

Lecture Notes in Mechanical Engineering

PSR Srinivasa Sastry

Jiji C. V.

D. V. A. Raghavamurthy

Samba Siva Rao *Editors*

Advances in Small Satellite Technologies

Proceedings of 1st International
Conference on Small Satellites

 Springer

Lecture Notes in Mechanical Engineering

Lecture Notes in Mechanical Engineering (LNME) publishes the latest developments in Mechanical Engineering—quickly, informally and with high quality. Original research reported in proceedings and post-proceedings represents the core of LNME. Volumes published in LNME embrace all aspects, subfields and new challenges of mechanical engineering. Topics in the series include:

- Engineering Design
- Machinery and Machine Elements
- Mechanical Structures and Stress Analysis
- Automotive Engineering
- Engine Technology
- Aerospace Technology and Astronautics
- Nanotechnology and Microengineering
- Control, Robotics, Mechatronics
- MEMS
- Theoretical and Applied Mechanics
- Dynamical Systems, Control
- Fluid Mechanics
- Engineering Thermodynamics, Heat and Mass Transfer
- Manufacturing
- Precision Engineering, Instrumentation, Measurement
- Materials Engineering
- Tribology and Surface Technology

To submit a proposal or request further information, please contact the Springer Editor in your country:

China: Li Shen at li.shen@springer.com

India: Priya Vyas at priya.vyas@springer.com

Rest of Asia, Australia, New Zealand: Swati Meherishi at swati.meherishi@springer.com

All other countries: Dr. Leontina Di Cecco at Leontina.dicecco@springer.com

To submit a proposal for a monograph, please check our Springer Tracts in Mechanical Engineering at <http://www.springer.com/series/11693> or contact Leontina.dicecco@springer.com

Indexed by SCOPUS. The books of the series are submitted for indexing to Web of Science.

More information about this series at <http://www.springer.com/series/11236>

PSR Srinivasa Sastry · Jiji C. V. ·
D. V. A. Raghavamurthy · Samba Siva Rao
Editors

Advances in Small Satellite Technologies

Proceedings of 1st International Conference
on Small Satellites

 Springer

Editors

PSR Srinivasa Sastry
Directorate of Space Systems
and Technologies
Hyderabad, Telangana, India

D. V. A. Raghavamurthy
Veltech University
Chennai, Tamil Nadu, India

Jiji C. V.
Department of Electronics
and Communication
College of Engineering
Trivandrum, Kerala, India

Samba Siva Rao
PES University
Bengaluru, Karnataka, India

ISSN 2195-4356

ISSN 2195-4364 (electronic)

Lecture Notes in Mechanical Engineering

ISBN 978-981-15-1723-5

ISBN 978-981-15-1724-2 (eBook)

<https://doi.org/10.1007/978-981-15-1724-2>

© Springer Nature Singapore Pte Ltd. 2020, corrected publication 2021

This work is subject to copyright. All rights are reserved by the Publisher, whether the whole or part of the material is concerned, specifically the rights of translation, reprinting, reuse of illustrations, recitation, broadcasting, reproduction on microfilms or in any other physical way, and transmission or information storage and retrieval, electronic adaptation, computer software, or by similar or dissimilar methodology now known or hereafter developed.

The use of general descriptive names, registered names, trademarks, service marks, etc. in this publication does not imply, even in the absence of a specific statement, that such names are exempt from the relevant protective laws and regulations and therefore free for general use.

The publisher, the authors and the editors are safe to assume that the advice and information in this book are believed to be true and accurate at the date of publication. Neither the publisher nor the authors or the editors give a warranty, expressed or implied, with respect to the material contained herein or for any errors or omissions that may have been made. The publisher remains neutral with regard to jurisdictional claims in published maps and institutional affiliations.

This Springer imprint is published by the registered company Springer Nature Singapore Pte Ltd. The registered company address is: 152 Beach Road, #21-01/04 Gateway East, Singapore 189721, Singapore

Preface

The International Conference on Small Satellites (ICSS-2019) is organized by the Society for Small Satellites and Systems (SSSS) and the Sensors Research Society (SRS). Recent advances in technologies related to small satellites and miniaturized sensors brought SSSS and SRS together organizing ICSS-2019 at Research Center Imarat (RCI). The efforts and steadfastness of the ICSS organizing team must be appreciated who made sure that this event is held on time and flawlessly.

Small satellites are playing an important role in space applications. They are faster to build, cost-effective, and better packaged due to the use of latest technologies. Small satellite platforms can be adapted for optical IR, thermal, and radar imaging (micro-SAR) remote sensing with good resolutions. This conference will provide a common platform for professionals from industries, industry, and universities to bring out their novel ideas and research and development work related to small satellites.

This conference came at the right time and aimed at bringing various stakeholders from academia, research institutions, and industry onto a common platform to share, discuss, and deliberate the critical issues in the related technologies and future trends. This conference was enriched with keynote addresses and invited talks by eminent persons from various countries and a large number of contributory papers. To benefit the students and young researchers, a satellite design workshop was organized with focused talks.

The proceedings of ICSS-2019 consists of full manuscripts accepted from scientists, academicians, researchers, and students worldwide. The theme of the conference is small satellites, big constellation. The papers are grouped in seven technical sessions, namely orbit and attitude control and dynamics; payloads and applications; power systems; small satellite system engineering and production; satellite constellations, mission design; and space robotics and mechanical engineering. A total of 121 papers were reviewed by specialists from different fields, and among them, 49 papers are selected for publication in the proceedings with rich content, clear focus, and high academic level. The acceptance rate was 44%, implying that only the quality papers were accepted. Plagiarism detection software Turnitin was used to scan each research paper. The proceedings had excellent

practical and promotional value, and we hope it would provide reference and help to all officials and scientific and technical personnel at different levels in the field of design and development of small satellites. This conference had created a platform for all to further the research, development, and operation of small satellites benefiting the society at large.

Thanks are due to the contributing authors and co-authors for their valuable submissions. However, the editors are not responsible for any statement made or any opinion expressed by the authors. All the queries should be directed to the respective authors. The papers were received with the presumption of being original work of the authors, not submitted elsewhere. The submissions were received after disseminating the Springer policies and procedures on paper submissions and copyrights. The editors have tried their best to accomplish their jobs within the narrow time frame; therefore, errors, if any, may genially be absolved.

Hyderabad, India
Chennai, India
Bengaluru, India
Trivandrum, India

PSR Srinivasa Sastry
Dr. D. V. A. Raghavamurthy
Dr. Samba Siva Rao
Dr. Jiji C. V.

Contents

Miniature Sensors for Space

44 Channels Multi-sensors Interface CMOS IC for Telemetry Application	3
Pradeep Kumar Dixena, Ashish Ranjan Prasad, Divya Kumar Garg, Amitesh Tripathi, Sushant Gaurav, P. Veeranna and P. Gangadhara	

Study of Concurrent Piezo Actuation and Sensing on Drift Stability of CVGs	13
Nisha S. Dathan, G. S. Anish, K. Usha and S. Paul Pandian	

A Quantitative Comparator of Heuristic Methods for Optimal Route in Hilly Terrain	23
Sudhir Porwal and Sangeeta Khare	

Orbit and Attitude Control and Dynamics

Simulation of the Dynamics and Control of Tethered Small Satellite Deployment	33
G. R. Sangeetha and Harikumar Ganesan	

Design and Development of Mass Optimised Latching Solenoid Valve for Chandrayaan-2 Lander Propulsion	41
Venkata Sunil Sai Nukala, Subrata Chakrabarti, D. Venkittaraman and M. Radhakrishnan	

De-Tumbling Controller of NIUSAT: Design, Simulation and On-Orbit Performance	49
F. Aaron Raphael Raja, Vivek Diwan and K. Samuel	

The Configurable Attitude Sensor and Actuator Simulation in the RSAT Test System	57
M. Roshini, Vishal Rao and M. Mahendra Nayak	

Optimal Nonlinear Dynamic Inversion-Based Flight Control System Design for an Aerospace Vehicle	65
R. Laxman, Arnab Maity, G. Mallikarjun Rao and R. Kranthi Kumar	
Closed-Loop Simulation for Attitude Control of Nano-satellite	87
Riya, Sanket Chirame, Anant A. Joshi, Ram Milan Kumar Verma, Sumit Agrawal, Ravit Anand, Shrita Singh, Sanskriti Bhansali, Piyush Jirwankar and Niket Parikh	
Real-Time Autonomous Navigation Scheme for Pointing Small Data Relay Satellite to LEO Using NavIC and GNSS Measurements	99
Monica Dantuluri, Ishita Ganjoo and Vinod Kumar	
Mission and Control Configuration for Spin to Three-Axis Stabilization for Small Satellite	115
A. L. Satheesha, S. Kannan and M. P. Ramachandran	
Slew Rate and Control Constrained Spacecraft Attitude Maneuver with Reaction Wheel Failure	119
Anuradha Sahu, Arun Kumar Mahodaya and Shreesha Chokkadi	
Payloads and Applications	
Novel Seed Point Selection Technique for Dual-Pol SAR Images	135
Manish Pratap Singh, Sanjay and A. Mishra	
SAR Payload Remote Sensing Satellite Mission Analysis for Global Coverage	145
Devi Prasad Panda, Kalpana Bandi and PSR Srinivasa Sastry	
Detection of Camouflaged Targets in Hyperspectral Images	155
Asheesh Kumar Gautam, Phool Preet, T. S. Rawat, Pinaki Roy Chowdhury and L. K. Sinha	
Spectroscopic Imaging of Nebular Gas: CubeSat-Based Spectrograph to Explore Nebular Astrophysics Through Imaging Spectrometry	163
C. Shanti Prabha, B. G. Nair, Ambily Suresh, Margarita Safonova, K. Nirmal and Jayant Murthy	
Visible and Near-Infrared (VNIR) Hyperspectral Payload Electronics	175
Hem Shikha and A. K. Sahay	
Design of Hyperspectral Imaging Sensor for Small Satellite in LEO	187
Vinay Kumar, A. K. Sahay and H. P. S. Panwar	

Opto-Mechanical Design of Short Wave Infrared Camera for Small Satellite 193
 Bharat Ram Meena, Shekhar Tomar, A. K. Sahay and H. P. S. Panwar

Absolute Radiometric Calibration of VNIR Hyperspectral Imaging Payload 201
 Maneesh Pawar, H. P. S. Panwar and A. K. Sahay

Design of Primary Mirror Mount for Spaceborne EO Payload 207
 Shekhar Tomar and Bharat Ram Meena

Weight Optimization of Primary Mirror Used in EO Payload for Small Satellite 215
 Shekhar Tomar and Bharat Ram Meena

Real-Time Embedded Software for Stabilized Electro-Optical System 221
 Ram Saran, Shashi Singh, Avnish Kumar and Rajeiv Marathe

Development of THz Photometer for Solar Flare Observation from Nanosatellite Platform 227
 S. P. Karanth, M. A. Sumesh, M. Dilip Yadav, H. R. N. Murthy, A. Edward Raj, S. Somashekar, S. Bhaskar Raju, K. V. Sriram and A. S. Laxmiprasad

Integrated High Speed and High Capacity Base-Band Data Handling —Solid-State Recorder for Small Satellite Applications 237
 Saswata Maitra, S. Chandrakanth, R. M. K. Guptha, P. Neeraja, K. L. Raja Sekhar and T. Venkata Mani

A Novel Space-Based AIS Receiver Architecture for Maritime Surveillance 249
 D. Mallikarjuna Reddy and S. Anuradha

Power Systems

Overview of Space Grade Power Supply Modules for Satellite 257
 J. Nesh, Bhoopendra Kumar Singh, Vinod Chippalkatti and G. Chandrashekar

Grounding Schemes for Small Satellite Systems 273
 P. Srinivas, Kumar Rahasyam, N. Beebamma and PSR Srinivasa Sastry

High Energy and High-Power Lithium Polymer Cells for Space and Satellite Application 283
 S. Loganathan, C. Althaf and S. Noorulla Basha

Deep Learning-Based Automatic Micro-crack Inspection in Space-Grade Solar Cells	293
Sharvari Gundawar, Nitish Kumar, N. Raghu Meetei, Ganesan Krishna Priya, Suresh E. Puthanveetil and Muthusamy Sankaran	
Microsat: Solar Array Exposed Materials Protection from Atomic Oxygen	309
K. H. Sucheta, B. R. Uma and R. NukaRaju	
Quality and Reliability	
Quality Assessment Techniques for Small Satellite Images	319
V. S. Biju, K. Balan, S. Sathiamurthi and K. S. Mani	
RETRACTED CHAPTER: Usage of COTS/EEE Parts in Space Applications—An Overview	327
H. V. Harish	
Remote Sensing, Deep Space Exploration	
Image Fusion Techniques for Spatial Resolution Enhancement of AWiFS Sensor Data	339
K. S. R. Radhika, C. V. Rao and V. Kamakshi Prasad	
Optimal Multiple Finite Burn Strategies for Trans-lunar and Trans-planetary Manoeuvres	347
Garima Aggarwal and R. V. Ramanan	
RF	
RF Signal Conditioning Module for Digital Receiver	365
Ranjit Kumar Dora, N. Veena, E. Vasanth, S. S. Rana and Vinod Chippalkatti	
Investigation of Beam Switching Phased Array Concept in Multi-layer Graphene-Based Active Antenna Setup for Small Satellite Applications	375
D. V. A. Ragavamoorthy and Prasanna Ram	
Satellite Constellations, Mission Design	
Satellite Constellation Design Studies for Missile Early Warning	385
Devi Prasad Panda, Kalpana Bandi, PSR Srinivasa Sastry and K. Rambabu	

Continuous Coverage of Fixed Location on Earth by LEO Satellite Constellation 397
 A. Vairavan and Rukmini Banda

Small Satellite System Engineering and Production

Design, Development and Validation of Fault-Tolerant Processor and Integrated Development Environment for Space and Defence Applications: Indigenous Initiative 413
 P. Balasubramanian, B. Kusuma Kumari, S. Kalyan Kumar, Anil N. Terkar, Chnab Sankar, Sudhanshu Kumar, Vikram Singh Parihar, J. V. R. Sagar and C. Ramesh Reddy

On-Orbit Real-Time Avionics Package Identification Using Vision-Based Machine Learning Techniques 429
 B. S. Sajeendran and R. Durairaj

Quality Assurance Practices for Student Satellite Teams 439
 Yash Sanghvi, Anmol Sikka and Aniruddha Ravindra Ranade

Challenges in Design of Very High-Speed Data Acquisition System for High-Altitude Application 451
 M. S. P. Srikar, H. R. Naveen Kumar, S. Amruth Kumar, N. Veena, Vasanth, S. S. Rana, Vinod Chippalkatti, R. K. Niranjana and N. Sarada

Space Applications

Design of Indian Navigation Satellite System-Based Traffic Management for Entire City 463
 Shwetank and Shailendra C. Badwaik

Techno-Commercial Aspects of Space-Based Startups Ecosystem in India 475
 Hemant M. Jain and Yashesh P. Rana

Space Robotics and Mechanical

Thermal Investigation of Power Supply Module (QDR-PSM) for Space Application Using Numerical and Experimental Approach 493
 B. K. Sharath, Santosh Jotteppa, Shashank Dibbi, Vinod Chippalkatti, P. Rajendran and M. Uma Ravindra

Analytical Thermal Modeling of Deployed and Body Mount Solar Panel and Its Comparison with Numerical Approaches for Small Satellite 509
 G. Ramu and Prateek Nagvanshi

Design Approach to Antenna Deployment System for Nano-Satellite Applications 523
Aditya Patki, Karan Jagdale and Mrigi Munjal

Satellite Structure of Advitiy (Second Student Satellite of IIT Bombay) 535
Hemil Kothari, Pushkar Lohiya, Abu Zubair and Shreeya Singh

Retraction Note to: Usage of COTS/EEE Parts in Space Applications—An Overview C1
H. V. Harish

About the Editors

PSR Srinivasa Sastry is the Project Director for the first LEO Satellite of Defence Research and Development Organization. In RCI he has worked for the development of hydraulic and electro-mechanical actuation systems for AGNI, A1 to A5 and Interceptor Missiles AD, and designed and developed several electro-hydraulic and electro-mechanical actuators, analog and digital controllers

Jiji C. V. is a Professor in the Department of Electronics and Communication, College of Engineering Trivandrum (CET), where his research focuses on computer vision, image processing, computational photography and signal processing. He has done his M. Tech and PhD from Indian Institute of Technology Bombay. He is also a visiting researcher in the University of Trento, Italy.

D. V. A. Raghavamurthy is a the Director of Aerospace Research in Veltech University. He joined ISRO as a Systems Engineer after his M.Sc.(Tech) from REC Warangal, and worked on numerous satellite projects, including Bhaskara-II, TES, and IRS satellites. He was Project Director of Cartosat-1, IMS-1, YouthSat, SARAL and first Project Director of Chandrayaan 2. He had also been involved in small satellite projects till 2013, when he became the Director of the Earth Observations System in ISRO Head Quarters and was responsible for Earth observing satellites, missions and applications till his retirement in 2016.

Samba Siva Rao is a Professor in the Electrical and Communications Engineering Department in PES University and the Director of the Crucible of Research & Innovation (CORI), Bangalore. An engineering graduate from College of Engineering, Kakinada, (Andhra University), he obtained his Ph.D from BITS, Pilani, and was associated with ISRO in various capacities for 37 years, till his retirement as Deputy Director from ISRO Satellite Centre in June 2011. In ISRO he was responsible for the development of high bit rate data transmitters for all IRS series of satellites and various RF and microwave systems in S, C, X, Ku and Ka bands for IRS and INSAT missions, and was also associated with the planning of communication satellites and development of associated technologies.

Miniature Sensors for Space

44 Channels Multi-sensors Interface CMOS IC for Telemetry Application



Pradeep Kumar Dixena, Ashish Ranjan Prasad, Divya Kumar Garg, Amitesh Tripathi, Sushant Gaurav, P. Veeranna and P. Gangadhara

Abstract In the telemetry system, multiple types of sensors are used for monitoring the physical and structural parameters of a system. These parameters are helpful for understanding the behavior of the system and to improve the performance of the system. Telemetry system integrates all the signal conditioning circuits for different types of sensors and provides digital data in the form of serial interface. To provide a compact and energy-efficient solution for telemetry, a 44 channels multi-sensors interface is implemented in single CMOS IC. In telemetry system, different types of sensors have been used which provide an output voltage in range of micro volt to 10 V. Each sensor has different noise, bandwidth and filtering requirement. This sensor interface chip (SIC) provides an integrated solution for different types of sensors used in the telemetry system. SIC used advanced circuit techniques to achieve better sensitivity and accuracy and also used the combination of high-voltage and low-voltage breakdown transistors for high level of integration. SIC has been designed and fabricated using 180 nm CMOS technology. Die area for this chip is 8 mm x 8 mm, and the package area is 20 mm × 20 mm. This chip has been tested for 10-bit accuracy of all sensor channel interface. Total power consumption of this chip is 800 mW.

Keywords Sensor interface · Multi-sensors · Telemetry

1 Introduction

Sensor interface chip has been designed for telemetry application. Telemetry is the process by which an object's characteristics are measured, and the result is transmitted to a distant station where they are displayed, recorded and analyzed. Telemetry

P. K. Dixena (✉) · A. R. Prasad · D. K. Garg · A. Tripathi · S. Gaurav
ANURAG, DRDO, Hyderabad, India
e-mail: pradeep.kumar@anurag.drdo.in

P. Veeranna · P. Gangadhara
RCI, DRDO, Hyderabad, India

© Springer Nature Singapore Pte Ltd. 2020
PSR. S. Sastry et al. (eds.), *Advances in Small Satellite Technologies*,
Lecture Notes in Mechanical Engineering,
https://doi.org/10.1007/978-981-15-1724-2_1

data is of immense use in evaluating various subsystem performances, i.e. propulsion, control guidance, structure analysis and aerodynamics. The telemetry data is extensively used in detecting the failure or under performance of subsystem and help in incorporating the necessary change in the subsystem so that optimum performance is obtained. Most important part of the telemetry system is sensor and signal conditioning circuit which interfaces physical signal to electrical signal and provides information about health of the complete system.

Sensor interface IC is targeted to integrate signal conditioning and sensor excitation circuits of ten different types of sensors used in telemetry along with multiple numbers of channels. This chip has been designed to reduce the number of discrete components and PCB boards in on-board subsystem, which will also reduce the number of cables, wiring lengths, size and weight along with energy consumption. Since the number of component reduces, it increases the reliability of the telemetry subsystem and also reduces the cost. It will also standardize and provide programmability to the telemetry system. The sensors' outputs are converted into digital serial data and made available on a standard serial SPI bus.

The SIC is implemented with a number of optimized high-performance front-end circuit for various types of sensors. The SIC samples the sensor signals and converts them into digital signal using in-built analog to digital converter. To realize a low-cost chip and low-cost IC technology, CMOS technology has been used. To overcome the drawbacks of the CMOS technology and obtain high performance, in the SIC design many advanced techniques and concepts [1–3], such as auto-calibration for offset and gain errors, chopping, low noise circuit implementation, temperature-independent bias and current generation, high-speed multiplexing and ADC, digital FIR filtering are used. To provide high-voltage constant current excitation and over-voltage protection high-voltage CMOS cell, resistors and diodes have been used which can stand up to 60 V.

2 General Description

Sensor interface chip (SIC) incorporates signal conditioning and excitation circuits for different kinds of sensors. Main requirement of signal conditioning circuit is to provide enough gain and filtering for further signal processing. Signal conditioning circuit should be designed such that it should introduce very low circuit noise to the desired sensor signal. Another requirement of signal conditioning block is to provide variable gain so it can support various sensor signal output ranges and provide DC voltage programming such that it can compensate various types of DC offset generated due to wire length and mismatch of components.

The sensor interface chip (SIC) is a mixed signal CMOS IC which integrates analog front end for sensor interface along with analog to digital converter and digital filtering. SIC converts sensing element signals into a serial digital output. These signals are in Serial Peripheral Interface (SPI) format which can easily read

by FPGA, DSP or microcontroller for further signal processing and recording. The SIC provide interfaces for:

- Resistance temperature detector (RTD) type PT100 for temperature range of -100 to 600 °C
- Thermocouple Sensor type-C for temperature range of -100 to 3000 °C
- Strain sensor, bridge type with resistance change of 350 ± 0.7 , 350 ± 1.4 , 350 ± 2.8 and 350 ± 5.6 Ω
- Pressure sensor, with signal output of $0-5$ and ± 2.5 V
- Acceleration sensor, bridge type with voltage range 7.5 V ± 150 mV
- Vibration and shock sensor, IEPE type with voltage output range 12 ± 5 V
- Acoustic sensor, IEPE type with voltage output range 12 ± 8 V
- Electrical signal sensing, single ended with output range ± 10 V
- Electrical signal sensing differential ended with output range $0-20$, $0-40$ and $0-80$ V.

3 System Level Implementation

Figure 1 shows the functional block diagram of the sensor interface chip. Sensor interface chip (SIC) integrates signal conditioning, excitation of above-mentioned sensors and output of signal conditioning circuits for all sensor channels are multiplexed and converted into a digital data by on-chip analog to digital converter (12-bit ADC), and converted digital data after filtering is made available serially on a standard Serial Peripheral Interface (SPI) bus.

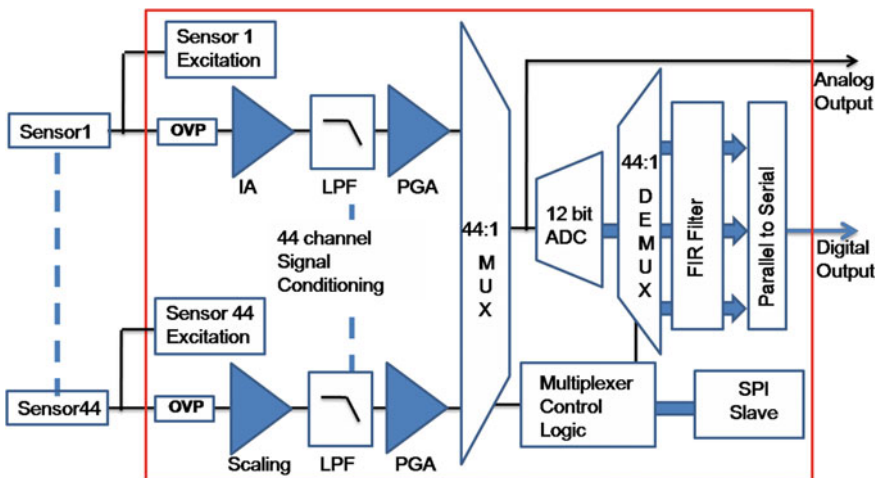


Fig. 1 Sensor interface chip block diagram

The basic building block of SIC is three op-amp-based instrumentation amplifier [4], which provides very high common mode noise rejection, analog low-pass filter used for high-frequency noise rejection and anti-aliasing filtering for ADC and programmable gain amplifier to adjust the signal gain and signal swing and match to ADC input swing. For some sensors, voltage swing is higher compared to supply voltage [5]. To accommodate higher voltage swing, the resistive divider scaling circuit has been used. This scaling circuit has been designed in such a way that it makes sure that input voltage of CMOS op-amp should not cross supply voltage.

High-frequency analog multiplexer has been used to sample the sensing signal. Multiplexer control signal is provided by state machine, and multiplexing scheme is optimized in such a way that it can accommodate very high and very low-frequency sensing signal in moderate rate. Signal-to-noise ratio of each signal conditioning circuit is maintained to get accuracy of 10-bit full-scale swing. Output of multiplexer is connected to high sampling 12-bit pipeline ADC. After ADC, digital de-multiplexer has been used to separate different sensor digital output. De-multiplexer is also controlled by same state machine to ensure synchronization between analog multiplexing and digital de-multiplexing. After de-multiplexing, sensor digital data is passed parallel through cascaded integrated comb (CIC) structure and digital finite impulse response (FIR) low-pass filter [6]. CIC filter down samples the ADC data and brings down the sampling rate of sensor bandwidth, and FIR filter provides desired low cut-off frequency and sampling rate of each sensor channel. Output of FIR filter is stored in SPI register and can be read by providing the SPI address data for defined sensor channel.

4 Block Level Implementation

This chip incorporates from very low-voltage sensing (in the range of micro volts) to very high-voltage sensing (in the range of 24 V) requirements. For very low-voltage sensing, noise is the most important aspect to design signal conditioning circuit, whereas for high-voltage sensing circuit, linearity as well as circuit breakdown is an important aspect. Different type of sensor requires different type of excitation, which is in the form of either constant current or constant voltage. The SIC chip provides the current/voltage excitation with programmable fine-tuning.

4.1 *Interface Circuit for Sensor Output Voltage Less Than Supply Voltage*

RTD, strain and thermocouple are examples of such type of sensors. This type of sensor output voltage is less than supply voltage and voltage swing vary from μV to mV only. Signal conditioning circuit of this type sensor should provide very high gain

along with very low noise to maintain desired SNR. CMOS technology has problem of flicker noise, which causes very high noise density at lower frequency. Most of the sensors are having very low-frequency response which falls in the range of device flicker noise. This type of sensor signal frequency is in the range of 10–20 Hz. To provide better sensitivity, CMOS op-amp should be designed in such a way that it provides very low flicker noise [7] and satisfies the 10-bit SNR requirement.

Figure 2 shows the block diagram of two-wire RTD sensor interface circuit. RTD sensor provides sensing of temperature in terms of resistance. For the temperature range of -100 to $+600$ °C, the resistance of PT100 RTD sensor changes from 60 to 320 Ω . To measure this change, a constant current of 1 mA has been flown through RTD sensor, which provides differential voltage change of 260 mV. This constant current has been generated using cascoded current mirror, and to provide constant reference DC bias, a feedback amplifier has been used.

Front end of RTD sensor composes of three op-amp-based instrumentation amplifier along with over-voltage protection (OVP) circuit. Instrumentation amplifier along with programmable gain amplifier provides the gain in the range of 2 V/260 mV, so full ADC swing can be achieved. After the instrumentation amplifier, analog low-pass filter (LPF) with cut-off frequency of 1 K has been used to filter high-frequency noise and anti-aliasing filter for ADC. Since sensor signal bandwidth is 10–20 Hz, 1 K LPF has been implemented to save silicon area. Lower frequency requires much higher passive component which occupies very large area. To achieve sensor signal bandwidth, very low cut-off frequency in range of 10–20 Hz digital FIR filter has been used after ADC. After LPF, programmable gain amplifier has been used to provide variable signal swing and gain. For RTD sensor signal conditioning chain, multiplexer sampling rate is 4 K, four times of LPF cut-off frequency. After analog to digital conversion and digital de-multiplexing and filtering, output of RTD sensor signal is stored in SPI register. RTD sensor signal conditioning chain also consists of a 8-bit digital to analog converter to provide DC offset correction which can be easily controlled by SPI configuration.

Figure 3 shows the detailed front-end circuit for RTD sensor interface. In all modes, the design target of the whole system is better than 10-bits. Similar architecture has been used for thermocouple and strain sensor signal conditioning circuit.

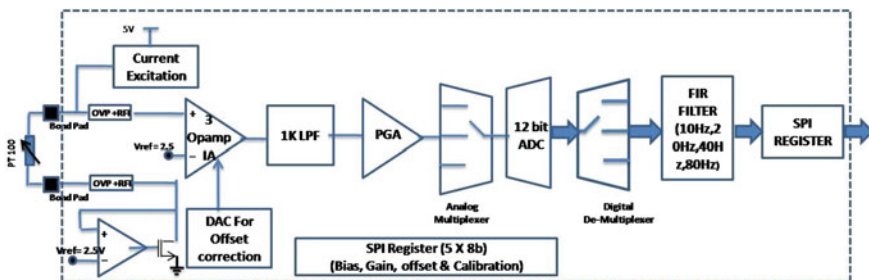


Fig. 2 Block diagram of two-wire RTD sensor interface circuit

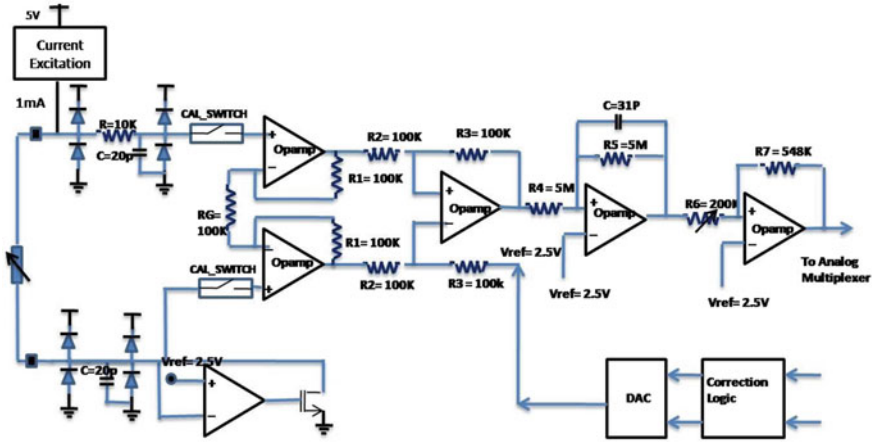


Fig. 3 Detailed front-end circuit for RTD sensor interface

The only difference is signal conditioning gain and excitation circuits. Thermocouple sensor only requires DC biasing, whereas strain sensor requires a low drop out (LDO) voltage regulator and bridge network for input voltage.

4.2 Interface Circuit for Sensor Output Voltage More Than Supply Voltage

Vibration, shock and acoustic sensor are of Integrated Electronics Piezo-Electric (IEPE) type, and voltage output of these sensors is in the range of 12 V DC voltage and voltage swing of ± 5 V. Electrical signal measurement is also a type of high-voltage measurement.

Figure 4 shows the block diagram of IEPE vibration sensor interface circuit. IEPE sensor requires excitation of 4 mA constant current from 24 V DC supply voltage.

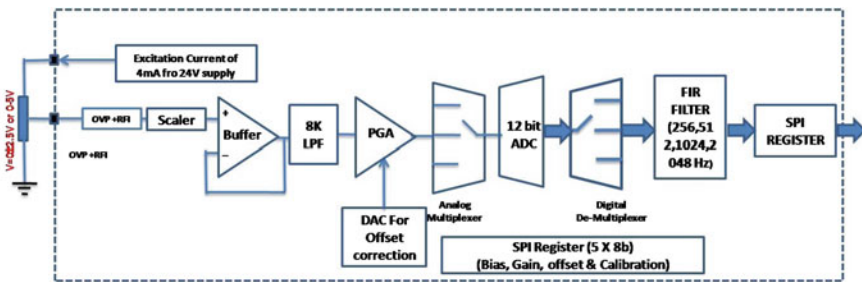
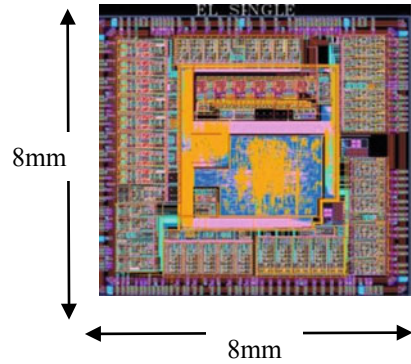


Fig. 4 Block diagram of IEPE vibration sensor interface circuit

Fig. 5 Layout of the fabricated SIC chip



This excitation circuit has been designed using high breakdown LDMOS transistor so it can withstand higher-voltage swing. Scaling network has been used as front end for this type of sensors. Scalar network has been designed using high-voltage breakdown resistor and diode. Scaling network makes sure that the input to the CMOS buffer is less than the normal supply voltage (5 V). Scalar and buffer circuits have been designed, i.e. sizing of scaling resistor and sizing of buffer transistor such that it has maintained required SNR of 10-bit. After buffer, second-order analog low-pass filter and programmable gain amplifier have been used. In the design, a digital to analog converter (DAC) output has been fed to PGA for DC offset correction and to provide DC bias shift to the input signal. For this sensor multiplexer, the sampling and ADC sampling are at 32 kHz, which is four times of LPF frequency. Desired sensor bandwidth is maintained using digital FIR filter.

5 SIC Chip Implementation

The SIC chip has been implemented using a 180 nm analog CMOS process with power management option, and the whole chip area is around 64 mm² (8 mm × 8 mm). All the analog blocks are fully custom designed and layout. There are also digital parts for digital FIR filtering and control and serial communication with the FPGA/DSP/MCU. Figure 5 shows the layouts of the fabricated SIC chip.

6 Test Set-Up and Experiment Results

The SIC chip has been tested for its functionality using the evaluation board and standard measurement system. Figure 6 shows the test set-up for RTD sensor interface circuit. Standard variable resistor simulator has been used to mimic the RTD sensor resistance change due to temperature.

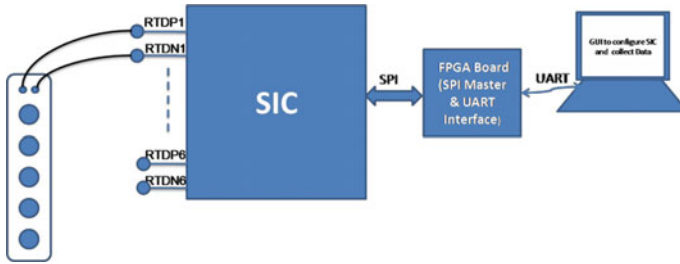


Fig. 6 Test set-up for RTD sensor signal conditioning chain

From RTD datasheet [8] for different temperature, corresponding resistance has been chosen and applied as the input of RTD signal conditioning circuit, and corresponding ADC output has been recorded. Table 1 shows the ADC output of RTD channel in decimal format for ADC output range of ± 512 . Figure 7 shows the pictorial plot of measured data.

Figure 8 shows the test set-up for vibration sensor (IEPE) interface circuit. IEPE sensor simulator has been used to mimic the vibration sensor output voltage. Table 2

Table 1 ADC output of RTD sensor channels

S. No.	Temp.	Res.	RTD1	RTD2	RTD3	RTD4	RTD5	RTD6
1	-100	60.25	-481	-480	-478	-478	-484	-480
2	0	100	-338	-335	-336	-336	-340	-337
3	100	138.5	-200	-198	-198	-198	-201	-200
4	200	175.8	-66	-65	-64	-65	-66	-66
5	300	212	64	65	65	65	66	65
6	400	247	190	189	191	191	193	191
7	500	280.9	312	310	313	312	316	312
8	600	313.6	429	427	430	428	435	430

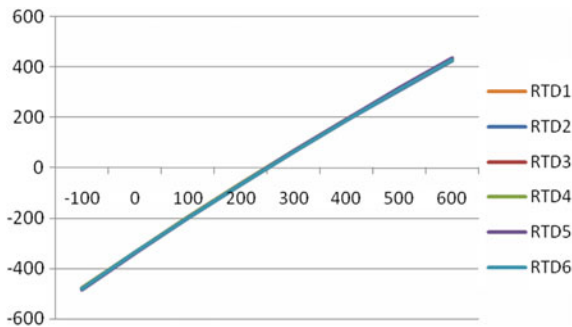


Fig. 7 RTD sensor channels measurement result

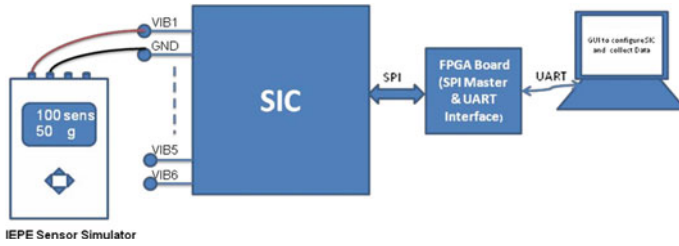


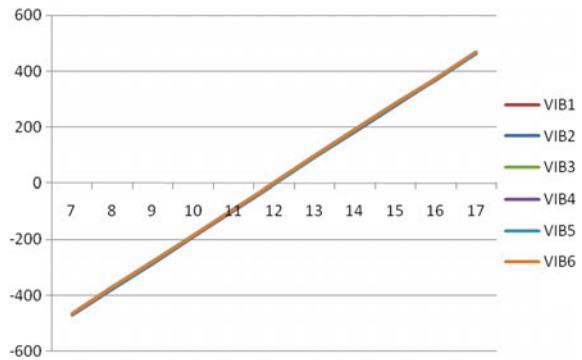
Fig. 8 Test set-up for vibration sensor signal conditioning chain

Table 2 ADC output of vibration sensor channels

S. No.	Input (V)	VIB1	VIB2	VIB3	VIB4	VIB5	VIB6
1	7	-468	-466	-466	-470	-468	-465
2	8	-375	-374	-373	-377	-375	-371
3	9	-282	-279	-280	-285	-283	-279
4	10	-188	-187	-187	-190	-188	-186
5	11	-96	-94	-92	-96	-94	-91
6	12	-2	-3	-2	-4	-3	3
7	13	92	92	94	91	90	97
8	14	185	187	188	183	185	191
9	15	277	280	279	277	278	284
10	16	371	371	374	370	371	375
11	17	464	465	467	463	463	469

shows the ADC output, and Fig. 9 shows the pictorial plot for all vibration sensor channel ADC outputs.

Fig. 9 Vibration sensor channels measurement result



A full set of measurement carried out at the moment of this paper is submitted, and all of the measurement modes have been tested carefully and verified. The overall speed and accuracy have been checked over the design target.

7 Conclusions

In this paper, a 44 channel sensor interface chip has been presented. As compared to an existing interface, the SIC offers a large variety and number of sensor channel integration compared to existing sensor interface ICs. Moreover, in the SIC, an optimized multiplexing scheme has been incorporated which takes care of the different bandwidth requirements of different variety of sensors. It also provides a standard Serial Peripheral Interface (SPI) bus for reading sensor data in serial digital form at higher speeds, which can be easily integrated with any other digital system. This chip uses advanced techniques and concepts, including auto-calibration, chopping technique, low noise circuit design and dynamic sampling. A prototype has been built and tested. A resolution and linearity of 10-bits have been achieved in a measurement. Chip size after packaging is only 20 mm × 20 mm, and it consumes power only 800 mW from 5 V supply. The SIC chip is very suitable to be realizing an integrated compact and miniaturized, low power and high-performance telemetry system, which can be used in avionics applications.

References

1. Rajavi B (2002) Design of analog CMOS integrated circuits. Tata McGraw-Hill, New Delhi
2. Carusone TC, Johns D, Martin K (2013) Analog integrated circuit design. Wiley, New York
3. van der Goes F, Meijer GCM (1997) A universal transducer interface for capacitive and resistive sensor elements. *Analog Integr Circuit Signal Process* 14(3):249–260
4. MT-063 tutorial. Basic three OPAMP in-amp configuration. Analog devices
5. Vetelino J, Reghu A (2013) Introduction to sensors. CRC Press, New York
6. Mehta K, Vinitha CS, Tulsani H (2104) A novel class of selective Cascaded Comb (CIC) FIR filters with passband compensation. In: 2014 IEEE international symposium on signal processing and information technology, Noida, 2104, pp 13–18
7. Kiely R (2017) Understanding and eliminating 1/f noise. *Analog Devices*
8. Technical information data bulletin. Platinum 100 Ohm (Pt 100) α 0.00385, temperature v/s resistance table. www.tnp-instruments.com

Study of Concurrent Piezo Actuation and Sensing on Drift Stability of CVGs



Nisha S. Dathan, G. S. Anish, K. Usha and S. Paul Pandian

Abstract Vibratory gyroscopes with piezoelectric transducers have found substantial number of applications where low drift rate is easily achievable with low cost, low weight and high reliability. However, piezoelectric transducers are prone to aging effects that cannot be compensated and hence affect gyro drift and scale factor stability. In this paper, two methods of using same piezoelectric transducer element for actuation and sensing are designed and evaluated for improving gyro performance.

Keywords CVG · TFG · PZT · Concurrent drive and sense

1 Introduction

The inertia and stiffness introduced by a piezoelectric element and bonding epoxy can significantly contribute to the performance of a vibratory gyroscope. Small dispersions in thickness of piezoelectric element and/or bonding layer as well as its mechanical and electrical material properties can result in asymmetry in the resonator calling for tight component level tolerance and process control. Though this requirement is indispensable in piezoelectric resonators, contribution of piezo imperfections can be significantly reduced by going for single set of piezoelectric transducers for actuation and sensing. First method studied in the paper makes use of the inherent piezoelectric capacitance in parallel with piezoelectric element. The input voltage is applied simultaneously to the piezo element and a reference capacitance, which by

N. S. Dathan (✉) · G. S. Anish · K. Usha · S. Paul Pandian
ISRO Inertial Systems Unit, Vattiyookavu, Thiruvananthapuram, Kerala 695013, India
e-mail: nisha_dathan@vssc.gov.in

G. S. Anish
e-mail: anish_gs@vssc.gov.in

K. Usha
e-mail: k_usha@vssc.gov.in

S. Paul Pandian
e-mail: s_paul_pandian@vssc.gov.in

matching with the known piezoelectric capacitance can give out signal proportional to the strain rate [1]. The second method employs a time-multiplexed discontinuous excitation and sensing.

2 CVG Details

Coriolis Vibratory Gyro works on the principle of energy transfer from a driven mode to sense mode due to Coriolis force generation. The Coriolis force, F_c , is given by

$$F_c = 2mV\Omega \quad (1)$$

where m is the mass of the resonator, v is the driving velocity, and Ω is the angular velocity to be measured.

2.1 CVG Configuration

TFG used for the study is a four-tine configuration with high rate capability and high accuracy. The gyro has four control loops, viz. frequency control, vibration amplitude control loop, force feedback loop and quadrature control loop.

TFG is driven using a set of four piezoelectric ceramic plates for drive mode excitation. Another spatially displaced set of four piezos are used to take feedback for excitation amplitude control. Conventionally, these eight sets of piezos are used for frequency control and amplitude control of drive mode. Another set of eight orthogonal piezos are used for force feedback control and quadrature control. However, the gyro is configured for open-loop operation for this study to minimize the effects of control loop stiffness on the performance, i.e., of the eight orthogonal piezos, only four sets are used to take rate output in open loop. Though gyro bandwidth is limited, it has no bearing on the drift stability.

2.2 Piezoelectric Transducer Specification

Piezo material composition is lead zirconate titanate (PZT). Relative dielectric constant is 1750, mechanical quality Q_m is 75, piezoelectric strain coefficients d_{33} and d_{31} are 400×10^{-12} C/N and -170×10^{-12} C/N, respectively. The piezo dimensions are $2.5 \times 2 \times 0.2$ (mm) with tolerance of $+0.0/-0.05$ mm. PZT transducers are bonded using conductive epoxy.

3 Concurrent Sensing Techniques

In these techniques, the same piezo element is used for both actuation and sensing [5]. Two such techniques are discussed. The first one is based on drive and sense using a matched RC network, and the second one is based on time division multiplexing.

3.1 Concurrent Drive and Sense Using Matched RC Network

In the first method of concurrent sensing circuit, each piezo is simultaneously used as an actuator and sensor via a strain rate circuit [7]. The inherent piezoelectric capacitance in parallel to the piezoelectric transformer is matched to an equivalent capacitance, and differential readout is done. Piezo current is the sum total of current through the transformer and current through the inherent capacitance. This relation is implied in the sensor equation [1].

$$\theta^T \dot{r} = B_q i - C_p \dot{v} \tag{2}$$

where θ is the mechanical and electrical coupling factor, r is the displacement coordinate vector, B_q is the forcing function, C is the capacitance, and v is the voltage.

3.1.1 Design Details

An R-C-based matching network is designed for strain rate measurement for 1.7 nF capacitance of the drive piezo element. In Fig. 1, the V_1 and V_2 can be derived from

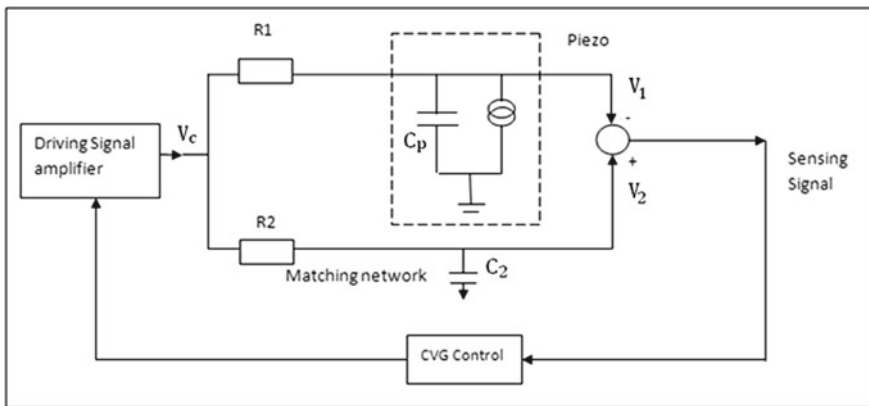


Fig. 1 Concurrent drive and sense using matched capacitance network

circuit theory in terms of the input voltage V_c and circuit parameters R_1 , R_2 , C_p and C_2 in the s domain [1]. Without losing generality, the strain rate signal of the piezoelectric element is determined by subtracting V_1 from V_2 .

$$V_1 = \frac{V_c - i_{\text{mech}} R_1}{s R_1 C_p + 1} \quad (3)$$

$$V_2 = \frac{V_c}{s R_2 C_2 + 1} \quad (4)$$

R_1 and R_2 are chosen 806Ω , and C_2 is chosen to be 1.7 nF , close to the value of drive capacitance of the piezo load. A potentiometer is used to match both time constants exactly to cancel out the driving voltage. An instrumentation amplifier is used as second stage which gives the sensed voltage which is proportional to the vibration rate.

3.2 Time-Multiplexed Switched Drive and Sense

The second method uses a time division multiplexing scheme [3, 6] to actuate the piezo and sense the output. The proposed scheme is shown in Fig. 2.

3.2.1 Design Details

The critical design parameters in this method include the multiplexing frequency, driving band, sensing band and guard band. These time periods should be chosen in optimum proportion to ensure proper functioning of the multiplexer circuit. If the actuation band is too high, it can reduce the time available for sensing the external

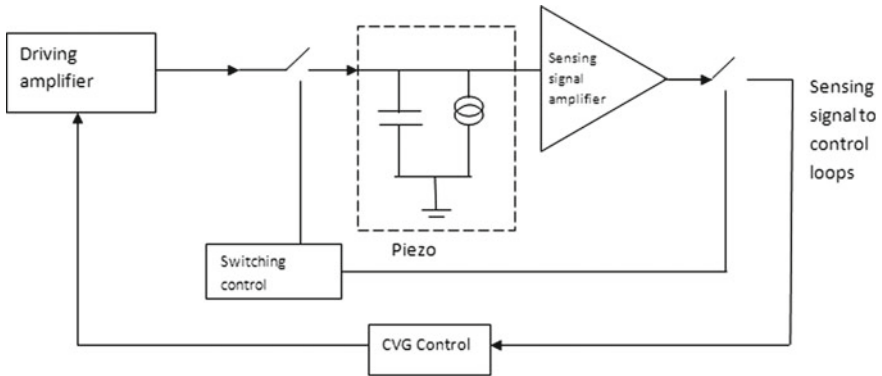
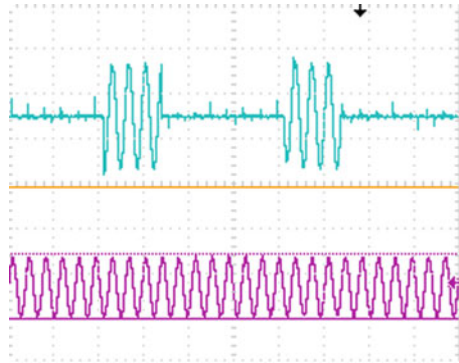


Fig. 2 Time-multiplexed switched drive and sense

Fig. 3 Waveforms for switched drive and direct feedback signal indicating minimal ripple



rate, while if actuation band is too low, the amplitude of the sensed signal will be too low. Similarly, if the guard band is too low, undesirable transition noise can affect the control loop. Moreover, a long no-actuation zone can result in Q -dependent decay of sense signal. For optimum actuation and minimizing the transition noises, for maximum multiplexing rate of 500 Hz, actuation time of 50% time period and sensing duration of 32% time period are used with a guard band of 18% of time period. Hi 201-based CMOS analog switches are used to implement the time division multiplexing scheme. Waveforms for a multiplexing frequency of 500 Hz for a TFG of frequency 5.423 kHz are shown in Fig. 3.

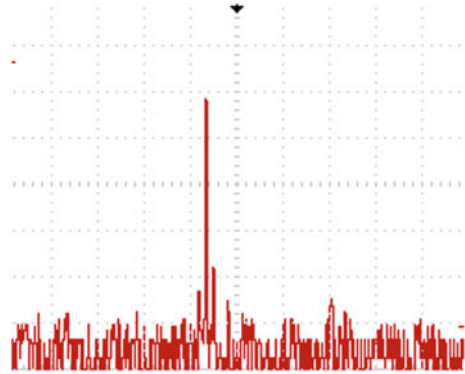
3.2.2 Effect of Multiplexing Frequency

The time-multiplexed frequency to too low value can result in dropping of TFG sense output due to lose of energy in the TFG whereas using too high multiplexing frequency will reduce the number of cycles of excitation obtained for sensing thus constraining sensor electronics. Further, the correlation of noise in the sensing circuit is seen to vary inversely as the multiplexing frequency decreases. Lower frequencies increase the ripple content in the sense signal due to decay of piezo amplitude during sensing phase. FFT of sense output shows side bands at switching frequency away from resonant frequency (Fig. 4). The ripple being Q dependent, the design is optimized for a multiplexing frequency range of 50–500 Hz for a TFG with $Q \approx 3300$.

3.2.3 Effect of Parasitic Capacitance of Analog Switch

Higher value of parasitic capacitance may interfere with sensing circuit as the observed sense signal using same piezo appears as a superimposed waveform on the actuation signal on account of parasitic capacitances. This varying bias can interfere with the control loop, and so, a bleeder resistance is used to discharge the parasitic

Fig. 4 FFT of direct feedback signal for 200 Hz multiplexing frequency



capacitances associated with analog switch. The resistance value if becomes too high will result in very slow discharge and if its value is too low can load the piezo thus reducing the magnitude of sensing output, and hence, it is optimally fixed.

4 Experimental Details

The study on drift stability was carried out in a tuning fork gyroscope with PZT transducers bonded using conductive epoxy. Q and frequency split was of the order of 3300 and 1.4 Hz, respectively. Open-loop frequency response of TFG was measured using conventional drive and sense piezos as well as with concurrent time-multiplexed switched drive and sense scheme. In conventional scheme, resonant frequency of the sense mode was seen to decrease as drive voltage increases. With switched drive, same drive voltage results in lower deflection due to restricted duty cycle. Hence, comparison was made on switched drive with conventional sensing and concurrent sensing. Resonant frequency behavior with respect to drive amplitude was seen to be similar for both cases (Fig. 5), i.e., resonant frequency variations with drive amplitude are not contributed by the sense piezo elements. Figure 6 indicates frequency response for different switching frequencies.

TFG is trimmed for frequency and amplitude control with conventional method using separate drive and sense piezo elements. PLL-based frequency loop is set for closed-loop operation at drive mode resonance of 5.423 kHz. Drive mode feedback amplitude is set for approximately 3 Vpp. With rate sensing in open loop, drift stability and temperature sensitivity are assessed. The mode of CVG operation configured for the experiment is shown in Fig. 7. Gyro scale factor is $80 \mu\text{V}/(^{\circ}/\text{s})$.

ADS1278-based data acquisition system is used to ensure high accuracy voltage readout, and quadrature phase encoder-based frequency analyzer with 25 MHz resolution is used for measuring frequency. Rate output voltage is acquired at 20 ms time intervals, whereas frequency is updated at 10 s time interval.

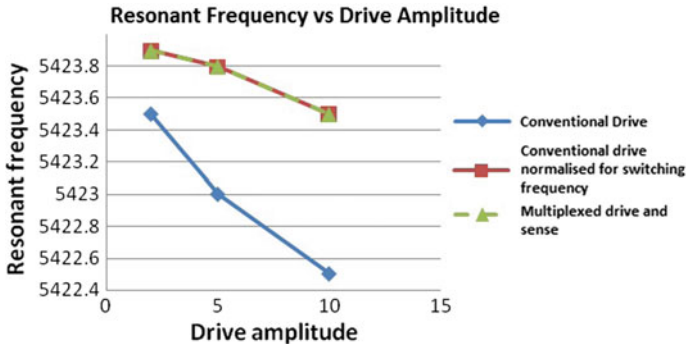


Fig. 5 Resonant frequency versus drive amplitude

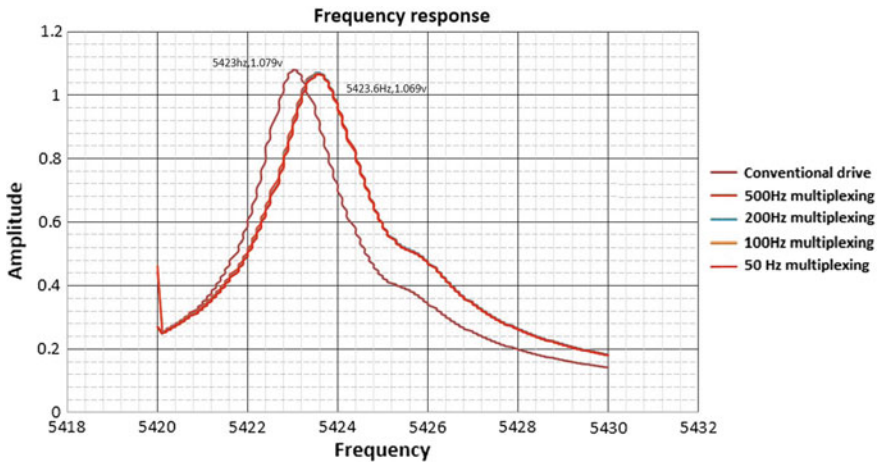


Fig. 6 Frequency response plot for different multiplexing frequencies

Time-multiplexed switched drive and sense circuit is interfaced to TFG. Multiplexing frequency is chosen as 500 Hz to keep sense signal ripple below 1%. To maintain same feedback amplitude and thereby same stiffness in the amplitude control loop, a gain of 3.3 is introduced in the switched concurrent sense output. With no loop trimming adjustments, drive mode feedback amplitude stabilized at 2.72 Vpp. However, drive mode excitation amplitude increased from 2.2 to 7 Vpp for 500 Hz multiplexing frequency. This is attributed to duty cycle limited drive amplitude. Frequency loop stabilized at 5.424 kHz with ± 10 Hz variation as observed in oscilloscope. Frequency analyzer measurement was with 10 s accumulation and hence could not measure the oscillatory behavior. However, presence of frequency variation was not seen to affect drift. Drift stability and temperature sensitivity were assessed in this condition.

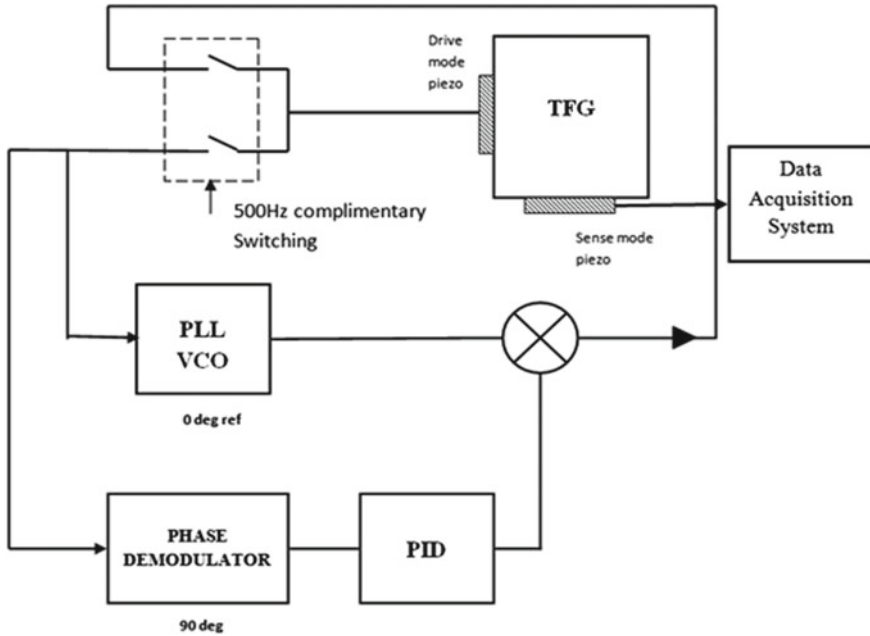


Fig. 7 TFG evaluation method

5 Results

Both methods discussed in the paper offer the advantage of using the same piezo for both actuation and sensing, thereby making truly collated control possible. They also eliminate the non linearity [4] and capacitive coupling problems associated with separate sensor and actuator piezos [2, 8]. However, these advantages come at the expense of reduced drive voltage. In the first method, an R-C-based matching network was designed for 1.7 nF capacitance of piezo element, and frequency response was evaluated. The second method was realized using analog switches for switching drive signal and sensing amplifier outputs.

5.1 Comparison of the Two Methods of Concurrent Sensing

The multiplexing method was found to be easier to configure and interface to the piezoelectric sensors. The multiplexing frequency has to be much larger than the bandwidth of the sensor to avoid any loss of bandwidth of the integrated system. The matched RC network-based concurrent sensing circuit on the other hand avoids this problem by sensing continuously over the entire time but gives time rate of strain as output and therefore requires modification of control loops. It also suffers from the

Table 1 Temperature sensitivity and amplitude control for conventional and concurrent drive

Parameter	Conventional mode	Concurrent drive and sense mode
Temperature sensitivity of rate bias (mV/°C)	11.4	2
Amplitude control requirement (V/°C)	0.57	1.43

problem of reduced sensing amplitude as the $R_1 C_1 \omega$ which is also the proportional constant is designed to be $\ll 1$ to keep the sensing output proportional to rate of strain, but this can be resolved by adding an extra amplifier stage. Also since the concurrent sensing circuit relies on time constant matching, careful trimming is essential.

5.2 Effect on Drift Stability

Since the introduction of second method of time-multiplexed concurrent sense required less modification in TFG loop dynamics, the method was adopted for evaluation of drift stability and thermal sensitivity.

The experiments were carried out in CVG open-loop mode with no quadrature control and no force feedback control. Results of the experiment are tabulated in Table 1.

Temperature sensitivity of bias improved from 11.4 to 2 mV/°C for a temperature range of 25–60 °C. Warm-up characteristics also improved. Drive mode amplitude control was seen to affect rate less. Frequency drift in conventional mode was 1 Hz, whereas this could not be correctly determined in the time switched scheme due to discontinuous pulses corrupting frequency estimation. More than five-fold difference in temperature sensitivity is attributed to the sense piezo characteristics. Similar improvement can be expected when quadrature control on orthogonal piezos is also done in concurrent drive and sense mode. Moreover, effect of spatially co-located orthogonal modes also benefits control loop stiffness.

Temperature-induced errors due to the temperature sensitivity of mechanical and electrical material properties of piezoelectric ceramics are significantly reduced by the proposed scheme. Based on obtained results, one-order improvement is expected on drift stability of the tuning fork gyroscope.

Acknowledgements We thank Smt. Jyothi Janardanan and Shri. Ajay P. Roy of ISRO Inertial Systems Unit, Vattiyoorkavu, Thiruvananthapuram, for their support in understanding characteristics of piezoelectric gyroscopes, their control requirements and trimming of control loops.

References

1. Yang SM, Chiu JS (1993) Dither-motor design with concurrent sensing and actuating piezoelectric materials. IOP 1994
2. Dosch JJ, Inman DJ, Garcia E (1992) A self sensing piezoelectric actuator for collated control. *J Intell Mater Syst Struct* 3:166
3. Lee J, Yun SW, Rhim J (2016) Design and verification of a digital controller for a 2-piece hemispherical resonator gyroscope. *Sensors* 16:555
4. Liu YY, Ozaki R, Morita T (2015) Investigation of nonlinearity in piezoelectric transducers. *Sensors Actuators A* 227:31–38
5. Simmers GE, Hodokins JR, Mascarenas DD, Park G, Sohn H (2004) Improved piezoelectric self-sensing actuation. *J Intell Mater Syst Struct* 15
6. Chew ZJ, Ruan T, Zhu M, Bafleur M, Dilhac J-M (2017) Single piezoelectric transducer as strain sensor and energy harvester using time-multiplexing operation. *IEEE Trans Ind Electron* 64(12):9646–9656
7. Ferris LS, Weitzner MA (1989) Velocity control system using piezoelectric transducers. US Patent 4,856,901
8. Anderson EH, Haeood NW, Goodiffe JM (1992) Self-sensing piezoelectric actuation: analysis and application to controlled structures. AIM-92-2465-CP

A Quantitative Comparator of Heuristic Methods for Optimal Route in Hilly Terrain



Sudhir Porwal and Sangeeta Khare

Abstract The computation of optimal route for various kinds of automatic or manned vehicles on hilly terrain is an important task in route planning applications. In the absence of a road network, the topography factors of the terrain (slope, elevation, etc.) and the climbing angle of the vehicle play an important role in the computation of the optimal route between two points. This kind of problem has been addressed in the artificial intelligence domain, and the graph search algorithms can be applied to find a solution. The A* algorithm and various versions of A* have been reported in the literature to achieve the faster results while maintaining the optimality criteria of the solution. The speed-up in all the versions of A* algorithms is achieved through the use of heuristic knowledge available in the problem domain. There may exist various heuristic functions that fulfil the admissibility criteria but produce different results as far as the speed and the optimality are concerned. This paper presents a performance measure for quantitative comparison of the various heuristics functions that can be used for optimal route selection in hilly terrain.

Keywords Search tree · Graph search · Optimal route · Heuristic methods · Terrain model

1 Introduction

The selection of the optimal route between two points has been a very popular problem for researchers from various domains like GIS, robotics, game programming. In most of the cases, the input is represented as connected graph $G = (V, E)$. The V represents a set of vertices (the various destination points), and the E represents the edges, i.e. each edge connects the two vertices. Every edge is also associated with some weight or cost that fixes the optimality criteria of the route selection. If the

S. Porwal (✉) · S. Khare
Defence Electronics Applications Laboratory, Dehradun 248001, India
e-mail: sudhir.porwal@deal.drdo.in

S. Khare
e-mail: sangeetakhare@deal.drdo.in

© Springer Nature Singapore Pte Ltd. 2020
PSR. S. Sastry et al. (eds.), *Advances in Small Satellite Technologies*,
Lecture Notes in Mechanical Engineering,
https://doi.org/10.1007/978-981-15-1724-2_3

length of the edge is used as the cost factor (more the length then more is the cost), the optimal route selection returns the shortest route possible between two points. The slope of the edge is also an important cost factor especially in cross-country movement where the road network is not present and the movement of vehicles is avoided on steep slopes to mitigate any possibility of accident or mishap. The computation of the optimal route over a given road network is somewhat faster as the size of the road network graph is not very large. A dense road network of a city may merely have few hundreds of vertices and few thousands of edges in the road network. It is much faster to produce the optimal solution for route selection in a smaller graph as the depth of the spanning tree during the graph search is not too high and the result can be produced in a faster manner. The cross-country route selection makes use of the digital geographic data of the terrain (e.g., digital elevation model), and the associated graph may have millions of vertices and edges. The graph search algorithms like depth-first search (DFS), breadth-first search (BFS) [1], Dijkstra's algorithm [2] guarantee to produce optimal route but expand too many nodes during the graph search and thus result in slow performance. The A* heuristic-based graph search algorithm [3] is one of the best-known algorithms for graph search that makes use of some heuristic knowledge and uses the criteria of the best-first search. The A* algorithm expands less number of graph nodes, and search is guided towards the destination node using the heuristic information during the search. It results in less number of node expansions and thus results in a performance boost up during the search. The general graph search algorithms use some cost estimation function that computes the actual cost of route from start node to some intermediate node. The nodes are reordered based on these cost values, and one node is selected for further expansion. On the other hand, the heuristic-based algorithms also add an estimation of the route cost from an intermediate node to the destination node. The use of heuristic information guides the search towards the destination node and results in less number of node expansions before the search terminates.

The various time, storage and optimality requirements have given birth to many modified versions of A* algorithm for route planning. The researchers have reported their work like dynamically pruned A* method [4], using bidirectional search [5], using experience graphs [6] and learning-based adaptive A* algorithm [7] to further improve the performance of the heuristic-based graph search algorithms. These optimizations are suitable for a class of problems and cannot straightway be used for optimal route selection problem in various domains. The Lingkun et al. [8], Geisberger et al. [9], Abraham et al. [10] have studied the problem and provided the optimized solution for road networks. A well-defined theoretical study of the performance was presented by Bast [11].

The work presented in this article makes use of standard A* algorithm for cross-country optimal path selection using the Digital Terrain Elevation Data (DTED). The various heuristic methods are used to compare the performance using the proposed comparator. All the selected heuristic function also satisfies the admissibility criteria [12]. The problem definition is presented in Sect. 2, the performance comparison and criteria are discussed in Sect. 3 and the paper concludes in Sect. 4.

2 Problem Definition

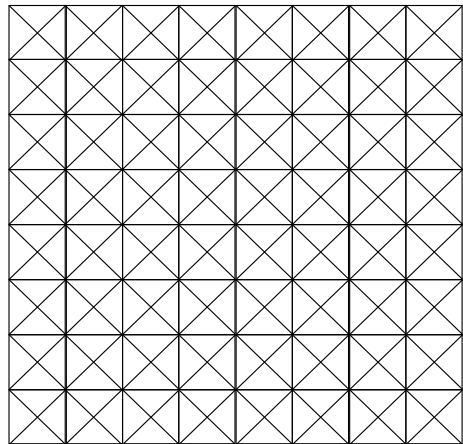
The vehicles, like tank, bridge carrier, trucks in armed forces, generally follow the cross-country routes for the movement. These vehicles have their critical climb angles that should not be neglected during movement to avoid any casualty. The planning of a safe route with minimum cost requires the knowledge about the terrain of operational area. With the advent of the GIS technology, the digital geographical data about the terrain can be stored, updated, managed and analysed for various situations. Using this digital geographical data, the route for a particular vehicle type can be selected beforehand and can be used for actual movement during the operation.

2.1 Graph Representation

The DTED is gridded terrain data that contains the ground height above mean sea level at each grid point. A connected graph needs to be prepared using the DTED so that a graph search algorithm can be employed over it for the selection of optimal route between two points. The DTED-based graph representation is shown in Fig. 1.

Each grid point represents the vertices of the graph, and every vertex is 8-way connected. Each vertex in the graph has eight in bound, and eight outbound edges except the vertices lying at the boundaries. The size of this graph increases rapidly as the size of operational area expands. The ASTER DTED data [13] is available at 30 m resolution. A graph representation of an operational area of 30×30 km using the ASTER data contains approximate one million vertices and 8 million edges. The optimal route selection on such a large graph may sometimes take unexpected time. It was observed that the performance of the algorithm is greatly affected by the selection of the heuristic function.

Fig. 1 Graph representation of DTED



2.2 Cost Estimation

The route between two vertices in the graph G is shown in Fig. 1, and it is a sequence of vertices $v_0, v_1 \dots v_n$, where $v_i \in V$ and $(v_i, v_{i+1}) \in E$ for $0 \leq i \leq n - 1$. Each edge between two adjacent vertices has some cost associated with it. If the length of the edge is assumed as the cost of the edge, the optimal route selection algorithm returns the shortest path. The criteria of optimality in the single weighted tree are always associated with the cost function. The graph search algorithm always tries to minimize the total cost of the route. The slope between two adjacent vertices is another criterion that can be used to compute the cost of the edges. In cross-country movement, the critical climb angle of vehicles needs to be addressed while selecting the optimal route. Thus in this work, the slope between two adjacent vertices and the critical climb angle of vehicle are used in cost estimation using the following procedure.

Procedure: Cost Estimation

Input: v_i, v_{i+1} // two adjacent vertices
max_height_diff = edge_lenght * tan(critical_climb_angle);
Cost = abs(DTED[i] - DTED[i+1]) * MAX_SLOPE_COST / max_height_diff;
If(cost > MAX_SLOPE_COST)
 Return INFINITY;
Else
 Return cost;

This procedure uses two constants **MAX_SLOPE_COST** and **INFINITY** that can be set to some values based on the implementation need. The **INFINITY** cost is assigned to those edges which can never be used by a vehicle type for movement. This computes the cost of the edge that varies linearly with the slope. DTED is an array that stores the height above mean sea level of each vertex in the graph.

2.3 Graph Search Procedure

The general graph search techniques like depth-first search (DFS) or breadth-first search (BFS) [1] can be applied for optimal route selection. The DFS technique uses the stack as internal data structure and backtracking to visit the graph nodes. The BFS technique uses the queue data structure and visit graph nodes based on their level of depth in the spanning tree. It guarantees to return an optimal route but consumes lots of time. The A* technique is modified BFS, that uses the priority queue as data structure and uses the heuristic information to visit the node with minimum cost value. The cost function $f(n)$ is described as $f(n) = g(n) + h(n)$, where $g(n)$ is the actual cost from start node to node 'n' and $h(n)$ provides an estimate of route cost from node 'n' to the goal node.

Table 1 Various heuristic functions

S. No	Name	Measure between point $P_1(a, b, c)$ and Point $P_2(x, y, z)$
1	Euclidean	$\sqrt{\{ \text{abs}(a-x)^2 + \text{abs}(b-y)^2 + \text{abs}(c-z)^2 \}}$
2	Manhattan	$\text{abs}(a-x) + \text{abs}(b-y) + \text{abs}(c-z)$
3	Chessboard	$\text{Max}[\text{abs}(a-x), \text{abs}(b-y), \text{abs}(c-z)]$

2.4 Heuristic Functions

The role of heuristic functions is to provide an estimate of the cost of the undiscovered route from some intermediate node 'n' to goal node. If it is assumed that an optimal route between start and goal node exists via node 'n'. If the actual cost of route from start node to node 'n' is $g^*(n)$ and actual cost of route from node 'n' to goal node is $h^*(n)$, the total route cost can be represented as $f^*(n) = g^*(n) + h^*(n)$. In various heuristic-based graph search techniques, it is desired that $f(n)$ should be a close estimate of $f^*(n)$. It can be achieved if $h(n)$ provides a close estimate of $h^*(n)$. The admissibility criteria [3] of a heuristic function that can produce an optimal route is that if $h(n) \leq h^*(n)$, i.e. $h(n)$ is a lower bound on $h^*(n)$. The selection of heuristic function is greatly dependent on the nature of input graph but it ensures the optimal route only if the admissibility criteria are satisfied.

Three different distance measures as shown in Table 1 are used as heuristic functions in our work to compute the cross-country optimal route for various kinds of vehicles. All the three distance measures satisfy the admissibility criteria thus capable of resulting in the optimal route.

3 Performance Comparison

The comparison of the heuristic power of different functions is generally done based on the experiences. It is required to build certain performance measures that can be calculated for comparison purposes. The penetration (P) is one of the popular performance measures [3]. It computes the extent to which a search is focused towards the goal, rather than searching in irrelevant areas. It is defined as $P = L/T$, where L is length of the path found to goal node and T is total number of nodes generated during the search.

3.1 Proposed Comparator Function

A performance measure cumulative cost (CCH) is proposed in this article that takes the cost of the route as well as the search completion time into account. It is a relative

measure that makes use of the fact that BFS always generates the optimal route. The result of algorithm under test is compared with BFS results, and CCH is computed.

Once the route has been searched, various parameters can be computed. The cost of the route using BFS can be computed as

$$C_{\text{BFS}} = \sum_{i=0}^{N-1} \text{cost}(x_i)$$

Similarly, the cost of route using heuristic-based method can be represented as

$$C_H = \sum_{i=0}^{M-1} \text{cost}(hx_i)$$

Here ‘ N ’ and ‘ M ’ are total number of nodes in route searched by BFS and heuristic-based method, respectively. The x_i and hx_i represent the route nodes in BFS and heuristic-based methods. The time taken to search the route using BFS algorithm and heuristic-based method is also represented as T_{BFS} and T_H , respectively. Now, the cumulative cost factor can be computed as

$$CC_H = \frac{C_H}{C_{\text{BFS}}} + \frac{T_H}{T_{\text{BFS}}}$$

The first fraction $F_1 = (C_H/C_{\text{BFS}})$ should always be greater than or equal to one, and the second fraction $F_2 = (T_H/T_{\text{BFS}})$ should always be less than one. A good heuristic method always tries to minimize the F_1 and F_2 both to achieve the optimality criteria. But in reality if F_1 is kept to its minimum, the F_2 increases and vice versa. The CC_H provides a measure that is a trade-off between optimality and the speed of execution of the algorithm.

4 Results

The BFS algorithm and A* algorithm with three different heuristic functions as shown in Table 1 are implemented in C++. A DTED data set of size 1024×1024 containing more than one million ground points is used to compute the optimal route between start and goal nodes. The selected routes are shown graphically in Fig. 2. The performance of the algorithms was recorded on the computer with Intel Xeon X5660 CPU with 8 GB of RAM. The performance measures like penetration (P) and cumulative cost (CC_H) are used to compare various algorithms. The minimum and maximum edge costs are assumed as 20 and 50, respectively. The detailed comparison is shown in Table 2.

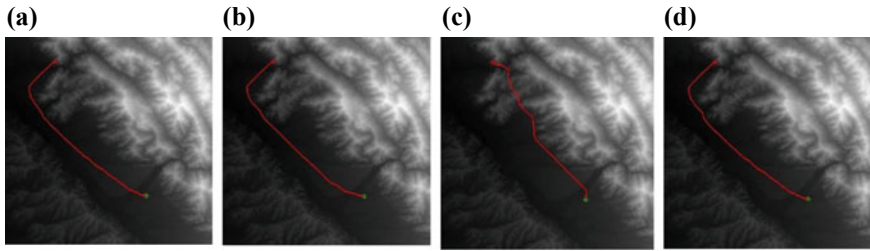


Fig. 2 Search results **a** BFS, using heuristic methods, **b** Euclidean, **c** Manhattan, **d** chessboard

Table 2 Performance comparison of various algorithms

S. No	Search method	C_H	T_H (sec)	F_1	F_2	CC_H	P
1	A* with Euclidean distance	15,567	9.42	1.021	0.0350	1.0560	0.00793
2	A* with Manhattan distance	16,707	2.12	1.096	0.0078	1.1038	0.01541
3	A* with chessboard distance	15,243	38.77	1.000	0.1443	1.1443	0.00390
		$C_{BFS} = 15,243, T_{BFS} = 268.526 \text{ s}, P_{BFS} = 0.00147$					

5 Conclusion and Future Work

It is evident from Table 2 that the A* algorithm with Euclidean distance metric works very well on hilly terrain in comparison with other heuristic method. The CC_H value for Euclidean distance metric is closest to 1; hence, it is the most suitable heuristic to be used for optimal route selection on hilly terrain. The penetrance (P) does not account for the search time, and its value is misleading for the selection of suitable heuristic method.

The heuristic method with Euclidean distance was also checked on various other routes on the same data set, and it was found that it is the most suitable heuristic for hilly terrain to compute the optimal route with optimum cost and time. This performance comparison can certainly help the route planner to choose the right heuristic based on the criticality of the operation and the availability of time.

The technique presented in this method uses a single-valued cost function that can easily be extended to accommodate multiple cost factors. The A* algorithm can further be optimized by using parallelization judiciously to reduce the search time significantly on multi-core machines.

Acknowledgements This work was done at Image Analysis Center (IAC), Defense Electronics Applications Laboratory (DEAL), Dehradun, India. The author is grateful to Dr. RS Pundir, Director, DEAL, for providing all his support and resources to complete this work.

References

1. Khantanapoka K, Chinnasarn K (2009) Pathfinding of 2D & 3D game real-time strategy with depth direction A* algorithm for multi-layer. In: Eight IEEE international symposium on natural language processing, pp 184–188
2. Dijkstra W (1959) A note on two problems in connection with graphs. *Numer Math* 1(1):269–271
3. Nilsson JN (1995) Principles of artificial intelligence. Narosa Publishing house, New Delhi
4. Wouter VT, Geraerts R (2015) Dynamically pruned A* for re-planning in navigation meshes. In: IEEE/RSJ international conference on intelligent robots and systems (IROS), Congress Center Hamburg, Germany, pp 2051–2057, 28 Sept–02 Oct
5. Ma H, Liang R (2013) Using bidirectional search to compute optimal shortest paths over multi-weight graphs. In: IEEE international conference on information science and cloud computing companion, pp 66–71
6. Phillips M, Likhachev M (2015) Speeding up heuristic computation in planning with experience graphs. In: IEEE international conference on robotics and automation (ICRA), Washington State Convention Center, Seattle, Washington, pp 893–899, 26–30 May
7. Bander JL, White CC III (1998) A heuristic search algorithm for path determination with learning. *IEEE Trans Syst Man Cybern Part A: Syst Hum* 28(1)
8. Lingkun W, Xiaokui X, Dingxiong D (2012) Shortest path and distance queries on road networks: an experimental evaluation. *Proc VLDB Endow* 5(5):406–417
9. Geisberger R, Sanders P, Schultes D (2008) Contraction hierarchies: faster and simpler hierarchical routing in road networks. In: International workshop on WEA, Springer, Heidelberg, pp 319–333
10. Abraham I, Fiat A, Goldberg AV et al (2010) Highway dimension, shortest paths, and provably efficient algorithms. In: Proceedings of the twenty first annual ACM-SIA Symposium on discrete algorithms, Society for Industrial and Applied Mathematics, pp 782–793
11. Bast H, Funke S, Matijecvic D (2006) Transit: ultrafast shortest path queries with linear time pre-processing. In Important proceedings of the 9th DIMACS implementation challenge, pp 175–192
12. Pearl J (1984) Heuristics: intelligent strategies for computer problem solving. Addison-Wesley, MA
13. <http://asterweb.jpl.nasa.gov>. Accessed 12 Nov 2018

Orbit and Attitude Control and Dynamics

Simulation of the Dynamics and Control of Tethered Small Satellite Deployment



G. R. Sangeetha and Harikumar Ganesan

Abstract This paper presents the simulation studies of the dynamics of short tethered satellite system during the deployment phase. The deployment dynamics of the tethered system is dominated by the tether oscillations and the three-dimensional attitude dynamics of the sub-satellite. The dynamic characters of the system are investigated, and probable control strategies that can be adopted for the faithful and hassle-free deployment of the tether are discussed. Tether is proposed to be released with an initial velocity with constant deceleration using tension in tether. Dynamics of a short tether of 10 m length connected to a 10 kg 3U sub-satellite is considered in the study. Deployment with tether in tension and without tension in tether is discussed.

Keywords Dynamics · Short tethered satellite · Tether oscillations · 10m tether

1 Introduction

India is entering an ambitious new trajectory in its space research and is steadily keeping pace with the developments in space arena across the globe. With more and more long-life exploration missions planned, on-orbit servicing, refueling, inspection and repair, executing repeated and monotonous maintenance operations are indispensable auxiliary functions. In addition, due to proliferated space activity over past 60 years, the number of space debris has reached a whopping 17,000 [1]. Of these, the small-sized debris is found to inflict profound damage to serve spacecrafts. This also calls for immediate human intervention.

An autonomous system that can independently carry out inspection and repair activities, as well as serve to collect small size debris in the immediate vicinity of the spacecraft, is the need of the hour. It is proposed to develop a smart sub-satellite tethered to a parent spacecraft, which can deploy itself, perform inspection and repair operations, collect space debris, return and re-attach to the parent body

G. R. Sangeetha (✉) · H. Ganesan
ISRO Inertial Systems Unit, Trivandrum, India
e-mail: sangeetha_gr@vssc.gov.in

© Springer Nature Singapore Pte Ltd. 2020
PSR. S. Sastry et al. (eds.), *Advances in Small Satellite Technologies*,
Lecture Notes in Mechanical Engineering,
https://doi.org/10.1007/978-981-15-1724-2_4

on its own. The operations of the smart sub-satellite were spread across three major phases—deployment, station keeping, and retrieval.

Space tether missions have a long history, beginning with the GEMINI-11 and GEMINI-12 missions, pioneered by NASA in 1996. Then, there was a brief lull for nearly 10 years, following which a number of tethered experiments have been carried out by various space agencies since the 1980s, details of which are listed in [2] and [6]. These missions have served to demonstrate various tethered system concepts such as generation of artificial gravity by spinning, gravity stabilization, upper atmospheric studies, generation of electrical energy using electrodynamic tethers. Though most theoretical studies, as well as early experiments, have concentrated on long tethers, the current focus is on short tethered system applicable to small satellites.

In this paper, the dynamics of the tethered sub-satellite during deployment is studied. The sub-satellite is of the 3U category with 10 kg mass. It is attached to the parent body through a 10-m-long tether. Two scenarios have been studied: (1) deployment assuming zero tension in tether, (2) deployment to nearly 5 m tether length under controlled tension. Case (1) is significant in developing initial insights into the qualitative and quantitative features of the tethered satellite motion. Case (2) is of practical importance in developing control laws for deployment.

The translational dynamics has been expressed both in terms of the motion of the CG of the sub-satellite in the 3D space and in terms of the in-plane and out-of-plane angles of the tether. The attitude dynamics has also been modeled to study the rotational dynamics of the sub-satellite with and without tension.

2 Assumptions

For the purpose of modeling the dominant dynamics, the base satellite is considered as a massive spacecraft, tether as massless, and the sub-satellite is of comparatively lower mass. The sub-satellite moves away from the base satellite due to delta V imparted by separation mechanism/thruster. The assumptions are as follows:

Sub-satellite Mass: 10 kg

Base satellite: Mass > 2 tons, circular sun-synchronous polar orbit at 800 km altitude, unperturbed by sub-satellite motion

Tether:	Material	Kevlar 49
	Young's modulus	83 GPa
	Tensile strength σ^* :	3.8 GPa
	Density ρ :	1.44 g/cm ³
	Length:	10 m
	Diameter of tether (cylindrical):	2 mm (45 g)

3 Translational Dynamics

The tethered satellite system is shown in Fig. 1. The base satellite is depicted as B , and the sub-satellite is depicted as A .

The motion of sub-satellite, A , has been developed based on

$$m_A w_A = T_A + F_A + G_A \tag{1}$$

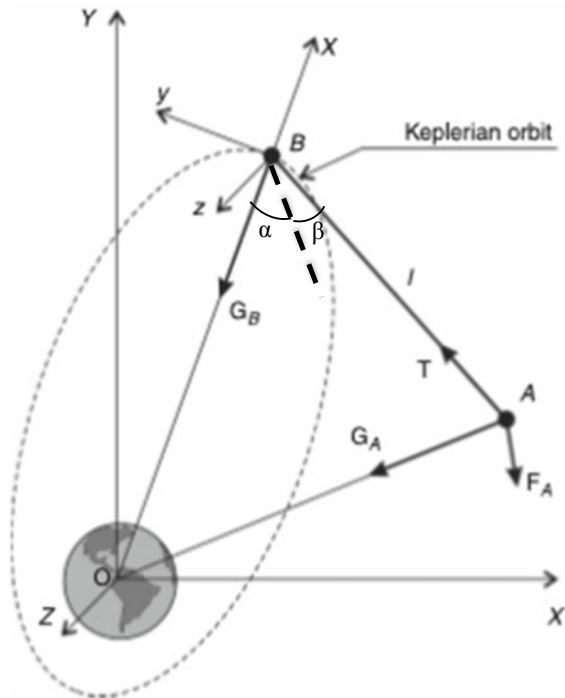
w_A —acceleration of the particle which is the sum of coriolis, relative, and reference-frame accelerations, T_A —tension in tether, F_A —non-gravitational forces, G_A —gravitational force on particle A .

The motion of base satellite, B , is modeled as follows based on the assumption of Keplerian motion for the vehicle:

$$\ddot{r}_B = -\frac{\mu r_B}{r_B^3} \tag{2}$$

The motion of the tethered satellite system in the base satellite orbital coordinate frame is as follows [2, 3]:

Fig. 1 Tethered satellite system depicted as point masses connected by a tether [2]



$$\left. \begin{aligned} \ddot{x} - 2\dot{y}\omega - \dot{\omega}y - (1 + 2k^{-1})\omega^2x &= \frac{T_x + F_x}{m_A} \\ \ddot{y} - 2\dot{x}\omega - \dot{\omega}x - (1 - k^{-1})\omega^2y &= \frac{T_y + F_y}{m_A} \\ \ddot{z} + k^{-1}\omega^2z &= \frac{T_z + F_z}{m_A} \end{aligned} \right\} \quad (3)$$

$$T = ES \left(\frac{\rho_A}{l_0} - 1 \right) \quad (4)$$

where T : tension force on tether attached from c.o.m, F : non-gravitational external forces, m_A : TSR mass, ω : orbital angular velocity, $k: 1 + e\cos(\Psi)$ where $e =$ eccentricity, $\Psi =$ true anomaly, E : Young's modulus of tether, S : cross-sectional area of tether, l_0 : length of tether, ρ_A : TSR radial position in xyz frame, r_B : radius vector of base satellite in geocentric coordinate system, μ : Earth's gravitational constant.

When the tether is massless rigid rod, the motion of the sub-satellite can be expressed in terms of the in-plane and out-of-plane angles of the tether. As given in Fig. 2, α denotes the in-plane angle and β denotes the out of plane angle and the x , y , z coordinates of the sub-satellite can be expressed as

$$x = -l \cos \alpha \cos \beta, \quad y = -l \sin \alpha \cos \beta, \quad z = -l \sin \beta$$

The dynamics of system in terms of tether angles is given as

$$\left. \begin{aligned} \ddot{\alpha} &= -2(\dot{\alpha} + \omega) \left(\frac{\dot{l}}{l} - \dot{\beta} \tan \beta \right) - 3\omega^2 \sin \alpha \cos \alpha + \frac{u_1}{m_A l^2 \cos^2 \beta} \\ \ddot{\beta} &= -2 \left(\frac{\dot{l}}{l} \dot{\beta} \right) - [(\dot{\alpha} + \omega)^2 + 3\omega^2 \cos^2 \alpha] \sin \beta \cos \beta - \frac{u_2}{m_A l^2} \\ \ddot{l} &= -l(\dot{\beta}^2 - \omega^2) + 3l\omega^2 \cos^2 \beta \cos^2 \alpha + l \cos^2 \beta (\dot{\alpha} + \omega)^2 - \frac{T}{m} + u_3 \end{aligned} \right\} \quad (5)$$

where u_1 , u_2 , and u_3 are the control forces, which is a resultant of the actual control force applied and the disturbances.

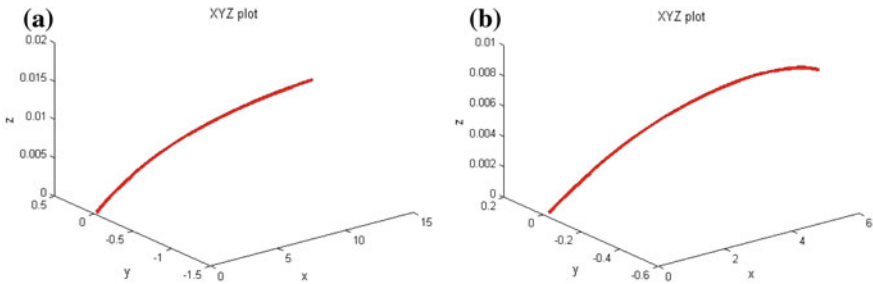


Fig. 2 a Plot of tether motion in 3D space (without tension). b Plot of tether motion in 3D space (with tension)

4 Attitude Dynamics

The attitude of the sub-satellite is coupled with the motion of the tether [4] and is given as

$$\left. \begin{aligned} I_{sy}\ddot{\theta}_s + (I_{sy} + m_s l)\ddot{\theta}_t - m_s \ddot{l}\theta_s + m_s \dot{l}\dot{\theta}_t &= 0 \\ I_{sx}\ddot{\varphi}_s - (I_{sx} + m_s l)\ddot{\theta}_t - m_s \ddot{l}\varphi_s - m_s \dot{l}\dot{\varphi}_t &= 0 \\ I_{sz}\ddot{\vartheta}_s + m_s l(\varphi_s \ddot{\theta}_t + \theta_s \ddot{\varphi}_t) &= 0 \end{aligned} \right\} \quad (6)$$

where θ_s = subsatellite pitch angle, φ_s = subsatellite roll angle, ϑ_s = subsatellite yaw angle.

5 Results and Inference

Based on the dynamic model for translational and rotational motion of sub-satellite, obtained above, simulation was performed to study the possibilities of deployment.

Case study: Ensure stable deployment to a length of 5 m in 100 ms and station keeping at 5 m for 500 s

The sub-satellite is deployed along the local vertical. The deployment conditions are as given below

$$\begin{aligned} \alpha_0 &= 0 \text{ degree (along local vertical - } Ox \text{ axis), } \dot{\alpha}_0 = 0.02^\circ/\text{s}, \\ \beta_0 &= 0 \text{ degree (in plane deployment), } \dot{\beta}_0 = 0.05^\circ/\text{s}, \end{aligned}$$

Initial length of tether = 0.2 m

Release velocity = 0.1 m/s

$$\theta_{s0} = 0.2^\circ, \dot{\theta}_{s0} = 0.05^\circ/\text{s}, \varphi_s = -0.1^\circ, \dot{\varphi}_s = -0.03^\circ/\text{s}, \vartheta_s = -0.5^\circ, \dot{\vartheta}_s = 0.1^\circ/\text{s}$$

Case 1: Deployment without tension in tether: It is seen that without any tension in the tether, the tether gets released to about 10 m in 100 s due to the initial velocity of 0.1 m/s. Also, acceleration of the order of $2 \times 10^{-5} \text{ m/s}^2$ is experienced by the tether due to the effect of Coriolis force. The rate of change of in-plane angle of the tether settles to the orbital rate of $0.06^\circ/\text{s}$ in 100 s, and hence, the in-plane tether angle deflects to 6° , as shown in Fig. 4a. The rate of change of out-of-plane angle of tether also settles to 0, and in the influence of the initial rate of $0.05^\circ/\text{s}$, the out-of-plane angle settles to 0.1° in 100 s. Even in the absence of tension in tether, the translational dynamics remains stable (Figs. 3, 5 and 6).

The attitude dynamics of the sub-satellite is coupled with the tether motion. The rate of in-plane and out-of-plane angles settles to zero and does not introduce any disturbance on the attitude; however, the acceleration on the tether introduces instability in attitude due to high rates coming on the sub-satellite.

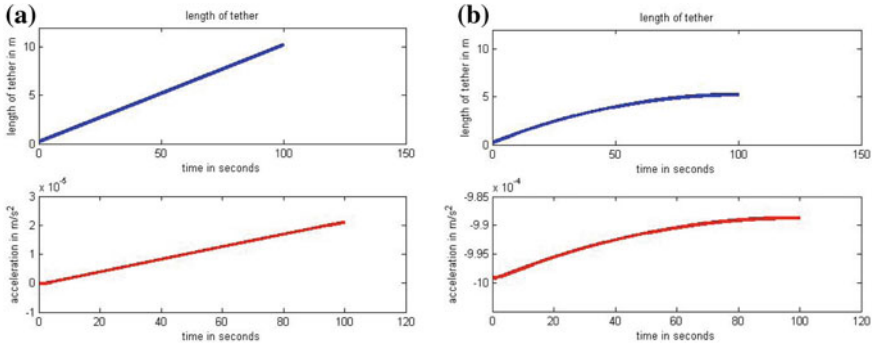


Fig. 3 a Deployed length and acceleration on tether (without tension). b Deployed length and acceleration on tether (with tension)

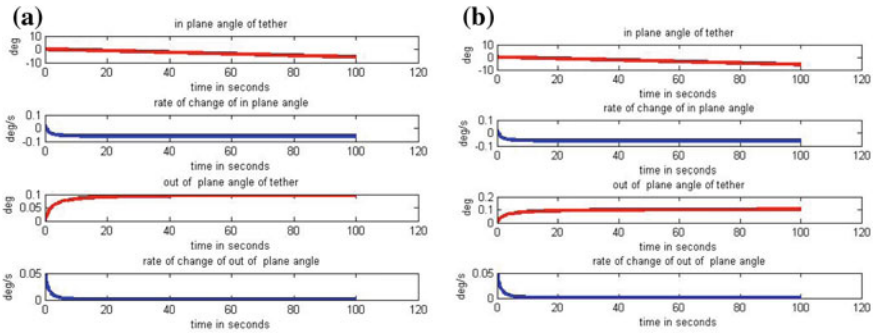


Fig. 4 a In-plane and out-of-plane angles of tether (without tension). b In-plane and out-of-plane angles of tether (with tension)

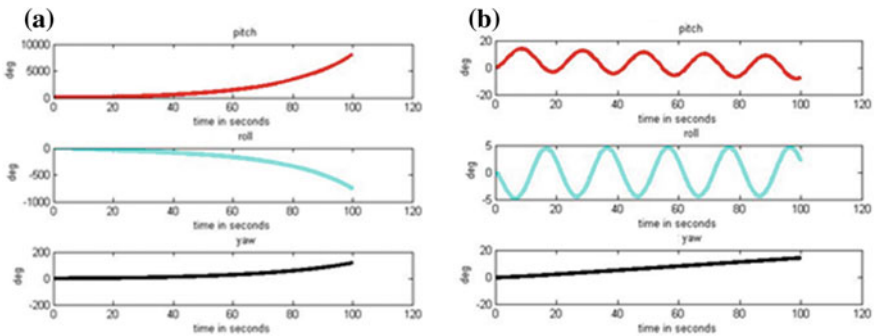


Fig. 5 a Sub-satellite attitude angles (without tension). b Sub-satellite attitude angles (with tension)

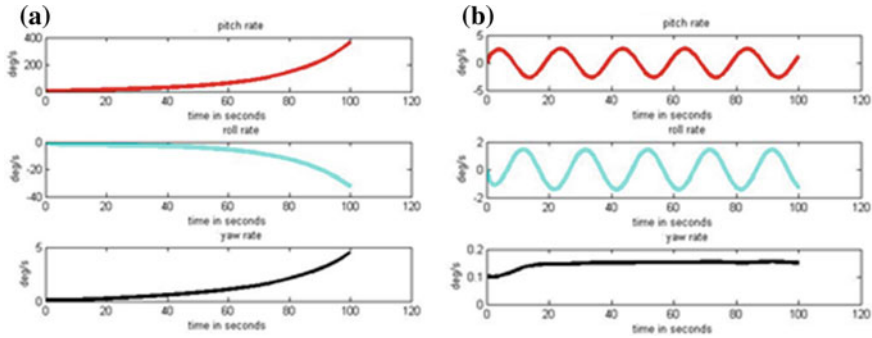


Fig. 6 **a** Sub-satellite attitude rates (without tension). **b** Sub-satellite attitude rates (with tension)

Case 2: Deployment with tension in tether: To ensure deployment of the tether to the desired length, the tether has to be maintained in tension. A tension which imparts an acceleration equivalent to 0.001 m/s^2 is given on the tether. The tether tension can be maintained to required value, by controlling the tether releasing mechanism [5].

In this scenario, it is seen that with the tension in the tether, required length of deployment is achieved and the in-plane and out-of-plane angles of the tether and the respective rates, follow the same trajectory as in the case of the deployment without tension, as expected. Due to the negative acceleration imparted on tether, the sub-satellite motion is stable and due to its coupling with the tether motion, the sub-satellite attitudes display vibratory sinusoidal motion with attitudes less than $\pm 10^\circ$ in pitch, $\pm 5^\circ$ in roll, and a gradual increase of up to 18° in yaw. The pitch and roll rates oscillate at $< \pm 3^\circ/\text{s}$, and the yaw rate settles to a constant value of $0.15^\circ/\text{s}$ due to which the yaw is seen to steadily increase.

The disturbance forces at the 800 km orbit have not been modeled. Aerodynamic drag would be a significant component. The presence of this could further dampen the swing in the attitude of the sub-satellite and reduce it to the level of vibrations [4].

6 Summary

The dynamics of deployment of a tethered satellite system has been studied. A controlled deployment method to achieve a desired station-keeping distance has been simulated.

References

1. Dubanchet V, Saussié D, Alazard D, Bérard C, Le Peuvedic C (2014) Modeling and control of a space robot for active debris removal. In: ESA GNC 2014 9th international ESA conference on guidance, navigation and control systems, Porto, Portugal 2–6 June 2014
2. Aslanov VS, Ledkov AS (2012) Dynamics of tethered satellite systems. Woodhead Publishing Limited, UK
3. Beletsky VV, Levin EM Dynamics of space tether systems, vol 83. Advances in the Astronautical Sciences, California
4. Liu Y, Zhou J (2016) Attitude dynamics and thrust control for short tethered sub-satellite in deployment. In: Proc IMechE Part G: J Aerosp Eng
5. Huang P, Zhang F et al (2016) Coordinated coupling control of tethered space robot using releasing characteristics of space tether. Adv Space Res Sci Direct
6. Yu BS, Wen H, Jin DP (2018) Review of deployment technology for tethered satellite systems. Acta Mech Sin 34(4):754–768. <https://doi.org/10.1007/s10409-018-0752-5>

Design and Development of Mass Optimised Latching Solenoid Valve for Chandrayaan-2 Lander Propulsion



Venkata Sunil Sai Nukala, Subrata Chakrabarti, D. Venkittaraman and M. Radhakrishnan

Abstract Chandrayaan-2 lander propulsion system employs a bipropellant thruster with a throttleable flow control valve (TCV) to vary the thrust produced by 800 N engines. A latching solenoid valve was proposed downstream of TCV to precisely admit/cut-off propellant supply to the engine as the latter does not inherently possess stringent leak tightness characteristics. The proposed valve employs a flexure guided plunger assembly to facilitate both continuous and pulse mode operation of the engine while preventing the possibility of cold welding/stiction between the sliding parts under space environment. A latching type of solenoid configuration was selected with balanced loading and permanent magnets to complement the solenoid in reducing the mass when compared to a conventional solenoid valve for the same application. In the selected configuration, switching of the valve position is accomplished by energising the solenoid coil and latching in the commanded position with the help of permanent magnets. Thus, the solenoid valve does not require continuous external supply, which results in negligible coil heating and very low power consumption. Two sets of proto models were realised which had undergone performance tests, 10,000 cycles of operation and 100 s duration hot test satisfactorily.

Keywords Propellant flow control · Solenoid · Permanent magnet · Flexure

1 Introduction

Chandrayaan-2 lander mission requires a liquid engine which can throttle to vary the thrust produced to facilitate de-boost and soft landing on the lunar surface. The thrust produced by 800 N engine is varied from 100 to 40% by throttling the propellant flow rate using a throttleable flow control valve (TCV). TCV does not inherently possess stringent leak tightness characteristics. Hence, a latching solenoid valve is proposed downstream of TCV to precisely admit/cut-off propellant supply to 800 N engine.

V. S. S. Nukala (✉) · S. Chakrabarti · D. Venkittaraman · M. Radhakrishnan
Control Systems and Components Entity, Liquid Propulsion Systems Centre, ISRO,
Thiruvananthapuram, Kerala 695 547, India

© Springer Nature Singapore Pte Ltd. 2020
PSR. S. Sastry et al. (eds.), *Advances in Small Satellite Technologies*,
Lecture Notes in Mechanical Engineering,
https://doi.org/10.1007/978-981-15-1724-2_5

Latching solenoid valve (Fig. 1) is basically a solenoid-operated shut-off valve with latching provision in the commanded position. Each bipropellant thruster has two valves (fuel and oxidiser) which are identical and is designed for the working medium with higher density. Electromagnetic flux produced by the solenoid is required to shift the position of the valve [2], and permanent magnetic flux is used for latching in the commanded position [3]. Breif specifications of the valve is given in Table 1.

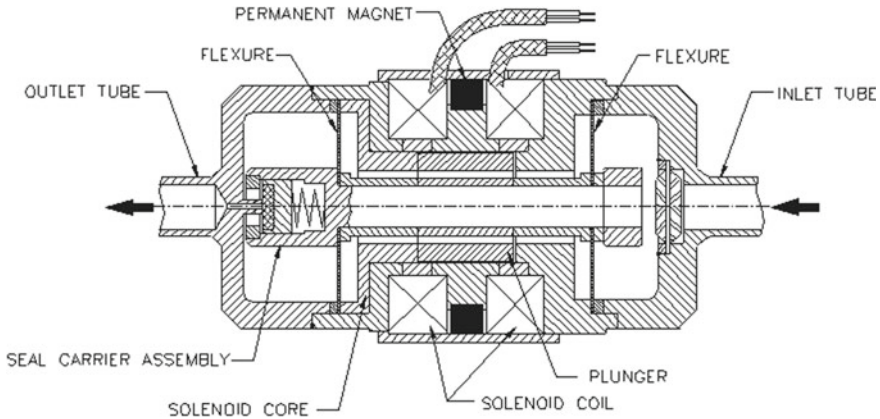


Fig. 1 Isolation latch valve

Table 1 Brief specifications of the valve

SI No	Parameter	Specification
1	Working fluid	N_2O_4 , MMH
2	Flow rate	162 g/s of oxidiser, 98 g/s of fuel
3	Maximum operating pressure	24 bar
4	Pressure drop at 162 g/s flow rate of oxidiser	3.5 bar
5	Working temperature	-7 to 60 °C
6	Supply voltage at coil terminal	21–14 VDC
7	Pull-in voltage (open and close)	≤ 11 VDC
8	Response time at 24 bar and 28 VDC	≤ 5 ms
9	Internal leakage at 24 bar	$\leq 1 \times 10^{-5}$ sccs of GHe
10	External leakage at 24 bar	$\leq 1 \times 10^{-6}$ sccs of GHe
11	Unit mass	≤ 220 g

2 Configuration

2.1 Description of Design

The latch valve has an axial configuration permitting straight flow of propellant through the valve. In order to accomplish precise guidance and sliding-free movement of the plunger inside solenoid bobbin bore, moving elements are suspended on a seal carrier assembly supported by flexures. This arrangement also results in minimising contaminant generation during valve actuation and improves fatigue life. Flexure (Fig. 2) is a flat spring designed to achieve required force–deflection characteristics, acts as a beam with fixed ends and ensures that moving elements are insensitive to lateral vibration loads. Stress analysis of the flexure is carried out, and the desired cyclic life is ensured in the design using the Soderberg criteria which inherently guards against yielding and is considered to be more conservative. Flexures have been calibrated and qualified for the intended number of actuations.

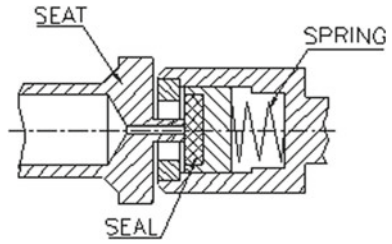
This method of guidance of plunger assembly facilitates both continuous and/or pulse mode operation of the 800 N Engine while preventing the possibility of cold welding or stiction between the sliding pair under space environment is compared to a direct sliding plunger type of valve, nor any coatings are required.

The port diameter is determined by the oxidiser flow requirements (162 g/s). Port diameter of 3.2 mm is selected, and corresponding valve stroke is provided accounting for the swell in soft seal material (PTFE) due to the thermal expansion and propellant wetting. Sealing is achieved by a flat PTFE seal pressing against a flat raised land-type stainless steel seat. PTFE seal element is preloaded with a helical spring in the valve closed condition. This floating spring configuration as depicted in Fig. 3 assures optimum seat bearing stress, self-alignment between the sealing surfaces. Inlet pressure generates additional interface sealing load. The seat stress provided should be adequate to permit sealing in unpressurised condition and at the same should be within the elastic limit at the operating pressure. For the present

Fig. 2 Flexure



Fig. 3 Floating spring configuration



design, maximum seat stress of 1.07 kg/mm^2 is provided which is within the yield limit for PTFE.

Solenoid bobbin comprises of soft magnetic material and non-magnetic material electron beam welded to form the magnetic circuit. AISI 446 is selected as the core material owing to its long-term compatibility with the propellants coupled with reasonably good magnetic properties. Non-linear BH characteristics of the core material are shown in Fig. 4.

Two coils are provided: one for opening and the other for closing the valve as shown in Fig. 5. The two coils are potted and hermetically sealed to prevent the entry

Fig. 4 Nonlinear BH curve for AISI 446

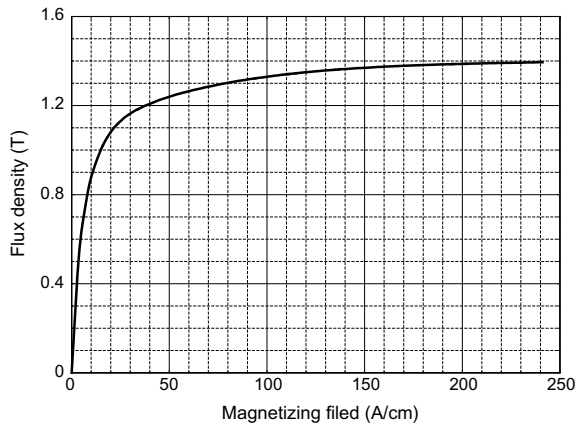
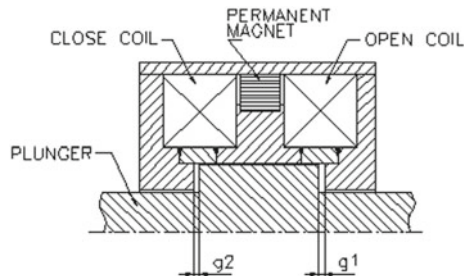


Fig. 5 Latching actuator schematic



of propellant vapours into the coil cavity. Electrical redundancy is available in the latch valve design without the incorporation of additional coils. If closing coil fails, valve can be closed by commanding open coil with reverse polarity. Similarly, the valve can be opened by commanding close coil with reverse polarity.

Five numbers of arc-shaped radially polarised samarium cobalt permanent magnets are employed to keep the valve latched in open/close position [3]. Permanent magnet is hermetically sealed from the working medium. Hence, no compatibility issues are associated with the selection of permanent magnetic material. Resultant force offered by the selected magnets is resistant to launch vibration and shock to prevent de-latching of the plunger from the commanded position. A 40-micron (abs) pleated disc filter is provided at the valve inlet. This ensures that the valve is contamination tolerant in achieving the stringent leakage specifications.

Thus, the latching type of solenoid configuration with balanced loading and permanent magnets to complement the solenoid optimises the actuator size when compared to a conventional solenoid valve for the same application.

All joints in the valve are electron beam welded. External leakage achieved through the valve is better than 1×10^{-6} secs.

3 Principle of Operation

Latching solenoid valve is normally closed. Plunger remains latched in the last commanded position with the aid of flux emanated from permanent magnets.

3.1 *Open Coil Energised*

In the valve closed position, permanent magnet attracts the plunger and latches it to the pole piece with air gap $g_2 = 0$, decoupling the closing spring force from the magnetic latch force. This electromagnetic actuator employs a radially polarised permanent magnet assembly to affect latching in both open and close positions. Two solenoid coils are provided to switch the plunger to the desired position. To open the valve, a short square wave voltage pulse is given to the open coil. This reduces the flux at the close pole piece (g_2) and builds up at the open pole (g_1) as shown in Fig. 6 [4]. When the attracting force exceeds the net closing forces with a margin, plunger moves towards open pole piece. After a small amount of pre-travel, the plunger assembly contacts the seal, overcomes the spring force and opens the valve. Plunger latches to the open pole piece, closing the air gap g_1 and the valve is kept open. Electrical power may be terminated, and the plunger latches in the open position.

Fig. 6 Flux distribution—open coil energised

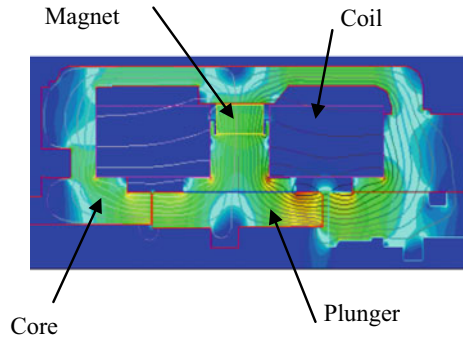
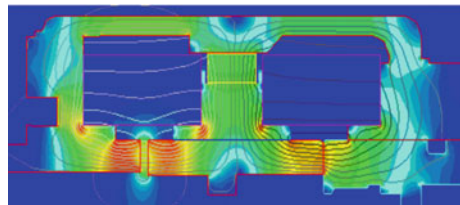


Fig. 7 Flux distribution—close coil energised



3.2 Close Coil Energised

To close the valve, a similar square wave voltage pulse is given to the close coil. This creates a magnetic flux which opposes the flux from the permanent magnet at air gap g_1 and adds to the permanent magnet flux at the other air gap g_2 as shown in Fig. 7 [4]. When the attractive force at gap g_2 becomes large enough, plunger is attracted towards the close pole piece and the air gap g_2 approaches zero. Power may then be terminated. For the present design, air gaps g_1 and g_2 are kept as 0.8 mm. Air gap is maintained within a tolerance band of 0.03 mm.

It may be noted that the poppet contacts the seat first during the closing process and the plunger over travels and latches to the close pole piece. This reduces the seat bearing stress, improves seal life and allows seal to align with seat under the spring load.

4 Testing

Two numbers of prototype valves were assembled and subjected to extensive developmental tests (Table 2) and the design parameters like operation at 24 bar inlet pressure, leak tightness under all operating conditions, dry coil excitation at rated voltage [1] valve response times were validated. Pull-in voltage measured for open

Table 2 Developmental test matrix

SI No	Test
1	Proof pressure test
2	Reference functional tests (a) Pull in voltage measurement (b) Response (c) Internal leakage (d) Stroke (e) Internal and external leak checks
3	Water calibration test
4	Dry excitation test (42 VDC, 120 s)
5	Performance test at -7 to 60 °C
6	Thermo vacuum test (-7 to 60 °C, 6 cycles)
7	Vibration test (20.89 g)
8	Shock test (50 g, 10 ms)
9	Life cycle test (10,000 cycles at 24 bar inlet pressure)

coil and close coil was less than 11 VDC, indicating adequate margins for valve operation.

During the water calibration test, pressure drop achieved was higher to meet the equivalent water flow rate. However, no reduction in valve stroke was observed. When the flow path was critically analysed, choking of the flow path between the flexure and the solenoid core was identified as the reason for the higher pressure drop, and the same was corrected to meet the mass flow rate and pressure drop requirements. Developmental tests as per the above test matrix were completed. In particular, significance is the temperature exposure test and life cycle test. Temperature exposure test, wherein the valve was subjected to various temperature conditions, envisaged during the mission by means of external heating. Design adequacy and performance margins were demonstrated under different temperature conditions. Life cycle test was carried out at 24 bar inlet pressure using de-ionised water to demonstrate the cyclic capability of the valve under the lowest pulse width (30 ms ON and 100 ms OFF). No degradation in performance was noticed. This test was limited to 10,000 cycles based on the end-user requirements. However, cyclic test can be extended as the moving elements are guided in flexures which ensure sliding free movement and consistent performance. Performance tests conducted after every stage of the test mentioned in the developmental test matrix were satisfactory.

5 Results and Discussion

Performance tests were carried out on two prototype valves realised. Pull-in voltage for opening and closing was measured to be 10.5 VDC against minimum supply voltage of 14 VDC. This ensures a sufficient margin exists for the valve operation.

Latching function in open and close positions was demonstrated. Latch force provided was adequate to hold the plunger to the respective pole piece during vibration simulation test. Valve opening and closing response times under operating conditions were better than 4.5 ms. Internal leak tightness achieved through the valve seating surface was 1.5×10^{-8} sccs using GHe medium. Water calibration test was carried out on the valve, and a pressure drop of 3.2 bar was observed for equivalent flow rate of oxidiser. The performance of the valve has been demonstrated successfully under extreme operating conditions (-7°C and 60°C). Post-cyclic (10,000) performance test results showed no degradation in the performance of the valves.

6 Conclusion

A latching solenoid valve with a flexure guided plunger is designed and developed for the supply/cut-off of propellants to 800 N engine. Switching of the valve position and latching in the commanded position have been successfully demonstrated under various operating environmental conditions. Latching type of solenoid design eliminates the requirement of continuous energisation of solenoid coil which results in negligible heating and very low power consumption. Thus, the present valve is capable of continuous and/or pulse mode operation. Developmental hardware has undergone water calibration, temperature exposure, cyclic actuations, vibration simulation test and 100 s duration test fire with 800 N engine satisfactorily. The performance of the valve is consistent throughout the developmental phase. Mass of the proto model was 210 g which is 40% of the mass of a conventional solenoid valve designed for the same application.

References

1. Angadi SV et al (2009) Reliability and life study of hydraulic solenoid valve. Part 2: Exp Study Eng Fail Anal 16:944–963
2. Roters Herbert C (1941) Electromagnetic devices. Wiley, New York
3. Parker RJ, Studders (1990) Permanent magnets and their application. Wiley, New York
4. Tao G et al (2002) Optimal design of the magnetic field of a high-speed response solenoid valve. J Mater Process Technol 129:555–558

De-Tumbling Controller of NIUSAT: Design, Simulation and On-Orbit Performance



F. Aaron Raphael Raja, Vivek Diwan and K. Samuel

Abstract NIUSAT was developed by the students of Noorul Islam Centre for Higher Education under the guidance of various faculties of our college and support from the ISRO experts. One of the most important problems that a satellite faces after being separated from the launcher is the tumbling. When the satellite has relatively high angular velocity, it is said to be tumbling. Tumbling occurs right after the release of the satellite from the launcher and also during the deployment of the nano-satellite from the launcher. The first task of attitude control system is to de-tumble the satellite. We have to bring down the angular velocities before starting to stabilize the satellite because the stabilization controllers may not have the capacity stabilize the satellite with high initial velocities. So taking considerations of these things, we have to design the de-tumbling controller in such a way that it takes reasonable measures to effectively reduce the tumbling of the satellite in a reasonable time. In this paper, we will describe the design details of the de-tumbling controller, digital simulation results and the on-orbit performance on board the NIUSAT nano-satellite.

1 Introduction

The satellite spins in an uncontrolled way after being released from the launcher. Before the satellite begins to use for normal operation, we must control the tumbling. This is the first process of the attitude determination and control system (ADCS). The tumbling is usually measured in deg/sec with respect to each of the three axes. Since it is practically impossible to completely de-tumble the satellite, the controller is switched off as soon as the angular velocity is brought down to a small value, since we do not have to waste the power/energy forever. For detumbling in NIUSAT, we have used the B-dot controller which is the most conventional method of detumbling

F. Aaron Raphael Raja (✉) · V. Diwan · K. Samuel
Department of Aerospace, Noorul Islam Centre for Higher Education, M1-36, Phase-6,
Avalapalli, Hosur 635109, India

© Springer Nature Singapore Pte Ltd. 2020
PSR. S. Sastry et al. (eds.), *Advances in Small Satellite Technologies*,
Lecture Notes in Mechanical Engineering,
https://doi.org/10.1007/978-981-15-1724-2_6

in a nano-satellite. The de-tumbling controller comprises magnetic torquers, magnetometers and the suitable control law to produce counteracting torque to bring down the tumbling rate of the satellite.

2 De-tumbling Controller

The B-Dot control law is a simple and reliable method that is suitable for this purpose. It uses three-axis magnetometer to measure and compute the magnitude of the dipole moment required by the magnetic torquers and to get the derivative of the earth's magnetic field vector in the rotating body frame. The torque equation is given by:

$$\mathbf{M}_b = -k * \mathbf{B_Dot}, k > 0$$

where

- M_b magnetic moment of the coil
- k positive control gain
- B_dot time derivative of the measured local magnetic field.

3 Magnetic Torquer

The magnetic torquers are nothing, but coils wound in loops, through which current is passed to create a magnetic field, which in turn interacts with the prevailing earth's magnetic field to generate small amount of torque on the satellite. They contribute in bringing the NIUSAT to a near-zero angular velocity, so that the three-axis stabilization can be carried out. Since our NIUSAT is a three-axis stabilized satellite, it equips with three magnetic torquers to provide torque about all the three axes. Generally, a nano-satellite has magnetic torquers placed perpendicular to each other, inside the side panels. As the magnetic torque will be produced by interacting with the magnetic field in all three directions, a magnetometer is required to measure the earth's magnetic field about each axis. The magnetic torquer is the primary mechanism for detumbling immediately after the separation from the launch vehicle. In the NIUSAT, three magnetic torquers, one at the bottom deck and other two on the side panels, are used. The design details of the magnetic torquer are given here.

The dimensions of the torquer coils are limited by the maximum space available in the side and bottom plates of the nano-satellite. The coils maximum outer dimensions are 200×150 mm, the inner dimensions are 180×130 mm, and the maximum thickness is 10 mm. The minimum magnetic moment (M) required for each coil is 0.1 Am^2 . The minimum supply voltage is 6 V, and OBC will generate the PWM signal for energizing the torquer. Based on the above requirements, the magnetic torquer coil specifications are arrived and are given below.

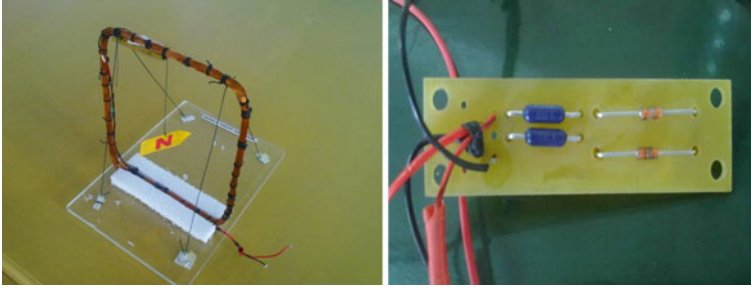


Fig. 1 Magnetic torquer with zener diode protection and current-limiting resistors

1. Outer dimensions are: 200×150 mm.
2. Type of wire/gauge: enamelled copper/32swg.
3. Number of turns: 200
4. Maximum magnetic moment (M) 0.234 Am^2 for side panels (xx , yy) and 0.375 Am^2 for bottom plate (zz) for a current of 50 mA to the coil
5. Thickness: less than 10 mm
6. Scale factor (AT/Volt): 2
7. Back-to-back Zener protection circuit incorporated to limit the voltage across the coil maximum of $\pm 9 \text{ V}$
8. Current limited by providing adequate series resistance in the coil drive circuit.
9. Area of the coil
 - Axx (mm^2): 23,400 mm^2
 - Ayy (mm^2): 23,400 mm^2
 - Azz (mm^2): 37,500 mm^2
10. Mass of the coil: 63 g.
11. Resistance: 35Ω
12. Inductance: 6.4 mH

The developmental model magnetic torquer with Zener diode protection and current-limiting resistors is given in Fig. 1.

4 Magnetometer

The magnetometer is a procured component from Honeywell International Inc., USA. The model selected for our nano-satellite is HMC5883L. The Honeywell HMC5883L is a surface-mount, multi-chip module designed for low-field magnetic sensing with a digital interface for applications such as low-cost compassing and magnetometry.

The HMC5883L includes the state-of-the-art, high-resolution HMC118X series magneto-resistive sensors plus an ASIC containing amplification, automatic degaussing strap drivers, offset cancellation, and a 12-bit ADC that enables 1° to 2° compass

heading accuracy. The I2C serial bus allows for easy interface with the OBC. The HMC5883L is a $3.0 \times 3.0 \times 0.9$ mm surface-mount 16-pin leadless chip carrier (LCC).

The HMC5883L utilizes Honeywell's Anisotropic Magneto-Resistive (AMR) technology that provides advantages over other magnetic sensor technologies. These anisotropic, directional sensors feature precision in-axis sensitivity and linearity. These sensors' solid-state construction with very low cross-axis sensitivity is designed to measure both the direction and the magnitude of Earth's magnetic fields, from milli-gauss to ± 8 gauss. Honeywell's magnetic sensors are among the most sensitive and reliable low-field sensors in the industry. The key benefits are as follows: low-power requirements, high-resolution output, easy data interface using I2C serial bus, and reduced costs.

5 Simulation Results

All simulations are done in MATLAB and Simulink. The International Geomagnetic Reference Field (IGRF) model was used to simulate the magnetic field vectors at various orbital altitudes of the NIUSAT. The simulations were carried out for various gain values of the de-tumbling controller. The simulation results for various gain values with initial tumbling rates of $5^\circ/\text{s}$ about all the three axes are given in Fig. 2a, b. The plots of de-tumbling controller performance with an expanded scale for the individual axis rates and the satellite net are given in Fig. 3a, b.

It can be seen from the above simulation results for lower gain values, the tumbling rates come close to zero about all three axes only after five orbits. This was not favourable because it would take a lot of time. So, the gain values were increased so that the de-tumbling to near-zero rates within two orbits is achieved. The detailed plot of satellite body rate versus time for the optimized gain values is given in Fig. 3a, b.

6 On-Orbit Performance of the De-Tumbling Controller

After a successful launch and separation of the NIUSAT from the launch vehicle, the tumbling rates expected about all the axes was about $5^\circ/\text{s}$. The NIUSAT was programmed to go to de-tumbling mode after the 40 min of delay after separation. When the NIUSAT came to the first visibility of the NIU ground station, the NIUSAT was already in sun tracking mode. This confirmed the excellent performance of the de-tumbling controller, where the satellite body rates of $5^\circ/\text{s}$ have come shown below $1^\circ/\text{s}$, within half an orbit as expected. The following plot (Fig. 4a, b) of the NIUSAT body rates and the magnetometer reading shows that the body rates are below about $0.2^\circ/\text{s}$.

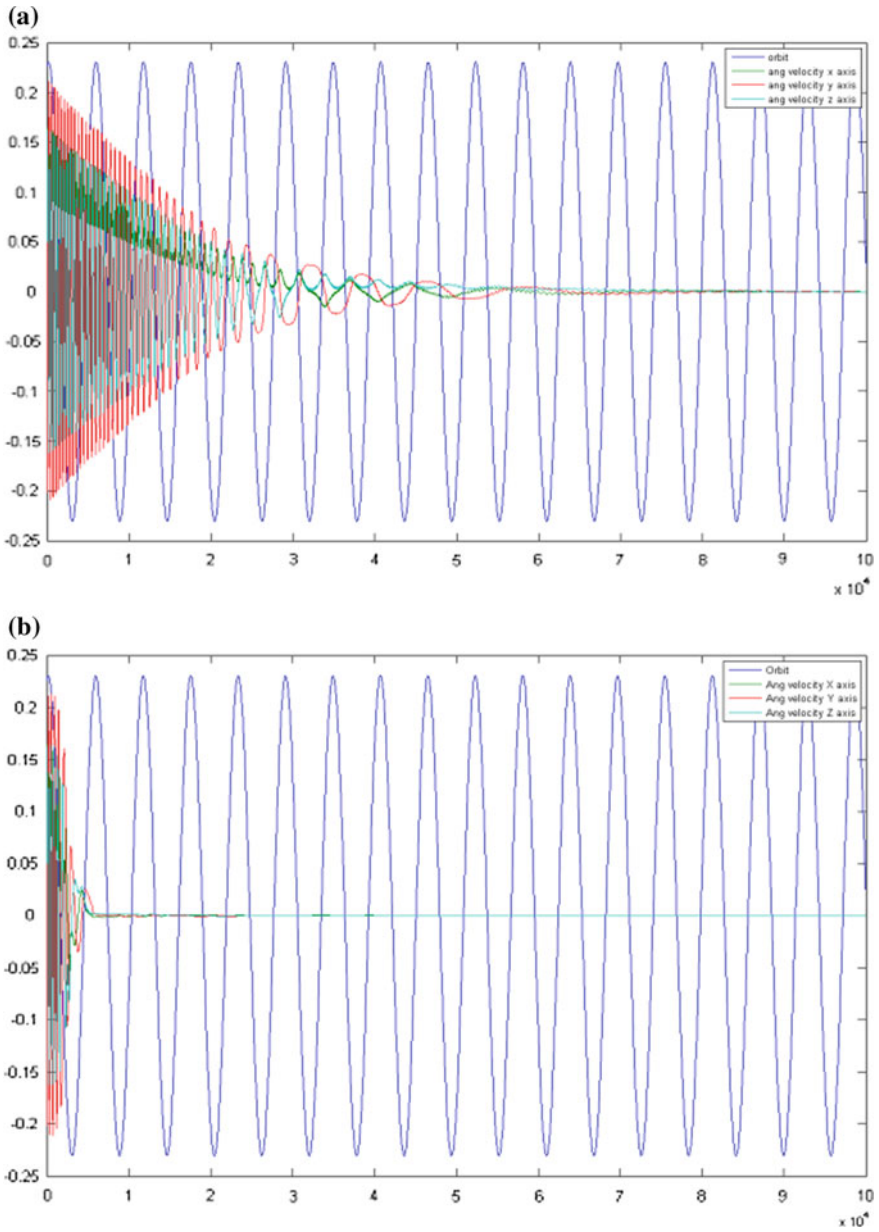


Fig. 2 a De-tumbling with minimum gain. b De-tumbling with increased gain

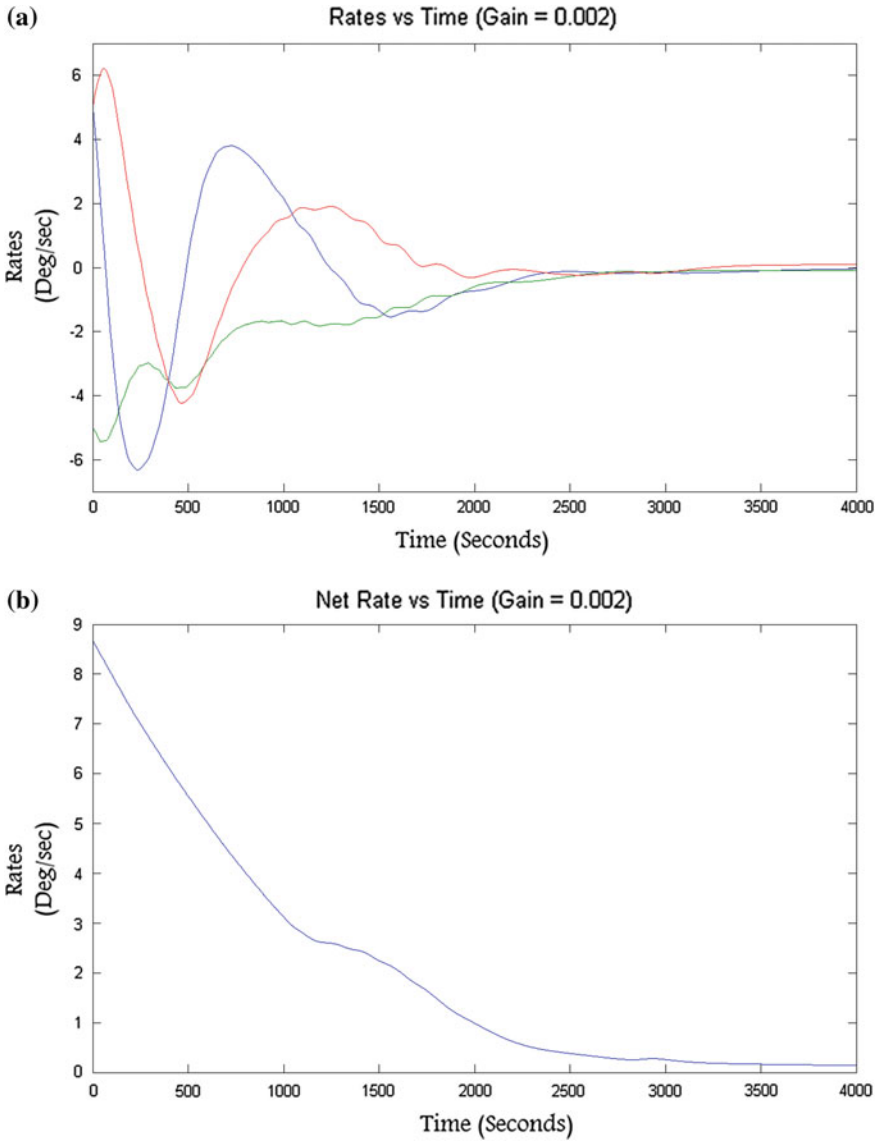


Fig. 3 a De-tumbling rates about each axis. b Net rate reduction versus time

7 Conclusion

After the separation of the NIUSAT from the launcher, the de-tumbling controller was actuated and the controller performance was quite satisfactory. On successful de-tumbling, the NIUSAT entered into sun tracking mode using the micro-reaction

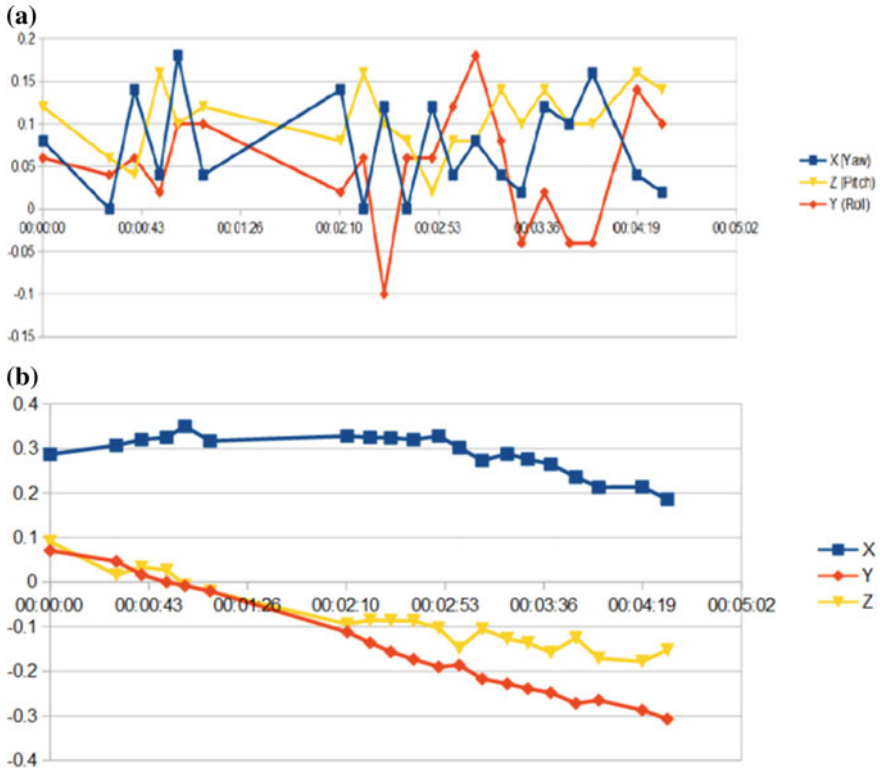


Fig. 4 **a** Body rates of NIUSAT during the first pass. **b** Magnetometer readings

wheels. The basics of attitude control were well understood, and the modelling and simulations have been carried out using the physical parameters of the NIUSAT nano-satellite.

The Configurable Attitude Sensor and Actuator Simulation in the RSAT Test System



M. Roshini, Vishal Rao and M. Mahendra Nayak

Abstract Satellite design involves the development of subsystems like telecommand, telemetry, attitude control, thermal control, structure, and payload. Testing the satellite on ground and qualification is an essential aspect to be considered while designing a satellite. A test system should be built to test and qualify all subsystems and their integrated behavior on ground. RSAT is a small satellite being developed at PES University with automatic identification system (AIS) as a payload. This paper presents the design aspects of such a test system for testing the attitude control system (ACS), which is flexible in terms of adding or removing any sensor or actuator. This paper is an attempt to present details on how the test system is made configurable for manual testing, automated testing, open-loop bench test, closed-loop attitude control testing and hardware-in-the-loop tests. The test system has been built as a generic tool making the system configurable for any satellite with ease.

Keywords User interface · Reconfiguration · Sensors · Actuators · Simulation

Abbreviations

SCHEMACS	Satellite control and health monitoring and communication system
FPGA	Field-programmable gate arrays
ZYBO	Zynq board (FPGA)
GPS	Global positioning system
IMU	Inertial magnetic unit

M. Roshini

V SEM, Electronics and Communication Engineering, PES University, Bangalore, Karnataka 560085, India

V. Rao

V SEM, Computer Science Engineering, PES University, Bangalore, Karnataka 560085, India

M. M. Nayak (✉)

Crucible of Research and Innovation, PES University, Bangalore, Karnataka 560085, India
e-mail: mmnayak@pes.edu

© Springer Nature Singapore Pte Ltd. 2020

PSR. S. Sastry et al. (eds.), *Advances in Small Satellite Technologies*,

Lecture Notes in Mechanical Engineering,

https://doi.org/10.1007/978-981-15-1724-2_7

MTC	Magnetic torquers
OBC	On-board computer
AODCS	Attitude-orbit determination and control system
AIS	Automatic identification system
EPS	Electric power system
DAC	Digital to analog converter
TCP/IP	Transmission control protocol over internet protocol
USB	Universal serial bus
SPI	Serial peripheral interface
RF Link	Radio frequency link
HILS	Hardware-in-the-loop simulation
ACS	Attitude control system

1 General Specifications

Figure 1 is a block diagram of RSAT. RSAT is a three-axis stabilized satellite making use of sun sensors and inertial magnetic unit (IMU). The GPS is used for on-board orbit determination. The actuators used are four reaction wheels and three magnetic torquers (MTC). For testing the satellite, one needs to build a test system which

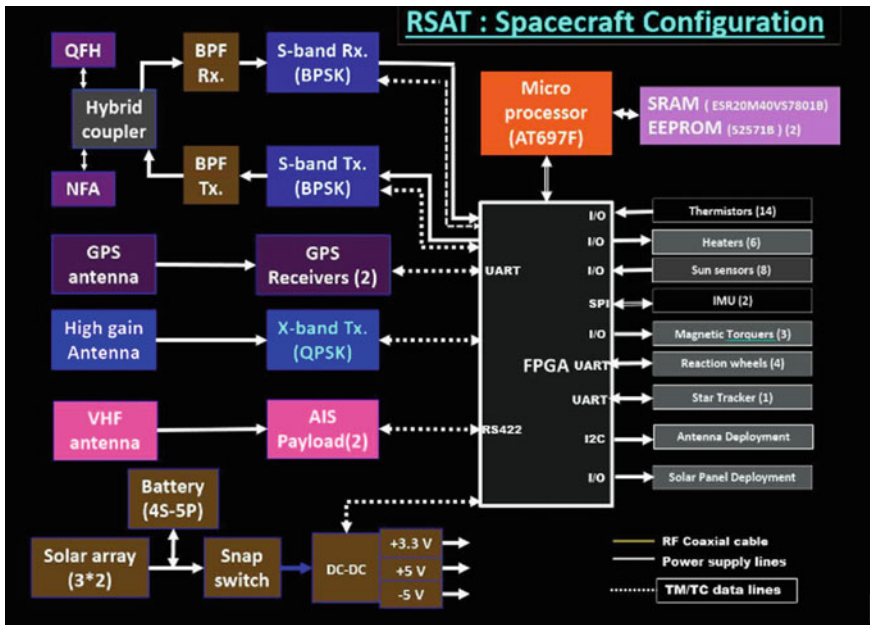


Fig. 1 Block diagram of RSAT

simulates the sensors and spacecraft dynamics driven by the electrical signals from the actuators. The test system needs to provide a platform for carrying out open-loop manual testing, open-loop automated testing, and closed-loop testing of the satellite. The test system should support hardware-in-the-loop simulation where actual sensors are mounted on the three-axis servo table and where the dynamics running on the test system drive the three-axis servo table.

2 Test System Specifications

Figure 2 is the block diagram of the test system for RSAT. Test system consists of telemetry, telecommand, analog sensors, IMU, and MTC. The test system also needs to simulate solar panel and antenna deployment mechanisms.

The PC drives an interface card which in turn simulates the sensor interfaces for the satellite. The interface card is driven through TCP/IP and USB interface. The telecommand and telemetry interfaces are simulated through TCP/IP, and sensor interface is simulated through USB. The list of sensors simulated by the test system

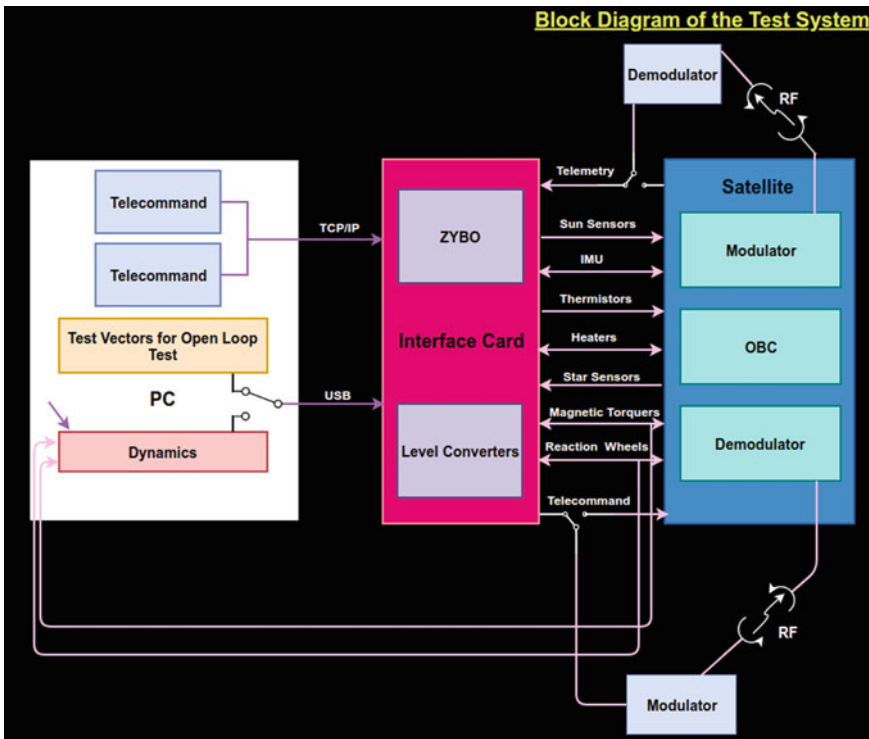


Fig. 2 Block diagram of the test system

Table 1 Sensor specifications

Part no. and manufacturer	Sensor	Interface to OBC	No. of channels	Data format and range	Update rate
Analog devices (ADIS16488A)	IMU	SPI	13	Signed 32 bits and 16 bits	16 ms
Accord (ACC-GPS_NANO)	GPS	UART	189	Hexadecimal	1 s
PES university	Sun sensors	Analog input (0–3.3 V)	16	Signed 12 bits	128 ms
Sinclair interplanetary (RW-0.01)	Reaction wheels (4)	UART	4	Floating point 32 bits	16 ms

is listed in Table 1. The actuator outputs are inputs to the interface card and drive the spacecraft dynamics being simulated in the PC.

The OBC has to perform several different tasks. The most important ones are to receive and respond to commands from the ground station (test system) as well as handle the general housekeeping of the satellite. The OBC needs to collect the telemetry data, format, and encode the data for transmitting to the ground station.

The following subsystems are integrated into the OBC–attitude–orbit determination and control system (AODCS), thermal system, automatic identification system (AIS) payload, telemetry, and telecommand.

In case of telecommand simulation, the required command code will be generated at the SCHEMACS running in the front-end PC. A 64-bit command is encoded to 320 bits, and those 320 bits were sent to the interface card through Ethernet cable using TCP/IP protocol. When the telecommand is connected to the OBC through the ground checkout connector, electrical simulation of the telecommand can be carried out. The test system also allows testing of telecommand through RF, when the command generated in test system is connected to the modulator.

The telemetry subsystem collects the data from various subsystems of the satellite and formats and randomizes the data into a suitable form and encodes it for transmitting to the ground station. The test system allows telemetry testing through electrical signals directly received from OBC or through RF while data is received through the demodulator.

The interface card is designed around the Zybo board (Zynq™-7000) and the level converter card designed for the specific spacecraft. The level converters are used to make sure that the inputs to and outputs from the OBC are in the required voltage range.

3 Open-Loop and Closed-Loop Testing Using Test System

The test system supports the testing the spacecraft on ground. It also supports manual open-loop tests, automated open-loop tests, and closed-loop tests.

In case of manual testing, a keyboard interface is provided through the user interface (UI) to the test sensor interfaces. The static inputs given are verified through telemetry. In case of automated tests, the test file is loaded and the user interface provides support to choose the file for automated open-loop tests. The test inputs could be changed at predefined frequency and actuator response (reaction wheel and magnetic torquers) is measured and compared with the expected result. The test system provides the support to define time interval between each test case.

In case of closed-loop tests, sensor inputs to the OBC are driven by spacecraft dynamics running on in the PC. Tests define initial condition of sensors and commands. Once the test starts, actuator outputs drive spacecraft (dynamics) and sensor inputs. Test system allows the user to define test scenarios and select appropriate test scenarios. SCHEMACS plot facility is used to collect specified telemetry data and plot the same. The sensor data plotted is compared with the expected closed-loop plot.

4 User Interface Overview

In Fig. 3, any number of sensors can be added to the ‘list of active sensors’ panel and can be accessed via a scroll bar. When a particular sensor is selected, the user is presented with an option of either entering the data manually into the channels of the sensor or the user can enter the name of the file which holds data of the sensor selected, and the user also needs to set the update rate, i.e., the time interval within

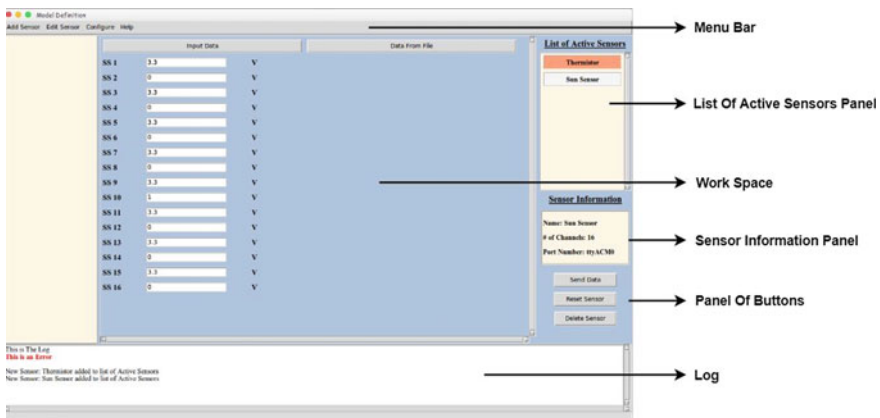


Fig. 3 Typical sensor user interface

which data from the file needs to be updated and sent. If the user has manually entered the values, they are sent instantaneously in an asynchronous manner once the ‘send data’ button is clicked.

The ‘sensor information’ panel holds the sensor name, number of channels present in sensor, and the port used for configuration of the active sensor.

The ‘send data’ button encodes the user input and sends it to interface board. ‘Reset sensor’ helps to set all the fields in the workspace to zero. ‘Delete sensor’ button deletes the sensor from the list of active sensors and also kills the work space for that particular sensor. The sensor being worked on in the workspace can be toggled using the sensor tabs in the ‘list of active sensor panel’.

The ‘log panel’ shows the actions that are taking place in the interface and also the errors detected in the interface.

5 Addition of New Sensors

The user interface can be used to configure any number of sensors as required. Figure 4 shows how to configure a new sensor. The user can select ‘configure new sensor’ from the ‘configure’ option in the menu bar.

The user can enter the required details of each sensor as shown in Fig. 4. After the user enters the number of channels of the sensor, he/she can configure the details

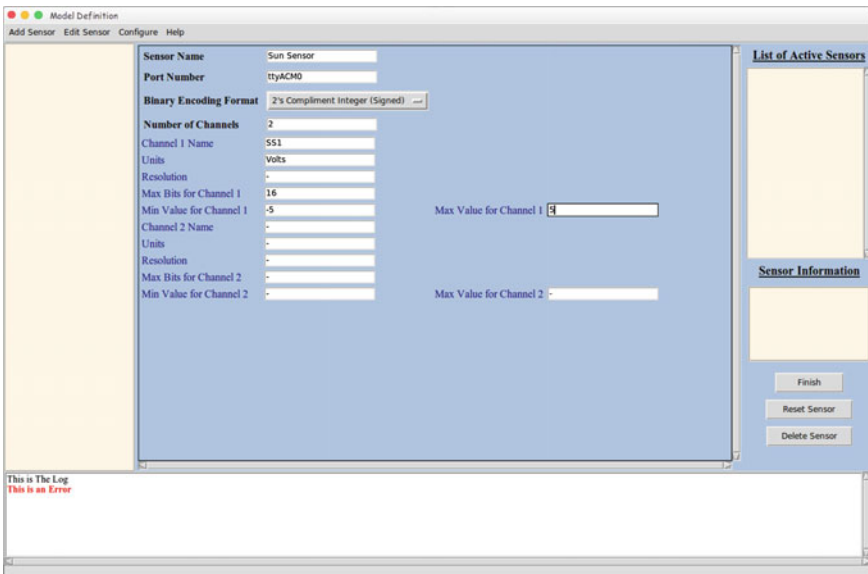


Fig. 4 Configuration of a new sensor

of each channel separately. The user can then click on ‘finish’ button, and the specifications of the sensor and each channel configured will automatically be stored by the user interface for future use. Each satellite can have any number of sensors with their own specifications. The user can set the number of channels for each sensor, the port of communication for that sensor and the binary encoding format for encoding the data before sending the data to the interface card. Each channel of the sensor may also be different and hence can be configured accordingly. The user can set name and the range of the values that this channel can take, i.e., the minimum and the maximum values, the number of bits required for the channel, the resolution of the channel, and the scientific unit of the channel’s value.

6 Reconfiguration for Any Satellite System

The tool has been developed so that it can be reconfigured to support any satellite. This makes the sensors and each of its channels generic, and this format can be used to represent any sensor for a given satellite. The interface is portable and can be used on any system. Since every sensor has some common attributes such as a name or a set of channels, the interface takes this into account and asks the user to specify the values of the common attributes. Once these attributes are set, the sensor is stored as a new unique instance of the generic sensor type. Similarly, each channel has common attributes which are specified by the user and this data is also stored. To add to the configurability, the edit option has been provided and this option can be used to make changes to the sensors’ data while using the tool in testing instead of creating a new sensor with the same data and deleting the old one. The edit option can be used to edit all the attributes of every sensor and all the attributes of each channel. This makes the interface easy to use.

7 Generic Test System

One way of developing a test system is to make a dedicated one for a specific satellite. Here, the test system has been developed as a generic tool, so that the sensors and actuators could be configured with ease for any satellite. The difference in configurations comes in the form of type of electrical interface (SPI, I2C, UART, etc.) used and the data representation (fixed point, floating point, etc.). The test system is generic because it is completely reconfigurable for any satellite. The addition or deletion of sensors and actuators is possible without any complications to ensure reuse of the test system for future satellites. The user interface is developed in Python script and can be executed on any operating system. A facility has been provided for manual and automated open-loop tests, closed-loop tests, and HILS. This makes the tool versatile and portable for multiple missions.

8 Conclusion and Future Work

RSAT test system is a generic tool built to ensure that the system could be easily reconfigured for future satellites. Ease of configurability, flexibility, and portability makes the system versatile. Any test engineer should be able to configure the system and start satellite testing in shortest possible time. The tool reduces the time required to start the test for any type of satellite where the sensors and actuators use standard interface buses. The tool could be easily configured for open-loop tests, closed-loop tests, and HILS tests. The interface card uses the Zybo board which has a processor and configurable FPGA. The interface to OBC is configurable using tools (VIVADO). The future enhancement is to provide a user interface to configure the hardware so that time required to set up test system is further reduced. Once this enhancement is in place, one needs to only design a level converter board while configuring the system for a new satellite.

References

1. RSAT On Board Computer Interface Design Document
2. RSAT OBC Preliminary design Document(PDR)
3. RSAT OBC Detailed Design Document(DDR)
4. RSAT Attitude Orbit Determination and Control System (AODCS) Design Document

Optimal Nonlinear Dynamic Inversion-Based Flight Control System Design for an Aerospace Vehicle



R. Laxman, Arnab Maity, G. Mallikarjun Rao and R. Kranthi Kumar

Abstract Design of flight control systems for an aerospace vehicle is a significant challenge to the control designer. Since the aerospace vehicle is highly nonlinear system, the linear control design may not be effective as well as does lead to large operational domains. Once the number of operating points increases, gain scheduling process in linear control technique becomes cumbersome. To overcome the demerits of linear control design techniques, the nonlinear control strategy techniques can be applied. This paper first discusses mathematical model of the aerospace vehicle. In the present work, the nonlinear control methods are designed to achieve effective performance of an aerospace vehicle without linearizing the plant dynamics. The vehicle dynamics are separated using timescale separation principle, and control synthesis is designed using nonlinear dynamic inversion (NDI) methodology as well as optimal dynamic inversion (ODI). Nonlinear dynamic inversion is the control synthesis technique in which the inherent dynamics of a dynamical system are cancelled out and replaced by desired performance parameters which are selected by the designer. Two-loop control structure is adopted based on vehicle dynamics. In this approach, the outer loop control law generates yaw rate, pitch rate and roll rate commands for the inner loop, based on the side slip angle, angle of attack and bank angle commands. These body rate commands are further tracked by inner loop control law by generating necessary control surface deflections. Since the number of control surfaces is more than the tracking objectives, the inner loop control law is designed by using optimal dynamic inversion (ODI) technique. Nonlinear dynamic inversion and optimal dynamic inversion methods are popular in the application of control design. The

R. Laxman (✉) · G. Mallikarjun Rao · R. Kranthi Kumar
RCI, DRDO, Hyderabad, India
e-mail: laxman.R@rcilab.in

G. Mallikarjun Rao
e-mail: Mallikrajunarao.G@rcilab.in

R. Kranthi Kumar
e-mail: kranthi.kumar@rcilab.in

A. Maity
Aerospace Department, IIT Bombay, Mumbai, India
e-mail: arnab@aero.iitb.ac.in

© Springer Nature Singapore Pte Ltd. 2020
PSR. S. Sastry et al. (eds.), *Advances in Small Satellite Technologies*,
Lecture Notes in Mechanical Engineering,
https://doi.org/10.1007/978-981-15-1724-2_8

detailed generic formulation for the NDI and ODI is discussed. Different perturbation studies on aerodynamic parameters are completed, and robustness of the design is validated. The second-order actuator model for the aerodynamic control surface (fins) is considered in this design. The nominal control law is designed and compared the simulation results for a step input of guidance profiles. Later nominal control design results are compared with respect to off-nominal cases like upper, lower bounds. All the design specification parameters show the satisfactory performance, and design is validated using different guidance profiles. To study the robustness of the control design against parameter uncertainty or model inaccuracies, the design is validated using different guidance profiles.

Keywords Nonlinear dynamic inversion · Optimal dynamic inversion · Guidance commands

1 Introduction

This paper explains about nonlinear dynamic inversion control design philosophy along with optimal dynamic inversion. However, the dynamic inversion can be applied to square systems and optimal dynamic inversion is applicable for non-square systems. Atmospheric re-entry is an important and critical part of any re-entry vehicle. The technical challenges of handling the different phases are always a significant task. In particular, the re-entry phase is very critical and this is due to enormous amount of heat generation during re-entry phase and for high structural loads. In such case, both should be handled carefully mainly for the safety point of view. During re-entry phase (altitude <60 km), aerodynamic forces become comparable with gravitational forces. The aerodynamic forces dominate more than the gravitational forces due to high density of atmosphere in re-entry. Consequently, axial and transverse loads acting on the re-entry vehicle become important issues while designing the atmospheric re-entry system. To address this kind of issues of re-entry system, the vehicle has to be equipped with high performance and reliable flight control system. Attitude control system for the vehicle needs to satisfy the desired tracking commands which are issued by guidance algorithm.

Dynamic inversion is a control strategy in which the inherent dynamics of nonlinear system are cancelled out and replaced with desired dynamics selected by the designer. In the last few decades, the dynamic inversion has more popular control design method for aircraft, re-entry vehicles, missile applications. Most of the literature has applied this methodology to both longitudinal and lateral/directional axes of the air crafts such as F-18 HARV, F-117A and F-16. A variety of approaches for designing guidance and control RLV has been proposed. The structure of the paper is divided into four sections. In the first section, introduction along with literature review has been briefly discussed. In the second section, the plant mathematical model [1] has been described. The generic philosophy of nonlinear dynamic inversion and optimal dynamic inversion along with aerodynamic control formulations

has also been explained in this section. In Sect. 3, the design of dynamic inversion and optimal dynamic inversion-based proportional–integral controller which can be used to the outer loop and inner loop of the control design has been briefly explained. Section 3 also explains about nominal control design by considering first-order actuator dynamics. In Sect. 4, the perturbation simulation results of the control system design are presented. Later aforementioned simulation results are compared with off-nominal simulation results. Conclusions and future scope of the control design technique are given at end.

1.1 Literature Review

Reference [2] has been discussed, preliminary mission design along with analysis of winged body RLV. The authors have also discussed trajectory optimization using quadratic programming. The trajectory optimization problem in this case is solved using optimal control method like path constraints, terminal constraints, etc. The proposed design has been validated using 2-DOF point mass model to see the performance of the design and robustness. Reference [3] has discussed the sliding mode control for designing the control system along with the sliding-based disturbance observer. Here, they have proposed the gain adoption logic for flight control design of RLV. This design methodology has been validated using 6-degree of freedom model, and results are generated with nominal and dispersion in the parameters. Reference [4] has proposed a guidance design methodology using optimal control technique like calculus of variations. Here, the authors have developed two different formulations for guidance using optimal path to go (OPTG) and adaptive production guidance (APG) methods. Similarly, Ref. [5] has implemented an integrated adaptive guidance and control for RLV. The authors proposed a time-variant LQR theory-based IAG&C approach. Both guidance and control design are discussed using optimal control techniques. They have designed a nonlinear dynamic inversion method which can be used to generate guidance commands. The IGC is simulated on high-fidelity environment like 6-DOF along with nonlinearities. Robustness of the design was demonstrated using Monte Carlo simulations. Reference [6] has proposed the control allocation design for RCS design using indexed control method. In this scenario, the authors addressed about the nonlinear control synthesis using reaction control system (RCS). This methodology was validated using point mass vehicle dynamics. Reference [7] has proposed a nonlinear control using dynamic inversion as well as optimal dynamic inversion (ODI) control techniques. This design method is also integrated along with state estimation using EKF for full state feedback. The authors have demonstrated the ODI/EKF-based control design using vehicle dynamics on six-DOF model for reusable launch vehicle (RLV).

In Ref. [8], the authors have proposed a nonlinear controller design, using model following neuro-adaptive method for reusable launch vehicle. This method assures the tracking of guidance commands in spite of uncertainties in the model. The authors have designed control design technique in two different methods, namely (a) nominal

design using dynamic inversion and (b) optimal dynamic inversion for RCS design. The simulation results with six-DOF dynamics along with realistic constraints like actuator dynamics, control bounds, RCS constraints, etc., clearly demonstrated the good command following as well as robustness of the overall design was presented. In the paper [9], the authors have proposed a nonlinear optimal guidance and control scheme for RLV in the pitch plane. In this scenario, the authors have discussed the guidance design using model predictive static programming technique which provides a finite nonlinear sub-optimal guidance law solution. Reference [10] has proposed the guidance design methodology using model predictive static programming which is a combination of model predictive control and approximate dynamic programming (ADP) which gives efficient technique to solve fixed finite horizon optimal control problems. The authors have designed the trajectory optimization problem and validated using 6-DOF simulation along with perturbation in the parameters.

In Ref. [11], the authors have proposed a new nonlinear control technique for ascent phase of reusable launch vehicle and designed using $\theta - D$ sub-optimal control method. This problem is a typical optimal control problem with quadratic cost function; in this design, the authors also elaborated by using comparative study of classical PID design along with $\theta - D$ method. In Ref. [12], the authors have developed a new approach of nonlinear robust controller designed using time-varying sliding mode manifold. Here, the authors also elaborated that using this method the system performance is more robust towards the model uncertainties/disturbances. The control system is designed using time-varying approach which will have more robust in terms of tracking of guidance command. The authors have proposed integrated guidance and control synthesized for RLV along with 6-DOF model. Trajectory design is done using optimal control like path constraints, terminal constraints, etc. Reference [13] has presented a new reconfigurable inner loop control law consisting of dynamic inversion and control allocation method. A new approach has been proposed in Ref. [14] for the development of autonomous guidance and control systems for RLV to handle large dispersion.

2 Dynamical Model of the Vehicle

2.1 Mathematical Model

The re-entry vehicle model used in this work is a automatic landing flight experiment vehicle (ALFLEX).

The aerodynamic parameters are given at one particular altitude (operating point), i.e. at re-entry altitude which is around 65 km. The input data for designing the control system is given at a particular operation point of the re-entry vehicle ALFLEX, i.e. Ref. [1]. The aerodynamic parameters and mass and inertia data are available at particular air density of $\rho = 1.156 \text{ kg/m}^3$.

The complete aerodynamic, inertia, gravitational parameters are given at one particular one operating point. These parameters include aerodynamic drag force coefficients, lift and side force coefficients along with rolling moment, pitching moment and yawing coefficients. The vehicle configuration parameters like mass, inertia and weight are also given in Table 1. The simplified plant model equations of motion along with certain assumptions include:

- Forward velocity (V), weight (W) and air density (ρ) are constant.
- Angle of attack (α) and side slip angle (β) are small.

Force-related equations:

$$\dot{\alpha} = -p\beta + q + \hat{z} + \frac{g}{V} \cos \phi \cos \theta \quad (1)$$

$$\dot{\beta} = p \sin \alpha - r \cos \alpha + \hat{y} + \frac{g}{V} \sin \phi \cos \theta \quad (2)$$

Moment equations:

$$\dot{p} = i_1 \left(-qr + i_a pq + \left(\frac{L}{I_x i_1} \right) \right) + \left(\frac{I_{xz}}{I_x} \right) \dot{r} \quad (3)$$

$$\dot{q} = i_2 (rp + i_b (-p^2 + r^2)) + \left(\frac{M}{I_y i_2} \right) \quad (4)$$

$$\dot{r} = i_3 \left(-pq - i_c qr + \left(\frac{N}{I_z i_3} \right) \right) + \left(\frac{I_{xz}}{I_z} \right) \dot{p} \quad (5)$$

The other kinematic equations:

$$\dot{\theta} = q \cos \phi - r \sin \phi \quad (6)$$

$$\dot{\phi} = p + (q \sin \phi \tan \theta + r \cos \phi) \tan \theta \quad (7)$$

$$\dot{\psi} = \frac{(r \cos \phi + q \sin \phi)}{\cos \theta} \quad (8)$$

Table 1 Physical data of re-entry vehicle

Parameter	Value	Parameter	Value
W (kg)	7448.0	S (m ²)	9.45
V (m/s)	73.84	b (m)	3.295
c (m)	3.154	I_{xx} (kg m ²)	407
I_{yy} (kg m ²)	1366	I_{zz} (kg m ²)	1643
I_{xz} (kg m ²)	10.4	–	–

Notations for the dynamics are: α : angle of attack, β : side slip angle and p, q, r : body rates in x -, y -, z -axes, respectively. ϕ, θ, ψ : are attitude angles in x -, y -, z -axes, whereas other force coefficient parameters are

$$\hat{y} = QSC_y \left(\frac{g}{WV} \right) \quad (9)$$

$$\hat{z} = QSC_z \left(\frac{g}{WV} \right) \quad (10)$$

$$\begin{aligned} C_z &= (C_{z0} + C_{z\alpha}(\alpha - \alpha_0) + C_{z\delta e}\delta_e - C_{z\delta e}\delta_{e0}) \\ C_y &= (C_{y\beta}\beta + C_{\delta r}\delta_r) \end{aligned} \quad (11)$$

The other inertia and its cross-coupling parameters are given as:

$$i_1 = \frac{I_z - I_y}{I_x}, \quad i_2 = \frac{I_z - I_x}{I_y}, \quad i_3 = \frac{I_y - I_x}{I_z}, \quad i_a = \frac{I_{xz}}{I_x} \frac{1}{i_1}, \quad i_b = \frac{I_{xz}}{I_y} \frac{1}{i_2}, \quad i_c = \frac{I_{xz}}{I_z} \frac{1}{i_3}$$

$$\hat{y} = \frac{gY_a}{WV}, \quad \hat{z} = \frac{gZ_a}{WV}, \quad \hat{l} = \frac{L}{i_1 I_x}, \quad \hat{m} = \frac{M}{i_2 I_y}, \quad \hat{n} = \frac{N}{i_3 I_z}$$

where Y_a and Z_a are aerodynamic forces and L, M, N aerodynamic moments about the centre of gravity and g is the gravity. The given simplified equations are highly nonlinear with cross-coupling between axes. The given data is for level flight with steady-state pitch angle θ_0 , and angle of attack α_0 is trivial trim point. Those original equations can be represented as state space form.

$$\dot{X} = F(x, \delta) \quad (12)$$

which can be further simplified as a control affine form in which state and control (input) can be separated. The equation can be rewritten as a nonlinear system is of the form where state and control can be separated.

The mass and inertia, velocity, initial conditions at the given altitude and the vehicle configuration are given in Table 1.

2.2 Aerodynamic Control

Some of the important equations are given to obtain the relation between aircraft control surfaces and missile control surface (aerodynamic control surface) as fins. These fins are control surfaces which are deflected using electro-mechanical actuators.

This cross form is converting from aileron, elevator, rudder to four control surfaces in the missile configuration. The relation between the aircraft control surfaces and four missile control surfaces is given below.

$$\begin{aligned}
\delta_a &= \left[\frac{\delta_1 + \delta_2 + \delta_3 + \delta_4}{4} \right] \\
\delta_e &= \left[\frac{\delta_1 + \delta_2 - \delta_3 - \delta_4}{4} \right] \\
\delta_r &= \left[\frac{-\delta_1 + \delta_2 + \delta_3 - \delta_4}{4} \right]
\end{aligned} \tag{13}$$

These cross form equations are converting from aileron, elevator, rudder to four control surfaces in the missile configuration mentioned [15]. The inner loop dynamics are written in terms of aforementioned control surfaces, i.e. $\delta_1, \delta_2, \delta_3, \delta_4$.

2.3 Generic Dynamic Inversion Philosophy

Gain scheduling methodology employs the well-developed linear control techniques to the control of nonlinear systems. In this process, a number of operating points are selected. At each of these points, the designer makes a linear time-varying approximation to the plant dynamics and designs a linear controller for each linearized plant. Between operating points, the parameter of compensators is interpolated which will result in a global compensator. The scheduling variable may not be one variable, or it can be multiple variables. But usual practice is to choosing the slowly varying parameter as the scheduling variable. Usually in flight control design, dynamic pressure and Mach number are chosen to be the scheduling parameters. The robustness and performance, and stability are guaranteed by extensive simulation studies like non-real-time simulation or real-time simulation method like hardware-in-the-loop simulation (HILS). The issue with this method is that there may be loss in the minimum phase property. In such case if the parameters of the model are updated during online, there may be chances of instability. So to avoid this kind of disadvantages in gain scheduling, some of the nonlinear control design techniques are available like dynamic inversion, optimal dynamic inversion, timescale separation with dynamic inversion, dynamic inversion augmentation with neuro-adaptive control design and model reference adaptive control. These control methods can be applied for control design which will make system more robust. The theory of nonlinear dynamic inversion and optimal dynamics is adopted from Ref. [16].

The general philosophy of the dynamic inversion is:

- Carry out the co-ordinate transformation such that the problem appears to be linear.
- Design the controller for the linear system using linear control design techniques.
- Obtain the original system using inverse transformation.
- The control design is carried out by enforcing error dynamics.

Given nonlinear dynamics can be represented as:

$$\dot{X} = f(X, U), \quad Y = CX \tag{14}$$

$X \in \mathcal{R}^N$, $U \in \mathcal{R}^m$, $Y \in \mathcal{R}^p$, the goal is to track the output $Y \rightarrow Y^*$, where Y^* is desired profile. Special cases were control affine and square system in which state and control can be separated.

$$\dot{X} = [f(X)] + [g(X)]U \quad (15)$$

$p = m$, and $g_Y(X)$ is non-singular.

Derive the output dynamics by taking differentiation of Y

$$\dot{Y} = \frac{\partial h}{\partial X} \dot{X} = \frac{\partial h}{\partial X} [f(X) + g(X)U] = f_Y(X) + g_Y(X)U \quad (16)$$

Define error of tracking as:

$$E(t) = [Y(t) - Y(t)^*] \quad (17)$$

Select a fixed gain $K > 0$ such that the first-order error dynamics are: $\dot{E} + KE = 0 \Rightarrow E = E_0 e^{-Kt} \rightarrow 0$ as $t \rightarrow \infty$ $\dot{Y} - [\dot{Y}^*] + K[Y - Y^*] = 0$.

Which can be further simplified

$$f_Y(X) + g_Y(X)U = \dot{Y}^* - K[Y - Y^*]$$

Therefore, solve for the controller

$$U = [g_Y(X)]^{-1} \{ \dot{Y}^* - K(Y - Y^*) - f_Y(X) \} \quad (18)$$

The order of the error dynamics is dictated by the relative degree of the problem, which can be defined as the number of time the output needs to be differentiated so that control variable appears explicitly in the equation. The designed control law (U) such that which cancels the non linearity. If the relative degree is well defined, then design done is mentioned earlier. The advantages of dynamic inversion design are:

- Simple design: No need of tedious gain scheduling hence some times called as universal gain scheduling.
- Easy online implementation since it leads to a closed-form solution.
- Asymptotic stability is guaranteed for the error dynamics.
- No problem if the parameters are updated.

2.4 Generic Theory of Optimal Dynamic Inversion

There are some issues in dynamic inversion control design like inverse does not exists for all time which is limiting case in dynamic inversion where the input matrix non-square where the no. of control surfaces are not equal to the no. of tracking

objectives. In such cases, if inverse does not exist, then do not update the control law unless $g_Y(X) > \epsilon$; otherwise, it may lead to performance degradation. When the number of control surfaces is less than no. of tracking objectives, perfect tracking is not possible. In another case where the no. of control surfaces is more than the tracking objectives, additional objectives can be demanded in the design. This type of approach is called optimal dynamic inversion (ODI). The number of control surfaces is four in our application, and the number of tracking objectives is three. Therefore, the formulation of optimal dynamic inversion is based on equality constrained problem by minimizing the augmented cost function. This type of control law is designed for only inner controller in our application. The formulations for this optimal control-based dynamic inversion control are same as NDI. In this case, the objective is to convert any three control surface forms of configuration to cross form (four fin control surfaces). The relation between these is given in Eq. (12) along with generic optimal control design formulation. All the theories related to NDI and ODI are adopted from Ref. [16] for control synthesis formulations.

The system dynamics and measurement model are represented by

$$\dot{X} = f(X, U), Y = CX \quad (19)$$

In this case if the number of control surfaces is more than no. of tracking objectives, the additional objectives can be demanded in the design. This type of design is called optimal dynamic inversion.

$X \in \mathcal{R}^N$, $U \in \mathcal{R}^m$, $Y \in \mathcal{R}^p$, the goal is to track the output $Y \rightarrow Y^*$, where Y^* is desired profile. Special cases were control affine and square system in which state and control can be separated.

$$\dot{X} = [f(X)] + [g(X)]U \quad (20)$$

$p = m$, and $g_Y(X)$ is non-singular.

Derive the output dynamics by taking differentiation of Y

$$\dot{Y} = \frac{\partial h}{\partial X} \dot{X} = \frac{\partial h}{\partial X} [f(X) + g(X)U] = f_Y(X) + g_Y(X)U \quad (21)$$

Define error of tracking as:

$$E(t) = [Y(t) - Y(t)^*] \quad (22)$$

Select a fixed gain $K > 0$ such that the first-order error dynamics are: $\dot{E} + KE = 0 \Rightarrow E = E_0 e^{-Kt} \rightarrow 0$ and as $t \rightarrow \infty \dot{Y} - [\dot{Y}^*] + K[Y - Y^*] = 0$.

Which can be further simplified

$$f_Y(X) + g_Y(X)U = \dot{Y}^* - K[Y - Y^*]$$

Therefore, solve for the control law

$$g_Y(X)U = \{\dot{Y}^* - K(Y - Y^*) - f_Y(X)\} \quad (23)$$

Since the g_Y is not square matrix, optimal dynamic inversion philosophy can be applied. Aforementioned equation can be rewritten as $AU = b$. Constructing the cost function minimize subjected to $AU = b$

- Minimize cost function:

$$J = \frac{1}{2}U^T R U \quad (24)$$

- Subjected to constraint: $AU = b$, where $A = g_Y(X)$

$$b = \{\dot{Y}^* - K(Y - Y^*) - f_Y(X)\}$$

- The complete solution can be obtained by augmenting the performance index:

$$J = \frac{1}{2}U^T R U, R = \text{diag}(r1, r2, r3, r4) \quad (25)$$

$$\bar{J} = \frac{1}{2}U^T R U + \lambda^T (AU - b) \quad (26)$$

- The necessary conditions are for the augmented cost function

$$\frac{\partial \bar{J}}{\partial U} = RU + A^T \lambda = 0 \quad (27)$$

$$\frac{\partial \bar{J}}{\partial \lambda} = AU - b = 0 \quad (28)$$

- Carrying out necessary simplifications, we can get the control equation

$$\begin{aligned} U &= -R^{-1}A^T \lambda \\ AU &= b \\ A(-R^{-1}A^T \lambda) &= b \\ \lambda &= -(ARA^T)^{-1}b \\ U &= R^{-1}A^T \left\{ (AR^{-1}A^T)^{-1} \right\} b \end{aligned} \quad (29)$$

where the notation is used for the simplification

$$A^+ = R^{-1}A^T \left\{ (AR^{-1}A^T)^{-1} \right\} \quad (30)$$

The control law is formulated, and if $R = I$ then the optimal dynamic inversion method can be applied if the system is not square.

3 Overall Control Design

3.1 Outer Loop Control

The complete vehicle dynamics are separated into two timescales and designed the controller using nonlinear dynamic inversion along with optimal dynamic inversion. The vehicle dynamics are separated as fast, slow dynamics using timescale approach. This type of control synthesis is two-loop control structure in which the outer loop commands are generated by guidance algorithm; further, these commands are converted into equivalent body rates (p, q, r) which are inputs to the inner loop controller. Similarly, the inner loop control generates the required deflection commands as per commanded profiles from outer loop and these deflections are forcing function to model (plant). This model generates outputs which are measurable by considering full state feedback. In this design, inner loop dynamics are faster than the outer loop dynamics. Generally, the inner loop dynamics are 3–5 times faster than outer loop dynamics. In this method of design, the inner loop dynamics 2–1.5 times faster than outer loop dynamics. The tuning method can be chosen as settling time requirement in the process. The outputs of the outer loop are used as the reference input of the inner loop. The outputs of the inner loop controller are sent to a pair of first-order actuator dynamics. This actuator commands are the forcing functions to the vehicle model (plant).

The desired commands are from guidance computer as a forcing function to the outer controller block. Further, these commands will generate commanded body rates to the inner loop. These commanded body rates are forcing function to inner loop controller, and these body rates will generate required control deflection which is input to the vehicle dynamics. The actual states coming out from vehicle dynamics are feedback through sensors and compared with the outer loop commanded and inner loop commanded profiles so that error can be minimized such that control action can take place. The block diagram is given in Fig. 1, which is a pictorial representation of control design using nonlinear dynamic inversion as well as other modern control techniques.

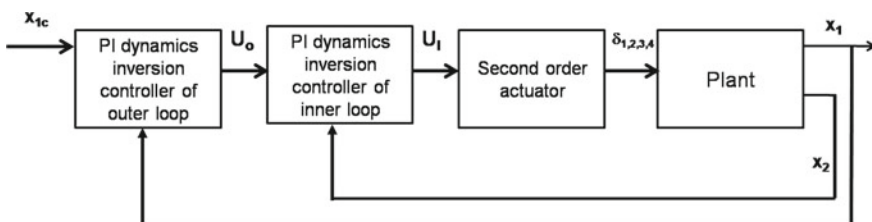


Fig. 1 Closed-loop system with PI dynamic inversion controller

Where the notations in Fig. 1 are

$$x_{1c} = [\alpha^* \beta^* \phi^*]'$$

$$x_1 = [\alpha \beta \phi]', \quad (31)$$

and

$$x_2 = [p \ q \ r]', \quad (32)$$

the control laws for inner loop and outer loop control systems are defined in the previous sections. The complete dynamics can be separated into two parameter timescales using time separation principle, and those dynamics are used for control design using dynamic inversion. The complete equations can be written as in the form of affine system. The vehicle dynamics are separated into fast and slow variables. The slow variables are considered as outer loop variables which are α , β , ϕ . The dynamics for the outer loop control are given as:

$$\begin{bmatrix} \dot{\alpha} \\ \dot{\beta} \\ \dot{\phi} \end{bmatrix} = \begin{bmatrix} -p\beta + q + \hat{z} + \frac{g}{v} \cos \phi \cos \theta \\ p \sin \alpha - r \cos \alpha + \hat{y} + \frac{g}{v} \sin \phi \cos \theta \\ p + q \sin \phi \tan \theta + r \cos \phi \tan \theta \end{bmatrix} \quad (33)$$

The dynamics are converted into control affine form as outer loop dynamics can be written in state space form

$$\dot{x}_o(t) = f_o(x_o, t) + G_o(x_o, t) U_o(t) \quad (34)$$

$$y_o(t) = C_o x_o(t) \quad (35)$$

where C_o is a $I_{3 \times 3}$ matrix for the output measurement. The detailed equations are given below, in which state and control input can be further simplified as

$$f_o(x_o, t) = \begin{bmatrix} \hat{z} + \frac{g}{v} \cos \phi \cos \theta \\ \hat{y} + \frac{g}{v} \sin \phi \cos \theta \\ 0 \end{bmatrix},$$

$$G_o(x_o, t) = \begin{bmatrix} -\beta & 1 & 0 \\ \sin \alpha & 0 & -\cos \alpha \\ 1 & \sin \phi \tan \theta & \cos \phi \tan \theta \end{bmatrix}$$

where state and control is given as

$$x_o = \begin{bmatrix} \alpha \\ \beta \\ \phi \end{bmatrix}, \quad U_o = \begin{bmatrix} p \\ q \\ r \end{bmatrix}$$

The derivation of control law using first order error dynamics using dynamic inversion philosophy. Let the desired/commanded tracking signals can be written as

$$x_o^* = \begin{bmatrix} \alpha^* \\ \beta^* \\ \phi^* \end{bmatrix} = \begin{bmatrix} \alpha^* \text{ {Computed from the guidance}} \\ 0 \\ \phi^* \text{ {Computed from the guidance}} \end{bmatrix} \quad (36)$$

Define the tracking error in outer loop as

$$e_o = x_o^* - x_o = \begin{bmatrix} \alpha^* \\ \beta^* \\ \phi^* \end{bmatrix} - \begin{bmatrix} \alpha \\ \beta \\ \phi \end{bmatrix} = \begin{bmatrix} \alpha^* - \alpha \\ \beta^* - \beta \\ \phi^* - \phi \end{bmatrix} \quad (37)$$

$$\dot{e}_o + K_{i_p} e_o + K_{i_o} \int_0^t (e_o dt) = 0 \quad (38)$$

$$\begin{bmatrix} p^* \\ q^* \\ r^* \end{bmatrix} = G_o^{-1} \times \left(\begin{bmatrix} \dot{\alpha}^* \\ \dot{\beta}^* \\ \dot{\phi}^* \end{bmatrix} + \begin{bmatrix} k_\alpha & 0 & 0 \\ 0 & k_\beta & 0 \\ 0 & 0 & k_\phi \end{bmatrix} e_o + K_{o_i} \int_0^t (e_o dt) - f(\alpha, \beta, \phi) \right) \quad (39)$$

3.2 Inner Loop Control

Similarly, the inner loop dynamics are p, q, r , which are considered as fast variables. The updating of inner loop dynamics must be 3–5 times faster than that of outer loop variables.

$$\begin{bmatrix} \dot{p} \\ \dot{q} \\ \dot{r} \end{bmatrix} = \begin{bmatrix} i_1(-qr + i_a pq + \frac{L}{i_{1rx}}) + (\frac{L_{xz}}{I_x})\dot{r} \\ i_2(rp + i_b(-p^2 + r^2)) + \frac{M}{i_{2ly}} \\ i_3(-pq - i_c qr + \frac{N}{i_{3lz}}) + (\frac{L_{xz}}{I_z})\dot{p} \end{bmatrix} \quad (40)$$

These inner loop dynamics can be written in the form of state and control as written for outer control design

$$\dot{x}_I = f_I(x_I, t) + G_I(x_I, t) U_I(t) \quad (41)$$

$$y_I(t) = C_I x_I(t) \quad (42)$$

where C_I is a $I_{3 \times 3}$ identity matrix for the output measurement where state and control is given by

$$x_I = \begin{bmatrix} p \\ q \\ r \end{bmatrix}, \quad U_I = \begin{bmatrix} \delta_1 \\ \delta_2 \\ \delta_3 \\ \delta_4 \end{bmatrix} \quad (43)$$

Similarly, the inner loop errors are defined as

$$e_i = x_i^* - x_i = \begin{bmatrix} p^* \\ q^* \\ r^* \end{bmatrix} - \begin{bmatrix} p \\ q \\ r \end{bmatrix} = \begin{bmatrix} p^* - p \\ q^* - q \\ r^* - r \end{bmatrix} \quad (44)$$

Since the system is assumed as the all states are measurable. Here in this case assuming that the relative degree is 1 i.e how many times differentiate the output equation the control term should appear in the equation.

$$\dot{e}_i + K_{i_p} e_i + K_{i_i} \int_0^t (e_i dt) = 0 \quad (45)$$

Therefore, the outer controller is derived as a function of states and desired dynamics, i.e. gains. These gains are $K_i = \frac{4}{\tau}$ where K_i is the channel gain and the outer loop is also function of control input and integral, proportional error constants. In similar way for the inner loop dynamics, controller equations can be derived using first-order error dynamics. The control law formulation is derived using optimal dynamic inversion method.

$$\begin{bmatrix} \delta_{1c} \\ \delta_{2c} \\ \delta_{3c} \\ \delta_{4c} \end{bmatrix} = R^{-1} A^T \left\{ (A R^{-1} A^T)^{-1} \right\} b$$

$$\begin{bmatrix} \delta_{1c} \\ \delta_{2c} \\ \delta_{3c} \\ \delta_{4c} \end{bmatrix} = (A^+)^{-1} \times \left\{ \begin{bmatrix} \dot{p}^* \\ \dot{q}^* \\ \dot{r}^* \end{bmatrix} + \begin{bmatrix} k_p & 0 & 0 \\ 0 & k_q & 0 \\ 0 & 0 & k_r \end{bmatrix} e_i + K_{i_i} \int_0^t e_i dt - f_R(x_2) \right\} \quad (46)$$

where k_p, k_q, k_r are the desired performance parameters (gains) and are functions of settling time or time constant of the system. The outer loop controller generates commands of p^*, q^*, r^* which are the desired commands for the inner loop control. The external commanded (guidance commands) profiles are given to the outer loop control as the value of 6° of angle of attack (α^*) as a step and 2° of roll angle (ϕ^*)

as a step and side slip angle (β^*) is forced to zero to avoid the undue yaw rate. The proportional and integral gains are tune-based iterative method and settling time of the desired performance where the control inputs are mapped from $\delta_a, \delta_e, \delta_r$ to cross form of $\delta_1, \delta_2, \delta_3, \delta_4$.

3.3 Nominal Control Design with Actuator Dynamics

The control deflections are generated by the inner loop controllers which are the forcing function to the actuator. These control surfaces will be deflected using servo electronics. These actuators can be modelled as a first-order or second-order system. In our simulation, we modelled the each actuator as a second-order dynamics. All these four models are similar in nature. These dynamics are considered into the simulation to study the controller performance under these dynamics. The actuator dynamics for the four actuators are given by the following mathematical equations. In this case, second-order actuator model parameters are given with natural frequency of $w_n = 250$ and damping ratio as $\zeta = 0.7$.

$$\ddot{\delta}_{o1} = -2\zeta w_n \dot{\delta}_{o1} - w_n^2 \delta_{o1} + w_n^2 \delta_1 \quad (47)$$

$$\ddot{\delta}_{o2} = -2\zeta w_n \dot{\delta}_{o2} - w_n^2 \delta_{o2} + w_n^2 \delta_2 \quad (48)$$

$$\ddot{\delta}_{o3} = -2\zeta w_n \dot{\delta}_{o3} - w_n^2 \delta_{o3} + w_n^2 \delta_3 \quad (49)$$

$$\ddot{\delta}_{o4} = -2\zeta w_n \dot{\delta}_{o4} - w_n^2 \delta_{o4} + w_n^2 \delta_4 \quad (50)$$

The actual aerodynamic control deflections observed by the vehicle are obtained through the actuator. The maximum deflections attainable from the aileron and rudder actuators are limited to 30° for all the four control fins, respectively. The outer loop controller gain values used in the simulation are given in Table 2. Similarly in the inner loop controller, the gain values used in the simulation are given in Table 3. These gains are adopted from the settling time of the desired dynamics.

Table 2 Outer loop gains

S. No.	Proportional gain	Integral gain
1	$K_\alpha = 4.0$	$K_{\alpha_i} = 0.02$
2	$K_\beta = 6.0$	$K_{\beta_i} = 1.8$
3	$K_\phi = 4.5$	$K_{\phi_i} = 0.02$

Table 3 Inner loop gains

S. No.	Proportional gain	Integral gain
1	$K_p = 4.9$	$K_{p_i} = 1.2$
2	$K_q = 7.5$	$K_{q_i} = 4.5$
3	$K_r = 6.4$	$K_{r_i} = 2.5$

3.4 Parameter Choice Principle

The gains in the simulations are taken from the settling time of the desired dynamics in the system. Taking the outer loop dynamics for the instance, α channel equations are taken. From the control law equation (32) and substitute into equation of α dynamics which is given in Eq. (27).

$$\dot{x}_1 = K_{\alpha_p}(x_{1c} - x_1) + K_{\alpha_i} \int_0^t (x_{1c} - x_1) dt \quad (51)$$

The above equation is a MIMO system with the three tracking objectives. We can apply the Laplace transform of Eq. (44) to get the transfer function

$$s\alpha(s) = K_{\alpha_p}(\alpha_c(s) - \alpha(s)) + \frac{K_{\alpha_i}}{s}(\alpha_c(s) - \alpha(s)) \quad (52)$$

Consequently,

$$G_{\alpha(s)} \approx \frac{\alpha(s)}{\alpha_c(s)} = \frac{sK_{\alpha_p} + K_{\alpha_i}}{s^2 + K_{\alpha_p}s + K_{\alpha_i}} \quad (53)$$

The aforementioned equation is the transfer function of the alpha channel control system. According to the Routh–Hurwitz criterion, if we choose $K_{\alpha_p} > 0$, $K_{\alpha_i} > 0$ the control system of (46) is stable. As per the timescale separation principle, the bandwidth of actuator should be more than triple the inner loop. The bandwidth of the inner loop should be more than the outer loop. Therefore, definition of bandwidth of the $G_{\alpha(s)}$ is expressed as in the form of gains

$$\omega_\alpha = \sqrt{(2K_{\alpha_i} + K_{\alpha_p}^2 + \sqrt{8K_{\alpha_i}^2 + 4K_{\alpha_i}K_{\alpha_p}^2 + K_{\alpha_p}^4})} \quad (54)$$

Thus, when we can choose K_{α_p} , K_{α_i} , ω_α should be one in three of the inner loop bandwidth. Similarly, we can obtain the limitation control parameters for other control systems.

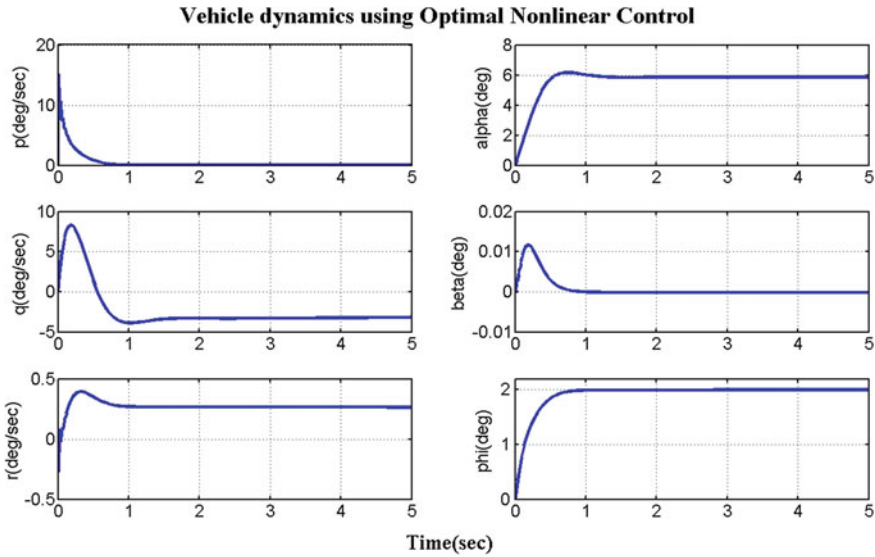


Fig. 2 Closed-loop state trajectory

3.5 Nominal Control Design Simulation Results

The control methodology is implemented in MATLAB and simulated results. The results show the satisfactory performance for the external guidance commands. The designed control system is tracking for the step guidance commands which is shown in Figs. 2, 3, 4 and 5. All the simulation results show satisfactory performance for given initial conditions.

4 Robustness Study

4.1 Perturbation Study

The designed control system is tracking well under nominal design, and the robustness of the design is further validated by perturbing the aerodynamic parameters by 0%. All the simulation results show satisfactory performance. The tracking of external guidance commands is given below.

To validate the robustness towards parameter uncertainty, some amount of perturbation/dispersion is introduced in the plant dynamics by keeping nominal controller as in the nominal design. The perturbations in the parameters are given as force coefficients are $\pm 10\%$, roll moment coefficient as $\pm 30\%$ and pitch and yaw coefficients as $\pm 15\%$. The results are shown with comparison nominal case, lower bound,

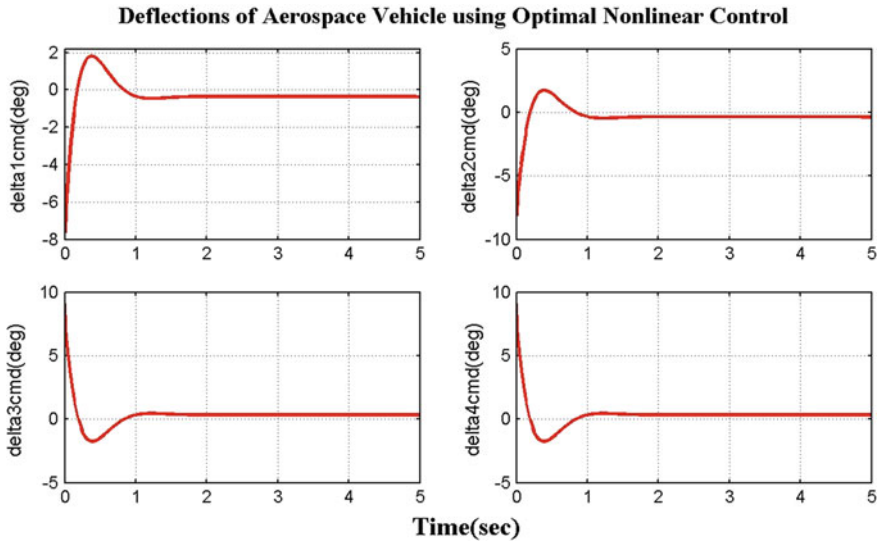


Fig. 3 Control trajectories

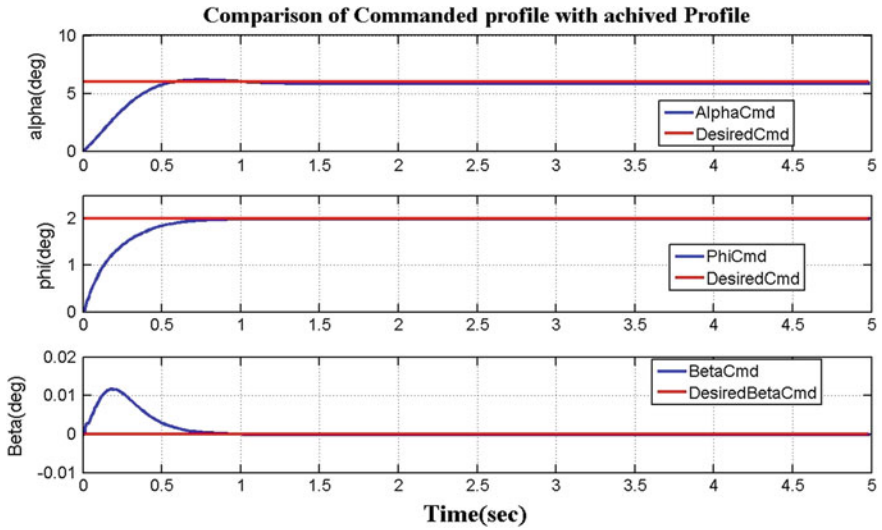


Fig. 4 State trajectories with step inputs

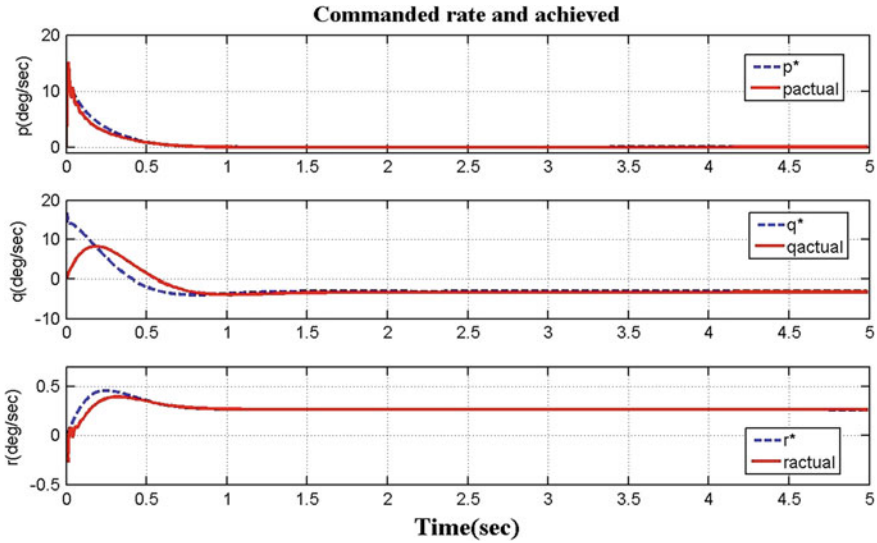


Fig. 5 Body rate comparison with actual

upper bound. These bounds are well matching with dispersion and show satisfactory performance. All three nominal, lower and upper bounds are compared with respect to actual obtained values which shows that the results are satisfactory as shown in Figs. 6, 7 and 8. In this simulation, the control commands are little chattering (due to perturbation) in the initial phase but latter is recovered.

The comparison of all three bounds (nominal, upper and lower) with control deflections and body rates computed has shown satisfactory performance which shows that the vehicle is under control and performing as per the desired dynamics (asymptotic stability). The vehicle fully under control and tracking objectives are met by considering the aforementioned perturbation in various critical aerodynamic parameters.

4.2 Tracking Performance with Perturbation

The aerodynamic parameter perturbation has been implemented to study the robustness of the design. The guidance commands are step signals in three channels, and the tracking performance is validated under such perturbations. The nominal, upper and lower bounds are generated, and controller tracking is validated. The results show the satisfactory performance along with the control signals, body rates, etc.

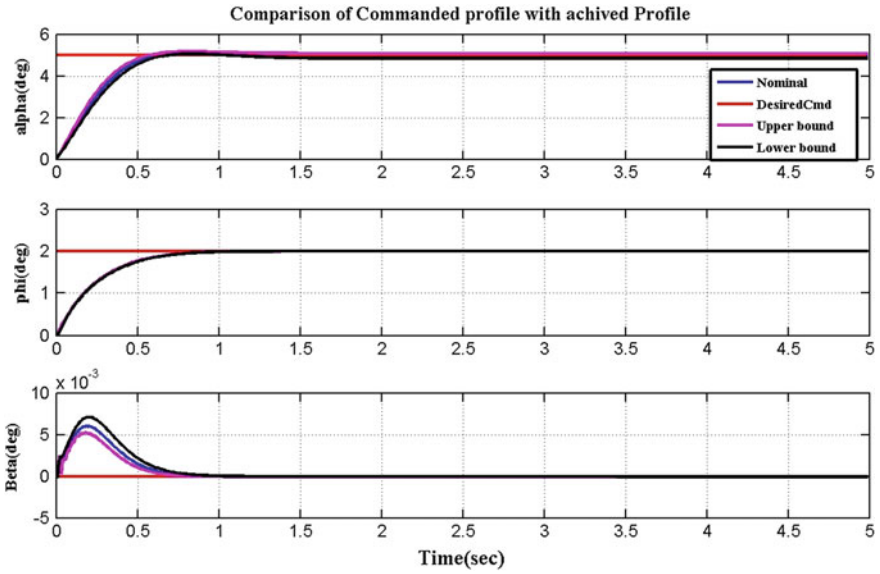


Fig. 6 Closed-loop trajectory with commanded profiles

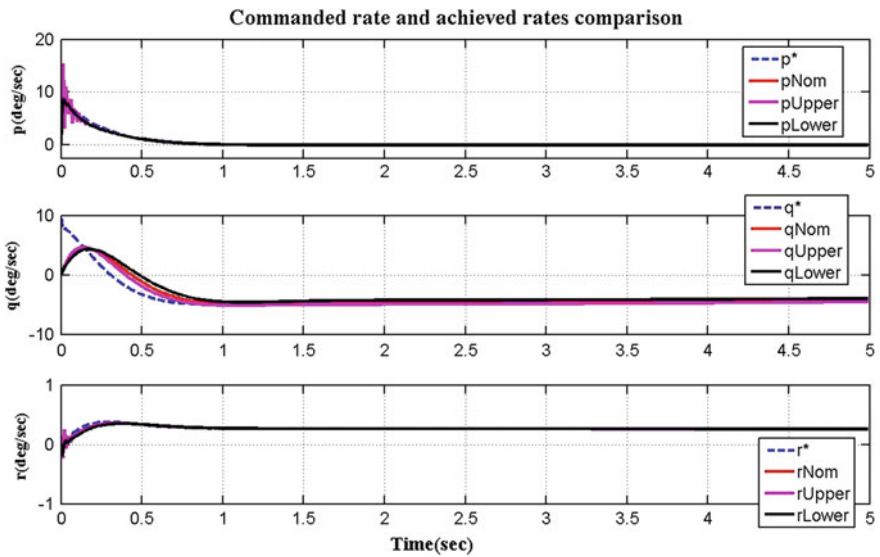


Fig. 7 Closed-loop body rate trajectory

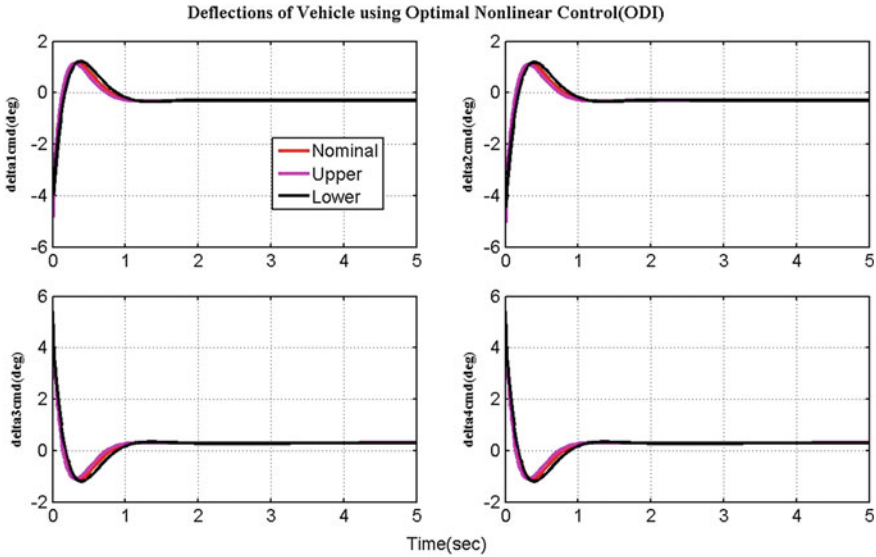


Fig. 8 Time history of control commands

4.3 Conclusions and Future Scope

Nonlinear dynamic inversion-based controller is designed using timescale separation principle. The outer loop controller is designed based on dynamic inversion with proportional–integral controller by considering first-order error dynamics. The inner loop controller is designed using optimal dynamic inversion because the number of aerodynamic control surfaces is four. The nominal control design is implemented at one particular operating point for which the aerodynamic data is available. Various robustness studies were performed like perturbations in the aerodynamic parameters, with different commanded profiles like step signal, sine signal, square signals, etc. All the results have shown satisfactory performance in terms of tracking objective and speed of response. The future scope in this design is to implement outer and inner loop controllers using neuro-adaptive design along with dynamic inversion-based nominal controller. In such case, this design will be more robust towards the parametric uncertainty/inaccuracy in the system. In such scenario, this type of algorithms can be applied.

Acknowledgements The authors acknowledge and express gratitude to Sri BHVS Narayana Murthy, Director of RCI, for his encouragement and support to write this paper.

References

1. Shivasundaram S (2004) Nonlinear systems in aviation, aerospace, aeronautics and astronautics: a book. *Advances in dynamics and control*
2. Brinda V, Arora RK, Janardhana E (2012) Mission analysis of a reusable launch vehicle technology demonstrator (RLV-TD). <https://doi.org/10.2514/6.2005-3291>
3. Hall CE, Shtessel YB (2012) Sliding mode control disturbance observer-based control a for reusable launch vehicle. *J Guidance Control Dyn.* <https://doi.org/10.2514/1.20151>
4. Schiermen JD, Ward DG, Monaco JF, Hull JR (2001) A re-configurable guidance approach for reusable launch vehicles
5. Anjay P, Swaminathan S (2016) Integrated adaptive guidance and control for the entry phase of winged RLV
6. Mu R, Zhang X (2014) Control allocation design of reaction control system for reusable launch vehicle. *Abstr Appl Anal* 2014
7. Das K, Purlupady C, Padhi R et al (2008) Optimal nonlinear control and estimation for a reusable launch vehicle during reentry phase
8. Mathavaraj S, Halbe O, Padhi R (2012) Robust control of a reusable launch vehicle in reentry phase using model following neuro adaptive design
9. Halbe O, Mathavaraj S, Sharmah P, Chawla C, Chetana P et al (2010) Nonlinear optimal reentry guidance and control of RLV in pitch plane. *IFAC Proc Vol 43*:142–147
10. Halbe O, Raja RG, Padhi R (2013) Robust reentry guidance of a reusable launch vehicle using model predictive static programming
11. Drake D, Xin M, Balakrishnan SN (2004) A new nonlinear control technique for ascent phase of reusable launch vehicles
12. Tain B, Fan W, Zong Q, Wang J, Wang F (2013) Nonlinear robust control for reusable launch vehicles in reentry phase based on time varying high order sliding mode. *J Franklin Inst* 350:1787–1807
13. Bollino KP, Oppenheimer MW, Doman DD (2006) Optimal guidance command generation and tracking for reusable launch vehicle reentry
14. Johnson EN, Calise AJ, Corban JE (2001) Reusable launch vehicle adaptive guidance and control using neural networks
15. Missile fin mechanizations
16. Padhi R NPTEL lecture notes of Lecture-34, Lecture-35
17. Schierman JD, Hull JR, Ward DG (2002) Adaptive guidance with trajectory reshaping for reusable launch vehicles
18. Zou Q, Wang F, Zou L, Zong Q (2015) Robust adaptive constrained back stepping flight controller design for re-entry reusable launch vehicle under input constraint. *Adv Mech Eng* 7(9):1–13
19. Georgie J, Valasek J (2003) Evaluation of longitudinal desired dynamics for dynamic inversion controlled generic reentry vehicle. *J Guidance Control Dyn* 26
20. Menon PP, Bates DG, Postlethwaite I, Macros A et al (2007) Worst case analysis of flight control laws for reentry vehicles. *IFAC Proc Vol 40*:317–322
21. Wallner EM, Well KH (2004) Nonlinear adaptive flight control for the X-38 vehicle
22. Macros A, Penn LF, Caramango A (2007) Atmospheric re-entry nonlinear dynamic inversion control design for the Hopper RLV concept
23. da costa RR, Chu QP, Mulder JA (2003) Reentry flight controller design using nonlinear dynamic inversion. *J Spacecr Rockets* 40(1)

Closed-Loop Simulation for Attitude Control of Nano-satellite



Riya, Sanket Chirame, Anant A. Joshi, Ram Milan Kumar Verma, Sumit Agrawal, Ravit Anand, Shrita Singh, Sanskriti Bhansali, Piyush Jirwankar and Niket Parikh

Abstract This document describes the implementation of a state estimator, and an attitude controller for Advityi, IIT Bombay's 2nd Student Satellite. The algorithms used by the estimator and the controller are described. A closed-loop simulation (CLS) framework for the testing of these algorithms is explained. A detailed description of each of the blocks in CLS framework has been provided. The problems faced due to actuation with magnetorquer are described. It also contains the description of practices followed to ensure the quality (correctness of results obtained and repeatability of the process).

Keywords Closed-loop simulation · Quality assurance · Estimator · Controller

1 Introduction

The requirements of attitude control and the challenges involved in realizing these in the case of nano-satellites in low earth orbit (LEO) are unique. The IIT Bombay Student Satellite, Advityi, belongs to this class of satellites, having a mass of 764 g, size of 10 cm × 10 cm × 11.5 cm and orbiting in a LEO of approximate altitude 600 km. The Attitude Determination and Controls Subsystem of Advityi aim to maintain earth-pointing orientation of satellite within an accuracy of $\pm 10^\circ$ because signals are received with detectable strength at minimum expense of power for transmission in earth-pointing orientation.

The closed-loop simulation framework is developed for the analysis and on ground-verification of chosen estimators and controllers. The estimation and control accuracy of the system are monitored in this framework and necessary design

Riya (✉) · S. Chirame · A. A. Joshi · R. M. K. Verma · S. Agrawal · R. Anand · S. Singh · S. Bhansali · P. Jirwankar · N. Parikh
Student Satellite Lab, Aerospace Department, IIT Bombay, Powai, Mumbai 400076, India
e-mail: riyasingh@iitb.ac.in
URL: <https://www.aero.iitb.ac.in/satlab/>

Riya
Mechanical Department, IIT Bombay, Powai, Mumbai 400076, India

© Springer Nature Singapore Pte Ltd. 2020
PSR. S. Sastry et al. (eds.), *Advances in Small Satellite Technologies*,
Lecture Notes in Mechanical Engineering,
https://doi.org/10.1007/978-981-15-1724-2_9

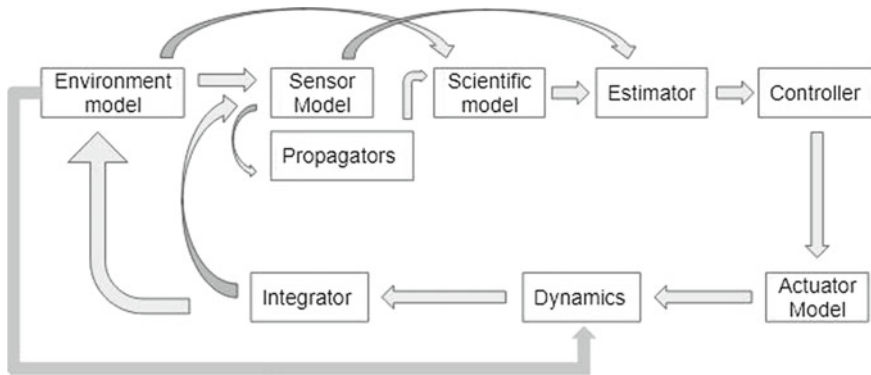


Fig. 1 Block diagram of CLS framework

changes are made based on the results. State vector refers to the attributes of satellite which are propagated in simulation. The main aim of simulation is to check that these attributes are within desired tolerance limits. For our simulation state consists of seven values—initial 4 values for quaternion corresponding to a rotation matrix used for rotating a vector from orbit frame to body frame (qBO) and latter 3 values for angular velocity of body frame with respect to orbit frame (earth-pointing frame) expressed in body frame. A simulation framework for modeling attitude dynamics of satellite typically comprises of different blocks as shown in Fig. 1. The rest of article is structured as follows. In Sect. 2, we introduce environment models used for simulation of environmental parameters. Sections 3–5 contain description of sensor models, propagator and scientific models, respectively. In Sect. 6, we describe the chosen estimator algorithm. Section 7 discusses two control modes and analysis of candidate control algorithms. Section 8 contains details of actuator modeling. Section 9 describes the attitude and angular velocity propagation step. Section 10 shows the simulation result we have obtained using the framework. Section 11 summarizes the guidelines followed to ensure the quality of framework and the correctness of results.

2 Environment Model

The environment model determines the external environmental parameters as a function of the state of satellite at some particular time. All the parameters that are modeled are explained below.

- Simplified Gravitational Perturbation model (SGP4) [1]: The SGP4 model is a standard gravity model for earth. It is a sophisticated model which iteratively calculates earth's gravity at any point by including effects like J2, J3, secular effects of gravitation, periodic effects of gravitation, short-term perturbations. The inputs to this model are orbital elements of the satellite orbit (sun synchronous,

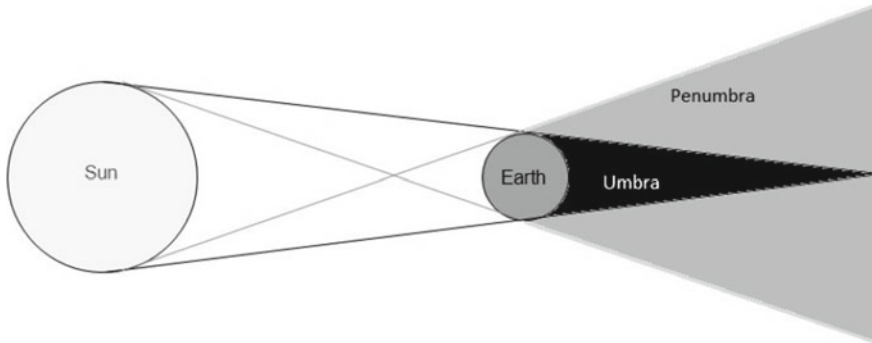


Fig. 2 Shadow of earth due to sun

500–800 km altitude) in the form of a two-line element (TLE). The output is the position and velocity vector in the Earth-Centered Inertial Frame (ECIF).

- Sun model [2]: The sun model takes the time elapsed (from the latest vernal equinox) as its input and gives the sun vector in ECIF as the output.
- Light model: The light model takes the position of the satellite as its input and tells us whether the satellite is in the light region or in the eclipsed region (shadow of the earth on the satellite as shown in Fig. 2). The satellite is assumed to be a point mass while earth and the sun are assumed to be spheres of finite radius. When the satellite is in either umbra or penumbra, it is assumed to be in eclipse region. Otherwise it is in the light region.
- Magnetic Field model: This block takes position of the satellite in the ECIF as input and calculates the geomagnetic field vector in the ECIF. The International Geomagnetic Reference Field 2011 (IGRF-11) [3] model is used. It models the earth's magnetism as a magnet with the desired order of polarity (dipole, quadrupole, octupole, etc.). For ground simulation, a 12th order model [4] is used. IGRF library [5] requires latitude, longitude, and altitude as input and generates magnetic field vector in North-East-Down (NED) frame. We perform intermediate frame transformation to obtain desired results.
- Disturbance model [6, 7]: The satellite, in its orbit, is acted upon by various forces applied by external environmental entities. These forces result in torques which cause the satellite to go out of the desired attitude. Thus, it is essential that we consider these effects during simulation. Based on comparison of order of magnitudes of torques, it has been concluded that the following three torques have critical effect on a nano-satellite like Advitiy.
 - Aerodynamic Torque: For a satellite in low earth orbit, the major disturbance torque is exerted by aerodynamic drag. The drag arises from friction between satellite and atmosphere and is in a direction opposite to that of satellite's velocity vector. Its order of magnitude is 10^{-9} Nm.
 - Solar Radiation Torque: Radiation hitting the surface of the satellite has momentum associated with it and thus due to absorption and reflection of radiation,

forces act on satellite which generates a torque around the center of mass. The majority solar radiation experienced by the satellite is due to radiation emitted from the sun. Thus, it is assumed not to act in the eclipse region. Its order of magnitude is 10^{-10} Nm.

- Gravity Gradient Torque: An extended object in a non-uniform gravitational field experiences a torque in general due to different forces acting at different parts of the object. Its order of magnitude is 10^{-11} Nm.

3 Sensor Model

Following sensors are going to be used in Advitiy, so they are modeled to be included in simulations.

- **GPS model:** Position and velocity inputs from SGP4 are taken and noise and bias is added to it to generate output of GPS.
- **Gyroscope model:** Angular velocity of body frame with respect to orbit frame expressed in body frame is given as input to it and it converts it into angular velocity of body frame with respect to Earth Centered Inertial Frame (ECIF) expressed in body frame and adds noises and bias to it.
- **Magnetometer model:** It takes magnetic field data from IGRF in ECIF and converts it into magnetic field in body frame and adds noises and bias to it.
- **Sun sensor model:** It takes sun vector in ECIF from sun model converts it into sun vector in body frame. Since, in the sun sensors, output is electric current value which is processed using analog-to-digital convertor (ADC), quantization due to ADC is introduced into the model along with introduction of noise. Comparing the generated sun sensor reading with a cutoff value, it is tested whether satellite is in eclipse or not. The output of block is sun-vector in body frame or null values depending on satellite's presence in eclipse.

4 Propagator

Since GPS can not be operated continuously on satellite due to power constraints, J2 propagator [8] will be used to determine position and velocity of the satellite during the duration for which GPS is off. So, J2 propagator is modeled in the simulation too.

It uses the SGP output as an initial condition and numerically solves the differential equation to obtain the position and velocity of the satellite. We use Runge Kutta 4th order (RK-4) method [14] for numerical integration.

5 Scientific Model

They are used to generate sun vector and magnetic field vector in orbit frame. They take sun vector and magnetic field vector in ECIF and convert them in orbit frame using quaternion corresponding to rotation matrix from ECIF to orbit frame [9]. The rotation matrix is generated by position obtained from propagator.

6 Estimator

It is not possible to obtain a direct measurement of the attitude of the satellite. It has to be calculated using the measurements from other sensors like coarse sun sensor, magnetometer, etc. These sensors have their inherent electronic noise. This makes deterministic attitude calculation difficult. Thus, attitude has to be estimated using some estimation techniques. Multiplicative Extended Kalman Filter (MEKF) is the primary attitude estimator in Advitii which addresses the non-linear nature of system and constraints associated with the quaternion framework. Quaternion Estimate (QuEst) algorithm will be used for providing an initial estimate to the filter.

- **QuEst:** Kalman filter requires an initial estimate of attitude. QuEst will be used for obtaining this initial attitude estimate between orbit and body frame. QuEst algorithm uses two of non-parallel vectors in body frame and corresponding two vectors in orbit frame. Attitude is estimated by minimizing the Wahba's loss function [9]. In our case, QuEst will use the following two vectors:
 - Sun vector: The body frame components will be measured by the onboard coarse sun sensor. The orbit frame sun vector will be computed using the onboard mathematical sun model. In CLS, these vectors will be obtained using sun sensor model and scientific model, respectively.
 - Magnetic field vector: The body frame components are measured using onboard three-axis magnetometer. The orbit frame components will be computed using the onboard IGRF magnetic field model. In CLS, these vectors will be obtained using magnetometer model and scientific model, respectively.

Due to requirement of sun vector, QuEst will be taken only when the satellite is not in the eclipse region.

- **Multiplicative Extended Kalman Filter** [9]: Despite being a relatively complex and computationally demanding, we are implementing it because of following reasons:
 - Unlike QuEst, Kalman Filtering is a dynamic attitude estimator. It incorporates into it the past measurements made in time and hence is a better method.
 - We are using quaternions to represent the attitude. In EKF, error in quaternion is defined as algebraic difference between the true quaternion and its estimate.

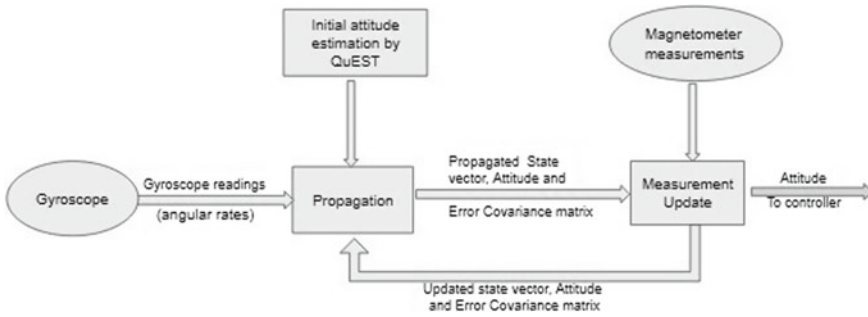


Fig. 3 Schematic of MEKF operation

If we are to keep the estimate unbiased, the unit norm constraint of quaternion is violated. So instead MEKF is used where the true quaternion is the product of an error quaternion and the estimate. Here, product of two unit quaternions is a unit quaternion resolving the issue.

- A typical EKF uses a dynamic model of the system in the propagation step. However, we are using gyro measurements instead for propagation. This has the advantage of avoiding inherent difficulties in modeling torques acting on a spacecraft. Also gyro measurements are usually more accurate than the models. All gyros have inherent variable bias which could cause inaccuracies in the propagated model. So the rate gyro bias is included in the state vector along with the quaternion and is used to correct the raw gyro measurements.

Figure 3 contains the flowchart which depicts the algorithm of MEKF. State vector of our estimator is taken to be change in angle corresponding to attitude change and change in angular rates bias. The initial estimate (i.e., of state vector and corresponding covariance matrix) for the filter is fed through QuEst which uses measurements from coarse sun sensor and magnetometer for the task. Angular rates from gyroscope readings are used to propagate previous estimates of state vector and corresponding covariance matrix. The propagated state vector and corresponding covariance matrix are then updated for next instance using magnetometer readings. The updated attitude is then fed to controller and state vector is input for next iteration of filter.

7 Controller

The goal of controller of the satellite will be to align the body frame with orbit frame. This control law should be robust to the disturbances faced by the satellite in orbit. This means that even in the presence of disturbance torque, the satellite's attitude should be within desired bound of the reference attitude. The satellite will have two control modes.

- **Detumbling mode:** The first mode is detumbling. When it is separated from the launch vehicle, the satellite has high initial angular velocity of body frame with respect to orbit frame. The detumbling control law will be used to reduce the body angular velocity with respect to orbit frame. This will be achieved using B-dot controller [9]. The estimate of angular velocities will be obtained from magnetometer data.

B-dot control law is based on the fact that the earth's magnetic field in the body frame changes with time due to motion of the satellite. Note that the change due to translational motion of the satellite is neglected as contribution due to high angular rates during detumbling is considerably larger. The controller aims to make this rate of change of earth's magnetic field equal to zero. The required magnetic moment is proportional to the magnitude of the derivative of body-fixed magnetic field but opposite in direction.

A magnetic actuation-based controller [10] was also reviewed. The magnetic moment is determined using the body-fixed earth's magnetic field vector and angular velocity vector of the body with respect to inertial frame. But it was later rejected as it required gyroscope data, which was not possible to obtain reliably since the estimator cannot be executed in detumbling mode to correct the drifting bias of the gyroscope.

- **Nominal Mode:** Once the angular rates are within desired bounds, the satellite control law will switch to nominal mode. The nominal controller will control the attitude of satellite. Advitiy will have active control in the eclipse phase as well. This decision was based on the fact that half of the passes of Advitiy over India are in eclipse phase. If angular velocities increase beyond the bounds, then controller mode will switch back to detumbling to reduce angular velocities.

The control laws implemented in previous small satellite missions have been reviewed. The following controllers are currently under consideration:

- **Quaternion Feedback Controller [9]:** This controller is implemented in lots of previous missions. This is like a simple PID controller. The control torque is directly proportional to the error quaternion and error angular velocity and a few other non-linear terms. This controller is a continuous controller which guarantees asymptotic tracking if the torque applied is exactly equal to the torque demanded and if there are no disturbances present. In case of disturbances and discretized magnetic actuation, its performance degrades significantly.
- **Adaptive Controller:** The first controller in this category is a variable gain controller [12] which exactly rejects gravity gradient and designed for magnetically actuated systems. This overcomes the two major shortcomings of the quaternion feedback controller.

Another controller in this category estimates the upper bound on the disturbances acting on the satellite [13]. The implementation of this controller is computationally simple but the tuning is difficult. Work on this controller has been halted since it was not designed specifically for magnetic actuation. Both of these controllers have not been implemented in previous satellite missions. However, they overcome some of the shortcomings of quaternion feedback controller.

8 Actuator Model

As we have seen in Sect. 7, depending on control algorithm used, output of controller block can be desired torque or desired magnetic moment. So, two types of actuator models have been developed depending on two possible cases of output of controller block. Type A will take magnetic moment required directly as input while type B takes torque required as input and magnetic moment required is calculated by

$$\mathbf{m} = (\mathbf{B} \times \boldsymbol{\tau}) / \|\mathbf{B}\|^2$$

where (bold character represents vector) \mathbf{m} is required magnetic moment, \mathbf{B} is magnetic field at that location, $\boldsymbol{\tau}$ is the torque required. This formula comes from the logic that since we cannot generate torque along magnetic field, so maximum efficiency (in terms of power consumed) will be in the case of magnetic moment perpendicular to both the magnetic field and torque required (as component of magnetic moment in direction of magnetic field will not contribute to torque).

For both the types, once we get the required magnetic moment, electric current required is calculated using the relation $\mathbf{m} = n I A$ where n is number of turns of wire in magnetorquer (same for all 3), I is a vector containing the required current in 3 magnetorquers aligned along x , y , z axis of body frame and A is the area of magnetorquers. Then, we assume magnetorquers to be purely resistive only. So, required voltage is calculated as $V = I \times R$ where V represents voltage required, I represents current required and R represents resistance of magnetorquers. From the required voltage to actual current, we are following three approaches on the basis of ease of implementation.

- We will model the actuator as resistive circuit only in the most basic framework. So, in this case the required current obtained will be equal to the actual current.
- We will improve the basic model and model the actuator as an LR circuit. Voltage for a control cycle (the time taken by onboard computing to complete one loop of execution of all the commands) will be given and current for the environment cycle (integration time step used for satellite attitude dynamics simulation) will be calculated using

$$I = ((1 - e^{-tR/L})(V - i_p R)) / R$$

where i_p is current in torquers at the end of previous control cycle and t is the time elapsed after beginning of current control cycle.

- We will introduce the fact that voltage supplied to panels is not Direct Current but Pulse Width Modulation. So, during ON time

$$I = ((1 - e^{-tR/L})(V - i_p R)) / R$$

and during OFF time

$$I = (e^{-t'R/L})V_p/R$$

where t' is the time after change of mode (ON mode or OFF mode and V_p is the voltage during previous mode).

9 Dynamics and Integrator

Dynamics and integrator are used to find next state of satellite using current state of satellite and total torque (sum of disturbance torque and control torque) acting on the satellite. Dynamics block calculates the derivative of state vector.

The integrator uses the derivative of the state calculated by the dynamics block and integrates it using RK-4 method to get next state. The new state is given as input to the environment and sensor block for continuation of loop thus making it closed.

10 Simulation Results

Simulation of uncontrolled satellite in eclipse region to determine the need of control in eclipse (Fig. 4)

Initial Angular Rates— $[0\ 0\ 0]^{\circ}/s$ along the X, Y, Z body axes, respectively.

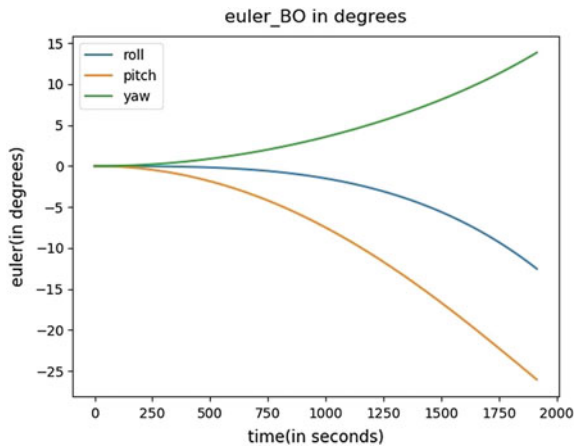
Initial Euler Angles— 0° roll, 0° pitch, 0° yaw

Duration—From start of eclipse to end of eclipse

Disturbance torques—Present

Control torques—Absent.

Fig. 4 Euler angles versus time



One should observe that value of maximum euler angle is 25° at the end of eclipse even if the satellite was completely earth pointing and its angular velocity with respect to earth-pointing frame of reference was zero at the start of eclipse. Since in real scenarios it is likely to be already deviated at the start of eclipse, the attitude deviations at the end of the eclipse will be worse. Since half of the passes of Advitiy over India are in eclipse, to transmit the signals with maximum efficiency, satellite has to be controlled during eclipse.

11 Quality Assurance

Following quality assurance (QA) practices is essential to minimize chances of mission failure. So, a rigorous procedure is followed to ensure the results generated from simulation are correct and the framework is easy to understand and debug. A document containing guidelines of writing codes and reviewing it has been made. It also consists of instructions for naming the files so that one can infer the type of document/code and its version from just looking at the name. Naming conventions of various elements of code such as functions and variables have also been described to maintain consistency across different codes and avoid confusion. Comments are added along with the header of functions where its inputs, outputs, and objective are defined. Comments are also added in the code to explain any mathematical or logical operation. The author of the code also writes a readme file, which gives information on the technical aspects of the code, i.e., the mathematical formulae and scientific laws used with references at the end.

An exhaustive set of test cases is also prepared, where expected outputs for particular inputs are written for each function in code. Finally, a test code is written using unittest module [11] to automate the process of checking whether the actual output from the functions of code match the expected output for the test case inputs. Process has been automated to remove manual error while testing. Now, a second person reviews all the steps identified above and also the correctness and logical consistency of code in general. The author of the code prepares a QA report based on existing format in place for it and includes there the links for code, readme file, and test code. The reviewer writes his suggestions in this QA report, which are then implemented in the code by the author.

GitHub is used for version control. A master repository is maintained for all codes, their readme files, test cases, and test codes. Individual team members update their personal GitHub repository after each change made in their code, and then push the completed and reviewed code to the master repository. A team member has been entrusted with responsibility of maintaining the master repository and ensuring that the laid down guidelines are followed by everyone involved in the development of framework.

References

1. Hoots FR, Roehrich RL, Kelso TS (1980) Spacetrack report No. 3. Project Spacetrack Reports, Office of Astrodynamics, Aerospace Defense Center, ADC/DO6, Peterson AFB, CO
2. Curtis HD (2013) Orbital mechanics for engineering students. Butterworth Heinemann, Oxford
3. Finlay C et al (2010) International Geomagnetic Reference Field: the eleventh generation. *Geophys J Int* 183(3):1216–1230
4. Thébault E et al (2015) International Geomagnetic Reference Field: the 12th generation. *Earth Planets Space* 67
5. <https://github.com/scivision/igrf12>
6. Montenbruck O, Gill E (2000) Satellite orbits models, methods and applications. Springer, Berlin
7. Wertz JR (1978) Spacecraft attitude determination and control. Springer, Netherlands
8. Sidi MJ (1997) Spacecraft dynamics and control: a practical engineering approach. Cambridge University Press, Cambridge
9. Landis Markley F, Crassidis JL (2014) Fundamentals of spacecraft attitude determination and control. Springer, New York
10. Avanzini G, Giulietti F (2012) Magnetic detumbling of a rigid spacecraft. *J Guid Control Dyn* 35(4):1326–1334
11. <https://docs.python.org/2/library/unittest.html>
12. Lovera M, Astolfi A (2006) Global magnetic attitude control of spacecraft in the presence of gravity gradient. *IEEE Trans Aerosp Electron Syst* 42(3):796–805
13. Cai W, Liao X, Song DY (2008) Indirect robust adaptive fault-tolerant control for attitude tracking of spacecraft. *J Guidance Control Dyn* 31(5):1456–1463
14. Conte SD, De Boor C (2017) Elementary numerical analysis: an algorithmic approach (Vol. 78). SIAM.

Real-Time Autonomous Navigation Scheme for Pointing Small Data Relay Satellite to LEO Using NavIC and GNSS Measurements



Monica Dantuluri, Ishita Ganjoo and Vinod Kumar

Abstract The continuous communication link to the ground station is the prime requirement of any space mission. Presently, the LEO is primarily used for remote sensing, science, and human in space program. The visibility of the low Earth orbit (LEO) to the ground station is limited for a maximum of ~20 min, with four to five orbital visibilities over a day. This requires a huge network of ground stations. About two-third coverage of the orbit of LEO satellite is possible, with about 40 stations located geographically over different places on the globe. The most of the Earth's surface is covered by water; a majority of ground stations need to be located on ships resulting in exorbitant costs of the ground network. Data relay satellite system with three satellite geosynchronous orbit (GEO) presents a very elegant solution in this context and provides a stable link between satellite in LEO and ground station. In the global scenario, the evolution of Tracking and Data Relay Satellite System (TDRSS) is developed by NASA to support communications and tracking services for its LEO spacecraft. The modern space technologies with low-cost microelectronics and microelectromechanical systems (MEMS) technology have enabled building small satellites in a short time. They have the advantage of low mass, low power consumption, low cost, and quick accessibility to space with launch-on-demand services. Small satellites have successfully demonstrated ground satellite and inter-satellite laser communication, which transmits data bit rates orders of magnitudes greater than the radio communication. The efforts are being made to design onboard controller as a generic 6-DOF control system capable of autonomous orientation, orbit, and formation control of multiple satellites in orbit. We use the small data relay satellites at GEO to keep in contact with LEO satellite for continuous data transfer coverage and better navigation accuracy.

Keywords Low Earth Orbit (LEO) · Geosynchronous Orbit (GEO) · Tracking and Data Relay Satellite System (TDRSS) · Navigation by Indian Constellation (NavIC) · Global Navigation Satellite System (GNSS) · Extended Kalman Filter (EKF) · Reduced Dynamics

M. Dantuluri · I. Ganjoo · V. Kumar (✉)

Control Dynamics and Simulation Group, U R Rao Satellite Centre, Bangalore 560017, India
e-mail: vinod@ursc.gov.in

1 Introduction

In this paper, we investigate the autonomous navigation system to point small data relay satellite at geosynchronous orbit (GEO) to the low Earth orbit (LEO) satellite, using observables from Navigation by Indian Constellation (NavIC) satellite and/or from Global Navigation Satellite System (GNSS). The approach applying GNSS receiver to autonomous navigation system of data relay satellite has many advantages over conventional ground-based telemetry and tele-command methods. In addition to reducing the workloads of ground tracking network, it also improves the coverage and navigation accuracy of LEO satellite [1].

The autonomous onboard navigation system needs precise information of the absolute state of the spacecraft as well as relative state of the spacecraft in the formation. The relative navigation requires inter-satellite communication at ultra-high frequency. There exists a gap in the observability of the states of a satellite. This gap can be bridged by using Global Navigation Satellite System (GNSS) or by novel infrared earth sensor and star sensor-based autonomous navigation techniques. In this work, we have used GNSS including NavIC for kinematic position, velocity, and time (PVT) estimation [2–6].

Since, the formulation of kinematics is geometric. It is prone to cycle slip, data outages, due to weak GNSS geometry, which leads to large dilution of precision (DOP). When the measurements are not available, dynamics continues to provide the estimates with slight degraded accuracy. So, combining the GNSS/NavIC measurements with dynamics in an extended Kalman filter (EKF) provides continuity in the PVT estimates.

The reference frames used in this paper are earth-centered inertial (ECI) and earth-centered-earth-fixed (ECEF) reference frame [3]. The vectors and scalars can be deduced from the context in which they are used.

The paper contains six sections, where Sect. 2 discusses the LEO satellite visibility to GEO constellation. The real-time kinematic relative position estimation of LEO satellite at small data relay satellite is discussed in Sect. 3. Sect. 4 discusses the real-time reduced dynamic relative position estimation of LEO satellite at small data relay satellite. Sect. 5 discusses about the antenna orientation angles required to point the GEO satellite to LEO satellite. The conclusion and directions for the future research work are described in Sect. 6.

2 LEO Satellite Visibility to GEO Constellation

In this section, we present the visibility of LEO satellite to the small GEO satellites in constellation. The GEO satellites are assumed to be located at 34° , 134° , and 270° East longitude. Table 1 describes the parameters for these satellites. The altitude of LEO satellites is near 599.0 km and is much lower than that of geosynchronous orbits, which is around 35,786 km. With three small satellites at GEO altitude, near

Table 1 LEO spacecraft orbital elements

Orbital elements	LEO spacecraft	GEO#1 @ 34° East longitude	GEO#2 @ 134° East longitude	GEO#3 @ 270° East longitude
Semi-major axis (a , km)	6981.1	42,164.001	42,164.002	42,164.009
Eccentricity (\vec{e})	0.0016	0.0006	0.00065	0.000045
Inclination (\vec{i} , °)	98.7838	0.075	0.08	0.039
Argument of perigee (ω) (°)	61.1330	62.89	109.99	109.98
RAAN (Ω)	-177.5759	167.9497	152.85	52.20
Mean anomaly (°)	-156.6613	62.35	-104.92	-104.95
Orbit epoch	25 Apr 2018, 11:20:00 UTCG	25 Apr 2018, 11:20:00 UTCG	25 Apr 2018, 11:20:00 UTCG	25 Apr 2018, 11:20:00 UTCG

seamless visibility of the LEO satellite is ensured, as shown in Fig. 1. From this figure, it can be deduced that a near continuous visibility of LEO is observed except for small duration where cones from GEO to LEO intersects. This will help in the transmission of payload data from LEO satellite to the nearest available GEO satellite and to ground station situated at 13.0342° North and 77.5124° East Longitude. The parameters used to generate measurements are provided in Table 2.

Fig. 1 Visibility of LEO satellite at GEO satellites at 34°, 134°, and 270° East longitude

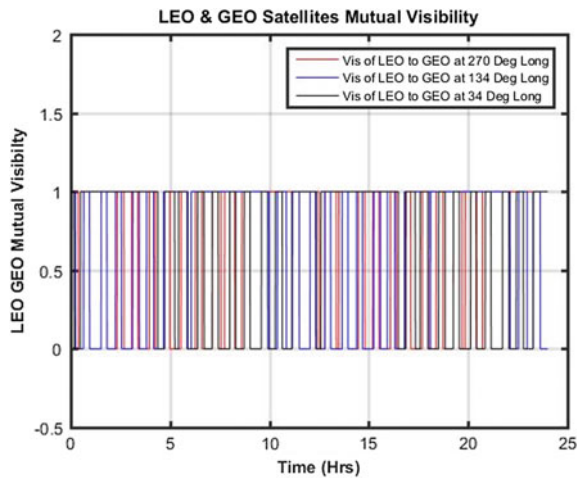


Table 2 Parameters for measurements generation

	Parameters	Data value
1	Propagation signal frequency	L5 band ($f = 1176.45$ MHz, $\lambda = 0.2548$ m)
2	Receiver code phase noise, SD (σ_ρ)	0.5 m (3σ) zero mean discrete white noise
3	Code phase frequency	(i) 1.023 MHz (standard positioning services) (ii) 2.046 MHz (restricted services)
4	Receiver carrier phase noise, SD (σ_ϕ)	0.025 cycles = 0.64 cm ($3 - \sigma$) zero mean discrete white noise
5	Receiver clock bias	(i) deterministic model: $c * 10e-06 = 3000$ m, i.e., 10 μ s; random walk model
6	Ephemeris update	2 h

3 Real-Time Kinematic Relative Position Estimation of LEO Satellite at Small Data Relay Satellites

Differential Navigation Method: The absolute position estimation is carried out using the algorithm described in Misra and Enge, Sect. 5.1.1 [2]. Figure 2 shows the conceptual scheme for the navigation for computing relative position estimation and pointing data relay satellite at GEO to LEO, using NavIC and GPS observables.

A. Relative Position Estimation

For computing relative position kinematically, let us assume relative position vector $\Delta x_r = [\Delta \vec{r} \ \Delta b]^T$; where $\Delta \vec{r}$ is the relative position vector and Δb represents the relative clock bias between LEO and GEO receivers. Their estimates are represented by $\Delta \hat{x}_r$.

The following observation formulation can be formed to relate the single difference between-receiver pseudorange measurements from the same, i.e., k th NavIC, that is Navigation by Indian Constellation is a new regional navigation system developed by Indian Space Research Organisation (ISRO).

$$\Delta P^{(k)}(t_1) = |\vec{r}_{\text{loc}}(t) + \Delta \vec{r}(t) - \vec{r}_{\text{NavIC}}^{(k)}(t - \tau)| - |\vec{r}_{\text{loc}}(t) - \vec{r}_{\text{NavIC}}^{(k)}(t - \tau)| + \Delta b + \sqrt{2}\epsilon_\rho^{(k)} \quad (1)$$

The NavIC/GNSS measurements consist of biased and noisy estimates of ranges to the satellites. The major sources of these errors and biases are unknown bias in receiver clock relative to NavIC/GNSS time, errors in code, carrier phase measurements, and the errors in the satellite clock and ephemerides. The satellite and receiver clock bias errors are estimated while the integer ambiguity is removed by taking between-receiver and between-measurement-epoch difference. With this, the receiver obtains its absolute position (r), velocity \dot{r} and time. These estimates as well as the measurements of the remote receiver communicated through the radio modem are then used in the relative positioning algorithm.

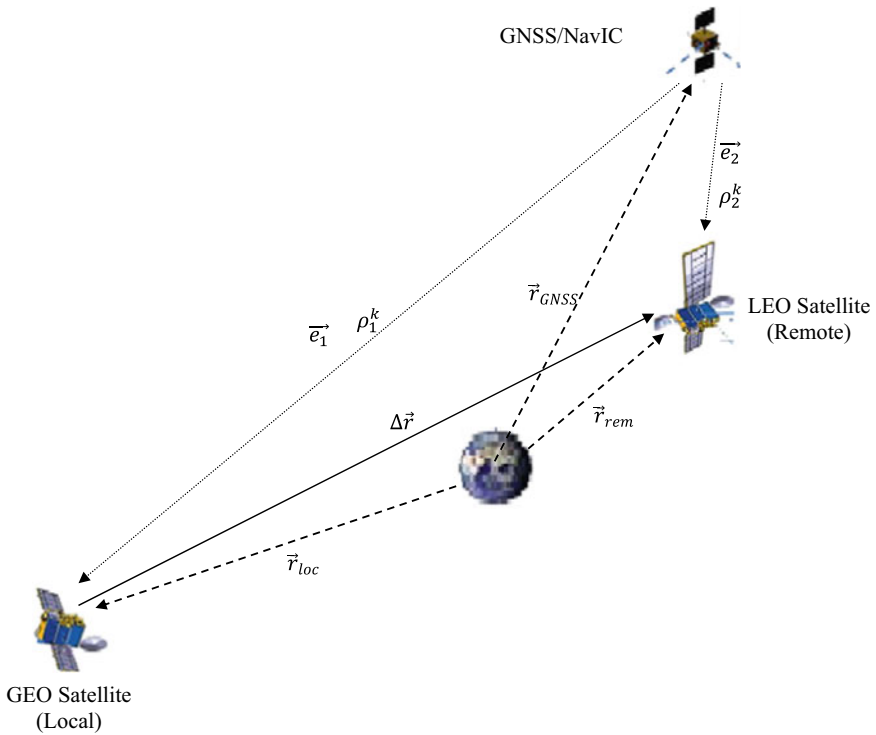


Fig. 2 Relative navigation concept using GNSS observables

B. Mathematical Formulation

The correction $\delta \hat{x}_r$ to the a priori estimates of the relative position vector and receiver clock bias $\Delta \hat{x}_r$ is obtained using following relation. It is assumed that the covariance of noise in all the K observables is equal [2–5]:

$$\delta \hat{x}_r = (G_{rem}^T G_{rem})^{-1} G_{rem}^T [\Delta P(t) - \Delta \hat{P}(j)] \tag{2}$$

where

$$G_{rem} = \begin{bmatrix} (e_{rem}^{(1)})^T & 1 \\ (e_{rem}^{(2)})^T & 1 \\ \cdot & \cdot \\ \cdot & \cdot \\ (e_{rem}^{(K)})^T & 1 \end{bmatrix}_{k \times 4} \tag{3}$$

and the unit vector $e_{rem}^{(k)}$, from the k th NavIC to the estimated position of remote GEO is estimated iteratively from its definition as in Chap. 3, Eq. (3.25) [3]:

$$e_{\text{rem}}^{(k)} = \frac{\vec{r}_{\text{rem}} - \vec{r}_{\text{NavIC}}^{(k)}}{\left| \vec{r}_{\text{rem}} - \vec{r}_{\text{NavIC}}^{(k)} \right|} \quad \text{where } k = 1, 2, 3, \dots, K \quad (4)$$

Finally, the estimates of the relative position and the receiver delta clock bias can be computed using the following equation:

$$\Delta \hat{x}_r(j) = \Delta \hat{x}_r(j-1) + \delta \hat{x}_r \quad (5)$$

Using the estimates of its variables the term $\Delta \hat{P}(j)$ in Eq. (1) is estimated in the j th iteration from the following relation:

$$\Delta \hat{P}(j) = \left| \vec{r}_{\text{loc}}(t) + \Delta \vec{r}(t) - \vec{r}_{\text{NavIC}}^{(k)}(t - \tau) \right| - \left| \vec{r}_{\text{loc}}(t) - \vec{r}_{\text{NavIC}}^{(k)}(t - \tau) \right| + \Delta b \quad (6)$$

$$\Delta \vec{r} = \Delta \hat{x}_r(1:3) \quad \text{and} \quad \Delta b = \Delta \hat{x}_r(4)$$

The iterative solution (1) is refined until the condition $\|\delta \hat{x}_r\| \leq 2\sqrt{K}\sigma_\rho$ meter, which is achieved. The limiting value of the term $\|\delta \hat{x}_r\|$ depends on the number of NavIC's and the standard deviation (SD) σ_ρ of receiver's code phase noise.

Figure 3 shows the number of common GNSS/NavIC satellite, visible to small data relay satellite, and LEO satellite. The sufficient number (i.e., at-least 4) of common GNSS satellites for relative position estimation is available only for a short duration. However, this is sufficient for fixing the relative position. The relative position estimation error achieved with this arrangement is shown in Fig. 4. This computation is limited to common GNSS satellites; hence, states are available only for 2 h wherever four or more satellites are in field of view, as shown in Fig. 3, providing an accuracy

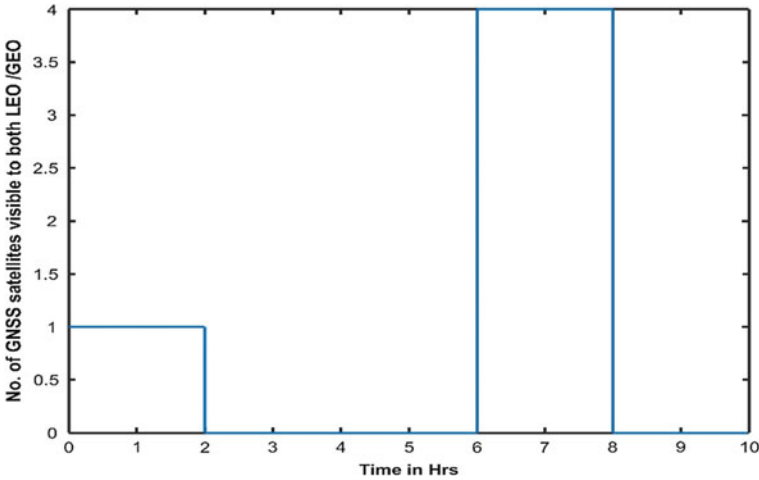


Fig. 3 No. of common GNSS satellites visible to both LEO and GEO

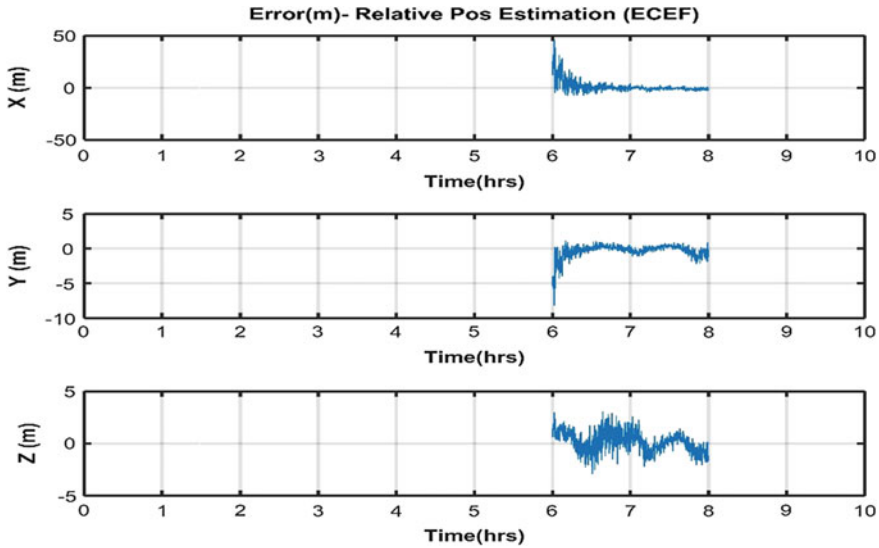


Fig. 4 Error in relative position vector using relative navigation formulation

of [2, 3, 5] m in ECEF frame. The data relay satellite will require continuous precise estimation of LEO orbital parameters. This estimation period can be increased by transferring the measurements from LEO to small data relay satellite using other data relay satellite in the constellation. Hence, they help improve the prediction capability of data relay satellite at GEO. The seamless communication to a LEO is possible by placing three small satellites at GEO at 34° , 134° , and 270° East longitude, with high-speed optical inter-satellite communication. In next section, we have combined the NavIC/GNSS measurements with dynamics in an extended Kalman filter (EKF), thus providing continuity in the PVT estimates [3].

4 Real-Time Reduced Dynamic Relative Position Estimation of LEO Satellite at Small Data Relay Satellites

In this section, we have incorporated high fidelity translational motion dynamics model for relative position estimation. It is assumed that the LEO satellite is able to transfer the available NavIC/GNSS observables to GEO small satellite constellation.

A. High Fidelity Force Models

The translational motion dynamics model for a satellite under perturbational forces, F , is given by the following equation [3–7],

$$\ddot{\mathbf{r}} = -\frac{\mu}{r^3}\mathbf{r} + a_{\text{prt}}(t, \mathbf{r}, \dot{\mathbf{r}}, \mathbf{p}) \quad (7)$$

where u_1 and u_2 are the zero mean rate and acceleration white noise, respectively, defined for the clock bias and bias rate. The states x_8 , x_9 and x_{10} are used to estimate the empirical accelerations.

The above state space Eq. (10) can be represented by:

$$\dot{\mathbf{x}} = \mathbf{f}(\mathbf{x}, \mathbf{a}, t) + \mathbf{w} \quad (11)$$

where acceleration vector comprises of $a_{3 \times 1} = \sum (a_{\text{central}}, a_{J2}, a_{\text{Sun}}, a_{\text{Moon}}, a_{\text{SRP}}, a_{\text{drag}}, a_{\text{thr}})$. The $\mathbf{f}(\mathbf{x}, \mathbf{a}, t)$ term in Eq. (11) is a nonlinear vector function. The column vector \mathbf{w} represents the white noise. For further details, refer [3] and cited references.

C. Orbit Propagation: Estimation Model

The estimation model is formulated with 12 states by adding three states for empirical acceleration. The empirical acceleration is formulated as first-order exponentially correlated Markov process. Hence, 12×1 state estimation vector is:

$$\hat{\mathbf{x}}^T = [\hat{\mathbf{r}}, \hat{\mathbf{v}}, \hat{\mathbf{C}}_r, \hat{\mathbf{a}}_{\text{emp}}, \hat{\mathbf{b}}]^T \quad (12)$$

Then complete state space model can be written as:

$$\begin{bmatrix} \dot{\hat{x}}_1 \\ \dot{\hat{x}}_2 \\ \dot{\hat{x}}_3 \\ \dot{\hat{x}}_4 \\ \dot{\hat{x}}_5 \\ \dot{\hat{x}}_6 \\ \dot{\hat{x}}_7 \\ \dot{\hat{x}}_8 \\ \dot{\hat{x}}_9 \\ \dot{\hat{x}}_{10} \\ \dot{\hat{x}}_{11} \\ \dot{\hat{x}}_{12} \end{bmatrix} = \begin{bmatrix} \hat{x}_4 \\ \hat{x}_5 \\ \hat{x}_6 \\ \hat{a}_x \\ \hat{a}_y \\ \hat{a}_z \\ 0 \\ -\beta_x \hat{x}_8 \\ -\beta_y \hat{x}_9 \\ -\beta_z \hat{x}_{10} \\ 0 \\ \hat{x}_{11} \end{bmatrix} \quad (13)$$

where $\hat{x}_{1, \dots, 6}, \hat{x}_7, \hat{x}_{8, 9, 10}, \hat{x}_{11, 12}$ are the position, velocity, solar radiation pressure coefficient, empirical accelerations, the receiver clock bias rate, and its bias, respectively. Equation (13) can be written as:

$$\dot{\hat{\mathbf{x}}} = \mathbf{f}(\hat{\mathbf{x}}, \hat{\mathbf{a}}, t) \quad (14)$$

where $\hat{\mathbf{a}}_{3 \times 1} = \sum (\hat{a}_{\text{central}}, \hat{a}_{J2}, \hat{a}_{\text{Sun}}, \hat{a}_{\text{Moon}}, \hat{a}_{\text{SRP}}, \hat{\mathbf{a}}_e)$ being the summation of estimated perturbational accelerations and hence, $\mathbf{f}(\hat{\mathbf{x}}, \hat{\mathbf{a}}, t)$ is a nonlinear vector.

D. Formulation of Extended Kalman Filter from NavIC/GNSS Observables

In the EKF, with reduced dynamics, the observables of NavIC/GNSS are fused with s/c translational motion dynamics. As usual, EKF outputs are fed back to the estimation model dynamics after the measurement updates along with covariance matrix. The EKF continues to provide the accurate estimation of states, in the presence of pseudorange measurements. Whenever outages of measurements occur, the estimation of states continues with the high fidelity translational motion dynamics. In this case, estimation accuracy will be degraded.

The NavIC/GNSS measurements update of the LEO satellite is carried out using the following formulation [3, 4],

$$z_1^{(k)}(x_1, t_1) = \rho_1^{(k)} + c(\delta t_u - \delta t^{(k)}) + \epsilon_\rho + \epsilon_{\text{eph}}^{(k)} \quad (\text{where } k = 1, 2, \dots, K) \quad (15)$$

$$\rho_1^{(k)} = \left[\left(x - X_{\text{NavIC}}^{(k)} \right)^2 + \left(y - Y_{\text{NavIC}}^{(k)} \right)^2 + \left(z - Z_{\text{NavIC}}^{(k)} \right)^2 \right]^{1/2}; \quad (16)$$

where $[X_{\text{NavIC}}, Y_{\text{NavIC}}, Z_{\text{NavIC}}]^T$ is the position vector of the k th NavIC/GNSS satellite at the signal transmission time. This signal has transit time delays, so it is compensated for these delays. Since the dynamics model of the LEO satellite is in the ECI frame and the received signal from NavIC/GNSS is in ECEF frame, so frame transformation from ECEF to ECI frame is carried out. In Eq. (15) δt_u and $\delta t^{(k)}$ are the receiver clock offsets of the LEO, and the k th NavIC/GNSS satellite clock offset, respectively. The NavIC/GNSS satellite clock offset is obtained from the navigation signal parameters sent to GEO. We need to model the delay from LEO to GEO appropriately in the formulation. The ϵ_ρ is white Gaussian noise having zero mean and standard deviation σ_p . The ephemeris error of NavIC/GNSS ($\epsilon_{\text{eph}}^{(k)}$), which is a non-white noise. Presently, it is not accounted herewith. The impact of this is studied in [8–10].

The *measurement innovation* is defined as:

$$v = z_1 - \hat{z}_e(x_1, t_1) \quad (17)$$

where z_1 and \hat{z}_e being the pseudorange measurements and estimated pseudorange measurements obtained from observations file and navigation file, respectively.

The formulation of the measurement sensitivity matrix is as given below:

$$H_i = \frac{\partial \hat{z}_c(x_1, t_1)}{\partial x_1} = \left[\frac{\left(\hat{x} - X_{\text{NavIC}}^{(k)} \right)}{\rho}, \frac{\left(\hat{y} - Y_{\text{NavIC}}^{(k)} \right)}{\rho}, \frac{\left(\hat{z} - Z_{\text{NavIC}}^{(k)} \right)}{\rho}, 0, 0, 0, 0, 0, 0, 0, 1 \right] \quad (18)$$

The measurement update phase: At this stage, measurement update of the estimates and the error covariance is performed. This is followed by the Kalman gains computation. The Kalman gain provides a measure of confidence on the measurements. The measurement covariance matrix R , with uncorrelated measurements, is given as below:

$$R_i = (\sigma^2) \begin{bmatrix} 1 & \cdots & 0 \\ \vdots & \ddots & \vdots \\ 0 & \cdots & 1 \end{bmatrix} m^2 \quad \text{where: } \sigma = 0.3 \text{ m} \quad (19)$$

The Kalman gain is used to update the state vector estimation error covariance matrix, computed as [3, 4]:

$$\hat{P}_1 = (I - K_1 H_1) P_1^- (I - K_1 H_1)^T + K_1 R_1 K_1^T \quad (20)$$

As usual, the innovation ν Eq. (17) is used to update the nonlinear state vector, Eq. (13):

$$\hat{x}_1 = x_1^- + K_1 \nu, \quad (21)$$

Equations (15)–(21) are executed in a sequence, provided the observations occur at the same time instant. Otherwise, the high fidelity translational motion dynamics Eq. (13) states is propagated to the next measurement epoch.

E. Simulation Results with Reduced Dynamics Formulation

This section presents the simulation results for reduced dynamics relative position estimation between LEO and GEO satellite. It can be seen from Fig. 5 that reduced dynamics has provided the continuous improved estimation of the relative position during NavIC/GNSS visibility period. The accuracy during this period is [50, 20, 40] m in ECI frame. Also, during NavIC non-visibility period the orbit estimation is carried out with translational motion dynamics. Figure 6 shows the relative position between LEO and GEO satellite for over 7 h.

5 Computation of Antenna Orientation Angle Requirement

For data transfer between LEO and ground station via small GEO Satellites, the antenna of GEO satellite has to be steered to LEO satellite to establish line-of-sight (LOS) communication between LEO and GEO satellites. Steering angle is the angle between current antenna pointing vector and LEO–GEO relative position vector. The steering can be realized by moving the antenna about elevation and azimuth angles. The azimuth angle is defined as the in-plane rotation required while elevation angle

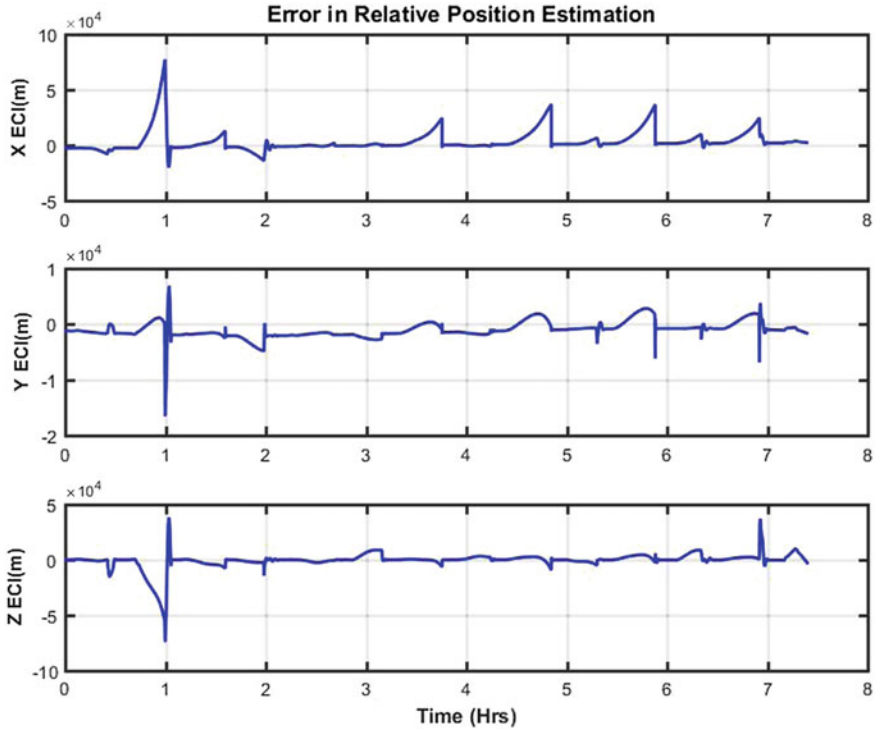


Fig. 5 Relative position estimation error

is defined as the out of plane rotation angle required to point the antenna beam from GEO to LEO.

The GEO orbit normal unit vector \vec{r}_{on} is computed as

$$\vec{r}_{on} = \vec{r}_{pos} \times \vec{r}_{vel} \tag{22}$$

The relative position vector is resolved into two components: one along the GEO orbit normal, i.e., \vec{r}_{relpos_on} and the other in the orbital plane unit vector, i.e., \vec{r}_{relpos_pln} .

$$\vec{r}_{relpos_on} = (\vec{r}_{relpos} \cdot \vec{r}_{on})\vec{r}_{on} \tag{23}$$

$$\vec{r}_{relpos_pln} = \vec{r}_{relpos} - \vec{r}_{relpos_on} \tag{24}$$

From Eqs. (23) and (24), the elevation (el) and azimuth (az) angles are computed. The corresponding plots for GEO at 270° East is shown in Fig. 7, thus establishing the requirement for continuous tracking of the antenna.

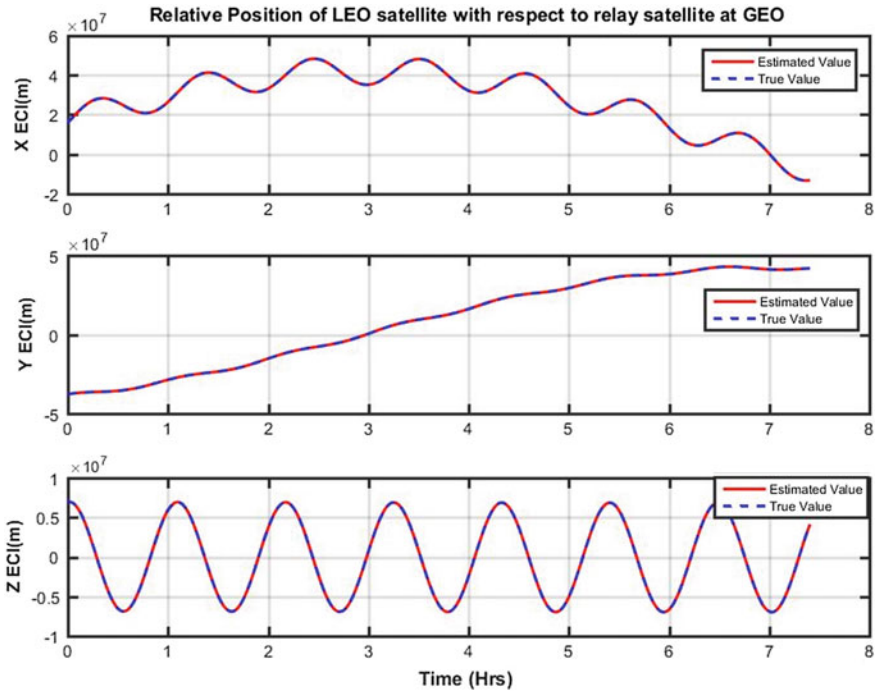


Fig. 6 Estimated relative position

6 Conclusion and Further Research Directions

This research work investigates the feasibility of using NavIC/GNSS measurements to determine the position of LEO satellite at data relay satellites at GEO altitude. Three small satellites are assumed at 34° , 134° , and 270° East longitude for this study. The visibility study of LEO satellite to GEO satellite is studied, providing possibility of continuous communication to ground station. The real-time kinematic relative position estimation between LEO and GEO satellites is carried out using NavIC/GNSS measurements. The common satellites to both the LEO and GEO are used to estimate the relative position, providing an estimation error of [2, 3, 5] m in ECEF frame of reference. This is further augmented with reduced dynamics in an extended Kalman filter. It is assumed that LEO satellite is transferring its GNSS observables to available GEO satellite for computation of the relative position. Whenever GNSS measurements are not available, the estimation is continued with degraded accuracy. The accuracy achieved during GNSS measurement period is of the order of [50, 20 40] m in ECI frame of reference. The computation of antenna orientation angle is carried out to move and track the LEO satellite for transfer of data anytime in the orbit using high-speed optical communication.

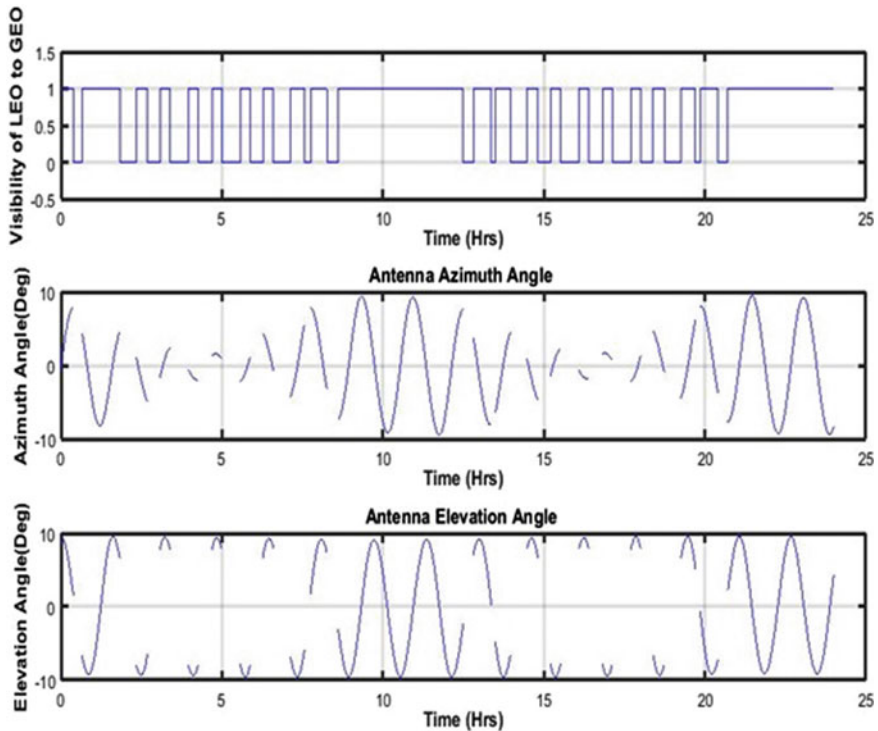


Fig. 7 Azimuth and elevation for GEO antenna at 270° East

In the future, these schemes should be extended to multiple LEO satellites data download. In view of optical communication that requires stringent pointing and control, the development of efficient formation flying algorithm is required.

Acknowledgements This research work was carried out at U. R. Rao Satellite Centre, Bangalore. The authors acknowledge the support and encouragement by Mr. Avinash K. Kulkarni, Division Head, Dr. N. K. Philip, Group Director, Control Dynamics and Simulation Group, Mr. Subramanya Udupa, Deputy Director, Control and Digital Area and Mr. P. Kunhikrishnan, Director, U. R. Rao Satellite Centre, for their motivation to pursue this practical and challenging research field.

References

1. Praveen Reddy G et al (2018) Study of data relay satellite system and its relevance to Indian context. *Int J Pure Appl Math* 118(16):1227–1244
2. Misra P, Enge P (2001) *Global positioning system: signals, measurements and performance*. Ganga-Jamuna Press, Lincoln, MA

3. Kumar V (2015) Autonomous navigation and station-keeping of geostationary satellites in formation using Indian regional space-based navigation system. Ph.D. dissertation, Department of Aerospace Engineering, IIT Bombay
4. Kumar V, Hablani HB (2017) Autonomous formation-keeping of geostationary satellites with regional navigation satellites and reduced dynamics. *AIAA J Guidance Control Dyn* 40:563–583. <http://arc.aiaa.org/doi/abs/10.2514/1.G001652>
5. Montenbruck O, Ebinuma T, Glenn Lightsey E, Leung S (2002) A real-time kinematic GPS sensor for spacecraft relative navigation. *Aerosp Sci Technol* 6:435–449. [https://doi.org/10.1016/s1270-9638\(02\)01185-9](https://doi.org/10.1016/s1270-9638(02)01185-9)
6. Kumar V, Hablani HB, Pandiyan R (2015) Kinematic navigation of geostationary satellites formation using Indian regional navigation satellites observables. *J Guidance Control Dyn* 38(9):1856–1864. <http://arc.aiaa.org/doi/abs/10.2514/1.G000864>
7. Montenbruck O, Gill E (2001) *Satellite orbits: models, methods and applications*, chapters 3 and 7. Springer, Berlin
8. Agrawal BN (1986) *Design of geosynchronous spacecraft*, chapter 2. Prentice-Hall, Inc., Englewood Cliffs, NJ
9. Sidi MJ (1997) *Spacecraft dynamics and control*, chapter 2. Cambridge University Press, Cambridge, UK
10. Montenbruck O, Steigenberger P, Riley S (2015) IRNSS orbit determination and broadcast ephemeris assessment. Paper presented at ION ITM 2015, Dana Point, CA, 26–28 Jan 2015

Mission and Control Configuration for Spin to Three-Axis Stabilization for Small Satellite



A. L. Satheesha, S. Kannan and M. P. Ramachandran

Abstract Describes the mission, control and attitude determination meant for spin stabilization to three-axis stabilization by using momentum bias system. Advantage of the proposed minimal configuration is better for small satellite using off-the-shelf component. There is clear advantage to spin up and spin down of the wheel in this configuration. Attitude determination is now simpler and reliable for the payload pointing to earth or solar panel tracking the sun when the pitch is held to orbit normal.

Keywords Spin stabilization · Momentum bias stabilization · Attitude determination · Magnetometer · Sun sensor

1 Introduction

Commercial and research interest by the companies, universities and organizations in small satellite design, building, realization and maintain are immense. This is in line with large computer now being available in smart phones. This is driven by the advancement in commercial electronic with various sensors in smart phones and other applications [1]. Launch of small satellite is depending mainly as piggy-bag along with large satellite. There are many small satellite launch vehicle research announcements. ISRO launched the HAMSAT way back in 2005 and it was a very successful mission. Later, Indian universities were guided to build the small satellites by ISRO. ANUSAT was first one such mission by ANNA UNIVERSITY. After this, many follow on missions were done by the INDIAN universities. Challenges in building small satellites by university are limited to ground resources to handle and

A. L. Satheesha (✉) · S. Kannan · M. P. Ramachandran
Flight Dynamics Group, U. R. Rao Satellite Center, Vimanapura Post, Bengaluru 560017, India
e-mail: alsatish@isac.gov.in

S. Kannan
e-mail: kannan@isac.gov.in

M. P. Ramachandran
e-mail: mprama@isac.gov.in

© Springer Nature Singapore Pte Ltd. 2020
PSR. S. Sastry et al. (eds.), *Advances in Small Satellite Technologies*,
Lecture Notes in Mechanical Engineering,
https://doi.org/10.1007/978-981-15-1724-2_11

maintain the satellite, using the commercial off-the-shelf components. In this paper, mission and control design scheme for simple three-axis stabilization are envisaged with minimal hardware.

2 Challenges in Configuration of Small Satellite

Satellite configuration is complex multidisciplinary task that involves power budgeting, control scheme for attitude stabilization, communication, thermal management and payload requirement, etc. For small satellite, above complex tasks need to be done with commercial off-the-shelf components which might not have been qualified for space radiation level. Ground infrastructure to support many satellites needs to be minimized. Thrusters are not considered in most of the small satellites. Cost considerations are equally important. These requirements triggered the authors to work out a simple concept of mission and control where three-axis momentum bias system is achieved after intermediate step of spin-axis stabilization.

3 Mission Design

Power hardware battery and solar panel should support the minimum load to support the communication, onboard-processor, magnetometer and torque's requirement during the initial acquisition. Highly inclined orbit is, however, required for functioning of negative $B \cdot \dot{\theta}$ law of control. Based on the local time of sun synchronous orbit, solar panel configuration will be decided so that minimum required power can be generated when spacecraft is spinning. For the sun synchronous orbit with 10:30 local time, the cosine of the angle between sun and orbit normal is around 0.9—this is parameter where 1 denotes full solar power generation. Hence, sun point panel can generate power with 90% of the peak power. Maximum moment of inertia axis should be spin axis that is, pitch axis and it is desirable to keep the cross moment of inertia considerably small. This ensures stability. To have better control, wheels about all the axes will compensate the cross moment of inertia effect in fine controlling the spacecraft attitude. Since the pitch axis is held to orbit normal, attitude determination will be the rotation of the other two axes about pitch. Hence only pitch rotation angle need to be determined. This can be determined using magnetometer Yaw and roll components. This can also be determined more accurately using sun vector measurement in yaw-roll plane. This is described in Sect. 5. It is well known that magnetic torquer activity will affect the magnetometer measurement. Hence, magnetic measurement and magnetic torquers operation need to be at different time slot.

Mission planning need to be done such that good power margin should be ensured during high power consuming activities like payload data download, torquers activity. Payload operation attitude with yaw looking to earth with constant pitch rate and

maximizing the power attitude with sun tracking (pitch is still along the –ve orbit normal) with zero pitch rate need to be properly planned such that good power generation and storage should be ensured.

4 Attitude Stabilization and Control

After injection, first step of the attitude stabilization is to kill the rate in the yaw and roll axes, align the pitch axis along the negative orbit normal with required spin rate. This can be achieved with magnetometer and two magnetic torquers using negative $B\dot{\cdot}$ law to align the spin axis to orbit normal and cross product law for the spin-rate control [2] as done in HAMSAT for highly inclined orbits. Disturbance torques due to environment and spacecraft moment of inertia will decide torques and wheel capacity. Spin-axis attitude determination and spin rate can be computed with magnetometer. Yet as mentioned earlier, the active torquers period and magnetometer measurement cannot be carried out simultaneously. Hence, the control and the measurement and attitude determination times will be in different slots. Spacecraft maximum moment of inertia should be spin axis, i.e. pitch to support this mode of acquisition. This can be achieved with proper mass and structural design. Once this is achievable, the wheel about spin axis is rotated such that angular momentum is transferred to wheel and spacecraft body is three-axis stabilized in momentum-biased configuration. Wheel switch ON is considered only after the spin-axis stabilization is achieved to save the power and make acquisition simple.

It is important to note that as the angular momentum vector is same as in spin-stabilization configuration, hence, negative $B\dot{\cdot}$ control law can be applied to make the pitch (or negative pitch) along the orbit normal. Single wheel controls the pitch rotation of spacecraft body. Less capacity wheel may be required based on moment of inertia matrix. Similar control was used for safe mode in case of RADAR satellite. Sun-synchronous dawn–dusk orbit (RADARSAT) negative pitch aligning to orbit normal makes it power safe. Another advantage of this configuration any power anomaly need the wheel spin down will transfer the angular momentum to body with body spin axis near to orbit normal. Spin configuration should generate sufficient power only to support the Onboard-computer, minimal communication, magnetometer and torquer. Normally, spin rate of about 2–3 rpm is required to compensate the disturbance torque in low earth orbit. Wheel capacity should be able to take this angular momentum. Hence wheel sizing is based on spacecraft moment of inertia about spin axis and spin rate. Once spin rate of spacecraft body is transferred to wheel, three axis is stabilized and can track the orbit frame with orbital rate. Negative $B\dot{\cdot}$ control law will act to hold the pitch in negative orbit normal. For earth pointing pitch attitude reference is required. This can be provided by the roll and yaw components of magnetometer reading detail are discussed in Sect. 5. In this case, attitude determination becomes single angle (pitch only) attitude determination problem assuming that pitch axis is pointing to orbit normal. Inertial held attitude can maximum power generation such that solar panel towards the sun. Still pitch will point to negative orbit

normal. This is similar to solar panel drive used for rotation of solar panel in earth pointing satellite. From this step, we can achieve zero moment system by dumping the wheel speed using magnetic torquer—in this case, other simplicity will be lost and wheels control along all the principle axis is required.

5 Determination of Attitude and Rate

Here, confirmation of spin-axis position is required. This can be done using magnetometer pitch axis measurement [3]. Spin rate higher than 0.5 °/s can be detected using magnetometer data. Pitch angle measurement and reference only required once spacecraft is achieved the three-axis stabilization with momentum bias system. Pitch rotation need to be determined and this can be done by just computing the phase of the magnetic field vector in yaw–roll plane w.r.t say yaw axis. This can be compared with desired phase angle for earth pointing and control to the required attitude. Similar scheme can be used with sun vector measurement with sun vector body frame measurement in yaw–roll plane. (Coarse Analog sun sensor will do this measurement) Sun sensor measurement will not change from orbit to orbit and only changes with the season. This can be used for better earth pointing and sun pointing. For better attitude, accuracy during optical payload pointing sun sensor phase can be used. But magnetometer yaw–roll phase angle will change w.r.t path in the orbit. Difference between the phase angle in yaw–roll plan between the sun and magnetometer may be used to find the path of the satellite orbit, and it may be correlated to station visibility. Momentum-biased system makes the attitude determination lot simpler and observability issue of “magnetometer only attitude determination” is removed when one axis is fixed.

Overall for simple symmetric moment of inertia balance small satellite three-axis-controlled mission can be achieved with single wheels and two magnetic torquers with magnetometer and coarse analog sun sensor.

Acknowledgements Author like to acknowledge the support for encouragement provided by our group director Mrs. Dakshayani B. P. and our Deputy Director Mr. Kiran B. S. Authors would like to acknowledge the discussion and encouragement from Control Group director Dr. Philip N. K. and their team. Authors thank Centre Director Mr. Kunhikrishnan for supporting this activity.

References

1. Boshuizen C, Mason J, Klupar P, Spanhake S Results from the planet labs flock constellation. In: 28th annual AIAA/USU conference on small satellites
2. Natarajan P, Pandey PN, Agrwal VK, Malik NK (2007) Autonomous spin axis and spin rate control for hamsat. In: 58th international astronomical congress
3. Thompson RH Magnetometer bias determination and spin-axis attitude estimation for the AMPTE mission. J Guid 7(4)

Slew Rate and Control Constrained Spacecraft Attitude Maneuver with Reaction Wheel Failure



Anuradha Sahu, Arun Kumar Mahodaya and Shreesha Chokkadi

Abstract Attitude maneuvers are required for reorienting the satellite for meeting various mission objectives. A higher satellite slew rate during maneuvers is a desirable characteristic for any mission design. At the same time, a higher slew rate demands a higher actuator torque capacity which is always constrained due to the physical limits of the actuator. This paper discusses the satellite attitude maneuver problem under slew rate and actuator capacity constraints. A quaternion feedback controller with quaternion and angular rate feedback is implemented to achieve a rest to rest reorientation maneuver. The control gains are computed based on the slew rate limits while the control commands incorporate the actuator limits. Three different configurations of four reaction wheels, (a) pyramid configuration, (b) skew configuration with three wheels along the body axes and the fourth wheel along body diagonal and (c) skew configuration with skew angle of 45° , are studied. The paper further discusses single reaction wheel failure conditions for all the three configurations and demonstrates satellite rest to rest maneuver within the slew rate and actuator limits.

Keywords Attitude maneuver · Slew rate · Quaternion feedback controller · Pyramid and skew configuration

1 Introduction

Attitude control system (ACS) is of significant importance among subsystems of spacecraft which governs the pointing accuracy of space mission. Designing high

A. Sahu · S. Chokkadi

Instrumentation and Control Engineering, Manipal Institute of Technology,
Manipal Academy of Higher Education (MAHE), Manipal, Karnataka 576104, India
e-mail: shreesha.c@manipal.edu

A. K. Mahodaya (✉)

Research Centre Imarat, Defence Research and Development Organisation (DRDO),
Hyderabad 500069, India
e-mail: arunkumar.mahodaya@rcilab.in

© Springer Nature Singapore Pte Ltd. 2020
PSR. S. Sastry et al. (eds.), *Advances in Small Satellite Technologies*,
Lecture Notes in Mechanical Engineering,
https://doi.org/10.1007/978-981-15-1724-2_12

performance ACS subsystem is always a challenging task, specially providing fast maneuver with available actuator torque limit. For maximum torque, reaction thruster is considered to be a good selection but at the cost of high fuel consumption. Alternatively, momentum exchange devices are proven to be the best option, utilizing only electrical power [1]. Since reaction wheels are widely installed as actuators in most of the spacecrafts for attitude control recently, the wheel input torque saturation problem has been a main area of concern. Large angle slew maneuver is driven by the torque capability of the actuator used in ACS subsystem and commanded control algorithm. Boskovic et al. have designed a globally stable control algorithm to take into account the input saturation limit of the actuator and parameter uncertainty [2]. Tian Lin et al. have designed a varying input saturation model for a set of three flywheels and provided a controller with feedback to take into consideration the stability of control process [3]. Cruz et al. [4] have proposed a saturation and inertia free controller for motion to spin tracking case. However, efforts discussed above have been mainly focused on the saturation limit of the actuators but have not considered the problem associated with high agility of the satellite. Most literature has been focusing on the minimum or near minimum time maneuvers associated with saturation problem. Weiss et al. [5] in their paper presented the algorithm with inertia uncertainty and near minimum time attitude control problem with eigen axis rotation using classical PD controller. Wie et al. [6] have proposed the cascade saturation control problem with slew rate as well as input saturation limits for rest to rest case. However, there is no illustration for the verification of controller's capability with wheel failure mode. This paper deals with quaternion feedback regulation control for rest to rest maneuver of the spacecraft for large angle reorientation within the torque limit of the actuator and within the slew rate constraint, with reaction wheel failure modes. In this paper, three different configurations of reaction wheel are used for performance comparison.

2 Satellite Modeling

In this section, a rigid spacecraft body at lower earth orbit (LEO) is considered with reaction wheels used as actuators. The dynamics of spacecraft and quaternion kinematics have been discussed, along with the distribution matrix of all three configurations of actuator. An asymmetric rigid spacecraft body, say B , is considered with center of mass C . The whole spacecraft system say s/c consists of the body B and four symmetric wheels W_i , whose center of mass is C_i , where $i = 1-4$ for four wheels. All the calculations will be done relative to a fixed inertial frame N .

2.1 Reaction Wheel Configuration

The angular momentum of wheel for four-wheel configuration is given by [7]:

$${}^N H^{W_i/C_i} = [I^{W_i/C_i}] \{ {}^N w^{W_i} \} \quad (1)$$

where ${}^N H^{W_i/C_i}$ is the momentum of i th wheel measured from its own center of mass, relative to inertial frame, $[I^{W_i/C_i}]$ is the moment of inertia matrix of i th wheel and $\{ {}^N w^{W_i} \}$ is the angular velocity of reaction wheel in wheel frame relative to the inertial frame and is given as,

$$\{ {}^N w^{W_i} \} = \{ {}^N w^B \} + \Omega_i \{ d_i \} \quad (2)$$

where $\{ d_i \}$ is the unit vector of i th wheel along its spin axis and Ω_i is the angular velocity of i th wheel

Thus angular momentum is rewritten in compact form for four wheels as,

$${}^N H^{W_i/C_i} = [A] \{ \Omega \} \quad (3)$$

where $A = [I^{W_1/C_1} \{ d_1 \} \quad I^{W_2/C_2} \{ d_2 \} \quad I^{W_3/C_3} \{ d_3 \} \quad I^{W_4/C_4} \{ d_4 \}]$

$$\Omega_i = [\Omega_1 \quad \Omega_2 \quad \Omega_3 \quad \Omega_4]^T$$

$$D_{3 \times 4} = [\{ d_1 \} \quad \{ d_2 \} \quad \{ d_3 \} \quad \{ d_4 \}]$$

The torque in satellite body frame is given by;

$$T_{c(3 \times 1)} = D_{(3 \times 4)} \tau_{RW(4 \times 1)} \quad (4)$$

where D is a 3×4 distribution matrix which transforms the torque from wheel frame to body frame. τ_{RW} is a 4×1 matrix gives reaction wheel torque in wheel frame along each wheel axis.

To obtain τ_{RW} , the Moore–Penrose pseudo-inverse method is used [8, 9] to obtain inverse of distribution matrix,

$$D_{4 \times 3}^f = D^T (D D^T)^{-1} \quad (5)$$

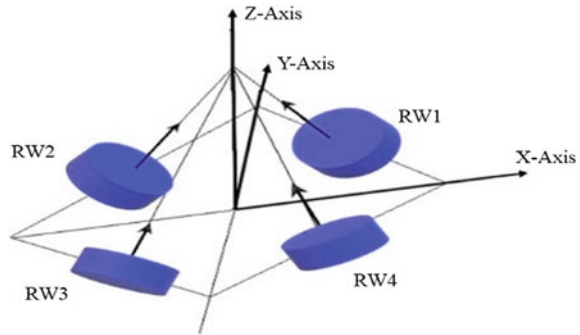
$$\tau_{RW(4 \times 1)} = D_{(4 \times 3)}^f T_{c(3 \times 1)} \quad (6)$$

Different configurations which have been considered in the paper are as follows:

Configuration (a)

The distribution matrix of a pyramid configuration shown in Fig. 1 with $\alpha = 35^\circ$ and $\beta = 45^\circ$ is given as:

Fig. 1 Reaction wheel configuration (a)



$$D = \begin{bmatrix} \cos(\alpha) * \cos(\beta) & \cos(\alpha) * -\cos(\beta) & \cos(\alpha) * -\cos(\beta) & \cos(\alpha) * \cos(\beta) \\ \cos(\alpha) * \sin(\beta) & \cos(\alpha) * \sin(\beta) & \cos(\alpha) * -\sin(\beta) & \cos(\alpha) * -\sin(\beta) \\ \sin(\alpha) & \sin(\alpha) & \sin(\alpha) & \sin(\alpha) \end{bmatrix} \tag{7}$$

Configuration (b)

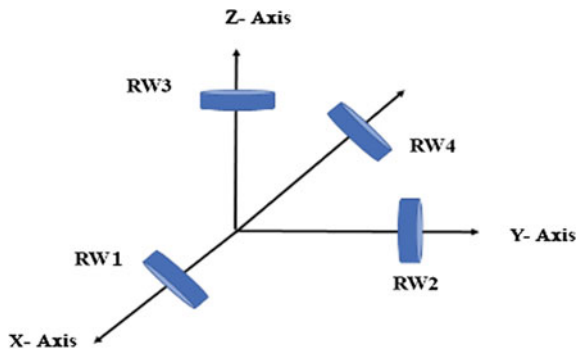
The configuration three wheels are kept along the roll, pitch and yaw axes of the spacecraft body, respectively, and the fourth wheel is kept along body diagonal, shown in Fig. 2, corresponding distribution matrix is given by;

$$D = \begin{bmatrix} 1 & 0 & 0 & 1/\sqrt{3} \\ 0 & 1 & 0 & 1/\sqrt{3} \\ 0 & 0 & 1 & 1/\sqrt{3} \end{bmatrix} \tag{8}$$

Configuration (c)

This is skew configuration with all wheels skewed by an angle 45° as shown in Fig. 3 [6]. The distribution matrix with $\beta = 45^\circ$ is given by:

Fig. 2 Reaction wheel configuration (b)



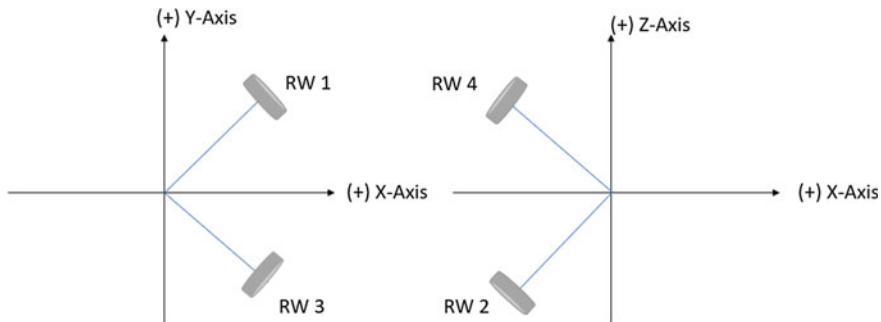


Fig. 3 Reaction wheel configuration (c)

$$D = \begin{bmatrix} \cos(\beta) & -\cos(\beta) & \cos(\beta) & -\cos(\beta) \\ \sin(\beta) & 0 & -\sin(\beta) & 0 \\ 0 & -\sin(\beta) & 0 & \sin(\beta) \end{bmatrix} \quad (9)$$

2.2 Satellite Dynamics

From Euler's equation of motion [1, 7]:

$$N_{\text{ext}} = {}^N H^{B/C} + {}^N w^B \times {}^N H^{B/C} \quad (10)$$

where N_{ext} is the external torque, ${}^N H^{B/C}$ is angular momentum of the spacecraft measured from its center of mass C in B relative to N and ${}^N w^B$ is the angular body rate of the satellite in body relative to inertial.

Considering the spacecraft equation of motion in Eq. (10) along with the wheel dynamics from Eq. (3) and representing in matrix form:

$$N_{\text{ext}} = [I_s]\{\dot{w}\} + \{\tilde{w}\}[I_s]\{w\} + [A]\{\dot{\Omega}\} + \{\tilde{w}\}[A]\{\Omega\} \quad (11)$$

where $[I_s]$ is a 3×3 spacecraft inertia matrix, $\{w\}$ is a 3×1 matrix representing the spacecraft angular body rates along roll, pitch and yaw axis.

For no external torque applied to the spacecraft, i.e., $N_{\text{ext}} = 0$, we have;

$$\dot{w} = -[I_s^{-1}][\{\tilde{w}\}[I_s]\{w\} + [A]\{\dot{\Omega}\} + \{\tilde{w}\}[A]\{\Omega\}] \quad (12)$$

where $\{\tilde{w}\}$ is a skew symmetric matrix given by;

$$\tilde{w} = \begin{bmatrix} 0 & -w_3 & w_2 \\ w_3 & 0 & -w_1 \\ -w_2 & w_1 & 0 \end{bmatrix} \quad (13)$$

$[A]\{\dot{\Omega}\} = \dot{h}_w = -N_{\text{ctrl}}$ is the control torque input to the reaction wheel, in opposite direction to the satellite rotation, gives:

$$\dot{w} = -[I_s^{-1}][\{\tilde{w}\}[I_s]\{w\} + \{\tilde{w}\}[A]\{\Omega\} - N_{\text{ctrl}}] \quad (14)$$

2.3 Quaternion Kinematics

The satellite error kinematics is represented using attitude error quaternion, $q = [q_1 \ q_2 \ q_3 \ q_4]^T$, where the vector part $[q_1 \ q_2 \ q_3]^T$ represents the axis of rotation and the scalar q_4 gives the angle of rotation. The error kinematics of satellite is given as [5]:

$$\dot{q} = \frac{1}{2}\{\tilde{w}\}q \quad (15)$$

$$\dot{q} = \frac{1}{2} \begin{bmatrix} 0 & w_3 & -w_2 & w_1 \\ -w_3 & 0 & w_1 & w_2 \\ w_2 & -w_1 & 0 & w_3 \\ -w_1 & -w_2 & -w_3 & 0 \end{bmatrix} q \quad (16)$$

Equation (15) can be separated for scalar term q_4 which gives:

$$\dot{q} = -\frac{1}{2} \begin{bmatrix} 0 & -w_3 & w_2 \\ w_3 & 0 & -w_1 \\ -w_2 & w_1 & 0 \\ w_1 & w_2 & w_3 \end{bmatrix} \begin{bmatrix} q_1 \\ q_2 \\ q_3 \end{bmatrix} + \frac{1}{2} \begin{bmatrix} q_4 & 0 & 0 \\ 0 & q_4 & 0 \\ 0 & 0 & q_4 \end{bmatrix} \begin{bmatrix} w_1 \\ w_2 \\ w_3 \end{bmatrix} \quad (17)$$

The kinematic equation can be written as $q = [g^T, q_4]$ where $g = [q_1 \ q_2 \ q_3]^T$ is the vector component of quaternion.

$$\frac{d}{dt} \begin{bmatrix} g \\ q_4 \end{bmatrix} = \frac{1}{2} \begin{bmatrix} -[\tilde{w}]_{3 \times 3} \\ -w^T \end{bmatrix} g + \frac{1}{2} q_4 \begin{bmatrix} I_{3 \times 3} \\ 0 \end{bmatrix} w \quad (18)$$

3 Feedback Control with Slew Rate and Torque Constraint

The satellite dynamics and kinematics from Eqs. (14) and (18) is combined in order to get a nonlinear equation of the form:

$$x = f(w_1, w_2, w_3, q_1, q_2, q_3, h_1, h_2, h_3, h_4) \quad (19)$$

The input is the control torque given by the reaction wheels;

$$u = [N_x \ N_y \ N_z] \quad (20)$$

The feedback control without considering any constraint consists of feedback error quaternion and angular body rates, which are given as [4, 9]:

$$u = N_{ctrl} = T_c = K_q q_e + K_w w \quad (21)$$

where u is the input torque given to the reaction wheels, K_q and K_w are proportional and derivative gains, respectively, which are 3×3 matrix selected according to the desired reorientation conditions.

When torque limit is to be included, reaction wheel torque required to be kept in the same direction as control torque, the maximum condition and saturation limit are considered as [6]:

$$\rho = \max |(T * \tau_{RW})_i| \quad (22)$$

where

$$T = \text{diag} \left(\frac{1}{\tau_{1RW\max}}, \frac{1}{\tau_{2RW\max}}, \frac{1}{\tau_{3RW\max}}, \frac{1}{\tau_{4RW\max}} \right) \quad (23)$$

And thus the saturation limit of the reaction wheel control torque is then defined as:

$$\tau = \text{sat}(\tau_{RW}) = \begin{cases} \tau_{RW} & \text{if } \rho \leq 1 \\ \tau_{RW}/\rho & \text{if } \rho > 1 \end{cases} \quad (24)$$

where ρ is a positive scalar function of τ_{RW} which characterizes the largeness of τ_{RW} to limit the torque value.

The control command law considering the slew rate and torque constraint is

$$u = T_c = \rho^{\text{sat}}(K_q \text{sat}(P q_e) + K_w w) \quad (25)$$

$$K_q = \text{diag}(k_1, k_2, k_3) * I_s \quad (26)$$

$$K_w = cI_s \quad (27)$$

$$P = \text{diag}(p_1, p_2, p_3) \quad (28)$$

$$K_q P = kI_s \quad (29)$$

The value of k_i is selected as; $k_i = c \frac{|q_{i(0)}|}{\|q_{(0)}\|} \dot{\theta}_{\max}$ for $i = 1, 2, 3$.

Where $[\text{sat}(Pq_e)]$ limits the slew rate of the satellite, keeping the saturation limits $|p_i q_i| = 1$, with t_c be the time at which there exists at least one axis such that $|p_i q_i(t_c)| = 1$ for all i and for duration $0 \leq t \leq t_c$.

The saturation for slew rate is given by $\text{sign}(Pq_e) = \begin{cases} +1 & \text{if } (Pq_e) > 0 \\ 0 & \text{if } (Pq_e) = 0 \\ -1 & \text{if } (Pq_e) < 0 \end{cases}$.

It is assumed that $q_{i(0)}$ is non-zero. The rest to rest reorientation maneuver consists of three phases [6]; (a) acceleration phase, (b) coast phase and (c) deceleration phase.

During the acceleration phase, the body rates accelerate at its fastest possible rate specified by $\dot{\theta}_{\max}$, for time $0 \leq t \leq t_s^*$ where t_s^* is the settling time after acceleration and is evaluated as $t_s^* \approx \frac{4}{c}$.

If a system is being controlled under saturation logic in a constrained maneuver problem and if there is a condition of $|p_i q_i| \geq 1$ for a large time instant, i.e., $t \leq t_c$, then during the time $[t_s^*, t_c]$ the spacecraft will rotate at constant velocity and is said to be in quasi-state mode [6]. The coast phase starts from $t = t_s^*$ and continues for the duration $t_s^* \leq t \leq t_c$, during this phase the angular rate changes very slowly and is calculated at any instant as;

$$w(t) \approx -\frac{|q_{i(0)}|}{\|q_{(0)}\|} \dot{\theta}_{\max}$$

for $i = 1, 2, 3$ for corresponding quaternion

where $i = 1, 2, 3$ for the corresponding quaternion and the time t_c is approximated as:

$$t_c \approx t_s^* + \frac{2}{\dot{\theta}_{\max}} \vartheta \quad (30)$$

where

$$\vartheta = \tan^{-1} \left(\frac{\|q_{(0)}\|}{q_4(t_s^*)} \right) \quad (31)$$

The quaternion errors and body rates reach zero as the deceleration phase arrives at $[t_c, \infty]$.

As deceleration phase approaches, for settling the spacecraft body rates to zero, we consider the 2nd order equation of the dynamics of slew rate required;

$$\ddot{\theta} + c\dot{\theta} + k\frac{\theta}{2} = 0 \quad (32)$$

Which gives the basis for selecting the parameters c and k for Eqs. (27) and (29) as:

$$c = 2\zeta w_n \quad (33)$$

$$k = 2w_n^2 \quad (34)$$

4 Wheel Failure Condition

The condition with failure of one wheel for each configuration of reaction wheels is discussed, where distribution matrix with wheel failure is obtained by removing the column corresponding to the failed one wheel, the matrix is then inverted and a row corresponding to the wheel failed is replaced with zero [8].

Equation (5) is used to calculate the inverse of distribution matrix in order to obtain the reaction wheel control torque in wheel frame from the body frame to evaluate the torque allocation matrix.

5 Simulation Results

The satellite is desired to make a maneuver of 120° giving initial quaternion $[\vec{q} \ q] = [0.2914 \ 0.2914 \ -0.7615 \ 0.5]^T$ with maximum slew rate of $\dot{\theta}_{\max} = 1.5^\circ/\text{s}$ and maximum torque saturation limit of each reaction wheel is 0.027 Nm . Considering a typical rest to rest maneuver, the initial body rates are taken as $w = [0 \ 0 \ 0]^T$. The parameters k and c are selected based on desired damping ratio as $\zeta = 1$ for critical damping and $w_n = 0.1 \text{ rad/s}$. Settling time relation is used as $t_s = \frac{8}{\zeta w_n}$ to account for nonlinear effect of $\sin(\phi/2)$ in 2nd order equation, which is replaced by $\phi/2$ in Eq. (32) for the purpose of gain selection. For better understanding of the results, the preferred configuration of the normal mode has been illustrated, and one of the wheel failure mode for all the configurations has been shown in the figures to represent the ability of controller to work with wheel failure mode with all the configurations.

Figure 4 shows the performance of configuration (b) in normal mode with all wheels working. The plot of body rates (left) in Fig. 4 and slew rate (right) represents that for time $[0 \ t_s^*]$, i.e., $t_s^* \approx \frac{4}{c} \approx 20 \text{ s}$, the body accelerates within slew rate limit

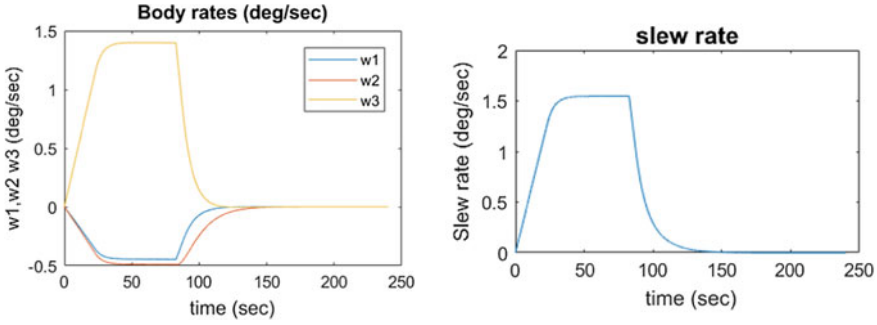


Fig. 4 Body rates (left) and slew rate (right) of configuration (b) with all wheels working

and then reaches quasi-state mode, i.e., for $[t_s^* \ t_c]$; $t_c \approx t_s^* + \frac{2}{\dot{\theta}_{\max}} \tan^{-1}\left(\frac{\|q_{(0)}\|}{q_4(t_s^*)}\right) \approx 91.35$ s, the spacecraft moves with almost constant velocity, the body rates moves very slowly with $w(t) = -\frac{|q_{i(0)}|}{\|q_{(0)}\|} \dot{\theta}_{\max}$. After the time interval t_c , the spacecraft starts decelerating and reaches target orientation during interval $[t_c \ t_\infty]$.

The numerical simulation has been performed using fourth-order Runge-Kutta integration method using MATLAB. The spacecraft error quaternion and angle error approaches zero with limited torque capacity of the actuator, represented in Fig. 5, shows the torque of each reaction wheels which is limited within 0.027 Nm to avoid saturation of reaction wheels.

Figures 6, 8 and 10 show the body rate and slew rate for one wheel failure mode (RW3 Failed) for configuration (a), (b) and (c), respectively. Even in the condition of one wheel failure, the controller is able to reorient the spacecraft under the desired slew rate and maximum torque limit (see Figs. 7, 9 and 11), however with a compromise in the attitude pointing accuracy. With respect to the time of reorientation and slew rate, all the three configurations of reaction wheels show approximately

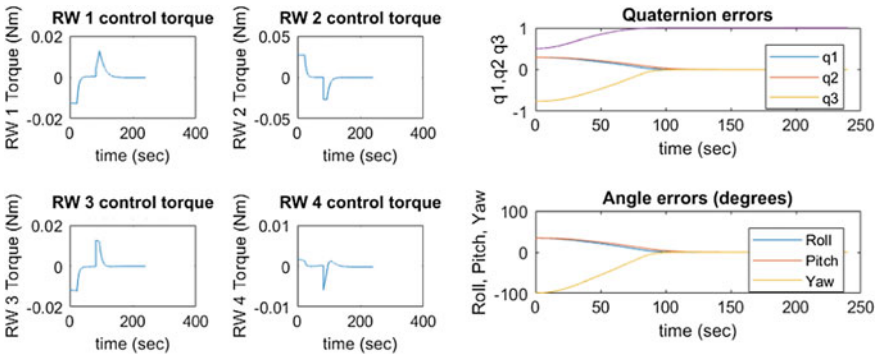


Fig. 5 Reaction wheel torque (left) and attitude error (right) for configuration (b), with all wheels working

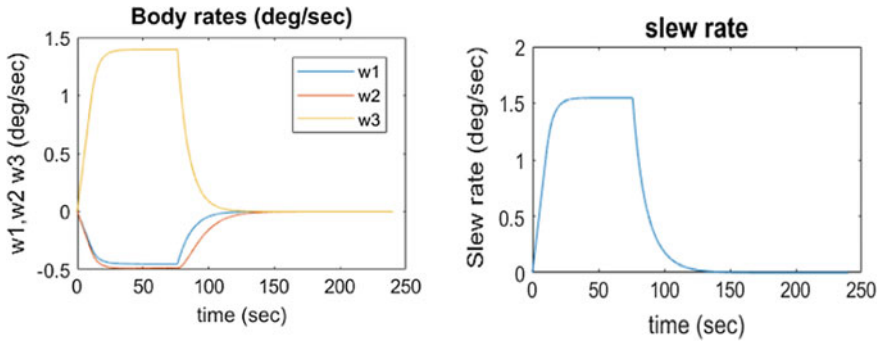


Fig. 6 Body rates (left) and slew rate (right) for configuration (a) with RW3 failure

similar performance but with respect to the torque utilization for rest to rest maneuver, configuration (b) performs as the most optimal configuration, utilizing minimum amount of torque in normal (no wheel failure) mode as given in Table 1.

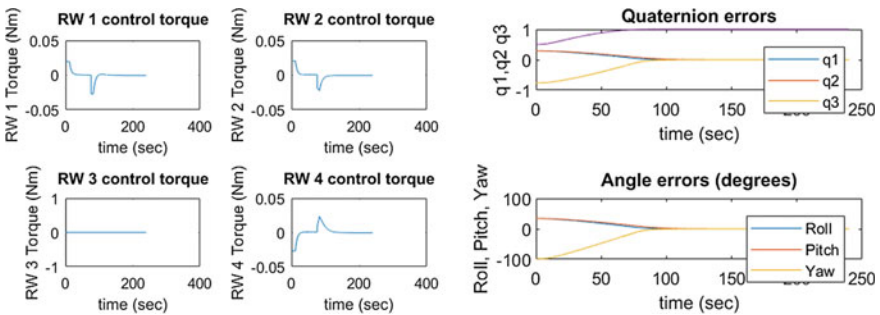


Fig. 7 Reaction wheel torque (left) and attitude error (right) with configuration (a), RW3 failure

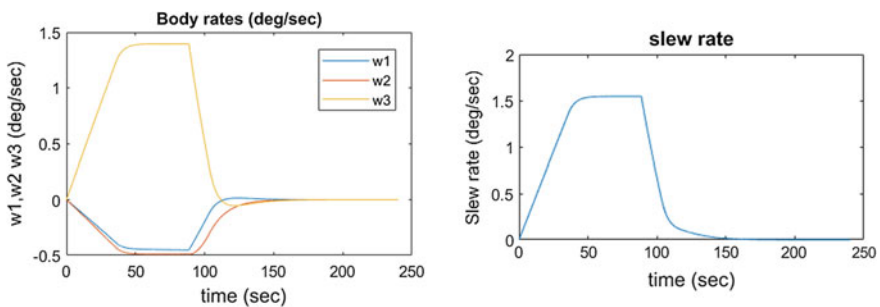


Fig. 8 Body rates (left) and slew rate (right) of configuration (b) with RW3 failure

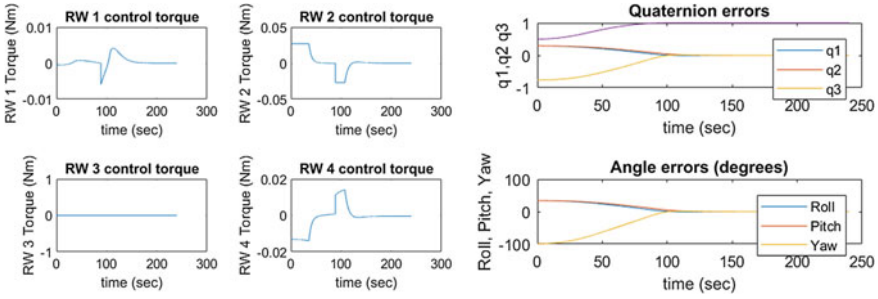


Fig. 9 Reaction wheel torque (left) and attitude error (right) with configuration (b), RW3 failure

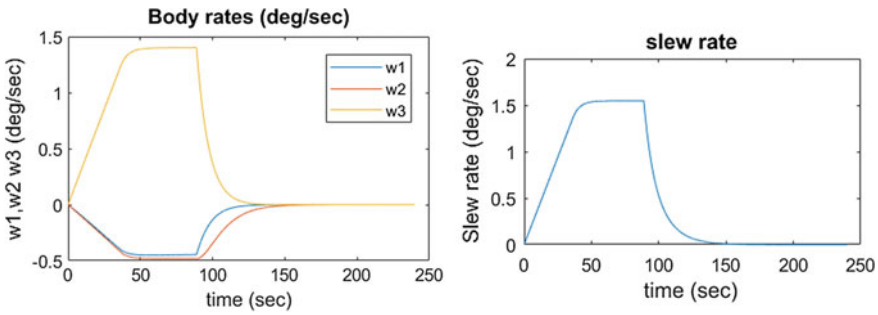


Fig. 10 Body rates (left) and slew rate (right) of configuration (c) with RW3 failure

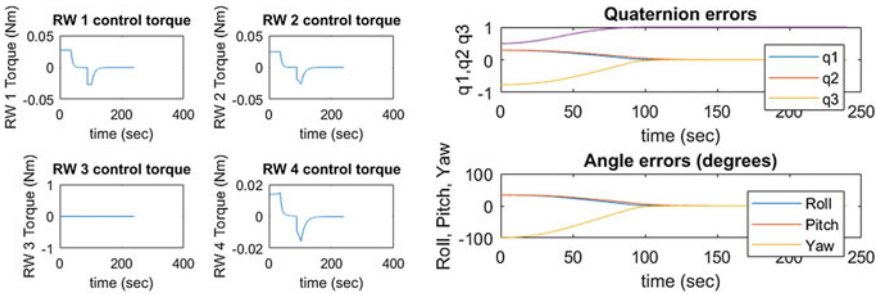


Fig. 11 Reaction wheel torque (left) and attitude error (right) with configuration (c), RW3 failure

Table 1 Net maximum torque requirement for rest to rest reorientation maneuver

	Configuration (a)	Configuration (b)	Configuration (c)
Torque in Nm	0.0406	0.0324	0.0372

6 Conclusion

The paper has discussed the control law for satellite maneuver, with slew rate and actuator constraints. The paper studied three different reaction wheel configurations having four wheels each. The slew maneuver capability was demonstrated in the nominal case of all wheels working as well as the case of single wheel failure. The slew rate and actuator maximum torque constraints were respected in all the cases. However, in case of one wheel failure, there was a slight degradation in the slew maneuver duration and the steady state attitude error.

The three configurations were compared with respect to the minimum torque demand. Slew rate performances with all wheels working in the nominal case are compared, and configuration (b) is the preferred configuration with respect to the minimum torque demand. This configuration also meets the requirement of single wheel failure with acceptable performance degradation and within the actuator physical limits.

References

1. Sidi MJ (1997) *Spacecraft dynamics and controls*, vol 1, no 7. Cambridge University Press, Cambridge, UK, pp 152–208
2. Boskovic JD, Li S-M, Mehra RK (2001) Robust adaptive variable structure control of spacecraft under control input saturation. *J Guid Control Dyn* 24:14–22
3. Lin T, Shinje XU (2012) Attitude control considering variable input saturation limit for a spacecraft equipped with flywheels. *Chin J Aeronaut* 25:437–445
4. Cruz G, Yang X, Weiss A (2011) Torque saturated, inertia free spacecraft attitude control. In: *AIAA guidance, navigation and control conference*, Portland, Oregon, pp 1–25
5. Weiss H, Wie B, Araposthathis A (1989) Quaternion feedback regulator for spacecraft eigenaxis rotations. *J Guidance* 12(3):375–380
6. Wie B, Lu J (1995) Feedback control logic for spacecraft eigenaxis rotations under slew rate and control constraints. *AIAA* 18(6):1372–1379
7. Junkins JL, Turner JD (1986) *Optimal spacecraft rotation manoeuvres*, vol 3. Elsevier, Amsterdam
8. Santosh K, Yuvaraj S, Rakshit, Sahay D, Tejaswini GS (2017) Reaction wheel control, testing and failure analysis for STUDSAT-2. *IEEE*, pp 1–11
9. Crassidis JL, Markley FL (2014) *Fundamentals of spacecraft attitude determination and control*. Springer, New York, pp 123–341

Payloads and Applications

Novel Seed Point Selection Technique for Dual-Pol SAR Images



Manish Pratap Singh, Sanjay and A. Mishra

Abstract In recent years, dual polarimetry has gained much importance among other earth observation missions due to its less complex architecture, larger swath coverage and low battery consumption. In this paper, a novel technique for automatic initial seed point selection for dual-pol data is proposed and its performance for different dual-pol combinations has been assessed. The proposed technique is independent of polarization combinations. Impact on classification when only 50% pixel is considered for selecting initial seed point is demonstrated. RISAT-1 quad-polarimetric data has been used for validating our result.

Keywords Dual-pol · Quad-pol · Wishart distance

1 Introduction

For dual-pol SAR data, different modes are possible like HH-HV, HH-VV and VV-HV. It is also a fact that though quad-polarimetric data contains maximum information, but often not used completely in the final implementation [1]. In quad-polarimetric, scattering values for four polarizations HH, HV, VH and VV are obtained, but in implementation phase it is assumed that HV and VH values are same as per the principle of reciprocity, or the average of HV and VH is taken for the further computations. Processing is done on T3 matrices which are a 3×3 semi-positive definite matrices instead of 4×4 semi-positive definite matrices. Very few literatures are available where 4×4 matrices are used for processing since not only the processing but its interpretation is also complex. In dual-pol data processing, all the information content is used in the final implementation of the algorithms. In dual-pol SAR data, for different combinations there are different target vectors and C2 matrices. H-Alpha (entropy/mean alpha angle) decomposition is the trademark for quad-pol data decomposition. For quad-pol data segmentation, the initial seed point is selected based on H-Alpha plane. Cloude [2] has shown that H-Alpha decomposition, similar to quad-pol case, is possible for dual-pol also. H-Alpha plane accuracy

M. P. Singh (✉) · Sanjay · A. Mishra

Defence Electronics Application Laboratory, Dehradun, Uttarakhand, India

© Springer Nature Singapore Pte Ltd. 2020

PSR. S. Sastry et al. (eds.), *Advances in Small Satellite Technologies*,

Lecture Notes in Mechanical Engineering,

https://doi.org/10.1007/978-981-15-1724-2_13

depends on the selected dual-pol data combination as shown by Ji et al. [3]. It is also seen that for dual-pol data it is not possible to accurately define H-Alpha plane boundary [3]. Since for different dual-pol combinations H-Alpha plane is different, so selecting the initial seed point criteria is also different [3]. In quad-polarimetric data, Wishart segmentation is applied after getting initial seed point. It is also observed that Wishart classifier is very robust and its convergence dependency on initial seed point is not so strong [4]. Even when initial cluster centers are selected randomly, the convergence is relatively fast. For different dual-pol data combinations, a different H-Alpha plane was proposed by Ji et al. [3].

2 Proposed Technique

H-Alpha decomposition and Wishart classification are widely used, and it is also very effective and robust for classifying the quad-polarimetric data. We have applied the H-Alpha decomposition technique for classifying dual-pol data. For different dual-pol combinations, different target vectors and coherency matrices are defined [3]. Target vectors and coherency matrices for different dual-pol data combinations are given in Eqs. (2–10) of Appendix. The proposed technique is independent of the selected dual-pol combination, and a *mode*-based initial seed point selection technique is proposed. In the proposed technique, we may vary the number of classes according to our requirements. H-Alpha parameter computation for each pixel takes a lot of time since it involves computation of eigenvalues and eigenvectors. Wishart segmentation is a very robust segmentation technique, and its stability does not depend much on initial seeds. Using these facts, only fifty percent pixels for initial seed selection are considered.

2.1 Preprocessing

We compute a 2×2 coherency matrix corresponding to each pixel. Speckle noise is inherent property of SAR images and since it may affect classification accuracy, Refined Lee filter is applied to remove speckle noise from the dual-pol data. Bias in H-Alpha parameter is one of the main issues for not getting the correct result [5]. Generally, entropy (H) value increases with the amount of averaging and averaging has least effect on Alpha values. After a certain number of looks, H and Alpha values become constant. In order to remove bias in H and Alpha parameter, Refined Lee filter of size 5×5 , and 3×3 sub-window size is used. Computing eigenvalues and eigenvectors only for alternate pixels saves a lot of complex computation. H and Alpha parameters are also computed for alternate pixels. The range of H is $[0, 1]$ and that of Alpha is $[0, 90]$. Rescaling H values which are in the range from $[0, 1]$ to $[0, 90]$ is done so that they are compatible with Alpha values.

2.2 Initial Seed Point Selection

For histogram computation and initial seed point selection, the advantages of robustness of Wishart classifier are taken into account and only 50% pixels are considered for initial seed point selection. Fifty percent pixels are chosen by taking alternate pixels from input data samples. The histogram of the dual-pol data $\text{Hist}[][]$ is computed. First *mode* (μ) is selected from this $\text{Hist}[][]$. To ensure minimum distance from each *mode* point, we choose a distance d and the points which come under this distance range from $\mu-d$ to $\mu+d$ not considered for the next *mode* selection. Distance 'd' varies with the number of clusters. For initial seed point selection, only H and Alpha values are computed and for further computation H and Alpha computation does not come. From next iteration onward, all the processing is done on coherency matrices.

2.3 Wishart Classification and Convergence

Coherency matrix of polarimetric SAR images follows Wishart distribution. After getting the desired number of seed points (here the number is eight), k-mean clustering technique using Wishart distance is applied. Based on H and Alpha parameters, we get the mean coherency matrices for each cluster. In the classification stage, Wishart distance between coherency matrix of current pixel and coherency matrices of all the cluster centroids is computed. This pixel is assigned to that cluster for which the computed distance is minimum. This process is applied to all the pixels of the input image, thus completing an iteration. Many iterations are performed so that the classifier converges and becomes stable. The convergence criteria used in this technique is the number of pixels changing their clusters in successive iterations. The clustering process stops when the number of pixels affected is less than 1% of the total pixels. Wishart distance defined for dual polarimetric is similar to the quad-polarimetric Wishart distance.

$$D_w(C, V_i) = \ln(|V_i|) + \text{Trace}(V_i^{-1}C) \quad (1)$$

C is the coherency matrix of image pixel, and V_i is the coherency matrix of the seed vector corresponding to the i th cluster. Here V_i, C is 2×2 semi-positive definite matrices. Here $D_w(C, V_i)$ corresponds to Wishart distance between coherency matrix of image pixel and the coherency matrix of the seed vector.

3 Test Area and Data Set

Single look complex (SLC) quad-pol data of RISAT-1 satellite of Ahmednagar, Maharashtra, has been used for validating the proposed technique. Each SLC image

Table 1 Different parameters of the data set of RISAT-1 satellite

Date of acquisition	18-07-2013	Incidence angle	40.83612
Center latitude	21.496715	Center longitude	79.147291
Upper left latitude	21.380718	Upper left longitude	79.307805
Upper right latitude	21.327082	Upper right longitude	79.062090
Lower right latitude	21.613096	Lower right longitude	78.989015
Lower left latitude	21.666830	Lower left longitude	79.235062

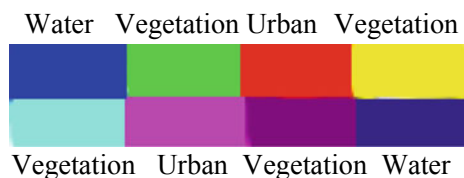
pixel has 4-byte long data in which 2 bytes are real part and 2 bytes are imaginary part. Image is taken in fine resolution strip map (FRS-2) mode. Since quad-pol data contains information about HH, HV, VH, VV polarization, three dual-pol data combinations (HH-HV, HH-VV and VV-HV) have been used here. Different parameters of the RISAT-1 satellite are given in Table 1.

4 Results

The proposed technique has been applied to vegetation, water body and urban areas. We have validated the result by taking the training sample from the data itself. In this eight class classification, we have broadly classified it into three classes (Fig. 1).

There is no generalized technique for visualizing dual-pol data as we get in quad-polarimetric data. For quad-polarimetric data, Pauli RGB is the most acceptable way for visualization. Pauli RGB image of the area is shown in Fig. 2 A. In Pauli RGB image, red color is for double-bounce scattering, green for volume scattering and blue for single-bounce scattering phenomena. Data sample is taken by verifying it with optical data of the corresponding area. Results for different dual-pol combinations when we take 100% pixels for computing initial seeds are exactly the same when only 50% pixels are considered for initial seed point selection. Results of each dual-pol combinations when only 50% pixels are considered for computing initial seed are given in Fig. 2(b–d).

Fig. 1 Color given to each pixel



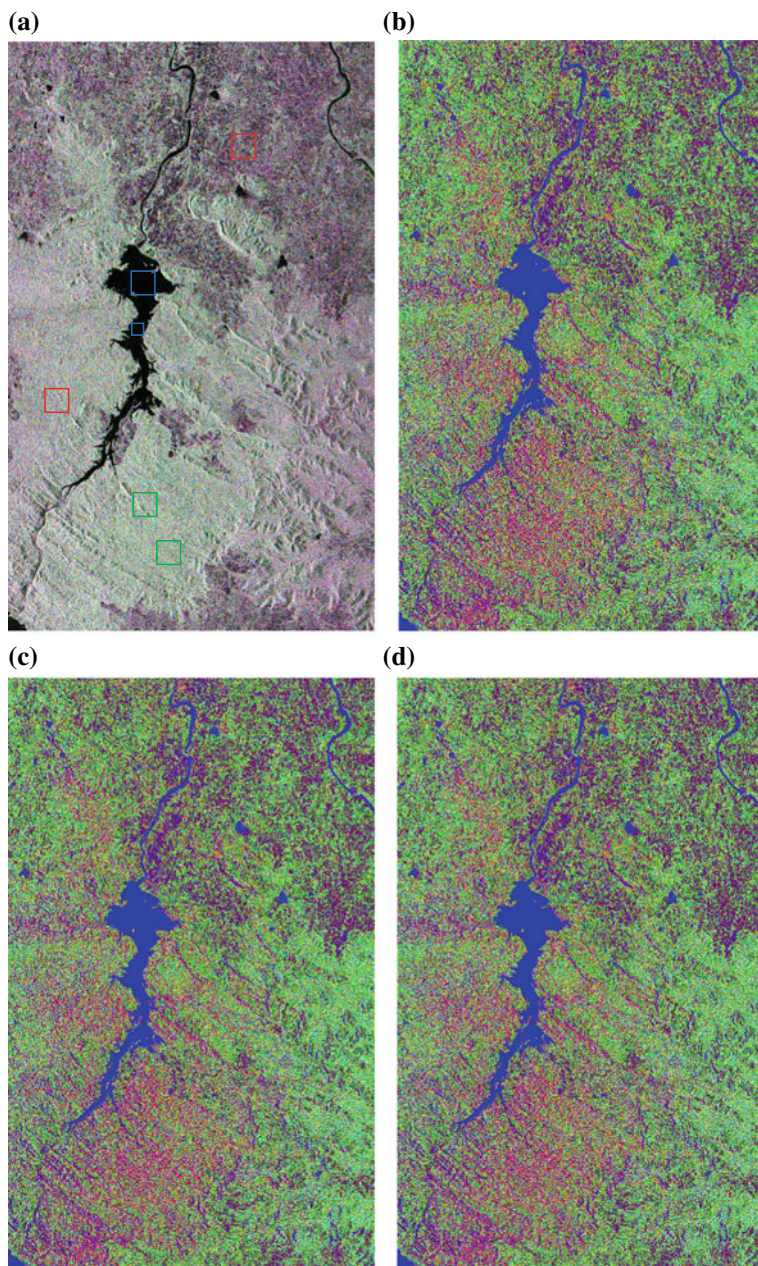


Fig. 2 a Pauli RGB image of the test area; in the image selected, red boxes are urban areas, blue boxes are water body and green boxes are vegetation. b HH-VV classification. c HH-HV classification. d VV-HV classification

We have taken the analysis of results consolidated in the form of confusion matrix which is given in Table 2.

5 Conclusion

The proposed algorithm is suitable for the varying number of classes as per the user requirement. It computes initial seed points independent of the chosen dual-pol combination. It was found that HH-VV combination is good for classifying urban areas and water body, and other two combinations are good for classifying vegetation areas. It is better to consider only 50 or 40% of the total pixels while computing initial seed point, as the results are not significantly affected and also it is computationally less expensive. HH-VV dual-pol combination is suitable for applying H-Alpha parameter-based Wishart segmentation as it can distinguish single- and double-bounce scattering. Since water pixels are classified correctly in all dual-pol combination, it is concluded that all dual-pol combinations are suitable for finding anomalies in water bodies and also soil moisture content. Complexity of algorithms in dual-pol data is not as complex as quad-polarimetric data. Selection of suitable polarization combination is required to cater for the desired purpose while planning small satellite space missions. For specific targets, more work is required to be carried out for the selection of appropriate dual-polarization combination.

Acknowledgements The authors are grateful to Dr. Rishipal Singh Pundir, Director, DEAL, Dehradun, for granting permission to publish this work. The authors also express their gratitude to Dr. Sangeeta Khare, Group Head, IAC, DEAL, and V. S. Rathi, Group Director, IAC, DEAL, for their encouragement.

Appendix A: Target Vector for Different Dual-Pol Combinations

Fully polarimetric data is used for the analysis of SAR polarimetry. SAR sensor alternately transmits H- and V-polarized pulses and, for each transmitted pulse, coherently receives both H and V polarizations. In this way, we get fully polarimetric data. We represent this information in scattering matrix [S], which embodies the polarimetric information.

$$S = \begin{bmatrix} S_{hh} & S_{hv} \\ S_{hv} & S_{vv} \end{bmatrix} \quad (2)$$

For quad-pol case assuming reciprocity, which we assume for monostatic radar case (where transmitter and receiver are the same). Target vector on Pauli basis is as follows:

Table 2 Accuracy assessment for various parameters using confusion matrix (U: urban class, W: water, V: vegetation, OA: overall accuracy)
 100% pixel used for calculating initial seed points

		100% pixel used for calculating initial seed points						50% pixel used for calculating initial seed points					
		HH-VV		HH-HV		VV-HV		HH-VV		HH-HV		VV-HV	
		W	U	V	U	W	V	W	U	V	U	W	V
W		99.3	0.0	0.7	0.0	97.1	0.0	97.4	0.0	0.7	0.0	97.4	0.0
U		0.3	83.0	16.7	62.8	2.0	35.2	1.7	61.4	16.7	83.0	1.7	61.4
V		8.2	15.3	76.5	11.3	7.1	81.6	7.1	14.3	76.5	11.3	7.1	14.3
OA		86.26		80.5		79.13		86.26		80.5		79.13	

$$K = \frac{1}{\sqrt{2}} \begin{bmatrix} S_{hh} + S_{vv} \\ S_{hh} - S_{vv} \\ 2S_{hv} \end{bmatrix} \quad (3)$$

In dual-pol SAR data, we get precisely half of the full polarimetric scattering matrix elements. Analysis of dual-pol data starts from an inherently inferior position in terms of the image information content. The importance of this lost information depends both on the dual-pol imaging mode, e.g., (HH, HV), (VV, HV) or (HH, VV). For each polarimetric imaging mode, we get different target vectors and coherency matrices which are explained in the subsections.

A.1 HH and VV

We get scattering matrix for HH and VV combination as

$$S = \begin{bmatrix} S_{hh} & 0 \\ 0 & S_{vv} \end{bmatrix} \quad (4)$$

And the corresponding scattering vector based on the Pauli basis as

$$k_{hh-vv} = \frac{1}{\sqrt{2}} \begin{bmatrix} S_{hh} + S_{vv} \\ S_{hh} - S_{vv} \end{bmatrix} \quad (5)$$

The coherency matrix we get for the target vector by multiplying target vector to its transpose conjugate.

$$\langle C_{hh-vv} \rangle = \frac{1}{L} \sum_{i=1}^L k_i k_i^H \quad (6)$$

A.2 HH and HV

We get scattering matrix for HH and HV combination as

$$S = \begin{bmatrix} S_{hh} & S_{hv} \\ S_{hv} & 0 \end{bmatrix} \quad (7)$$

And the corresponding scattering vector based on the Pauli basis as

$$k_{hh-hv} = \begin{bmatrix} S_{hh} \\ 2S_{hv} \end{bmatrix} \quad (8)$$

A.3 VV and HV

We get scattering matrix for VV and HV combination as

$$S = \begin{bmatrix} 0 & S_{hv} \\ S_{hv} & S_{vv} \end{bmatrix} \quad (9)$$

And the corresponding scattering vector based on the Pauli basis as

$$k_{vv-hv} = \begin{bmatrix} S_{vv} \\ 2S_{hv} \end{bmatrix} \quad (10)$$

References

1. Raney RK (2016) Comparing compact and quadrature polarimetric SAR performance. *IEEE Geosci Remote Sens Lett* 13(6):861–864
2. Cloude SR (2007) The dual polarisation entropy alpha decomposition: a palsar case study. In: *Proceedings of the 3rd international workshop on science and applications of SAR polarimetry and polarimetric interferometry*, Frascati, Italy
3. Ji K, Wu Y (2015) Scattering mechanism extraction by a modified cloude-pottier decomposition for dual polarization SAR. *Remote Sens* 7:7447–7470. ISSN 2072- 4292
4. Scheuchl B (2002) Sea ice classification using multi-frequency polarimetric SAR data. In: *2002 IEEE international geoscience and remote sensing symposium, IGARSS 02*, Toronto
5. Lee JS, Ainsworth JS, Kelly JP, Lopez-Martinez C (2008) Evaluation and bias removal of multilook effect on entropy/alpha/anisotropy in polarimetric SAR decomposition. *IEEE Trans Geosci Remote Sens* 46(10):3039–3052

SAR Payload Remote Sensing Satellite Mission Analysis for Global Coverage



Devi Prasad Panda, Kalpana Bandi and PSR Srinivasa Sastry

Abstract The purpose of this paper is to discuss the criteria to select the orbit for satellite with SAR payload which is best suitable for the mission. The requirements of the SAR payload are spelled out, and in turn how we convert those requirements to design of orbit is discussed. The constraints of SAR payload imaging over normal electro-optical payload will be detailed. Mission requirements and payload constraints are converted into specific orbital parameters. SAR payload geometry is discussed, and off-nadir angle, repeat cycle and revisit time relation is detailed. The superiority of the selected orbit is simulated and detailed in the paper. Global coverage analysis studies are simulated and presented.

Keywords Repeativity days · Revisit time · Global coverage · SAR payload · SAR geometry · Mission analysis

1 Introduction, SAR Geometry and Comparison with Electro-Optical Payload

In order to meet the mission and system requirements and P/L constraints, and to decrease the complexity of the satellite mission, orbit selection should be considered as a priority for all the LEO space missions (imaging payload like SAR or electro-optic applications). To decide the orbit for the satellite first input comes from the payload specifications and constraints (Table 1).

Typical SAR payload specifications required for mission studies are provided in Table 1.

In electro-optical payload, satellite can directly image at sub-satellite point but in SAR payload off-nadir angle about 10° typically is must to get the valid data of imaging. SAR geometry [4] is shown in Fig. 1. SAR payload incidence angle will be converted to satellite look angle or off-nadir angle as shown in Graph 1.

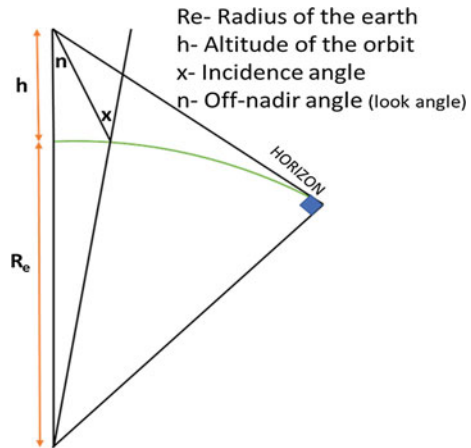
D. Prasad Panda (✉) · K. Bandi · P. S. Sastry
Directorate of Space Systems and Technologies (DSST), Research Centre Imarat (RCI),
Hyderabad, India
e-mail: devi.prasad@rcilab.in

© Springer Nature Singapore Pte Ltd. 2020
PSR. S. Sastry et al. (eds.), *Advances in Small Satellite Technologies*,
Lecture Notes in Mechanical Engineering,
https://doi.org/10.1007/978-981-15-1724-2_14

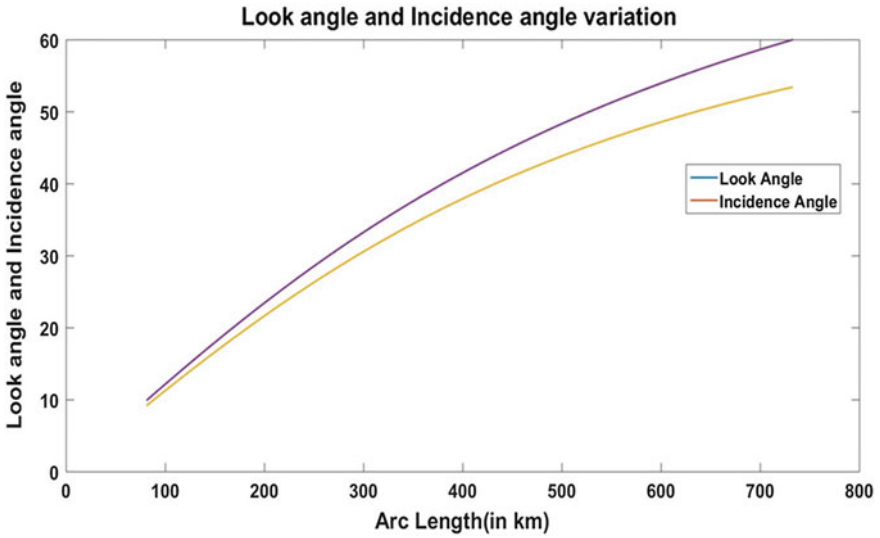
Table 1 Payload specifications and constraints

Parameter	Value (typical specifications of TechSAR)	
Incidence angle of operation	10°–60°	
Mode of operation	Resolution versus max incidence angle	
	2 m	28°
	3 m	35°
	5 m	42°
	10 m	51°
20 m	60°	
Payload constraints	Acquisition time	
	Swath will vary due to altitude and look angle of the satellite (slant range change)	
	Power consumption and thermal limitations	

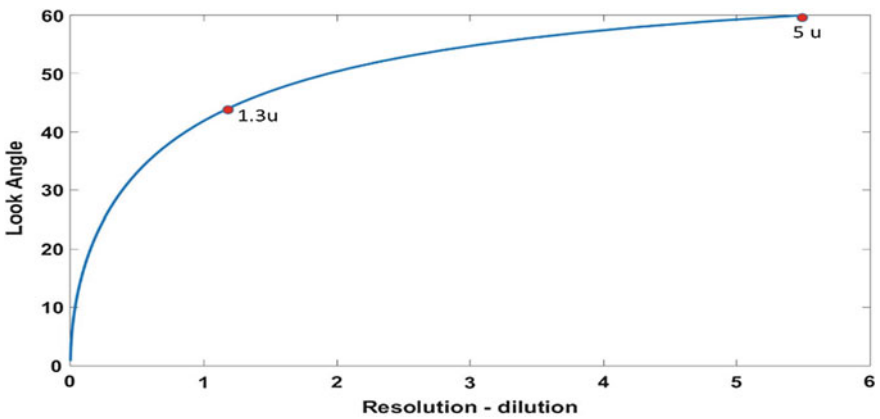
Fig. 1 SAR geometry



Unlike electro-optical payload, the SAR payload gives different modes of operations for different ranges because SAR is an active method of imaging where SAR payload transmits EM waves and receives the reflected and scattered EM waves from the object. Due to the power constraint in the satellite, all the slant ranges will not give the same resolutions. The tentative details are given in Table 1. The variation in the resolutions as look angle (slant range) increases is shown in Graph 2. The variations in the resolution for SAR payload for different slant ranges vary from 1 unit to 10 units depending on the mode of operation and slant range typically as shown in Fig. 2. For electro-optical payload, the change in resolution due to slant range is very small but it may change from 1 unit to 1.3 units because electro-optical payloads



Graph 1 Variation of arc length with incidence and off-nadir angle



Graph 2 Variation in resolution with satellite look angle

cannot image at a larger incidence angle which can be done in SAR payloads as shown in Fig. 2. As shown in Fig. 2, the satellite coverage area will have different resolution regions.

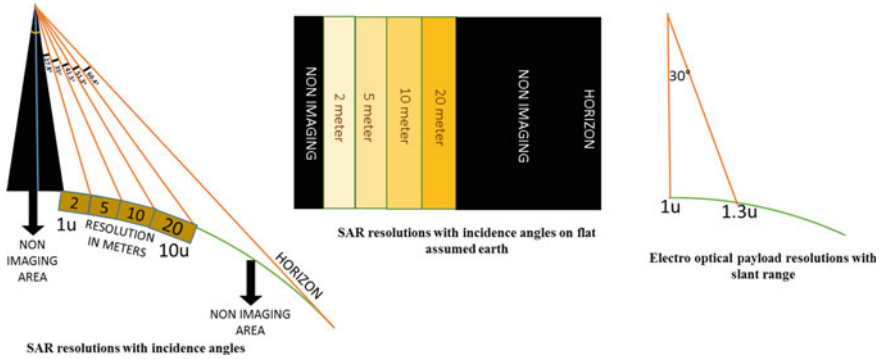


Fig. 2 SAR payload resolutions with different regions and incidence angles and electro-optical payload resolution change with off-nadir angle

2 Mission Requirements and Selection Criteria of the Orbit

The orbit selection of the satellite mission derives from mission requirements and payload constraints. Mission requirements broadly can be derived from the payload type and requirements of the user. From the mission objective

- Satellite will be in LEO type.
- Coverage (global/regional).
- Revisit to the same location and time with less than 7 days assumed.

Orbital parameters and design variables can be further explained in terms of their major effects on mission, and P/L operations are given in Table 2.

Repeativity of the orbit will decide the altitude (semi-major axis) of the orbit. If orbit altitude is selected, then sun-synchronicity orbit will generate the inclination of the orbit. Satellite altitude variation to be minimal satellite orbit should be frozen orbit [2], which will decide the eccentricity and argument of perigee. P/L illumination constraint will be converted to launch time of the satellite, which will decide RAAN [5] of the orbit. Orbital parameters and their major effects are given in Table 2.

After performing the above-different studies, the satellite orbit has been selected. The orbital parameters and design variables [1, 3] are selected for the mission study purpose (tentatively) and are given in Table 3. These studies are done only for presenting purpose, and all values are notional. Repeativity of the orbit is selected as 6 days.

3 Coverage Analysis for SAR Payload

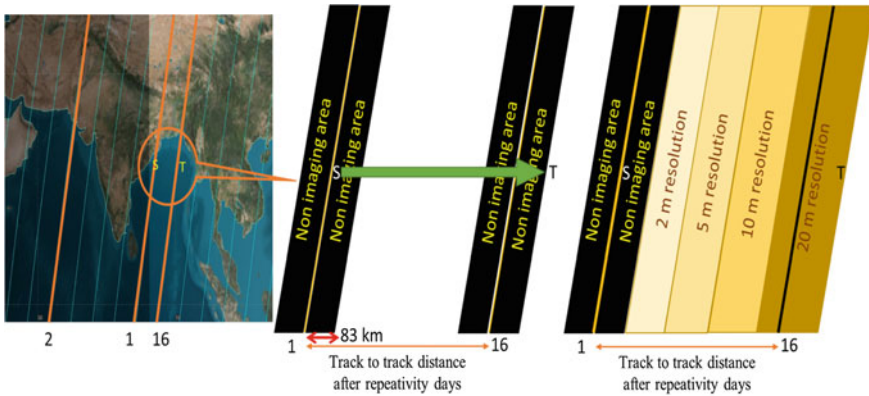
The ground track of the sun-synchronous satellite orbit is shown in Fig. 3. In Fig. 3,

Table 2 Orbital parameters and design variables and their major effects

Orbital parameters and design variables	Major effect	Basic of selection
Orbit type	Orientation toward sun	Sun-synchronous frozen orbit or inclined orbit
Altitude	Revisit time (<7 days) Coverage (global coverage) Image resolution (best possible) Eclipse time	Image quality <800 km resolution Life of the satellite (>500 km) Orbit maintenance and de-orbiting (>500 km less delta-V maintenance) (<800 km less delta-V de-orbiting)
Inclination	Latitude coverage Eclipse time Sun and zenith angle limit	Sun-synchronous orbit Latitude belt coverage
Eccentricity and argument of perigee	Altitude and velocity (circular or ellipse) Coverage	Sun synchronous-frozen orbit
RAAN	Eclipse cycle over year	Dependent on launch data P/L requirement
Repeat cycle	Revisit time Coverage	Revisit time requirements and coverage
Sensor and off-nadir angle	Complexity of the satellite Revisit time and overlapping area Coverage and revisit time	To obtain less off-nadir angle Sun zenith angle
Revisit time	Coverage Off-nadir pointing of satellite	Limitation for revisit time

Table 3 Orbital parameters and the type of orbit it generates

Parameter	Value	Effect and consequence
Orbit type	15 1/6 sun-synchronous frozen orbit	Sun-synchronous frozen orbit
Altitude (semi-major axis)	509.8 km	Repeativity, coverage
Eccentricity	0.001	Frozen orbit and velocity variation of satellite
Inclination	97.44°	Sun-synchronous condition, latitude coverage
Argument of perigee	90°	Frozen orbit condition
RAAN	Dawn–dusk orbit (seasonal eclipse)	Launch time and eclipse time
Path-to-path distance after repeativity days	532 km Off-nadir angle requirement approximately 50°	Off-nadir angle requirement



S denotes the satellite (sub satellite point) T denotes the target to image so that satellite can achieve global coverage. As shown in the figure all ground tracks are shown in repeativity days. T is selected in such a way that side track non imaging area should be covered by the satellite from the side track which will full fill our global coverage definition. In figure the non imaging area can be covered by next track satellite which is shown in the figure.

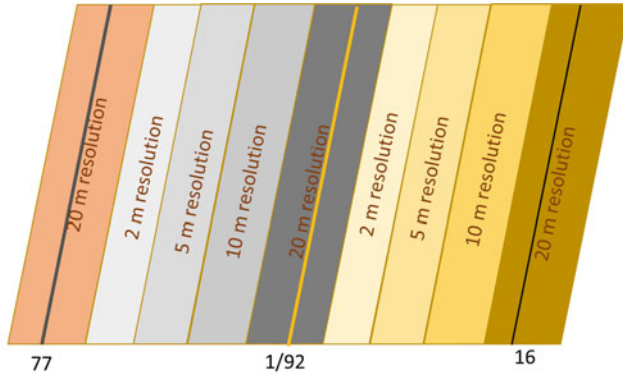
Fig. 3 Satellite coverage with small repeativity time and resolution pattern

S point represents the satellite and T is the target point to image, black area on the track is the minimum off-nadir angle block as shown in Fig. 3. To get the global coverage, the satellite has to see the next track from one side that is shown in Fig. 3 as T which is just next to non-imaging area of the next track. The angle requirement to see the point S to T is the look angle requirement of the satellite to provide global coverage. The look angle requirement of the satellite to get the global coverage should be less than the maximum incidence angle operation for the payload. For 6-day repeativity sun-synchronous orbit at 509.8 km with inclination 97.44° the non-imaging area arc length is about 83 km and the look angle requirement is 48.5° with the incidence angle requirement is about 54° which is well within the payload incidence angle specification.

As it is already explained that satellite coverage area will be divided with different resolutions. After desired repeativity of 6 days, the satellite coverage had different patches of regions with different resolutions as shown in Fig. 3. The most important part to be noted here is that the total global coverage is achieved for different resolutions but all areas are not having all types of resolutions which means some areas satellite can never see the resolution other than prescribed for the patch as shown in Fig. 4.

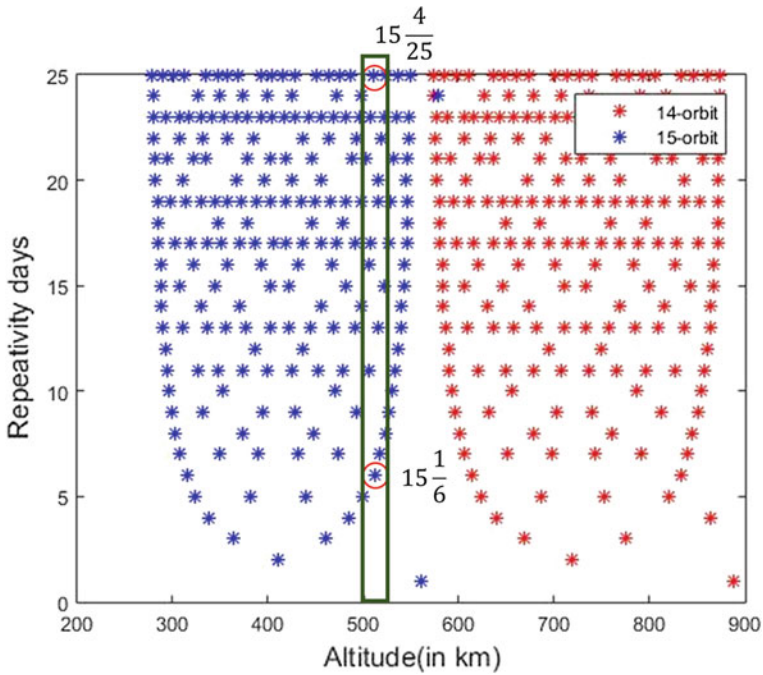
4 Selection Criteria of Repeativity Days Based on Coverage

To achieve global coverage with same revisit time (6 days) and get all resolutions for all areas, a different orbit should be selected which is having the form factor near to the old satellite orbit. 15/16 satellite orbit form factor is 0.167. If we select an orbit



After the repeativity days complete globe can be covered with different resolutions as shown in the figure. Due to the track drift restriction global coverage is possible but restricted to different resolutions at different places.

Fig. 4 Satellite coverage with patches and resolutions



Graph 3 Repeativity pattern orbits and altitude variations

near to the form factor as the old satellite orbit, the satellite can achieve the global coverage of 6 days with limited resolutions and after the new repeativity the satellite can give all resolutions globally in all regions.

Selecting a new orbit which gives all resolution in all regions is discussed. In this method, we have to take the form factor into consideration and simply calculate how many orbits we want to add in between the path-to-path for old orbit (depends on how many resolutions the satellite has to take over prescribed area). So that number can be simply multiplied top and bottom of the form factor and add or subtract 1 from the bottom of the form factor. Example $1/6$ is form factor we want to divide the orbit path-to-path distance into further four parts so the new orbit form factor can be $4/25$. For the same orbit, if we want to make five parts in between the old orbit path-to-path distance, we can select the orbit as $15\ 5/31$. The selected new orbit altitude variation should be minimal because the change in altitude can change the characteristics of the payload. Once the nearby orbits are selected, we have to check for coverage definitions for all the orbits and select the best one out of it. Satellite old orbit and new orbit can be observed in the repeativity graph. Those orbits should be very close enough in the altitude variation or form factor as shown in the Graph 3. Select the new orbit as $15\ 4/25$ repeativity orbit to show the effect of coverage by new orbit. As shown in Fig. 5 satellite ground track path pattern for new and old orbit, if we compare as the form factor is same satellite will give same revisit time as the old one but the track to track distance for old orbit is divided into further four parts in new orbit. Compared to the old satellite orbit, the new orbit selected can give global coverage as the old orbit revisit time, and it gives all resolutions for all regions

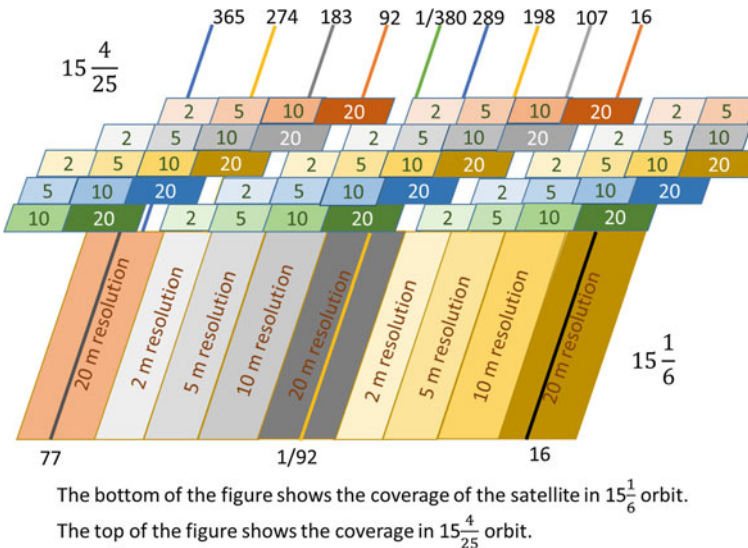


Fig. 5 Satellite coverage of patches for two different orbits

after prescribed new repeativity time. Global coverage of the newly selected orbit is shown in Fig. 5. All the areas are covered with different resolutions.

5 Conclusion

Mission analysis for low Earth orbit satellite with SAR payload is unlike electro-optical payload where resolutions will change very rapidly at a higher incidence angle. Due to this, global coverage is achieved within 7 days but the only constraint is that the satellite coverage will be divided in different resolutions, with that the satellite cannot see all other resolutions at prescribed patch. To achieve all the resolutions across the globe, the satellite will be injected in higher repeativity days orbit, which can give same revisit time as older orbit and also can give all resolutions after new (higher) repeativity days. With this method, the user can get all resolution images. Further, if the user wants to decrease the number of repeativity days, we have to plan for the constellations which can be discussed in future studies.

Acknowledgements Authors would like to express deep regards and profound respect to the director, RCI, for his support. Authors express sincere thanks to K. Rambabu and Dr. MSY Siva Prasad for their guidance. Authors extend sincere thanks to the colleagues of Directorate of Space Systems and Technologies, RCI, for their continuous support to complete this paper.

References

1. Wertz JR, Everett DF, Puschell JJ (eds) Space mission engineering: the new SMAD. University of South California, NASA Goddard Raytheon
2. Vallado DA (ed) Fundamentals of astrodynamics and applications
3. Wertz JR (ed) Space mission analysis and design (SMAD)
4. Chobotov VA (ed) Orbital mechanics
5. Curtis H (ed) Orbital mechanics for engineering students

Detection of Camouflaged Targets in Hyperspectral Images



Asheesh Kumar Gautam, Phool Preet, T. S. Rawat, Pinaki Roy Chowdhury and L. K. Sinha

Abstract This paper presents a study of a deterministic camouflaged target detection using hyperspectral images. Hyperspectral imagery has hundreds of spectral bands. This plethora of spectral information enables the detection of targets concealed by tree canopy or camouflage net. This problem cannot be addressed using high-resolution visible data alone because ‘shape information’ provided by such imagery cannot be used reliably in case of concealed targets. Hence, this problem is modeled as a target detection problem using ‘spectral information’ present in hyperspectral imagery. Moreover, the presence of concealing material such as canopy or cam net over the target necessitates the use of ‘sub-pixel’ target detectors.

Keywords Hyperspectral imagery · Adaptive Cosine/Coherence Estimator (ACE) · Camouflaged target · Sub pixel detection

1 Introduction

Remote sensing has been the mainstay for a host of military and civilian applications. These applications include object detection, surveillance, environmental monitoring, land-use classification, etc. For a very long time, multispectral images have been used in various remote sensing applications. Recently, hyperspectral imaging has emerged as the *technology of choice* for these applications. This shift in focus is due to the wealth of spectral information provided by hyperspectral images. Main focus of hyperspectral sensing is in the visible, near infrared and shortwave infrared region of spectral band covering from 0.3 to 2.5 μm .

The use of hyperspectral technology in various applications has also been boosted by the increasing availability of commercial aerial and satellite-based sensors. This article presents the use of hyperspectral data for one of the most important military applications namely target detection [1, 2]. In particular, the case of targets concealed by tree canopy or camouflaged net is studied and presented. Also, the effectiveness of modeling of concealed targets as sub-pixel targets is investigated.

A. K. Gautam (✉) · P. Preet · T. S. Rawat · P. Roy Chowdhury · L. K. Sinha
Defence Terrain Research Laboratory, DRDO, New Delhi, Delhi 110054, India

© Springer Nature Singapore Pte Ltd. 2020
PSR. S. Sastry et al. (eds.), *Advances in Small Satellite Technologies*,
Lecture Notes in Mechanical Engineering,
https://doi.org/10.1007/978-981-15-1724-2_15

2 Target detection in hyperspectral images

Target detection has always been one of the main military applications of remote sensing technologies. Target detection from panchromatic/multispectral satellite images generally uses the ‘*shape information*’ of the target. Hyperspectral (HX) sensors on the other hand use ‘*spectral information*’ of the target. Hyperspectral detectors generally have a trade-off between spatial and spectral resolution. This trade-off is deliberate because ‘*shape information*’ cannot always be used reliably for target detection. Hyperspectral detector exploits the ‘*spectral information*’ of the target and hence more suited for the application of detection of camouflaged target.

Traditionally, in any pattern recognition or target detection problem, the problem after being modeled as a supervised classification one is fed with training samples for model building. These samples are spatial in nature, and therefore, no spectral properties of the object in question are exploited. This exploitation of spectral properties is not that meaningful for both multispectral (MX) and panchromatic (PAN) data. Due to broad spectrum of MX imageries, spectral properties of target get normalised. Because of this reason, the pivotal point in image processing of MX data relies on geometry of the target and spatial resolution of the imaging sensor.

This study focuses on the detection of deterministic targets where the signature of the target is known and fixed. Herein, we wish to exploit the typical target object signatures in spectral domain, which are stored in a database upfront, and pose the problem of camouflaged target detection as a problem of matching rather than classification. The exploitation of target signatures is made possible because HX sensors image the target in a narrow band, thereby effectively utilizing the energy for a specific object. Beside this, the library of target signatures created upfront provides a kind of genetic footprint of the object treated as a target. This genetic footprint remains invariant for a specific object with an assumption that the material composition of the object remains same throughout.

Target detection from hyperspectral data is generally modeled as binary hypothesis testing problem: target absent and target present [1].

$$H_0 = \text{target absent}$$

$$H_1 = \text{target present}$$

This approach gives rise to detector known as ‘Likelihood Ratio Test.’ When likelihood ratio is greater than certain threshold η , then target present hypothesis is assumed to be true.

2.1 Detection of Sub-pixel Targets

Sub-pixel target detection problem is also modeled as binary hypothesis testing problem. The only difference is that now target pixel is assumed to have both target and

background which makes it a sub-pixel target. The observed spectrum of such pixel is the result of linear or nonlinear mixing of target and background spectra. Generally, target is described as subspace model, but background can be described by using either subspace model or statistical distribution model [1].

$$\begin{aligned} H_0 : x = v &\sim N(\mu, \Sigma) \text{ target absent} \\ H_1 : x = Sa + v &\text{ target present} \end{aligned}$$

Here background is described as random vector drawn from normal distribution, and target is described as a subspace plus background. This assumption leads to *Adaptive Detector* [3]

$$D(X) = \frac{x^T \Sigma^{-1} S (S^T \Sigma^{-1} S)^{-1} S^T \Sigma^{-1} x}{N + x^T \Sigma^{-1} x} \quad (1)$$

This detector assumes same covariance of background for both hypotheses. But area of background differs in two hypotheses. The correction for covariance leads to well-known *Adaptive Cosine/Coherence Estimator* (ACE) given by the following equation [4]

$$D(X) = \frac{x^T \Sigma^{-1} S (S^T \Sigma^{-1} S)^{-1} S^T \Sigma^{-1} x}{x^T \Sigma^{-1} x} \quad (2)$$

2.2 Detection of Camouflaged Targets

Detection of concealed targets which are under camouflage net or tree canopy can also be modeled as detection of sub-pixel target. In [5], a constrained energy minimization-based camouflaged target detection method is presented. The basic premise for modeling camouflaged target as sub-pixel target is that though the target is hidden, it is not *completely* covered by concealment, and its spectra also contribute (linearly or nonlinearly) in the observed pixel spectra. This assumption (visibility of target) is necessary as hyperspectral imagery does not exhibit any penetration, and hence, only camouflaged net and tree canopy cover are considered as concealment methods. Targets that are completely hidden such as under a sheet or other material cannot be detected using this technique.

3 Data and method

Experiments were conducted on the data acquired through spectro-radiometer in the range of 0.3–2.5 μm . Experiments have been conducted on the following target and background combination

1. Grass with soil (50–50%)
2. Grass soil rubber (25–25–50%)
3. Metallic net with grass (approx 50–50%)
4. Grass aggregate (50–50%).

The concealment of the target was simulated using grass cover. Target spectral data were acquired for aforementioned targets, in the laboratory environment, from different heights while keeping the point of view fixed to simulate the different mixing proportions. AVIRIS-NG HX data set of Udaipur region has been used for validating performance of ACE.

4 Results

Reflectance spectrum of target, background and mixed materials along with their respective images is shown below (Fig. 1).

Experiments were conducted in such a manner that each material will contribute a finite percentage in the final mixed spectrum. Abundance of each material in the experiments is mentioned in the previous section.

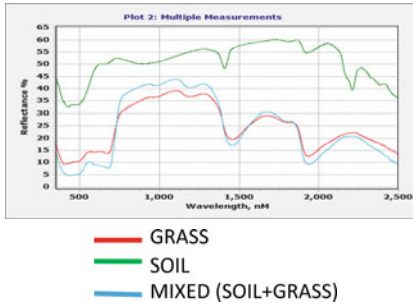
Now, the mixed spectrum is known, and background statistics is captured in the Table 1. The values in the table are computed using Eq. 2 given above. It is indicated in Table 1 given below that ACE gives the maximum value in case of the target material when large number of material combinations are presented which includes the target material also.

ACE has been tested on AVIRIS-NG data set with three different background thresholds 0.5, 0.7 and 0.9. Significance of this threshold value pertains to the abundance of the target material within the given pixels. This threshold is different from value η . Results look similar, but threshold with 0.7 gives better results than others. That is concluded after accuracy calculations which are based on ground truth samples collected on the ground (Fig. 2).

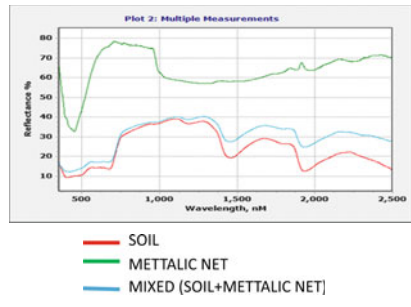
5 Conclusion and future directions

In this paper, we have demonstrated that the presence of hyperbands in HX imagery is a potential game changer. By this, we mean that, with the advent of HX image processing techniques, it is now more feasible to design and develop reasonably

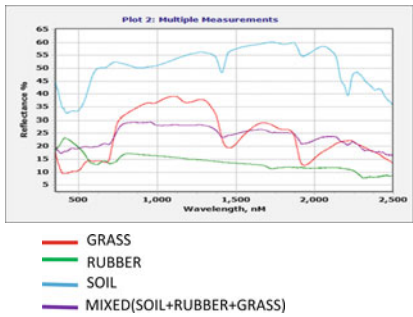
(a)



(b)



(c)



(d)

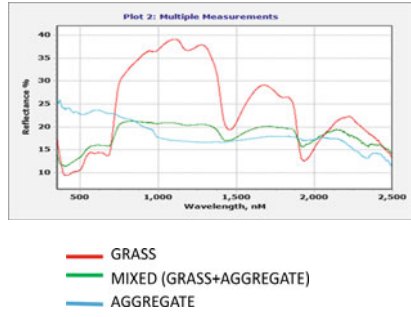


Fig. 1 a Reflectance spectrum of soil grass mixture and individual component with image, b Reflectance spectrum of grass metallic net mixture and individual component with image, c Reflectance spectrum of soil grass rubber mixture and individual component with image, d Reflectance spectrum of grass aggregate mixture and individual component with image

Table 1 ACE results of all available targets under the given experimental setup

Background-target	Grass	Soil	Rubber	Metallic net	Aggregate	Plastic	Aluminum
Grass-soil	–	0.64	0.01	0.19	0.12	0.09	0.015
Soil-grass	0.82	–	0.02	0.01	0.27	0.13	0.2
Grass-rubber	–	0.13	0.53	0.03	0.22	0.37	0.28
Rubber-grass	0.79	0.35	–	0.09	0.23	0.15	0.18
Grass-metallic net	–	0.03	0.06	0.49	0.17	0.07	0.08
Metallic net-grass	0.69	0.2	0.01	–	0.28	0.14	0.24
Grass-aggregate	–	0.3	0.04	0.02	0.66	0.21	0.34
Aggregate-grass	0.76	0.25	0.09	0.3	–	0.08	0.13

The values in bold italics represent primary target present

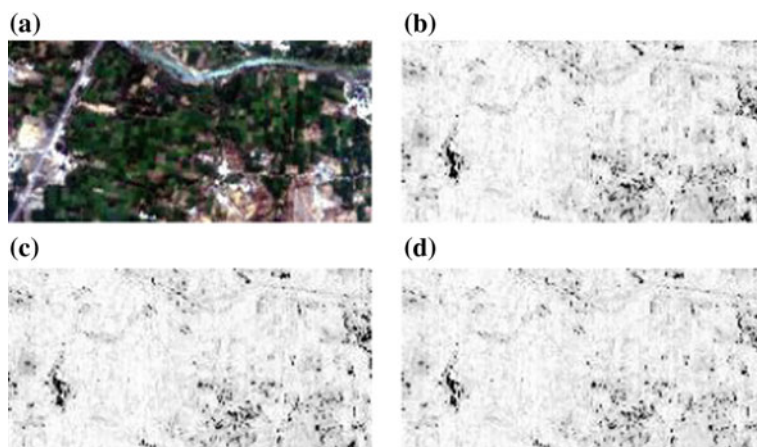


Fig. 2 a AVIRIS-NG data set of Udaipur region, b ACE output result with background threshold = 0.5, c ACE output result with background threshold = 0.7, d ACE output result with background threshold = 0.9

tractable solution for those problems which are very complex in MX domain. ACE as a detector was evaluated especially for sub-pixel target detection, where controlled experimentations were performed under various combinations of materials available in the laboratory. Though one must keep in mind that the identification of targets is solely based on spectral features, which can be a bit deceptive in the sense that two objects can have same material composition. In our view, for better overall accuracy, one should include fusion of HX along with either SAR or LiDAR imagery. This is the future course of work but will also greatly depend on availability of airborne SAR/LiDAR sensors.

Acknowledgements Authors are thankful to NISA program under which AVIRIS-NG HX image was made available.

References

1. Manolakis D, Marden D, Shaw GA (2003) Hyperspectral image processing for automatic target detection applications. *Lincoln Lab J* 14(1):79–116
2. Briottet X, Boucher Y, Dimmeler A, Malaplate A, Cini A, Diani M, Bekman HHPT et al (2006) Military applications of hyperspectral imagery. In: *Proceedings of SPIE6239*, pp 62390B
3. Kelly EJ (1986) An adaptive detection algorithm. *IEEE Trans Aerosp Electron Syst* 22(1):115–127
4. Kraut S, Scharf LL, McWhorter LT (2001) Adaptive subspace detectors. *IEEE Trans Signal Process* 49(1):1–16
5. Zuo Q, Guo B, Shen H, Yang M, Cheng K (2017) An improved target detection algorithm for camouflaged targets. In: *Proceedings of IEEE control conference (CCC)*, IEEE, pp 11478–11482

Spectroscopic Imaging of Nebular Gas: CubeSat-Based Spectrograph to Explore Nebular Astrophysics Through Imaging Spectrometry



C. Shanti Prabha, B. G. Nair, Ambily Suresh, Margarita Safonova, K. Nirmal and Jayant Murthy

Abstract An exciting part of the astrophysical spectrum is the far-ultraviolet (FUV: 90 to 180 nm), with a great density of absorption and emission lines. We are planning to develop an imaging spectrograph incorporated into a 6U ($300 \times 200 \times 100 \text{ mm}^3$) satellite to observe diffuse nebulae. The field of view is $4 \times 1'$ with a spatial resolution of 13" and a spectral resolution of 0.6 \AA (Resolution 2000). In this work, we present the selection of the components and the optical design of the spectrograph using hand calculations and Zemax software. To determine the positions of the components, ray tracing (sequential) is done.

Keywords Torus grating · Grating resolution · Spot size · CubeSat

1 Introduction

Our payload is a 6U size spectrograph designed for operation in the spectral range between 90 and 180 nm. The field of view is 4° with a spatial resolution of 13" and $1'$ with a spectral resolution of 0.065 nm (R 2000). The detector, provided by the University of Tübingen, will be a 40 mm GaN detector with a peak efficiency of 70%, which will have quantum efficiency better by a factor of 4 than the standard detectors with CsI photocathodes.

2 Science Goals

With the imaging spectrograph, we wish to observe CIII (97.7 nm), OVI (103.2/103.8 nm), CIV (1548/1550 nm), and many other lines emitted by hot gas in the halo and Lyman and Werner lines of H_2 to track cold gas, which is the dominant phase of interstellar medium. Emission of atomic lines shows the existence of hot

C. Shanti Prabha (✉) · B. G. Nair · A. Suresh · M. Safonova · K. Nirmal · J. Murthy
Indian Institute of Astrophysics, Koramangala Block II, Bangalore 560034, India

© Springer Nature Singapore Pte Ltd. 2020
PSR. S. Sastry et al. (eds.), *Advances in Small Satellite Technologies*,
Lecture Notes in Mechanical Engineering,
https://doi.org/10.1007/978-981-15-1724-2_16

gas. From the strength of the emission lines, the temperature of the gas may be estimated. We may also observe in the region: NII (108 nm), OI (98 nm), FeII (110 nm), CII (135 nm), etc.

Using the spectrograph, we wish to track emission lines over the entire spatial extent of a nebula, key to understanding its dynamics and evolution. For instance, observations of the Crab and Vela SNR with UVIT reveal a beautiful filamentary structure but understanding the nature of those filaments requires emission line mapping over the entire extent of the nebulae. Lines and the line ratios are sensitive indicators of the temperatures and densities in those regions.

2.1 Requirements

From the above science goals, we have determined that the instrument should satisfy the following requirements based on science goals, space constraints, or availability:

Requirements for designing the spectrograph

Component	Specification
Resolution	2000 at central wavelength
Lines per mm	1800
Spatial resolution	13''
Spectral resolution	0.065 nm
Imaging field of view (FOV)	4°
Spectrum direction FOV	1'
Wavelength range	90–180 nm
Grating size	20 mm × 20 mm
Detector pixel is cube of side	16 μm

3 Optical Layout

The layout consists of mirror, slit, and grating as shown in Fig. 1. No other components were chosen to keep the components minimum because each reflection causes a loss of intensity especially in the FUV region. The components are arranged as shown in the layout. The grating is in the Rowland configuration (the object, the grating, and the image fall on a circle). The Rowland configuration was also used in ALICE [4]

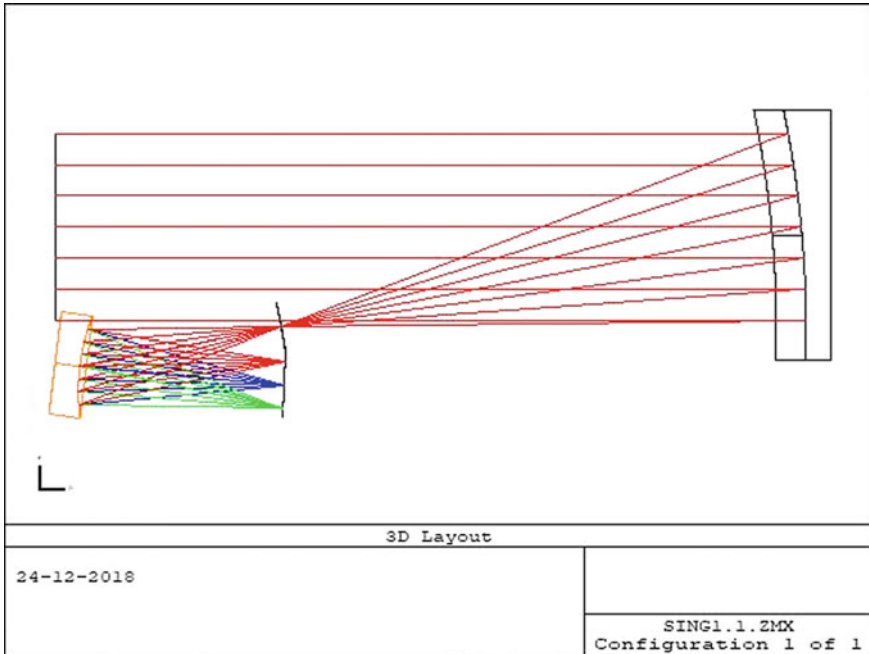


Fig. 1 The optical layout showing the mirror slit, grating, and detector after optimization using Zemax

3.1 Footprint of Optics

The longest side (6U) is taken to fit the focal lengths of the mirror and grating. The dimension of the mirror is 100 mm, 200 mm. The 200 mm side is to accommodate the 4° field of view (FOV) and the 100 mm side is to accommodate the $1'$ FOV. In the image plane also, the longer side is made to accommodate the 40 FOV. Thus, the 100 mm side of the mirror and the spectrum in the image plane lie along the 1U side of the CubeSat. The spatial direction of the image and the 200 mm side of the mirror are accommodated in the 2U side of the CubeSat.

4 Mirror

The mirror is made of Zerodur with a coating of silicon carbide (SiC). For space based instruments, we require a very fine surface finish $\sim \lambda/10$ to ensure the resolution since the image quality depends on the optical surfaces in the absence of an atmosphere. The coating thickness is calculated to maximize the absorptivity so as to

Table 1 Parameters of the mirror

Parameter	Value
Size	77 mm × 200 mm
Reflectivity	60%
Coating	Silicon carbide 100 nm

prevent back reflections from the second surface. The profile is parabolic to remove spherical aberration. An off-axis displacement is incorporated to shift the focal point of the mirror (Table 1).

5 Slit

As mentioned above, the field of view required is 4° by 1'. The slit dimensions were calculated accordingly:

$$\text{Plate scale} = 1/f = 1021.11''/\text{mm}.$$

Therefore in the imaging direction, for 4° field of view, slit width required = 4°/Plate scale = 14.102 mm.

And in the spectral direction, for 1' FOV, slit width = 1'/Plate scale = 58.76 m.

5.1 Spectral Resolution

We require a spectral resolution of 2000 at the central wavelength 135 nm. To obtain this resolution, we may require (as calculated below) a much smaller slit than 58.76 m. So, we will incorporate a dumbbell-shaped slit. The grating equation is given by Eq. 1 [3]

$$\sin\alpha + \sin\beta = n \frac{\lambda}{a} \tag{1}$$

where α is the angle of incidence, β is the angle of diffraction, n is the order of diffraction, λ is the wavelength and a is the distance between two rulings of the grating. Here, n is chosen to be 1 to get higher light output, a is 1/1800 mm and lies between 90 and 180 nm. Resolution R is defined by Eq. 2

$$R = \frac{\lambda}{d\lambda} \tag{2}$$

From Eq 1

$$d\lambda = a \cos \beta d\beta \quad (3)$$

Since α is constant for all wavelengths, $d\alpha = 0$. From the final design parameters, we can see that for 135 nm, $\alpha = 4:079^\circ$. In our case, $R = 2000$ is required at $\alpha = 135$ nm.

Radius of grating $R = 0.404$ m obtained after optimization in Zemax. Thus, $S = 11.206$ m. From the above calculations, we will have a dumbbell-shaped slit of length 14.102 mm, large width = 58.76 m, and small width = 11.206 m.

6 Grating

The grating is a 20 mm toroidal grating with 1800 lines per mm with SiC reflective coating. The surface has a reflectivity of 60%. The grating equation is given by Eq. 1.

The torus shape is determined by the radius of rotation and the radius of curvature. The major aberration in grating spectrographs in Rowland configuration is astigmatism. The torus shape is chosen to eliminate astigmatism as shown in Reference [1]. The torus grating creates stigmatic imaging at two wavelengths which can be adjusted according to our wavelength range. The condition for minimum astigmatism derived in Reference [1] in grating is given by Eq. 4

$$\cos \alpha \cos \beta = \frac{\rho}{R} \quad (4)$$

where R is the radius of curvature of the grating and ρ is the radius of rotation.

It has been shown in Reference [1] that by solving Eqs. 1 and 4, we can obtain α and β as in Eqs. 5 and 6

$$\sin \alpha = \pm \frac{\lambda}{2a} \pm \sqrt{1 + \left(\frac{\lambda}{2a}\right)^2 - \sqrt{\left(\frac{\lambda}{a}\right)^2 + \left(\frac{\rho}{R}\right)^2}} \quad (5)$$

$$\sin \beta = \pm \frac{\lambda}{2a} \mp \sqrt{1 + \left(\frac{\lambda}{2a}\right)^2 - \sqrt{\left(\frac{\lambda}{a}\right)^2 + \left(\frac{\rho}{R}\right)^2}} \quad (6)$$

Stigmatic imaging occurs at $\alpha = 0$, $\beta = 0$ and $\alpha = \beta$, as shown in Reference [1]. So from $\alpha = 0$, $\beta = 0$, we have Eq. 7.1 which gives the lower wavelength

$$\lambda_1 = \pm a \sqrt{1 - \left(\frac{\rho}{R}\right)^2} \quad (7.1)$$

and from $\alpha = \beta$, we have Eq. 7.2 which gives the higher wavelength.

$$\lambda_2 = 2a\sqrt{1 - \frac{\rho}{R}} \quad (7.2)$$

If we make $\lambda_1 = 135$ nm, we have $\rho/R = 0.97$ and $\lambda_2 = 192$ nm. R is determined depending on the focal length of the grating. From the values determined above, $\alpha = 13.11^\circ$ and $\beta = 0.91^\circ$ and blaze angle $\theta_B = 7^\circ$. These values have been taken as the starting point for optimization in Zemax software.

7 Optimization

7.1 Parameters to Be Considered While Optimizing

Distance between mirror and grating: The distance between mirror and grating is the sum of distance between mirror to slit and the distance between slit and grating. It should be small enough to be accommodated in the 3U side of the CubeSat along with the corresponding mechanical parts but large enough to remove aberrations and utilize the space.

Off-axis distance of the mirror: Should be small enough for the mirror and grating to fit in the 1U side but large enough to allow a wide aperture of mirror to receive light.

Slit location: The slit should be located exactly where the beam diameter is minimum between the mirror and the grating.

Grating to detector distance: The detector should be located where rays from all the wavelengths are focused. The grating, slit, and detector should be made to lie on a circle (Rowland circle).

The variables to be optimized were taken to be: **Radius of curvature of grating, Radius of rotation of grating, Radius of curvature of mirror.**

7.2 Parameter Values

After optimization, the following parameters were determined as shown in Table 2.

7.3 Spot Diagrams

The spot diagrams for 90 nm, 135 nm, and 180 nm are 127.539 m, 19.76 m, and 115.397 m, respectively. The spot diagrams are as shown in Figs. 2, 3, and 4.

Table 2 Simulated parameters

Parameter	Parameter	Value
ρ	Radius of rotation of grating	87 mm
R	Radius of curvature of grating	92 mm
α	Angle of incidence	18.309°
B	Angle of diffraction	4.079°
	Distance of mirror to slit	92.363 mm
	Off-axis displacement of mirror	40 mm
	Area of mirror used	77 mm × 200 mm
θ_B	Blaze angle	11.194°
	Radius of curvature of mirror	404 mm

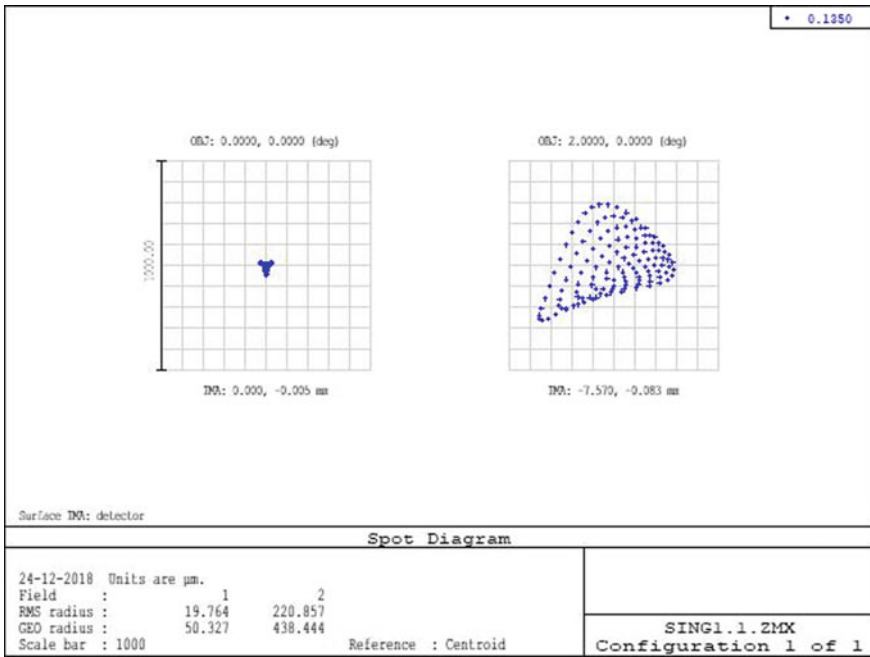


Fig. 2 Spot diagram at the wavelength 135 nm as obtained from Zemax. RMS spot size at center field = 19 microns

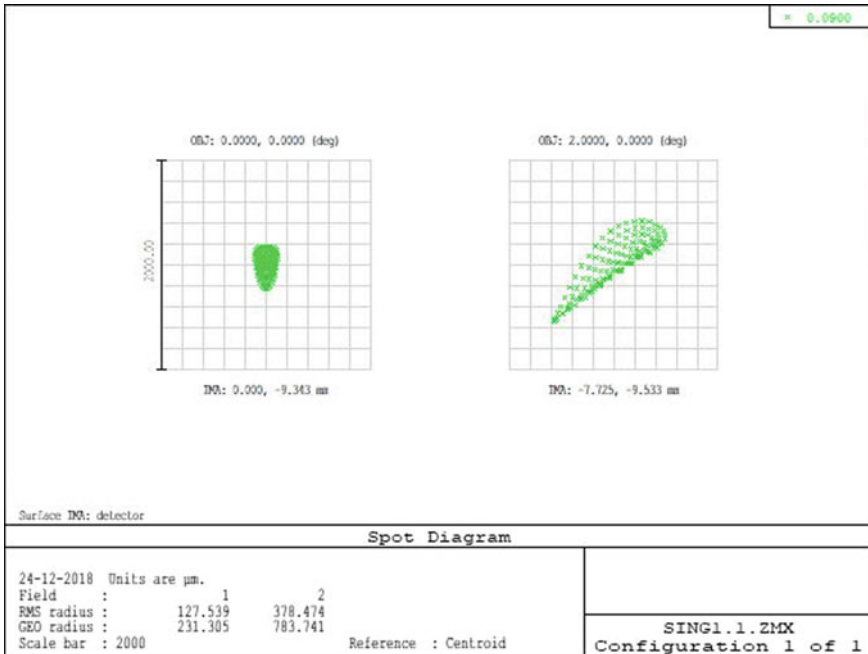


Fig. 3 Spot diagram at the wavelength 90 nm as obtained from Zemax. RMS spot size at center field = 127 microns

7.4 Spectral Resolution

The resolution of the spectrograph at the central wavelength 135 nm is 2000. The resolution of the spectrograph over the wavelength range is shown in Figs. 4, 5 and 6.

7.5 Throughput and Effective Area

The throughput of the spectrograph is given by the product of the reactivities of all the surfaces and the efficiency of the detector. The reflectivities of the mirror and grating are 60% and the maximum efficiency of the detector 70%. Therefore, the throughput of the spectrograph = 0.252. Effective area = throughput \times area of the mirror = $3.78 \times 10^{-3} \text{ m}^2$.

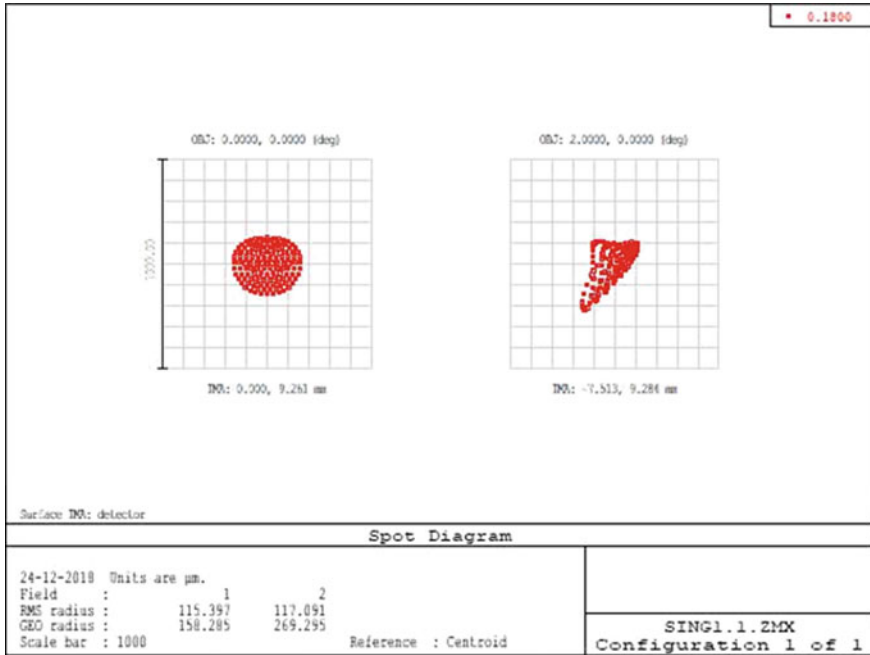


Fig. 4 Spot diagram at the wavelength 180 nm as obtained from Zemax. RMS spot size at center field = 115 microns

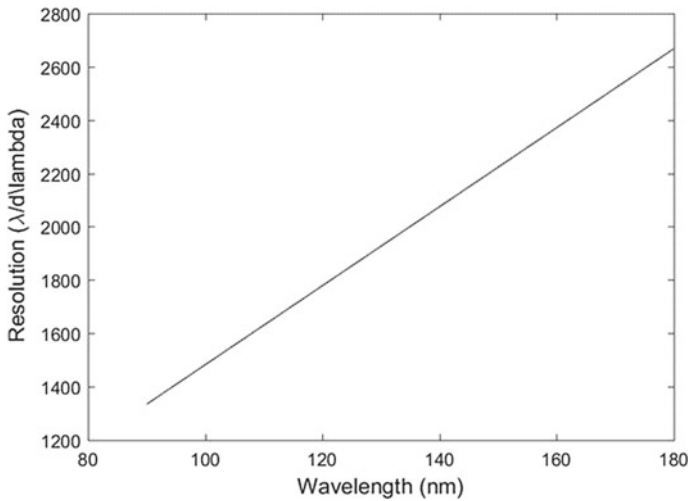


Fig. 5 Plot of resolution R of the grating versus wavelength in the range of 90–180 nm

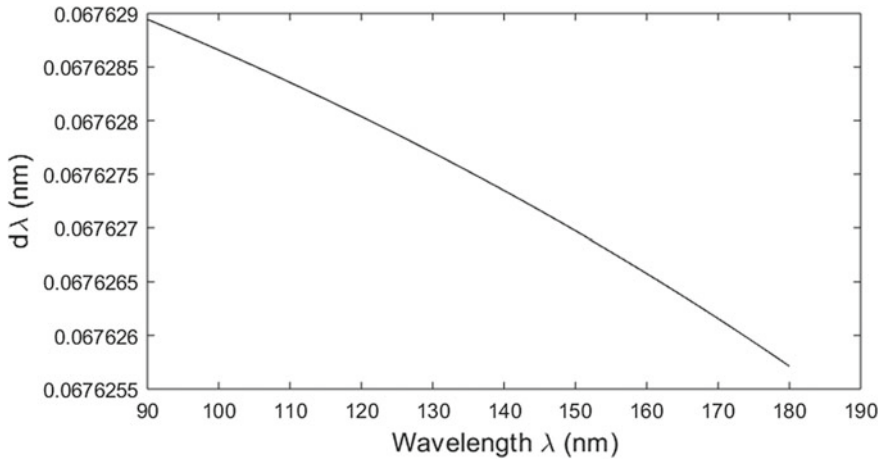


Fig. 6 Plot of resolution $d\lambda$ in nm versus wavelength in nm

8 Detector

The FUV detector will be made at the University of Tubingen (Reference [2]) with whom we have a collaboration. The FUV detector is sealed and it has a Cs-activated photoactive layer of GaN (or similarly advanced photocathode), with the help of (001)-MgF₂ GaN is operated in a semitransparent mode (Reference [2]). A coplanar cross-strip anode and stack of two long-life MCPs form the 2D plane of the detector (Reference [2]), which is combined with advanced readout electronics. An incoming UV photon passes through a window (fused silica/or MgF₂ or LiF) with low transmission from the far ultraviolet to the near ultraviolet (Reference [2]).

9 Conclusion

The optical design and optimization of the FUV spectrograph are completed. All parameters of the spectrograph after optimization are found to satisfy the science goals. As per the CubeSat design philosophy, we have conceived a compact and cost-effective design. Mechanical support structure will be designed and a finite-element-analysis study of the structure will be conducted. Mechanical design and analysis will be followed by thermal analysis. Once the thermal analysis phase is completed, the design will undergo a critical design review, and thereafter, we will proceed manufacturing of the qualification model.

References

1. Haber H (1949) The torus grating. *JOSA*
2. Conti L, Barnstedt J et al (2018) MCP detector development for UV space missions. [arXiv:1803.02895v1](https://arxiv.org/abs/1803.02895v1)
3. James J (2007) Spectrograph design fundamentals
4. Stern SA, Slater DC et al (1998) ALICE an ultraviolet imaging spectrometer for the Rosetta Orbiter. *Adv Space Res* 21(11):1517–1525

Visible and Near-Infrared (VNIR) Hyperspectral Payload Electronics



Hem Shikha and A. K. Sahay

Abstract In this paper, design of electronics for VNIR hyperspectral payload for the small satellite is presented. The payload comprises of imaging unit, linear variable filters (LVF), a CMOS sensor and electronics module. The LVF is used as a spectral filter before the sensor. The rectangular sensor being an array detector captures images in different bands in pushbroom fashion utilising satellite motion along the track. VNIR electronics captures sensor data, processes, rearranges and writes in memory to form hyperspectral data cube (H-cube). This high-speed data is transferred in real time to bus data handler (BDH) of satellite bus. This paper covers challenges and important aspects required for designing such payload electronics.

1 Introduction

With ever-increasing demand of remote sensing of earth data for monitoring important resources, disaster management, including flood, fire, chemical, biological or nuclear leakages, etc., and detection of targets of interest for national security, launch of small satellites with such payloads have gained importance. But the deployment of satellite with such payload comes with the high cost and huge effort. So, it is essential that each payload is to be utilised optimally for data acquisition and classification. In **EO remote sensing**, sensors detect solar radiation reflected or scattered from the earth, forming images resembling photographs taken by a camera high up in space. The wavelength region usually extends from the visible and near infrared (commonly abbreviated as VNIR) to the short-wave infrared (SWIR).

Optical remote sensing is characterised by following depending upon the number of spectral bands used in the imaging process:-

H. Shikha · A. K. Sahay (✉)
Vision Instrumentation (Aero and Space), Instruments Research and Development Establishment (IRDE), Dehradun 248008, India
e-mail: amithhappy@irde.drdo.in

H. Shikha
e-mail: hemsikha@irde.drdo.in

- (1) **Panchromatic imaging system**—the sensor detects only one band in a wide wavelength range. If this range coincides with the visible range, a greyscale image is seen. It is used to measure the brightness of targets but the spectral information is lost.
- (2) **Multispectral imaging system**—the sensor is able to detect a few spectral bands within a narrow wavelength. A multilayer image is obtained with both brightness and spectral information of the target observed.
- (3) **Super-spectral imaging system**—it has many more spectral channels as compared to multispectral imaging system. The bands have even narrower bandwidths enabling it to detect the finer spectral characteristics.
- (4) **Hyperspectral imaging system**—it acquires images in about a 100 or more contiguous bands enabling precise spectral information for better characterisation and identification of targets. It has useful applications such as in agriculture and coastal management.

1.1 Hyperspectral Imaging

In hyperspectral remote sensing or imaging, spectroscopy images are acquired in a large number of narrow contiguous spectral bands (typically >100). As a result, hyperspectral images are actually described as image cubes with two spatial dimensions and the third spectral dimension. It is used in a variety of applications including planetary and terrestrial geology, agriculture and urban studies. Each material has a unique spectral reflectance curve. Materials are identified from hyperspectral remote sensing images by comparing their spectra to a set of available reference spectra. Thus, the goal of hyperspectral camera (Fig. 1) is to obtain spectrum for each pixel of the image of a scene with the purpose of identifying materials of importance and determining the target. They collect information as a set of images, where each image represents a narrow waveband of EM spectrum. These images are then combined to form a hyperspectral data cube (H-cube) where two-dimensional images represent the spatial information and the third dimension represents the spectral content.

The hyperspectral imaging systems can be hand-held, air borne or space-borne systems.

The hyperspectral payload developed under this project will be a space-borne system mounted on a small satellite. It will cover wavelength band 450–2500 nm for the spectroscopic imaging from space-borne platforms. Two cameras will be developed to cover the entire band of wavelengths and the images will be recorded in an average of 10 nm wavelength bands in VNIR and 20 nm in SWIR region, respectively. First camera will cover the VNIR band from 450 to 900 nm, and second will cover the SWIR band from 900 to 2500 nm. Both cameras will work concurrently on the platform to record the complete band images. Both the cameras will provide ground sampling distance (GSD) of 12–15 m at 500 km altitude as a imaging payload

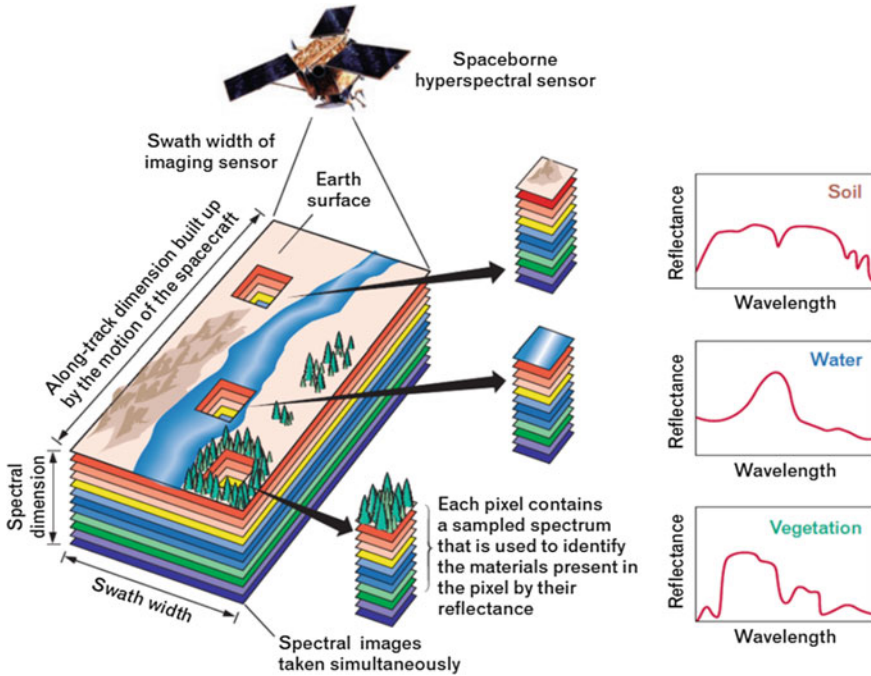


Fig. 1 Hyperspectral imaging sensor

for small satellites. VNIR camera will be realised based on VNIR CMOS image sensor (image sensor from M/S ON semiconductor), LVF filter and front-end optics.

2 System Configuration

The VNIR camera is designed to achieve ~10–15 m spatial resolution with high frame rate data capture capability. VNIR camera consists of a light gathering optical system, a spectral separation mechanism (linear variable filter), an area array detector (VNIR sensor) to capture and convert the scene radiances into an electrical signal as shown in Fig. 1. The processing electronics is required to acquire, calibrate and format data for cube generation. Further, this data is transferred using high-speed LVDS lines to BDH as per command received from BMU. The electronics module consists of (i) sensor mount card, (ii) FPGA-based processing card and (iii) power supply card. The raw data is captured in 42 bands and processed to form H-cube (Fig. 2). A graphical user interface (GUI), which is sensor configuration software, is designed for controlling important sensor parameters. The sensor is controlled through FPGA processing card via SPI interface and the image data is obtained through 12 parallel LVDS channels. It also describes the methodology adopted for

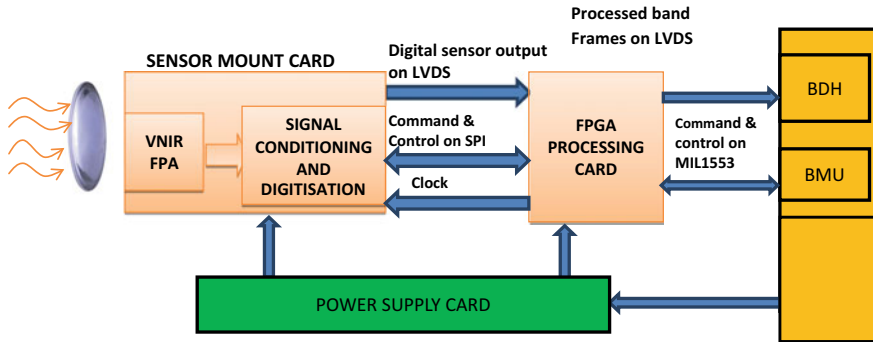


Fig. 2 System configuration

selecting sensor configuration through MIL1553 bus. The sensor data coming on high-speed serial links can drift due to various reasons which need to be addressed. This drift is corrected by per-pin skew compensation method (using bit and word alignment techniques) on each channel using ISERDES in FPGA. The link data integrity is incorporated using CRC code method. The polynomial used to generate the CRC checksum is $(x^{10} + x^9 + x^6 + x^3 + x^2 + x + 1)$. The generated H-cube is transferred through LVDS channels to satellite BDH for storage in solid-state recorder (SSR). Camlink interface is used for laboratory testing of the complete electronics module.

From project requirements, system parameters are deduced. From the satellite speed, time taken to travel distance equal to a spatial resolution corresponding to 1 pixel of the sensor, i.e. ground sampling distance (GSD) is calculated. If satellite speed is x km/s as projected on ground and resolution/projection of 1 pixel is y mts, then time taken to cover y mts is $(1/x * 1000) * y$ sec. This is the maximum integration time that can be used for image capture without blurring. The required integration time of the sensor depends on the brightness of the scene, the sensitivity of the detector and the aperture size. From spectral range of sensor and its active size, per pixel dispersion is calculated. Spectral resolution is decided by the number of pixel rows to be used in each band. If no. of lines per band is reduced, then spectral resolution will improve but it will increase the data rate. If no. of lines per band is increased, spectral resolution will become poor but frame rate and data rate will reduce.

The design of VNIR sensor processing electronics is done with reference to all the requirements of the project. It is described in detail in the next section.

3 VNIR Electronics

VNIR electronics is shown in Fig. 3. It consists of the following:

- (a) **Sensor mount card**
- (b) **FPGA-based processing card**
- (c) **Power supply card.**

(A) **Sensor mount card:**

Sensor mount card is a multilayer PCB for mounting of high-speed sensor and on-board bias generations for the sensor. The required input power supply for sensor card is provided by the power supply card. It also contains one high-density connector with locking facility for interfacing with signal processing card through Rigiflex cable. The readout process requires timing control and input control commands. So, input clock and control commands are given to this card by Xilinx FPGA-based signal processing card. The synchronisation signals, output clock and digitised image data are given as outputs from sensor card to SPC.

- (B) **Xilinx FPGA-based signal processing card (SPC)** generates all the control commands and clock required for sensor mount card. The data acquisition module of this card will capture image data from the sensor using synchronisation channel and clock signals which are given by the sensor card. The image data processing and formatting are done and then data cubes are generated. The output of the card is given as raw LVDS video on two buses (main and redundant) to BDH. Video output is also given through camlink transceiver for ground testing in laboratory to PC-based GUI. One LVDS pair is given for synchronisation with SWIR payload. MIL1553B interface is provided on this board for receiving of control commands and sending status to BMU/PC-based GUI.

- (C) **Power supply card** is developed for supplying power to the sensor mount card and signal processing card. It receives 28 V from relay and gives 5 V output.

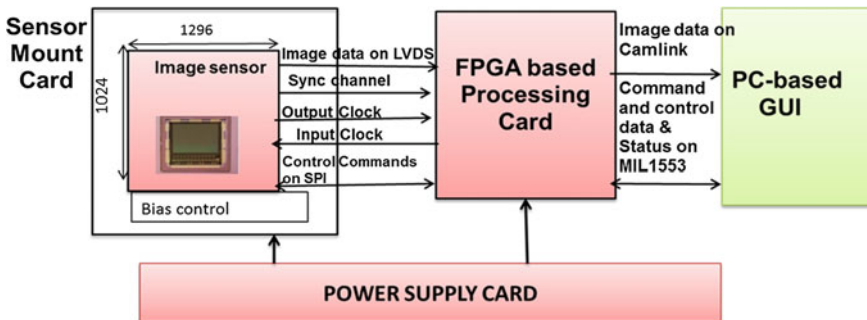


Fig. 3 VNIR electronics

3.1 Imaging Sensor

Imaging sensor is an important component of the imaging camera. The scene is imaged by the optics on the sensor. The sensor converts radiation from each pixel of scene into corresponding electrical signals. The numbers of electrons generated on the imaging pixel are dependent on the number of photons incident on it. The characteristic of imaging sensor of converting photons into electron is measured by the quantum efficiency. Higher is the quantum efficiency means the better response of the sensor for the small radiation. The electrons are stored into the resistors and then charge is converted into voltage using built-in electronics circuitry. The voltage measured corresponding to each pixel is the representation of the radiation intensity incident on it and hence the scene characteristics. Thus, the voltage of each pixel of imaging sensor regenerates the scene on the display.

3.2 Radiometric and Spectral Characteristics

The sensor used in this project captures images with 10 bit radiometric resolution using CMOS sensor technology. Individual pixels produce signal known as dark current even if they are not exposed to light. Dark currents are corrected by collecting a dark cube image while the sensor is not receiving light. Dark values are then subtracted from the digital number values of each image pixel. Additionally, pixels on the sensor may have different gain and offset components when reacting to incident photons. For this, radiometric and spectral calibrations were done.

The sensor will be used in windowing mode with the frame size of 1024×630 pixels due to the limited size of LVF. The spectral dispersion will be along the vertical direction with 630 pixels and each band will comprise of 15 rows of pixels. The spectral dispersion rate of the LVF is 0.7 nm per pixel. Thus, the spectral resolution achieved is 10.5 nm. To enhance the overall quantum efficiency, temporal binning is implemented by motion-compensated averaging of the pixels without losing spatial resolution. Using this setting, the dimensions of each captured band is 1024×15 per frame which represents a 15 line bands in the final hyperspectral image. Adjacent lines (successive frames) are captured along the satellite path to produce the final hyperspectral image cube, which has 42 spectral bands (all 15 line bands of same waveband stitched together). A PC-based GUI is used to upload the required settings over MIL 1553 line with the sensor as a remote terminal, and a PCI camlink frame grabber is used to acquire the frames successively. Custom hardware circuit board and software application were developed for the image acquisition including the camera synchronisation.

4 Data Acquisition and Pre-processing

Different kinds of techniques and processing are required for effective utilisation of hyperspectral sensors. Before starting the sensors to capture frames the fixed pattern noise (FPN) correction is enabled in the sensor. The on-chip column FPN correction is more reliable than an offline correction, as it compensates for supply and temperature variations. The first processing after data acquisition is stitching together the bands of same wavelength from different frames to form one complete image of a particular wavelength and all 42 such images bundled together forms a complete data cube. Then, radiometric and spectral calibrations are applied. Further processing, like atmospheric corrections, etc., is done on the ground.

To collect HIS data cube (or hypercube) requires either scanning (in a time interval) in the spectral or spatial domain. There are two main methods of scanning:

1. **Pushbroom:** In this technique, the second dimension of the detector collects simultaneously all the spectral information. This uses the forward motion of the platform to record successive scan lines and build up a 2-d image, perpendicular to flight direction. This technique is being used in our project.
2. **Whiskbroom:** In this case, an active scan mechanism is required to scan the spatial dimension orthogonal to the direction of the motion of the platform. Each line is scanned from one side of the sensor to the other using a rotating mirror.

Following steps show the spectral data collection and hyperspectral data cube generation process to be used in the hyperspectral camera to be developed in the project:

- (a) A pushbroom sensor on an airborne or space-borne platform collects spectral information for a one-dimensional row of cross-track pixels, called a *scan line*. Fifteen contiguous such scan lines form one spectral band.
- (b) The sensor captures frames after the shift of every single line in sensor and then motion-compensated averaging is done on these fifteen frames to get a single frame with improved SNR. The frame rate is decided as per the satellite speed.
- (c) After 42 such improved frames are obtained, the bands of corresponding wavelengths are stitched together and stored in the DDR memory as one data cube. The assembled three-dimensional hyperspectral data cube can be seen as a stack of two-dimensional spatial images, each corresponding to a particular narrow waveband.
- (d) Alternately, the spectral samples can be plotted for each pixel or for each class of material in the hyperspectral image. Distinguishing features in the spectra can be used for the detection and classification of material in a scene.
- (e) Readout of previous image data is done before or during exposure of sensor for integration of new scene so that new data does not erase the previous data. Clock at which sensor is to be operated and shuttering mode is chosen so that it satisfies the above criteria.

Figure 4 shows the algorithm involved for the acquisition of data for a hyperspec-

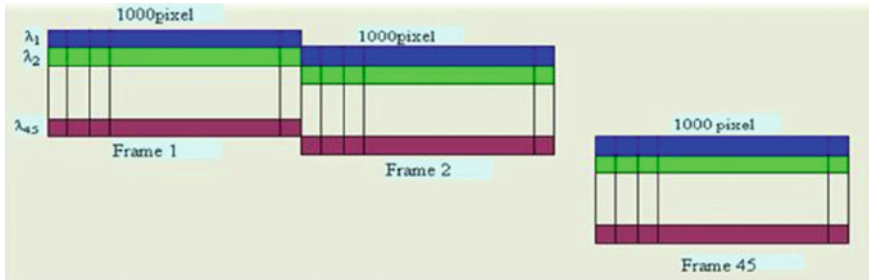


Fig. 4 Data acquisition and generation of hyperspectral data cube

tral data cube. After data acquisition is complete, the data cubes generated can be further processed using data pre-processing techniques.

Some of the data pre-processing techniques are described below [9]. The hyperspectral data cubes generated with the process described above contains large data volumes so the pre-processing becomes complex. The hyperspectral data quality is also affected by random sensor error and noise which tends to reduce the signal to noise ratio. Pre-processing of data is very essential as the data cubes generated are also affected by atmospheric errors. So, data pre-processing includes sensor and atmospheric error removal and image rectification.

(a) **Sensor error correction**

Most pushbroom sensors produce bad vertical lines on the images due to poor calibrated detectors. The bad lines have a constant or low value as compared to its neighbouring pixel. The DN values of the pixels are replaced with the values of their immediate left and right pixel for error correction.

(b) **Atmospheric correction**

The atmosphere is responsible for scattering the electromagnetic energy travelling from Sun to Earth's surface and from Earth's surface to the sensor. Therefore, the energy received by the sensor may be less than or more than the original one due to reflectance from Earth's surface alone. This effect on the image spectra is minimised using atmospheric correction.

5 Software Architecture

The software flow of the VNIR hyperspectral camera is shown in Fig. 5. As the satellite power supply unit is switched on, electronics draws power and its on status is sent through BMU to ground station. The ground station sends commands through sensor configuration software/BMU to VNIR camera. The FPGA signal processing board receives the commands and generates control signals and clocks for sensor. The sensor acquires pixel image data and sends to FPGA. The FPGA receives data, rearranges it and calibration coefficients are applied to it. The data

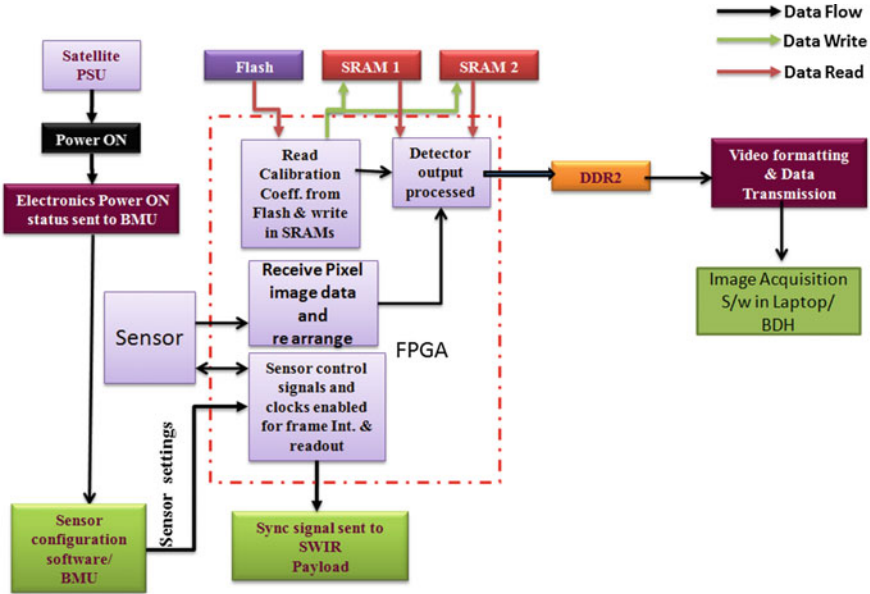


Fig. 5 Software architecture

is saved in DDR memory. The data cube generation algorithm is applied in DDR memory. The formatted data is transmitted to image acquisition software/BDH.

5.1 Image Acquisition Software

A software application is developed to acquire the hyperspectral images from FPGA-based SPC. The interface with satellite will be LVDS lines, but for testing in laboratory, the same data is output through camlink interface. It is captured though a PCI-based camlink frame grabber (IMPERX) and displayed on laptop.

5.2 Sensor Configuration Software

A Labview-based sensor configuration GUI has been developed which can configure sensor using FPGA without the need to reprogram the FPGA each time. For configuring the sensor to various settings, certain values are to be written to specified registers in the sensor through SPI interface. This is done by the FPGA on receipt of corresponding commands from the PC-based GUI. Designed Labview application can configure the sensor for operating modes, integration time, FPN correction enable or disable, window position set, PGA gain settings and offset settings. In

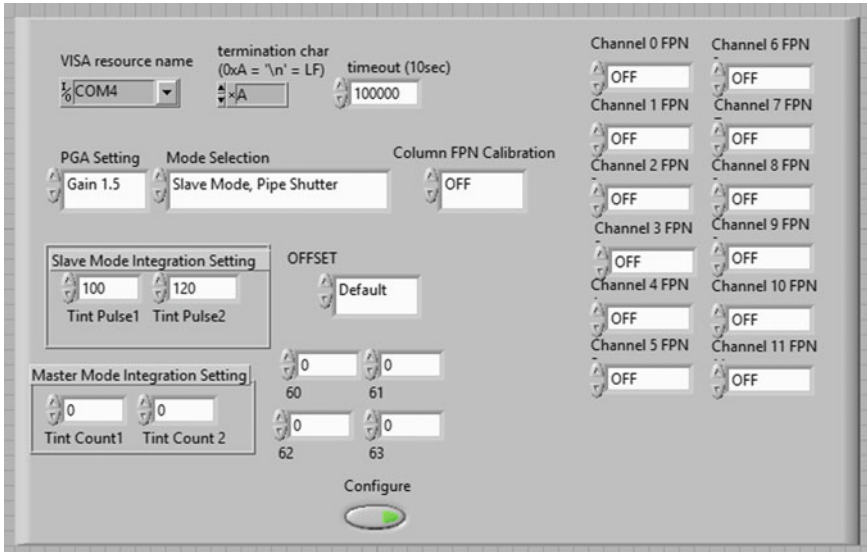


Fig. 6 Sensor configuration software

the actual scenario, these commands will come from bus monitoring unit (BMU) of satellite on MIL1553 lines (Fig 6).

6 Challenges Encountered

- Calibration and characterisation of sensor: The sensors that are expected to return accurate data require prelaunch characterisation. Sensors require a suite of prelaunch tests to establish performance parameters such as spectral bandpass and polarisation sensitivity to be used in the data processing.
- Radiometric and spectral calibration is required to be done for the sensor. Calibration is the process of measuring the relationship between sensor output (digital counts) and absolute radiant (radiance) input.
- Selection of radiation-hardened components has sufficient resources to satisfy the system requirements. These components come at an exorbitant cost and have a long lead time.
- Large memory is required on electronic boards to store data and run the hypercube generation algorithm with binning.
- All the processing has to be done with limited power requirement.



Fig. 7 Actual scene. Image acquired on software



Fig. 8 Simulated input scene (pseudo-coloured). Output image

7 Results

The laboratory set-up for data acquisition through VNIR camera was done.

First of all, a single image is captured by VNIR camera. The actual image and image received on image acquisition software are as shown in Fig. 7.

An algorithm is developed for image cube generation with image size of 1008×630 . Each band's size is of 15 lines. For the generation of data cube, we have developed a scheme in which each captured image is divided into 42 bands, each band comprising of 15 lines and stored in respective memory space using paging in DDR.

For demonstrating the above algorithm, we have developed a model in our laboratory where to replicate satellite movement, a video is played on a display as seen through a satellite and that is captured through the VNIR hypercam. By synchronising the movement of scene and integration time, 42 images are captured and bands are rearranged to generate the data cube. Figure 8 shows the results for the same.

8 Summary and Conclusion

A VNIR hyperspectral imaging system composed of an integrated set of off-the-shelf components is demonstrated. The electronics is designed around the industrial

equivalent of the space grade sensor On semi sensor LUPA 1300-2 and Xilinx Vertex V FPGA. It has been tested as a stand-alone system in the laboratory. Presently, all the interfaces have been tested with laptop through converters namely MIL1553 to USB converter and IMPREX camlink frame grabber.

Acknowledgements The analysis is primarily based on the evolution of electro-optical payloads at IRDE, Dehradun, and authors profusely thank their present and past colleagues. We are grateful to other colleagues at other DRDO centres, whose work has been used for taking the system parameters. Special thanks to Programme Director for useful discussions and for providing system details.

We sincerely thank Director, IRDE for allowing us to carry out this research and publication.

References

1. The role of small satellites in NASA and NOAA Earth observation programs
2. Abd-Elrahman A, Pand-Chhetri R, Vallad G (2011) Design and development of a multi-purpose low-cost hyperspectral imaging system. *Remote Sens* 3:570–586
3. Samudraiah DRM, Saxena M, Paul S, Narayanababu P, Kuriakose S, Kumar AK Payload configurations for efficient image acquisition—Indian perspective
4. Various payload documentation of IRDE

Design of Hyperspectral Imaging Sensor for Small Satellite in LEO



Vinay Kumar, A. K. Sahay and H. P. S. Panwar

Abstract Military applications such as reconnaissance, surveillance and detection of camouflaged targets require imaging payloads with state-of-the-art sensors in spectral wavebands covering visible NIR (VNIR), SWIR, and thermal IR (MWIR and LWIR) region. Hyperspectral imaging sensor is one of them. This type of sensor acquires both the spatial and spectral signatures of the scene simultaneously. These sensors can be designed using variable filter, prism, grating, or interferometric means. This paper presents the design of a hyperspectral imaging camera (HSIC) for the VNIR (450–900 nm) and SWIR (900–2500 nm) wavebands using linear variable filter (LVF). This camera has advanced features such as high spatial resolution (12 m at 500 km) and high spectral resolution (10–20 nm) and can be used for military applications from small satellites operating in LEO.

Keywords Hyperspectral · LVF · SNR

1 Introduction

Since last two decades, the development of airborne and space-borne hyperspectral sensors along with advanced classification algorithms has improved the discrimination of various targets of interest. These sensors enable the imaging of a scene over a large no. of discrete, contiguous, and narrow (~10 nm) spectral bands such that a complete spectral signature can be obtained from the scene. These sensors acquire spatial and spectral information collectively from the scene radiation by using either filters, prism, grating, or interferometric means along with an area array detector [1, 2]. All the design schemes of hyperspectral imaging camera have their own advantages and disadvantages in terms of size, weight, cost, and portability. The fundamental design parameters of hyperspectral imagers for remote sensing application are spatial resolution, spectral resolution, and signal-to-noise ratio (SNR) [3]. This paper presents

V. Kumar (✉) · A. K. Sahay · H. P. S. Panwar
Vision Instruments (Aero & Space Borne Systems) Division, Instruments Research and
Development Establishment (IRDE), 248008 Dehradun, India
e-mail: vinay.kumar@irde.drdo.in

© Springer Nature Singapore Pte Ltd. 2020
PSR. S. Sastry et al. (eds.), *Advances in Small Satellite Technologies*,
Lecture Notes in Mechanical Engineering,
https://doi.org/10.1007/978-981-15-1724-2_18

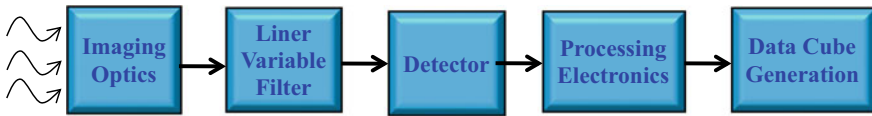


Fig. 1 Hyperspectral imager configuration using linear variable filter

hyperspectral imaging camera configuration for the VNIR-SWIR range using linear variable filter as a spectral dispersion mechanism (Fig. 1). This study summarizes the major system design considerations including specifications for front-end optics, linear variable filter and SNR analysis of proposed hyperspectral sensor using silicon and MCT detector arrays covering VNIR-SWIR waveband region, respectively.

2 Hyperspectral Imaging Sensor

The design of the proposed HSIC is similar to a normal imaging camera except for the inclusion of a spectral feature. It comprises imaging optics, LVF, area array detector, and processing electronics (Fig. 1). The focusing optics along with the detector pixel decides the spatial resolution of the imaging system. The LVF acts as a spectral separation device in the proposed camera. It decides the spectral resolution of the hyperspectral camera. The SNR of the system is derived by considering the cumulative effect of individual sensor components (e.g., collecting optics, filter, and detector) and scene radiance.

3 Design Analysis

The design of the proposed camera may be carried out by estimating parameters of front-end optics, LVF, and available state-of-the-art detectors, for getting optimum SNR of the system. This has been explained in the following subsections.

3.1 Front-End Optics

There exist a number of optical configurations for the light-gathering optical systems of hyperspectral imagers. In the proposed design, the collecting optics is RC type. The most important parameters related to collecting optics are spatial resolution at the detection range, optical aperture diameter, F#, and MTF. The design of the proposed HSIC is based on readily available detectors, i.e., 1024×1024 (pixel pitch: 14μ) Si-CMOS detector in VNIR and 1024×256 (pixel pitch: 30μ) cryogenically cooled (195 K) MCT detector in SWIR waveband. The required spatial resolution of 12 m at

Table 1 Sensor design parameter

Parameter		Value in VNIR waveband	Value in SWIR waveband
Detector	Format and pixel pitch	1024 × 1280 (14 μm) (Si-CMOS)	256 × 1000 (30 μm) (MCT)
	Readout noise	37e	149e
	Full well	30 K	500 K
LVF	Central wavelength	675 nm	1700 nm
	Spectral resolution	7 nm	21 nm
Front-end optics	Aperture and F#	153 mm (F#3.8), RC type	330 mm (F#3.8), RC type
	IFOV	24 μrad	24 μrad
	Spatial resolution	12 m at 500 km	12 m at 500 km
Sensor SNR	At 1.7 ms (integration time)	114	110

500 km altitude subtends an IFOV of 24 micro-radian. This calls for front-end optics with EFL of 583 and 1250 mm in VNIR and SWIR wavebands, respectively. F/3.8 of the collecting optics has been selected to achieve optimum SNR value (Sect. 3.3, Table 1). The mathematical expressions for spatial resolution and aperture diameter of collecting optics are given below:

$$\text{Spatial Resolution} = \text{IFOV} \times \text{Range} \quad (1)$$

$$\text{Aperture Diameter(m)} = \frac{0.00244 \times \text{Wavelength}(\mu\text{m}) \times \text{Range(km)}}{\text{Spatial Resolution(m)}} \quad (2)$$

3.2 LVF

The proposed camera is based on LVF. In order to get the spectral dispersion in such a wide waveband (VNIR-SWIR), it is proposed to have two separate LVFs. One LVF will be used in VNIR region and the other one in SWIR region. In order to get the required spectral resolution, the specifications of LVF and related parameters have been derived as follows:

$$\text{Linear Spectral Dispersion(nm/mm)} = \text{Spectral Band(nm)}/\text{Coated dimension(mm)} \quad (3)$$

$$\text{Spectral Resolution(nm)} = \text{FWHM} + (\text{linear dispersion} \times \text{spot size}) \quad (4)$$

where diffraction limited spot size = $2.44\lambda F\#$ and FWHM $\leq 1\%$ of central wavelength.

3.3 SNR Analysis of Hyperspectral Imaging Sensor

The system SNR is estimated by dividing signal electrons by noise electrons (generated in the detector). The electrons (signal and noise) generated in the detector may be estimated using following expressions:

$$\text{Spectral Radiance } L_\lambda = \frac{2hc^2}{\lambda^5 \left[\exp\left(\frac{hc}{\lambda kt}\right) - 1 \right]} \quad (5)$$

$$\text{Signal Electrons} = \frac{L_\lambda \Delta\lambda A_{\text{Aperture}} \text{IFOV}^2 \eta_{\text{OE}} \eta_{\text{QE}} t_{\text{int}}}{h\nu} \times \frac{R_{\text{Sun}}^2}{D_{\text{Sun_Earth}}} \quad (6)$$

$$\text{Noise} = \sqrt{\text{Photon_Noise}^2 + \text{Quantization_Noise}^2 + \text{Readout_Noise}^2} \quad (7)$$

$$\text{SNR} = \frac{\text{Signal Electrons}}{\text{Noise Electrons}} \quad (8)$$

where

$\Delta\lambda$ = Spectral bandwidth

A_{Aperture} = Aperture area of collecting optics

η_{OE} = Optical efficiency

η_{QE} = Quantum efficiency

R_{Sun} = Radius of Sun

$D_{\text{Sun_Earth}}$ = Distance between Sun and Earth

t_{int} = Integration time.

4 Results

The sensor parameters have been derived using major input parameters of the detector, spatial and spectral resolution at required range. The results have been summarized in Table 1.

5 Conclusion

The system design has been presented for the proposed hyperspectral imaging camera covering VNIR-SWIR spectral range. The proposed camera has advanced features such as high operating altitude (~500 km), high spatial resolution (12 m at 500 km), and high spectral resolution (10–20 nm). Further, this can be deployed from UAVs/aircraft providing GSD of the order of 25 cm at 10 km.

References

1. Hackwell JA et al (1996) LWIR/MWIR imaging hyper-spectral sensors for airborne and ground based remote sensing, vol 2819. SPIE
2. Singh B, Dowerah J (2010) Hyperspectral imaging: new generation remote sensing. Earth Sci India 3(iii)
3. Landgrebe DA (2003) Signal theory methods in multispectral remote sensing. Wiley series in Remote Sensing

Opto-Mechanical Design of Short Wave Infrared Camera for Small Satellite



Bharat Ram Meena, Shekhar Tomar, A. K. Sahay and H. P. S. Panwar

Abstract The objective of this paper is to design and analyse the opto-mechanical design of the SWIR camera for space applications. The opto-mechanical design includes, mounting of various optical elements using compliant flexures so that the optical elements are isolated from mechanical and thermal loads. To mitigate the effects of thermal cycles in space environment, special structural materials are used. Joining of the opto-mechanical is done using space grade adhesives to avoid various issues with the friction-based joining schemes. Opto-mechanical design approach is focused on ease of manufacturing, optical performance and survival in space environment. Finite element model of the entire assembly was established to analyse the design for static and dynamic design requirements.

Keywords Short wave infrared camera · Opto-mechanical design · Adhesive joints · Flexure mount

1 Introduction

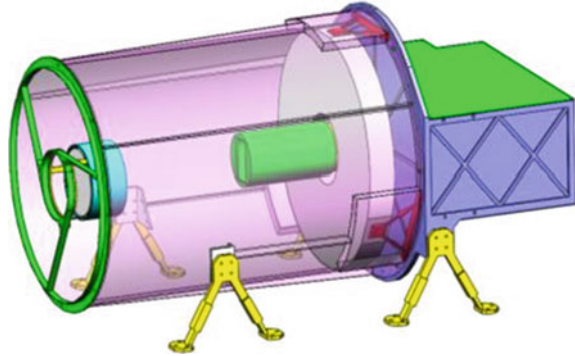
Electro-optical payloads are the integral part of the satellites launched for earth observations and remote sensing purposes. These payloads are mounted on the top surface of the satellite deck and have to perform their intended function in space environment. Short wave infrared camera (SWIR) is currently under development for remote sensing on earth surfaces at a sampling distance of 12 m for an altitude of 500 km. It will image the earth in 0.9–2.5 μm spectral bands.

While designing the payload the following opto-mechanical constraints need to be considered:

(i) overall size and weight of the system is constrained by the launch vehicle (ii) system must withstand the severe launch environment (iii) Optical design is very sensitive due to very tight optical tolerances (iv) optical alignment must be retained

B. R. Meena (✉) · S. Tomar · A. K. Sahay · H. P. S. Panwar
Vision Instruments (Aero & Space Borne Systems) Division, Instruments Research and Development Establishment, 248008 Dehradun, India
e-mail: bharatmeena@irde.drdo.in

Fig. 1 SWIR camera 3D model



throughout the working life of the system (v) The fundamental mode of the system has to be more than 100 Hz [1].

The 3-D solid model of the proposed SWIR camera design is shown in Fig. 1. This paper presents the opto-mechanical design procedure of SWIR camera as well as a demonstration of its validity through finite element analysis (FEA).

2 Opto-Mechanical Design Procedure

SWIR is an integrated compact camera assembly consisting of fore and relay optics assemblies. Due to the severe launch environment and working conditions in space, its design philosophy is totally different from land-based system. So, while designing SWIR camera care has been taken for survival in launch environment and long working life in space.

While designing the system, the emphasis is given to maintaining opto-mechanical tolerances at certain temperature range and behaviour of critical sub-assemblies under static and dynamic conditions. Optical and mechanical layout of the SWIR camera is shown in Fig. 2.

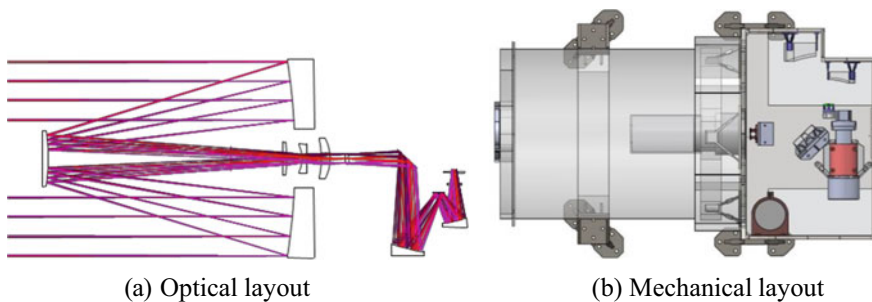


Fig. 2 Optical and mechanical layout of SWIR camera

2.1 Material Selection

To minimize the thermal effects, material selection is done very carefully. The principle of matched coefficient of thermal expansion (CTE) is used to select the material for mirror mounts and housing. Detector is the main source of thermal load and vibrations at the time of operation, so provision of thermal and vibration isolation has been done by designing a suitable isolation scheme.

2.2 Selection of Bonding (Adhesive) Material

Structural adhesive is used for optical-metallic and metallic-metallic components bonding. Certain mechanical properties possessed by adhesive make them more favourable as joining agents. These properties are: small stress concentration in adherents, stiff connection, excellent fatigue properties, no fretting problems, sealed against corrosion, smooth surface contour, relatively lightweight and damage tolerant.

In the design of SWIR camera, adhesives are used as bonding materials. While selecting the bonding materials certain properties have been taken into account which are [9]:

- A. The bonding material must possess high shear strength.
- B. The coefficient of thermal expansion must be as low as possible.
- C. Optimum viscosity at room temperatures.
- D. Optimum curing time at room temperatures.

2.3 Mounting of Optical Components

There are a number of optical elements which have to mount in such a way that both optical performance and structural stiffness are maintained. These mounts were driven by three principles: frictionless, kinematically constrained and matched coefficient of thermal expansion. Optical components are mounted using flexures.

Every optical sub-assembly is designed as a separate module for the ease of assembly and alignment. The optical components have been mounted using radially compliant isostatic flexures to compensate the assembly and manufacturing errors. These flexure mounts can also isolate the optical elements from the stresses generated due to thermal cycle. Space grade adhesive has been used to assemble the flexure with the optical elements. The properties of the adhesives are listed in Table 2 (Fig. 3).

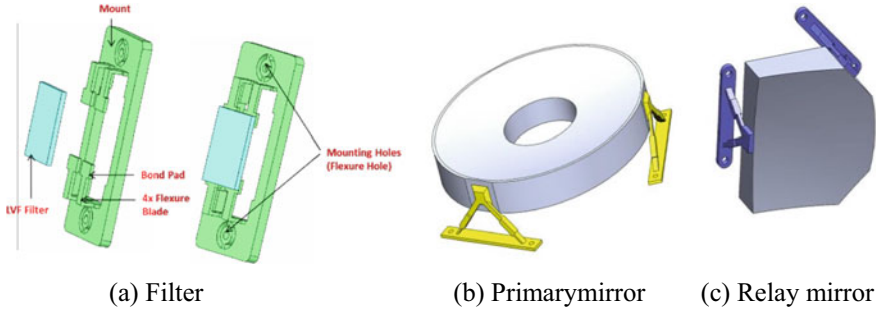


Fig. 3 Mounting scheme of various critical optical components **a** filter **b** primary mirror **c** relay mirror

3 Finite Element Modelling

A thorough finite element (FE) analysis of the entire system and subsystems has been carried out to optimize the functional and structural parameters of the system in launch environment. First, the system was analysed at 1 g gravity and it was ensured that the static deflections are within permissible limits.

Finite element model of the camera is established in a commercial FEA tool with 2-D shell elements (CQUAD 8). Smaller lenses and mirrors were excluded from the analysis and they were modelled as lumped masses. All the bolted connections are modelled as rigid beam elements (RBE2). The material properties in Tables 1 and 2 are used (Fig. 4).

3.1 Static Load Analysis

SWIR payload will experience quasi-static loads during a launch of 30 g for the axial and 30 g for the lateral directions. The axial direction (z-axis) is along the optical axis and x- and y-axis are the lateral directions. The stress distribution and deformed shape of the camera at 1 g is shown in figure.

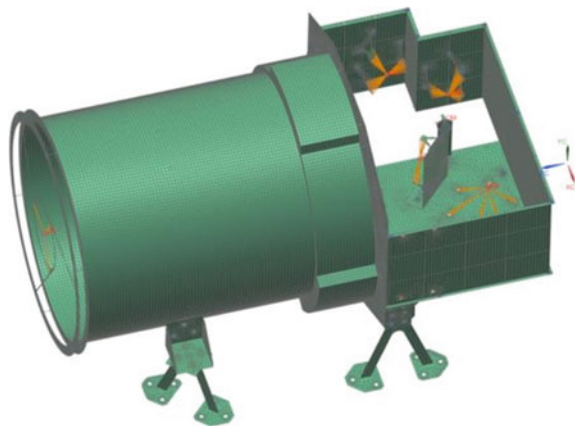
Table 1 Mechanical properties of opto-mechanical materials

Material	Density, ρ (kg/m ³)	Young's modulus, E (GPa)	Thermal expansion, α (10 ⁻⁶ /K)	Specific stiffness, E/ρ (GPa m ³ /kg)
Zerodur	2530	92	-0.09	36.4
Titanium	4428	104	9.0	24.4
Invar 36	8050	141	1	10.4

Table 2 Mechanical properties of space grade adhesives

Adhesive	Type	Shear strength at 24 °C (MPa)	Thermal expansion coefficient $1 \times 10^{-6}/^{\circ}\text{C}$	Recommended curing time	Temperature range (°C)
2216 B/A grey (3M)	2-part epoxy	22.1	102	30 min (98 °C) 120 min (66 °C)	-55 to 150
RTV 566(GE)	2-part epoxy	3.2	280	1 day (24 °C)	-115 to 260
Milbond (Summers)	2-part epoxy	14.5	72	180 min (71 °C)	-60 to 110

Fig. 4 Meshed model of the SWIR camera



System must survive the launch environment. Through many iterations it is ensured that the maximum stresses are well within safety limits (Fig. 5; Table 3).

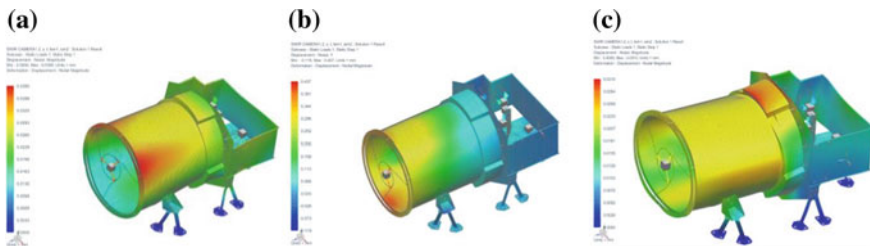


Fig. 5 Deflection plot when load is applied **a** along x-axis **b** along y-axis **c** along z-axis

Table 3 Maximum stress and margin of safety

Direction	Maximum stress for 1 g (MPa)	Max quasi-static load, (g)	Maximum stress (MPa)
X-axis	6.93	30	207.9
Y-axis	5.42	30	162.83
Z-axis	5.50	30	168.14

3.2 Thermal Analysis

Thermal analysis of the camera was carried out using ANSYS APDL analysis tool. The effect of the heat generated by the cryogenic cooler on the opto-mechanical components was analysed. To maintain the integrity of the structure under thermal loads, a heat pipe-based heat dissipation mechanism has been implemented in the design.

3.3 Modal Analysis

Payload mounted on a satellite can have resonance caused by their dynamic coupling to launch vibrations. In order to avoid these resonances, payload and satellite must have certain minimum fundamental vibration mode depending on the launch requirements. In case of SWIR camera, the minimum required natural frequency is 100 Hz in all three directions. First six natural frequencies and three modes shapes are shown in Fig. 6.

While doing the modal analysis, smaller electronics and fasteners are excluded from the analysis. Only modes with more than 85% mass participation are considered for the design purpose. Many design modifications and improvements are done with the help of finite element analysis to achieve the 100 Hz fundamental mode of vibration.

3.4 Weight Optimization of the Opto-Mechanical Components

In order to maintain the weight of the SWIR camera, finite element analysis method has been used to optimize the weight of the various opto-mechanical components. Primary mirror is shown in Fig. 7 which is the major weight contributing element. Its weight has been reduced by scooping the material from back side in hexagonal pockets. While reducing the weight, the surface figure of the primary mirror is maintained according to a pre-specified criterion.

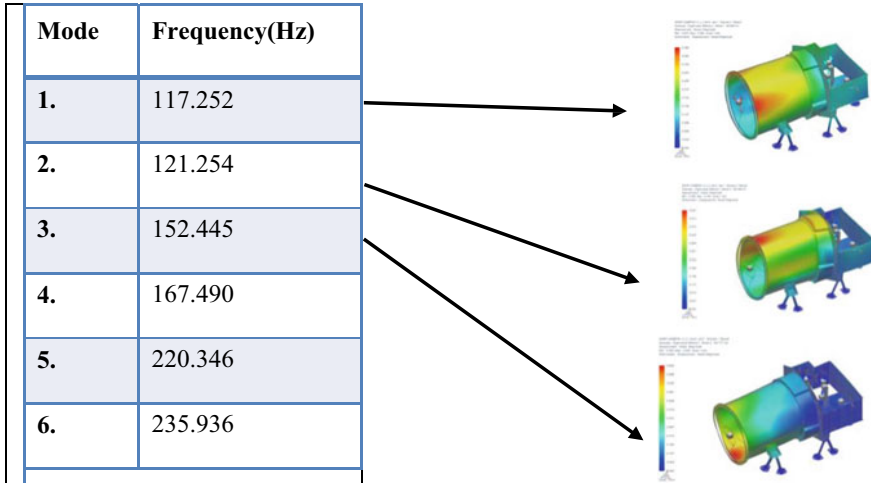
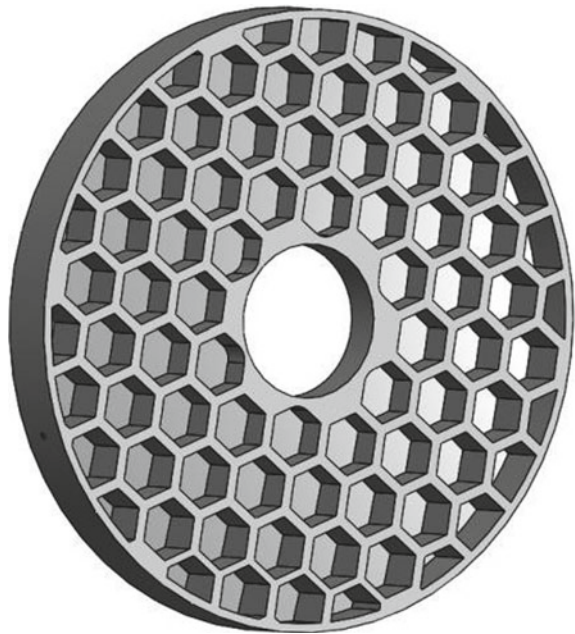


Fig. 6 First six natural frequencies and three mode shapes

Fig. 7 Weight optimization scheme in primary mirror



In mechanical components, housing is the main weight contributing component. Weight optimization of the housing is done using FE analysis. Based on the result of the modal and static load analysis, undesirable material is removed.

4 Conclusion

A compact opto-mechanical design of the SWIR camera has been carried out while taking care of the various opto-mechanical constraints. While selecting the material, matched CTE criterion was followed to take care of the thermal gradient induced stresses. Moreover, the optical components are mounted using the compliant flexure mounts. Adhesive-based joints are adopted while joining the opto-mechanical components which take care of any play in the joints. The design is demonstrated by finite element analysis to be stiff and stable enough to survive and operate the launch and in orbit space.

References

1. Chu C et al (2011) Design of bipod flexures for space mirror. In: International symposium on photoelectronic detection and imaging 2011: space exploration technologies and applications, vol 8196. International Society for Optics and Photonics
2. Lee J-H, Lee C-W, Kim Y-M, Kim J-W (2009) Optomechanical design of a compact imaging spectrometer for a microsatellite STSAT3. *J Opt Soc Korea* 13(2):193–200
3. Gupta N (2008) Hyperspectral imager development at Army Research Laboratory. In: Infrared technology and applications XXXIV, vol 6940. International Society for Optics and Photonics, p 69401P
4. Delp C, Duffy MA, Neill D, Sebring TA (2004) Optomechanical design of the discovery channel telescope prime focus assembly. In: Astronomical structures and mechanisms technology, vol 5495. International Society for Optics and Photonics, pp 216–228
5. Li Y (2012) Modeling and structural analysis of honeycomb structure mirror. In: Modern technologies in space- and ground-based telescopes and instrumentation II, vol 8450. International Society for Optics and Photonics, p. 84504K
6. Park K-S, Lee JH, Youn S-K (2005) Lightweight mirror design method using topology optimization. *Opt Eng* 44(5):053002
7. Doyle KB, Genberg VL, Michels GJ (2002) Integrated optomechanical analysis. vol 58. SPIE Press
8. Yan Y, Jin G, Yang H (2007) Design and analysis of large spaceborne light-weighted primary mirror and its support system. In: 3rd International symposium on advanced optical manufacturing and testing technologies: large mirrors and telescopes, vol 6721. International Society for Optics and Photonics, p 67210V
9. Daly JG, Daly DJ (2001) Structural adhesives for bonding optics to metals: a study of optomechanical stability. In: Optomechanical design and engineering 2001, vol 4444. International Society for Optics and Photonics, pp 177–185

Absolute Radiometric Calibration of VNIR Hyperspectral Imaging Payload



Maneesh Pawar, H. P. S. Panwar and A. K. Sahay

Abstract Presently, small satellites with hyperspectral imaging payloads have been used for target detection, environmental monitoring, and forest mapping. All these applications involve the same process of recording the spectra of target/object of interest over densely sampled contiguous spectrum, usually from 400 to 2500 nm. Once a target spectra is recorded, it is matched with reference spectra library for detection. The accuracy of spectra matching highly depends upon the accuracy of radiometric calibration of the hyperspectral imaging payload. This paper presents a study of three methods of absolute radiometric calibration used by various hyperspectral imaging systems in VNIR region, namely Hihara method, Mitsunaga method, and Xiujuan method. Out of the analyzed methods, Hihara method performs the best.

Keywords Hyperspectral imaging · Radiometric calibration · VNIR · Space-borne camera

1 Introduction

Accurate radiometric calibration is a basic characterization require for any quantitative application of hyperspectral imaging system. Radiometric calibration is a methodology that relates the value measured by an instrument, i.e., digital numbers (DN) with the absolute physical quantities such as spectral radiance. The model for this type of conversion is established with the help of auxiliary radiation sources with in-built calibrated CMOS detector. Photo-response of sensor is measured at varying levels of luminance by exposing the sensor to a radiation source. The radiance level of integrating sphere (radiation source) is varied with the help of calibrated halogen and tungsten lamps. The integrating sphere usually consists of multiple lamps which can be switched ON and OFF via software control to increase/decrease the radiance levels. The absolute levels of radiation are measured by in-built calibrated CMOS

M. Pawar (✉) · H. P. S. Panwar · A. K. Sahay
Vision Instruments (Aero & Space Borne Systems) Division, Instruments Research and Development Establishment, 248008 Dehradun, India
e-mail: maneesh.pawar@irde.drdo.in

© Springer Nature Singapore Pte Ltd. 2020
PSR. S. Sastry et al. (eds.), *Advances in Small Satellite Technologies*,
Lecture Notes in Mechanical Engineering,
https://doi.org/10.1007/978-981-15-1724-2_20

detector. The recorded DNs and absolute radiance levels are fitted into a calibration model to generate coefficients for each detector in array. At the time of analysis, application these coefficients are used to convert the DNs to physical quantity.

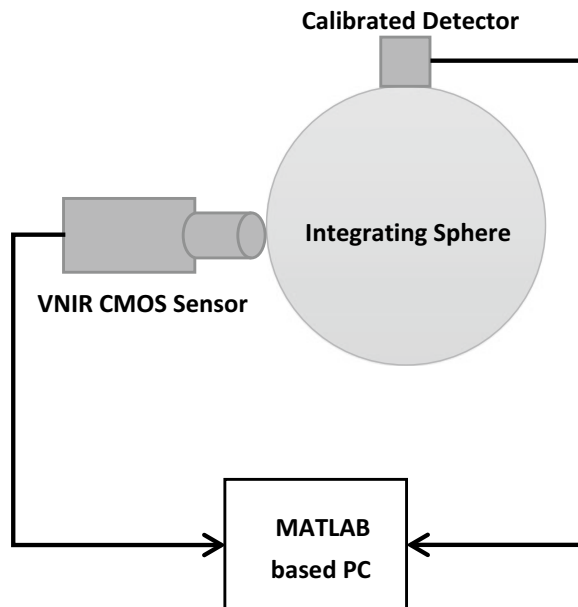
2 Methodology

Instead of relying on arbitrary simulated data, a high-speed CMOS image sensor has been interfaced with FPGA-based electronics to grab the DNs for each exposure for various radiance levels. Figure 1 shows the set up for calibration. The VNIR CMOS sensor along with optical assembly is mounted at exit pupil of integrating sphere. With the grabbed data from VNIR sensor at different radiance levels, the proposed work compares three popular radiometric calibration methods used in various satellite-based EO payloads.

1. Xiujuan method [1]: This method assumes the photo-response to be linear. Based on a gain and offset, the DNs are matched with the radiance recorded from in-built CMOS sensor. The pupil radiance, $L(\lambda)$ received by the imaging system is related to DN by a linear equation as shown in Fig. 4 as:

$$L(\lambda)_{ij} = a_{0ij} + a_{1ij}DN_{ij} \quad (1)$$

Fig. 1 Radiometric calibration set up



a_0 and a_1 are radiation calibration coefficient, that are eventually determined by calibration for each detector element. Using a least-square-fit method, a_0 and a_1 can be determined from multiple observations recorded at various intensity levels by exposing the detector array to different intensity levels of integrating sphere.

2. Mitsunaga method [2]: This method assumes the photo-response of individual elements to be polynomial in nature; hence, a straightforward polynomial fit is used for radiometric calibration.

Figure 3 shows that each detectors photo-repose, $L(\lambda)$ received by the imaging system is related to DN as follows:

$$L(\lambda)_{ij} = a_{3ij} + b_{3ij}DN_{ij} + c_{3ij}DN_{ij}^2 \tag{2}$$

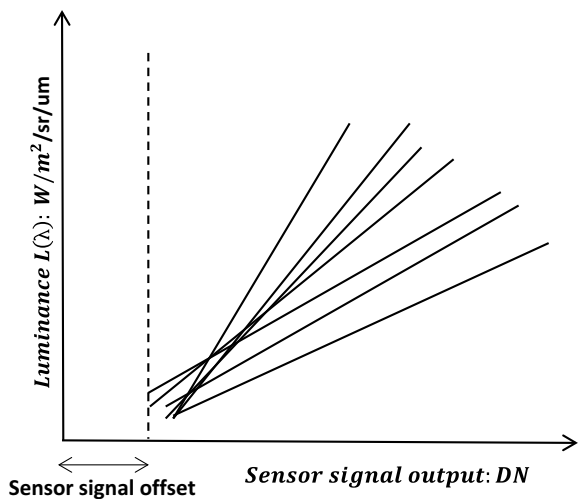
3. Hihara method [3]: This method uses the methodology of evaluating the characteristics of elements of CMOS sensor by production test. The characteristics of individual elements are segregated into few classes of responses.

Each element is assigned a class based on its photo-response. Based on the class model, the detector elements are calibrated. Figure 2 shows the segregation of detector elements via a production test. Class-I represents detectors with linear response, Class-II and Class-III represent detector elements with quadratic photo-response. Figure 2 shows that the pupil radiance, $L(\lambda)$ received by the imaging system for each class is related to DN as follows:

$$\text{Class - I: } L(\lambda)_{ij} = a_{1ij} + b_{1ij}DN_{ij} \tag{3}$$

$$\text{Class - II: } L(\lambda)_{ij} = a_{2ij}(DN_{ij} - c_{2ij})^2 + b_{2ij}(DN_{ij} - c_{2ij})^2 \tag{4}$$

Fig. 2 Xiujuan method assumption for photo-response



Class - III: Class - II: $L(\lambda)_{ij} = a_{3ij}(DN_{ij} - c_{3ij})^2 + b_{3ij}(DN_{ij} - c_{3ij})^2$ (5)

The calibration coefficients $a_1, b_1, a_2, b_2, c_2, a_3, b_3, c_3$ are determined by statistical investigation of luminance responses of corresponding class of detectors at various exposure levels of integrating sphere (Figs. 3 and 4; Table 1).

Fig. 3 Mitsunaga method assumption for photo-response

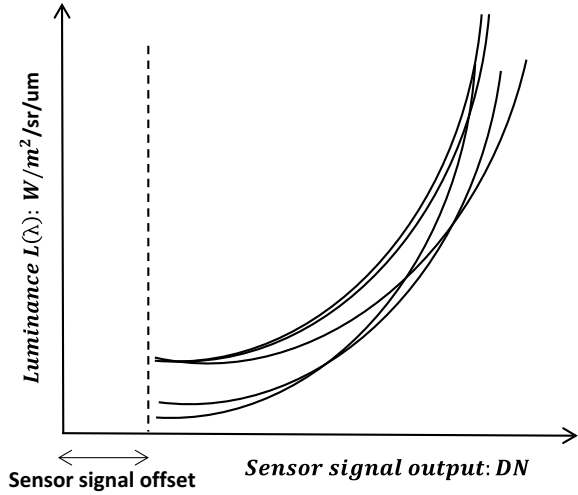


Fig. 4 Hihara calibration classification method

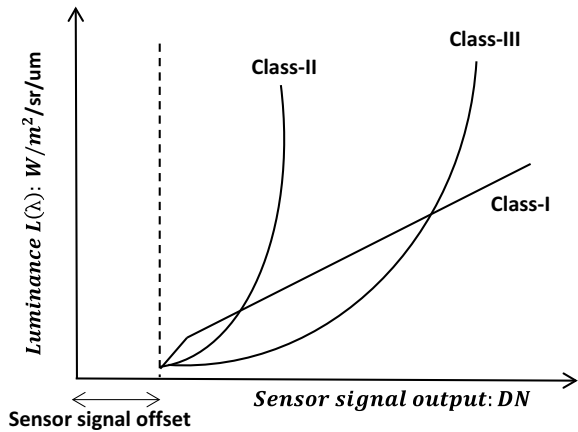


Table 1 Standard deviation of compared methods

Method	Standard deviation (%)
Xiujuan	20
Mitsunaga	13
Hihara	6

3 Results and Discussion

The VNIR CMOS sensor is interfaced with the PC via camlink interface for high-speed frame transfer. The calibrated detector is interfaced via USB interface; this common interface also controls the radiance levels of the integrated sphere through proprietary software. The MATLAB-based software captures the image frames at various luminance levels at 10-bit quantization. The MATLAB-based software also captures the actual luminance level at every luminance level from in-built calibrated detector. This captured data is used to fit explained calibration models.

In this paper, the standard deviation metric has been used for comparing the results of implemented methods. Hihara method with lowest variance outperforms all other methods. Xiujuan and Mitsunaga methods model each detector element with same photo-response model that is infact not true. Due to limitations of fabrication process of detectors on focal plane array, the photo-response of detector to detector varies. The Hihara method takes care of this variation by segregating detectors into different classes during a production test.

References

1. YU X, Sun Y, Fang A, Qi W (2014) Laboratory spectral calibration and radiometric calibration of hyper-spectral imaging spectrometer. In: 2nd International conference on systems and informatics (ICSAI)
2. Mitsunaga T, Nayar SK (1999) Radiometric self-calibration. In: Proceedings of CVPR
3. Hihara H, Moritani K, Inoue M, Hoshi Y, Iwasaki A, Takada J, Inada H, Suzuki M, Seki T, Ichikawa S, Tanii J (2015) Onboard Image Processing System for Hyperspectral Sensor. Sensors

Design of Primary Mirror Mount for Spaceborne EO Payload



Shekhar Tomar and Bharat Ram Meena

Abstract The paper is aimed at obtaining the optimum mount configuration for a Zerodur primary mirror for a Cassegrain spaceborne electro-optical payload. A bipod flexure design procedure is presented while taking various optomechanical design principles into account. Finite element model of the flexure is established in ANSYS APDL to analyse the design w.r.t optical and mechanical design parameters. In the design process of the mounts, thickness of the flexure notches; angle between the bipods; and height of the mounts are optimized for the best optical performance.

Keywords Mirror fixing device · Electro-optical surface figure · Zernike coefficients · Thermal stress

1 Introduction

There are several optomechanical design and performance requirements for the primary mirror of a Cassegrainian telescope system in space applications. The primary mirror is the light collecting element of the camera; so generally, it is the largest and heaviest optical element in the camera. Primary mirror is prone to stresses from the assembly errors, static loads induced due to gravity and thermal stresses induced due to differential heating [1]. So, there is a requirement to design mountings in such a way that all the design constraints are fulfilled, and the desired optical performance is achieved (Fig. 1).

A flexure is designed as an elastic element providing controlled motion. It has a small volume, no mechanical friction, no empty return and high move sensitivity [2, 3]. Through preferential trade-off between flexibility and stiffness, flexure mounts provide an accurate and stable method of mounting for large mirrors solving the problem of poor surface figure resulting from assembly errors, constraint and thermal stresses.

S. Tomar (✉) · B. R. Meena

Vision Instruments (Aero & Space Borne Systems) Division, Instruments Research and Development Establishment, 248008 Dehradun, India
e-mail: shekhartomar9@irde.drdo.in

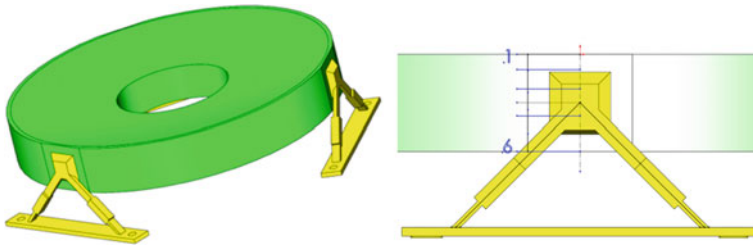


Fig. 1 Primary mirror mounted using bipod flexure

Reducing the stiffness to gain the compliance not only isolates vibrations, but also isolates a majority of mounting stress; more important is that when the environment temperature changes, the deformation of flexure could bridge the coefficient of thermal expansion (CTE) gap between the mirror material and the underlying supporting structure [4]. Flexure mounts generally provide flexibility in the radial direction while providing pseudo-kinematics support, both of which significantly aid in minimizing the stresses and strains in the mirror due to gravitational and thermal vibrations.

2 Design Requirements

While designing the mirror mounts certain design philosophy is followed. The fundamental requirement of a mount is to firmly hold the mirror. To hold it, all six degrees of freedom have to be constrained. While constraining the degrees of freedom, care has to be taken that the mounts are not over constraining the mirror. Over constraining leads to assembly stresses and moments in the mirror which severely deteriorate the surface figure.

Large size mirrors are prone to damage at the time of launching. The shock loads at the time of launching could go up to 30 g, so at such high loads, large mirrors made of highly brittle materials such as fused silica or Zerodur may get damaged. So, the mount designs should be such that the mirrors are isolated from launch loads. The system operating and survival requirements are listed in Table 1.

Table 1 Environmental specifications for SWIR camera

Description	Requirement
Launch load (survival)	30 g
Fundamental mode	100 Hz
Operational surface figure	$\lambda/10$ ($\lambda = 632.8$ nm)
Operational temperature range	10–30 °C
Survival temperature range	–10 to 50 °C

Spaceborne systems have to work in a broad temperature range depending on the orientation of the satellite with respect to the sun. The gap in CTE between mirror material and mount material will result in thermal stresses on the mirror. These stresses could produce significant amount of strains to deform the surface figure which ultimately leads to reduced performance of the system. So, the material selection should be done in such a way that the CTE of the mating components is as close as possible.

3 Design Configuration

This paper is aimed at the design and analysis of bipod flexure mounting for the primary mirror of a space Cassegrainian telescope. Optical systems require support structures that isolate the optical parts from mechanical loads. The mirror considered for the study is Zerodur aspheric mirror with a diameter of 160 mm and weight 1.2 kg.

The mount chosen for holding the primary mirror is a bipod flexure type. Three such mounts are symmetrically used to hold the mirror. Space grade adhesives are used to mount the mirror with flexures. Each flexure is stiff in axial and tangential directions and compliant in radial direction. This radial compliance isolates the mirror from assembly and thermal-induced stresses. The design configuration of the flexure is shown in Fig. 2.

The selection of material for the mirror mounts is very critical. The first criterion for selecting the material is matched coefficients of thermal expansion. Invar-36 is the material with CTE very close to Zerodur, so it is chosen as the material for mirror mount. The properties of the materials used are listed in Table 2.

The design principles used in choosing the bipod flexures are that they are frictionless, kinematically constrained and have matched coefficient of thermal expansion [2]. Joints based on friction are prone to loosening due to vibrations and shocks at the time of launch. Friction-based mounts are difficult to analyse and inherently less stable than frictionless mounts [2].

The flexures are used to provide moment isolation for the mirror to minimize surface figure distortion resulting from mount assembly error or distortion of the mount due to temperature change. The optical performance of the mirror highly depends on the design of the bipod flexure mount.

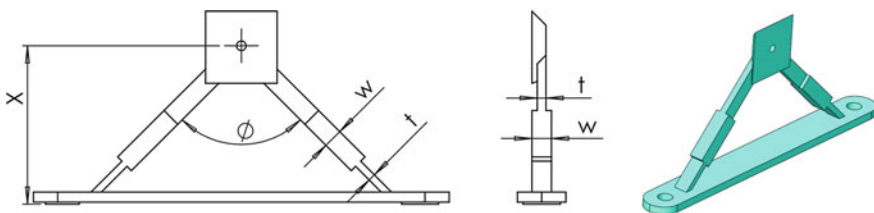


Fig. 2 Configuration of MFD

Table 2 Mechanical properties of optomechanical materials [5]

Material	Density, ρ (kg/m ³)	Young's modulus, E (GPa)	Thermal expansion, α (10 ⁻⁶ /K)	Specific stiffness, E/ρ (GPa m ³ /kg)
Zerodur	2530	92	-0.09	36.4
Titanium	4428	104	9.0	
Invar 36	8050	141	1	10.4

Finite element model approach is used to optimize the size and thickness of the flexure using ANSYS APDL. While optimizing the flexure notch thickness, the design variables considered are static displacement, surface figure and fundamental mode of vibration. The flexure geometry is optimized so that it would have just enough margins to survive launch loads and minimize the amount of stress that could be transmitted to optics while maintaining its integrity.

The minimum surface distortions occur in the mirror when the line of action of the flexure is passed through the mirror's centre of gravity. Before finalizing the design, many iterations are carried to optimize all the design variables.

4 Finite Element Modelling

Using the finite element analysis (FEA) method, the notch thickness (t), notch width (w), vertex angle (ϕ) and height (x) of the bipod flexure were optimized such that mirror surface figure distortions are minimum, and fundamental modal frequency is highest. Commercial FEA tool is used to model the mirror assembly. Flexure mounts and mirror are meshed as 3-D beam elements. Base of the flexures is fixed, and a load of 1 g is applied to the entire body. Meshed model, deflection, and stress plots of the mirror-flexure assembly are shown in Fig. 3.

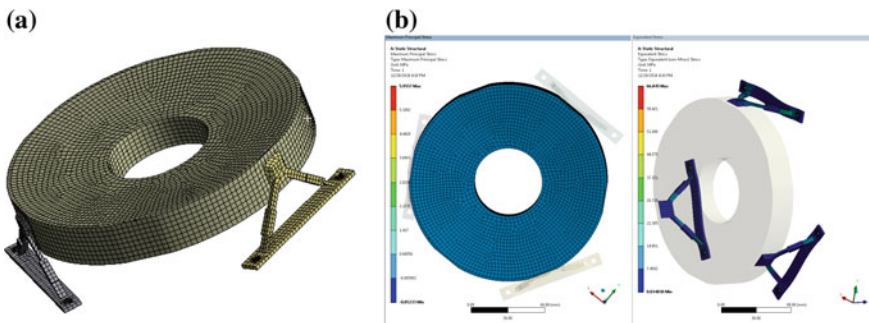


Fig. 3 a Meshed model of the flexure with mirror, b stress and deformation plots of flexure

To achieve the optimum design, iterations are done by varying the parameters and checking their effect on the components of the surface figure. The major components of the aberration or surface figure which are important from optical performance point of view are astigmatism, tilt, coma and trefoil.

In the first study, the arm angle (ϕ) is varied and surface figure data is extracted. Using a MATLAB code, the extracted data is processed to break it into various components of the surface. In a similar way, notch thickness, width and height of the flexure are varied to get the best results. Plots in Figs. 4, 5 and 6 show the variation of these components w.r.t to design parameters.

The results demonstrate that the bipod flexures could maintain the precision of the mirror surface figure under a load of external force and thermal constraints and also could keep the stability of the structure.

Based on the results from FE analysis plotted in Figs. 4, 5 and 6, optimum design parameters are chosen such that minimum surface distortion occurs.

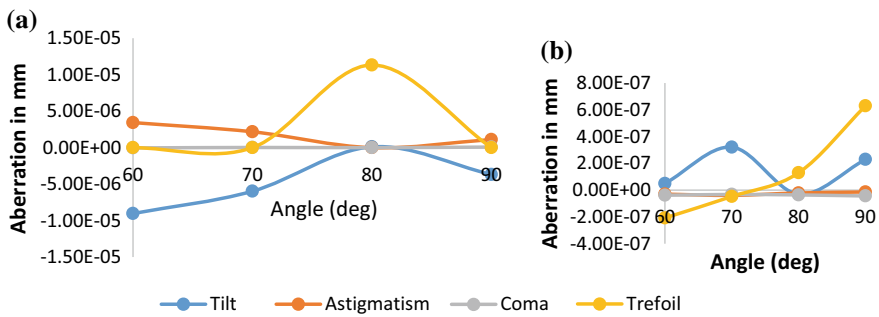


Fig. 4 Variation of surface figure with arm angle a at 1 g, b at $\Delta T = 10\text{ }^\circ\text{C}$

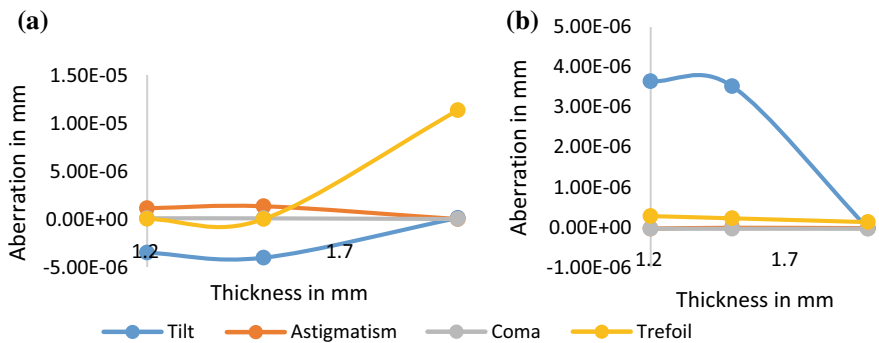


Fig. 5 Variation of surface figure with notch thickness (t) a at 1 g, b at $\Delta T = 10\text{ }^\circ\text{C}$

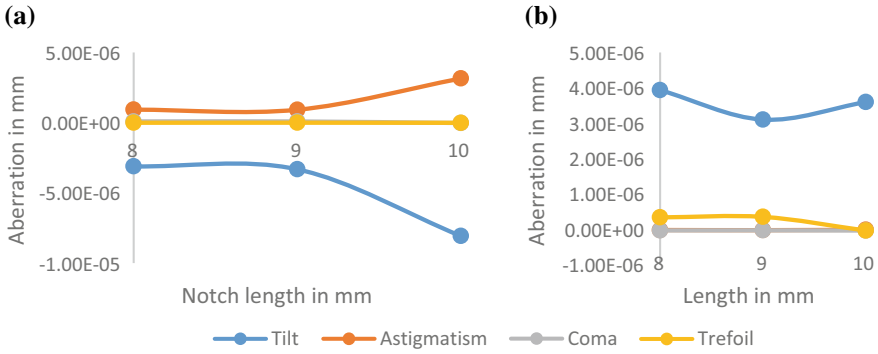


Fig. 6 Variation of surface figure with flexure height (l) **a** at 1 g, **b** at $\Delta T = 10^\circ\text{C}$

5 Results and Discussion

This paper presents the design criterion, and optimization procedure of the bipod flexure of mirror is used in a Cassegrainian space telescope. Design and optimization results demonstrate that the bipod flexures could keep the precision of the mirror surface figure under a load of external force and thermal constraints, and meanwhile, they could keep the stability of the structure. The optimum flexure mount with the least-induced surface figure parameters such as astigmatism, coma, tilt and trefoil has been identified.

References

1. Kihm H, Yang H-S, Rhee H-G, Lee Y-W (2015) Development of 1-m primary mirror for a spaceborne camera. In: Optomechanical Engineering 2015, vol 9573. International Society for Optics and Photonics, p 95730W
2. Weingrod I et al (2013) Design of bipod flexure mounts for the IRIS spectrometer. In: Optomechanical engineering 2013, vol 8836. International Society for Optics and Photonics
3. Vukobratovich D, Coronato P (2015) Unit moment analysis as a guide to mirror mount design. In: Optomechanical engineering 2015, vol 9573. International Society for Optics and Photonics, p 95730R
4. Chu C et al (2011) Design of bipod flexures for space mirror. In: International symposium on photoelectronic detection and imaging 2011: space exploration technologies and applications, vol 8196. International Society for Optics and Photonics
5. Kihm H, Presenter H-SY, Moon I-K, Lee Y-W. Adjustable bipod flexures for mounting mirrors in a satellite telescope
6. Doyle KB, Genberg VL, Michels GJ (2002) Integrated optomechanical analysis, vol 58. SPIE Press
7. Chan CY et al (2013) Design and analysis of isostatic mounts on a spaceborne lightweight primary mirror. In: Optomechanical Engineering 2013, vol 8836. International Society for Optics and Photonics

8. Daly JG, Daly DJ (2001) Structural adhesives for bonding optics to metals: a study of optomechanical stability. In: *Optomechanical design and engineering 2001*, vol 4444. International Society for Optics and Photonics, pp 177–185

Weight Optimization of Primary Mirror Used in EO Payload for Small Satellite



Shekhar Tomar and Bharat Ram Meena

Abstract This paper talks about the weight optimization scheme of the primary mirror of a space telescope. Comparative study of three lightweight structural schemes (hexagonal, triangular and square) for the primary mirror is done. For the study, finite element modelling method is used using as tool. While comparing the weight reduction, the comparison between the three schemes is carried out based on static deflection, surface figure of the mirror and fundamental modal frequency.

Keywords Bipod flexure mount · Zernike coefficient · Astigmatism · Cassegrainian telescope

1 Introduction

Astronomy and earth observation both require a larger optical collecting area to meet the higher-resolution requirements. At the same time, they need a low-weight mirror which can sustain inertial loads during launch and perform efficiently under zero gravity in space [1]. In Cassegrainian scheme of optical design, the primary mirror accounts for more than 90% of the total weight of the optics. To support such heavy mirror, the mechanical structure must also be strong enough to sustain the severe launch environment which results in increased overall payload weight. Heavy payload requires high launch capability vehicles which escalate the entire mission cost [2].

The mirror presented in this paper is Zerodur mirror with diameter 340 mm and clear aperture 332 mm. It is the most important component of the imaging telescope as the deformation in primary mirror surface figure affects the overall image quality of the system. The mirror weighs 7.9 kg. Such heavy mirrors have high static deflection which deteriorates the surface figure and optical alignment.

S. Tomar (✉) · B. R. Meena

Vision Instruments (Aero & Space Borne Systems) Division, Instruments Research and Development Establishment, 248008 Dehradun, India
e-mail: shekhartomar9@irde.drdo.in

© Springer Nature Singapore Pte Ltd. 2020
PSR. S. Sastry et al. (eds.), *Advances in Small Satellite Technologies*,
Lecture Notes in Mechanical Engineering,
https://doi.org/10.1007/978-981-15-1724-2_22

215

This paper describes the effective weight optimization scheme of the primary mirror while maintains the opto-mechanical design requirements [1]. Three weight reduction schemes have been studied, and comparison has been done using the finite element analysis method to achieve optimum solution.

2 Research Methodology

The primary mirror considered in the study is made of Zerodur having an outer diameter of 340 mm and with a hole of 80 mm diameter in the centre. A lightweight design with a ratio of approximately 70% is considered. The mirror is bonded with coefficient of thermal expansion (CTE) compatible material (Invar 36) flexure mount at three points on the periphery.

Weight reduction is done by scooping the material from the back side in three different shapes (triangular, square and hexagonal). Different weight reduction schemes are shown in Fig. 1. After removing the material from the back side of the mirror, the surface figure criterion $PV \leq \lambda/10$, $RMS \leq \lambda/50$ must meet.

Weight reduction from the mirror is done in such a way that the diameter of the inscribed circle made inside the triangular, square and hexagonal geometries is same as shown in Fig. 1. Other geometric parameters such as depth of cut and lightweight ratio are also kept same.

Using the finite element method, the design parameters such as astigmatism, static deflection due to gravity and fundamental modal frequency were compared. To analyse the deformations in surface figure, a MATLAB code was used to find out the Zernike coefficients. Structural strength and dynamic stiffness of the mirror subsystem in the thermal–structural coupling state were also analysed with the finite element method.

Some structure parameters having significant effects on the mechanical properties and mass of the mirror, such as the lightweight structure forms, thickness of the mirror, thickness of the rib, were used as design variables. The different lightweight

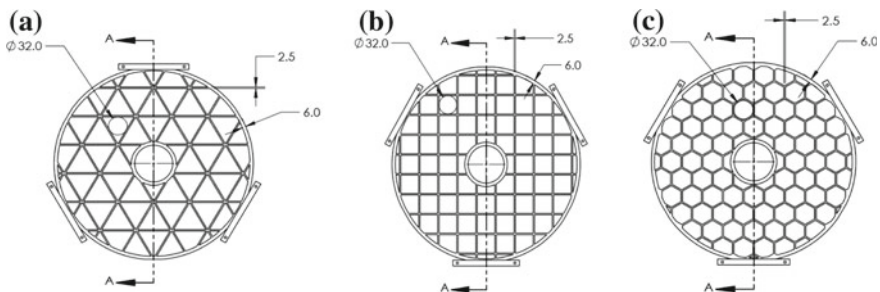


Fig. 1 Three different schemes of weight reduction: **a** triangular, **b** square, **c** hexagonal

structure the mirror takes, the lightweight ratio, the maximum deformation of the mirror suffered 1 g gravitational and their natural frequencies will vary too.

3 Results and Discussion

Finite element model of the mirror is established using commercial analysis tool. For the study purpose, three different geometries were generated using Solidworks modelling software. For the sake of objective comparison, mirror design parameters such as skin thickness, rim thickness, inner rim diameter and rib thickness are kept same for all three schemes.

Both mirror and its mount flexures are meshed using 3D solid elements. The interaction between flexure and mirror is taken as rigid connection. The six mounting holes of the flexure are fixed, and load of 1 g is applied to entire model. The load is applied in all three mutually perpendicular directions. Meshed geometry and stress plot of the mirror are shown in Fig. 2.

Other than the gravitational load, one iteration for all the design configurations is done with thermal load of 20 ± 10 °C. When the thermal load is applied, gravitational load is removed. Same surface figure parameters were recorded in this condition also.

Deformation plots under different loading conditions are shown in Fig. 3. Surface figure data in the form of PV and RMS are executed. The result of the analysis for three design configurations is summarized in Tables 1, 2, 3, 4 and 5. Using the MATLAB code, PV and RMS data are processed to get astigmatism value.

λ is the wavelength of the laser source (HeNe) used for the measurement of the surface figure. Its value is 632.8 nm.

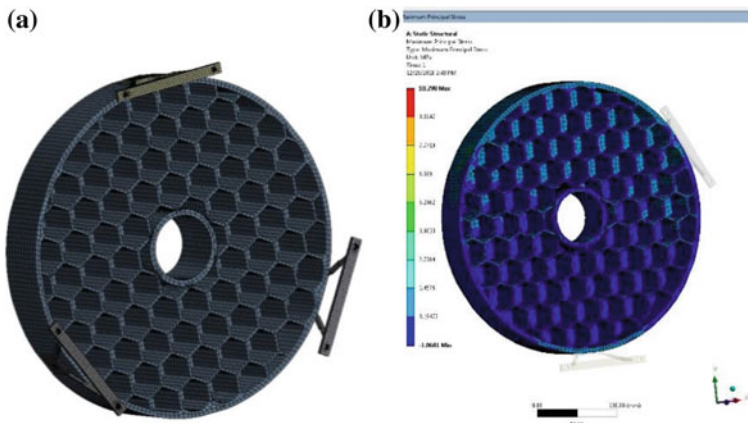


Fig. 2 a Meshed geometry of the mirror assembly, b stress plot at 1 g

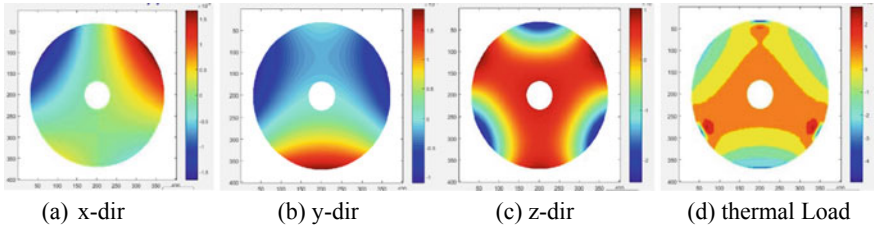


Fig. 3 Surface figure plot obtained from data processing in MATLAB

Table 1 Surface figure values for triangular pattern

Load direction	PV	RMS
X	0.16λ	0.03λ
Y	0.14λ	0.027λ
Z	0.4λ	0.08λ
Thermal	0.13λ	0.01λ

Table 2 Surface figure values for square pattern

Load direction	PV	RMS
X	0.73λ	0.13λ
Y	0.06λ	0.09λ
Z	0.4λ	0.09λ
Thermal	0.1λ	0.01λ

Table 3 Surface figure values for hexagonal pattern

Load direction	PV	RMS
X	0.09λ	0.13λ
Y	0.09λ	0.09λ
Z	0.11λ	0.09λ
Thermal	0.01λ	0.01λ

Table 4 Value of astigmatism surface figure values for three patterns

Load direction	Triangular	Square	Hexagonal
X	0.062λ	0.3λ	0.2λ
Y	0.001λ	0.001λ	0.001λ
Z	0.001λ	0.001λ	0.001λ
Thermal	0.001λ	0.001λ	0.001λ

Table 5 Surface figure values for hexagonal pattern

Parameter	Triangular	Square	Hexagonal
Lightweight ratio (%)	70	70	70
Natural frequency (Hz)	455.82	446.73	443.77
Maximum stress (MPa)	9.53	10.33	12.0

PV and RMS values obtained from the FE analysis are processed using a MATLAB code to get the astigmatism values. These values are listed in Table 4 for three different patterns for comparative study.

Dynamic response of the mirror was also analysed for three patterns. The maximum stress at 1 g load and fundamental natural frequency are listed in Table 5. The lightweight ratio kept is 70% for all three patterns.

4 Conclusion

The reflecting surface puts lot of constraints while optimizing the weight of the mirror. So, while choosing the weight reduction scheme, a thorough analysis must be done at the design stage. Using the finite element analysis, different schemes are compared and best schemes from an optical performance point of view are chosen. The analysis shows that the optical surface distortion (PV and RMS) is minimum in hexagonal weight reduction scheme. For all three schemes, static and dynamic structural requirements are same.

References

1. Yan Y, Jin G, Yang H (2007) Design and analysis of large spaceborne light-weighted primary mirror and its support system. In: 3rd International symposium on advanced optical manufacturing and testing technologies: large mirrors and telescopes, vol 6721. International Society for Optics and Photonics, p 67210V
2. Li Y (2012) Modeling and structural analysis of honeycomb structure mirror. In: Modern Technologies in Space-and Ground-based Telescopes and Instrumentation II, vol 8450. International Society for Optics and Photonics, p 84504K
3. Park K-S, Lee JH, Youn S-K (2005) Lightweight mirror design method using topology optimization. *Opt Eng* 44(5):053002
4. Doyle KB, Genberg VL, Michels GJ (2002) Integrated optomechanical analysis. vol 58. SPIE Press
5. Chan CY et al (2013) Design and analysis of isostatic mounts on a spaceborne lightweight primary mirror. In: Optomechanical engineering 2013, vol 8836. International Society for Optics and Photonics
6. Chu C et al (2011) Design of bipod flexures for space mirror. In: International symposium on photoelectronic detection and imaging 2011: space exploration technologies and applications, vol 8196. International Society for Optics and Photonics

Real-Time Embedded Software for Stabilized Electro-Optical System



Ram Saran, Shashi Singh, Avnish Kumar and Rajeev Marathe

Abstract Stabilized electro-optical system (SEOS) housed with electro-optical (EO) payloads is required for battlefield surveillance, positioning, pointing and tracking of ground, aerial and naval targets. SEOS are required for line-of-sight (LOS) stabilization by rejecting the host platform motion for accurate pointing and tracking. In such complex systems, the design of real-time embedded software becomes very challenging. Hard real-time implementation of stabilization and position and track control algorithms make it more critical. Interfacing and real-time handling of heterogeneous interfaces simultaneously and further make the embedded software complex. In this paper, we present an innovative real-time embedded software design and implementation for stabilized EO system.

1 Introduction

Electro-optical (EO) payloads: Typically, a day vision camera, infrared imaging (IR) camera and an eye-safe laser rangefinder (LRF) are required for battlefield surveillance, positioning, pointing, ranging and tracking of ground, aerial and naval targets. These EO payloads are installed on a 2- or 3-axis gimballed assembly [1] to get motion in yaw, pitch and roll axes. LOS of EO payloads gets highly disturbed when they are mounted and carried on a dynamic vehicle like a tank, UAV or fighter aircraft and/or when the target is in motion. In this situation, maintenance of LOS toward a dynamic target becomes highly complex. SEOS [2] is used to maintain the LOS by rejecting the host vehicle motion to get desired stabilization and tracking. An automatic video tracker (AVT) is also an important element of target engagement process. It is required for automatic detection, locking and tracking of targets. Man-machine Interface (MMI) [3] transmits the commands to the electronics unit through serial interface RS-232/Ethernet which transfers the commands to stabilized EO system (SEOS).

R. Saran (✉) · S. Singh · A. Kumar · R. Marathe
Instruments Research and Development Establishment (IRDE), DRDO, 248008 Dehradun, India
e-mail: ramsaran@irde.drdo.in

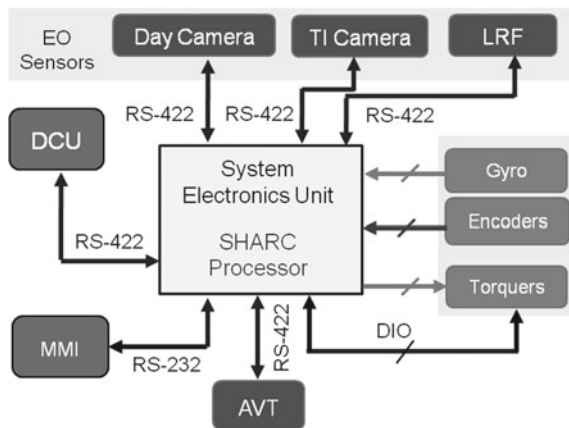
In such type of complex systems, the design of real-time embedded software [4] becomes very challenging. Hard real-time computing requirement of stabilization, position and track controller algorithms in $250 \mu\text{s}$ make it more critical. Interfacing and real-time simultaneous handling of command and control for multiple and heterogeneous interfaces like analog, discrete I/O, synchronous serial interface (SSI), RS-232, RS-422, RS-485 and Ethernet further make the embedded software design and implementation complex. The proposed real-time embedded software requirements and design for stabilized EO system are presented in Sect. 2. Result to demonstrate the real-time nature of embedded software is shown in Sect. 3. Finally, the paper is concluded in Sect. 4.

2 Embedded Software Requirements and Design

Real-time embedded software (RTES) is the main embedded application software for SEOS, specifically developed for analog devices' ADSP-213XX (SHARC) target hardware n'C' language. The target hardware and major interfaces, for which the RTES is developed, are also depicted in Fig. 1. The main design features of the RTES are as follows.

- Handling of Stabilized Gimbal Control
 - Reading servo sensors (2-axis gyro and encoders) at every $250 \mu\text{s}$ frame timer
 - Characterization of gimbal plant in 2-axis and 2-gimbal
 - Implementation of high-gain stabilization controller algorithm at 4 kHz ($250 \mu\text{s}$) frame timer
 - Implementation of position controller algorithm for quick positioning at 4 kHz ($250 \mu\text{s}$) frame timer

Fig. 1 Target hardware and interfaces of RTES



- Implementation of system modes of operation (STAB, POSITION, TRACK, SLAVE and STOW)
- Implementation of auto drift compensation algorithm
- High-speed data logging at 1 kHz, i.e., 1000 samples/sec (during testing and performance evaluation).
- Handling of EO sensors (day camera, TI and LRF) interfaces through RS-422 and RS-485 interfaces
- Handling of automatic video tracker (AVT) interface through RS-422 interface
- Handling of man-machine interface/display and control unit (DCU) through RS-232/RS-422 interfaces
- Handling of simulator (during testing and integration) through RS-232 interface.

Modes of operation of the system illustrate the overall operation of the embedded application software. In this document, modes are used to define a high-level operation of the RTES. The primary normal system mode operations of the RTES are defined below and shown in Fig. 2. The software flow diagram of RTES is shown in Fig. 3.

- Initialization (INIT)—system initialization
- Manual/Stab Mode (IND)—sight stabilized (and driven by joystick)
- Position Mode (SLAVE)—sight enslaves to the GS/launcher
- Stow Mode (STOW)—sight is positioned to a specified angle (AZ: 90°, EL: -20°)

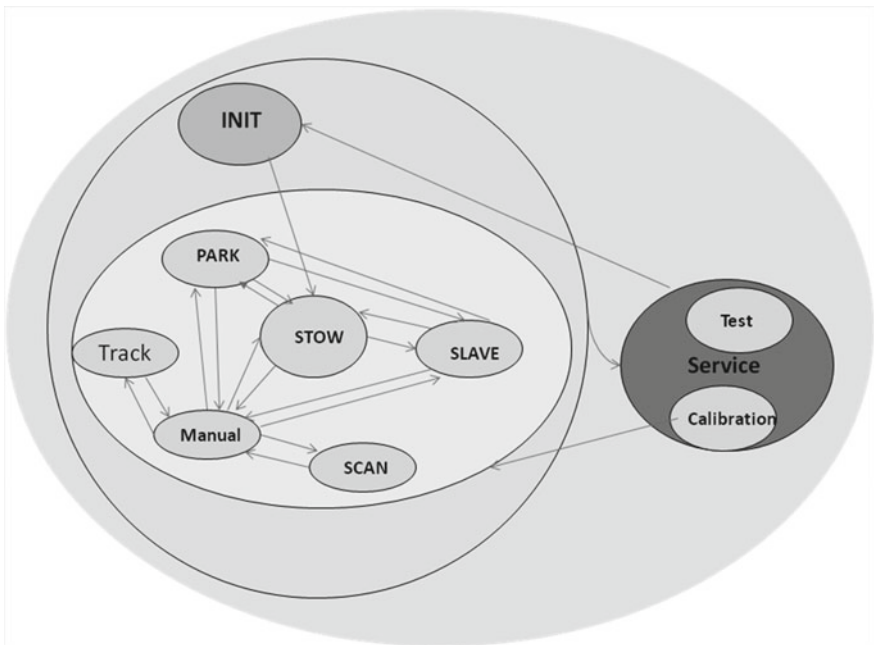


Fig. 2 State transition diagram for modes of operation of SEOS

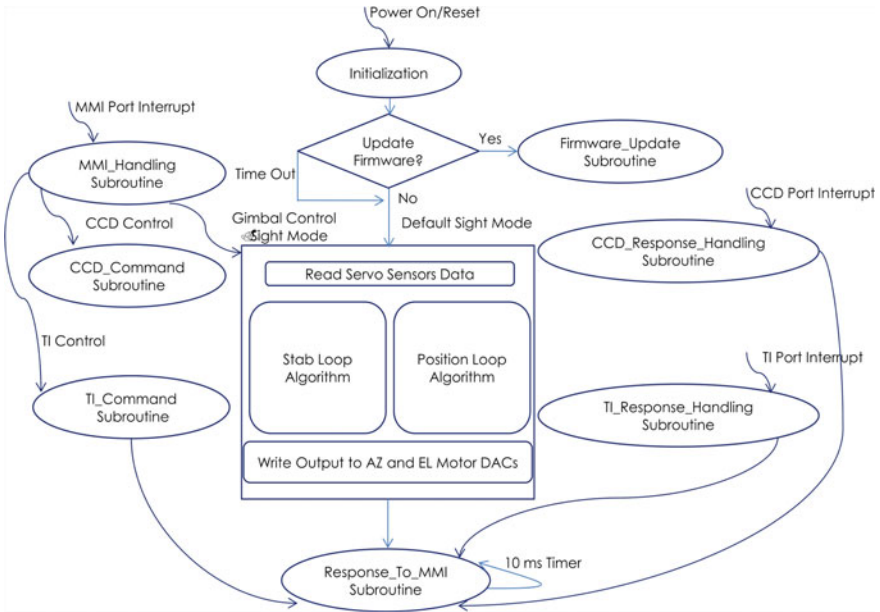


Fig. 3 RTES flow diagram

- Scan Mode (SCAN)—automatic scan in defined scan sector with defined scan rate
- Track Mode (TRACK)—automatic tracking of target (optional)
- Calibration Mode (CAL)—harmonization and drift calibration
- Test Mode (TEST)—maintenance of the EOSSS (BIT, firmware update, etc.).

3 Development of Man–Machine Interface (MMI) Software

Man–machine interface (MMI) has been developed using MATLAB GUIDE, MATLAB event-driven programming and MATLAB serial interface programming. The MMI is responsible for initiation of command to ESE for gimbal control and CCD camera and TI camera command and control. The main features of the EOSSS MMI are as follows.

- Selection of operation modes
- Control handle simulation
- LOS indicator
- Grouping of controls
- Monitoring of variables
- High-speed data logging

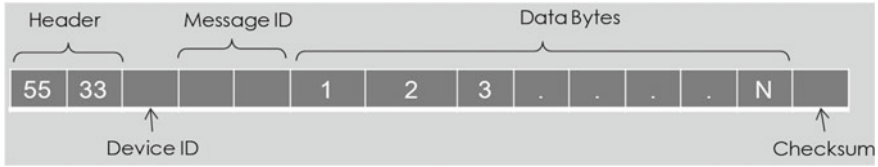


Fig. 4 MMI message format

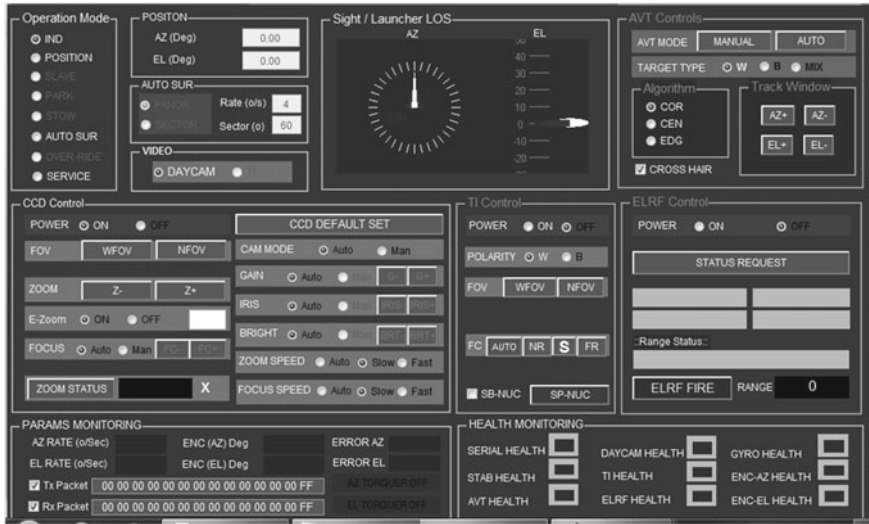


Fig. 5 Snapshot of MMI

- TX/RX packet monitoring

The message from MMI is fixed length of 14 bytes as given below. A snapshot of MMI software is shown in Figs. 4 and 5.

4 Results

Results demonstrate fulfillment of real-time execution requirement in addition to functional requirements. Figure 6 shows real-time completion of critical task of control algorithm in every 250 μ s.

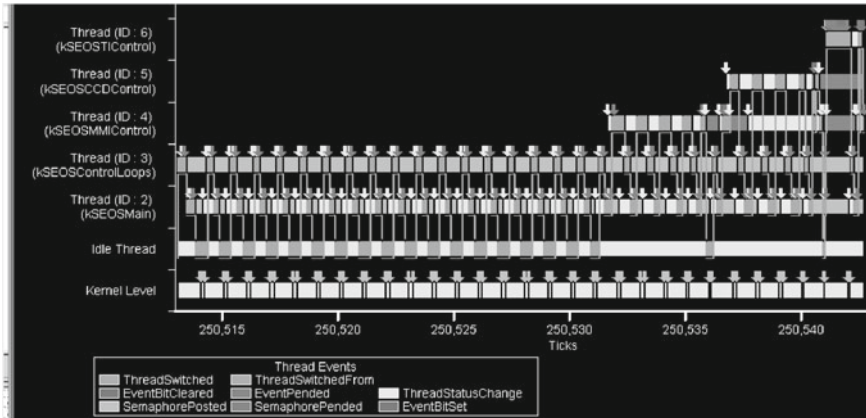


Fig. 6 Thread state showing the real-time execution of control loop within 250 μ s

5 Conclusion

Design and implementation of embedded software for SEOS is very challenging due to hard real-time constraint for control algorithms and real-time handling requirement of heterogeneous interfaces simultaneously.

References

1. Downey GA (2003) Electro-optical tracking considerations II. In: Proceedings of SPIE, acquisition, tracking, and pointing XVII, vol 5082. <https://doi.org/10.1117/12.487943>
2. Karr BA, Downey GA, Harris NA, (2018) Electro-optical tracking considerations III. In: Proceedings of SPIE, long-range imaging III, vol 10650. <https://doi.org/10.1117/12.2304796>
3. Saran R, Sharma S, Dhaka R, Kumar A (2014) Design of man-machine interface for stabilized electro-optical tracking system. MATLAB EXPO India 2014, Bangalore, India
4. Khamis A, Zydek D, Borowik G, Naidu DS (2013) Control system design based on modern embedded systems. In: International conference on computer aided systems theory—EUROCAST 2013. Springer lecture notes in computer science, vol 8112, pp 491–498

Development of THz Photometer for Solar Flare Observation from Nanosatellite Platform



S. P. Karanth, M. A. Sumesh, M. Dilip Yadav, H. R. N. Murthy, A. Edward Raj, S. Somashekar, S. Bhaskar Raju, K. V. Sriram and A. S. Laxmiprasad

Abstract Recent solar flare explorations reveal the presence of high-frequency components in sub-THz and THz regime, which are much more intense, compared to the RF counterpart, and understanding of origin is still ambiguous. Solar flare observations in THz region need to be carried out from space since the atmospheric attenuation hinders measurements from ground. Present paper discusses, in detail, the development of a photometer that operates in THz region from 0.1 to 7 THz in different spectral bands. Entire electro-opto-mechanical design was carried to meet the size, mass, and power constraints posed by inherent resource limitations of Nanosatellite platforms. A Cassegrain optical configuration was designed to collect the sun radiation with aperture effective area of 0.0027 m² with HDPE windows and resonant mesh filter for selective perception of THz radiation, rejecting the huge background of visible and NIR with a spectral selectivity of 10⁷:1. Sensitivity of the photometer was estimated to be 9 K/mV by calibration against the blackbody radiator. The minimum detectable temperature transient of the instrument is 30.6 SFU (1 SFU = 1 × 10⁻²² Wm⁻² Hz⁻¹).

Keywords Solar flare · Solar flux unit (SFU) · Sensitivity · Aperture efficiency · THz detector · Nanosatellite · Blackbody radiator · Mesh filter

1 Introduction

THz is a region of electromagnetic spectrum that lies between IR ($\lambda < 30 \mu$) and microwave ($\lambda > 3000 \mu$) which is significantly distinct in its spectral properties and interaction with mater. Salient characteristics of these radiations enable development of advanced instruments which can perform highly specific tasks, impossible with

S. P. Karanth · M. A. Sumesh (✉) · M. D. Yadav · H. R. N. Murthy · A. E. Raj · S. Somashekar · S. B. Raju · K. V. Sriram · A. S. Laxmiprasad
Laboratory for Electro-Optics Systems, Indian Space Research Organization,
Bengaluru 560058, India
e-mail: sumesh@leos.gov.in

© Springer Nature Singapore Pte Ltd. 2020
PSR. S. Sastry et al. (eds.), *Advances in Small Satellite Technologies*,
Lecture Notes in Mechanical Engineering,
https://doi.org/10.1007/978-981-15-1724-2_24

ordinary imaging and spectroscopic techniques. Ever since, the first infrared telescope devoted to space science was launched in 1996 that brought about stunning discoveries including the fact that 98% of the total photons constituting the galactic backgrounds are in FAR IR [1], and a remarkable boost was observed in the THz technology for space instrumentation. One of the most recent discoveries is that solar flares have a new spectral component in THz that peaks several orders of magnitude than the microwave and RF regions conventionally used for classifying solar hyperactivities [2]. Solar flares are intense burst of radiation due to explosive release of magnetic energy associated with sunspots. It is well known that the aftermath of solar flare is always harmful for mankind such as interruption of radio/wireless communication, malfunctioning of GPS, and disruption of power grid lines. In space sector, the hyperactivity in solar atmosphere leads to solar proton events leading to increased computational/memory errors in on-board processors, damage of space instruments, and health hazard to astronauts. An early warning could safeguard not only infrastructure and resources but also valuable lives, and the best way is to keep observing solar flares, since the geomagnetic storms trail solar flare by 3–5 days. This paper discusses the development of THz photometer for observation of solar flare from LEO orbit on a Nanosatellite.

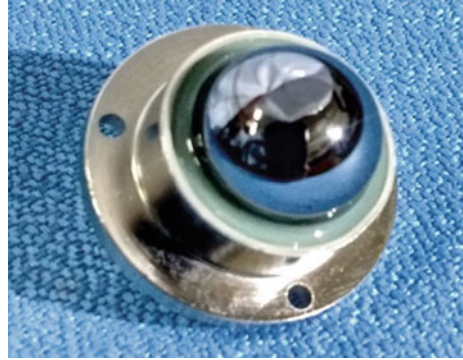
2 Mission Objective

Atmospheric attenuation hinders the solar burst observation from ground stations especially due to the water vapor absorption in the THz. Low-frequency observations in the atmospheric windows of 210 and 400 GHz are carried out by ground stations [3] in Argentina and Chile, where the precipitable water volume (PWV) is <0.28 mm. For observations in higher frequencies, one has to deploy the instruments in outer atmosphere, to overcome atmospheric attenuation. In this mission, it is planned to study the solar flare burst by deploying the THz photometer in low Earth orbit on a Nanosatellite Platform. The photometer shall observe solar burst in 7 THz with a bandwidth of ± 700 GHz. Two more ground-based identical photometers shall be tracking the sun in 634 GHz as well as 802 GHz coinciding with atmospheric windows. These ground photometers will be mounted on the Alt/Az stage of LEOS Astronomical Observatory. The data obtained from all these three photometers will be analyzed and cross-verified with the online space weather data in H- α and X-ray regimes.

3 THz Detector Development

LEOS has recently embarked upon developing THz detectors that can sense radiations with frequency from 0.1 GHz to 30 THz for space applications [4]. A hybrid detector concept was successfully implemented in which a quasi-optical element in

Fig. 1 Bolometric THz detector with HRFZ-Si hyper hemispherical lens



the form of a lithographic-printed microdipole antenna was integrated to the V_2O_5 sensing element at its feed that was optically immersed on to high-resistance float zone (HRFZ) silicon hyperhemispherical lens [5] (Fig. 1). V_2O_5 active element thermally isolated by Kapton render these devices extremely sensitive to IR radiation, while the microantenna harvests radiations with wavelength longer than that of IR, and net result is a hybrid device with broad spectral coverage ranging from longest edge of IR to shortest edge of microwave (from 30 THz down to 0.1 GHz) with a dynamic range of >32 dB throughout.

4 THz Instrument Development

Design activities pertaining to optical, mechanical, and electronic configuration within the payload as well as the space craft interface have been carried out in compliance with Nanosatellite platform resource constraints such as weight less than 5 kg, center of gravity (CG) within 50 mm away from the payload interface, and power maximum of 8 W. Within these constraints, crux of the problem is suppressing the visible and IR region of solar emission and selectively detecting the THz radiation, which turns out to be an extremely feeble signal (0.67 mW m^{-2} at 3 THz against 1378 Wm^{-2} of total sun radiation). The spectral irradiance of solar power at outer space is estimated using Planck's radiation law. The emission peaks at $\sim 500 \text{ nm}$, and the majority of radiation (99.5%) belong to shorter wavelength ($< 5 \mu\text{m}$). The spectral radiant emittance of the blackbody ($\text{Wm}^{-2} \text{sr}^{-1} \text{THz}^{-1}$) was estimated using Planck's radiation law:

$$L(f, T) = \frac{2hf^3}{c^2} \left(\frac{1}{e^{\left(\frac{hf}{k_B T}\right)} - 1} \right) \quad (1)$$

where h = Planck's constant, k_B = Boltzmann's constant, f = frequency in THz, T = temperature of blackbody, and c = speed of light in vacuum.

Radiant emittance $M(T)$ of the blackbody is the integral of $L(f, T)$ with respect to f and is now to be associated with the spectral transmittance characteristics of the THz window, $\eta(f)$

$$M(T) = \int_{f_1}^{f_2} \eta(f) \cdot \frac{2hf^3}{c^2} \left(\frac{1}{e^{\left(\frac{hf}{k_B T}\right)} - 1} \right) df \tag{2}$$

Power falling on the detector ϕ_{det} is estimated from the geometry as:

$$\phi_{det} = M(T) A_{bb} \Omega_{det,bb} \tag{3}$$

where A_{bb} = aperture area of blackbody and $\Omega_{det,bb}$ = solid angle subtended by detector on source. Also, from the graph, it is evident that the fraction of radiation in terahertz is extremely small compared to the emission in visible IR regime as shown in Fig. 2. In the case of 3 THz, this fraction turns out to be about 0.2 ppm which renders the measurement extremely difficult in the presence of continuum solar radiation. Suppressing the visible and IR regions of solar radiation and selectively detecting the THz radiation in the specified frequency band requires special filters with high spectral selectivity of the order 10 [6] in order to carry out a meaningful measurement of THz emission from the sun. This is especially true in the case of thermal detectors which have a wide range of spectral response (UV to THz). This spectral selectivity of 0.2 ppm was achieved by a novel technique of microroughening of reflective optical components [7], together with nickel mesh filter for selective transmission of THz radiation [6] and also the optical throughput of the combination. With this

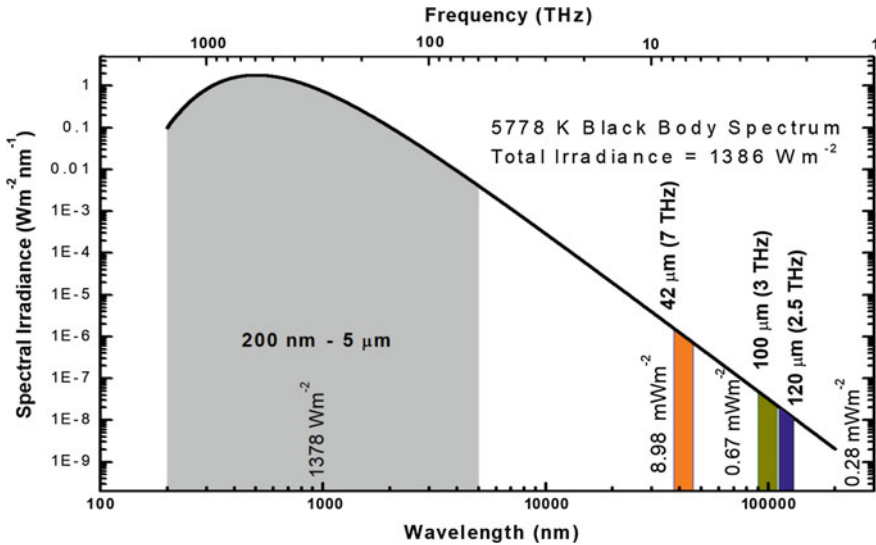
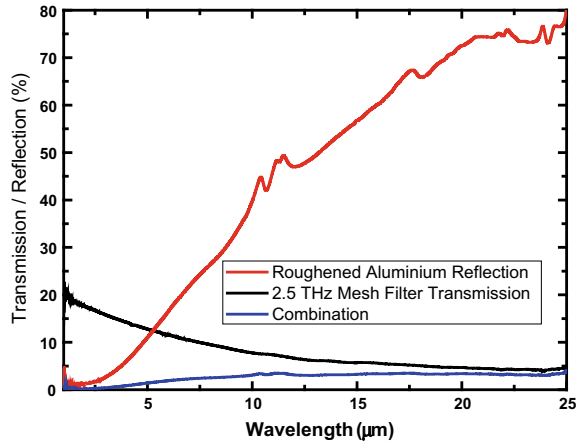


Fig. 2 Spectral emission in outer space at AM0 condition

Fig. 3 Reflection and transmittance characteristics of the roughened mirror and mesh filter, respectively



combination, the UV, visible, and NIR region is suppressed to $<1\%$ for $\lambda < 5 \mu\text{m}$ and $<0.5\%$ for $\lambda < 5 \mu\text{m}$ as shown in Fig. 3.

A prototype instrument was developed and demonstrated using a blackbody radiator as an artificial sun [8]. Reflective optical system based on Cassegrain configuration was chosen as the front-end optics, due to its compactness and convenience in integrating with detector system. Optical design was carried out comprising of primary concave mirror 75-mm-dia. secondary convex mirror of 20-m-dia., to achieve an IFOV of $\pm 1^\circ$, with a focal length of 100 mm and detector size of 2 mm. As per this design, metal mirrors were fabricated using aluminum and characterized for their focal length, field of view, and optical performance in conjunction with THz detectors. Since the payload has size, weight, and power constraints imposed by Nanosatellite requirements, a resonant fork optical modulator (CH-10 from EOPC, USA) was integrated with the optical assembly for performance evaluation. The chopper is tuned for jitter-free operation at 20 Hz (matched to peak performance frequency of detector) with stability better than 0.005%.

Solar spectral emission at THz region is extremely low compared to the continuum spectrum, and design of signal processing front-end electronics is highly challenging in terms of the dynamic range requirement. Only lock-in amplifier-based electronics can extract such deep-buried signals from noisy ambient. A very compact lock-in amplifier was designed and integrated to the sensor electronics, and dynamic range as high as 110 dB was achieved. A 16-bit Σ - Δ -based ADC with sampling rate of 800 Hz was used for converting the analog DC output of front-end signal processor for further processing by on-board intelligence (Atmega328P). An accurate (± 2 ppm) real-time clock (RTC) with built-in TCXO is used for time keeping and one-time synchronized to UT. An on-board memory of 4 GB (microSD card) is used for storing the payload data till it is transferred to spacecraft mother board as supplementary for 8 GB spacecraft memory. Block diagram of the instrument architecture is given in Fig. 4. The Bluetooth feature is not adopted for on-board usage, but it facilitates easy

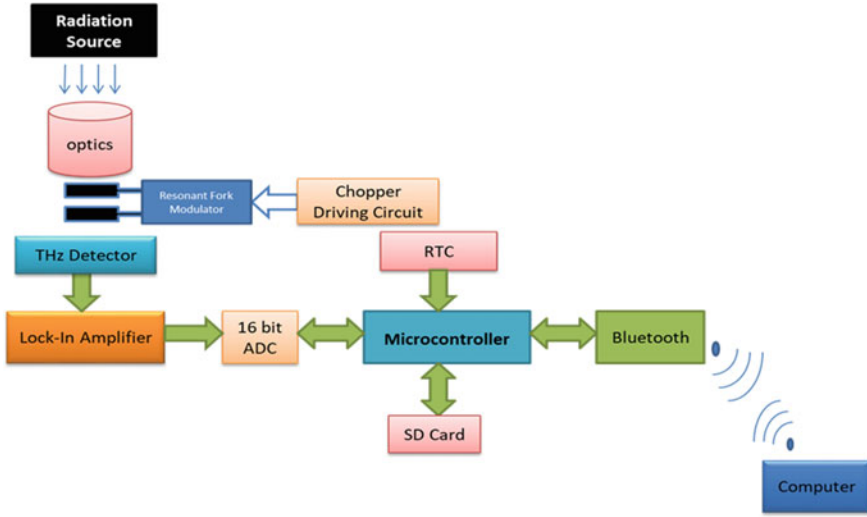
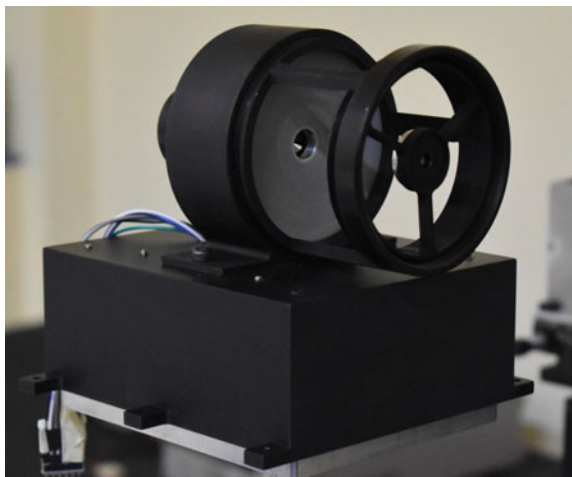


Fig. 4 Schematic block diagram of the photometer components

integration and testing at laboratory as well as field tests, doing away with hassles of harness.

The instrument features with Serial Peripheral Interface (SPI) bus for communication with the on-board processor of the Nanosatellite. A compact, stiff, and light-weight mechanical housing was designed and fabricated to accommodate all the subsystems of the entire instrument. The mechanical interface is chosen to match the +VE YAW panel of Nanosatellite pointing the optics toward -VE PITCH (sun pointing). Figure 5 shows photograph of THz photometer developed at LEOS.

Fig. 5 Photograph of THz photometer developed at LEOS for solar flare observation



5 Results

Instrument noise was critically observed for a long period of time. The source of noise includes, components from electronic noise, mechanical vibrations and jitter from chopper and detector noise. The total noise conforms to Gaussian nature of fluctuations with a standard deviation of $30 \mu\text{V}$ (RMS). Figure 6 shows snapshot of noise plot of THz photometer output.

Simulation of the instrument responding to solar burst was acquired using tungsten–halogen source (2800 k). The first-cut data while drift scanning the radiometer is shown in Fig. 7. A prototype model laboratory tests have been carried out using artificial sun to calibrate the THz photometer. Blackbody source was maintained at various temperatures for calibrating the developed THz photometer. The sensitivity of about 9 K/mV was observed which is as per the design and is on par with the literature reports [9] as shown in Fig. 8.

The conversion factor for the temperature variation is derived by calibrating the photometer in front of blackbody source as an artificial sun. Radiometric resolution of a photometer is given in Eq. 4 [9].

$$\Delta S = 2k_B\Delta T/A_e \quad (4)$$

where ΔT is the minimum resolvable excess temperature transient in THz spectrum, A_e is the aperture effective area, and k_B is Boltzmann constant. Noise measured from THz photometer is $30 \mu\text{V}$. The minimum resolvable excess temperature (ΔT) is 0.3 K . The aperture effective area is given in Eq. 5.

$$A_e = \eta_{\text{Transmission}} \times A_{\text{primaryoptics}} \quad (5)$$

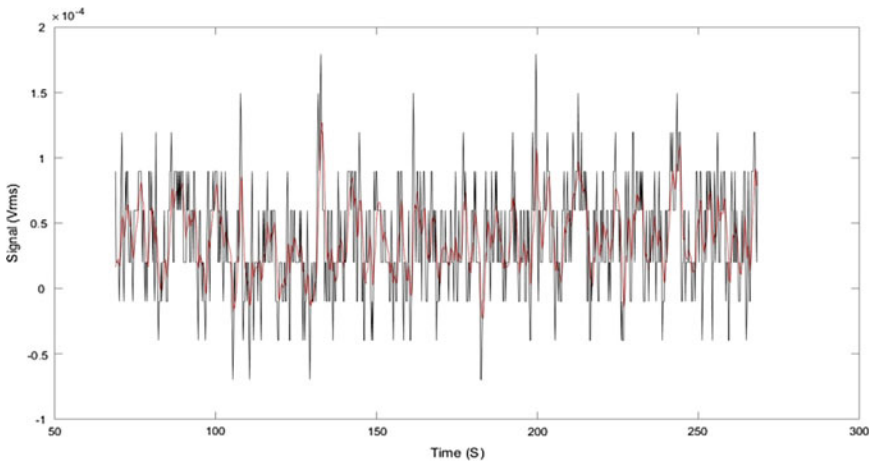


Fig. 6 Snapshot of noise plot of THz photometer

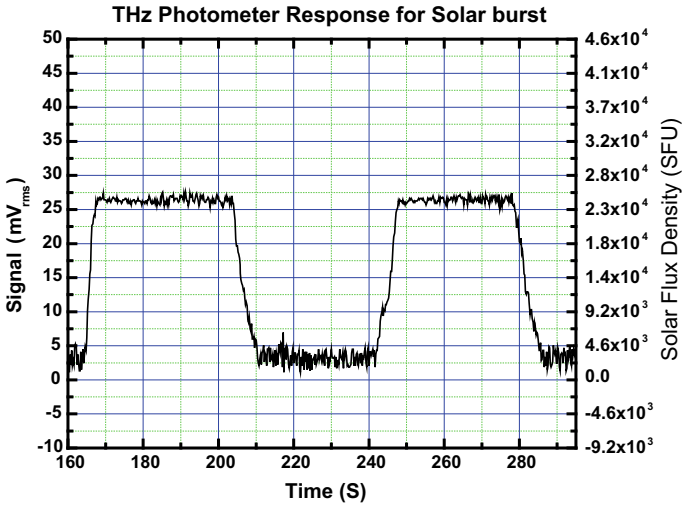


Fig. 7 Simulation of solar burst carried out by acquiring first-cut data in front of tungsten-halogen source (2800 k) while drift scanning the radiometer

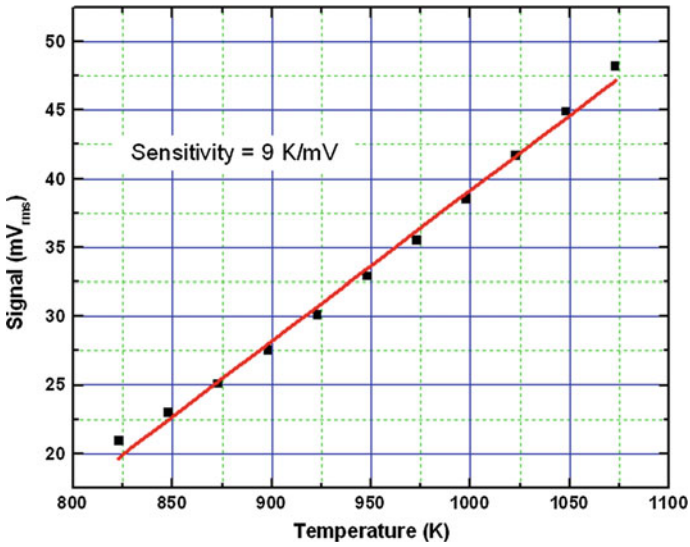


Fig. 8 Calibration of THz photometer with HDPE and mesh filter (2.5 THz) using blackbody radiation source

Table 1 Technical specifications of the developed THz photometer

S. No.	Parameter	Specification
1.	Operating frequency	7, 3, and 2.5 THz
2.	Bandwidth (FWHM)	$\pm 10\%$ of central frequency
3.	Resolution	30.6 SFU ($1-\sigma$)
4.	Field of view	$\pm 1^\circ$
5.	Optics configuration	Cassegrain
6.	Detector type	Uncooled THz detector
7.	Payload memory	4 GB (flash memory)
8.	Weight	1.5 kg
9.	Size	150 mm \times 150 mm \times 150 mm
10.	Power requirement	9–18 V DC
11.	Power consumption	4.5 W
12.	Communication	SPI
13.	Data update rate	10 samples per second
14.	Location of the instrument	+VE yaw panel
15.	Orientation	–VE pitch (sun pointing)

where $\eta_{\text{Transmission}}$ is aperture efficiency and $A_{\text{primaryoptics}}$ is the aperture physical area. Aperture physical area is 0.0044 m^{-2} , aperture efficiency is 60% by taking all layers into consideration, and aperture effective area is 0.0027 m^2 . The minimum detectable temperature transient of the instrument is 30.6 SFU ($1 \text{ SFU} = 1 \times 10^{-22} \text{ Wm}^{-2} \text{ Hz}^{-1}$). Simulation of the instrument responding to solar burst was acquired using tungsten–halogen source (2800 K). The first-cut data while drift scanning the radiometer is shown in Fig. 8. Field testing of the instrument is progressing in the LEOS Astronomical Observatory with the photometer mounted on the Alt/Az stage configured in sun tracking mode. The entire instrument weighs 1.5 kg (with the scope of further reducing to 1.2 kg) and consumes 4.5 W maximum. Technical specifications of the developed THz photometer is listed in Table 1.

6 Conclusion

A THz photometer was developed for observation of solar flare from low Earth orbits on a nanosatellite platform. The required spectral selectivity of 0.2 ppm was achieved by a cascade of different technologies for effective suppression of UV, visible, and IR radiation in the solar spectrum while selectively perceiving the THz component. An ultra-low noise front-end electronics based on lock-in-detection technique was adopted for achieving a dynamic range of 110 dB. With a sensitivity of 9 K/mV,

the photometer is capable of detecting the solar bursts with intensities as low as 30.6 SFU. Instrument capability was estimated by simulation of solar bursts while drift scanning the radiometer in front of tungsten–halogen source (color temperature: 2800 K). Field test and calibration are progressing, and it is planned to deploy the instrument in one of the forthcoming nanosatellites of ISRO.

Acknowledgements The authors are thankful to Shri Ganesh Shanbhogue, Group Director, PPEG, LEOS, for providing financial grant for carrying out the work presented in this paper.

References

1. Neugebauer G, Beichman CA, Soifer BT (1984) Early results from the infrared astronomical satellite. *Science* 224(4644):4–21
2. Kaufman P, White SM, Marcon R et al (2015) Bright 30 THz impulsive solar bursts. *J Geophys Res: Space Phys* 120(6):4155–4163
3. Kaufmann P, Klopff JM (2011) THz solar telescope for detection flare synchrotron radiation, *IEEE*. 978-1-4244-6051-9
4. Sumesh MA, Karanth SP, Thomas B, Rao GM, Viswanathan M, Chakraborty P, Rao GN (2017) Performance-enhanced bolometric terahertz detectors based on V₂O₅ for 15–30 THz. *J Infrared, Millimeter, Terahertz Waves* 38(2):135–142
5. Sumesh MA, Thomas B, Vijesh TV, Rao GM, Viswanathan M, Karanth SP (2018) Optically immersed bolometer ir detectors based on v₂o₅ thin films with polyimide thermal impedance control layer for space applications. *J Infrared, Millimeter, Terahertz Waves* 39(1):6–23
6. Kaufmann P, Abrantes A, Bortolucci EC, Caspi A, Fernandes LOT, Kropotov G, Kudaka AS, Laurent G, Machado N, Marcon R, Marun A, Nikolaev VA, Hidalgo Ramirez RF, Raulin JP, Saint Hilaire P, Shih A, Silva CM, Timofeevsky AV (2016) THz solar observations on board of a trans-antarctic stratospheric balloon flights, *IEEE*
7. Marcon R et al (2012) Terahertz photometer to observe solar flares in continuum. *J Infrared, Millimeter Terahertz Waves* 33:192–205
8. Kaufmann P, Marcon R, Marun A, Kudaka AS, Bortolucci E, Beny Zakia M, Cassiano MM, Pereyra P, Godoy R, Timofeevsky AV, Nikolaev VA, Diniz JA, Pereira Alves da Silva AM, Fernandes LOT (2010) Selective spectral detection of continuum terahertz radiation, millimeter, submillimeter, and far-infrared detectors and instrumentation for astronomy. In: *Proceedings of SPIE* 7741, p 774125
9. Kaufmann P, Fernandes LOT, Kudaka AS, Machado N, Abrantes A (2013) The performance of THz photometers for solar flare observations from space, *IEEE*

Integrated High Speed and High Capacity Base-Band Data Handling—Solid-State Recorder for Small Satellite Applications



Saswata Maitra, S. Chandrakanth, R. M. K. Guptha, P. Neeraja, K. L. Raja Sekhar and T. Venkata Mani

Abstract Defense satellites with hyperspectral imaging (HSI) and synthetic-aperture radar (SAR) payloads capture high-resolution images. The voluminous data captured by payload needs to be processed and stored for transmission to ground station upon visibility for analysis. Data from payloads has to be acquired by data handling system and to be stored in memory after required processing. This paper describes novel and efficient hardware architecture of high speed, high capacity, miniaturized, non-volatile, redundant and radiation tolerant integrated base-band data handling (BDH)—solid-state recorder (SSR) system for polar lower earth observation (LEO) small satellite applications.

Keywords Integrated base-band data handling · Solid-state recorder · Payload · Lower earth observation · Radiation tolerant

1 Introduction

Integrated BDH-SSR is a critical subsystem used in satellite applications for storage of high speed voluminous data captured by payload and transmits the stored data to ground station on demand for processing and analysis. Payloads that are widely used for capturing images in polar lower earth observation (LEO) small satellite applications are hyperspectral imaging (HSI) and synthetic-aperture radar (SAR). The images captured are sent to integrated BDH-SSR on high speed communication channel for storage. The major functional requirements of BDH-SSR are to acquire data from payloads, time stamp and format the received data as per CCSDS

S. Maitra (✉)
DNEC, RCI, DRDO, Hyderabad, India
e-mail: saswata.maitra@rcilab.in

S. Chandrakanth · R. M. K. Guptha · P. Neeraja · K. L. Raja Sekhar · T. Venkata Mani
Research Centre Imarat, Dr. APJ Abdul Kalam Missile Complex, 500 069 Hyderabad, Telangana, India

guidelines, encode the formatted data for error detection and correction, and store in non-volatile memory. The stored data has to be encrypted and randomized during downlink to ground station.

Contemporary designs mostly have data handling and storage (volatile) as two separate systems. The proposed design has data handling and storage functionalities integrated in single system which is capable of acquiring payload data at the rate of 1.6 Gbps and storage capacity of 2.25 Tbits. BDH-SSR design uses NAND Flash Memory as basic storage element because of its non-volatility and high density. The system is specifically designed to withstand radiation effects in Polar LEO.

Two identical BDH-SSR PCBs are integrated in single chassis for cold standby redundancy. This paper gives a description of the hardware architecture evolved to meet the functional, timing and environmental requirements of BDH-SSR and the challenges encountered in the realization of integrated BDH-SSR system.

2 System Description

Integrated BDH-SSR unit is interfaced to Payload System, Bus Management Unit (BMU), X-Band System and Electrical Power System (EPS) as shown in Fig. 1. BSH-SSR receives payload data through 16 LVDS channels each having a data rate of 100 Mbps. BDH-SSR communicates with BMU over MIL-STD-1553B bus as remote terminal (RT) to receive time stamping data and operational commands. The received data is formatted, time stamped and packetized for encoding. The encoded data is then stored in solid-state recorder consisting of non-volatile high density NAND Flash Memory banks. The unit is also interfaced to Payload and X-Band System on low voltage differential signaling (LVDS) communication channels. Upon receiving

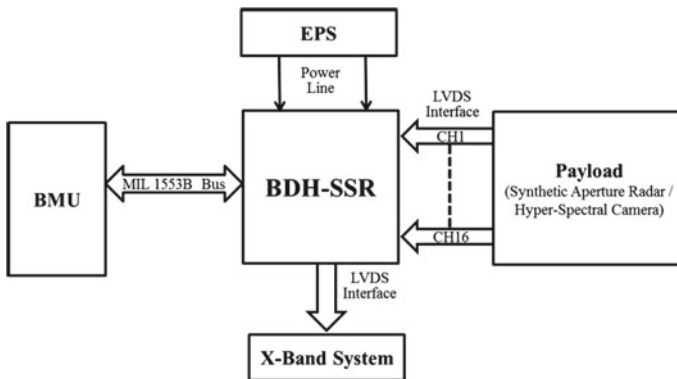


Fig. 1 Interface block diagram of BDH-SSR

playback command from BMU, recorded data from SSR will be transmitted to X-Band System at the rate of 660 Mbps. The recorded data is encrypted and randomized before transmission to X-Band System. BDH-SSR main and redundant has separate power interface to EPS for operation.

3 System Requirement

BDH-SSR unit has to meet the following requirements:

- (i) **Radiation Tolerant:** BDH-SSR unit has to be radiation tolerant as the satellite is aimed for Polar LEO. The radiation level to which the unit is exposed in Polar LEO is given in Table 1.
- (ii) **Functional requirement:** BDH-SSR has three modes of operation consisting of data acquisition and record, data erase, playback mode, standby mode and self-diagnostic mode. These modes are invoked based on the operational commands from BMU.
 - (a) **Data acquisition and Record mode:** In this mode, the data from payload is received and then initiates and continues for recording in SSR until stop command from BMU is received.
 - (b) **Data erase mode:** On erase command from BMU, erase operation of SSR is carried out prior to start of data acquisition.
 - (c) **Playback mode:** Transmission of data is carried out in playback mode. This is initiated by BMU command during which the stored data is read from SSR, encrypted and randomized before transmission to ground station via downlink.
 - (d) **Standby mode:** This mode is reached after initialization on Power-On with hardware or software reset command. Then BDH-SSR waits for further commands from BMU.
 - (e) **Self-diagnostic mode:** In this mode, the unit carries out testing of internal resources. Bus communication and memory checks are performed.
- iii) **Timing requirement:** BDH-SSR system has to receive data from payloads at the rate of 1.6 Gbps over 16 LVDS channels each having data rate of 100 Mbps. Also during playback mode, BDH-SSR has to transmit the stored data at 660 Mbps to X-band transmitter (Fig. 2).

Table 1 Radiation specifications

Radiation parameter	Min	Units
Total Ionizing Dose (TID)	50	Krad (Si)
Single-Event Latch-up immunity (SEL) transfer (LET) threshold	85	LET (MeV-cm ² /mg)
Single-Event Functional Interrupt (SEFI)	80	Mev-cm ² /mg
Single-Event Upset (SEU)	80	Mev-cm ² /mg
Total bits: 35 M		

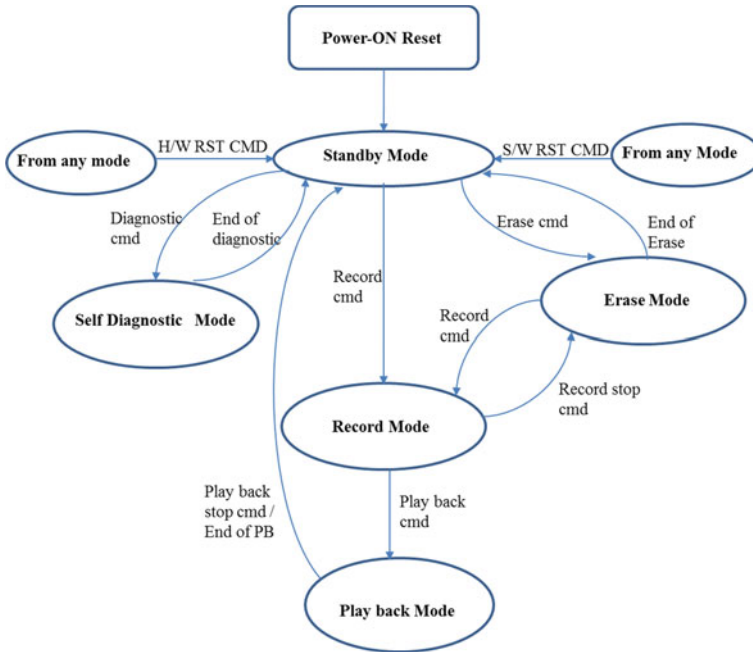


Fig. 2 BDH-SSR mode operation

- (iv) **Power requirement:** The unit draws power from power supply unit. BDH-SSR requires 50 W for its functionality.
- (v) **Lifetime:** The unit has to be operational in LEO for a period of five years.
- (vi) **Reliability:** Reliability has to be ensured at design level. Redundancy has to be incorporated for more reliability.

4 System Architecture and Design

Hardware design of BDH-SSR is based on Xilinx FPGA with embedded MicroBlaze Soft Processor, NAND Flash Memory Banks and Magneto-Resistive RAMs (MRAM) as shown in Fig. 3. Parallel and pipelined architecture are adopted in BDH-SSR for data acquisition at high speed of 1.6 Gbps and to overcome slow write cycles of NAND flash. The major functionality of the unit is achieved using custom IP cores for data acquisition, NAND Flash Memory controller, bad block management, formatting, RS encoding, playback interface logic, encryption and randomization. All the IP cores are implemented along with MIL-STD-1553B IP core, UART IP core and MicroBlaze Soft Processor in a single FPGA.

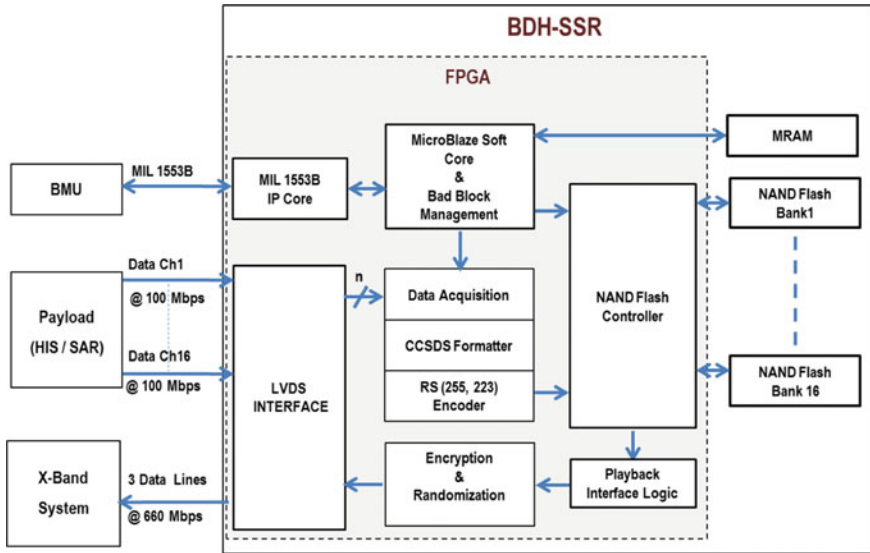


Fig. 3 Architectural block diagram of BDH-SSR

Hyperspectral imaging system (HIS) comprises of VNIR and SWIR camera with separate electronics. The throughput is 840 Mbps and 240 Mbps for VNIR and SWIR, respectively. The throughput of synthetic-aperture radar (SAR) payload is 1.6 Gbps. BDH-SSR receives data from both payloads over the 16 parallel LVDS channels. The high throughput of SAR and HSIS demands high density memory storage. The stored data is sent to ground station upon visibility. BDH-SSR unit is powered on only during data recording mode and playback mode to meet the power budget of the mission. Hence, SSR design is based on high density non-volatile NAND flash ICs to provide the recorder capacity of 2.25 Tbits. NAND flash devices are of high density but with slower reading and programming speed. The maximum programming speed achieved in a single NAND flash device is 70 Mbps. The major challenge in designing SSR is to write the incoming payload data at the rate of 100 Mbps to NAND flash. Pipelined architecture is adopted for programming NAND flash with 100 Mbps incoming data from payload.

4.1 Data Acquisition

LVDS standard is an ideal solution for high speed and low power applications. Due to differential signaling and reduced voltage levels, LVDS induces a much lower EMI in other subsystems and also provides noise immunity. LVDS interface only has a common mode input range of 2.4 V. LVDS output driver provides 350 mV, nominal into a 100 Ω load. Twisted pair double-shielded cables are used to connect

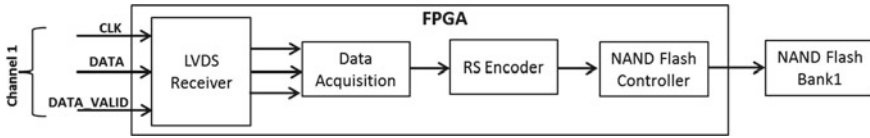


Fig. 4 Internal architecture of single-channel data acquisition and recording

between payload and BDH-SSR. Each LVDS channel from payload to BDH-SSR comprises of data, data valid and clock signals. Data from payload is transmitted in synchronous to clock (125 MHz) with 80% duty cycle of data valid signal. Hence, 100 Mbps effective data rate is achieved.

To mitigate signal skew and jitter, LVDS cross-point switch, configured as repeater, is used for acquiring data from payload. In-built LVDS transceivers of Xilinx FPGA receive LVDS output of cross-point switch and store the data in Block RAM modules of Xilinx FPGA. Incoming data is grouped into sets of 8K bytes corresponding to one page of NAND Flash Memory and is stored in separate BRAM modules.

Figure 4 shows the complete path for data acquisition and storing in NAND flash on one channel.

4.2 Data Formatting

Data stored in BRAM is read and formatted by inclusion of time stamp and headers. The formatting is required by the ground station to decode and process the received data.

4.3 Reed Solomon (255,223) Encoding

The formatted data is encoded before storing into flash memory. RS encoding scheme is used to detect and correct burst errors occurring during transmission. RS (255,223) encoder implemented in FPGA that can detect 32 errors and correct 16 errors. RS coding has proved to be a good compromise between redundant information required and hardware complexity (Figs. 5 and 6).

4.4 NAND Flash Controller

NAND flash is a non-volatile memory with high storage density, fast access time and low power requirement. NAND Flash Memory is based on single-level cell

Fig. 5 Device organization

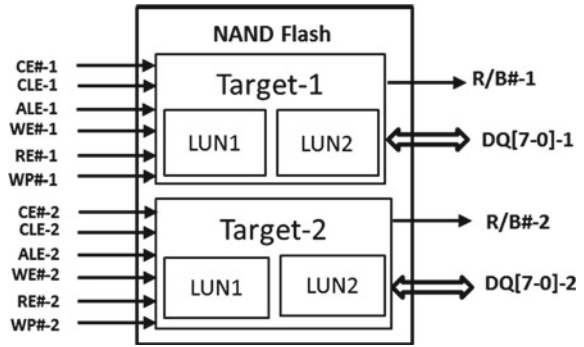
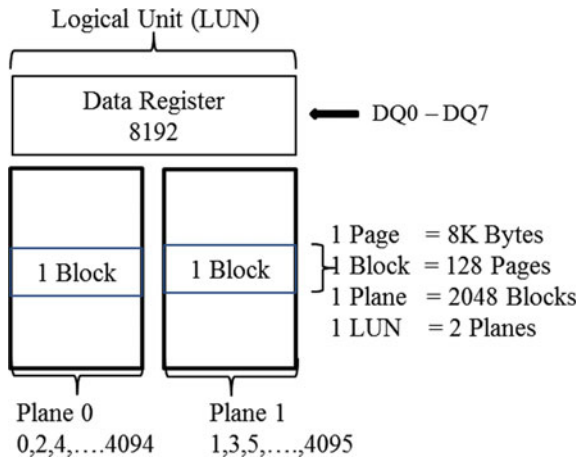


Fig. 6 Array organization



technology. It is highly reliable, ceramic hermetically sealed with in-built TID shielding.

In NAND flash device, command, address and data share the same bus resulting in low I/O bandwidth. The programming time also consumes large proportion in the timing of flash operation of the order of 560 μ s. The slow programming speed is a critical factor to the I/O bandwidth of the system. Selected NAND Flash IC has two targets and each target has two logic units (LUN). The device chosen has two isolated buses thereby enabling pipelined programming as shown in Fig. 7. When

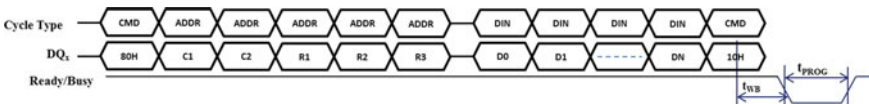


Fig. 7 Timing diagram of NAND flash page programming

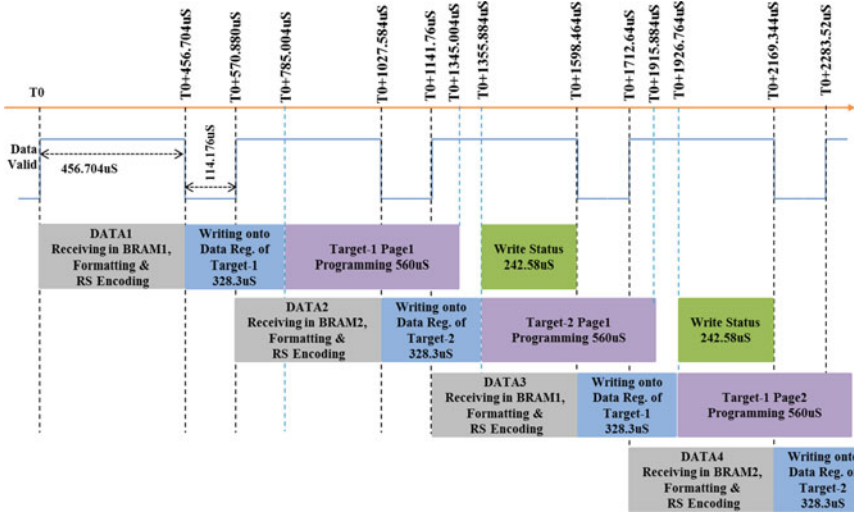


Fig. 8 Timing diagram of data acquisition and data storage

first target is in programming mode, the second target is loaded with data. Use of pipelined architecture enables to meet the timing requirements of the mission.

- a. Time required for issuing command and writing page data to data register of FLASH with **100% de-rating** = $t_{WC} + 5 * t_{WC} + t_{ADL} + (m * t_{WC}) + t_{WC} + t_{WB} = 328.3 \mu s$
- b. Time required to transfer DATA from data register to memory = $t_{PROG_{max}} = 560 \mu s$
- c. Effective Flash write speed = $64 * 1024/888.3 \mu s = 73.77 \text{ Mbps}$

Figure 8 shows the pipelined architecture implemented in FPGA for data acquisition and storage.

- a. Data is received only during only ON period (456.704 μs) of data valid signal.
- b. Consider the first data (DATA1) starts receiving in FPGA BRAM1 at T0 instance.
- c. At T0 + 456.704 μs , DATA1 receiving in BRAM1 is completed and the DATA1 starts writing onto the data registers of Target-1.
- d. At T0 + 785.004 μs , DATA1 is completely written onto the data register of Target-1. At this instance, Target-1 enters into page programming mode. Hence, multiplexed IO bus will be free.
- e. DATA2 starts receiving in FPGA BRAM2 at T0 + 570.880 μs and completes at T0 + 1027.584 μs . At T0 + 1027.584 μs instance, it starts writing onto the data register of Target-2.
- f. At T0 + 1355.884 μs , DATA2 is completely written onto the data register of Target-2. At this instance, Target-2 enters into page programming mode and multiplexed IO bus will be free.

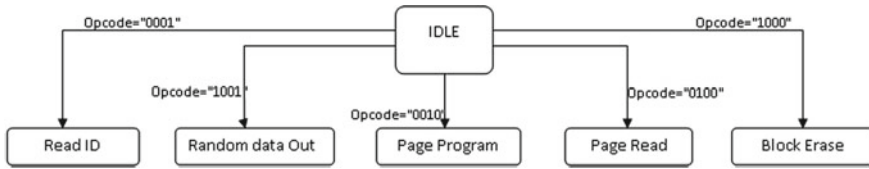


Fig. 9 Operating modes of NAND flash controller

- g. At $T_0 + 1141.76 \mu\text{s}$, DATA3 starts receiving in BRAM1 and is completed at $T_0 + 1598.464 \mu\text{s}$. At this instance, it starts writing onto the data register of Target-1.
- h. At $T_0 + 1926.7644 \mu\text{s}$, DATA3 is completely written onto the data register of Target-1. Target-1 enters into page programming mode. Hence, multiplexed IO bus will be free.
- i. At $T_0 + 1712.646 \mu\text{s}$, DATA4 starts receiving in BRAM2 and is completed at $T_0 + 2169.344 \mu\text{s}$. At this instance, it starts writing onto the data register of Target-2.
- j. The NAND flash controller will repeat the same cycle for incoming data.

Custom NAND Flash Memory controller IP core is developed that performs the read ID, page read, page write and block erase operations. All the timings are 50% derated to meet the harsh environmental requirements. The encoded data is continuously written in NAND Flash Page by Page. The implemented NAND flash controller has various operating modes as shown in Fig. 9. The command from BMU is decoded and corresponding opcode is generated for various modes of operation.

4.5 Bad Block Management and Wear Leveling

NAND flash technology has inherent limitations. Bad blocks are those which contain invalid bits. Due to production yield constraints, NAND flash ships with a number of bad blocks that are not to be used. Moreover, with time and after multiple erase cycles, the memory will tend to wear and become less reliable and bad blocks may develop during lifetime. Hence, bad block management, ECC and wear leveling techniques are implemented.

10% extra NAND flash storage is provided in the design to deal with bad blocks. Bad block information is written prior to shipping of the ICs. Specific algorithm provided by the vendor is implemented in HDL for recognition of bad blocks. Bad block table is prepared by software in the initial stage on Power-On and then is updated after each erase cycle. Blocks contained in bad block table are not addressable. The bad block table is stored in MRAM and updated whenever a bad block is identified. The table also gives the alternate address for storage corresponding to each bad block encountered during data storage.

Wear leveling uses NAND flash device evenly and maximizes its life span. Wear leveling technique remaps the same logic address to different physical memory in each program cycle.

4.6 *MicroBlaze Soft Core*

MicroBlaze V8.2 is a 32-bit RISC softcore that is implemented in VIRTEX-5 FPGA. It has 32-bit general purpose registers and 32-bit address bus with three stage pipeline. It has local memory bus and processor local bus (PLB). One MIL-1553B controller, UART controller and MRAM controller are interfaced on PLB to the processor. UART is used for debugging purposes. Logical address to physical address translation is carried out by processor. MicroBlaze V8.2 takes approximately 330 LUTs in Virtex-5 FPGA.

5 Major Challenges

The major challenges encountered during the design of BDH-SSR are listed below.

Component availability: The components used in BDH-SSR design are required to be radiation hardened or radiation tolerant. The major challenge is limited availability of radiation tolerant components meeting the TID, SEE and SEU specifications.

Handling high data rate 1.6 Gbps for 1 m distance: LVDS interface with multiple acquisition channels is provided to meet the high data rate.

Signal integrity issues of high speed LVDS signals: The layout guidelines for LVDS signal routing are followed with proper termination and grounding for avoiding cross-talk effects and EMI/EMC.

Small form factor: BDH and SSR functionality are integrated in a single PCB. Also, two identical PCBs are assembled in the mechanical chassis to provide cold standby redundancy.

Thermal considerations: Conduction cooled PCBs are used. Two thermal planes are included in the PCB stack and thermal vias are provided to mitigate thermal issues. Heat sink is used to dissipate heat.

6 Results

The proto board of BDH-SSR is realized and IP cores (data acquisition, NAND flash controller, RS encoding) are implemented in FPGA. Figure 10a shows the test setup consisting of BDH-SSR proto board and payload simulator board. Data is continuously transmitted from payload simulator at the rate of 300 Mbps and

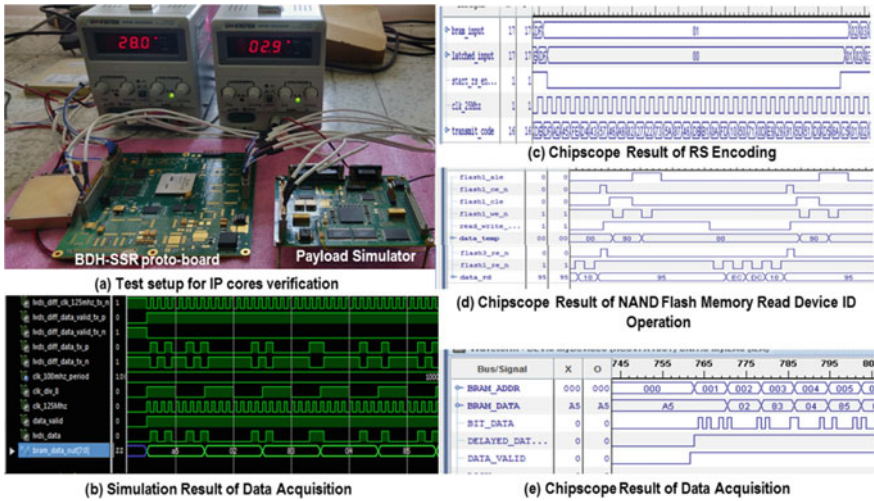


Fig. 10 Test setup and implementation results

acquired through LVDS receiver in Virtex-5 FPGA on BDH-SSR board. The data is then stored in BRAM in FPGA and verified using ChipScope hardware debugging tool. Figure b shows the simulation result of data acquisition and Figure e shows the implementation result of the same. RS encoding results are shown in Figure c and verified by comparison with MATLAB and ModelSim simulation results. Figure d shows the read ID operation results of NAND Flash Memory. Erase, write and read operations of NAND flash are also verified.

7 Conclusion

BDH-SSR is the first indigenously designed system which is radiation tolerant with high data rate acquisition, high density non-volatile storage capability and cold standby redundancy. The design meets the requirements of both HSI and SAR payloads. The storage capacity of the system caters for higher acquisition times for immediate future requirements. SERDES architecture is being explored for data acquisition as well as transmission to ground station, which shall reduce cable looming to great extent and at the same time achieving higher data rates.

References

1. Micron 64 Gb, 128 Gb, 256 Gb, 512 Gb Asynchronous/Synchronous NAND Features

2. Mir I, Mcewan AA, Perrins N (2012) A high performance reconfigurable architecture for flash file systems. In: Welch PH et al (eds) *Communicating process architectures 2012*. Open Channel Publishing Ltd.
3. Qin G, Xie M, Liu G, Jiao L, Zhou B (2012) A tri-level parallel architecture for NAND flash storage system. In: *5th international conference on BioMedical engineering and informatics*
4. *White Paper on Flash File System Overview*. Intel Corporation
5. Mitiukhina N (2014) Overview of the NAND flash high-speed interfacing and controller architecture. In: *IEE 5008 memory system final report 0060805*
6. Clarke CKP (2002) Reed-Solomon error correction. R&D White Paper WHP031, British Broadcasting Corporation

A Novel Space-Based AIS Receiver Architecture for Maritime Surveillance



D. Mallikarjuna Reddy and S. Anuradha

Abstract This paper presents a novel space-based automatic identification system (AIS) receiver architecture meant for maritime surveillance. The receiver performance has been simulated in the presence of three AIS Tx signal messages colliding in different combinations of frequency, time and power. Doppler shift due to the LEO satellite moving at a velocity of 7.5 km/s at an altitude of 600–900 km, and the delay in signal transmission was also induced in the AIS Tx signals to fully characterize the AIS receiver. The architecture proposed in this paper is suited for on-board processing on any nanosatellite with enhanced message and ship detection capability. The performance parameters of the proposed AIS receiver in the collision environment have been tabulated in the results' section.

Keywords AIS · LEO · GMSK · SOTDMA · Maritime

1 Introduction

Terrestrial AIS communication system was developed to provide identification and location information to vessels and shore stations by exchanging different types of messages containing position, identification, course, speed and other voyage details. This helps vessels to have the knowledge of other ships in their neighborhood and thus avoid collisions in the sea. AIS also offers ship monitoring services to coastal guards.

Automatic identification system (AIS) messages comprise 1-min SOTDMA frame with each frame consisting of 2250 slots. Each slot takes around 26.67 ms and are transmitted over two AIS frequencies 161.975 and 162.025 MHz with a transmit power of 12.5 W. This was designed for a coverage region of 40 nautical mile diameter called SOTDMA cell. The SOTDMA protocol ensures message collision avoidance

D. Mallikarjuna Reddy (✉) · S. Anuradha
Department of ECE, National Institute of Technology, Warangal, Telangana, India
e-mail: mallikarjuna.reddy@rcilab.in

S. Anuradha
e-mail: anuradha@nitw.ac.in

© Springer Nature Singapore Pte Ltd. 2020
PSR. S. Sastry et al. (eds.), *Advances in Small Satellite Technologies*,
Lecture Notes in Mechanical Engineering,
https://doi.org/10.1007/978-981-15-1724-2_26

within that region. The total number of messages received in 1 min over the two AIS frequencies is around 4500 [1] from a single cell.

Limitation in the range for the terrestrial AIS communication system due to line of sight has grown interest for detecting and tracking ships in the deep seas and areas not reachable by normal ground-based systems. For improved security and countering of illegal operations, there is a need to detect and monitor ships which are at very long distances from the shores. Space-based AIS system has been presented as a potential solution to overcome the limitations of existing terrestrial AIS systems and provide detection service coverage on any part of the globe.

Field of view from a low earth orbit (LEO) satellite covers hundreds of SOTDMA cells, and hence, the messages received by the AIS receiver from space platform will likely be experiencing collisions. Link budget ([1], Table 6) for a 950 km altitude LEO satellite with 12.5 W isotropic radiated power transmitter, at a maximum slant range of 3606 km has energy-per-bit to noise spectral density (E_b/N_0) of 8.3 dB. This shows that the architecture for space-based AIS receiver should be capable of decoding messages in the interference scenario rather than the noise.

A novel receiver architecture suitable for on-board processing on a LEO satellite for decoding the AIS messages in the collision environment is proposed in this paper. Characteristics of AIS signals received by a LEO satellite from ships are provided in Sect. 2, a parallel demodulation receiver architecture in Sect. 3 and decoding and validation of messages in different signal collision scenarios in Sect. 4. Overall performance of AIS receiver is captured in the results' section.

2 Technical Characteristics and AIS Message Construction

A. AIS Transmission Frame Structure

AIS message packet length is of 256 bits transmitted in small slot of 26.67 ms at a rate of 9600 bps using a binary GMSK modulation over two VHF carriers. Each SOTDMA (Self-Organized Time Division Multiple Access) cell is designed to cope with path delays of not longer than 12 bits, which translates into a maximum range of 200 nautical miles, but the RF coverage is limited to about 40 nautical miles. All transmissions by the ships in this range follow SOTDMA protocol and are collision free.

B. AIS Encoder Section

AIS packet message of 256 bits as shown in Fig. 1 as shown in Fig. 2. The start flag and end flag each of 8 bits are represented by "7E" used for message synchronization. In the data field bit stuffing is carried out to avoid data resembling the start or end flag.

C. GMSK Conversion and Modulation

The NRZ coded AIS packet will first be converted into bipolar data and is GMSK converted using the filter and integrator sections (Fig. 3).

Ramp up (8 bits)	Training Sequence (24 bits)	Start flag (8 bits)	Data (168 bits)	FCS (16 bits)	End Flag (8 bits)	Buffer (24 bits)
-------------------------	------------------------------------	----------------------------	------------------------	----------------------	--------------------------	-------------------------

Fig. 1 AIS message packet structure

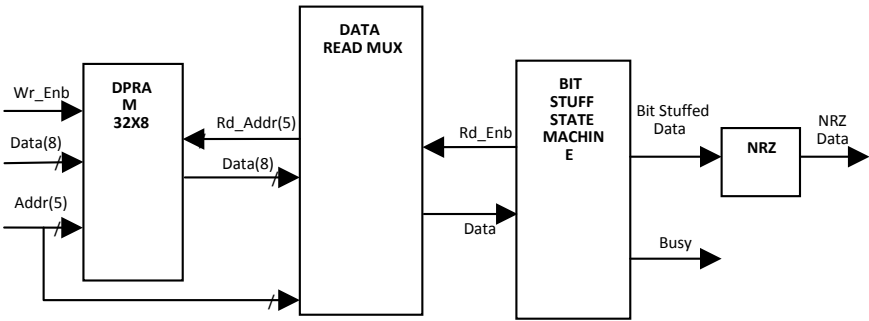


Fig. 2 AIS packet construction



Fig. 3 GMSK conversion

The accumulated data from the integrator section is I&Q modulated using a quadrature NCO generating sine and cosine signals, multiplier and adder section as shown in Fig. 4.

Each AIS enabled ship can transmit the messages on two channels 161.975 and 162.025 MHz with a bandwidth of 25 kHz on each channel alternatively with a reporting interval between 2 s and 6 min. SOTDMA cell frame is composed of 2250 slots where the ships can transmit their messages. This frame is transmitted on the

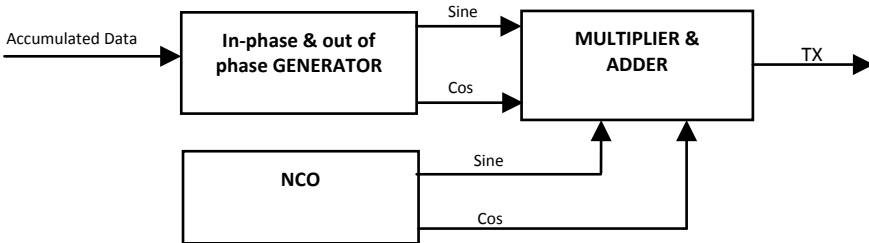


Fig. 4 Modulator

two frequency channels and each ship transmitter’s hop continuously between them. The TDMA frame length accommodating 2250 slots for the ships to transmit 256 bits each in the allocated slot at a rate of 9600 bps will be around 60 s.

3 Proposed Parallel Decoder Architecture for Space-Based on-Board Processing AIS Receiver

A novel parallel decoder AIS receiver is proposed in this section. A total of 19 parallel decoders structure each catering a doppler shift of ± 200 Hz to cover the complete range of the expected Doppler shift from -3800 to $+3800$ Hz. To receive the AIS messages on both the channels, two such blocks are used for decoding the AIS messages. The band-pass filter in the RF front end will limit the channel bandwidth to around 125 kHz. The two channels are digitally down converted using an NCO to zero IF and near zero IF signals. Each channel occupies a bandwidth of 25 kHz with the central frequencies $161.975\text{ MHz} \pm 12.5\text{ kHz}$ and $162.025\text{ MHz} \pm 12.5\text{ kHz}$ (Fig. 5).

On each channel and for each chain, the signal is GMSK demodulated by using the CORDIC algorithm. For each chain, matched filter with eight different thresholds has been configured for proper demodulation of the AIS messages in the collision scenario with difference in the power level (Fig. 6).

The matched filter demodulated data is passed through a trellis structure for error correction. On the extracted bits, CRC check is carried out for AIS message validation. A total of 2^{16} combinations of CRC check need to be computed to validate the CRC of each AIS message packet.

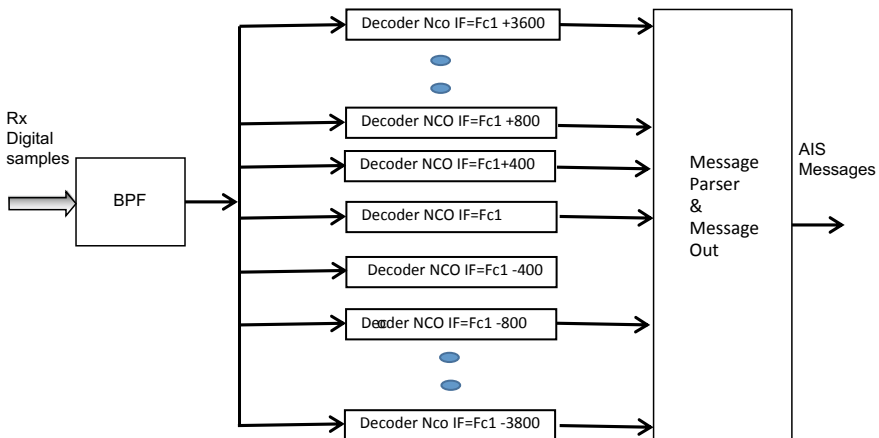


Fig. 5 Proposed AIS receiver architecture

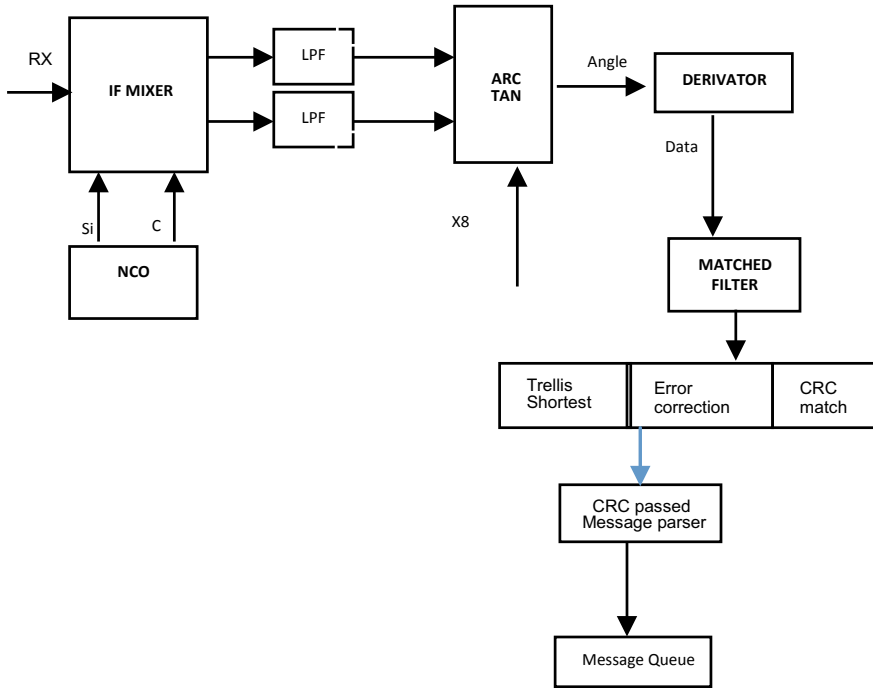


Fig. 6 Internal structure for each decoder

4 Performance Results

The performance details of the proposed novel AIS receiver are presented for (a) collision case and (b) non-collision case in Tables 1 and 2, respectively. In the non-collision case, the receiver works as a simple GMSK demodulator and at the sensitivity level of -110 dBm, the PER was around 10% for both the channels.

In the case of collision scenario, different combinations of signals named User #1 and User #2 with varying Doppler and power levels between them have been simulated, and the results are detailed in Table 2.

Table 1 PER in non-collision scenario with Doppler variation

Sensitivity of receiver	-110 dBm
Ch1: 161.975 MHz Doppler variation from -3800 to 3800 Hz	PER = 10%
Ch1: 162.025 MHz Doppler variation from -3800 to 3800 Hz	PER = 10%

Table 2 PER in collision scenario with Doppler variation

Sensitivity of receiver in collision case		–105 dBm	
S. No.	Doppler difference between the User #1 and User #2 (Hz)	Signal to interference ratio (dB)	Packet error rate (%)
1	±400	(i) 5	70
		(ii) 6	60
		(iii) 7	30
2	±800	(i) 6	60
		(ii) 7	50
		(iii) 8	30
3	±1600	(i) 8	70
		(ii) 9	40
		(iii) 10	30
4	±2400	(i) 10	75
		(ii) 11	40
		(iii) 12	20
5	±3800	(i) 12	60
		(ii) 13	20

5 Conclusion

A novel AIS receiver is proposed in this paper, and the results for both collision and non-collision scenario have been presented. The implementation of this AIS receiver with a capability for on-board message extraction on a small satellite using software defined radio devices is feasible with low power consumption, small size and low weight.

References

1. Report ITU-R M-2084, “Satellite Detection of Automatic Identification System Messages” (2006)

Power Systems

Overview of Space Grade Power Supply Modules for Satellite



J. Nesh, Bhoopendra Kumar Singh, Vinod Chippalkatti
and G. Chandrashekar

Abstract This paper aims at the overview in design and development of reliable and robust space grade power supplies for satellite subsystems. The satellite is using six types of power supplies modules (PSM) which provide total of 20 isolated outputs. All converters are designed by using forward converter topology followed by post-Mag-Amp regulator for each output to meet the required specifications. Voltage mode with feed-forward control technique has been adopted to provide better CS101 performance. The converters deliver the output power from 15 to 110 W for different PSMs for the lower input voltage range of 32–42 V at a switching frequency of 150 kHz with sync. This paper also covers specification, design procedure and practical test results. Flight models have been developed, and practical electrical results have been validated in environmental tests like thermo-vacuum cycling test, operational temperature test, vibration test, etc.

Keywords Forward converter · Hybrid microcircuits (HMC) · Subsystems · Mag-Amp

1 Introduction

The circuits designed for space applications are required to operate reliably under extreme temperature conditions. All the six types of PSMs are meeting the environmental conditions required for satellite. PSM1 to PSM6 powers-up the respective

J. Nesh (✉) · B. K. Singh · V. Chippalkatti · G. Chandrashekar
Centum Electronics Ltd, Yelahanka, India
e-mail: neshj@centumelectronics.com

B. K. Singh
e-mail: bksingh@centumelectronics.com

V. Chippalkatti
e-mail: vinod@centumelectronics.com

G. Chandrashekar
e-mail: chandrashekhar.g@drlr.drdo.in

subsystems, PSM1 (1 output) power-up Subsystem-1, PSM2 (2 output) power-up Subsystem-2, PSM3 (2 output) power-up Subsystem-3, PSM4 (5 output) power-up Subsystem-4, PSM5 (6 output) power-up Subsystem-5 and PSM6 (4 output) power-up Subsystem-6. Design is done keeping the reliability, modularity, size and mass as central aspect that also meets the specifications. Switching frequency is selected 150 kHz to optimize the switching losses, mass, size of filters and transformer design. PSM also provides the under-voltage shutdown, output overvoltage protection, input overcurrent protection and output short-circuit protection. It is having sync-out and sync-in facility to synchronize all the PSM. In all the converters, hybrid microcircuits (HMC) are used to bring down the size and mass. Four types of HMCs are used in all PSMs so that the manufacturing becomes uncomplicated and faster. HMCs contain PWM circuitry, start-up circuit, input under-voltage protection, I/P current monitoring, I/P short-circuit protection, relay driver circuits for both relays, control circuitries of Mag-Amp regulator for each output and O/P overvoltage protection circuits, etc. PSMs are having output voltage ranging from 3.35 to 16 V with efficiency of 65–76% at 100% load condition. All the PSMs meet the EMI/EMC specifications MIL-STD-461C Class A2 with 120% resistive load.

2 Converter Specifications

- Input voltage range: 32 VDC to 42 VDC
- Outputs
 - PSM1 output: 5 V/3.6 A
 - PSM2 output: 9 V/5.5 A, –9 V/0.5 A
 - PSM3 output: 9 V/3.6A, –9 V/0.9 A
 - PSM4 output: 16 V/1.8 A, –15 V/0.6 A, 5 V/1.8 A, 5 V/2.4 A, 15 V/2.4 A
 - PSM5 output: 3.42 V/10.8 A, 15 V/0.6 A, –5 V/0.36 A, 3.42 V/10.8 A, 15 V/0.3 A, 5 V/3.6 A
 - PSM6 output: 3.35 V/14.4 A, 15 V/0.3 A, –5 V/0.24 A, 5 V/1.2 A
- Load regulation: $\pm 1\%$ (50–100% load)
- Line regulation: $\pm 0.5\%$
- Operating frequency: 150 kHz \pm 2 kHz (with Sync)
- Ripple: 30 mVpk-pk
- Spike: 50 mV/75 mVpk-pk (for 9 V/15 V/16 V Outputs)
- Operating temperature: –15 to +55 °C in Vacuum
- EMI/EMC: MIL-STD-461C
- Output voltage (rise time): Rise time should be <20 ms
- Efficiency (100% load): $\geq 60\%$ (PSM1,5 & 6) & $\geq 70\%$ (PSM2,3 & 4)

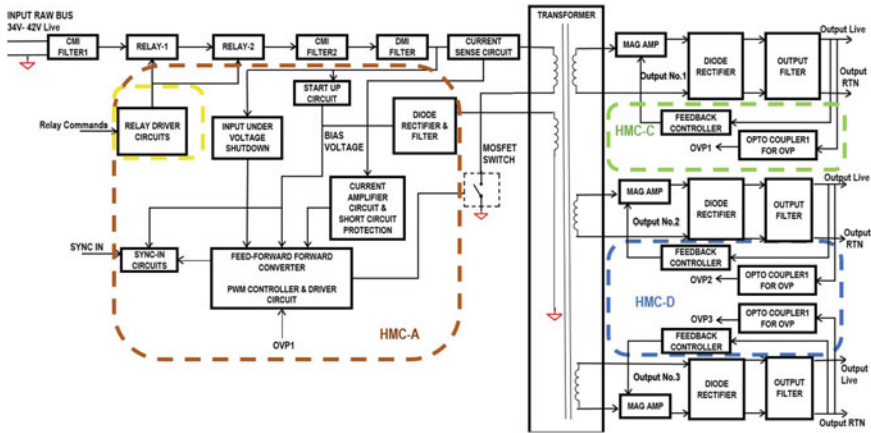


Fig. 2 Generic block diagram for PSMs

PCB and housed in aluminium housing. There are different PCB layouts for each type of PSM. Power MOSFET will be mounted on mechanical housing for better thermal flow and similarly few secondary diodes. Initial operating current to PWM controller is supplied by start-up circuit and switching starts. To reduce the losses, the start-up circuit is disabled, as PWM controller takes power from the auxiliary winding of the transformer. The auxiliary voltage is rectified and filtered by ultrafast recovery diode, inductor and capacitor filter, respectively. The filtered voltage is given to PWM controller. Transformers are required for galvanic isolation between input and output voltages and for voltage and current scaling. Steps involved in the isolation transformer design for DC–DC converter are explained in [2]. The secondary side output voltage is regulated with the help of feedback controller circuit. Filter inductor should be chosen to be sufficiently large such that under expected range of load current variation [1], secondary output is regulated output for all specified load changes. The feedback controller circuit in each Mag-Amp circuit provides the necessary correction for load changes. This is done by comparing changes in output voltage with reference voltage level. Thus, output in secondary will be regulated by Mag-Amp coil by using feedback signal from feedback controller circuit. These sections are shown as blocks in Fig. 2.

4 Modularity in Design

The forward converter topology is used for all the six types of PSMs. The status monitoring, input current sensing, relay control and protection circuits are kept same for the PSMs. Four types of HMC's (A, B, C and D as shown in Table 1) are used in realizing six types of PSMs. HMC-A consists of primary side control circuitry and relay control circuitry. HMC-B consists of primary side control circuitry without

Table 1 HMC types used in PSMs

HMC Type	PSM1	PSM2	PSM3	PSM4	PSM5	PSM6
HMC-A (primary control with relay control circuit)	1	1	1	1	1	1
HMC-B (primary control without relay control circuit)	–	–	–	1	1	–
HMC-C (single output feedback control)	1	–	–	1	2	–
HMC-D (dual output feedback control)	–	1	1	2	2	2

relay control circuitry. HMC-C consists of single output feedback control and HMC-D consists of dual output feedback control. Based on the no. of outputs and relay control circuit section, the HMC types are decided, Modularity improves the design and reduces the overall testing time, higher quality assembly and fabrication is also achieved.

HMC-A: It contains PWM circuitry, start-up circuit, ultrafast rectifier diodes of the bias winding, input under-voltage protection, I/P current monitoring, I/P short-circuit protection, relay driver circuits for both relays, etc. Package dimension for HMC-A is 2.3'' × 1.4'' × 0.18'' and substrate dimension is 1.86'' × 1.00'' × 0.025''. HMC-A will be used for all PSMs.

HMC-B: It is similar to HMC-A in all aspects except the relay driver circuitry. Relay driver circuitry is not provided in HMC-B.

HMC-D: It contains control circuitries of Mag-Amp regulator for each output and O/P overvoltage protection circuits. It is used for regulating the dual outputs. Package dimension for HMC-D is 1.27'' × 0.77'' × 0.18'', and substrate dimension is 1'' × 0.5'' × 0.025''.

HMC-C: HMC-C circuitry is similar to HMC-D except it regulates single output.

5 Size and Mass Optimization

The overall system size is reduced with the help of stacking the subsystem over the power supply in PSM1 and PSM6 as shown in Fig. 3. The stacking improved the overall system performance and reduced the overall length of the interconnection harness which also helps in the reduction of overall system mass. The reduction in mass of the overall system is one of the main concerns in space projects (PSM size and mass details are shown in Table 2). The long harness between the PSM and corresponding load gives very poor EMI/EMC performance, and it is difficult to meet the integrated payload performance even though the individual package might have complied with all the specifications. Long harness wires deteriorate the ripple

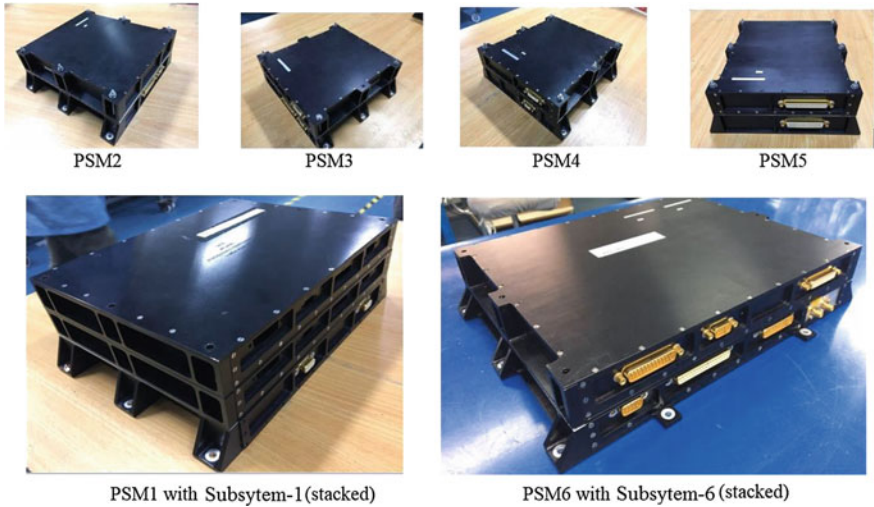


Fig. 3 PSM1 to PSM6 final assembly

Table 2 PSM size and mass details

S. No.	Description	FM size in mm	Mass of FM units (g)
1	Subsystem-6 with PSM-6	334 × 270 × 75	4280
2	Subsystem-1 with PSM-1	281 × 194 × 105	3700
3	PSM-2	216 × 204 × 90	2175
4	PSM-3	216 × 204 × 90	2712
5	PSM-4	216 × 204 × 90	2766
6	PSM-5	220 × 218 × 90	3003

as well as line/load regulation specifications. Structural and thermal analysis has been completed for all the units, and the mounting directions have been finalized accordingly so that it meets the vibration test also.

6 PSM Analysis Performed

The design is completed after many stages of analysis, testing of development models. During design, the following analyses are performed.

Table 3 PSM reliability factors

PSM	Reliability factor (R)
PSM1	0.995
PSM2	0.992
PSM3	0.995
PSM4	0.991
PSM5	0.991
PSM6	0.994

6.1 Derating Analysis

ISRO satellite derating guidelines have been used for PSMs. Each component including all resistors, capacitors, semiconductors, connectors, magnetics and relays has gone through derating analysis, and all PSMs have passed the criteria with enough margin. This margin keeps all components at lesser stress levels, which give PSMs a better reliability.

6.2 Reliability Analysis

MIL-HDBK-217F guidelines have been used for the calculation of component failure rates for PSMs. All the PSMs can achieve reliability factor ($R \geq 0.99$ (PSM reliability factors are shown in Table 3) for the mission time of 5 years and the equation used is

$$R = e^{-0.2t/MTBF} \tag{1}$$

t: Mission time

MTBF: Mean time between failures (years)

PSM reliability analysis is one of the most important analyses, and failure rate with respect to time shows much more clarity about the overall reliability of the system.

6.3 FMECA (Failure Mode, Effects and Criticality Analysis)

FMECA helped us to identify potential failure modes for a product or process, to assess the risk associated with those failure modes, to rank the issues in terms of importance and to identify and carry out corrective actions to address the most serious concerns. Severity level of each effect of failure has been assigned for all PSMs that helped in elimination, reduced failures, starting with the highest priority ones.

6.4 Worst Case Analysis (WCA)

PSM WCA accounts for component variability and determines circuit performance under extreme environmental and operating conditions. Following components are considered in the analysis, since these components have direct impact on the outputs:

- Error Due to Gain Resistor
- Error due to reference voltage (LM136) (@ Mag-Amp controller circuit)
- Error due to OP-Amp LM158 (@ Mag-Amp controller circuit)

The overall error (%) is $\leq 1.58\%$ in all PSMs due to ageing, temperature variation and radiation effects.

7 Practical Results' Validation

PSM1 to PSM6 are electrically tested against specifications individually with test jigs as well as manually depending on the test conditions. Table 4 shows automated tests and manual tests matrix. The automated jigs provide the reports in very less time compared to the manual measurement, and manual methods are used when the test set-up and measurement method are complex. Each PSM reading is captured in this way. Automated jigs are used during initial bench test, thermovac test and final bench tests. Electrical testing is done by applying the input DC voltage (34–42 V)

Table 4 Auto/manual test matrix

Test	Manual test	Automation test
Isolation measurement	✓	X
Relay control test @ 36 V	✓	✓
Input/output parameter measurement ripple and spike	✓	✓
Switching frequency @ 100 load	✓	X
Current monitoring voltage and TM status	✓	X
Calculations of efficiency, settability and regulation	✓	✓
Load transient response @ 42 V, 50–100% and 100–50%	✓	X
Turn on transient	✓	X
I/P under-voltage protection test @ 100% load	✓	✓
Surge current @ 42 V & 100% Load	✓	X
Output overvoltage protection @ 36 V _{in} and 10% Load	✓	X
Capacitive load test @ 36 V _{in} and 120% load	✓	✓
Noise immunity test @ 36 V and 100% load	✓	✓
I/P overcurrent protection @ 31 V and 120% load	✓	X
Short-Circuit Protection Test @ 31 V And 120% load	✓	X

and by giving SELECT and ON signal (5 V, 64 ms) to the unit. Press DESELECT and OFF signal to turn OFF the unit for all PSMs.

Fabrication of the PSM is done, and it has passed through the following test sequence.

7.1 Initial Bench Test

Once the card level testing is completed, the board is fixed inside the chassis and potting, echo-bonding, conformal coating, etc. are done.

7.2 EMI/EMC Test

EMI/EMC tests are performed with 120% resistive load and with actual subsystem also using space grade harness. Flight equivalent grounding scheme is mandatory during the test. Four types of test are done in EMI/EMC test.

- Conducted emission tests: CE01, CE03, CE07 (CE03 test set-up is shown in Fig. 4)
- Conducted susceptibility tests: CS01, CS02, CS06
- Radiated emission tests: RE02
- Radiated susceptibility tests: RS02, RS03

All the above tests have been completed successfully at ISAC Bangalore, and flight equivalent grounding scheme (shown in Table 5) is used for the test.

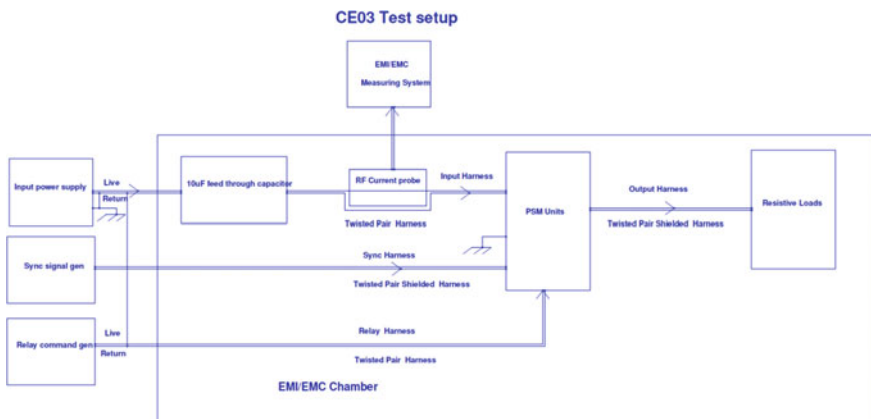


Fig. 4 CE03 test set-up

Table 5 Flight equivalent grounding scheme

Flight equivalent grounding scheme	
Input harness (input connector)	1. Input power line are TPS wires, TPS shield is connected to the connector via lug
	2. TM status live is ordinary wire
	3. Current monitoring live is ordinary shielded wire. Shield is connected to the connector via lug. Current Monitoring return is Connected to SGRP
	4. Sync-in and Sync-out wires are TPS wires. Shield is Connected to the connector Via Lug
	5. Primary return is shorted to control room chassis
Relay connector	1. ALL relay command wires are ordinary (O) wires
	2. Relay command returns are shorted to primary return
	3. Primary return is shorted to control room chassis
Output connector	1. Output wires are twisted pair shielded wires
	2. All output returns are shorted and connected to chassis at load end
	3. All shields are shorted and connected to connector via lug in connector side
	4. All shields are shorted and connected to load chassis at load side

7.3 Vibration Test

Each PSM is subjected to pre-low-level resonance search, random vibration and post-low-level resonance search. The fundamental frequency of all the PSMs is above 200 Hz, and it is meeting the specification requirement. The test sequence is low-level resonance search (LLS) → Random → LLS. All the PSM units passed the vibration test successfully.

7.4 Thermovac Test

The FM units are tested from $-10\text{ }^{\circ}\text{C}$ to $+50\text{ }^{\circ}\text{C}$. All the possible electrical readings are taken at 32, 36 and 42 V. Relay ON and OFF test, ripple, input/output measurements and efficiency are checked. All the units are tested at 100% resistive load condition. All PSMs completed the thermovac test. The thermovac test profile is shown in Fig. 5.

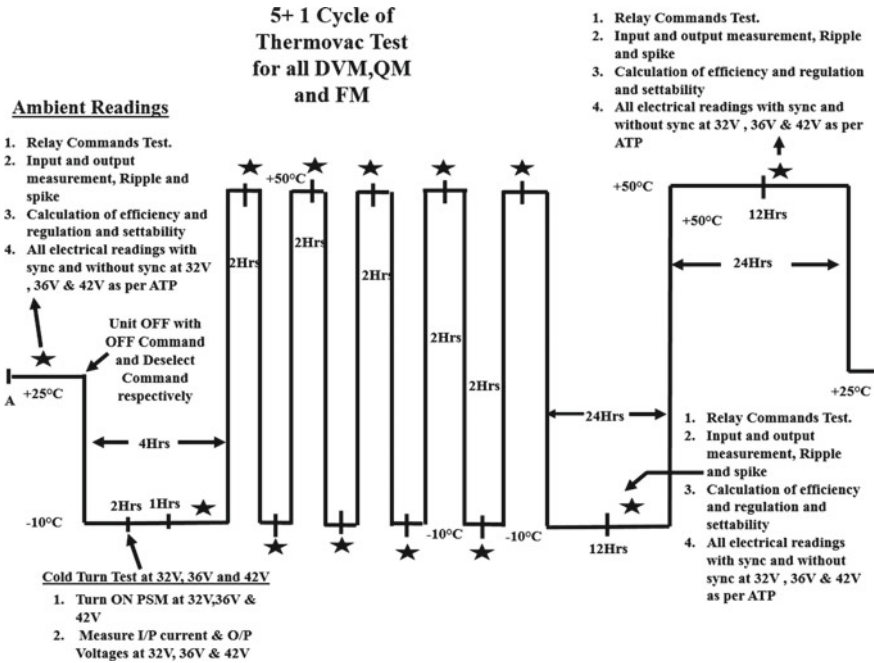


Fig. 5 Thermovac test profile

7.5 Final Bench Test

In the final bench test, all the electrical readings like isolation measurement, input/output parameter measurement, ripple, spike, switching frequency @100% load, calculations of efficiency, settability, regulation, load transient response @ 42 V 50–100% also 100–50%, turn on transient and all protection tests are once again cross-checked and data is captured. The ripple waveforms of PSM outputs are shown in Figs. 6 and 7.

The 12 PSMs are designed to deliver overall output power of 662 W (efficiency chart is shown in Table 6) to the subsystem (Figs. 8 and 9).

8 Integration Tests and Results

Electrical tests, thermovac, EMI/EMC, etc. are performed with subsystems after the completion of PSM final bench test. The actual output load current when connected with the subsystem is shown in Table 7. Integration level EMI/EMC test and thermovac tests with subsystems has been completed successfully.

Fig. 6 Ripple of +3.3 V/9 A O/P is 3.8 mV

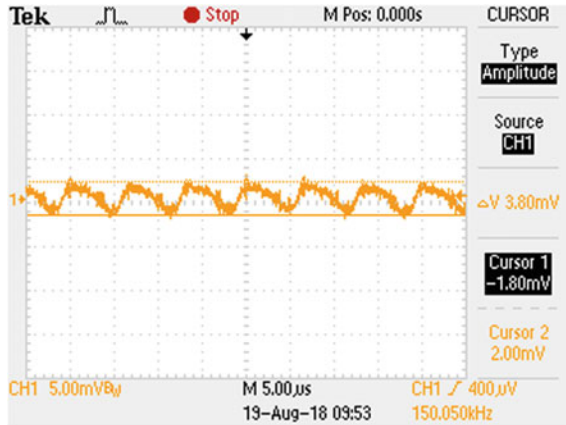
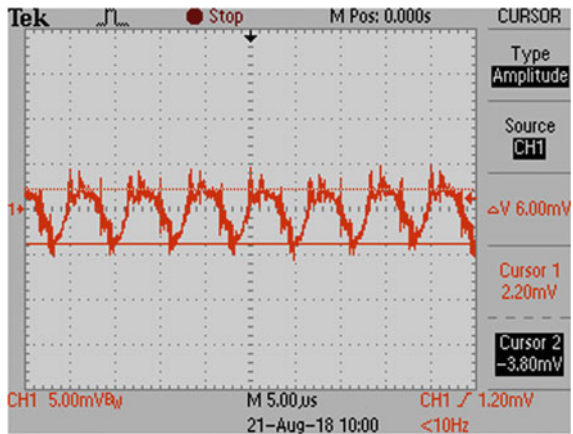


Fig. 7 Ripple of +16 V/1.5 A O/P is 6 mV



9 Conclusion

Topology selection of the power supply plays a vital and effective role in developing a switched mode power supply. The converter performance has features of low ripple voltage, better line regulation and good load transient response. The modularity in design and the mechanical stacking of the subsystems has reduced the overall size significantly. Protection against under-voltage, short-circuit and output overvoltage is provided to improve the reliability of the power supply. Electrical, environmental and EMI/EMC tests have been completed for all the PSMs.

Table 6 Efficiency chart of PSM1-PSM6 at 100% load condition

PSMs	Output voltage (V)	Output 100% current (A)	Output wattage (W)	Total output power (W)	Efficiency (%)
PSM1	5	3	15	15	69.61
PSM2	9	5.5	49.5	64	74.43
	-9	0.5	4.5		
PSM3	9	3	27	33.75	76.4
	-9	0.75	6.75		
PSM4	16	1.5	24	79	75.8
	-15	0.5	7.5		
	5	1.5	7.5		
	5	2	10		
	15	2	30		
PSM5	3.42	9	30.78	89.31	67.61
	15	0.5	7.5		
	-5	0.3	1.5		
	3.42	9	30.78		
	15	0.25	3.75		
	5	3	15		
PSM6	3.35	12	40.2	49.95	65.09
	15	0.25	3.75		
	-5	0.2	1		
	5	1	5		
				331.01	

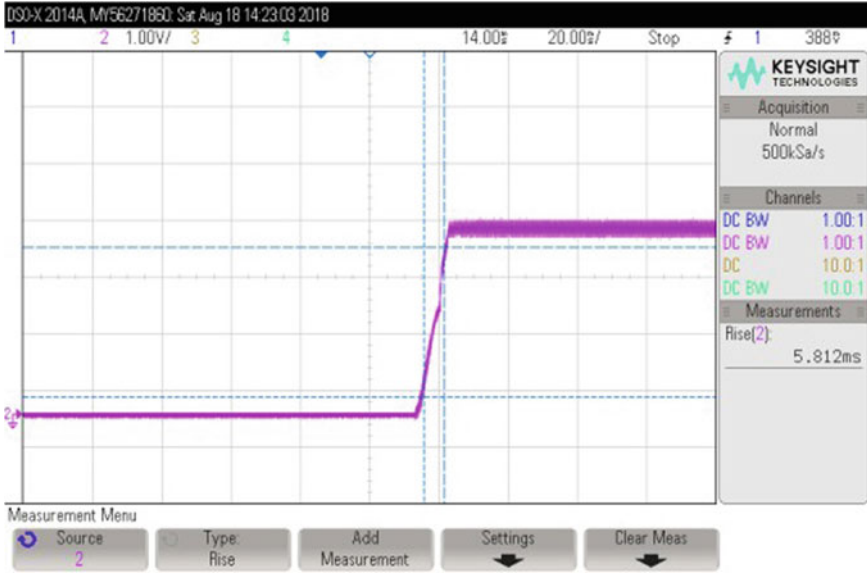


Fig. 8 Rise time of +3.3 V/9 A O/P is 5.8 ms

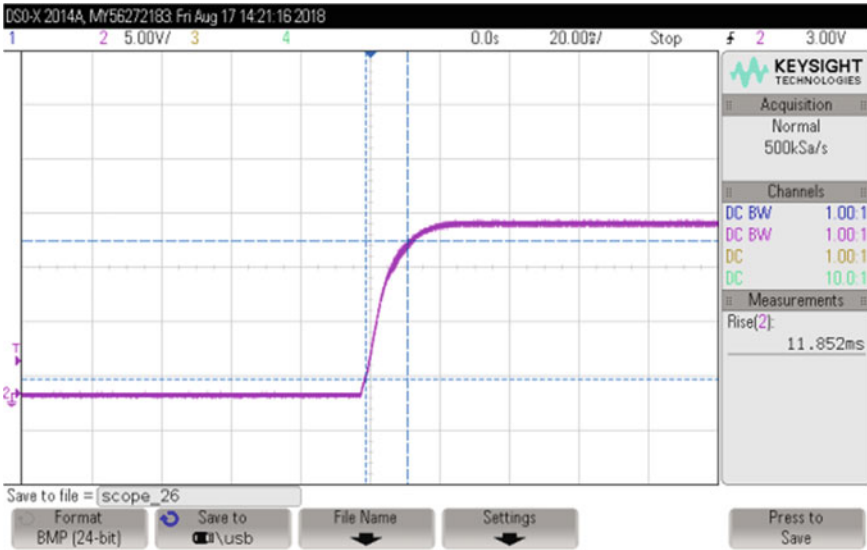


Fig. 9 Rise time of +16 V/1.5A O/P is 11.852 ms

Table 7 Actual subsystem load current with PSM

PSM units	100% load	Actual load (subsystem load)
PSM1	5 V/3 A	5 V/0.4 A
PSM2	9 V/5.5 A	9 V/4.481 A
	-9 V/0.5 A	-9 V/0.283 A
PSM3	9 V/3 A	9 V/1.4 A
	-9 V/0.75 A	-9 V/0.2 A
PSM4	16 V/1.5 A	16 V/1.391 A
	-15 V/0.5 A	-15 V/0.161 A
	5 V/1.5 A	5 V/1.08 A
	5 V/2 A	5 V/0.075 A
	15 V/2 A	15 V/1.1 A
PSM5	3.3 V/9 A	3.3 V/4.45 A
	15 V/0.5 A	15 V/0.3 A
	-5 V/0.3 A	-5 V/0.2 A
	3.3 V/9 A	3.3 V/5.41 A
	15 V/0.25 A	15 V/0.2 A
	5 V/3 A	5 V/2 A
PSM6	3.3 V/12 A	3.3 V/7 A
	15 V/0.25 A	15 V/0.1 A
	-5 V/0.2 A	-5 V/0.1 A
	5 V/1 A	5 V/1.0 A

Acknowledgements We are grateful to Mr. **Mallavarapu Apparao**, Managing Director, Centum Electronics Limited, Bangalore, for his encouragement and constant support for this work.

References

1. Pressman AI (1999) Switching power supply design, second edition. McGraw-Hill International
2. Umanand L, Bhat SR (2003) Design of magnetic components for switched mode power converters, 1st edition. New Age Publishers, (Paperback)

Grounding Schemes for Small Satellite Systems



P. Srinivas, Kumar Rahasyam, N. Beebamma and PSR Srinivasa Sastry

Abstract Grounding is very essential part of any electrical and electronic system design. Spacecraft is a complex system consisting of multiple complex subsystems electrically connected to each other. Most operations in satellites take place autonomously based on measurements; improper measurements may lead to unintended operation. Spurious triggering of switches and relays due to EMI is also very dangerous in satellites as it consists pyros and propulsion. Spacecraft charging will cause arcing in satellite which may lead to failure of subsystems. These situations sometimes lead to loss of whole satellite and make it irretrievable. Proper grounding is very essential to avoid these kinds of problems. The associated costs of any failure of on orbit satellite are very huge; hence, minute care shall be taken from the design phase to avoid any such problems. The objective of grounding is to ensure the proper operation of the spacecraft and reduction in electromagnetic interference. A good grounding design critically looks into these aspects and tries to minimize such occurrences and henceforth helps in reducing the noise coupling. This paper briefly presents the spacecraft grounding requirements, design approaches, grounding scheme philosophy at satellite level and discusses the different types of grounding schemes in small satellites. This paper also deals with advantages and disadvantages of different grounding schemes in small satellites.

Keywords Grounding · Small satellite · Distributed single-point grounding · Spacecraft charging · EMI/EMC · SGRP

1 Introduction

The term “ground” has been used since olden days in electrical circuits. The earth is considered as a sink for electrical currents and acts as equipotential plane for reference. In airborne/space-borne systems, metallic structures, frames, housings, etc. are electrically connected together forming an equipotential potential plane and

P. Srinivas (✉) · K. Rahasyam · N. Beebamma · P. S. Sastry
RCI, DRDO, Hyderabad, India
e-mail: p.srinivas@rcilab.in

© Springer Nature Singapore Pte Ltd. 2020
PSR. S. Sastry et al. (eds.), *Advances in Small Satellite Technologies*,
Lecture Notes in Mechanical Engineering,
https://doi.org/10.1007/978-981-15-1724-2_28

it is considered as ground plane. In subsystems, circuits are electrically referenced to this structure, which acts as reference plane.

As per IEEE Std 142-2007, grounding is defined as “A conducting path, whether intentional or accidental, between an electrical circuit or equipment and the earth, or to some other body that serves in place of the earth” [1].

Major purposes of spacecraft grounding are:

- to prevent the accumulation of stray electric charges (electrostatic charges on insulating surfaces) [2]
- to provide low resistance path to ground and prevent unwanted voltages from appearing between units
- to reduce electromagnetic interference between the circuits arising due to electromagnetic and electrostatic coupling phenomena
- to provide an equipotential reference surface for circuits
- to protect against shock hazards arising from harness damage.

2 Spacecraft Grounding Requirements and Design Approaches

The following points regarding the ground shall be ensured during the design of electrical and electronic systems

- (1) Ground plane shall act as an equipotential reference to all systems, subsystems, structures and other connected elements.
- (2) Power return through ground plane shall be avoided. Power supply lines shall be provided with dedicated return lines.
- (3) Separate returns shall be ensured for power and signal lines.
- (4) Separate grounds for signal and power circuits are to be maintained. They shall be electrically isolated from each other except at the point of reference. Each circuit reference shall be connected to structure at one point only.
- (5) Within the subsystem, separate ground planes shall be established for analogue and digital circuits, and both shall be connected to each at only one point.

3 Grounding Plane Requirements

A good ground plane is very essential for obtaining reliable, interference-free equipment operation. An ideal ground system offers a zero-impedance to all signals and will provide an equipotential common reference throughout the system. A ground plane shall have low segment inductances, and it must be able to absorb all signals while remaining stable.

A ground plane shall be constructed of low impedance material. Practically, a spacecraft structure consists of a number of parts, viz. equipment panels, decks, brackets and interface ring. The construction of these parts is generally with a honeycomb structure having aluminium/CFRP face-skins. The formation of the entire structure is realized by the mechanical assembly of all these parts. An equipotential surface of all these structural components has to be realized by the process of bonding. This bonding ensures to equalize the potential between the items and thus ensures that minimum potential difference develops between the structural components over a broad range of frequency, typically from DC to several tens of MHz. Non-conductive adhesives, formation of oxides and in case of CFRP the basic characteristics of the material itself will be problem in achieving equipotential surface. Care shall be taken such as not mounting any electrically active equipment on CFRP, providing copper mesh, etc. to overcome these problems and ensure good ground plane throughout the satellite.

3.1 Characteristics of Ground Plane

A ground plane is predominantly resistive for frequencies below 1 MHz. In a given frequency region, the resistance/sq. of a ground plane is same for all the thickness of the face-skin.

The equation for determining the impedance between two points on a plane is:

$$Z_{gp} = (R_{DC} + j \cdot Z_{RF}) \cdot \left[1 + \tan \frac{2\pi \cdot d}{\lambda} \right]$$

R_{DC} = DC resistance of the metal ground plane

The value of R_{DC} is given by

$$R_{DC} = \frac{1000}{\sigma t_{mm}} \Omega/\text{sq.}$$

where

σ = conductivity of the metal (for copper σ is 5.80×10^7 mhos/m and

t_{mm} = metal thickness in mm

The RF impedance of a metal ground plane, Z_{RF} is

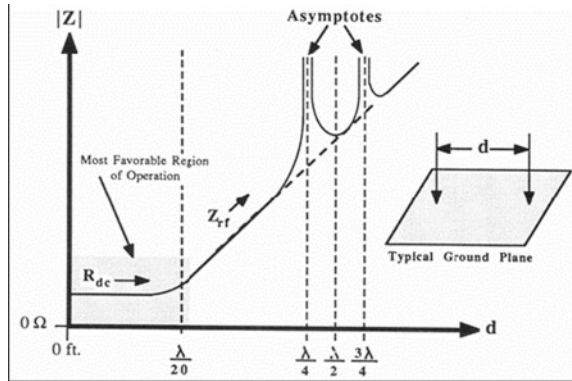
$$Z_{RF} = \frac{369 \sqrt{\mu_r f_{MHz} / \sigma_r}}{1 - e^{-t/\delta}} \mu\Omega/\text{sq}$$

μ_r is the permeability relative to copper

δ is the skin depth in mm = $\sqrt{\mu_r f_{MHz} / \sigma_r}$

The impedance between two points in a ground plane will approximate the above Ω/sq value provided the ground plane is at least as wide as the distance between the two ground points, and this distance, d , is short compared with a wavelength, λ .

Fig. 1 Impedance between connection points on typical ground plane as a function of separation of the connection points (in terms of wavelengths)



Beyond 1 MHz, the ground plane impedance of a 0.1 mm or a 10 mm thick ground plane is same.

Asymptotic rises in impedance may be expected at the first resonant point encountered (0.25λ) on the plane and at each succeeding odd-order multiples. Even order multiples (0.5λ) approach the expected impedance along the dotted line (see Fig. 1). The most favourable area of operation for the ground plane is in the range $< \lambda/20$ at the highest frequency of concern.

Except when the harmonically repeating asymptotic points are being approached, the ground plane offers three to four orders of magnitude less impedance than single wire of any practical cross-sectional area connected across distance “ d ”.

4 Types of Grounding Systems [3, 4]

A common grounding scheme will not work for all systems or circuits. A ground configuration suitable to low-frequency systems cannot be used for high frequencies if used causes detrimental effects. Different types of grounding schemes are discussed here. Depending on the application, criticality, frequency and other parameters, suitable grounding scheme for a system is selected.

4.1 Single-Point Grounding

The single-point grounding scheme is shown in Fig. 2. In this configuration, all the subsystems circuit common points are connected to ground at single ground reference point (SGRP). This single point is connected to satellite structure. Individual wires will be brought from all subsystem circuit commons and connected to single reference point. There is no connection between secondary of the subsystem circuit and chassis within the subsystem. Isolation between subsystems circuit common

Fig. 2 Single-point (star) grounding

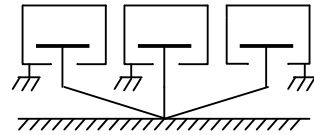
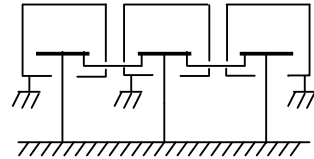


Fig. 3 Multiple-point grounding



points is available. There is only one path to available to ground reference point from each subsystem, thereby eliminating ground loops. As all the circuit common points are connected to one point, this scheme can also be called as “star ground”.

At low frequencies, single-point grounding scheme is very effective. As the frequencies increase, long wires will pose higher inductance and this will reduce the effectiveness of grounding and subsystem common point will have nonzero potential with respect to ground reference point.

4.2 Multiple-Point Grounding

Multiple-point grounding scheme is shown in Fig. 3. As the name suggests, subsystems are connected to ground through multiple points. Each subsystem circuit common is connected to ground at nearest point instead of taking them to single reference point.

In this configuration, each circuit common is grounded to spacecraft structure directly and also indirectly through the connections to other subsystems. This grounding scheme is widely used in radio frequency (RF) subsystems. There is no isolation between subsystems.

4.3 Distributed Single-Point Grounding

Distributed Single-point grounding in contrast with single-point grounding, subsystem circuit common is connected to structure(ground reference) at nearest point instead of taking them to single reference point as shown in Fig. 4. This connection path will be made as short as possible. Each subsystem will have a single path to the chassis (the zero-voltage reference). Subsystems are designed in such a way that current in structure is zero. All subsystems have a common DC voltage reference potential (the interconnected structure). Ground connection wires are made

Fig. 4 Multiple single-point grounding

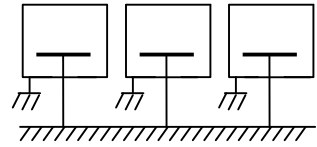
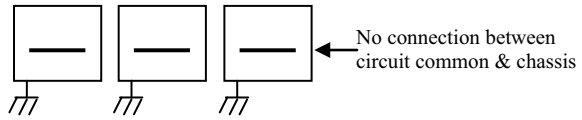


Fig. 5 Floating (isolated) grounds



small there by making the AC impedance between each circuit common and chassis minimum. There is no direct connection between two subsystem circuit commons. Modern spacecrafts (S/C) employ this grounding architecture, as this scheme offers isolation of interfaces and structure currents are minimized.

4.4 Floating Ground System

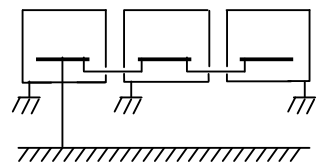
Subsystem circuit commons are not referenced to any point in this configuration, so it is called floating ground system. Figure 5 shows floating ground system. Absence of electrical connection between circuit common and chassis may cause differential potential build-up due to spacecraft charging and can lead to arcing and failure. Due to isolated circuit commons, subsystems will become vulnerable to noise from parasitic paths; hence, this scheme is not preferred.

If the subsystem design requires isolation between circuit common and chassis, a bleed resistor of high value which has negligible effect on electrical circuit to be connected between them. Bleed resistor provides the path for discharge of any stray charge present on circuit to ground, thus providing a “soft” ground reference.

4.5 Daisy-Chain Ground System

Subsystems circuit commons connected to each other forming a chain and at one point this chain is connected to ground reference point. Figure 6 shows a daisy-chained

Fig. 6 Daisy-chained ground system



ground system.

Shared return wires cause common mode voltage differences (circuits “talk” to each other through common mode impedance coupling). There can be a potential difference between circuit common to ground reference point and also between two circuit commons as each subsystem is not connected to ground reference point through shortest distance.

5 Grounding Configuration for Small Satellites

Advancement in electronics enabled the reduction in the size of components and packing of multiple devices into single device. Thereby, the circuits are becoming smaller in size and complex in functionality. Complexity of small satellite subsystems is ever increasing to accommodate the more functionality within smaller size. Care shall be taken in selection of suitable grounding scheme and also proper implementation for reliable operation of subsystems in small satellites.

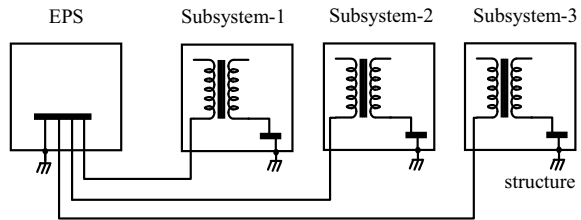
In spacecraft, no conducting surface shall be left floating. Even for the components within the subsystem, unconnected pins shall be either grounded or to be connected to Vcc depending on functionality. All conducting surfaces which are not part of any electrical circuit, primary and secondary circuit commons shall be connected to ground. If conducting surfaces are not grounded, spacecraft charging causes potential build-up between floating surfaces and may cause arcing and lead to failure.

Isolated (floating) ground system is not recommended and highly discouraged from usage in spacecrafts due to floating conducting surfaces and also other associated disadvantages. Daisy-chained configuration is simple, but impedance of daisy chain connecting elements will cause different subsystem circuit commons at different potentials and also EMI problems. Multiple-point grounding offers multiple paths to return currents, thereby forming ground loops. This gives rise to EMI problems.

Single-point grounding connects all subsystems to single ground reference point, thereby avoiding ground loops, hence less EMI. Distributed parasitic capacitances between units and cables in single-point grounding system provide parasitic path to ground at higher frequencies. Impedance of ground leads force more current to flow through parasitic paths. This is problematic if the interconnection cable lengths are longer than $\lambda/20$. Noise currents flowing in the connection to ground plane will develop a potential difference between the ground plane and circuit. Long conductors act as antenna at high frequencies. If the connection between circuit and ground plane is long, the RF signals can couple with the conductor which cause a voltage difference between ground plane and circuit, and this may interfere with the correct operation of the equipment. It is sometimes possible that the resonant frequencies of even small inductances acting with circuit capacitance often fall within the operating frequency of the circuit.

Distributed single-point grounding eliminates these problems by connecting the individual circuit common to ground plane with shortest distance, thereby reducing the reactance between circuit common to ground plane. Each subsystem is connected

Fig. 7 Small satellite of distributed single-point grounding configuration



to ground plane at one point only; hence, ground loops are avoided and EMI problems are reduced.

6 Typical Small Satellite Grounding Configuration

Considering the advantages and disadvantages of different grounding schemes discussed in Sects. 4 and 5, distributed single-point grounding is preferred for small satellite systems. A typical configuration of distributed single-point grounding is shown in Fig. 7.

Spacecraft subsystems are supplied from electrical power system (EPS) at bus voltage. Isolated DC–DC converters present inside the individual subsystem will convert the incoming supply to required voltage levels. Isolated DC–DC converter primary side power supply return will be brought to EPS. In EPS where power returns of all the subsystems are brought, they are connected to a common point called “single ground reference point (SGRP)”. SGRP is connected to satellite structure at only one point. Except at SGRP primary power returns are not connected anywhere to chassis. As the individual return wires are brought from the subsystems to EPS, ground will not carry current and used as reference point only.

Circuits within the subsystem are referred to isolated DC–DC converter negative terminal on secondary side, and this is called circuit common for subsystem. This circuit common is connected to subsystem chassis at only one single point. Subsystem chassis is mounted on spacecraft structure ensuring proper contact for minimum resistance. Spacecraft structure acts as ground (common reference) plane for entire spacecraft. It is ensured that sufficient isolation is available between circuit common and subsystem chassis when the connection between these two is removed at the single point. There is no direct connection between circuit commons of two subsystems, thereby avoiding ground loops.

7 Conclusion

This paper discussed the need for grounding in satellites and effect of improper grounding. Different types of grounding schemes and their applicability to small

satellites were considered. Based on the advantages and disadvantages of different grounding schemes, it was found that distributed single-point grounding is most suitable for small satellite systems due to reduced impedance of return paths and avoiding ground loops.

References

1. IEEE Std 142-2007
2. NASA Reference Publication 1374—Electronic systems failures and anomalies attributed to electromagnetic interference
3. MIL-HDBK-419A—Military handbook grounding, bonding, and shielding for electronic equipments and facilities
4. NASA-HANDBOOK-4001—Electrical grounding architecture for unmanned spacecraft

High Energy and High-Power Lithium Polymer Cells for Space and Satellite Application



S. Loganathan, C. Althaf and S. Noorulla Basha

Abstract Evaluation studies were carried out to assess the suitability of high energy and high-power 75 Ah lithium polymer cells for space and satellite applications. The study includes evaluation of cell nominal capacity, Ah efficiency at different discharge rates, loss of capacity on storage and performance of the cell at different discharge rates. It also explains about the fast chargeability, self-discharge characteristic of the cell and effect of temperature on the performance of the cells. The study has been carried out at different temperatures ranging -30 to 60 °C at different C rates (0.5C to 6C). The cells were charged at constant current of 0.5C until the on-charge voltage reaches 4.2 V, then soaked at different temperatures from -30 to 60 °C for 16 h and discharged at different currents varying 0.5C to 6C. The above experiment was repeated by charging at different currents and discharging at 1C at 23 °C. The self-discharge characteristics were analysed by charging at constant current of 0.5C then stored for the period of 1 day, 7 days, 14 days and 28 days and discharged at 0.5C at 23 °C. The suitability of low temperature operation for satellite and space application was discussed and the results were presented.

Keywords Batteries · Space and satellites · Lithium polymer · Efficiency · Temperature effects · C rates · Charging · Discharging · Self discharge · MATLAB

1 Introduction

Batteries are used in virtually all space applications. The primary goal of any space energy storage technology is to provide power at the highest possible specific energy with sufficient durability in the mission environment and in the case of rechargeable storage, sufficient cycle life. There are many ways that flight systems can deal with

S. Loganathan (✉) · S. Noorulla Basha
Research Centre Imarat, Hyderabad, Telangana 500069, India
e-mail: loganathans@rcilab.in

C. Althaf (✉)
Manipal Institute of Technology, Manipal 576104, India
e-mail: althaf.c@learner.manipal.edu

© Springer Nature Singapore Pte Ltd. 2020
PSR. S. Sastry et al. (eds.), *Advances in Small Satellite Technologies*,
Lecture Notes in Mechanical Engineering,
https://doi.org/10.1007/978-981-15-1724-2_29

the challenges, but the least expensive ways are often those where the technologies are able to work directly in the environment. The missions to space are outer planetary, inner planetary, mars and small body missions. Batteries are used as primary and secondary sources in space missions. Researchers are investigating on advance batteries that can provide more specific energy than current lithium batteries. Nickel Cadmium and Nickel Hydrogen batteries are secondary batteries used in many space applications which were later replaced by Li-ion battery. Lithium, being the lightest metallic element, low equivalent weight (6.941) and high standard electrode potential (-3.04V Vs SHE) has higher energy density and high specific energy which is twice that of Nickel Cadmium and Nickel Hydrogen batteries [1].

The 75 Ah high energy and high-power superior lithium polymer cell is a rechargeable type battery with wide operating temperature. The selected cell is developed and manufactured by M/s XALT Energy, LLC which was formerly known as Dow Kokam, head quartered at Midland, Michigan, with nickel manganese cobalt cathode cells and graphite anodes (NMC/G). The high-energy lithium polymer cells are used in spacecraft for the equipment and payload during Sun eclipse periods, for night-time or eclipse-time experimentation, for communicating and data transmission, to keep the electronics warm and for load levelling (to augment nuclear power source). The high-power lithium polymer cells are used during launch and post-launch (until the deployment of solar panels in inner planetary missions), for firing pyros and firing rockets for attitude control, to correct cruise anomalies or support trajectory control maneuvers of the spacecraft. The nominal voltage of both high energy and high-power cell is 3.7 V and has upper voltage limit of 4.2 V. MATLAB and Origin software were used to plot and analyse the data. The purpose of this study is to identify candidate advanced energy storage technologies that will enable or significantly enhance the capabilities of future planetary science mission concepts.

1.1 Mission Specific Needs

- Outer Planet Orbital Missions: Rechargeable batteries with long calendar and cycle life and compliance with planetary protection requirements for Ocean Worlds.
- Outer Planet Surface Missions: Primary batteries with low temperature ($<-60\text{ }^{\circ}\text{C}$) performance, radiation survivability, compliance with planetary protection requirements (OW).
- Venus Aerial Missions: Rechargeable batteries that can survive high temperature ($25\text{--}350\text{ }^{\circ}\text{C}$), high pressure and corrosive environments
- Mars Aerial Missions: Rechargeable batteries with wide operating temperature capability ($-40\text{ to }40\text{ }^{\circ}\text{C}$), high-power capability and compliance with planetary protection requirements
- Small Body Orbital Missions: Rechargeable batteries with long calendar and cycle life with wide operating temperature capability ($-40\text{ to }40\text{ }^{\circ}\text{C}$) [2].

2 Experiment

2.1 High-Power Lithium Polymer Cell

In this study, constant current charging of cell was done delta power supply (100 V/50 V, 37.5 A/75 A). The cells were initially charged at constant current of $C/2$ (37.5 A) until the voltage reaches 4.2 V and constant voltage charging of 4.2 V is maintained for 1 h or until the current decayed to 1 A. The cells were soaked for the period of 16–24 h in climatic chambers at different temperatures (-30 , -20 , -10 , 0 , 45 and 60 °C). After the completion of respective soaking period, the cells were discharged at $C/2$, $1C$, $2C$, $3C$, $4C$, $5C$ and $6C$ at different temperatures by using programmable DC electronic load bank (Chroma 100 A/1000 A, 16 V/80 V 15.6 kW). The temperature sensors were placed at four different position of the cell to ensure that the same temperature was maintained. At this case, the discharge studies of HP Li-polymer cell at different C rates at above-mentioned temperatures were analysed. This study explains about the effect of temperatures at different rates from $0.5C$ to $6C$ at constant temperature and vice versa.

The fast chargeability test of selected HP Li-polymer cell was carried out at $C/2$, $1C$, $1.5C$, $2C$, $2.5C$ and $3C$ at constant temperature (23 °C) and discharged at constant current of $1C$ at 23 °C. Self-discharge studies were carried out by charging at constant current of $C/2$ rate maintained at room temperature then stored for the period of 1 day, 7 days, 14 days and 28 days. After the completion of respective storage time interval, the cell is discharged at $C/2$ rate.

2.2 High Energy Lithium Polymer Cell

Experimental analysis of HE Li-polymer cell was carried out initially by charging at constant current of $C/2$ (37.5 A) using delta power supply (100 V/50 V, 37.5 A/75 A), until the voltage reaches 4.2 V and constant voltage charging of 4.2 V is maintained for 1 h or until the current decayed to 1 A. The cells were soaked for the period of 16–24 h in climatic chambers at different temperatures (-20 , -10 , 0 , 45 and 60 °C). After the completion of respective soaking period, the cells were discharged at $C/2$, $1C$, $2C$, $3C$ at different temperatures by using programmable DC electronic load bank (Chroma 100 A/1000 A, 16 V/80 V 15.6 kW). The temperature sensors were placed at four different position of the cell to ensure that the same temperature was maintained. At this case, the discharge studies of HE Li-polymer cell at different C rates at above-mentioned temperatures were analysed. This study explains about the effect of temperatures at different rates from $0.5C$ to $6C$ at constant temperature and vice versa.

Self-discharge studies were carried out by charging at constant current of $C/2$ rate maintained at room temperature then stored for the period of 1 day, 7 days, 14 days and 28 days. After the completion of respective storage time interval, the

cell is discharged at $C/2$ rate. The fast chargeability test of selected HE Li-polymer cell was carried out at 1C, 1.5C and 2C, at different temperature (0, 23 and 45 °C) and discharged at constant current of 1C at 23 °C.

3 Results and Discussion

Evaluation studies were carried out to assess the suitability of high power and high-energy 75 Ah lithium polymer cell for space and satellite applications. The experiments were carried out for both high energy and high-power lithium polymer cells with different temperature ranging $-30, -20, -10, 23, 45$ and 60 °C at different C rates (0.5C to 6C) with keeping temperature as constant and vice versa.

3.1 Effect of Temperature

High-Power Lithium Polymer cells were initially charged at 0.5C at constant temperature of 23 °C and discharged at 0.5C, 1C, 2C, 3C, 4C, 5C and 6C at different temperatures ($-30, -20, -10, 0, 23, 45$ and 60 °C). At this case the discharge studies of HP Li-Polymer cell at different C-rates at above-mentioned temperatures were analysed. Results show that the HP Li-polymer cells delivered the energy with greater efficiency of 96.6% discharged at 1C (75 A) at 23 °C (Fig. 1). The cell has capability to deliver energy at -30 °C with 73.3% efficiency at 1C rate. It was also noted that the HP Li-polymer cell failed to deliver energy at -30 °C when discharged

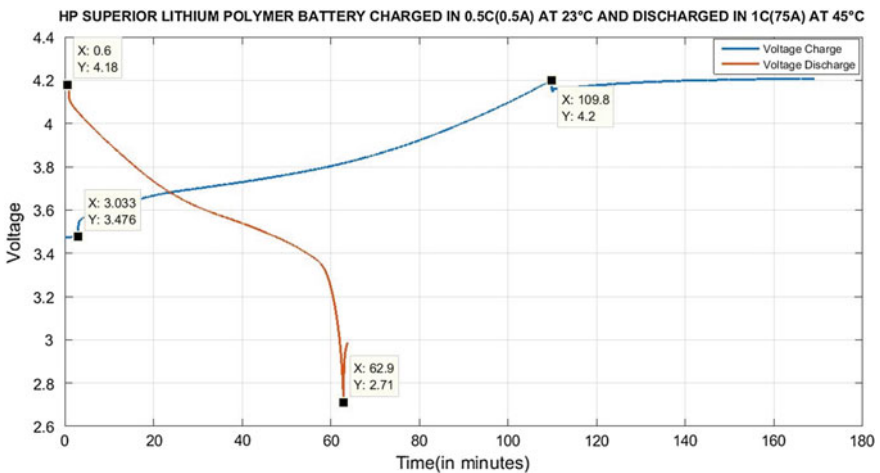


Fig. 1 Graphical representation of HP Li-polymer cell charged in $C/2$ (37.5 A) at 23 °C and discharged in 1C(75 A) at 45 °C

at 2C rate with the cut-off voltage of 2.7 V. At 0 °C, HP Li-polymer cell could deliver energy with greater efficiency of 75% at 6C rate when compared to -10 °C, where the cell failed to meet its target.

At 45 °C, it is observed that the cell was able to deliver the energy even at 5C rate with slightly overstepping its operating temperature limit of 62 °C. When the cell is discharged in 1C (75 A) at 60 °C, there was gradual increase in its operating temperature beyond the limit and failed to meet the mission requirement (Figs. 2 and 3).

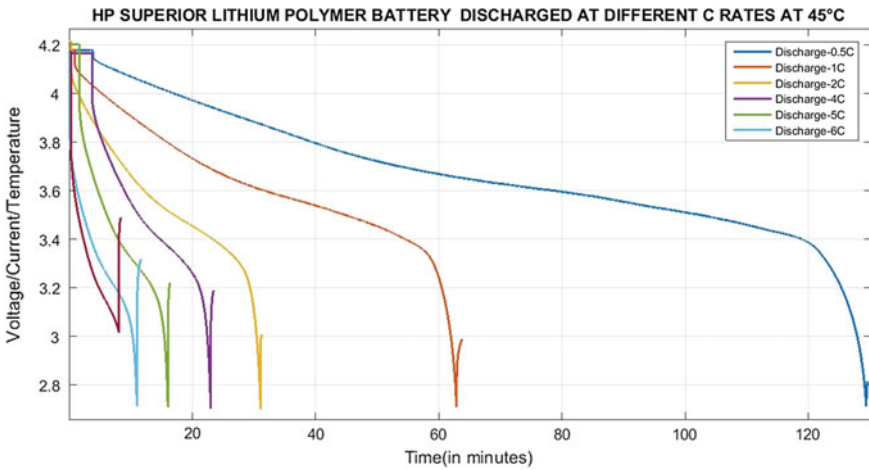


Fig. 2 Graphical representation of HP Li-polymer cell discharged in 0.5C(37.5 A), 1C(75 A), 2C(150 A), 3C(225 A), 4C(300 A), 5C(375 A), 6C(450 A) at 45 °C

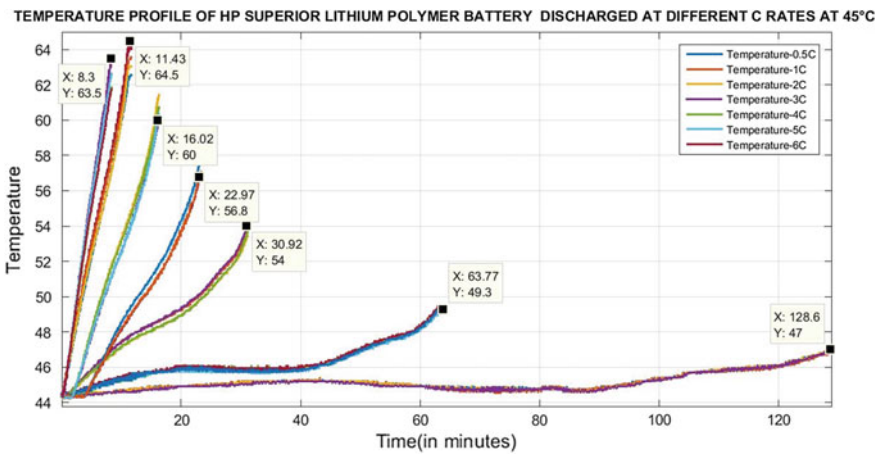


Fig. 3 Graphical representation of overall temperature curve-HP lithium polymer cell discharged in 0.5C(37.5 A), 1C(75 A), 2C(150 A), 3C(225 A), 4C(300 A), 5C(375 A), 6C(450 A) at 45 °C

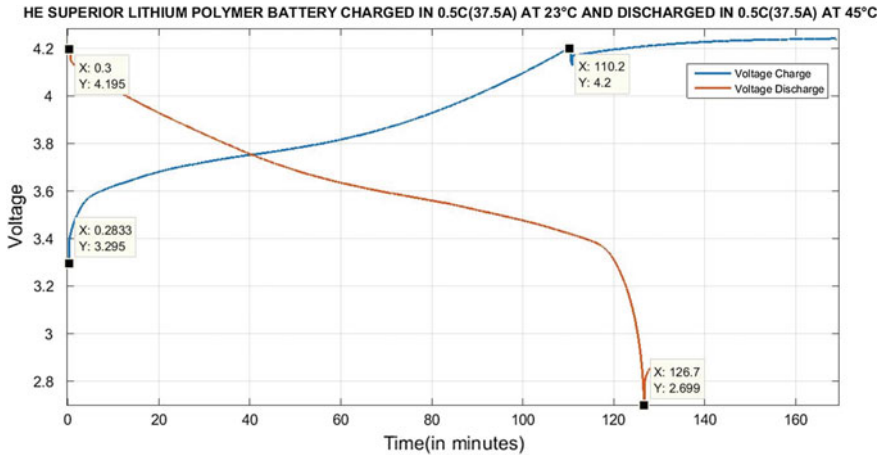


Fig. 4 Graphical representation of voltage curve of HE lithium polymer cell charged in 0.5C(37.5 A) at 23 °C and discharged in 0.5C(37.5 A) at 45 °C

The High-Energy Lithium Polymer cells were charged at 0.5C at constant temperature of 23 °C and discharged at 0.5C, 1C, 2C and 3C at different temperatures (−20, −10, 0, 23, 45 and 60 °C). Results show that the HE Li-polymer cells delivered the energy with greater efficiency of 100% discharged at 1C (75 A) at 23 °C. At lower temperature (−20 °C), the performance of the cell was effective (76.6% @ C/2 and 80% @ 1C) when compared to HP Li-polymer cell. It was also noted that the HP Li-polymer cell failed to deliver energy at 45 °C when discharged at 3C rate, it crossed its operating temperature limit of 62 °C (Figs. 4 and 5).

3.2 Fast Chargeability Characteristics

The fast chargeability test for both high energy and high-power cells was analysed. Results show that the HP Li-polymer cell can be charged even at 3C rate at 23 °C and the cell can even be charged at 3C(225 A) with the charging efficiency of 50%. At 23 °C, the cell was able to charge at 95.83% at 0.5C (37.5 A) within its operating temperature limit. Figure 6 shows the performance of high-power lithium polymer cell charged at different C rates.

The fast chargeability test of selected HE Li-polymer cell was carried out at 1C, 1.5C, 2C at different temperature (23, 45 °C) and discharged at constant current of 1C at 23°C. The results showed that the cell can even be charged at 2C (150 A) with the charging efficiency of 76%. The cell was able to charge at higher temperature (45 °C) at 86.6% at 1C (75 A). When charged at 2C (150 A), the performance of the cell was 75% (Fig. 7).

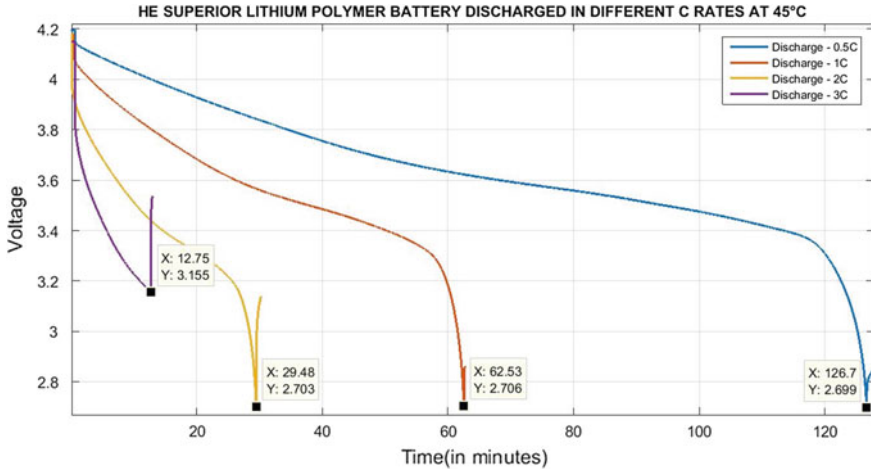


Fig. 5 Graphical representation of HP Li-polymer cell discharged in 0.5C(37.5 A), 1C(75 A), 2C(150 A), 3C(225 A) at 45 °C

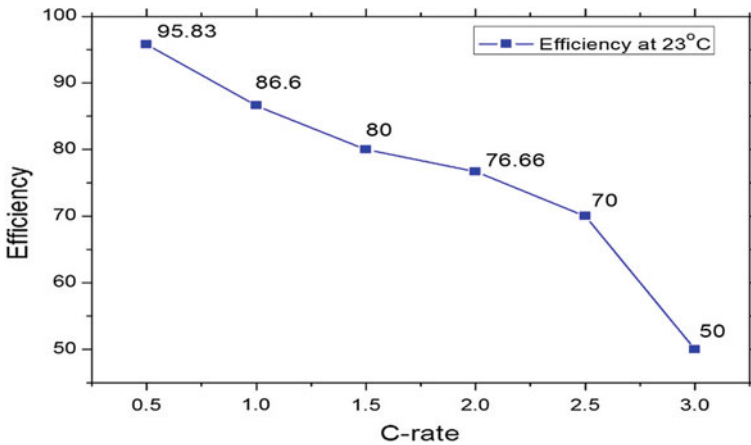


Fig. 6 Graphical representation of HP lithium polymer cell charged in different C rates at 23 °C

3.3 Self-discharge Characteristics

Self-discharge studies on high energy and high-power lithium polymer cell were performed. The cells were charged at constant current of 0.5C then stored for the period of 1 day, 7 days, 14 days, and 28 days and discharged at 0.5C at 23 °C. The self-discharge studies of HP Li-polymer cell is in progress. For HE Li-polymer cell, it is observed that there was no loss of energy when the cell is discharged after 7th and 14th day periodic storage. At 21st and 28th day of storage, there is a slight deflection

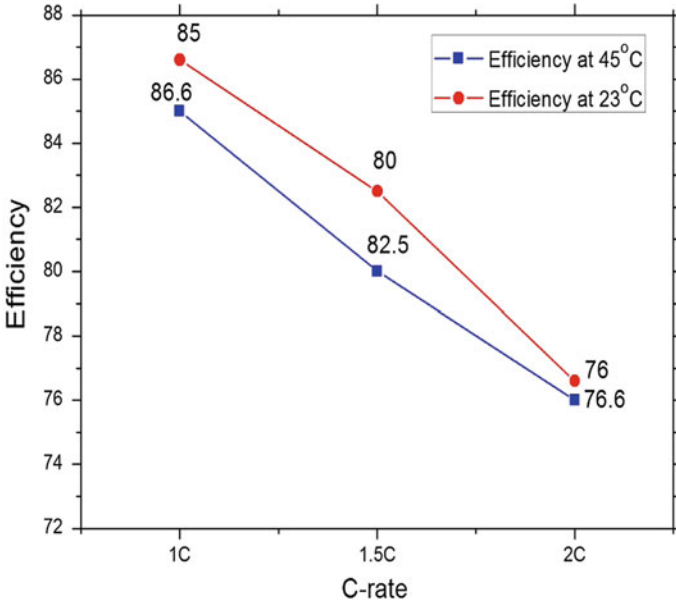


Fig. 7 Graphical representation of HE lithium polymer cell charged in different C rates at 23 and 45 °C

in the performance of cell that it could deliver the energy with the efficiency of 97.5% on 21st day of storage and 96.6% at 28th day. This shows that the cell has less self-discharge reactions on the cell at 23 °C (Fig. 8).

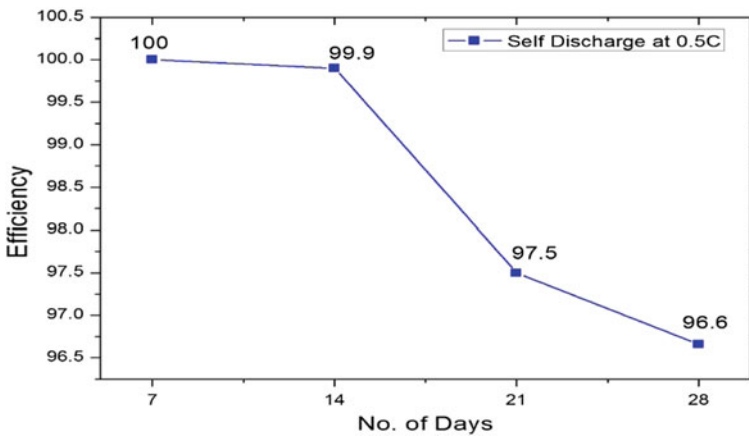


Fig. 8 Graphical representation of HE lithium polymer cell discharged in 0.5C (37.5 A) at 23 °C after periodic storage of 7, 14, 21 and 28 days

4 Conclusion

Evaluation studies to assess the suitability of high energy and high-power 75 Ah lithium polymer cells for space and satellite applications were carried out. The study has been carried out at different temperature ranging -30 to 60 °C at different C rates (0.5C to 6C). The performance of HE Li-polymer cell was promising when compared to HP Li-polymer cell. But at higher C rates, the HE cell failed to operate without overstepping its operating temperature. At 45 °C, it is observed that the HP Li-polymer cell was able to deliver the energy even at 5C rate with slightly overstepping its operating temperature limit of 62 °C. Self-discharge characteristic results after 7 days, 14 days, 21 days and 28 days showed that HE Li-polymer cell able to deliver the energy with 96.6% after 28th day of periodic interval. Both the cells were able to perform at lower temperature with greater efficiency when compared to other lithium ion cells. In future, these cells could able to perform with improved efficiency replacing current lithium ion batteries for space and satellite applications.

Acknowledgements The author would like to thank the Director-RCI, Technology Director-DSST for their support and guidance for successful completion of this work.

References

1. Reddy TB (2011) Linden's handbook of batteries, 4th ed, p 33.2. McGraw-Hill, New York, United Kingdom
2. Bauer P (1968) Batteries for space power systems, written under contract for NASA by TRwr Systems, Redondo Beach, California, NASA SP-172, May 1968

Deep Learning-Based Automatic Micro-crack Inspection in Space-Grade Solar Cells



Sharvari Gundawar, Nitish Kumar, N. Raghu Meetei,
Ganesan Krishna Priya, Suresh E. Puthanveetil and Muthusamy Sankaran

Abstract Spacecraft power systems reliability is critical parameter for mission success. Multiple checks and inspections are carried out for each component for power subsystems. In this paper, a novel automated solar cell micro-crack inspection tool is presented which is based on convolutional neural network (CNNs) to classify space-grade multi-junction solar cells taken under electroluminescence condition. The whole system is named ELSIS, which stands for “Electroluminescence Smart Inspection System”. It is an end-to-end automated system that acquires images under electroluminescence condition as arrays, identifies each cell and classifies them into two classes namely the cells that exhibit micro-cracks and cells and those that are free of micro-crack. ELSIS is developed with the objective to reduce the tedious and time-consuming manual effort required to identify micro-cracks and to increase the reliability of the solar cell modules by minimizing the human errors which may arise during the manual inspection of thousands of solar cells for spacecraft by automating the whole process. The CNNs for ELSIS have been developed in TensorFlow framework in Python based on InceptionV3 architecture. ELSIS is augmented with the latest image processing techniques that are applied to acquire EL images, which are modules containing array of solar cells (Fig. 1). ELSIS thus identifies and

S. Gundawar (✉) · N. Kumar · G. Krishna Priya · S. E. Puthanveetil
Power Systems Group, URSC, U R Rao Satellite Centre, Bangalore 560017, India
e-mail: sharvari@isac.gov.in

N. Kumar
e-mail: nitish@isac.gov.in

G. Krishna Priya
e-mail: priya@isac.gov.in

S. E. Puthanveetil
e-mail: eps@isac.gov.in

N. R. Meetei
DTDI, ISRO HQ, Bangalore, India
e-mail: nraghu@isro.gov.in

M. Sankaran
Communication & Power Area, URSC, Bangalore 560017, India
e-mail: msankar@isac.gov.in

© Springer Nature Singapore Pte Ltd. 2020
PSR. S. Sastry et al. (eds.), *Advances in Small Satellite Technologies*,
Lecture Notes in Mechanical Engineering,
https://doi.org/10.1007/978-981-15-1724-2_30

produces individual solar cells from the arrays and indexed and stored. The deep learning network was trained on a large number of solar cell >6000 images such that cross-entropy of the network settles within an accepted constant value. The trained network when tested for a large sample size of ~3000 new solar cells yielded a very reliable >98% accuracy. ELSIS helps in capacity building for scale manufacturing of satellites with stringent power budget, making it imperative to have zero defect solar cells.

Keywords Solar cells · Electroluminescence · Neural networks · Transfer learning · Convolutional neural networks

1 Introduction

Satellites can operate for long periods only if they have a reliable energy source. The satellites operating in the inner solar system usually rely on photovoltaic solar panels as a primary source of power. At present, ISRO spacecraft are using variants of InGaP/InGaAs/Ge multi-junction solar cell with efficiency ~30% at 1AM0. Such solar cells are welded into modules which are in turn then bonded onto solar panels. For space applications, solar panel fabrication is often done at the nodal agency with their size and design customized to the need of a particular mission. To obtain an efficient solar power generation system, it is necessary to have solar cells with zero defects which greatly affects the power generation. Micro-crack is one such defect. This defect propagates when it goes through the hazardous environment which space provides, leading to the formation of major cracks. This results in degradation of the solar power generation system [1, 2]. Each satellite consists of many solar panels where each panel in turn comprises of hundreds of space-grade solar cells. Hence, it is imperative to avoid any micro-cracks on the solar cell panel to obtain a product with high reliability and high efficiency.

Chances of occurrences of cross-shaped (X) micro-cracks (Fig. 1) are high while welding of large number of solar cells into modules. This happens despite welding with optimized weld parameters due to minor deviations in cell thickness, metallization and presence of minor crystal defects at the weld locations. This work mainly

Fig. 1 EL image with welding micro-cracks

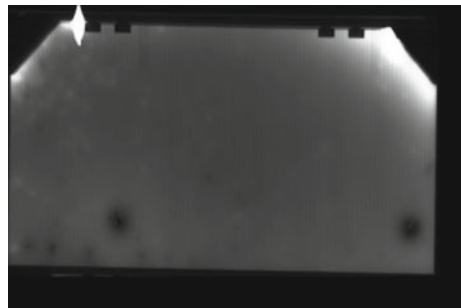
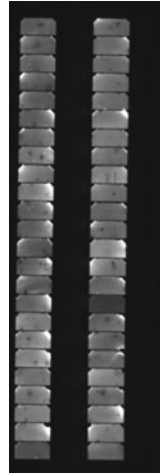


Fig. 2 Solar cell module EL Image



focuses on detecting these weld point micro-cracks in an automatic way. One way to detect these defects (and other semi-conductor defects) is electroluminescence imaging [1, 2].

1.1 Electroluminescence Imaging

Electroluminescence imaging is based on the radiant inter-band recombination of excited charge carriers in solar cells. In this method, a solar cell module (Fig. 2) is operated as a light-emitting diode (LED) by passing electric current through it and the radiation due to the recombination effects is detected through sensitive cameras. EL is a non-destructive, high-resolution method.

1.2 Inspection of EL Images

The usual method to detect these cracks is through visual inspection of solar cell modules or manually inspecting the EL images of the modules. As there is a large quantity of solar cells to be inspected, using manual or semi-manual methods is very labourious and tedious. Experts are needed for such methods, making it a very expensive exercise. The given method intends to identify the micro-cracks automatically without any expert need, using convolutional neural network-based deep learning algorithm.

1.3 Supervised Learning

Supervised learning is a machine learning technique used for inferring a function from given training data. The data consists of pairs consisting of an input object (typically a vector) and a desired output value. This technique analyses the training data and produces an inferred function, which can be used to map new data [3]. Supervised learning has proved its potential in areas like handwriting recognition, pattern recognition, bioinformatics, speech recognition, etc. [3]. Supervised learning can be realized using neural networks for classification of data. Neural networks have already been used to identify cracks in concrete structures [4].

1.4 Related Work

Previous work has been done in using computer inspection for crack detection in EL images of solar cells including detection using texture analysis [5] and Fourier image reconstruction [6]. The micro-cracks with simple straight line geometry were detected by these methods. These image processing algorithms are insufficient for large-scale applications as manual intervention is still needed for each and every cell. Matched filters have also been used for crack detection but cracks with higher length could only be identified [7]. Tsai et al. [8] have presented the detection of cracks using independent component analysis (ICA). Anwar and Abdullah [9], in 2015, presented a technique to detect micro-cracks using an improved anisotropic diffusion algorithm and segmentation method. The algorithms described above are for single solar cells, and thus, solar cell module inspection cannot be done automatically. Bharathkumar and Ashokkumar [10], in 2013, proposed a method to identify cracks in solar panels using bacterial foraging optimization algorithm. To the best of authors' knowledge, the proposed method has been used for the first time for detection of micro-cracks in solar cell modules and the algorithm is fully developed so that it can be used straightaway without any additional software or human interpretation.

The algorithm presented here uses deep learning-based classification to identify the micro-cracks due to welding. The detection goal is challenging due to the presence of heterogeneous background of the multi-junction cell images.

An EL image of a solar cell module (collection of cells welded) is taken as an input and undergoes the following steps—(i) The cells in the module are identified and indexed; (ii) a trained deep neural network is used to check for micro-cracks.

2 Image Separation—Cell Identification and Indexing

Electroluminescence (EL) image of a solar cell module is obtained by the module-level EL unit. This EL image contains module of solar cells as shown in Fig. 2. The

micro-crack identification is done for each cell separately; hence, they have to be cropped out of the module image.

2.1 Cropping Out Cells from the Solar Cell Module

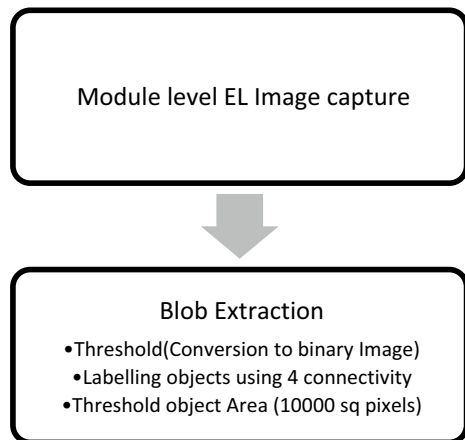
A solar cell module image consists of modules with varying number of solar cells. They need to be separated so that individual images of each cell can be analysed.

The process of cropping out cells from the solar cell module EL image is shown in Fig. 3. An EL solar cell module image is obtained as a greyscale image with 256 levels (8 bit). The value of each pixel lies between 0 and 1. To identify cells from a solar cell module image, the image is first converted to a binary image. For this purpose, an appropriate threshold has to be determined. Threshold technique used here is a combination of two threshold techniques (Otsu’s threshold method [11] and iso-data method [12]). Intermediate threshold is obtained using Otsu’s method, and then, iso-data method is applied to get the final threshold. The details will be discussed in threshold technique section.

Finding the optimum threshold without merging or missing out the cell after conversion to binary is another challenge. Firstly, if the chosen threshold is above the optimum, many cells can be missed out as shown in (Fig. 5). Secondly, if the chosen threshold is below the optimum value, the cells can merge and could be detected as a single cell as shown in (Fig. 4). Being so sensitive, a complex threshold technique has been executed as given below.

The solar cell module EL image (range 0–1) is taken as an input. In case the greyscale values of the image do not cover the entire range of 0–1, then the image is enhanced by expanding the values to the entire range 0–1 to obtain an image as named I (Figs. 4a and 5a).

Fig. 3 Flow chart to identify solar cells from a solar cell module image



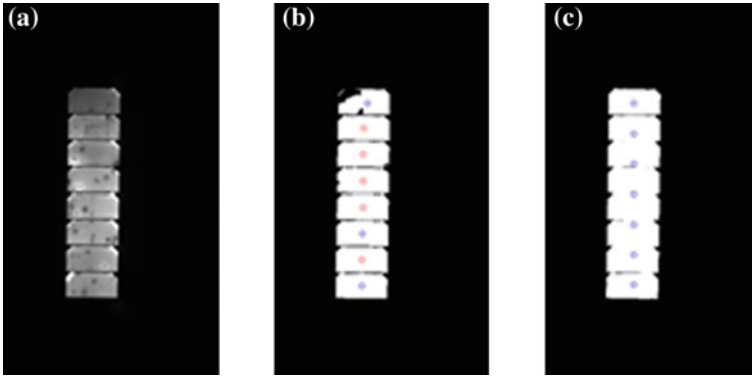


Fig. 4 Cells merged. **a** Original image has 8 cells (I), **b** 8 cells are identified (threshold by original image) and **c** 7 cells identified (threshold by brightened image) [circles represent cells discovered by the software]

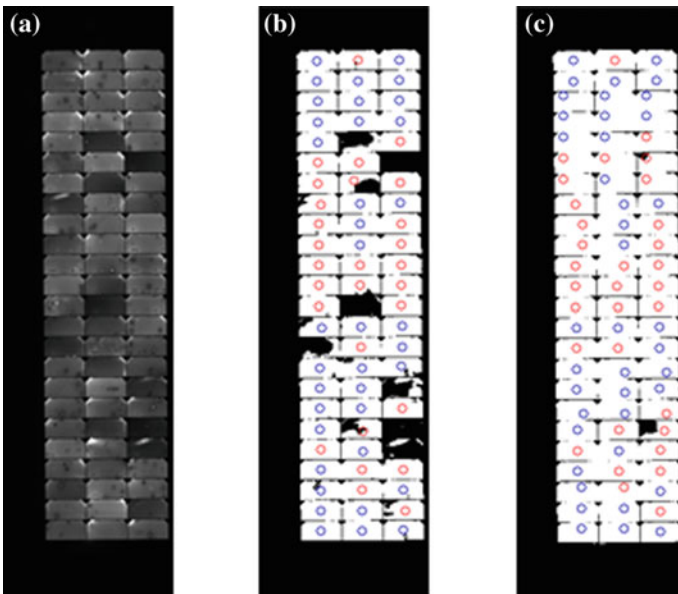


Fig. 5 Cells missed. **a** Original Image has 72 cells (I), **b** 65 cells are identified (threshold by original image) and **c** 72 cells identified (threshold by brightened image) [circles represent cells discovered by the software]

The intensity of image I is increased 5 times so that relatively dark cells are also identified. We denote this image as J.

The threshold technique proposed is used to identify solar cells in the module images I and J.

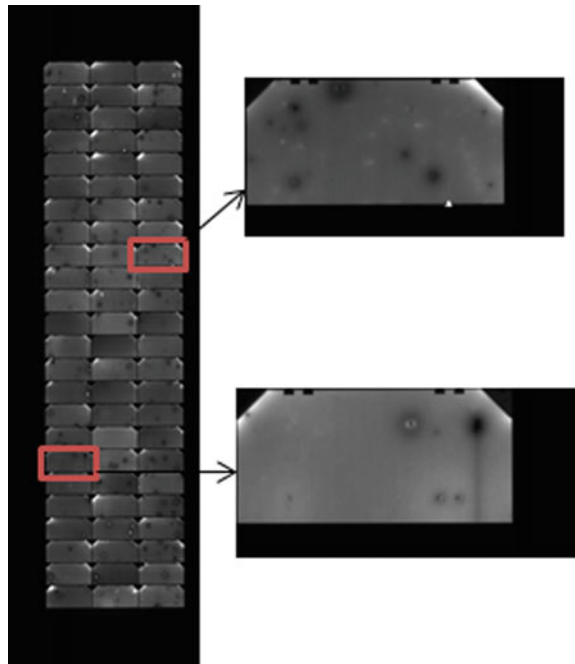
Out of the images I and J, the image giving maximum number of cells after applying threshold is considered.

In case all the cells are equally illuminated (Fig. 4a), image J may be too bright and cells are likely to merge and applying threshold would give number of cells lesser than the actual number (Fig. 4c). So, identification of cells can be done by applying the threshold technique on image I (Fig. 4b).

In case cells are with less intensity, that is, dark cells are present in a solar cell module image(Fig. 5a), there is a possibility of missing out cells after applying threshold to image I (Fig. 5b) and would give number of cells lesser than the actual number. As illumination is high in image J, dark cells are brightened too. So, identification of cells can be done by applying the threshold technique on image J (Fig. 5c).

After conversion to a binary image, the solar cell module image is checked for individual cells using blob extraction [13]. In this, foreground pixels (foreground pixel value is 1) which are surrounded by background pixels (background pixel value is 0) from the cardinal directions(North, South, East, West) are labelled as one single object (4-connected objects [13]). Only objects with area above 1000 sq pixels are identified as solar cells (Fig. 6).

Fig. 6 Solar cells cropped from a solar cell module image



2.2 Uniformity and Positioning of Cells

After identification, these cells go through an image enhancement technique. Here, the grey-level range in which the cells lie (which is always in between 0 and 1) is expanded to the entire range (0–1). This makes the micro-cracks (and other dark spots in the background) appear with an enhanced contrast with the background.

The location of each cell is determined by the position of the centroid of each cell with respect to the entire image. This location is then used to position each cell in the module. Thus, the position of each identified cell is obtained. The separated solar cells are then fed to the neural networks for training and testing which are given in details in Sect. 3.

2.3 Threshold Technique

The Otsu's algorithm assumes that the image contains two classes of pixels [foreground pixels (solar cells) and background pixels (background)]. It then calculates the optimum threshold separating the two classes so that the intra-class variance (σ_w^2) is minimal that is, the inter-class variance (σ_b^2) is maximal [8]. The intra-class variance (σ_w^2) is defined by weighted sum of variances of both the classes [$\sigma_0^2(t)$ and $\sigma_1^2(t)$].

$$\sigma_w^2 = \omega_0(t)\sigma_0^2(t) + \omega_1(t)\sigma_1^2(t) \quad (1)$$

where weights $\omega_0(t)$ and $\omega_1(t)$ are the probability of the classes with threshold t . These weights are computed as the sum of all the probabilities (p_0 and p_1 , resp.) of greyscales lying in the classes. In other words, all pixels with grey-levels 0 to $t - 1$ belong to background class and all pixels with grey-levels t to L belong to solar cells class, where t is the threshold and L is the maximum grey-level value.

$$\omega_0(t) = \sum_{i=0}^{t-1} p_0(i) \quad (2)$$

$$\omega_1(t) = \sum_{i=t}^L p_1(i) \quad (3)$$

$$\sigma_b^2 = \sigma^2 - \sigma_w^2 \quad (4)$$

So, we get

$$\sigma_b^2 = \omega_0(t)\omega_1(t)(\mu_0(t) - \mu_1(t))^2 \quad (5)$$

where

$$\mu_0(t) = \sum_{i=0}^{t-1} ip_0(i)/\omega_0(t) \quad (6)$$

And

$$\mu_1(t) = \sum_{i=t}^L ip_1(i)/\omega_1(t) \quad (7)$$

The desired threshold corresponds to the maximum of inter-class variance (8).

$$t = \max(\sigma_b^2) \quad (8)$$

The obtained threshold (t) is then fine-tuned by finding the average of the mean of the foreground (m_f) and background (m_b) pixels [12] as given is Eq. (11).

$$m_b = \sum_{i=1}^b gs_b(i)/b \quad (9)$$

$$m_f = \sum_{i=1}^f gs_f(i)/f \quad (10)$$

$$t^* = (m_f + m_b)/2 \quad (11)$$

where gs_b and gs_f are the greyscale values and b and f are the number of pixels of the background and foreground region, respectively.

The final threshold obtained (t^*) is then used to threshold the image.

3 Deep Learning-Based Image Classification

3.1 Deep Learning

A deep learning architecture is a stack of several neuron-based layers, which are subject to learning and is trained to compute nonlinear input–output mappings. Each layer in the stack mutates its input to decrease variance of the representation. With multiple nonlinear layers, a system can implement extremely intricate functions

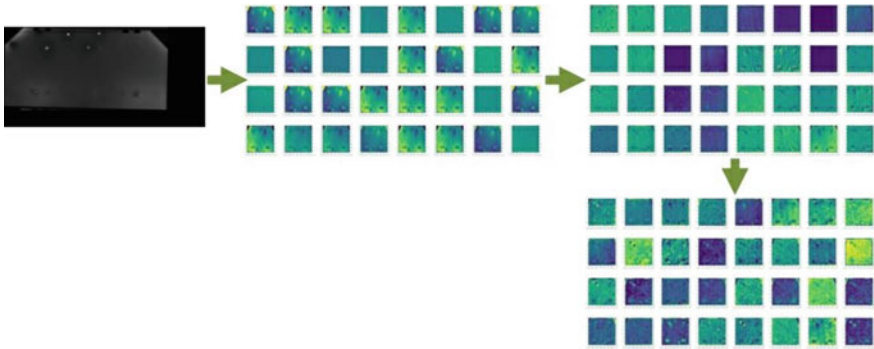


Fig. 7 A glimpse of abstraction in InceptionV3 when a solar cell is fed in (deep learning allows computational models that are composed of multiple processing layers to learn representations of data with multiple levels of abstraction)

of its inputs that are simultaneously sensitive to minute details—like cracks—and insensitive to large irrelevant variations such as the background, pose, lighting and surrounding objects—like the unwanted features of solar cells [14].

Deep learning allows computational models that are composed of multiple processing layers to learn representations of data with multiple levels of abstraction (Fig. 7). Deep learning network has the capability to uncover intricate structure in large data sets. Such networks are trained using the back-propagation algorithm to indicate how a machine should change its internal parameters that are used to compute the representation in each layer from the representation in the previous layer. Revolution is brought about by deep convolutional nets in processing images as well as other domains [14].

Deep learning possesses automatic feature extraction capability reducing the need for feature engineering. The algorithms for deep learning can be adapted to new problems relatively easily. So, we can adapt our technique to classify solar cells for other defects as well, given the appropriate training dataset.

The downside of deep learning image classification is that the network training may take weeks to complete even on high-performance hardware. It would also require humungous amount of data. A way to utilize this powerful tool is through “Transfer learning”.

3.2 Transfer Learning

Transfer learning is an approach in which knowledge learnt in a task is transferred to improve the learning of another related task. It ensures better and faster learning of parameters. In transfer learning, classification layer is learned (end layer) and all the other layers are “transferred” from a pre-trained model (Fig. 8). InceptionV3 model [15] is proposed for transfer learning in this paper as shown in Fig. 10. Our model

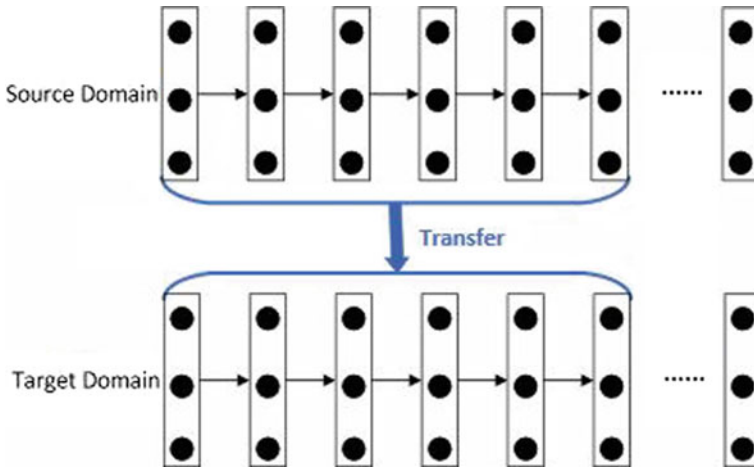


Fig. 8 Sketch map of network-based deep transfer learning. First, network was trained in source domain with large-scale training data set. Second, partial of network pre-trained for source domain are transfer to be a part of new network designed for target domain [16]

was initially trained using the ImageNet database. ImageNet is an image data set that contains thousands of different scenes and objects to train and evaluate network models for image classification.

In transfer learning, the model in target domain is not required to be trained from scratch, which can significantly reduce the demand of training data and training time in the target domain [16].

In transfer learning, we reuse the feature extraction layers of the InceptionV3 model and retrain the classification layer (Fig. 9). After separation of solar cells, they are fed into the feature extraction layers for pre-processing. These pre-processed feature vectors are fed into the classification layer to give out the result in 0 (crack absent) or 1 (crack present).

The InceptionV3 is named after the inception modules it uses. Modules are the heavily engineered blocks of neural network used in a deep learning architecture to increase the performance as highlighted in Fig. 10.

3.3 Adam Optimizer

The adaptive moment estimation (Adam) optimization algorithm is an extension to stochastic gradient descent which is being recently adopted for deep learning applications in computer vision. We have used Adam optimizer for optimizing parameters (training) of the classification layer. It has inherited features from RMSProp and Adadelata optimization algorithms for optimizing weights. In addition to storing an exponentially decaying average of past squared gradients v_t like Adadelata and

Fig. 9 Last layer (final_training_ops) [obtained through TensorBoard]

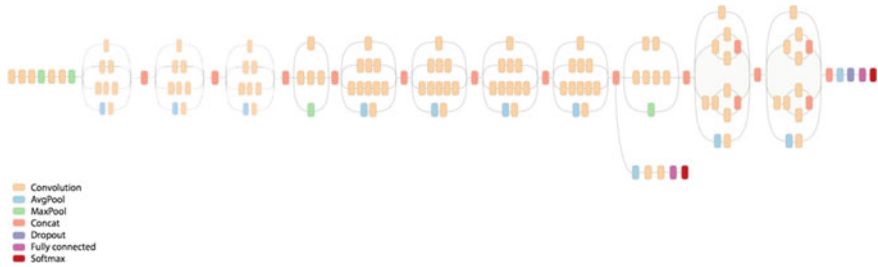
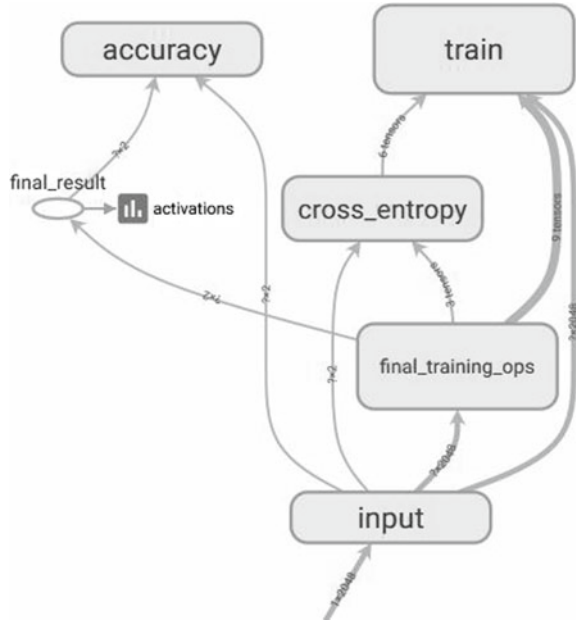


Fig. 10 InceptionV3 neural network architecture [obtained through TensorBoard]

RMSprop, Adam also keeps an exponentially decaying average of past gradients m_t , similar to momentum as given the Eqs. (16) and (15). The authors show empirically that Adam works well in practice and compares favourably to other adaptive learning method algorithms [17].

The Adam optimizer works as given in the pseudo-algorithm [18] given below.
Require:

- $\alpha \leftarrow 0.001$ (step size),
- $\beta_1 \leftarrow 0.9$ and $\beta_2 \leftarrow 0.99$ (Exponential decay rates for the moment estimates)
- $\epsilon \leftarrow 1e^{-8}$ (a small constant for numerical stability)
- $f(\theta)$ (Stochastic objective function with parameters θ)
- θ_0 (Initial parameter vector), $t_0 \leftarrow 0$ (Initialize timestep)
- $m_0 \leftarrow 0$ (Initialize 1st moment vector), $v_0 \leftarrow 0$ (Initialize 2nd moment vector)

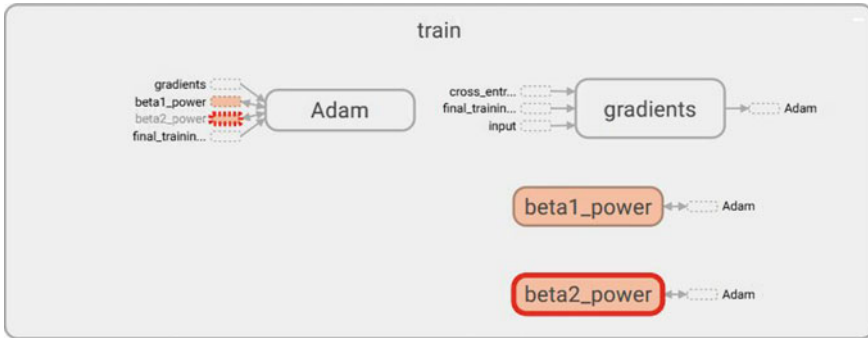


Fig. 11 Training module for the network, Adam optimizer is used [obtained through TensorBoard]

while θ_t not converged do

$$t \leftarrow t + 1 \tag{12}$$

$$g_t \leftarrow \nabla_{\theta} f_t(\theta_{t-1}) \text{ (Get gradients w.r.t. stochastic objective at timestep } t) \tag{13}$$

$$m_t \leftarrow \beta_1 * m_{t-1} + (1 - \beta_1) * g_t \text{ (Update biased first moment estimate)} \tag{14}$$

$$v_t \leftarrow \beta_2 * v_{t-1} + (1 - \beta_2) * g_t^2 \text{ (Update biased first moment estimate)} \tag{15}$$

$$\hat{m}_t \leftarrow m_t / (1 - \beta_1^t) \text{ (Compute bias - corrected first moment estimate)} \tag{16}$$

$$\hat{v}_t \leftarrow v_t / (1 - \beta_2^t) \text{ (Compute bias-corrected second raw moment estimate)} \tag{17}$$

$$\theta_t \leftarrow \theta_{t-1} - \alpha * \hat{m}_t / (\sqrt{\hat{v}_t} + \epsilon) \text{ (Update parameters)} \tag{18}$$

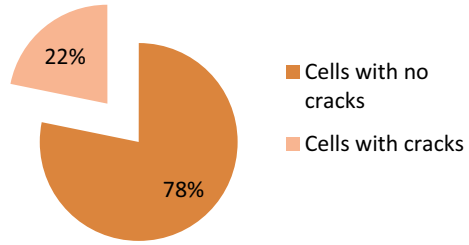
end while

return θ_t (Resulting parameters).

3.4 Training the Model

The data set was collected concurrently with the EL testing of different modules used in various satellites (Fig. 12). This data set was partitioned into separate training, validation and testing sets with 70-10-20 percentage split. For training, a total of 5000 iterations with batch size of 100 were performed. After every 100 training

Fig. 12 Training data



iterations, the model was applied to the validation data set, with a batch size of 100, to evaluate performance on unseen data.

4 Results

We trained the network for 5000 steps and achieved the training accuracy of 98% as shown in Fig. 13a. We used metric called cross-entropy to measure the loss in achieving the correct classification, which has decreased with training as expected (Fig. 13b).

We have tested the trained network for about 3000 images from various satellites. We obtained images of multi-junction solar cell modules used satellites solar panels. The confusion matrix of the solar cells tested is given in Table 1.

In Table 1, from the 2463 cells detected as good, 2419 were without cracks and 44 were observed with cracks. Out of 2702 cells without cracks, 2419 were detected

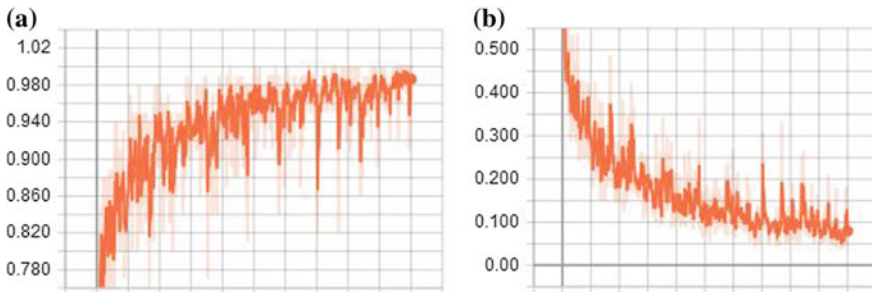


Fig. 13 a Training accuracy for 5000 steps and b cross-entropy for 5000 steps while training

Table 1 Confusion matrix for the tested solar cell images used in various satellites

	Total	True good	True crack
Detected as good	2463	2419	44
Detected as cracks	485	283	202
Total	2948	246	246

without cracks and 283 were detected as cracked cells.

$$p = \frac{tp}{tp + fp}, \quad tp = 2419 \text{ and } fp = 44 \quad (19)$$

$$r = \frac{tp}{tp + fn}, \quad tp = 2419 \text{ and } fn = 283 \quad (20)$$

$$F1 = 2 * p * r / (p + r) \quad (21)$$

We obtained precision accuracy (p) in detecting good cells as 98.21% and recall (r) as 89.52%. The F1 accuracy is another measure for the performance of neural network that is more important in cases where there is an imbalance of dataset. As shown in Fig. (12, the data imbalance shows less number of cracked cells than the good cells, and hence a need for F1 score is underlined here. Using the Eq. (21) data in Table 1, F1 score for identifying good cells is 0.936689. Due to stringent requirements of space conditions and very strict guidelines followed in ISRO, False Positives (fp) are not a concern as every cell flagged as defective is rechecked manually. Only the cells identified as good are not checked and they are passed automatically. Hence, precision of detecting good cells is the key performance parameter in ELSIS, which is 98.21%.

5 Conclusion

The software is tested for 3000 solar cells and an accuracy of 98% is achieved in classifying cells with no micro-cracks, thereby reducing inspection time to a great extent. This software thus reduces the tedious and time-consuming manual effort and increases the reliability of the solar cell modules by minimizing the human errors which may arise during the manual inspection of thousands of solar cells for spacecraft by automating the whole process. This is a step forward towards the automation of all the streamlined activities in the realization of solar panel for satellites. Automation of inspection systems will save the precious expert hours and can be channelized for developmental purposes.

Acknowledgements The team of authors would like to acknowledge the contributions of Mrs. Amudha E., in-charge of EL inspection system for her round the clock support and Aditya Singh for his assistance in preparing the dataset. We would like to thank Mr. Vasudevan R. whose meticulous work in identifying and classifying the various defects was the foundational work on which the whole system was designed.

References

1. Zimmermann CG (2006) Assessing the in-orbit impact of cell cracks -an electroluminescence study of crack propagation. In: Photovoltaic energy conversion, Conference Record, IEEE
2. Köntges M, Kunze I, Kajari-Schröder S, Breitenmoser X, Bjørneklett B (2011) The risk of power loss in crystalline silicon based photovoltaic modules due to microcracks. Elsevier, pp 4
3. Supervised Learning webpage on Wikipedia. https://en.wikipedia.org/wiki/Supervised_learning (2007)
4. Moon H-G, Kim J-H (2011) Intelligent crack detecting algorithm on concrete crack image using neural network. Department of Civil and Environmental Engineering, Yonsei University, Seoul, Korea (2011)
5. Bastari A, Bruni A, Cristalli C (2010) Classification of silicon solar cells using electroluminescence texture analysis. In: 2010 IEEE international symposium on industrial electronics, Bari, pp 1722–1727
6. Tsai D-M, Wu S-C, Li W-C (2012) Defect detection of solar cells in electroluminescence images using Fourier image reconstruction. *Sol Energy Mater Sol Cells* 99:250–262
7. Spataru S, Hacke P, Sera D (2016) Automatic detection and evaluation of solar cell microcracks in electroluminescence images using matched filters. In: 2016 IEEE 43rd photovoltaic specialists conference (PVSC), Portland, OR, pp 1602–1607
8. Tsai D-M, Wu S-C, Chiu W-Y (2013) Defect detection in solar modules using ICA basis images. *IEEE Trans Ind Inf*
9. Anwar SA, Abdullah MZ (2015) Micro-crack detection of multicrystalline solar cells featuring an improved anisotropic diffusion filter and image segmentation technique. *Eurasip J Image Video Process*
10. Bharathkumar S, Ashokkumar K (2006) Solar cell panel crack detection using bacterial foraging optimization algorithm. *Int J Sci Eng Technol Res*
11. Otsu's Method webpage on Wikipedia website, https://en.wikipedia.org/wiki/Otsu%27s_method (2017)
12. Velasco F (1980 Nov) Thresholding using the ISODATA clustering algorithm. *IEEE Trans Syst Man Cybern* 10(11):771–774
13. Connected-component labelling webpage on Wikipedia website, https://en.wikipedia.org/wiki/Connected-component_labeling (2017)
14. LeCun Y, Bengio Y, Hinton G (2015) Deep learning. *Nature* 521(7553):436
15. Szegedy C, Vanhoucke V, Ioffe S, Shlens J (2015 Dec 11) Rethinking the inception architecture for computer vision. [arXiv:1512.00567v3](https://arxiv.org/abs/1512.00567v3)
16. Tan C, Sun F, Kong T, Zhang W, Yang C, Liu C (6 Aug 2018) A survey on deep transfer learning. [arXiv:1808.01974v1](https://arxiv.org/abs/1808.01974v1)
17. Ruder S (2016) An overview of gradient descent optimization algorithms. arXiv preprint:1609.04747
18. Kingma DP, Ba JL (2015) Adam: a method for stochastic optimization. ICLR

Microsat: Solar Array Exposed Materials Protection from Atomic Oxygen



K. H. Sucheta, B. R. Uma and R. NukaRaju

Abstract Microsat is the third satellite in the series of remote sensing micro-satellites by ISRO. It is a low earth orbit (LEO) spacecraft, launched into a 350-km circular orbit on 12 January 2018. The orbit of 350 km poses lot of constraints on the satellite with respect to space environment as well as atmospheric drag. The major concern is from atomic oxygen present in the LEO environment. The interaction between atomic oxygen and spacecraft surfaces produces significant changes in the mass, surface morphology, electrical and optical properties of the spacecraft materials through erosion and oxidation. The major exposed materials of solar panels, viz. silver, Kapton and epoxy, are vulnerable to atomic oxygen effect. For LEO missions (<500 km), erosion rates of solar array materials can be high and can cause degradation in their mechanical, thermal and electrical properties. In recent years, many nanosatellites and student satellites are launched into low earth orbits for technology demonstration. Hence, understanding of the performance degradation of solar array exposed materials is very critical for the low-altitude satellites. To protect the exposed surfaces, mitigation technique needs to be adopted. In this chapter, the effect of atomic oxygen on the solar array exposed materials, details of the protection coatings, its qualification and on-board performance are presented.

Keywords Indian Space Research Organization (ISRO) · Solar array · Low earth orbit (LEO) · Atomic oxygen · Ultraviolet radiation · UTP (Upper trip point) · LTP (Lower trip point)

K. H. Sucheta (✉) · B. R. Uma (✉) · R. NukaRaju (✉)
Solar Panel Division, Power Systems Group, URSC, Bangalore 560017, India
e-mail: sucheta@ursc.gov.in

B. R. Uma
e-mail: uma@ursc.gov.in

R. NukaRaju
e-mail: mraju@ursc.gov.in

© Springer Nature Singapore Pte Ltd. 2020
PSR. S. Sastry et al. (eds.), *Advances in Small Satellite Technologies*,
Lecture Notes in Mechanical Engineering,
https://doi.org/10.1007/978-981-15-1724-2_31

1 Introduction

Atomic oxygen is the predominant species in the upper atmosphere (200–600 km). Atomic oxygen is formed due to the dissociation [1] of O_2 by ultraviolet (100–200 nm wavelength) radiation. The interaction between atomic oxygen and spacecraft surfaces can produce significant changes in the mass, surface morphology, electrical, thermal and optical properties of the spacecraft materials through erosion and oxidation. Atomic oxygen has a high number density and ram impact energy at altitudes between 200 and 650 km. The orbiting spacecraft motion (approx. 7.7 km/s) through the atmospheric atomic oxygen can generate a flux to the spacecraft surfaces with significant energy of about 5 eV. This energy is sufficient enough to initiate numerous chemical and physical events on the surface it impacts. The changes in the surface properties are directly related to the atomic oxygen fluence or total integrated flux incident on material surfaces. The atomic fluence incident on the exposed surface is dependent on parameters, such as 11-year solar cycle activity (F10.7), Geomagnetic Index (Ap Index), the orbital velocity vector, spacecraft orbital parameters, such as altitude, surface orientation, local time and mission life. Atomic oxygen fluence increases with the increase in solar activity and decreases with the increase in the satellite altitude. The product of fluence and the erosion yield (re-activity coefficient) of the material will give the material erosion depth. The accurate prediction of the material erosion is very important in determining the life of the system. The effect of atomic oxygen and erosion rates of different solar array exposed materials for Microsat was calculated using SPENVIS environmental models. From the analysis, it is evident that the erosion rates are predominantly high and it needs to be protected from the atomic oxygen for the better performance of the system.

The Microsat is a low earth orbit satellite launched to an altitude of 350 km by PSLV launch vehicle on 12 January 2018. Because of the low altitude of 350 km, the impact of atomic oxygen is very high. In order to overcome the erosion of materials, as mitigation technique, atomic oxygen-resistant coatings were used on exposed materials of Microsat solar array. The performance of the solar array with these coatings is as per design and is found to be satisfactory.

In recent years, many nanosatellites and student satellites are launched into orbit. These nanosatellites are becoming popular because of their smaller size, lower mass and cost. In nanosatellites, many new technologies can be tested and demonstrated. Because of lower mass and size constraint, the nanosatellite subsystems do not have redundant systems. This requires the nanosatellite subsystems to work without failure. Generally, nanosatellites are launched into the lower-altitude orbits; hence, it is essential that these satellites need to be protected from the effect of atomic oxygen.

2 Study of Atomic Oxygen Effect

Experiments conducted during early space shuttle flights to understand the effects of exposure of a variety of materials to the LEO environment, viz. Space Transport System (STS), NASA's Long Duration Exposure Facility (LDEF) and Limited Duration Candidate Exposure (LDCE) material exposure experiments, the Russian space station Mir, Materials International Space Station Experiment (MISSE) series flown on the exterior of the International Space Station (ISS), Hubble Space Telescope, etc., have shown that atomic oxygen in LEO environment causes erosion of sensitive material surfaces, and prolonged exposure will result in degraded system performance [2] and eventually lead to premature mission failure.

Figure 1 depicts a Kapton H flight sample (three layered) pre and post atomic oxygen exposure, which was part of MISSE 2 PEACE (Polymer Erosion and contamination Experiment) Polymers Experiment carried out on board ISS. During flight, the top layer had completely eroded due to atomic oxygen. The second layer was eroded partially, and the third layer was exposed to atomic oxygen [3].

Hence, ATOX is considered as one of the most serious hazard to spacecraft materials, and it is essential to protect the exposed surfaces of the solar array with atomic oxygen-resistant coating materials.

The effect of atomic oxygen on solar array exposed materials was studied in detail using SPENVIS model. A study has been carried out to assess the effect of atomic oxygen on the solar array exposed materials for Microsat mission by considering the orbit parameters—total period of exposure and ram direction.

2.1 Calculation of Atomic Oxygen Fluence

The atomic oxygen density was calculated using SPENVIS model. The atomic oxygen density depends on

- Altitude,
- Year of launch,
- Day of the year,

Fig. 1 Kapton H sample pre- and post-flight



- Geomagnetic Index (Ap Index),
- Solar Flux (F10.7).

The atomic oxygen flux was estimated by using

$$\text{Atomic oxygen flux} = \text{Atomic oxygen density} * \text{Space craft ram velocity.}$$

$$\text{Atomic oxygen fluence} = \text{Atomic oxygen flux} * \text{Total mission life.}$$

With the above input, the erosion rates of various spacecraft exposed materials were calculated for each satellite axis (pitch, yaw and roll) with respect to ram. The erosion levels for each axis are listed in Tables 1 and 2. From the analysis, it is clear that if exposed materials are not protected from the atomic oxygen, because of the high erosion rate, the materials especially solar array front-side Kapton and epoxy used in CFRP will erode within the mission life.

Table 1 Erosion depth in one year for materials in front surface

Erosion depth in one year for materials in front surface due to atomic oxygen						
Satellite axis with respect to ram	Total cumulative fluence (cm ⁻²)	Erosion for different materials (μ)				
		Kapton	Silver	Carbon	Epoxy	Teflon
+Y	1.73E+20	5.19	18.16	2.59	2.94	0.06
+R	1.91E+21	57.18	200.13	28.59	32.40	0.71
+P	4.19E+20	12.57	43.98	6.28	7.12	0.15
-Y	1.69E+20	5.07	17.74	2.53	2.87	0.06
-R	0.00E+00	0.00	0.00	0.00	0.00	0.00
-P	4.10E+20	12.31	43.10	6.16	6.98	0.15

Table 2 Erosion depth in one year for materials in rear surface

Erosion depth in one year for materials in rear surface due to atomic oxygen						
Satellite axis with respect to ram	Total cumulative fluence (cm ⁻²)	Erosion for different materials (μ)				
		Kapton	Silver	Carbon	Epoxy	Teflon
+Y	1.69E+20	5.07	17.74	2.53	2.87	0.06
+R	0.00E+00	0.00	0.00	0.00	0.00	0.00
+P	4.10E+20	12.31	43.10	6.16	6.98	0.15
-Y	1.73E+20	5.19	18.16	2.59	2.94	0.06
-R	1.91E+21	57.18	200.13	28.59	32.40	0.71
-P	4.19E+20	12.57	43.98	6.28	7.12	0.15

2.2 Mitigation

To protect the exposed materials, a mitigation technique of applying the atomic oxygen-resistant coating materials on the exposed surfaces was adopted. An extensive literature survey was made to identify suitable atomic oxygen-resistant coating materials. The list of various solar array exposed materials is shown in Table 3. The list of base materials and the atomic oxygen-resistant coating materials used for their protection is shown in Table 4.

The resistant coating materials were process qualified by adopting suitable application process and various evaluation tests. A qualification coupon was fabricated, wherein the exposed surfaces were coated with different atomic oxygen-resistant coating materials. The coupon was tested for 30,000 ambient thermal cycles between +100 and -100 °C for low earth orbit environment condition. The coupon successfully completed the test, and there were no anomalous test results observed. These mitigation techniques can be adopted to all low earth orbit (LEO) satellites.

Table 3 List of solar array exposed materials

S. No.	Description	Material used
1	Solar cell cover glass	Cerium-doped micro-sheet
2	Solar cell end termination	Silver-plated Kovar
3	Substrate	Aluminium honeycomb core with CFRP face skin and Kapton insulator layer on cell side.
4	Harness	Spec-55 wires (Teflon-coated wires)
5	Solar cell adhesive	RTV-S-691
6	Crimp barrels	Nickel-plated copper
7	Crimp sleeves	Polyurethane
8	Connector	ITT Cannon (shell)
9	Clamps	Anodized aluminium clamps
10	Harness tying thread	Wax-coated nylon

Table 4 List of base materials and atomic oxygen-resistant coating materials used

S. No.	Base material	Atomic oxygen-resistant coating material used
1	Kapton surface	MAP ATOX-41B
2	Silver-plated Kovar interconnectors and silver-plated copper busbars	MAP ATOX-41B
3	On CFRP substrate	CV 1148

3 Microsat Solar Array

Microsat solar array consists of rigid deployable sun-orienting solar array comprising of two panels, one on each wing. There is no SADA to track the sun. The solar panels are made sun pointing by orienting the spacecraft body along one axis. Microsat solar array consists of rigid, deployable solar panels. The solar panel substrates are composite structures with a rigid aluminium honeycomb core of thickness 14.15 mm and 0.1-mm-thick woven CFRP fabric face sheet co-cured with 0.05-mm-thick Kapton insulator on cell side. The solar panels are in the roll axis/plane. There are two solar panels of size $0.810\text{ m} \times 0.830\text{ m}$ and $0.915\text{ m} \times 0.830\text{ m}$, one per wing. The total array area is 1.36 m^2 .

In order to meet the higher specific power requirements, high-efficient triple-junction solar cells are used for power generation. Atomic oxygen-resistant coating materials and processes were adopted to protect the exposed surfaces of Microsat solar array. The solar panel's front and rear sides are shown in Figs. 2 and 3.

The array is designed to generate a maximum power of 320 W at end of life of 1 year at equinox, normal incidence, at a maximum bus voltage of 42 V. The required power is to be distributed from single raw bus of 30–42 V.

Fig. 2 Solar panel front side



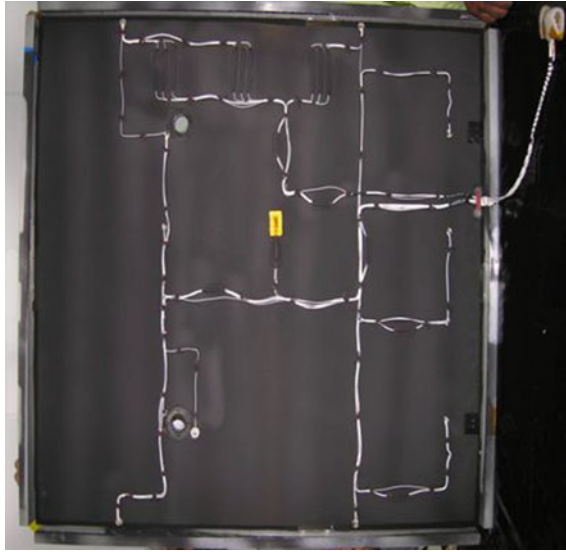


Fig. 3 Solar panel rear side

3.1 In-Orbit Performance of Microsat Solar Array

Microsat was launched on 12 January 2018 to a 350-km circular orbit by Polar Satellite Launch Vehicle (PSLV) from Sriharikota (SHAR), India.

The solar array supported the spacecraft power requirement and battery charging requirement except during eclipse throughout the mission. The power electronics is designed for UTP- and LTP-based battery charge management.

The on-board parameters to verify the solar array performance of Microsat Spacecraft are:

- Current delivered by solar array to the loads/load currents,
- Status of inclusion/exclusion of the solar array strings,
- Solar panel rear-side temperature,
- Solar panel off-set from sun normal.

Using these data available in telemetry, a method was established for estimating the total power generation capacity of the solar array. The in-orbit telemetry-derived generation estimate was compared against the theoretical predictions throughout the mission. The Microsat solar array observed performance with respect to estimated performance is shown in Fig. 4.

The uncertainty of ~2% as shown in Fig. 4 in observed performance with respect to estimated performance can be attributed to the telemetry error and probability of non-occurrence of losses due to mismatch, orientation and assembly losses.

From observation, it is evident that the performance of the solar array is as per design and estimation. The in-orbit performance of the solar array is normal which

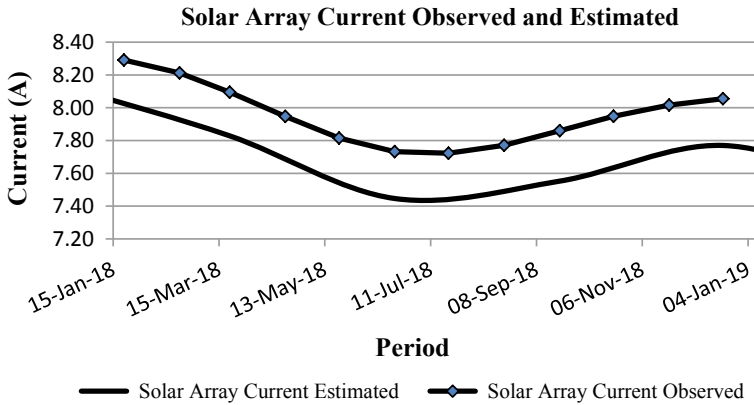


Fig. 4 Solar array performance

clearly indicates that the atomic oxygen protection coating has protected the solar array exposed materials. The atomic oxygen-resistant coating has survived the on-board atomic oxygen environment.

4 Conclusions

Microsat is one of the satellites in the series of remote sensing micro-satellites launched to a 350-km circular orbit, where atomic oxygen is of major concern. The Microsat solar array with atomic oxygen-resistant coating has survived the atomic oxygen orbital environment, and the performance of the solar array is as per the design and prediction. Hence, these mitigation techniques are adoptable to nanosatellites, which are the future technology development frontiers in satellite technology.

Acknowledgements The authors are grateful to Director, URSC, Deputy Director, CPA and GD, PSG, Head, SPD for their guidance and support for this work. We wish to acknowledge the SPENVIS web-based software team for the usage of their program. Also we wish to thank all individuals of solar panel division for their contribution in realizing the solar array for Microsat.

References

1. MISSE PEACE Polymers Atomic Oxygen Erosion Results, NASA/TM-2006-214482. In: Proceedings of the 2006 MISSE post-retrieval conference sponsored by the U.S. Air Force Research Laboratory Orlando, Florida, 26–30 June 2006
2. NASA/SDIO Space environmental effects on materials workshop, NASA-CP-3035; Reddy R et al (1992) Effect of the low earth orbit atomic oxygen environment on solar array materials. ESA J 16
3. Spacecraft Polymers Atomic Oxygen Durability handbook, NASA-HDBK-6024

Quality and Reliability

Quality Assessment Techniques for Small Satellite Images



V. S. Biju, K. Balan, S. Sathiamurthi and K. S. Mani

Abstract Recently, the occupancy of small satellite in space is increasing, and one potential application of this is satellite imaging. The difference in acquisition conditions of satellite images makes it susceptible to much degradation compared to normal images. The common degradations are motion blur, low resolution and noise due to low light conditions, rain, snow, etc. Since small satellites are planned to be launched in big numbers, the number of image data to be analyzed will be higher, and this calls for some automatic techniques for assessing the quality of acquired images. Even though perceptual image quality assessment is a much explored area, there is not much work done in the area of satellite image quality assessment. In this paper, we review different techniques used for satellite image quality assessment and suggest some techniques which can also be used. The first method that we propose extracts GIST feature from satellite images and then uses a shallow neural network to predict the quality of the image from these features. The second method uses a deep convolutional neural network (CNN) with a shallow fully connected neural network to predict satellite image quality.

Keywords Image quality assessment · Satellite images · Deep CNN · Small satellites

1 Introduction

Recently, there is tremendous growth in the use of small satellites for different applications. The lower launch costs, lower development cost, lower development time and mass production possibilities make it a good business prospect for private industries. Forming satellite constellations, in-orbit inspection of bigger satellites and different technology demonstrations are some of the unique applications of small satellites. At

V. S. Biju (✉) · K. Balan · S. Sathiamurthi · K. S. Mani
Reliability and Quality Assurance Area, ISRO Inertial Systems Unit, Trivandrum,
Kerala 695013, India
e-mail: vs_biju@vssc.gov.in

© Springer Nature Singapore Pte Ltd. 2020
PSR. S. Sastry et al. (eds.), *Advances in Small Satellite Technologies*,
Lecture Notes in Mechanical Engineering,
https://doi.org/10.1007/978-981-15-1724-2_32

the same time, small satellites are widely used for imaging purposes also. The number of satellites, and hence, the number of images captured will be in large quantities in the case of small satellites. Two main types of satellite images are panchromatic and multispectral. The former will have a higher spatial resolution; whereas, the later will have rich spectral content. These images may undergo a different type of degradations while acquisition. Some common degradation is motion blur, low resolution and noise due to low light, rain, snow, etc. Also, there can be degradations while stitching the stripes of images to make a big image. Image quality assessment (QA) is the technique of assessing the quality of an image either perceived by human beings or for an application using a computer algorithm. Image QA algorithms are used for testing the performance of different image filters, fusion methods, acquisition systems and many others. It is also used to screen out bad images from a large collection of acquired images.

There is plenty of work done in the area of image quality assessment for predicting the perceived quality of images by a human being. The image quality assessment algorithms are generally classified into three categories. They are the full reference (FR), reduced reference (RR) and no reference (NR) image quality assessment (IQA) methods. In FR-IQA, we assess the quality of the test image w.r.t. a reference image. This methodology can be applied in applications where we have the reference image like image compression, image transmission over a channel, etc. In RR-IQA, quality of the test image is assessed with only partial information about the reference image. In most of the cases, we will have only the test image and no reference images. This falls under the category of NR-IQA. Mean squared error (MSE) and structural similarity index (SSIM) [1] are two of the most common FR-IQA indices. BRISQUE, NIQE and DIVIINE [2] are some of the popular indices for NR-IQA. Since satellite images are generally not used for human perception, these common techniques may not be of good use. In this paper, we will have a review of the existing techniques for satellite image quality assessment and propose some new techniques which can be used.

2 Existing Methods for Satellite Image Quality Assessment

Multispectral images will have data in different bands, and they are fused to create a single image. Babawuro et al. [3] have analyzed the effect of structural similarity index (SSIM) for assessing the quality of fused multispectral images. SSIM is a full reference image quality index which is computed as the product of luminance similarity, contrast similarity and structural similarity between two images. SSIM is expressed mathematically as

$$\text{SSIM}(x, y) = \frac{2\mu_x * \mu_y + C_1}{\mu_x^2 + \mu_y^2 + C_1} * \frac{2\sigma_x * \sigma_y + C_2}{\sigma_x^2 + \sigma_y^2 + C_2} * \frac{\sigma_{xy} + C_3}{\sigma_x * \sigma_y + C_3} \quad (1)$$

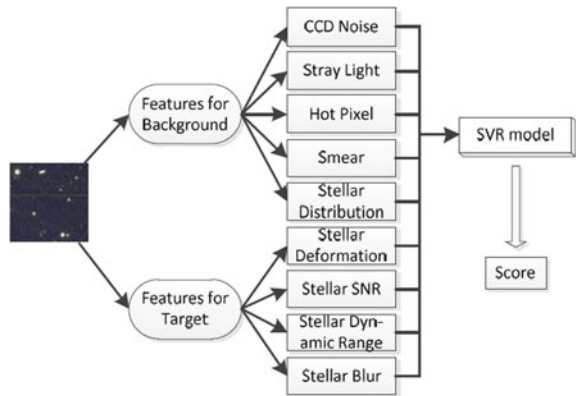
where x and y are two images, μ denotes the weighted mean of a patch around a pixel, σ denotes weighted standard deviation of a patch around a pixel, σ_{xy} denotes cross-correlation between two image patches, and C_1 , C_2 and C_3 are small constants used to avoid singularities.

They have tested this method on very high-resolution multispectral images from Quick Bird satellite. The multispectral images are fused to create true color images. The noisy images of the same scene are also generated since it leads to the deformed structure of the image. They have compared different sets of good and degraded images using different image quality metrics. According to their results, SSIM is able to capture distortions in the fused image up to some extent, and this can be used as a coarse index to assess the quality of fused multispectral images.

Zhang et al. [4] have proposed a no reference method for satellite image QA based on an indicator system. Their algorithm extracts different features from the image and then uses support vector regression (SVR) to predict the quality of the image from these features. They extract five features for background and four features for target from the image and give this as input to the SVR. A block diagram of their method is given in Fig. 1. They have done the experiments using multiple satellite images from geo orbit. These images are spread across three years and different seasons. Images are taken from different locations in space and contain images of different quality. They are able to predict the image quality quite well using this method with a MSE of 0.00046.

Crespi et al. [5] propose a method to evaluate the radiometric quality of high-resolution satellite images using noise and resolution characteristics. They find out the noise in homogenous image regions from pixel standard deviations and analyze the variation of noise w.r.t. pixel intensity. The noise in an image region is computed from the standard deviation of pixels in 3×3 image patches. The standard deviation values are sorted, and the average of smallest 5% is used for noise computation since the higher standard deviations are caused by image textures. An indicator of signal-to-noise ratio is computed as

Fig. 1 Block diagram of satellite image quality prediction algorithm by Zhang et al. [4]



$$R = \frac{D_{\max} - D_{\min}}{\sigma_s} \quad (2)$$

D_{\max} and D_{\min} denote the highest and lowest pixel value in the region, and σ_s denotes the mean of the lowest 5% standard deviations.

To get the resolution characteristics, they use modulation transfer function (MTF) of the image. First, a line spread function is computed from edges in the image, and then its Fourier transform is taken to get the MTF.

3 Proposed New Methods for Satellite Image Quality Assessment

Recently, artificial neural networks are gaining more and more popularity. They are being used for many computer vision applications like image classification, object detection, image denoising and image super resolution. In all these applications, artificial neural networks are giving state-of-the-art performance. The increase in amount of annotated data and the increase in computational power have lead to the recent advances in this field. This made us to think the possibilities of using the same for satellite image QA. We propose two methods for satellite image QA using neural networks.

3.1 *Satellite Image Quality Assessment Using GIST Features and a Shallow Network*

The basic idea behind our first method is to extract feature from the image using some standard techniques and then use a shallow network to predict the image quality using these features. We can either use local image features or global features for this purpose. If we use local features, some kind of aggregation has to be applied on that. So, here we decided to use one global image feature called GIST [6] in the initial step. In GIST, rather than viewing the image as a collection of different objects, a holistic model of the image is made. GIST is an image feature used mainly for applications like scene categorization. A set of five perceptual dimensions, namely openness, naturalness, roughness, ruggedness and expansion are used to represent the holistic nature of the image in low dimension. These five features are obtained from the amplitude spectrum of windowed Fourier transform of the image. GIST gives a feature vector of size 512 for each image, and we train a shallow neural network to predict image quality from these features.

The neural network that we propose is of three layers. Layer-1 has 16 nodes, layer-2 has four nodes, and layer-3 has one node. In effect, it is a regressor function trying to predict a scalar from a vector of size 512. The number of layers and nodes

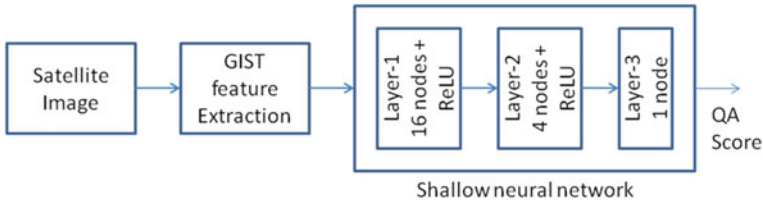


Fig. 2 Block diagram of satellite image quality prediction using GIST features and a three-layered neural network

can be increased depending on the size of the dataset that we have. We propose to use ReLU activation function for the first two layers and linear activation function for the last layer. The network can be trained using Adam optimizer for 50 epochs. The number of epoch can also be adjusted depending upon the dataset size. A basic block diagram of our proposed method is given in Fig. 2.

The above algorithm can be implemented in Python with Keras library for the neural network.

3.2 *Satellite Image Quality Assessment Using a Deep Convolutional Neural Network*

In Sect. 3.1, we have used GIST algorithm for extracting features from the image. But recently, it has been shown in the literature that many of the deep convolutional neural network features trained for applications like image classifications can be used as general-purpose features [7]. So, here we also would like to use deep convolutional features and fully connected network for predicting the quality of satellite images. The main constraint in training a deep CNN is the huge annotated data requirement. Since we may not be having enough data to train a CNN from scratch, we decided to use convolutional layers from a pre-trained network and augment it with fully connected layers.

There are numerous of the shelf trained networks available. We propose to take convolutional layers from a network called VGG-16 [8] which is trained for image classification on ImageNet dataset. VGG-16 has 13 convolutional layers. The number of channels increases gradually from 64 to 512 in powers of two. All convolutional kernels are of size 3×3 . The shallow network is the same as that in previous section. A block diagram of our proposed method is given in Fig. 3.

Training methodology for this network is as follows. First, the fully connected layers alone will be trained using Adam optimizer for 30 epochs. The weights of deep CNN layers from VGG-16 will not be varied during this phase of training. Once the new layers are trained properly, in the next step, the last nine convolutional layers from VGG-16 will be fine-tuned using stochastic gradient descent optimizer

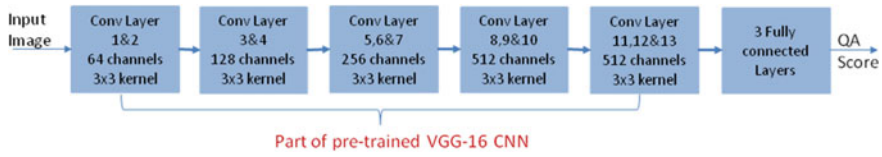


Fig. 3 Block diagram of satellite image quality prediction using deep CNN features and a three-layered neural network

and a low learning rate. The first two blocks of VGG-19 are not fine-tuned because generally initial layers in a deep network represent low-level image features which are common to many applications.

One problem that we faced here is the non-uniformity in size of the image that is used for training and testing. The input image size should be fixed for the proper working of the network since the output size of the convolutional layers depends upon the input image size. So, here we decided to split the input image to patches of size 256×256 and feed these patches to the quality prediction network. The quality score for the input image is found as the average of quality scores of all patches in that image.

4 Conclusion

The significance of image quality assessment is very high for small satellites considering the large number of image that will be captured and the possibility of cheap sensors to be used. In this paper, we review some of the existing methods for satellite image quality assessment. We also propose two new methods for satellite image quality assessment using artificial neural networks considering the recent advancement in the field. In the first method, we have designed a framework for the extraction of GIST features from the image and prediction of image quality from these features using a shallow neural network. We have also proposed a method in which deep convolutional features are extracted from the image using parts of pre-trained VGG-16 network followed by a three-layered neural network for predicting quality from these features.

References

1. Wang Z, Bovik AC, Sheikh HR, Simoncelli EP (2004) Image quality assessment: from error visibility to structural similarity. *IEEE Trans Image Process* 13(4):600–612
2. Mittal A, Moorthy AK, Bovik AC (2012) No-reference image quality assessment in the spatial domain. *IEEE Trans Image Process* 21(12):4695–4708
3. Babawuro U, Beiji Z (2011) Satellite imagery quality evaluation using image quality metrics for quantitative cadastral analysis. *Int J Comput Appl Eng Sci* 1

4. Zhang D, Wang K, Jin Y, Bian P, Tan J (2016) NR image quality assessment of satellite image. In: ICSP2016
5. Crespi M, Vendictis LD (2009) A procedure for high resolution satellite imagery quality assessment. *Sensors* 9(5):3289–3313
6. Oliva A, Torralba A (2001) Modeling the shape of the scene: a holistic representation of the spatial envelope. *Int J Comput Vision* 42(3):145–175
7. Bianco S, Celona L, Napoletano P, Schettini R (2016) On the use of deep learning for blind image quality assessment. *CoRR*, vol. abs/1602.05531
8. Simonyan K, Zisserman A (2014) Very deep convolutional networks for large-scale image recognition. *CoRR*, vol. abs/1409.1556

RETRACTED CHAPTER: Usage of COTS/EEE Parts in Space Applications—An Overview



H. V. Harish

Abstract Many challenging space application requirements can be met using COTS. The time comes (better sooner than later) for the policymakers to reach a consensus on applying the COTS philosophy to space applications. This policy change is critical for the space industry. This paper attempts to suggest different issues to be tackled in order to meet technical, quality assurance, and cost requirements using COTS. A less heavy package results in a smaller payload for the same board dimension; this provides a huge weight advantage for space missions because the payload mass defines the launch vehicle requirements. Potential reduction in cost can be achieved by using various methods like screening, accelerated testing, or partial qualification techniques to complement the existing commercial qualification as well as by the reduced package materials costs. Assessment of the risk associated with potentially lower reliability devices, engineers within the commercial and aerospace industries are using trade-off and risk analysis to attain reducing satellite system cost while increasing performance and maintaining high reliability.

Keywords COTS · EEE Parts · Space

1 Introduction

For decades military/space electrical, electronic, and electromechanical (EEE) parts have proved to be suitable for use in military and space applications [NASA's Office of Safety & Mission Assurance (OSMA) evaluates newly available and advanced electronic parts for programs and projects under its EEE parts program.]. The traditional MIL-SPEC [US defense standard/military specification] methodology is based

The original version of this chapter was retracted: The Editors have retracted this book chapter because it contains material that substantially overlaps with content from a blog post by a different author "Dan Friedlander (2016)". The retraction note to this chapter is available at https://doi.org/10.1007/978-981-15-1724-2_50

H. V. Harish (✉)
Director Spur India, Bangalore 560075, India
e-mail: harish@spurindia.com

on risk avoidance by testing the finished parts. Yet, global developments, like declining availability and budget constraints, have triggered the need to find an alternative solution. The alternative solution was officialized in 1994 by US Secretary of Defense William Perry's directive, imposing the use of commercial off-the-shelf (COTS) parts in military applications, exempting space applications. After decades of successful use of COTS in military applications, the above change has been proved viable. Many challenging space application requirements can be met only using COTS. The time comes (better sooner than later) for the policymakers to reach a consensus on applying the COTS philosophy to space applications. This policy change is critical for the space industry. This paper attempts to suggest different issues to be tackled in order to meet technical, quality assurance, and cost requirements using COTS. The term "COTS" in this paper refers to commercial EEE parts, including plastic-encapsulated active ones.

2 EEE Parts Control Concepts

US Secretary of Defense William Perry's 1994 directive officially started the transition from the use of military electrical, electronic, and electromechanical (EEE) parts in military applications to the use of commercial EEE parts (or COTS) in military applications. Space applications were exempted from meeting the directive requirements; however, the same drivers to this cultural change (like parts availability) apply also to the space industry.

3 MIL-SPEC Versus COTS

The following table compares the main principles of the two subject concepts.

For COTS, the main idea is:

MIL-SPEC	COTS
Risk avoidance	Risk management
Parts testing	Statistical Process Control (SPC)
Small-volume production	High-volume production

- Risk management: It is the project responsibility to manage the risk. The risk cannot be zeroed, even by most stringent measures.
- Process control: The process builds reliability into the part.
- Production level: High-volume results in reliability.

4 Quality Versus Reliability

Quality and reliability are two different terms to be understood: Quality is the conformance to requirements at the start of use. Reliability is the probability of parts to meet the relevant specification over the time, under the worst operational conditions. Reliability is quality changing over time. In other words, quality is a snapshot at the start of the life, and reliability is a motion picture over the life.

5 Part Testing Versus Process Control

Given the above quality/reliability clarification, it is clear that reliability cannot be tested into the part. The qualification and screening are not considered as a substitute for manufacturing control, but rather as risk mitigation measures. Consequently, the way to address the reliability issue is by Statistical Process Control (SPC). The process (design followed by manufacturing) builds reliability into the part. In the environment of high-volume commercial EEE parts production, the SPC works well, resulting in very low failure rates at start of use timing. That does not mean that the part testing is worthless. The MIL-SPEC focuses on part testing and much less on process control.

The Statistical Process Control does not work for a low-volume production, like space/military EEE parts production. The testing mitigates the lack of statistics value. The reliability is built into the part. The quality is addressed by testing. That is the positive side. Usually, the risk of damaging the parts during testing is ignored by policymakers. Any part-level extra testing (outside the necessary manufacturer's inline testing) of the actual units to be flown results in higher risk than testing them. Selected sample testing is OK. The tested sample should not be used for flight. The manufacturer of military-qualified parts is not incentivized to improve the process. Changes involve time and money to meet the qualification requirements. The qualification addresses the quality. Process improvements addressing reliability may be skipped, and the specification met anyway at parts delivery timing. This is not the case with COTS; the focus is on process control. The high-volume production justifies the efficient implementation of statistics. Consequently, the reliability is addressed. The COTS manufacturer, freed from the MIL-SPEC restrictions, can continuously monitor the process and continuously improve it. The term "high-reliability" or "hi-rel" is used exclusively for space/military ones. It is wrong to conclude that by definition all COTS are non-hi-rel parts. Decades of COTS use in military applications proved that COTS are reliable enough for the specific mission. The mission conditions in military are often more severe than in space, except radiation. The mission duration is often longer than a space mission.

6 Reliability Prediction

The leading document for reliability prediction has, for decades, been MIL-HDBK-217. This handbook, on the reliability prediction of electronic equipment, systematically suppressed the use of non-military parts in military applications. In spite of the wide usage of the above document, after the 1994 William Perry's directive, it has been declared unreliable. On February 15, 1996, a memorandum signed by Assistant Secretary of the Army/Research, Development, Acquisition, Gilbert Decker, stated: "In particular, MIL-HDBK-217, Reliability Prediction of Electronic Equipment, is not to appear in an RFP (request for proposal) as it been shown to be unreliable and its use can lead to erroneous and misleading reliability prediction." It has to be remembered that the reliability prediction model is based on the Arrhenius equation, a formula for the temperature dependence of reaction rates, considering one stress. Various experts claim that there is ample evidence that a straightforward application of the Arrhenius equation, with activation energies determined from high-temperature accelerated stress testing, is not the right way to deal with the matter.

7 Space Qualified

The term "space qualified" has to be fully understood in order not to be misused. The definition is space systems, subsystems, and components which meet the specification relevant to their use. For example, often parts qualified to MIL-SPEC quality level "S" are called "space qualified." Quality level "S" is the highest quality level and should not be automatically interpreted as "S" = "space." Level "S", without specified radiation hardness assurance (RHA) for space systems requirement in the specific part specification, ignores fully or partially the radiation in space.

8 Military versus Space Application

The exclusive requirements for space are radiation, outgassing, vacuum, microgravity, and atomic oxygen. Proper selected COTS (including non-hermetic ones) can meet these requirements.

COTS for space applications/issues are to be revisited.

In order to progress in the process of massive introduction of COTS in space applications, well-rooted requirements shall be revisited within the risk management philosophy, in order to save time and money. Following are some suggested revisit targets:

8.1 Reliability Prediction

Too often, technical specifications/scopes of work (SOW) specify an absolute reliability limit to be met, penalizing use of COTS. The use of the term shall be revisited in order to use it within its limitations. MIL-HDBK-217F explicitly states its limitations: “a reliability prediction should never be assumed to represent the expected field reliability.” A misinterpretation may lead to not justifiable extra cost. Anyway, as MIL-HDBK-217F admits, “those who view the prediction only as a number which must exceed a specified value can usually find the way to achieve their goal without any impact on the system.”

8.2 Market-Driven Availability

In view of the many years of official use of COTS in military applications, it is obvious that the required results did not materialize. The military-qualified and space-qualified EEE parts share in the EEE parts global market is less than 0.5 percent in terms of dollar value. Nobody can stop a manufacturer from leaving a market found not to be profitable. Keeping the traditional approach means that we learn from history that we do not learn from history. The future EEE parts availability has to be secured for military applications and for space applications, as well. The business decisions are much stronger than any EEE parts policy.

8.3 Hermeticity Requirement Versus Plastic

The importance of package hermeticity is not arguable. The problems encountered in early stages (from the 60 s) with non-hermetic plastic-encapsulated semiconductors caused the military and space parts policymakers to have serious concerns of their use in military and space applications. Of course, the “hermeticity” of the plastic parts cannot compete with the hermeticity of the hermetic parts. The goal should be “enough” not the “best.”

8.4 COTS Post-procurement Testing

The needed COTS introduction into space applications is shadowed by the high non-recurring engineering (NRE) involved. The high NRE is driven by post-procurement testing requirements derived from the well-rooted traditional approach of part testing.

9 Radiation TID

It is the user's responsibility to find a way to assess the total ionizing dose (TID) withstanding capability of any part and use it accordingly. The following issues should be revisited.

9.1 Radiation Design Margin (RDM)

The RDM requirement provides a systematic approach to managing the mission risk posed by uncertainties in both the radiation model and hardware susceptibility to radiation. RDM takes into account traditionally an historic lot-to-lot variation that may be different today due to better manufacturing process control (SPC) and improvements. Revisit may lead to applied RDM reduction, leading to more COTS being able to withstand the radiation requirements.

9.2 Lot-to-Lot TID Testing Requirement

In view of the improved process control (SPC) and high-volume statistics validity, the lot-to-lot and within-a-lot variation issue is worth to be revisited. From the point of view of radiation testing, military-level-qualified parts and COTS have the same lack of die traceability problem of not being wafer traceable. The space industry turns a blind eye on the lack of wafer traceability for the traditionally acceptable military-level parts, but penalizes COTS in space because of same traceability issue!

9.3 Part TID Tolerance Level

The part TID withstanding capability level is established by radiation testing and is defined as the TID level at which the part goes out the specification limits for the first time. To relax the requirement, another practice is applied by those having a meaningful database. It is not a good engineering practice, because it relies on out-of-spec part operation toward the end-of-life phase of the mission. The higher level achieved is called design part TID withstanding capability level. The design worst-case analysis (WCA) shall validate the above practice. Revisiting the above widely used practice may lead to new ideas of easing the introduction of relatively TID weak COTS in space applications. On the other hand, it may lead to the conclusion that when operating outside the spec, the risk is too high.

9.4 EEE Parts Shielding

The use of more effective shield material lowers the predicted mission TID level seen by a part. Consequently, the required part TID tolerance is decreasing, and more parts become suitable for the space application (from TID points of view). There are better than aluminum materials (like tantalum), and there are more effective shielding techniques (like multilayer shields). Active shields (like magnetic) are in research stage.

10 Radiation-Induced Latch-up (SEL)

SEL, one of the single-event effects, is destructive. The mitigation consists of a latch-up protection circuit to quickly disconnect the damaging current. To implement such mitigation, the latch-up current shall be known from the SEL testing. The SEL testing is performed in heavy-ion accelerators and involves high cost and a long time. In order to reduce cost and time, the following issues should be revisited:

10.1 SEL Test Method

Revisiting the traditional method versus another method may lead to cost reduction and time savings. Another SEL test method, worth being considered, is the less expensive pulsed laser SEL (and other SEE) testing, proved as efficient. By the way, the pulsed laser source may play an important role in bit mapping, mitigating multiple bit upsets (MBU). Another known SEL test method is Californium 252, if used within its limitations.

10.2 SEL Rate Prediction

There is a practice, to be revisited for validity and increased use, based on comparison with the reliability figure of the part. It states that if the SEL probability is less than one-tenth of the relevant reliability figure, the part may be used for flight as is.

10.3 Part Technology/Process

To help the rather complicated, difficult task of COTS SEL assessment, there is a strong need for knowledge of the relevant part technology/process basic data.

The following information is needed: technology, process, foundry, and die revision. Alliances in the space industry can substantially contribute to avoid testing duplications.

11 Destructive Physical Analysis (DPA)

The DPA, focusing on the process-related issues, is not a removable post-procurement activity. Saying that it does not mean that the DPA testing depth should not be revisited for optimization.

12 Upscreening

“Upscreening” means a raise of confidence level for using the part in the given space application. Upscreening traditionally is performed 100 percent, but it can also reach its goal by sample testing. The rationale behind sample (not to be flown) testing is the conviction that any handling of flight parts may damage them. It is worth paying attention to the NASA warning in official document PEM-INST-001: “There are numerous data indicating that improper handling and testing of the parts can introduce more defects than are screened out. The traditional post-procurement 100 percent upscreening requirement at part level needs to be revisited. MIL-STD-883, Method 1015, Burn-in Screen, states that “burn-in is performed for the purpose of eliminating marginal devices, those with inherent defects or defects resulting from manufacturing aberrations which are evidenced as time and stress dependent failures. In the absence of burn-in, these defective devices would be expected to result in infant mortality or early life time failures under use conditions.” As seen above, everything starts and ends within the manufacturing process of the die. Manufacturing defects may result in failures. The present COTS are manufactured in a rigorous statistical process controlled high-volume production regime. That results in a substantial better outgoing parts quality. The reliability cannot be addressed by upscreening. Extensive design, production, and operational use of COTS (as procured) in military applications in harsh environments, resulted in successful experiences. As the technologies advance and the functional integration at part level increases, the electrical post-procurement testing becomes more and more difficult, inefficient, and costly.

13 Qualification

The successful use of COTS parts in military applications (very long operational life is often applicable) supports the viability of use of COTS in space applications. NASA PEM-INST-001 states: “For all PEMs, qualification by flight history or similarity is

not acceptable.” It is not understood why NASA is still following the traditional way of thinking, imposing such a general restriction on all PEMs. Qualification and reliability monitoring are performed routinely by best-in-class parts manufacturers.

14 Procurement Strategy

Usually, the majority of the players in the space industry do not have all the skills and infrastructure to manage the EEE parts procurement alone. It is preferred to outsource these activities to specialized companies, the so-called parts procurement agencies. The procurement methodology for COTS can follow the one practiced for space parts. Centralization of the relevant activities is even more beneficial for COTS (reduction of duplicate NRE).

15 Summary

The 1994 Perry move meant reversal of EEE parts selection priority for military applications: First priority is given to use COTS. The focus went to process control, as the fundament of part reliability. The 1994 move to use of COTS in military has been proven successful. For space applications, there is a hesitating move to permit the use of COTS, keeping the traditional EEE parts selection priority: first priority to space parts. This methodology is a “choice” permit to use COTS in space, within the 100 percent testing regime (moved to post-procurement phase) of the traditional (pre-Perry directive) philosophy. The minuscule military/space market life is finite and unpredictable. The present methodology viability depends on the EEE parts availability driven by business decisions. Consequently, the above methodology is not a secure solution. A revised, pragmatic space tailored COTS methodology has to be established and officially recognized. The methodology has to be based on the concept of process control rather than finished 100 percent part testing. There is a strong technical need for use of complex parts built using advanced technologies, available only as COTS. There is a strong need for cost reduction and schedule shortening. Educated decisions on eliminating not value-added activities are a must for cost reduction. As per the present methodology, the COTS part ownership cost is often higher than the procurement cost of space parts. There is no unsolvable technical issue to block the use of selected COTS in space applications.

Absolute reliability figure shall not be specified as a requirement to be met. Reliability prediction models shall be understood and not misused. The EEE parts availability assurance shall be considered a high-priority, critical parameter in their selection process. A new approach is needed to better secure the parts availability. COTS post-procurement testing shall be optimized, eliminating activities that do not add value. The present methodology has to be revisited for optimization and adaptation

to the reality. Shared parts radiation databases shall be established to avoid duplicate testing. Focus on part types reduction and orders consolidation.

16 Conclusion

The time has come (better sooner than later) for policymakers to reach a consensus on applying a realistic COTS philosophy to space applications. There is no unsolvable technical issue to block the use of selected COTS in space applications. The resistance to change is the main obstacle to overcome.

Acknowledgements The author thanks Dr. M. Ravindra—Deputy Director, RQA, ISRO Satellite Centre, for valuable suggestions, The author also expresses gratitude to Director, IAC, Dr. Venkateshwarra Sharma S, Deputy Director, SPA, Mr. V. Venkatesh, Group Director, PMSC, and Abdul Rehman Khan for providing support and encouragement to present this paper in the conference.



H. V. Harish He received his B. Tech (1992) from University Visvesvaraya College of Engineering, Bangalore. Since 1993, he is involved in procurement of Hi Rel EEE parts for space application. He has over 20 years of experience in EEE parts procurement area and also has been involved in component screening and testing. He is also a life member of IMAPS India Chapter and AOC India Chapter and has contributed as a main coordinator for International Conference on Electronic Warfare.

Remote Sensing, Deep Space Exploration

Image Fusion Techniques for Spatial Resolution Enhancement of AWiFS Sensor Data



K. S. R. Radhika, C. V. Rao and V. Kamakshi Prasad

Abstract Different characteristics of two or more images can be combined to achieve the merits of both in the resultant image. In proposed work image fusion is performed on pair of images, LISS-III and AWiFS of Resourcesat-I satellite (ISRO) LISS-III sensor data have high-spatial resolution, whereas AWiFS sensor data has high temporal resolution and larger swath. Different techniques namely regression, support vector machines (SVM), non-subsampled contourlet transform (NSCT) are used for acquiring images with high temporal, finer spatial and larger swath. The results of the resultant images with high resolutions are found to be satisfactory.

Keywords LISS-III data · AWiFS data · LR-HR image pair · Fusion · Regression · NSCT · SVM

1 Introduction

Satellite data is the essential data for Earth observations applications. This data is important for many environmental monitoring applications. India is agricultural-based country. Close monitoring is required for crop study applications. Some crops with short duration require data with high resolutions for analysis. Indian spaceborne sensors have certain technological limitations of acquiring all the resolution high. Satellite data is described using resolutions viz., spatial, radiometric, spectral and radiometric resolutions [1]. The resolutions of the two sensors AWiFS and LISS-III of Resourcesat-I satellite are given in Table 1.

These two sensor data are considered for the proposed work because the spectral resolution of both sensors is the same. Both sensor data can be acquired on the same

K. S. R. Radhika (✉)
DMS SVH College of Engineering, Machilipatnam, India

C. V. Rao
National Remote Sensing Centre, Hyderabad, India

V. Kamakshi Prasad
JNTUH, Hyderabad, India

Table 1 Properties of AWiFS, LISS-III data

Sensor	Swath (km)	Temporal resolution (days)	Spatial resolution (m)	Spectral bands	Wavelength ranges (μm)
LISS-III	740	5	56	Band 2	0.52–0.59
				Band 3	0.62–0.68
				Band 4	0.77–0.86
				Band 5	1.55–1.70
AWiFS	140	24	23.5	Band 2	0.52–0.59
				Band 3	0.62–0.68
				Band 4	0.77–0.86
				Band 5	1.55–1.70

date and same geographical area. Resourcesat-I satellite has three sensors on board viz., AWiFS, LISS-III and LISS-IV. The acquisition of two sensors along path is shown in Fig. 1. In simultaneous acquisition, the overlapping regions of this pair of image sensors are shown in Fig. 2.

Fig. 1 AWiFS, LISS-III swath along path

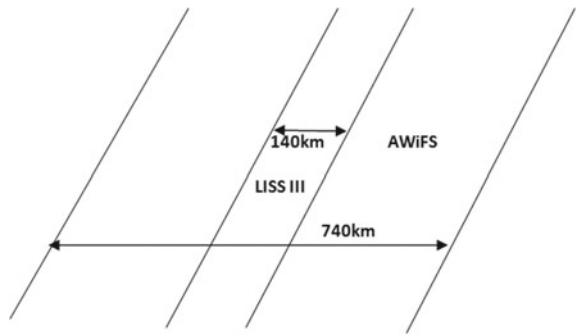
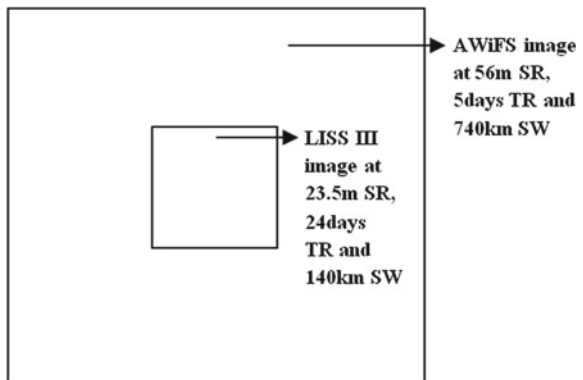


Fig. 2 Cross section along the path of two images



2 Back Ground

Two sensors data, Landsat and MODIS which have different temporal and spatial resolutions, are fused to improve temporal resolution. An algorithm STAARCH is developed and tested in Canada area of 185×185 km. This algorithm showed the landscape changes for the total disturbed area with improved results [2].

A novel method on image fusion is performed to enhance the radiometric resolution. This technique used sensor data (LISS-III, LISS-IV, AWiFS) of Resourcesat-I satellite which are having different resolutions. The resulted 10-bit image with spatial resolution 23.5 m showed discerning object classes with better accuracy for classification [3].

Data fusion is performed on high-resolution imagery and individual band LSR image using Modification Brovey Transforms (MBT). QuickBird and IKONOS images are fused using the methods MBT, Discrete Wavelet Transforms and Smoothing Filter-based Intensity Modulation. The resultant image preserved both spatial and spectral information. The results describe the strength of the prescribed method [4].

Fusion of LSHT and HSLT image is performed to generate high-spatial and high temporal (HSHT) images. The procedure is performed in two steps. In the first step, sparse representation is used and in latter, fusion using high-pass modulation is performed on LSHT, HSLT imageries [5].

3 Methodology

A. Description:

In Fig. 1, 140 km swath of LISS-III (HR) can be expanded to 740 km swath of AWiFS (LR) assuming that there may be similar Earth's surface objects in nonoverlapping area as that of objects in overlapping area by using single image super resolution method. Here, information (i.e., objects) related to both images in 140 km area is used as database for prediction in outer box area as shown in Fig. 3.

The spatial resolution (SR) of HR is less than SR of LR, i.e., SR ratio is 2.38. 2.38×2.38 pixels of HR are equivalent to single pixel of LR. In proposed method, both the images are acquired on same date and location; therefore, direct subpixel correspondence exists between LR pixel and HR pixel. In order to procure direct subpixel and HR pixel, interpolation (nearest neighbor) technique is used. By this technique, equalization is done for 2×2 pixel of HR to one pixel of LR as shown in Fig. 3. Because of the interpolation, there will be no change in reflectance values, but there will be problem of mixed-pixel responses. This problem of discrete pixel is resolved in the proposed method prediction of HR pixel which uses subpixel correspondence of LR-HR pair.

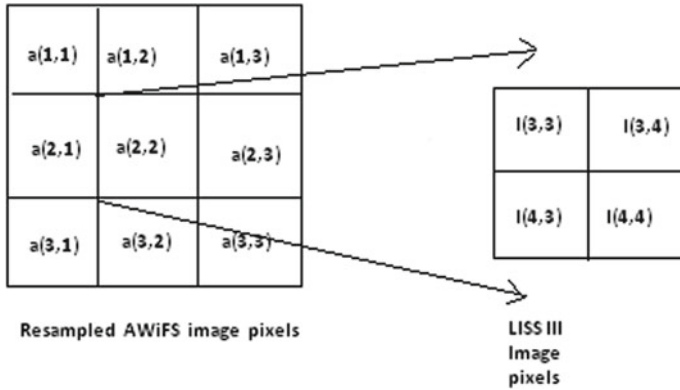


Fig. 3 Relationship between resampled pixel in AWiFS and LISS-III

B. Image-to-Image Registration:

This step is an essential precondition that is to be performed on the image pair HR-LR to create pixel-to-pixel correspondence. The HR is used as a reference image; the LR image is registered to HR image using control point method. 23.5 m pixel size of HR image is changed to 28 m by resampling. One pixel of LR image and 2 × 2 pixel block of HR image are made equivalent, because SR of LR image is 56 m. One-to-one relationship is obtained between LR-HR image pair.

C. LR-HR Normalization:

The SR of LR and HR images is 23.5 m and 56 m, respectively. Therefore, 2.4 pixels of HR span over LR single pixel. The radiometric resolutions of LR and HR images are 10-bit and 8-bit, respectively. Radiometric normalization in radiance domain given in (1) and (2) is performed, because of no Direct Digital Number (DN) comparison.

$$L_r = (L_d / DN_{max}(L)) * SaturationRadiance(L) \tag{1}$$

$$D_N = L_r * (DN_{max}(A) / SaturationRadiance(A)) \tag{2}$$

where L is LISS-III and A is AWiFS.

D. Prediction of HR image:

In prediction phase, image fusion using three different techniques is proposed in this work. The proposed methods are tested on two datasets. Figures 4 and 5 belong to Dataset-I original AWiFS and LISS-III images. Similarly, another dataset is also considered for testing. Input images are downloaded from BHUVAN website of NRSC, Hyderabad [7].

Fig. 4 AWiFS

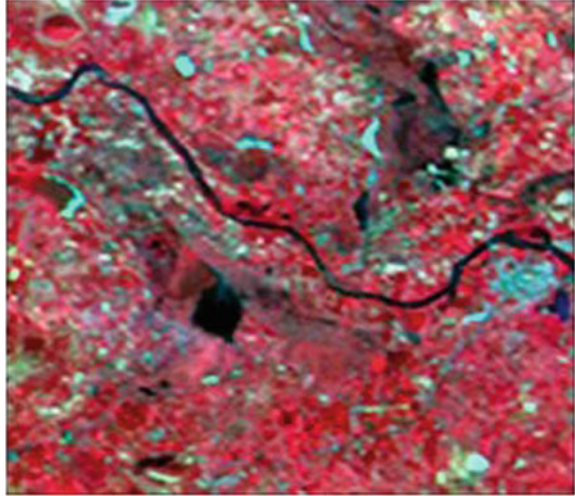


Fig. 5 LISS-III



● **Using Regression:**

The data in the overlapped area is used to train the regressor. In regression, there are two types of regression, namely linear and curvilinear. In linear regression, $y = a + bx$ where a, b are arbitrary constants and y is dependant variable on x . Similarly, in curvilinear, $y = a + b_1x + b_2x^2$ where a, b_1, b_2 are constants and y is dependant variable on independent variable x . The overlapping area, where both LR and HR images exist, is taken for training and then y is predicted using this trained data.

- **Using SVM:**

In the overlapping area, both the images appear over a span of 140 km. This region is given for SVM training. A 5×5 patch in LR image is given for its center pixel in HR image; this is a tuple in training database. Similarly, the total overlapped area is considered for training which is given for SVM-train, further creates trained database.

Later, this trained database is used to predict HR pixel to respective LR patch using SVM-predict [6].

- **Using NSCT:**

In overlapping areas, both LR and HR images are considered. Then applying NSCT, each is decomposed into seven contourlet coefficients, four high levels, two midlevel and one low-level frequencies. Training is performed separately on each and seven training databases are created. Later, these trained databases are used for prediction of seven contourlet coefficients belonging to HR image, corresponding to the respective LR image. Finally, inverse NSCT is applied for the predicted HR image [8].

4 Results

In this section, the proposed methodologies, namely the regression, SVM, NSCT predicted images are compared with the original image. All the methods are processed on the individual four bands of the image. The images are displayed in false-color composite (4, 3, 2). Figure 5 is the original HR image. Figure 6 is the predicted HR

Fig. 6 Using regression



image using regression. Figure 7 is the predicted HR image using SVM. Figure 8 is the predicted HR image using NSCT. All the three outputs are almost nearer to the original image.

The quality of the predicted images is assessed using quality assessment parameters like root means squared error (RMSE), correction coefficient (CC), R^2 , etc. The RMSE of the original and predicted images is shown in Table 2. The proposed method is tested on two data sets.

Fig. 7 Using SVM



Fig. 8 Using NSCT

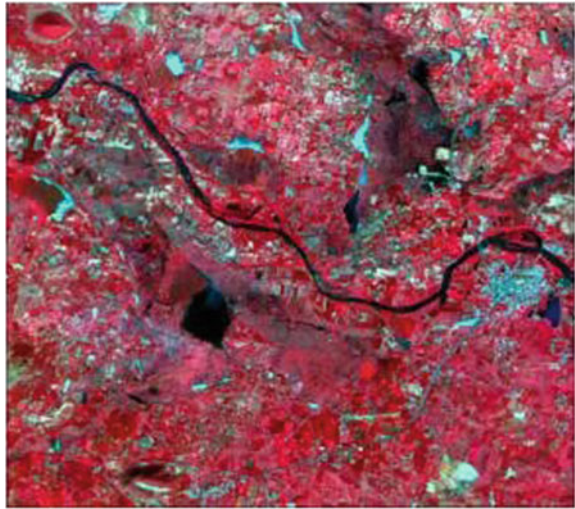


Table 2 Root means squared error

Method	Dataset-I				Dataset-II			
	B2	B3	B4	B5	B2	B3	B4	B5
Regression	2.9916	2.9998	3.3056	3.7626	2.4399	2.3005	2.4587	3.2891
SVM	2.5177 e-004	2.5177 e-004	2.5076 e-004	2.5328 e-004	2.5328 e-004	2.5227 e-004	2.5379 e-004	2.5303 e-004
NSCT	0.0032	0.0026	0.0138	0.0049	0.0027	0.0033	0.0035	0.0039

5 Conclusion

Using the proposed methodologies, the spatial resolution is enhanced for a LR images; therefore, the swath of 140 km can be expanded to 740 km assuming similar Earth's surface features in the nonoverlapping area as that in overlapping area. The quality assessment parameters are also found to be satisfactory for the predicted LISS-III image corresponding to the AWIFS image. Since the proposed methodologies are proved to be satisfied, this can be extended to the nonoverlapping area.

References

1. Jenen JR Introductory digital image processing, a remote sensing perspective
2. Hilker T, Wulder MA, Coops NC, Linke J, Mc Dermid G, Masek JG, Gao F, White JC (2009) A new data fusion model for high spatial- and temporal- resolution mapping of forest disturbance based on Landsat and MODIS. *Remote Sens Environ* 113:1613–1627
3. Rao CV, Rao KMM, Shasidhar Reddy P, Pujar G (2008) A novel method for enhancement of radiometric resolution using image fusion. *Int J Appl Earth Obs Geoinformation* 10:165–174
4. Li W, Zhang Q (2008) Study on data fusion methods with optimal information preservation between spectral and spatial based on high resolution imagery. *Arch Photogrammetry Remote Sens Spat Inf Sci XXXVII*, 1227–1232
5. Song H, Huang B (2012) Spatiotemporal satellite image fusion through one-pair image learning. *IEEE Trans Geosci Remote Sens* 1–13
6. Radhika KSR, Rao CV, Kamakshi Prasad V (2016) Enhancement of AWiFS spatial resolution with SVM learning. In: *International advanced computing conference, IACC*. IEEE, Bhimavaram, pp 178–183
7. National Remote Sensing Centre. <https://bhuvan.nrsc.gov.in>
8. Rao CV, Malleswara Rao J, Senthil Kumar A, Lakshmi B, Dadwal VK (2015) Expansion of LISS III swath using AWiFS wider swath data and contourlet coefficients learning. *GIScience Remote Sens* 52(1):78–93

Optimal Multiple Finite Burn Strategies for Trans-lunar and Trans-planetary Manoeuvres



Garima Aggarwal and R. V. Ramanan

Abstract In Chandrayaan I Mission and Mars Orbiter Mission, ISRO put the spacecraft from Earth Parking Orbit to the trans-lunar/trans-planetary injection point through a series of orbit-raising manoeuvres around Earth. The start time and duration of each burn, along with the size of the intermediate orbits and the burn sequence, must be designed, such that at the end of manoeuvres, the trans-lunar/trans-planetary injection epoch is achieved. This study aims to design the optimal multiple finite burn orbit-raising manoeuvres for trans-lunar and trans-planetary manoeuvres, using differential evolution as the optimization technique. The reduction in the computational time is achieved through multi-threading.

Keywords Orbit-raising manoeuvres · Finite burn loss · Differential evolution · Chandrayaan I Mission · Mars orbiter mission · Multi-threading

1 Introduction

ISRO has conducted several space missions, notably, Chandrayaan I Mission and Mars Orbiter Mission. The spacecraft which carried the experimental payloads for the two missions had to orbit around the Moon/Mars in Lunar/Planet Parking Orbit. There are a series of manoeuvres before the spacecraft reaches that orbit. The spacecraft is first injected by the launch vehicle into Earth Parking Orbit (EPO). The apogee/energy of the orbit is gradually increased until the spacecraft is injected into the trans-lunar/trans-mars trajectory. The spacecraft is then captured in an orbit around Moon/Mars through another sequence of manoeuvres. The orbit-raising manoeuvres are executed through finite burns for a specified duration around perigee. The burns are directed using velocity steering, in which the thrust direction is continuously aligned in the direction of the velocity of the spacecraft. It is well known that finite burn results in loss in the propellant mass. The finite burn loss can be reduced

G. Aggarwal · R. V. Ramanan (✉)

Department of Aerospace Engineering, Indian Institute of Space Science and Technology, Thiruvananthapuram, India

by executing the burn when the spacecraft is close to the perigee/apogee of the orbit, which makes the gravitational force perpendicular to the thrust direction [1].

2 Problem Formulation

The orbit-raising manoeuvres by ISRO are executed using a 440 N liquid thruster. The velocity impulse to be imparted is of the order of 1 km/s. This results in large burn duration and hence, large finite burn losses for a single burn. If the velocity impulse is imparted in multiple burns near the perigee, it will reduce the finite burn loss. For Chandrayaan I Mission, energy requirements of up to 160 m/s could be saved, which translates to around 40 kg of payload for the Chandrayaan I spacecraft. Also, these finite burn manoeuvres must be carried out such that there is no unplanned apsis line rotation. Further, there can be additional constraints, which are specific to different missions. For example, Chandrayaan I Mission had an additional constraint that the spacecraft should be visible from any one of the ISRO ground stations during each burn. Designing the multiple burns that save propellant mass and satisfy the constraints is an important task. The burn sequence (orbit numbers), intermediate orbit sizes, burn start time and the duration of burn must be chosen to satisfy the constraints and to make the spacecraft at perigee at the trans-lunar/planetary epoch.

3 Solution Procedure

This study devises an optimal strategy that consists of sequence of the orbit-raising manoeuvres which makes the spacecraft to be at the trans-lunar/trans-Mars injection point at the specified injection Epoch. This study formulates the problem as an optimization problem with unknown design parameters as the burn sequence, intermediate orbit size, the start time and duration of each burn. Differential evolution (DE), an optimization technique, is used to determine the unknowns because of its effectiveness to find a global optimal solution. Differential evolution does not require an initial guess but finds solution from a specified set of bounds on the unknown design variables [2]. Because the problem involves numerical integration of equations of motion, including perturbations, the process of finding the global optimal solution under finite burn requires enormous computational time [3, 4].

To reduce the computational time, a novel scheme has been devised. In this scheme, initial estimates of some of the unknowns are generated first by assuming impulsive burn in the optimization process, and then, these initial estimates are used in the optimization process with finite burn to generate the refined estimates. The optimization process assuming impulsive burn generates initial estimates for two unknowns (i) the sequence of burns and (ii) intermediate orbit sizes. The initial estimates of intermediate orbit sizes are used to generate initial estimates of the start time and duration of each burn assuming symmetric burn around perigee. The objective

function for the optimal impulsive burn strategy is set as minimizing the deviations in the trans-lunar injection (TLI) epoch and the final target orbit elements. These estimates are used in the optimization process where the orbit raising is modelled with finite burn. The intermediate orbit sizes obtained in this optimization process are used as target intermediate orbits for the finite burn optimization. It is to be noted that the intermediate orbit sizes may undergo changes in finite burn strategy, due to visibility constraint.

The initial estimates on burn start and burn duration obtained in optimization process assuming impulsive burn are used to fix the bounds of the design variables in the optimization process with finite burn. These initial estimates help narrow down the bounds and hence reduce the computational time of the optimization process with finite burn. In the optimal finite burn strategy, the objective function includes minimizing the deviation in the intermediate orbit sizes, AOP during each burn, the TLI epoch and the final target orbit elements. In optimizing the above objective functions, suitable weights have been added to the terms of the objective function. Despite the smaller bounds, the computational time for the optimization process with finite burn is about half a day. In order to further reduce the computational time, multi-threading has also been implemented in the C++ code, developed to find the optimal burn strategy.

4 Differential Evolution

Differential evolution (DE) is a meta-heuristic procedure that optimizes a problem by maintaining a population of candidate solutions and creating new candidate solutions by combining existing ones using crossover probability and then keeping whichever candidate solution has the best score or fitness on the optimization problem at hand. DE can search very large spaces of candidate solutions, thus ensuring global solution. Three operations (i) mutation, (ii) crossover and (iii) selection are used to introduce variation in the population of candidates. The DE scheme is used in this study is $\text{rand}/1/\text{bin}$, which means that the vector to be mutated is selected at random, only one difference vector is used for mutation, and crossover is determined by independent binomial experiments. The performance of DE is influenced by three parameters (i) crossover probability (CR); (ii) population size (NP) and (iii) mutation factor (F). Further details of the DE algorithm can be found in [2].

5 Algorithms

5.1 Optimization Process with Impulsive Burn

The unknowns in the impulsive burn strategy are the size of the intermediate phasing orbits around the Earth. The number of burns is fixed.

1. Fix bounds on the sizes of the intermediate phasing orbits. If there are four burns, then there will be four such bounds.
2. Select values for sizes of the intermediate orbits randomly from their respective bounds.
3. Propagate the orbit from injection epoch to an orbit pass which satisfies the visibility constraint from a network of tracking stations. Note that the propagation is not by using numerical integration. It is an approximate analytical process. After every orbital lap, Right Ascension of Ascending Node (RAAN) and Argument of Perigee (AOP) of the orbit are to be updated to account for J2 effect [1]. The other orbital elements are kept the same, and the state vector at perigee is computed. The check of visibility is done for this state vector. A constraint for an elevation angle of at least 7° at perigee has been imposed. This is done to later ensure visibility over the burn arc for finite burn.
4. Introduce impulsive burns at the perigee to achieve the next immediate intermediate orbit size. The velocity requirement at the burn location is given by

$$\Delta v_B = \sqrt{\mu \left(\frac{2}{r_B} - \frac{1}{a_1} \right)} - \sqrt{\mu \left(\frac{2}{r_B} - \frac{1}{a_2} \right)}$$

where r_B is the radius of the burn location and a_1, a_2 are the semi-major axes of the initial and target orbits.

5. Repeat steps (3) and (4) till the number of burns (fixed a priori) is completed.

Maximum number of orbital laps in the same orbit has been fixed to four. In case of non-visibility of spacecraft for four consecutive perigee of the same orbit, impose a heavy penalty in the objective function, which will eventually lead to rejection of the proposed solution.
6. Find the apogee of the achieved orbit after all prefixed number of burns and compute $|h_{\text{achieved}} - h_{\text{target}}|$.
7. Find the time elapsed to reach the perigee of the final intermediate orbit and compute $|\text{TLI Epoch}_{\text{achieved}} - \text{TLI Epoch}_{\text{target}}|$.
8. Check the visibility of the spacecraft at TLI epoch. In case of non-visibility, heavy penalty is to be imposed on the objective function.
9. The objective function is set as

$$F = w_1 X |\text{TLI Epoch}_{\text{achieved}} - \text{TLI Epoch}_{\text{target}}| + w_2 X |h_{\text{achieved}} - h_{\text{target}}| \\ + \text{Penalty for burn non-visibility at the perigees}$$

where w_i are weights for the i th terms in the objective function. The weights in the objective function have been fixed after several trials and are very specific to a mission. For Chandrayaan I Mission later described in Sect. 6.1, the weights are $w_1 = 500$, $w_2 = 1$, Penalty = 108.

10. Build a population of a fixed size (NP) by repeating the steps (2) to (9). The population is a $NP \times (n + 1)$ matrix, where n is the number of unknowns, and the last column will be the value of the objective function.
11. The DE optimization is carried out on the current generation, and the population is updated by repeating the steps (3) to (9) till the termination criteria are met.

The output obtained from the impulsive burn strategy gives the size of the intermediate orbits, which in turn are used to find the burn start time assuming symmetric burn and duration of each burn for finite burn implementation.

Given the initial mass of the spacecraft before each burn, ideal rocket equation gives the burn-out mass of the spacecraft after each burn:

$$\Delta v_B = g_0 I_{sp} \ln \left(\frac{M_{\text{initial}}}{M_{\text{final}}} \right)$$

where $g_0 = 9.81$ m/s and I_{sp} is the specific impulse of the spacecraft. The burn time is given by

$$\begin{aligned} \dot{m} &= \frac{\text{Thrust}}{g_0 I_{sp}} \\ \text{Burn time} &= \frac{M_{\text{initial}} - M_{\text{final}}}{\dot{m}} \end{aligned}$$

Thus, the estimated burn start time = Time of passage at perigee – estimated burn time/2, assuming symmetric burn.

5.2 Optimization Process with Finite Burn

The unknowns in the finite burn optimization process are the burn start time and burn duration of each burn. Previous Sect. 5.1 described how to find an initial estimate of burn start time and burn duration, which is used to fix bounds on these unknown parameters. The burn sequence and the intermediate orbit sizes are fixed to the values which are obtained in the optimization process with impulsive burn. These intermediate orbit sizes are used as targets to be achieved after each burn. However, achieving them exactly is not possible. During finite burn, the perigee altitude undergoes changes, which in turn changes the orbital period, and so, the target apogee altitudes after each burn also undergo small changes. The error in the achieved apogee altitudes can vary from 0.1% for the initial burns to 2% for the end burns. The objective function is formed to minimize these changes.

1. Fix bounds on unknowns of all burns: burn start times and burn durations.
2. Select values randomly from their respective bound for all unknowns.

3. Propagate the orbit from injection epoch to an orbit pass already identified with impulsive burn. Note that the propagation is using numerical integration of equations of motion that includes perturbation due to J2 effect of non-spherical Earth. Unlike in the impulsive burn, the state vector gets updated in this numerical integration.
4. Execute the finite burns at the selected burn start time for the selected burn duration for each burn. Check visibility of the spacecraft at all times during burn. In case of non-visibility of spacecraft during any burn, impose a heavy penalty in the objective function, which will eventually lead to rejection of the proposed solution.
5. Find the apogee of the achieved intermediate orbit and compute $|h_{\text{achieved},i} - h_{\text{target},i}|$ for the i th burn. Also, find the change in AOP of the orbit after the burn.
6. Repeat the steps (3) to (5) for all burns.
7. Find the true anomaly at the TLI epoch.
8. Check the visibility of the spacecraft at TLI epoch. In case of non-visibility, impose heavy penalty on the objective function.
9. The objective function for finite burn strategy is as follows:

$$\begin{aligned}
 f = & w_{11}(\text{Error in AOP}_1) + w_{12}|h_{\text{achieved},1} - h_{\text{target},1}| + w_{21}(\text{Error in AOP}) \\
 & + w_{22}|h_{\text{achieved},2} - h_{\text{target},2}| + \dots + w_{\text{TLI}}(\text{TA}_{\text{TLI}}) \\
 & + \text{Penalties for non visibilities during each burn and at TLI Epoch.}
 \end{aligned}$$

where w_{i1} represent the weights for error in AOP for i th burn and w_{i2} represent the weights for error in apogee altitude for i th burn. The weights in the objective function have been fixed after several trials and are very specific to a mission. For Chandrayaan I Mission later described in Sect. 6.1, the weights are $w_{11} = 105$, $w_{12} = 2$, $w_{21} = 2000$, $w_{22} = 10^{-3}$, $w_{31} = 104$, $w_{32} = 10^{-4}$, $w_{41} = 104$, $w_{\text{TLI}} = 5000$, Penalty = 1010. They can be easily set after studying the trend in the objective function on changing weights.

10. Build a population of a fixed size (NP) by repeating the steps (2)–(9). The population is a $\text{NP} \times (n + 1)$ matrix where n is the number of unknowns, and the last column will be the value of the objective function.
11. The DE optimization is carried out on the current generation, and the population is updated by repeating the steps (3)–(9) till the termination criteria are met.

6 Numerical Results

A C++ code has been developed based on the procedures discussed in the sections above. To fix values for the DE parameters, a few trial runs have been carried out for an orbit-raising manoeuvre. The combination of the parameters which gave least error and minimal computational time is $F = 0.4$, $\text{CR} = 0.5$ and $\text{NP} = 40$. These set of parameters are specific to a sample orbital manoeuvre, but they have given

satisfactory results for the other manoeuvres and missions discussed. To validate the formulation and the code, the following missions have been reproduced: (i) Chandrayaan I Mission and (ii) Mars Orbiter Mission (MOM).

6.1 Chandrayaan I Mission

India’s first Moon mission Chandrayaan-1 carrying eleven scientific instruments for the purpose of expanding scientific knowledge about the Moon was launched on 22 October 2008 from Satish Dhawan Space Centre, Sriharikota, India, by India’s PSLV-C11. The spacecraft was injected into transfer orbit of $254.4 \times 22,932.7$ km with inclination of 17.9° at 2008-10-22 01:10:19.081 UTC. The spacecraft was put into Moon’s polar circular orbit of about 100×100 km on 12 November 2008 by carrying out sequence of Earth and lunar bound manoeuvres.

For this study, the spacecraft is assumed to be initially in EPO of $250 \text{ km} \times 22,881 \text{ km}$. The following constraints were introduced in the optimization processes.

1. The spacecraft should be visible during each burn from any of the ISRO ground stations, as mentioned in Table 1 (Fig. 1).
2. No rotation of the apsis line of the intermediate orbits, during burn.
3. Reach perigee of the last intermediate orbit at TLI epoch.
4. Visibility at perigee of the last intermediate orbit for TLI burn.

The parameters used in the study are given in Table 2. The optimization process assuming impulsive burn generated a burn sequence (4, 6, 7, 10, 11) which implies five burns at the 4th, 6th, 7th, 10th and 11th perigees of the orbit and the related orbit sizes. This sequence of burns and the intermediate orbit sizes are chosen ensuring visibility at the perigee of the orbit. The burn sequence and the intermediate orbit sizes are given in Table 3. The velocity impulse required and the burn duration corresponding to the intermediate orbit sizes and the mass of the spacecraft after each burn have been computed using equations mentioned in Sect. 5.1. The values have been tabulated in Table 3.

It is to be noted this burn sequence was the same sequence proposed by ISRO. However, due to failure of burn at the 6th perigee, ISRO had to revise its burn strategy.

The optimization process with finite burn is attempted using the results of impulsive burn. The bounds on the start time and duration of each burn are fixed around

Table 1 ISRO ground stations for Chandrayaan I Mission

Station	Latitude	Longitude
Trivandrum	8.536°N	76.78°E
Bangalore	13.03°N	7.51°E
Biak	1.10°S	136.05°E
Brunei	4.97°N	114.88°E
Port Blair	11.64°N	92.71°E



Fig. 1 ISRO ground stations for tracking Chandrayaan I spacecraft

Table 2 Chandrayaan I Mission specifications

Specification	Value	Units
Thrust	408	N
I_{sp}	318	s
Initial mass	1380	kg
PSLV injection epoch	22-10-2008 01:10:19.081	UTC
TLI epoch	03-11-2008 23:15:00	UTC
Target orbit	380,000	km
Number of burns	5	—

Table 3 Impulsive burn results for Chandrayaan I Mission

Burn at perigee	h_a (km)	Delta v (m/s)	Mass (kg)	Burn duration (s)
4	37,393.45	318.37	1246.07	1023.69
6	68,507.62	291.22	1126.35	831.70
7	106,428.12	146.68	1070.49	388.14
10	230,983.46	158.67	1013.17	398.22
11 (TLI)	380,000.00	57.11	993.29	138.06
Total		972.05	993.29	

the values, given in Table 3. The bounds on the burn duration are set within ± 40 s, whereas the bounds on the burn start time are different for each burn. It is set as ± 500 s for the first burn and increases to ± 1700 s for the last burn. The intermediate orbit sizes, along with few other parameters, have been used in the objective function of finite burn process, with suitable weights.

To validate the formulation of the finite burn, the first burn of the mission has been reproduced and compared to the actual mission, as shown in Table 4.

Small deviations in the current design from the Chandrayaan I Mission occur due to difference in the force model. The code accounts only for the J2 effect due to non-spherical Earth and not the forces, like solar radiation pressure, gravitational forces due to third bodies, other harmonics of Earth’s oblateness, etc.

Table 5 gives the modified burn duration, the true anomaly of the burn start and

Table 4 First burn design from this study and the Chandrayaan I Mission

Orbit parameter	3rd lap burn start	4th perigee (with burn)	4th lap burn end	Chandrayaan Mission	Units
h_p	256.07	258.34	292.19	292.02	km
h_a	22,857.16	26,161.28	37,351.26	37,425.47	km
a	179,314.61	19,587.81	25,199.73	25,236.75	km
e	0.630097	0.661201	0.735307	0.735702	–
Inclination	17.89	17.89	17.89	17.89	°
RAAN	353.09	35.08	353.06	353.07	°
AOP	170.06	169.73	171.73	171.73	°
TA	333.37	0.01	54.57	54.58	°
Time passed since 22/10/08 01:10:19.081	94,679.00	94,994.00	95,739.34		s
Burn duration			1060.34	1063.24	s

Table 5 Finite burn strategy for Chandrayaan I Mission

Burn at perigee	h_a (km)	TA burn start (°)	TA burn end (°)	Delta v (m/s)	Mass (kg)	Burn duration (s)
4	37,351	333.37	54.57	330.39	1241.27	1060.34
6	68,507	323.05	33.87	287.16	1128.45	846.73
7	107,371	340.57	15.94	150.52	1075.28	397.43
10	235,350	340.17	16.61	162.4	1020.72	404.73
11 (TLI)	380,000	351.98	4.27	54.6	1003	133.13
Total				995.071	1003	

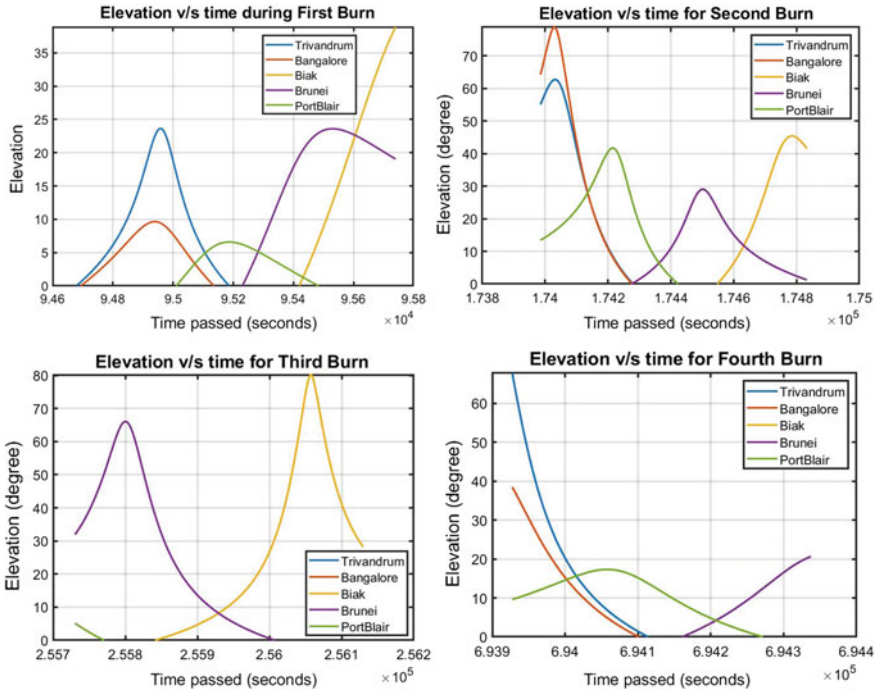


Fig. 2 Visibility at different ISRO ground stations during different burns for tracking Chandrayaan I spacecraft

the burn end of each burn. It also gives the modified orbit sizes and the corresponding velocity requirements.

A single burn for TLI would require 1134.5 m/s against the 995.07 m/s with multiple burns. This could cut down the payload mass of the spacecraft by around 40 kg.

Figure 2 presents the plots for elevation of the spacecraft from different ISRO ground stations mentioned in Table 1.

6.2 Mars Orbiter Mission (MOM)

The Mars Orbiter Mission (MOM) is India’s first interplanetary mission. The Mars Orbiter Mission probe was lifted-off from Satish Dhawan Space Centre, using a PSLV rocket at 09:52.39.5 UTC on 5 November 2013. The MOM probe spent about a month in Earth orbit, where it made a series of six apogee-raising orbital manoeuvres before trans-Mars injection on 30 November 2013 (UTC) [5].

For this study, the spacecraft is assumed to be initially in EPO of $240 \text{ km} \times 23,563 \text{ km}$. The following constraints were introduced in the optimization processes.

Table 6 ISRO ground stations for MOM

Station	Latitude	Longitude
Mauritius	20.35°S	57.55°E
Bangalore	13.03°N	7.51°E
HBK	25.89°S	27.68°E
Alcantara	2.40°N	44.41E

1. The spacecraft should be visible during the beginning of each burn from any of the ISRO ground stations, as mentioned in Table 6 (Fig. 3).
2. No rotation of the apsis line of the intermediate orbits, during burn.
3. Reach perigee of the last intermediate orbit at TMI Epoch.
4. Visibility at perigee of the last intermediate orbit for TMI burn.

The parameters used in the study are given in Table 7. The target is to reach



Fig. 3 ISRO ground stations for tracking MOM Orbiter spacecraft

Table 7 Mars Orbiter Mission specifications

Specification	Value	Units
Thrust	425	N
I_{sp}	315	s
Initial mass	1340	kg
PSLV injection epoch	05-11-2013 09:52:39.5	UTC
TMI epoch	30-11-2013 19:30:00	UTC
Number of burns	5	–

Table 8 Impulsive burn results for MOM

Perigee	h_a (km)	Delta v (m/s)	Mass (kg)	Burn duration (s)
0	23,563.37		1340.00	
5	28,224.61	123.41	1287.52	381.43
8	40,201.14	214.31	1201.23	627.22
10	72,605.17	272.71	1099.73	737.75
13	119,733.40	155.77	1045.65	393.09
15	190,533.00	97.27	1013.24	235.59
Total		614.75	837.42	

an apogee altitude of 192,874 km from an initial apogee altitude of 23,563 km. The optimization process assuming impulsive burn generated a burn sequence (5, 8, 10, 13, 15, 19) which implies six burns at the 5th, 8th, 10th, 13th, 15th and 19th perigees of the orbit. The burn at the 19th perigee would set the spacecraft in a hyperbolic orbit, along which the spacecraft escapes the Earth. This sequence of burns and the intermediate orbit sizes are chosen ensuring visibility at the perigee of the orbit. The burn sequence and the intermediate orbit sizes are given in Table 8. The velocity impulse required and the burn duration corresponding to the intermediate orbit sizes and the mass of the spacecraft after each burn have been computed using equations mentioned in Sect. 5.1. The values have been tabulated in Table 8. This results in velocity requirement of 1452.17 km/s, only for the impulsive orbit-raising manoeuvres to reach the target orbit before injection into trans-Mars trajectory. This burn strategy is the same as proposed by ISRO for MOM Mission. But ISRO could not implement this burn strategy due to incomplete 4th burn at the 13th perigee of the orbit.

To find an optimal finite burn strategy, bounds on the start time and duration of each burn are fixed around the values, given in Table 8. The bounds on the burn duration are set within ± 150 s, whereas the bounds on the burn start time are different for each burn. It is set as ± 500 s for the first burn and increases to $\pm 20,000$ s for the last burn. The intermediate orbit sizes, along with few other parameters, have been used in the objective function of finite burn process, with suitable weights. The optimal finite burn strategy obtained is given in Table 9.

It is evident that the velocity impulse during finite burns for MOM is around 904.62 km/s.

The visibility plots, shown in Fig. 4, clearly show that the visibility constraint has not been rigidly been applied for MOM because of the rarity in the opportunity for the interplanetary mission. ISRO did eventually opt for partial blind burns to avoid delay or failure in mission.

Table 9 Finite burn strategy for Mars Orbiter Mission

Burn at perigee	h_a (km)	TA burn start (°)	TA burn end (°)	Delta v (m/s)	Mass (kg)	Burn duration (s)
5	28,237.38	341.02	13.81	124.11	1287.23	383.56
8	40,501.48	330.32	25.085	220.31	1198.62	644.03
10	73,750.47	325.65	29.91	278.42	1095.31	750.88
13	120,222.31	340.29	14.97	151.59	1042.86	381.25
15	236,694.48	344.98	13.64	130.19	999.824	312.82
Total				904.62	999.824	

7 Multi-threading in Optimization

Multi-threading is a specialized form of multitasking, which deals with the concurrent execution of pieces of the same program. A multithreaded program contains two or more parts that can run concurrently. Multi-threading has been implemented in the scheme of differential evolution, only to evaluate the cost function of individuals in a specific generation simultaneously. Evaluation of the cost function is computationally dominating and thus demands parallelization. A sample lunar mission has been studied to highlight the importance of multi-threading to reduce computational time. The mission specifications are the same as shown in Table 2. The apogee altitude of the orbit is to be increased from 22,861 to 71,592 km in two burns. The mission, thus, has four unknowns—burn start time and burn end time of each burn.

The computational time to find the optimal solution was reduced by eight times, after implementing multi-threading on a four-core processor (Table 10). The time taken to find the optimal five-burn strategy for Chandrayaan I Mission, with ten unknowns, took around 80 min with multi-threading. Without the visibility constraint for Mars Orbiter Mission, the computational time to find an optimal solution for ten unknowns is around 10–15 min. The computational time increases exponentially with increase in the number of unknowns. This brings out the need of multi-threading to reduce the computational time for an optimal solution. This computational time for the missions is aimed to be less than the orbital time periods of the spacecraft. This gives enough time to compute optimal finite burn strategy, in case of failure of a burn or any immediate necessary change in burn strategy.

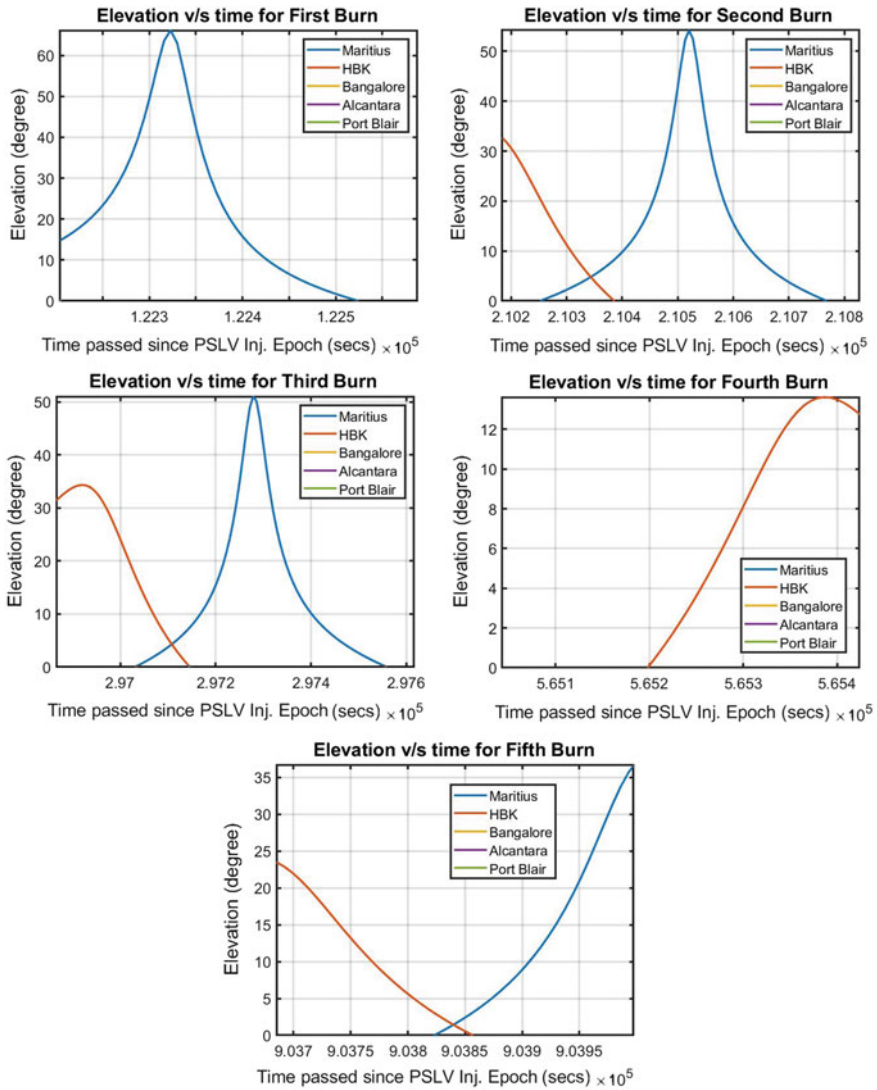


Fig. 4 Visibility at different ISRO ground stations during different burns for tracking MOM spacecraft

Table 10 Computational time for lunar strategy using single and multi-threading

	Unknown variables				Computational time (min)	Generations in DE for computation
	1st burn start time (s)	2nd burn start time	1st burn duration	2nd burn duration		
Single-thread	94,707.051	168,384.810	861.07	966.61	11.13	178
Multi-thread	94,707.051	168,384.810	861.07	966.61	1.34	178

Acknowledgements We are thankful to Ansuman Palo, an undergraduate student of IIST, who provided his expertise that greatly assisted the implementation of multi-threading in the C++ code. We are always also grateful to our families for the moral support extended to us.

References

1. Vladimir A (2002) Chobotov, orbital mechanics, 3rd edn. AIAA Education Series, Virginia
2. Pedersen M (2010) Good parameters for differential evolution. Hvass Laboratories, Technical Report no. HL1002
3. Curtis H (2005) Orbital mechanics for engineering students, 3rd edn. Elsevier Ltd., Great Britain
4. Suresh BN, Sivan K (2015) Integrated design for space transportation system. Springer, India
5. Ramanan RV, Adimurthy V (2014) Mars Orbiter mission: overview. Planex 4(1)

RF

RF Signal Conditioning Module for Digital Receiver



Ranjit Kumar Dora, N. Veena, E. Vasanth, S. S. Rana
and Vinod Chippalkatti

Abstract A multichannel digital receiver is required for estimating several signal parameters such as instantaneous frequency, pulse width, pulse amplitude, PRF as well as direction of arrival of signals. In this paper, a five-channel signal conditioning module is developed for the multichannel digital receiver that is capable of operating in 160–180 MHz and 750–1250 MHz bands with 40 dB dynamic range at the input (−38 to 2 dBm).

Keywords Digital receivers · Signal conditioning circuits · DIFM and DF receivers

1 Introduction

Multichannel digital receiver developed at Centum estimates the direction of arrival of signal using Baseline Interferometry (BLI) technique and frequency measurements using Digital Instantaneous Frequency Measurements (DIFM) technique. The digital receiver is realized using RF signal conditioning circuits, high-speed ADCs, FPGA logics, high-speed RAM look up tables and a central supervisory microcontroller interface unit. Multichannel digital receiver has the following major functions:

R. K. Dora (✉) · N. Veena · E. Vasanth · S. S. Rana · V. Chippalkatti
Centum Electronics Ltd., No. 44, KHB Industrial Area, Yelahanka New Town, Bangalore,
Karnataka 560106, India
e-mail: ranjitikumard@centumelectronics.com

N. Veena
e-mail: veenan@centumelectronics.com

E. Vasanth
e-mail: vasanthe@centumelectronics.com

S. S. Rana
e-mail: ssrana@centumelectronics.com

V. Chippalkatti
e-mail: vinod@centumelectronics.com

© Springer Nature Singapore Pte Ltd. 2020
PSR. S. Sastry et al. (eds.), *Advances in Small Satellite Technologies*,
Lecture Notes in Mechanical Engineering,
https://doi.org/10.1007/978-981-15-1724-2_36

- Video threshold detection to aid the data acquisition.
- Measurement of the signal frequency using Digital Instantaneous Frequency Measurement (DIFM) technique.
- Measurement of various parameters such as amplitude and pulse width using the analogue video signal. The high-speed comparator for threshold detection is also implemented for generating the data valid trigger.
- High-speed ADCs used for digitizing the IF channels at 1000 ± 250 MHz or 160 ± 20 MHz for instantaneous frequency measurement.
- Computation of angle of arrival (AOA) by Baseline Interferometry (BLI) technique by simultaneously sampling the four IF signals corresponding to four antenna elements of the Azimuth/Elevation array.
- Generation of Pulse Description Word (PDW) and sending the same to satellite Baseband Data Handling (BDH) system via LVDS link. The controller and 1553 communication protocol are realized in Actel AX2000 FPGA as soft IPs.
- The regulated power for digital receiver is generated using highly efficient Electronic Power Conditioner (EPC).

2 Signal Conditioning

Multichannel digital receiver is an important sub-system for measuring several pulse parameters such as instantaneous frequency, amplitude, the direction of arrival and pulse width of the radar signals in real time in the 0.5–18 GHz band. Following are the salient features of the signal conditioning module:

- Flat response over 140–180 MHz and 750–1250 MHz bands.
- Keep voltage level at ADC input within safe limits and compress the 40 dB input signal dynamic range to less than 10 dB at ADC input.
- The digital receiver accepts four channels of amplitude/phase-matched IF signals in the frequency range of 1000 ± 250 MHz/ 160 ± 20 MHz. In addition, the fifth IF channel for instantaneous frequency measurement and two video channels for signal detection/threshold and pulse parameters estimation are also available at the input.

The IF signals are suitably amplified in signal conditioning circuits and passed through 3 dB hybrid to generate I and Q signals, which are digitized using high-speed ADC's. The FPGAs receive the digitized signals from four channels and estimate phase, frequency and angle of arrival of the signal. The video channel is used to generate the data valid trigger, and this enables the measurement of the pulse width. The output from the receiver is packetized as Pulse Description Word (PDW) and given to Baseband Data handling (BDH) system for transmission to the ground.

The paper discusses various topologies considered to arrive at the optimum configuration of the Signal Conditioning Module which provide the following functions:

- Suitable amplification using low noise front-end amplifier.
- Keep the ADC input voltage level within safe limit.
- Split the IF signal into two bands at 160 ± 20 MHz and 1000 ± 250 MHz and provide necessary filtering for limiting the out of band noise.
- Generation of IQ components for both frequency bands by using 3 dB hybrid coupler.
- Providing balanced signal at the ADC input using a broadband balun (common input for 160 and 1000 MHz channels selectable using two SPDT switches).
- Suitable level adjustment of the signal to get the same voltage at the ADC input for both 160 and 1000 MHz channels.

As the IF signal is used for accurate determination of amplitude and phase of the incoming signal, the following design aspects need special attention:

- Low noise front end
- Sharp cut-off filters to remove out of band noise.
- Very accurate amplitude and phase balance between I and Q channels over 0 to 40 °C temperature range.
- Minimal amplitude/phase distortion between the input and output over the complete signal dynamic range. This puts severe restriction in selecting hard limiters for protection purpose.
- Significant signal level at the ADC input corresponding to the minimum signal level at the receiver input.
- Protection of various amplifiers and ADC's against high level of spurious signals.

3 Design Methodology

3.1 Specifications

Table 1 gives detailed specifications for the signal conditioning circuit.

3.2 Design Approach

For ease of implementation and better channel to channel matching, the signal conditioning circuit is realized using the following two modules:

- Amplifier–Limiter Module-1
- Filter-IQ Module-2.

Figure 1 shows the block diagram of Module-1 wherein a combination of amplifiers and limiters is used. Four amplifiers, each having gain of 16 dB and three limiters with insertion loss of 2 dB each are used to reduce dynamic range from 40 dB to less

Table 1 Specifications

S. no.	Parameters	Specifications
1.	Four RF inputs	750–1250/140–180 MHz
2.	Input and output impedance	50 Ω
3.	Input signal range	−38 to +2 dBm
4.	Noise figure	3 dB
5.	Harmonic level	−50 dBc with respect to carrier at +2 dBm input power
6.	Gain matching	± 1dB (Among all the channels)
7.	Phase matching (Among all the channels)	i. ±5° (at ambient temperature) ii. ±8° (over the complete temp range)
8.	Voltage and currents	i. 5 V/300 mA, 15 V/10 mA
9.	Controls	CMOS compatible



Fig. 1 Module-1—amplifier–limiter

than 10 dB. The amplifier can withstand maximum input power of 24 dBm and has 1 dB compression point at 19 dBm. Limiter has a maximum input power of 20 dBm and an output power of 2 dBm for power exceeding +2 dBm. The maximum output power of amplifier–limiter card is around 18 dBm.

Figure 2 shows the block diagram of filter-IQ card. Filter-IQ card consists of SP2T switches for selecting 140 MHz/1000 MHz band, BPF’s at 160 MHz and 1 GHz, attenuator pad for level adjustment, hybrid coupler and power divider.

Figure 3 shows amplifier–limiter card. Output of amplifier–limiter card acts as an input to the filter-IQ card. Figure 4 shows filter-IQ card. The first component in filter-

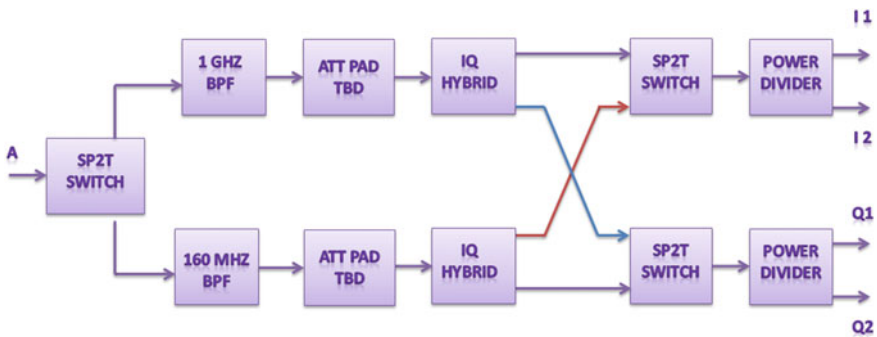


Fig. 2 Module-2—Filter-IQ

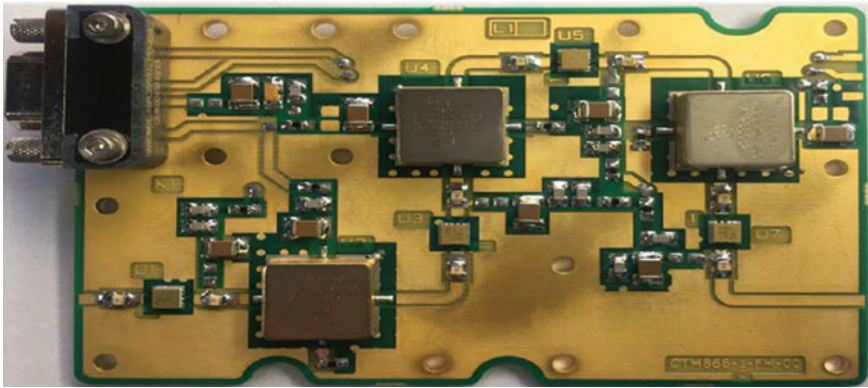


Fig. 3 Amplifier-limiter card

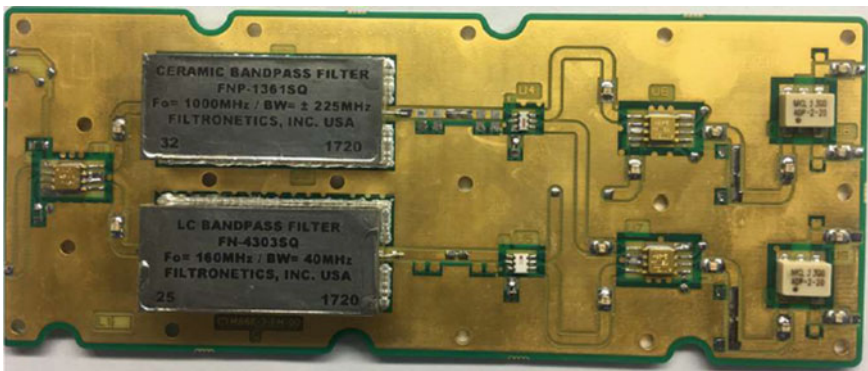


Fig. 4 Filter-IQ card

IQ card is SP2T switch, which helps to select either 1000 MHz path or 160 MHz path. In 1000 MHz path, input signal from switch passes through BPF having bandwidth of 500 MHz, and in 160 MHz path BPF has bandwidth of 40 MHz. The attenuator pad which follows the filter is used for power tuning based on the requirement of ADC (4 dBm for 1000 MHz and 0 dBm for 160 MHz). The hybrid coupler splits the input signal with 90° phase difference. Two SP2T switches following 160 MHz/1000 MHz hybrids select I/Q from either 160 MHz or 1000 MHz channels. Figure 5 shows the photographs of the flight model of the five-channel RF Signal Conditioning Module for the digital receiver.

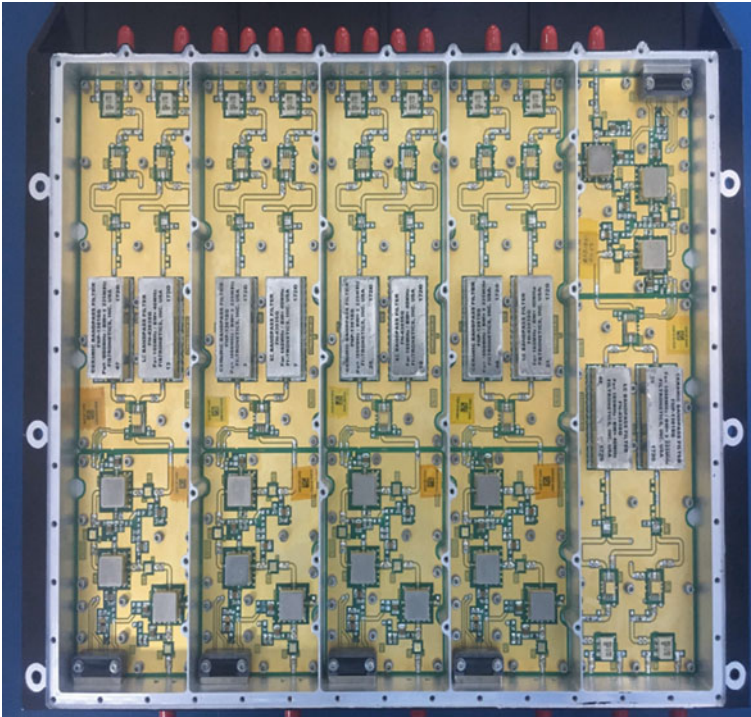


Fig. 5 RF signal conditioning module for digital receiver

3.3 Chain Budgeting

Tables 2 and 3 give the chain budgeting for 160 MHz and 1000 MHz channels, respectively.

4 Results

4.1 Gain Measurements

Figures 6 and 7 are the gain measurement plots for 160 MHz band and 1000 MHz band, respectively, at -40 dBm input power level. However, as the input power increases, the limiters go into compression and the output remains nearly constant over the entire input dynamic range of 40 dB.

Table 2 Chain budgeting for 160 MHz band

IP power (dBm)	160 MHz			
	-40.0		0.0	
	Gain/Loss	OP	Gain/Loss	OP
Amplifier 0	16.0	-24.0	16.0	16.0
Limiter 0	-2.0	-26.0	-2.0	2.0
Amplifier 1	16.0	-10.0	16.0	18.0
Limiter 1	-2.0	-12.0	-2.0	2.0
Amplifier 2	16.0	4.0	16.0	18.0
Limiter 2	-2.0	2.0	-2.0	2.0
Amplifier 3	16.0	18.0	16.0	18.0
Switch-1	-1.5	16.5	-1.5	16.5
BPF	-4.5	12.0	-4.5	12.0
Att Pad	-3.5	8.5	-3.5	8.5
Hyb-coupler	-3.5	5.0	-3.5	5.0
Switch-2	-1.5	3.5	-1.5	3.5
Power divider	-3.5	0.0	-3.5	0.0
Balun	-1.0	-1.0	-1.0	-1.0

Table 3 Chain budgeting for 1000 MHz band

IP power (dBm)	1000 MHz			
	-40.0		0.0	
	Gain/Loss	OP	Gain/Loss	OP
Amplifier 0	16.0	-24.0	16.0	16.0
Limiter 0	-2.0	-26.0	-2.0	2.0
Amplifier 1	16.0	-10.0	16.0	18.0
Limiter 1	-2.0	-12.0	-2.0	2.0
Amplifier 2	16.0	4.0	16.0	18.0
Limiter 2	-2.0	2.0	-2.0	2.0
Amplifier 3	16.0	18.0	16.0	18.0
Switch-1	-1.5	16.5	-1.5	16.5
BPF	-1.5	15.0	-1.5	15.0
Att Pad	-2.5	12.5	-2.5	12.5
Hyb-coupler	-3.5	9.0	-3.5	9.0
Switch-2	-1.5	7.5	-1.5	7.5
Power divider	-3.5	4.0	-3.5	4.0
Balun	-1.0	3.0	-1.0	3.0

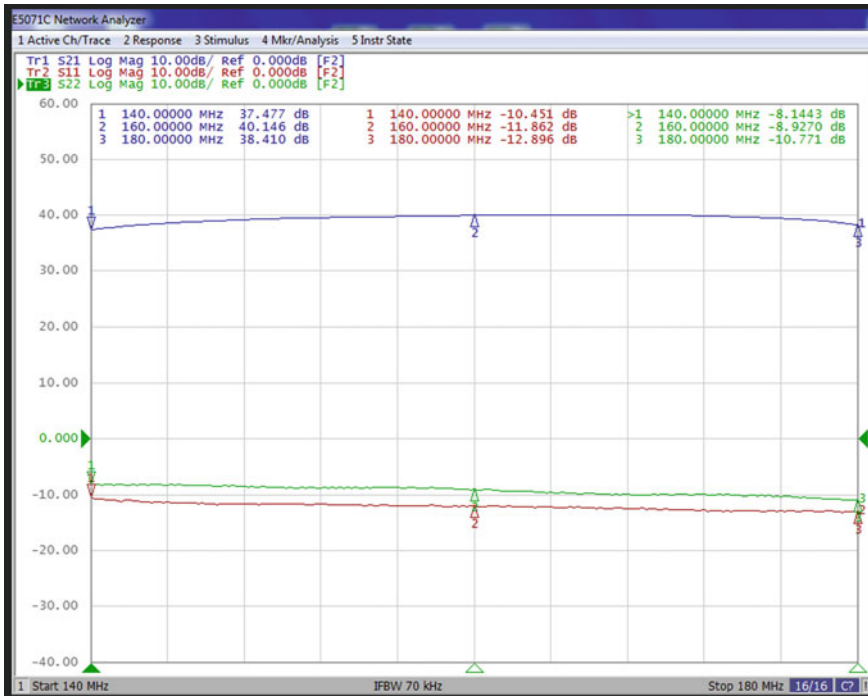


Fig. 6 Gain measurement for 160 MHz band

4.2 Power Measurements

Table 4 shows power measurements at different frequencies for input power -40 dBm and 0 dBm. As the insertion phase for all the four DF channels should be same, the power variations of the order of 2 dB over the band are not corrected using equalizer network so as not to disturb the insertion phase.

5 Conclusion

A design of RF signal conditioning module for multichannel digital receiver is presented. The module consists of two cards, amplifier–limiter card and filter-IQ card which ensure almost constant input at the ADC over the entire 40 dB dynamic range. The unit developed has been tested under various environmental conditions such as temperature, vibrations, thermal vacuum and EMI/EMC.

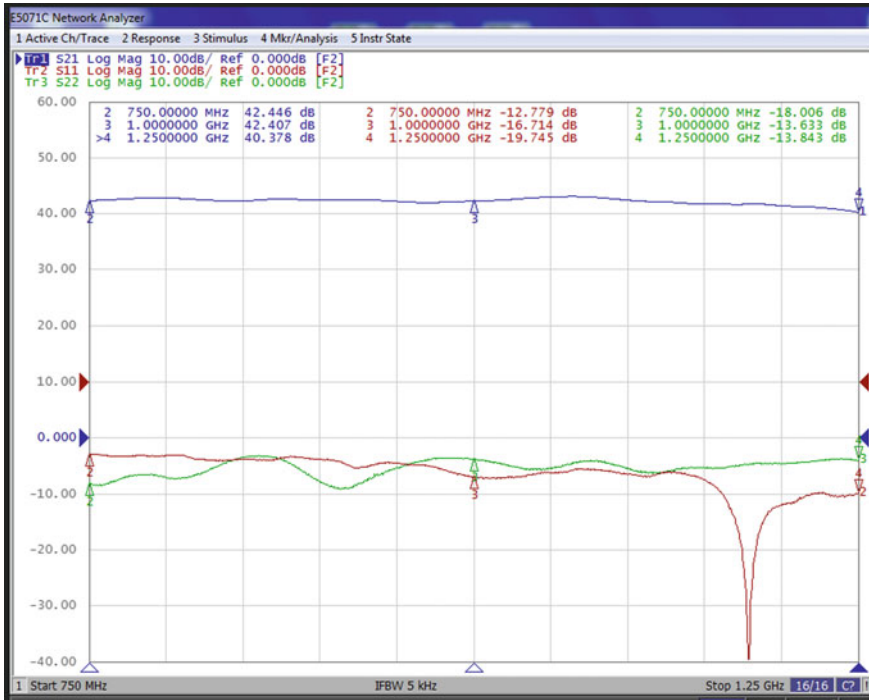


Fig. 7 Gain measurement for 1000 MHz band

Table 4 Power measurements

S. No.	Frequency (MHz)	IP power -40 dBm	IP power 0 dBm
1	140	-3.6	-3.28
2	160	-0.58	-0.24
3	180	-1.71	-1.37
4	750	1.88	-0.10
5	1000	1.91	0.74
6	1250	-0.53	-1.74

Investigation of Beam Switching Phased Array Concept in Multi-layer Graphene-Based Active Antenna Setup for Small Satellite Applications



D. V. A. Ragavamoorthy and Prasanna Ram

Abstract Small satellite constellations are becoming space systems capable of operational space application products delivery and services. As the number of satellites are becoming large in each constellation of satellites, many of the operations of the satellite need to be smart with intelligence or expert systems. To achieve this, technology of the satellite sub-systems need to be improved for enabling such operations. One of the crucial sub-systems for data transfer is the communication sub-system and antenna design. With constellations, the inter-satellite links become very essential for exchanging health keeping, command, control, scheduling and mission data so that wherever the satellite is in the globe, for crucial link establishes with ground at any time. Beam switching with phased array concept, though used in many missions, a continuous development to make it small, light weight and more efficient, is a continuous effort.

Keywords Stacking · Graphene · Multilayer · Patch antenna · Satellite Communication

1 Introduction

In this paper, a multi-layer 8×8 array fabricated with graphene material for beam switching is presented. The innovation of the proposed project is the flexibility nature of the antenna suitable of retrofitting nature anywhere on the satellite bus structure. The quad layer graphene prototype will have the beam changing ability by external switching making it suitable for active antenna technique for constellation applications. The beam angle and beam width will be controlled by the delay in the switching time. The graphene patches are $50 \text{ mm} \times 50 \text{ mm}$ in dimension and the λ

D. V. A. Ragavamoorthy

Aeronautical Engineering and Director Aerospace Research, Vel Tech Rangarajan Dr. Sagunthala R&D Institute of Science and Technology, Avadi, Chennai, India

P. Ram (✉)

Department of Electronics and Communication Engineering, Vel Tech Rangarajan Dr. Sagunthala R&D Institute of Science and Technology, Avadi, Chennai, India

© Springer Nature Singapore Pte Ltd. 2020

PSR. S. Sastry et al. (eds.), *Advances in Small Satellite Technologies*,

Lecture Notes in Mechanical Engineering,

https://doi.org/10.1007/978-981-15-1724-2_37

rule distance will be 120 mm between the antennae for 2.5 GHz. The gap between the antennas will be 20 mm. The substrate will be flexible polymer substrate suitable for retrofitting body mounting over the satellite surface. The main purpose of using graphene is to avoid the lattice resistance due to change in the temperature, and the reduction of bending loss which will not be suitable in the case of graphene flexible films. The second advantage of using graphene is the bandwidth enhancement property of the radiating material which will be appropriate for the active antenna mechanisms. The beam angle change will be achieved by predicted delay switching. Usability of the concept in the constellation of satellites with antenna beam switching for inter-satellite communications is examined (Figs. 1, 2 and 3). Effect of stacking with radiating material [1], rotated stacking for circular beam forming [2], stacked patch antenna for independent frequency [3], stacking structure for frequency tuning [4], single feed stacking for parameter enhancement [5], stacking with lens structure [6], Dual band stacking structure [7], Stacking of single patch with couple feeding [8]. The Fig. 1 shows the dimension of the stacking structure. Figure 2 shows the side view of the stacking structure of the layers. Figure 3 shows the full structure of the stacked array. Figure 4 shows the single patch polarization. Figure 5 shows the beam formation of the array structure. Table 1 shows the comparison of effect of graphene on different substrates. Table 2 shows the effect of stacking without airgap in fabrication. Table 3 shows the effect of airgap in the stacking layers.

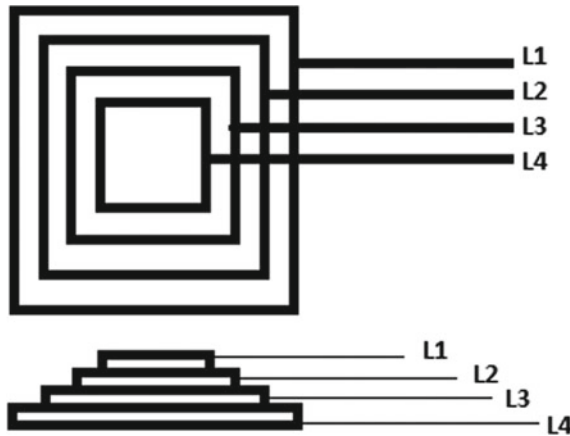


Fig. 1 Single cell with quad layer graphene antennas, top view and side view, L1, L2, L3, L4: feeding lines

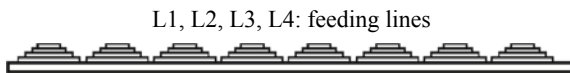
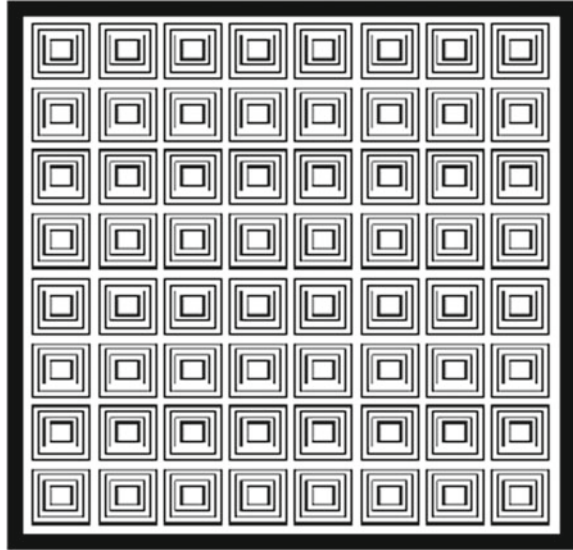


Fig. 2 Mounting of 8 quad layer antenna on substrate, side view

Fig. 3 8×8 array of quad layer antenna mounted on substrate, top view



2 Phase-Increment Calculating

$$x = d \cdot \sin \Theta_s$$

$$\Delta\varphi = (360 * d \cdot \sin \Theta_s) / \lambda$$

where

$\Delta\varphi$ = phase shift between two successive elements, d = distance between the radiating elements and Θ_s = beam steering.

In Table 1, the effect of a layer of material in the antenna parameter has been discussed and the variation in the reading shows that the material changes the effect in terms of material property and the substrate plays the vital role in the antenna beam switching property. The table also shows that the effect of lattice formation is very important as shown in Fig. 4.

The above radiation pattern shows the change in the beam switching due to the change in the feeding points of the same antenna array and they are more suitable for the active antenna techniques (Fig. 5).

The layers over the material can be due to the printing techniques and they may create the air gaps, so we designed the simulation and they will show the effect of the air gaps in the stacking parameter of the antenna over the different substrates. And it is clearly shown in Tables 2 and 3.

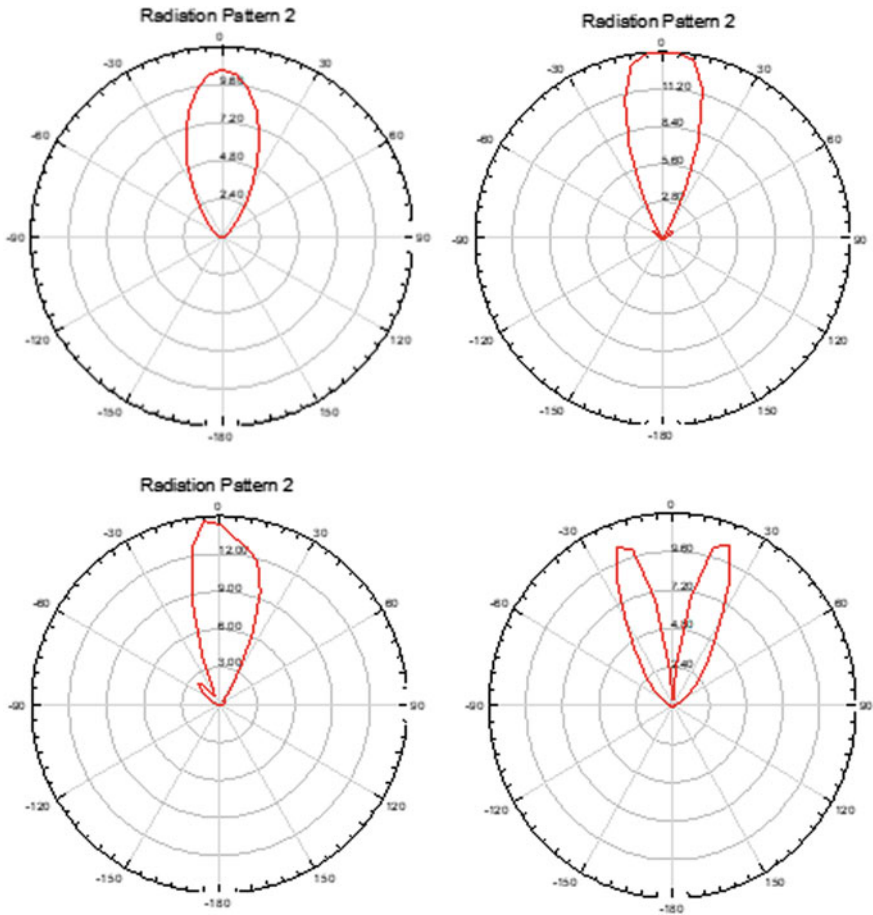


Fig. 4 Beam Forming. Radiation pattern shows the beam switching

3 Conclusion

In the above paper, we tried the effect of layers and the effect of air gap in the antenna formation. Due the effect of feeding, the beam formation will be controlled and the usage of graphene material will be suitable for the effect of faster response in the beam formation of the antenna.

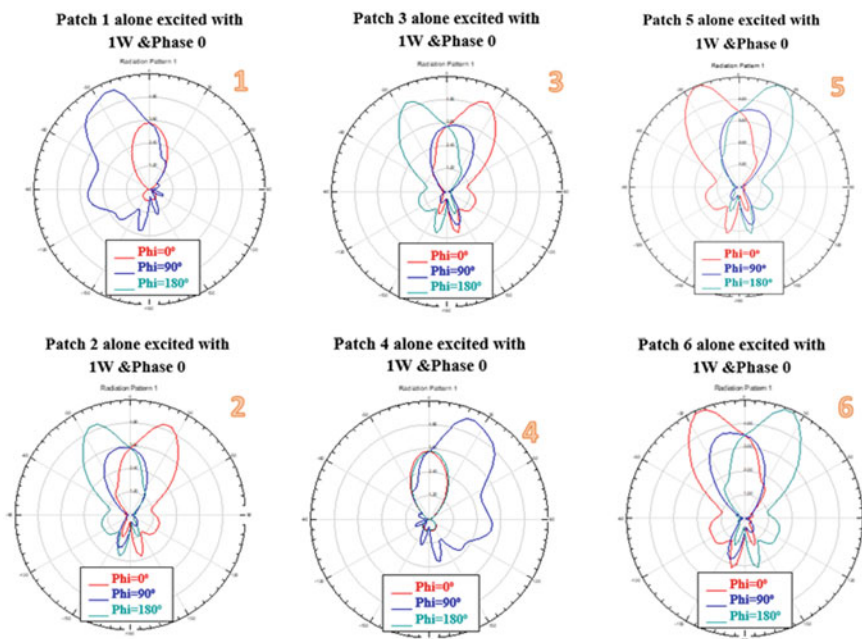


Fig. 5 Radiation pattern shows beam formation in different direction

Table 1 Performance of the proposed system. Comparison of copper and graphene on different substrates

Parameter	Simulated	Copper fabrication (measured)	Graphene fabrication (measured)	Graphene fabrication (measured)	Graphene fabrication (measured)
Antenna material	Copper	Copper	Graphene	Graphene	Graphene
Substrate material	FR4	FR4	FR4	Paper	Polystyrene
Impedance matching (Ω)	50	50	50	50	50
Material occupancy (cm^2)	10.32	10.32	10.32	10.32	10.32
Dielectric measurement	4.4	4.4	***	3.4	3.2
Substrate thickness (mm)	1.6	1.6	1.6	0.25	0.1
Material thickness (mm)	0.035	0.020	0.020	0.020	0.020
Substrate area (cm^2)	92.16	92.16	92.16	92.16	92.16
Return loss	-27.54 dB	-31.08 dB	-35.43 dB	-15.74 dB	-20.80
Gain (dB)	+3.2	+2.7	+4	+4.5	+4.5
VSWR	1.4	1.14	1.01	1.386	1.205
Bandwidth (MHz)	53.3	46	75.5	70	67
Frequency (GHz)	2.45	2.56	2.45	2.42	2.42

Table 2 Shows the effect of antenna without airgap in printing

Parameters	Copper on FR4	Copper on paper (dielectric constant = 3.4)	Copper on paper (dielectric constant = 2.4 based on literature)	Graphene on FR4	Graphene on paper (dielectric constant = 3.4)	Graphene on paper (dielectric constant = 2.4)
Return loss (dB)	-27.6	-27.95	-27.8	-22.25	-22.35	-22.45
VSWR	1.075	1.075	1.075	1.095	1.095	1.093
Bandwidth (MHz)	64.8	61.5	61.5	65.69	61.5	61.66
Resonance frequency (GHz)	2.39	2.39	2.39	2.39	2.39	2.4

Table 3 Shows the effect of antenna without airgap in printing

Antenna material	Patch radius (mm)	Substrate	Substrate thickness (mm)	Feed length (mm)	Return loss (dB)	VSWR	Bandwidth (MHz)
Copper	17.64	FR4 (dielectric constant = 4.4)	1.6	31	-24.93	1.12	77.55102
Graphene	17.64	FR4 (dielectric constant = 4.4)	1.6	31	-22.2	1.17	63.26
Graphene	19.64	Paper (dielectric constant = 3.4)	0.255	27	-22.6	1.159	63.39
Graphene	20.14	Polyester (dielectric constant = 3.2)	0.1	27	-21.5	1.183	73.4

References

1. Tang M-C, Chen X, Li M, Ziolkowski RW (2017) Bandwidth-enhanced, compact, single-feed, low-profile, multilayered, circularly polarized patch antenna. *IEEE Antennas Wirel Propag Lett* 16
2. Oraizi H, Pazoki R (2013) Wideband circularly polarized aperture-fed rotated stacked patch antenna. *IEEE Trans. Antennas Propag* 61(3)

3. Ge L, Li M, Wang J, Gu H (2017) Unidirectional dual-band stacked patch antenna with independent frequency reconfiguration. *IEEE Antennas Wirel Propag Lett* 16:113
4. Yang G-M, Xing X, Daigle A, Liu M, Obi O, Stoute S, Naishadham K, Sun NX (2009) Tunable miniaturized patch antennas with self-biased multilayer magnetic films. *IEEE Trans Antennas Propag* 57(7)
5. Yang W, Zhou J, Yu Z, Li L (2014) Single-fed low profile broadband circularly polarized stacked patch antenna. *IEEE Trans Antennas Propag* 62(10)
6. Al-Tikriti M, Koch S, Member, Uno M, Member (2006) A compact broadband stacked microstrip array antenna using eggcup-type of lens. *IEEE Microw Wirel Compon Lett* 16(4)
7. Tsai Y-L, Huang C-C (2017) A dual-band LHCP stacked patch antenna array. 978-1-5386-0465-6/17/\$31.00 ©2017 IEEE ISAP2017, Phuket, Thailand
8. Liang Z, Liu J, Li Y, Member, Long Y, Senior Member, A dual-frequency broad band design of coupled-fed stacked microstrip monopolar patch antenna for WLAN application. *IEEE Antennas Wirel Propag Lett* 15

Satellite Constellations, Mission Design

Satellite Constellation Design Studies for Missile Early Warning



Devi Prasad Panda, Kalpana Bandi, PSR Srinivasa Sastry and K. Rambabu

Abstract Missile early warning system enables the defence services to detect the missile launches. IR imaging sensors on satellite platform can detect vehicle plumes from the launcher, and it can send the data to the ground station. Orbit design and constellation study analysis of missile early warning system is carried out to get the global coverage. The constellation consists of three or four GEO stationary satellites, four highly elliptical orbit (HEO) satellite orbits in two planes to cover higher latitudes on earth and low earth orbit satellites to cover the specific area of interest to track the launcher in middle stage. Number of satellites in the constellation estimated and optimized to cover area of interest. GEO satellite, HEO satellite coverage analysis and LEO satellite orbit parameters analysed. The complete scenario of missile defence scheme is presented.

Keywords Missile early warning · Satellite early warning system · Space-based missile defence

1 Introduction

Missile defence plays a vital role in national security. Missile defence systems are a type of missile defence intended to shield a country against incoming missiles, such as ICBMs or other ballistic missiles. The USA, Russia, France, India and Israel have the missile defence systems. India has ground-based RADAR capability of missile defence which has certain constraints like limited field of view and less time of reaction due to earth curvature. This limits warning time against an ICBM attack to about 10 min the warning may be even less against ship or sea-launched ballistic missile (SLBMs). The other type of early warning system is IR sensors on satellites.

A satellite can detect a missile almost immediately after launch by detecting the infrared radiation from its rocket plume. Space-based system could provide the

D. P. Panda (✉) · K. Bandi · P. S. Sastry · K. Rambabu
Directorate of Space Systems and Technologies (DSST), Research Centre Imarat (RCI),
Hyderabad, India
e-mail: devi.prasad@reilab.in

maximum warning time of about 30 min against ICBMs and 15–20 min against SLBMs. So, space-based missile defence has an advantage that it can detect the launch in initial phases and track the missile and provide the launch trajectory to the control station. The satellites and ground-based RADARs are intended to complement each other. In this scenario, user has more time to respond and initiate counter-attack by activating appropriate means like ship, ground or air-based missile defence system.

Satellite early warning system is developed initially by Russia and USA, but they are not up to the mark to meet the missile defence purpose. US air force entered into a contract with Lockheed Martin to launch satellite early warning system in GEO and HEO altogether seven satellites. In that, HEO satellites are launched as a part of USA-184 and USA 200 in 2006 and 2008, respectively. Two GEO satellites are also launched under this program. As part of the Russian satellite early warning system under EKS program, six satellites will be launched in HEO orbit. First satellite was launched in Tundra orbit on 17th November 2015 under this program.

2 Space-Based Missile Defence

Missile launch has three phases in the trajectory. They are boost phase, mid-course and terminal phase as shown in Fig. 1. The boost phase can be detected by GEO

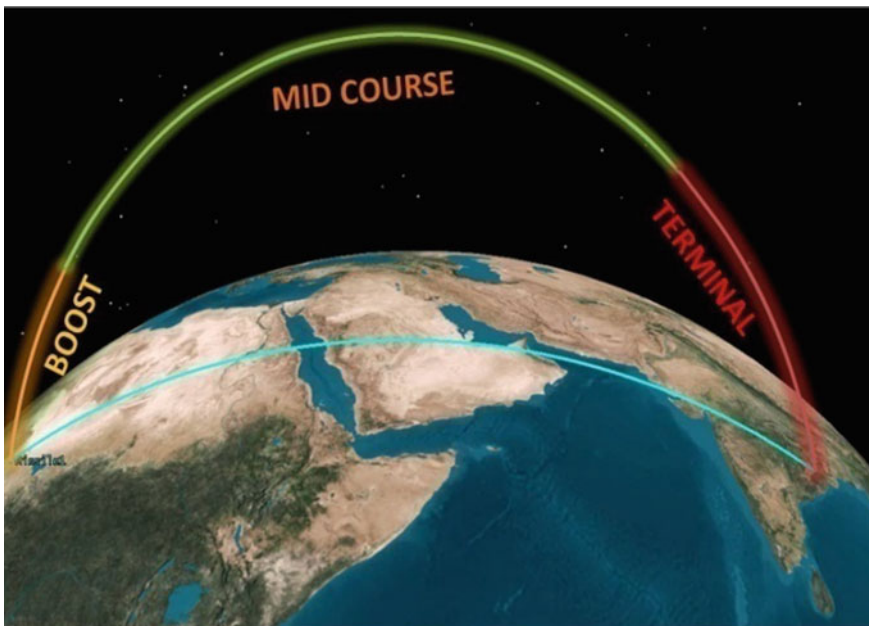


Fig. 1 Missile launch different phases

satellite or HEO satellite as the plumes are at high temperatures. All ground-based missile defence systems always track at terminal phase of the missile leaving very less reaction time. Once the launch is detected by GEO or HEO satellites, the coordinates of launch and trajectory can be computed and transmitted to LEO satellites which can start track the missile in mid-course.

2.1 GEO Stationary Orbit and Coverage

GEO stationary orbit is a circular orbit with a radius of 42,164 km and inclination of 0° . A satellite in such orbit has an orbital period equal to earth rotational period which is one sidereal day (1436 min).

The GEO stationary satellites will cover the entire globe except higher latitudes (greater than 81°). Theoretically, one GEO stationary satellite can cover 42% of earth in one stretch as shown in Fig. 2 with elevation circles around.

2.2 Highly Elliptical Orbit (HEO)

Highly elliptical orbit is an elliptical orbit with a low altitude of perigee (<1000 km) and a high altitude of apogee (36,000 km approx.). These extremely elongated orbits have the advantage of long dwell times at a point in the sky during the approach to, and descent from, apogee. HEO orbits offer visibility over earth polar regions, which most GEO stationary satellites lack. The widely usable orbits like Molniya, Tundra and Super Tundra are classified as HEO.

2.2.1 Molniya Orbit and Coverage

Molniya orbit is with a perigee around 500 km and an apogee around 36,000 km and inclination of 63.4° exactly which is called critical inclination, argument of perigee at 90° or 270° with time period of 12 h. The critical inclination of the orbit fixes the perigee position. The orbit is recurrent with a cycle of one day: the ground track passes through the same point every day as shown in Fig. 3. Satellites in this orbit are better suited for the higher latitudes. The subsatellite point remains approximately fixed for ± 3 h around apogee, as shown in Fig. 4. The characteristics of the Molniya orbit are shown in Table 1.

$$\frac{d\omega}{dt} = \frac{3nj_2 R_0^2 (4 - 5 \sin^2 i)}{4a^2 (1 - e^2)^2}$$

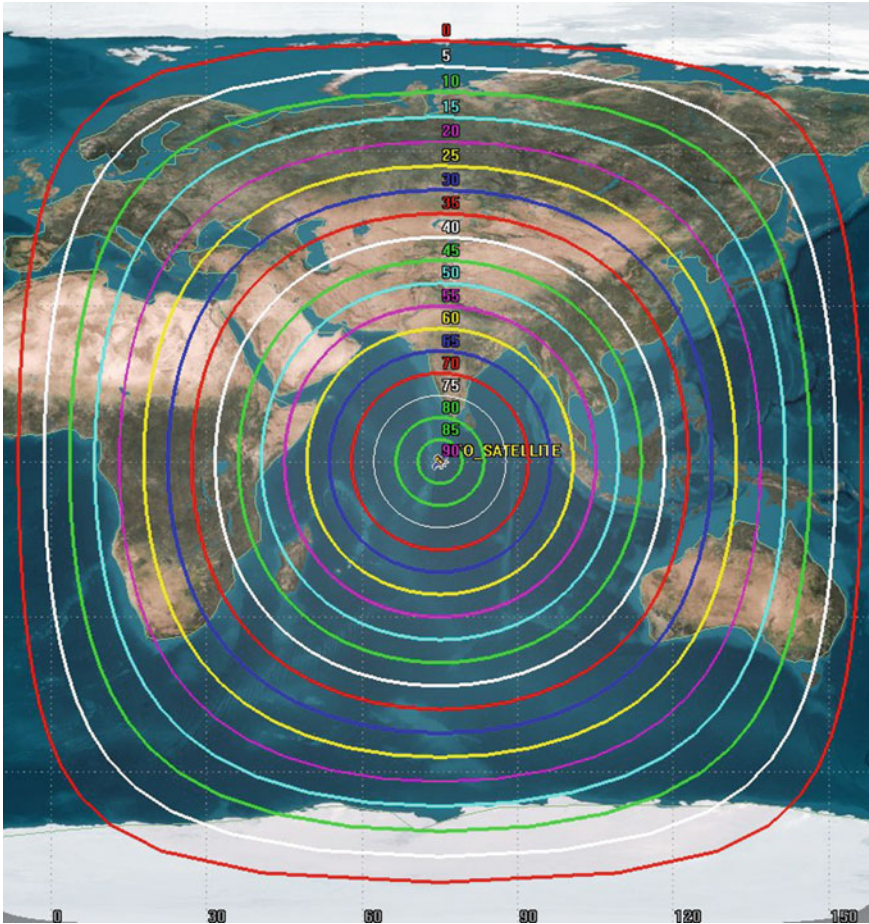


Fig. 2 GEO stationary coverage with elevation circles

where

- J_2 2nd order earth oblateness constant ($J_2 = 0.001082$)
- a Semi-major axis
- e Eccentricity
- i Inclination
- n Periodicity
- R_0 Earth mean radius.

The inclinations of 63.4° and 116.6° solve the above equation, and generally, the former is selected which resulted in frozen perigee.

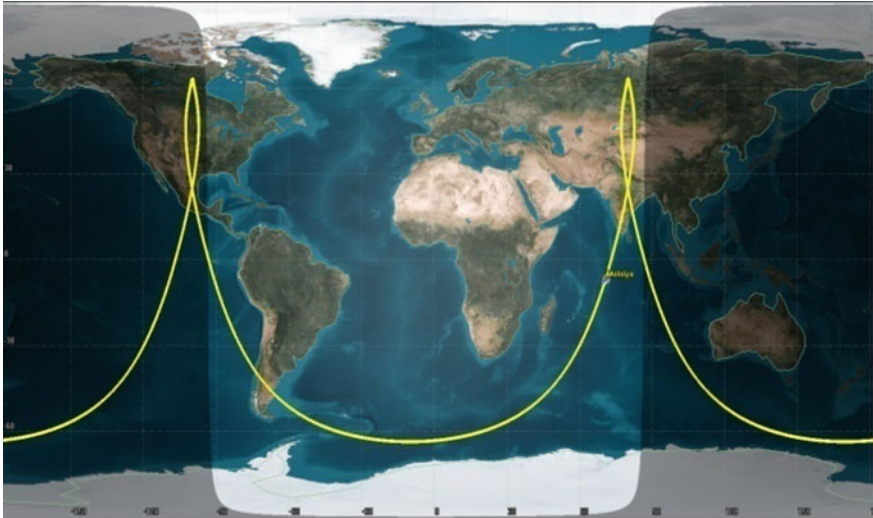


Fig. 3 Recurrent ground track of Molniya orbit



Fig. 4 Satellite subpoint at apogee ± 3 h

Table 1 Molniya orbit parameters

Orbital parameter	Value
Apogee altitude	39,850 km
Perigee altitude	500 km
Inclination	63.4°
Argument of perigee	270°

3 Constellation Design

3.1 GEO Stationary Satellite Constellation

The global coverage is achieved with three satellites in GEO stationary orbit coverage overlap of 0° – 30° elevations can be ensured as shown in Fig. 5. For optimal coverage of Indian subcontinent and neighbouring regions is obtained by appropriate selection of location of two satellites. The third satellite is placed to cover the remaining part of the earth to complete the global coverage at any time. The optimal satellite positions in the constellation are East 15° , East 135° and West 105° with respect to GMT. Specifications of the GEO stationary constellation are summarized in Table 2.

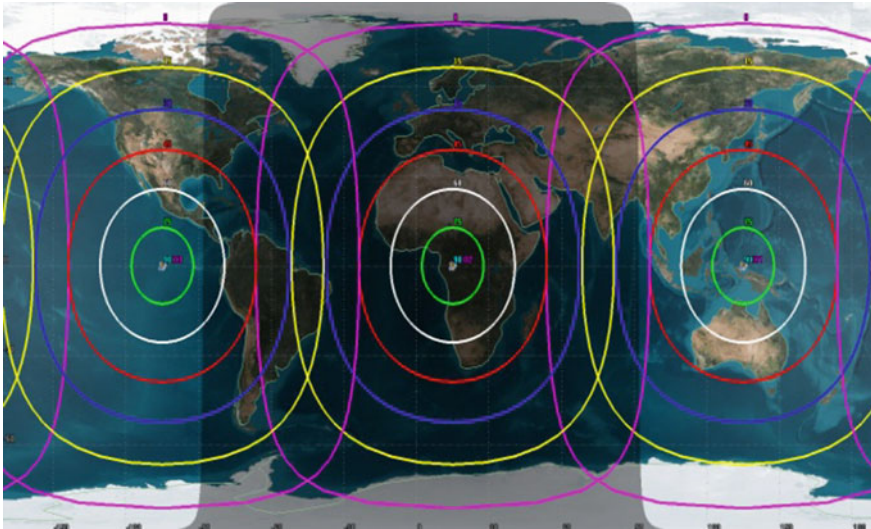


Fig. 5 GEO constellation coverage

Table 2 GEO constellation satellites details

Satellite name	Longitude of ascending node
GEO1	135° (east 135°)
GEO2	15° (east 15°)
GEO3	255° (west 105°)

3.2 Molniya Satellite Constellation

Four Molniya satellites can cover the entire higher latitudes in the northern hemisphere and our area of interest near India and neighbouring countries. One Molniya orbit is selected in such a way that it crosses the apogee over India. In this plane, two satellites are needed with 6 h gap as to have the continuous coverage over India. Other two satellites with RAAN shifted by 180° . As on 21 March 2016, the RAAN values are 79° and 259° . Then, four satellites can cover the entire northern hemisphere any time, as shown in Fig. 6a, b.

3.3 LEO Satellite Constellation Design

The mid-course tracking has to be carried out by the satellite in LEO. Once the launch is detected by GEO or HEO satellite, the coordinates will be sent to both ground station and to the LEO satellites which are able to track the launch. The area of coverage decides the number of satellite required in the constellation. LEO satellites will have very limited coverage area due to its altitude constraint. Our area of interest is about $+55^\circ$ northern latitudes and -45° max southern latitudes.

Constellation design analysis is done based on

- (a) The maximum latitude coverage requirement
- (b) Optimized satellite availability for tracking
- (c) Availability of LEO satellite to the GEO or HEO to send the data to the ground control station.

Orbital parameters and constellation details of LEO satellites are shown in Tables 3 and 4.

4 Missile Early Warning System Concept

Space-based missile early warning system is a two-tier system. Tier 1 consists of space system to track the launch in boost phase and mid-course. Tier 2 consists of ground-based RADARs to track during the terminal phase. Tier 1 further divided into two parts, one is GEO and HEO satellites which will detect the boost phase of launch, and the other is the LEO satellites which track the mid-course of launch as shown in Fig. 7. Complete scenario is shown in the flow chart in Fig. 8.

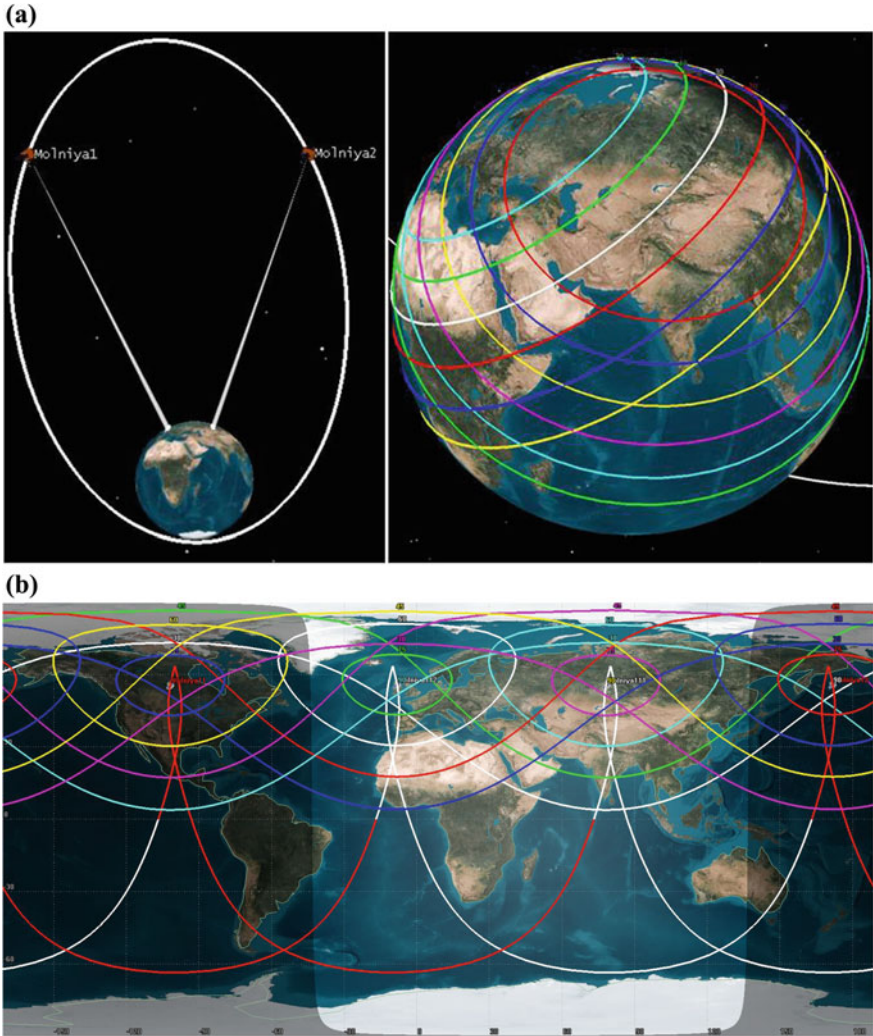


Fig. 6 a Two satellites in one Molniya plane and coverage, b HEO constellation total coverage on Northern hemisphere of earth

Table 3 Orbit parameters of LEO satellite

Orbit parameter	Value
Altitude	836 km
Repeativity	6 days
Orbit type	Circle
Inclination	55°
Repeativity orbits	85

Table 4 LEO constellation details

Parameter	Value
Number of walker planes	6
Number of satellites per plane	4
RAAN difference per plane	60°
Total satellites	24

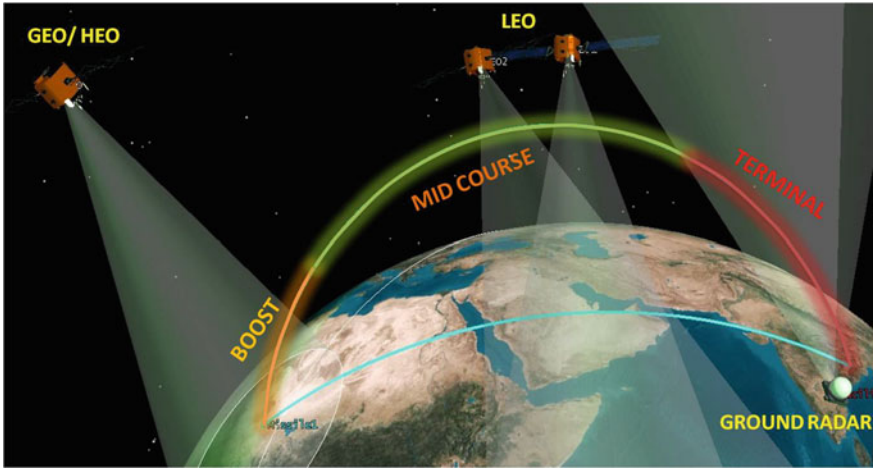


Fig. 7 Missile tracking in different phases with early warning system

4.1 LEO Satellite Visibility to GEO or HEO Studies

LEO satellite visibility studies are done based on geometrical studies only not based on communication link.

Number of LEO satellites availability to different GEO and HEOs are computed at different times and shown in Figs. 9 and 10.

From Figs. 9 and 10, LEO satellite availability to track the missile in mid-course can be arrived. Minimum of eight LEO satellites are always available to track the missile with this constellation. This constellation can track more number of launches at the same time as the LEO satellites availability is more.

4.2 Communication Systems

Any satellite in any constellation (i.e. LEO, GEO, HEO) can communicate over a two data link with any other constellation in addition to the ground station. All GEOs and HEOs are able to communicate each other as well as to ground station as shown in

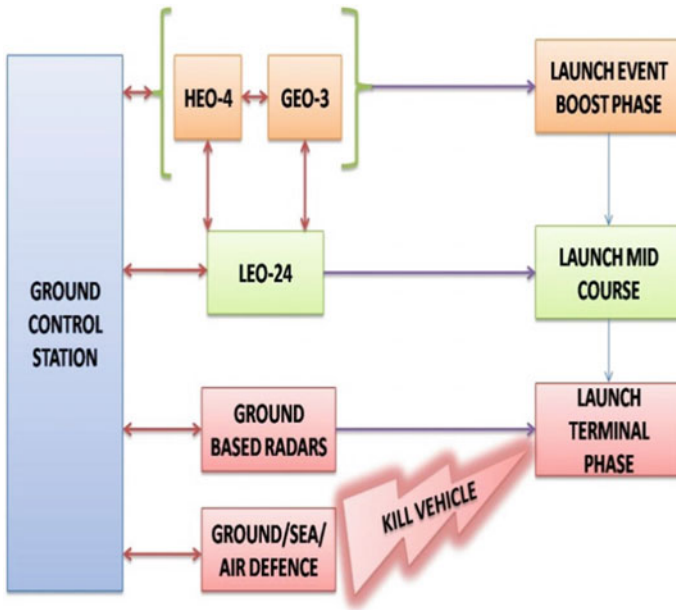


Fig. 8 Flow chart of space-based missile defence

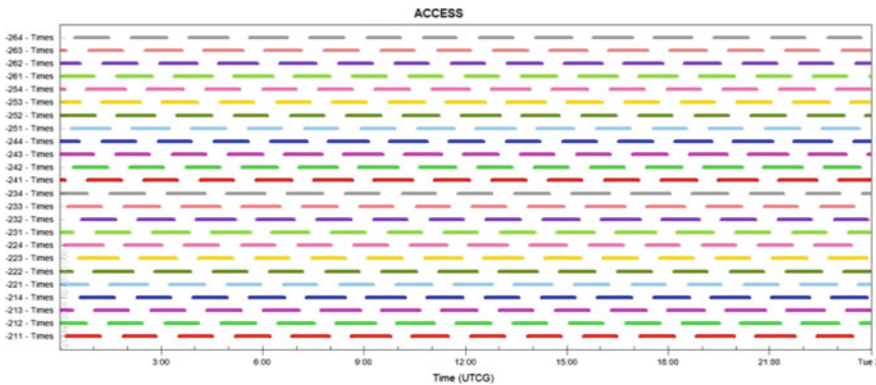


Fig. 9 GEO satellite visibility with LEO satellite

Fig. 11. Then, the ground station will compute the trajectory and alert the appropriate LEO for tracking. The LEO chain will hand over to ground-based tier-2 RADAR systems at appropriate time for activating countermeasures like launch kill vehicle as per the ballistic missile defence plan.

In this paper, we used MATLAB to determine the values of orbit period, Sun angle, Ground station accessibility times and coverage time over area of interest, etc. We also used Systems Tool Kit (STK) version 10.1.

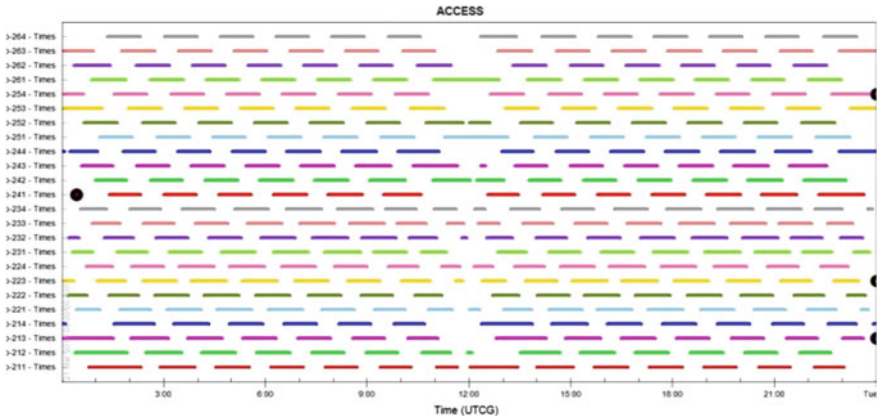


Fig. 10 HEO satellite visibility with LEO satellite

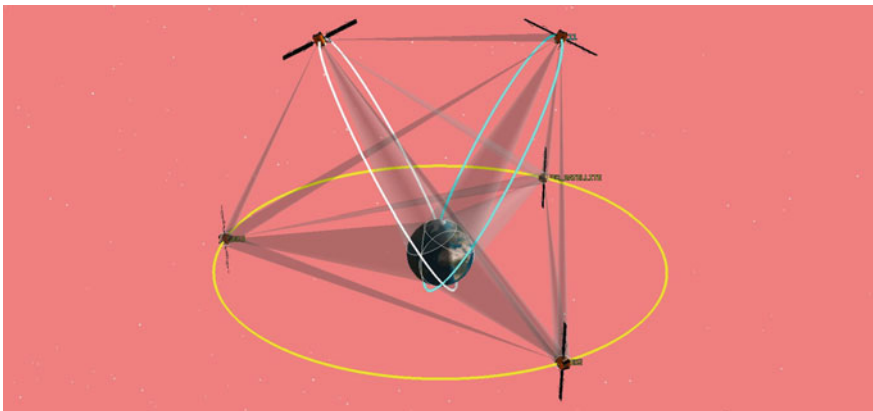


Fig. 11 Communication chain between GEOs and Molniya satellites

5 Conclusions

Missile defence is a growing area of concern across the globe. No nation with proper national security policy can afford to ignore anymore as number of countries entered the game of missiles. The most important issues in missile defence are the global coverage, in-terminable coverage and available reaction time. Three GEO stationary satellites, four Molniya satellites, 24 LEO satellites with IR sensors onboard can provide the capability to detect and track the missile. The studies presented optimal solution to address all above issues, particularly for Indian scenario.

Acknowledgements Authors would like to express deep regards and profound respect to Director, RCI for his support. Author expresses sincere thanks to Dr. MSY Siva Prasad for his guidance and constant support. Author extends sincere thanks to colleagues of Directorate of Space Systems and Technologies, RCI for their continuous encouragement and support to complete this paper.

References

1. Missile Defence Agency, The ballistic missile defence system fact sheet
2. Canavan GH, Missile defence for the 21st century
3. Missile warning system US space command
4. Martin L, Space based infrared system the next generation in persistent IR surveillance
5. Podvig P, The operational status of the russian space based early warning system
6. Vallo do DA, Fundamentals of astrodynamics and applications
7. Capderou M, Satellite orbits and missions
8. Wertz JR, Space mission analysis and design
9. Chobotov VA, Orbital mechanics
10. Curtis H, Orbital mechanics for engineering students

Continuous Coverage of Fixed Location on Earth by LEO Satellite Constellation



A. Vairavan and Rukmini Banda

Abstract Continuous coverage of a fixed location on Earth with the constellation of LEO satellite is considered. Target's relative velocity on Earth with respect to the satellite is analyzed for different orbit altitudes and inclinations. Characteristics of footprint with respect to central angle, footprint overlap, and coverage area are analyzed. A closed-form solution for the selection of true anomaly and RAAN separations is obtained. Time period and access time are analyzed with respect to the ground location of the target for different inclinations in order to obtain maximum possible access time of the satellite. Effects of RAAN rate and orbit inclinations are analyzed with respect to the Earth relative velocity for continuously covering certain latitude zones of the Earth. The geometry of footprint overlap is analyzed, and a closed-form expression for the maximum effective coverage angle is obtained.

Keywords LEO · Constellation · RAAN separation · Earth coverage factor · Satellite access time · Nodal drift

1 Introduction

The global trends in the Intelligence, Surveillance, and Reconnaissance (ISR) lead to the requirement for the constellation of small satellites to remotely monitor a location in any part of the world continuously in real time. Small satellite constellation design for ISR activities enhances the performance of the space sensors and provides more accurate information. Small satellite constellation plays a substantial role for accessing certain terrestrial regions for disaster management and also for providing high-quality imaging for military applications.

The accessibility time and coverage area depend on the footprint of the satellite and orbit design. By considering the ellipticity of the Earth, a mathematical treatment

A. Vairavan (✉)

Space Systems and Technology, Research Centre Imarat, Hyderabad 500069, India

R. Banda

System Engineering Division, DSST, Research Centre Imarat, Hyderabad 500069, India

e-mail: rukmini.banda@rcilab.in

© Springer Nature Singapore Pte Ltd. 2020

PSR. S. Sastry et al. (eds.), *Advances in Small Satellite Technologies*,

Lecture Notes in Mechanical Engineering,

https://doi.org/10.1007/978-981-15-1724-2_39

on the determination of look angles to geostationary communication satellite was presented in Ref. [1]. The Earth coverage analysis by a single LEO satellite at different altitude for low elevation angle was presented in [2].

In this paper, improvements of their work, with additional analysis, are presented in view of proposing a novel method for continuously monitoring a fixed location on Earth by the constellation of low Earth orbiting satellites. The remainder of the paper is arranged as follows: Sect. 2 describes the problem and satellite coverage on spherical Earth for different altitude. The two- and three-dimensional analyses of footprint and Earth coverage area are given in Sect. 3. Derivation for the estimation of true anomaly and RAAN separation for proposed constellation method are presented in Sect. 4, followed by satellite relative velocity and visibility time calculations in Sect. 5. Section 6 presents the simulation results, and the concluding remarks are given in Sect. 7.

2 Geometry of Spherical Earth and Satellite Coverage

Figure 1 represents a conventional spherical Earth and satellite coverage geometry. Here, α , λ , ϵ , and R_E denote the satellite viewing angle, Earth central angle, elevation angle, and Earth radius, respectively. Satellite altitude is denoted by h and is measured normal to the ground from the subsatellite point P_s as shown.

When the elevation angle, $\epsilon = 0$, $\alpha = \alpha_{max}$, and $\lambda = \lambda_{max}$. Hence, at zero elevation angle, the viewing angle and the possible coverage obtained by the satellite are maximum.

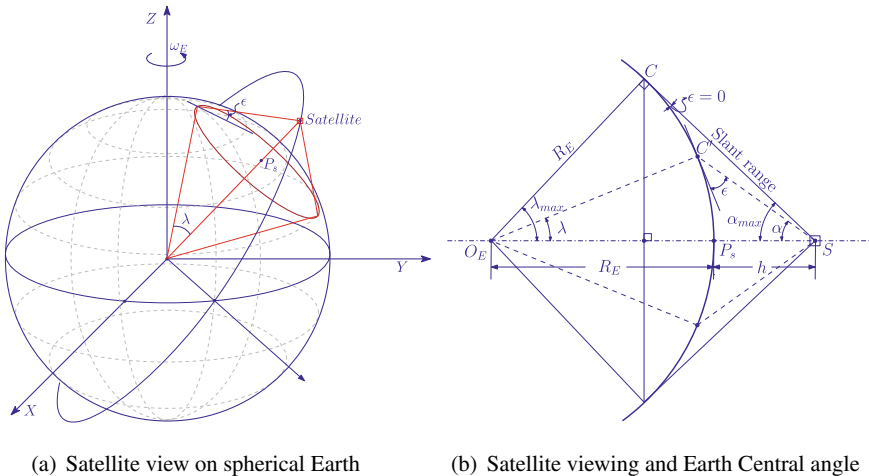


Fig. 1 Geometry of satellite coverage on spherical Earth

$$\lambda_{\max} = \cos^{-1}\left(\frac{R_E}{R_E + h}\right) \tag{1}$$

for a circular orbit, $a = R_E + h$.

2.1 Satellite Coverage Area on Earth for Different Altitude

The surface area of the spherical Earth is given by

$$A_{\text{Earth}} = 4\pi R_E^2 \tag{2}$$

From an altitude, h , the surface area of the spherical cap on Earth that can be viewed by the satellite can be obtained as

$$A_{\text{coverage}} = 2\pi R_E^2 \left(\frac{h}{R_E + h}\right) \tag{3}$$

Hence, the fraction of Earth surface that will be covered by a single satellite can be obtained from Eqs. (2) and (3) as

$$\text{Fraction of Earth Coverage} = \frac{1}{2} \left(\frac{h}{R_E + h}\right) \tag{4}$$

From Eq. (4), we can obtain the percentage of coverage of Earth surface by a single satellite for different altitude, assuming spherical Earth.

3 Analysis of Footprint and Earth Coverage Area

Figure 2 represents the footprint of multiple (three) satellites. Each circle represents the footprint obtained by a single satellite. Minimum overlap of footprint area of adjacent satellites is necessary to ensure the continuous coverage of the desired zonal area of Earth with minimum number of satellites. If the area to be monitored is a simple two-dimensional plane, this can be accomplished from the simple geometry, as shown in Fig. 2.

For a circular footprint, the area of overlap will be minimum if the centers of circles which form a triangle are at equal distance to each other. If the sides of the triangle are equal, the overlap area of two adjoining circle will be equal, and also be the minimum as shown in Fig. 2. But, the geometry of the footprints is affected by the three-dimensional shape of the Earth, and also by the rotational motion of Earth and satellites. Hence, it is difficult to maintain a minimum overlap continuously as shown in Fig. 2.

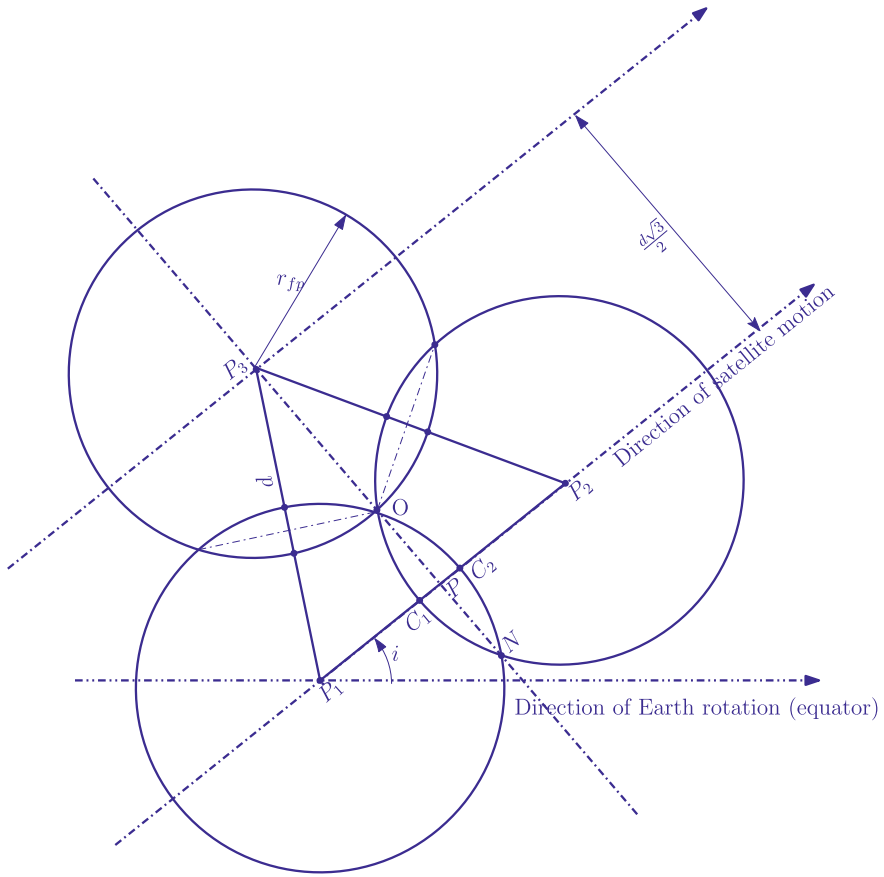


Fig. 2 Footprints of three satellites with minimum overlap

The footprint overlap will be minimum at the equator, and it will be maximum near poles due to Earth rotation about an axis and orbit motion with inclination. Continuous coverage at the equator with minimum overlap implies continuous coverage near poles.

The following sections present the analysis based on two dimensional footprint and coverage area, and are subsequently extended to three-dimensional space for obtaining true anomaly (θ_{sep}) and RAAN (Ω_{sep}) separation. Number of satellites required for continuous coverage with respect to the percentage coverage of the Earth by a single satellite is also deduced.

3.1 Footprint Area Analysis

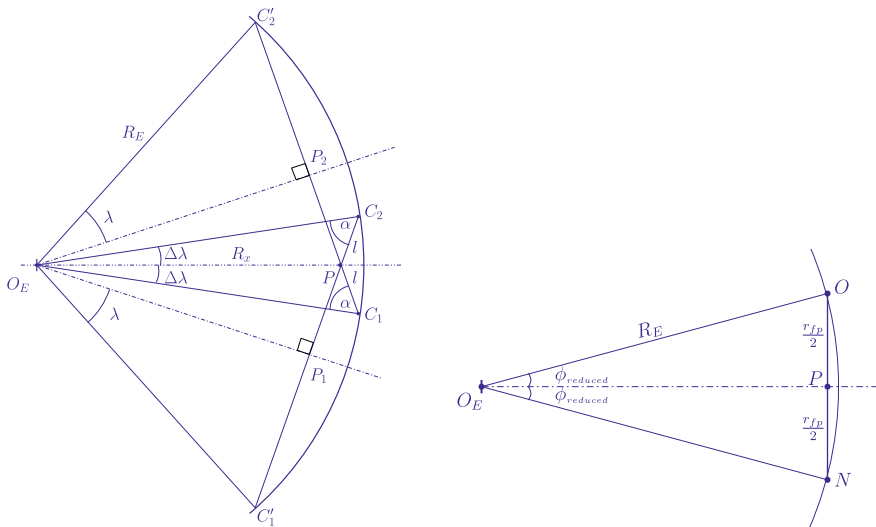
Let r_{fp} be the radius of the footprint as shown in Fig. (2). $P_1, P_2,$ and P_3 are centers of the circles of footprint, which forms an equilateral triangle $P_1P_2P_3$. $P_1P_2 = P_2P_3 = P_3P_1 = d$ denote the side lengths of the triangle. The three circles intersect at a common point, O , which is also the centroid of the triangle $P_1P_2P_3$. Point ‘ P ’ divides the length P_1P_2 equally, i.e., $P_1P = PP_2 = \frac{d}{2}$, and $OP \perp P_1P_2$. From the property of equilateral triangle, we can deduce the lengths $OP = \frac{d}{2\sqrt{3}}, OP_3 = \frac{d}{\sqrt{3}}$, and $PP_3 = \frac{3d}{2}$. Hence, from OP , the chord length of overlap segment of the circle can be deduced as $OP = \frac{r_{fp}}{2} \Rightarrow ON = r_{fp}$, is equivalent to the radius of footprint.

In Fig. 3, O_E represents the center of the Earth, and $O_EC_1 = O_EC_2 = R_E$. From triangle $O_EC_2C'_2$,

$$r_{fp} = R_E \sin \lambda \tag{5}$$

Equation (5) is a function of altitude, for the maximum central angle, it can also be expressed as

$$r_{fp} = R_E \sin \left[\cos^{-1} \left(\frac{R_E}{R_E + h} \right) \right] \tag{6}$$



(a) Coverage geometry of two satellites with overlap in central angles and footprints

(b) Reduced central angle due to the footprint overlap for continuous coverage

Fig. 3 Geometry of satellite coverage on spherical Earth

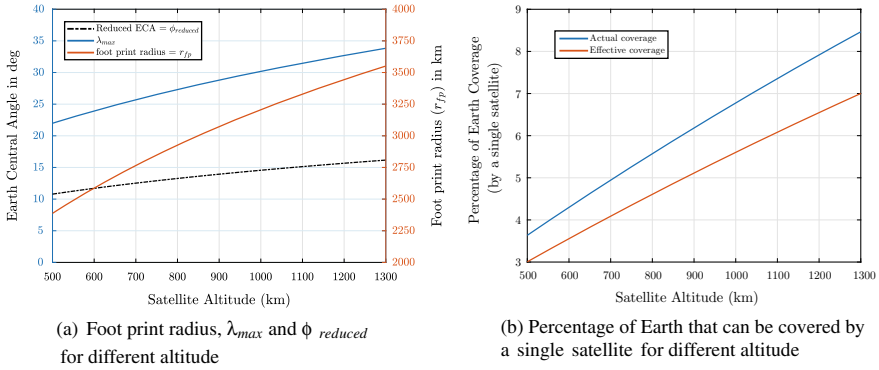


Fig. 4 Satellite footprint and percentage of Earth coverage for different altitude

The area of circular segment [3, 4] with radius r_{fp} and included angle $\frac{\pi}{3}$, is given as

$$A_{cs} = \frac{1}{2} R_E^2 \sin^2 \left[\cos^{-1} \left(\frac{R_E}{R_E + h} \right) \right] \left[\frac{\pi}{3} - \sin \frac{\pi}{3} \right] \tag{7}$$

and the area of the footprint can be obtained as

$$A_{fp} = \pi R_E^2 \sin^2 \left[\cos^{-1} \left(\frac{R_E}{R_E + h} \right) \right] \tag{8}$$

Since, each footprint circle overlaps with six adjacent circles, the effective footprint area can be obtained as

$$\text{Effective foot print area} = A_{fp} - 6 A_{cs} \tag{9}$$

Let the coverage factor be defined as

$$\text{Coverage factor} = \frac{\text{Effective foot print area}}{\text{Area of footprint}} \tag{10}$$

Using Eqs. (7) and (8) in Eq. (9) and substituting in Eq. (10), we get

$$\text{Coverage factor} = \frac{\pi}{3} \sin \frac{\pi}{3} \tag{11}$$

From Eq. (11), it is clear that the coverage factor is independent of altitude, h , and hence, the footprint radius, r_{fp} .

3.2 Earth Coverage Area

Product of Eqs. (4) and (11) yields the percentage of effective area on Earth that can be covered by a single satellite excluding the overlap, as given below.

$$\text{Percentage of coverage of Earth} = \frac{3}{2\pi} \left(\frac{h}{R_E + h} \right) \sin\left(\frac{\pi}{3}\right) \times 100 \quad (12)$$

For a circular orbit, $a = R_E + h$. Hence, Eq. (12) can be written as

$$\text{Percentage of coverage of Earth} = K \left(\frac{h}{a} \right) \times 100 \quad (13)$$

where K is a constant given by

$$K = \left(\frac{3}{2\pi} \right) \sin\left(\frac{\pi}{3}\right) \quad (14)$$

For a given altitude, h , Eq. (13) gives the percentage of coverage area obtained by a single satellite. From that, we can deduce the minimum number of satellites required to cover certain latitude zones and entire area of the Earth. The continuous coverage will be intermittent due to both the Earth and orbital rotation. These two motions cause accumulation of satellites at some place and no coverage at other places. This situation demands more number of satellites than the minimum number required as predicted from the Eq. (13).

4 True Anomaly (θ_{sep}) and RAAN (Ω_{sep}) Separation

The total number of satellites required for continuous coverage can be obtained by appropriately selecting the RAAN and true anomaly separation.

Now, extending this analysis in three-dimensional space, we can relate the separation lengths (refer Fig. 2) P_1P_2 , to true anomaly separation, θ_{sep} , and P_3P , to RAAN separation Ω_{sep} , which can be deduced as follows.

4.1 True Anomaly Separation (θ_{sep})

The satellite separation distance, d , is given by (refer Fig. 2)

$$d = \sqrt{3}r_{fp} \quad (15)$$

which is equivalent to sum of the lengths P_1P and PP_2 as shown in Fig. 3a,

$$d = P_1P + PP_2 \quad (16)$$

and also the lengths $P_1P = PP_2$. Let us denote the length of overlap ($C_1P = C_2P$) be l , length $O_E P$ be R_x , and the angles $\angle O_E C_1 P = \angle O_E C_2 P$ be α . By geometry, $\alpha = 90 - \lambda$. When $\lambda = \lambda_{\max}$, the satellite viewing angle $= \alpha$. From Figs. 2 and 3, we can write the length of overlap

$$l = r_{fp} \left(1 - \frac{\sqrt{3}}{2} \right) \quad (17)$$

In order to find true anomaly separation, θ_{sep} , the overlap angle $\Delta\lambda$ can be obtained as

$$\Delta\lambda = \cos^{-1} \left[\frac{R_E^2 + R_x^2 - l^2}{2R_E R_x} \right] \quad (18)$$

The unknown R_x in Eq. (18) can be obtained from the following expression

$$R_x = \sqrt{R_E^2 + l^2 - 2R_E l \cos \alpha} \quad (19)$$

Hence, by using Eq. (18), we can find the true anomaly separation, θ_{sep} as

$$\theta_{\text{sep}} = 2(\lambda - \Delta\lambda) \quad (20)$$

If $\lambda = \lambda_{\max}$, substituting Eqs. (1) and (18) in Eq. (20), θ_{sep} can be obtained as

$$\theta_{\text{sep}} = 2 \left\{ \cos^{-1} \left(\frac{R_E}{R_E + h} \right) - \cos^{-1} \left[\frac{R_E^2 + R_x^2 - l^2}{2R_E R_x} \right] \right\} \quad (21)$$

For continuous coverage, the reduced coverage angle due to footprint overlap is given by

$$\phi_{\text{reduced}} = \sin^{-1} \left(\frac{r_{fp}}{2R_E} \right) \quad (22)$$

For an altitude of 710 km, Eq. (1) gives $\lambda_{\max} = 25.864^\circ$. From Eqs. (20) and (22), we obtain $\theta_{\text{sep}} = 45.119^\circ$ and $\phi_{\text{reduced}} = 12.58^\circ$, respectively. Which means, if we distribute eight satellites in an orbit with an inclination of $i = 0^\circ$ and true anomaly separation of 45° , it can continuously cover the Earth only up to $\pm 12.58^\circ$ latitude zone (i.e., $\phi_{\text{reduced}} = 12.58^\circ$), though each satellite sweeps the area between $\pm 25.864^\circ$ latitude zones. Hence, within $\pm 12.58^\circ$ the latitude zone, the coverage is continuous, and between $\pm 12.58^\circ$ to $\pm 25.864^\circ$ the coverage is intermittent.

4.2 RAAN Separation (Ω_{sep})

Ideally, the plane or the RAAN separation angle can be obtained as (from the separation distance PP_3 , refer Fig. 2)

$$\Omega_{sep} = 2 \sin^{-1} \left(\frac{3 \cos(90 - i) r_{fp}}{4 R_E} \right) \quad (23)$$

But, it should be compensated for Earth rotational rate $\omega_E = 7.292115090 \times 10^{-5}$ rad/s, and orbital node drift rate at the equator, $\dot{\Omega}$, given in Eq. (25).

5 Satellite Relative Velocity and Access Time

Satellite access time depends on satellite relative velocity with respect to the ground and also latitude and longitude of the ground location. This section presents the analysis of these two quantities in order to increase the access time.

5.1 Satellite Relative Velocity

The satellite relative velocity with respect to ground location is given by

$$V_R^2 = V_E^2 + V_{Sat}^2 + 2V_E V_{Sat} \cos i \quad (24)$$

where V_{Sat} is the satellite velocity, V_E is the velocity at the ground location due to Earth rotation and is a function of latitude ϕ . $V_E \approx 465$ m/s at equator and *zero* at poles, and i denotes orbit inclination. When inclination $i = 90^\circ$, $V_{R,90^\circ} = \sqrt{V_{Sat}^2 + V_E^2}$. For ($0^\circ \leq i < 90^\circ$), $V_R < V_{R,90^\circ}$, and for ($90^\circ < i \leq 180^\circ$), $V_R > V_{R,90^\circ}$. Hence, the relative velocity given by Eq. (24) depends on the orbit inclination and location of the target on the ground, which is also affected by smaller amount of nodal drift rate of the orbital plane as given by Eq. (25).

$$\dot{\Omega} = -\frac{3}{2} \frac{J_2 \sqrt{\mu} R_E^2}{a^{\frac{7}{2}} (1 - e^2)^2} \cos i \quad (25)$$

where R_E is the Earth equatorial radius (6378.137 km), i is orbit inclination, μ is the Earth gravitational constant ($3.986004418 \times 10^{14}$ m³/s²), a is semi-major axis, e is eccentricity of the orbit, and $J_2 = 0.00108263$ is the perturbation constant (see Refs. [5, 6]). Combined effect of $\dot{\Omega}$, Earth latitude ϕ , and orbit inclination i are to be analyzed independently to achieve the desired access time.

5.2 Satellite Access Time to a Target Location on Earth

The access time of satellite to the ground station is given by

$$T_{\text{access}} = -\frac{T_p}{180} \cos^{-1} \left(\frac{\cos \lambda_{\text{max}}}{\cos \lambda_{\text{min}}} \right) \quad (26)$$

where T_p represents the orbital period, λ_{max} is the maximum central angle given in Eq. (1), and λ_{min} is the minimum central angle which depends on the relative location of the target with respect to the satellite. λ_{min} can be obtained from the spherical triangle [3, 4] as follows:

$$\lambda_{\text{min}} = \sin^{-1} \left\{ \sin \phi_{\text{pole}} \sin \phi_T + \cos \phi_{\text{pole}} \cos \phi_T \cos \Delta L \right\} \quad (27)$$

where ϕ_T and L_T , ϕ_{pole} and L_{pole} are the latitude and longitude of targets and orbit pole, respectively, which can be expressed as

$$\phi_{\text{pole}} = 90^\circ - i \quad (28)$$

$$L_{\text{pole}} = L_{\text{node}} - 90^\circ \quad (29)$$

Whereas, ΔL is the difference in longitudes of orbit pole and target, i.e., $\Delta L = L_{\text{pole}} - L_T$.

6 Simulation

Considering a satellite in an orbit of altitude $h = 710$ km, from Eq. (1) we obtain $\lambda_{\text{max}} = 25.8639^\circ$. From Eq. (6), the radius of the footprint can be obtained as $r_{\text{fp}} = 2782.368$ km. The actual coverage area by a single satellite is approximately 5% of the Earth surface as given by Eq. (4), but, due to overlap in the footprint it is reduced to 4.1419, by the factor K given in Eq. (14). This is the effective coverage area by a single satellite with footprint overlap as given by Eq. (13). From Eq. (17), the minimum overlap length $l = 372.77$ km, which gives the overlap angle $\Delta\lambda$, and the true anomaly separation $\theta_{\text{sep}} = 45.119^\circ$ and $\phi_{\text{reduced}} = 12.58^\circ$.

For an orbit with an inclination $i = 0^\circ$ and $\theta_{\text{sep}} = 45^\circ$, we need minimum of eight satellites to continuously cover $\pm 12.58^\circ$ latitude zone of Earth.

The time period is $T_p = 98.98$ min, for $h = 710$ km circular orbit. From Fig. 5b, the target is at 55° latitude, for $i = 0^\circ$ and $i = 15^\circ$ the satellite is not accessible to the target at any time. When $i = 30^\circ$, it is accessible to the target for a short duration of 3.76 min when the node crosses at 180° . More than 10 min of visibility time is achieved for all inclinations from $i = 45^\circ$ to 90° (Fig. 4).

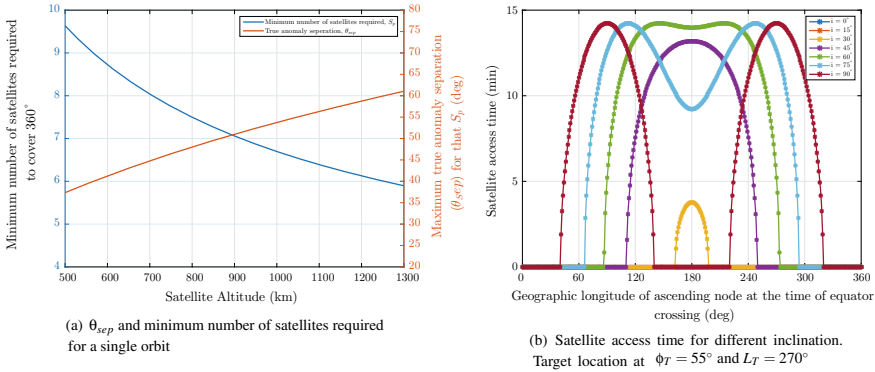


Fig. 5 True anomaly separation (θ_{sep}) and access time (T_{access})

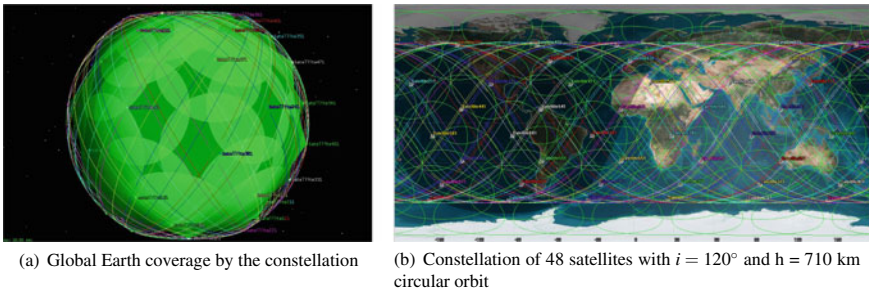


Fig. 6 Simulation result from STK

From Eq. (25), $\dot{\Omega} = 3.98527383 \times 10^{-5}$ deg/s, and the nodal shift of the orbit for a given time Δt is given by $\Delta\Omega = (\omega_E - \dot{\Omega})\Delta t$. For repeat ground track orbit, $\Delta t = 12.3728$ min give $\Delta\Omega = 3.0721^\circ$. And nodal shift for a period T_p is 24.5767° . From Eq. (23), we obtain $\Omega_{sep} = 32.9197^\circ$. Considering the nodal shift due to perturbation and drift of the single satellite, we get 60.5685° longitude distribution. Hence, the total number of satellite required for continuous coverage of Earth becomes $6 \times 8 = 48$. The results are simulated and validated in STK as shown in Fig. 6.

7 Conclusions

A constellation method is proposed to continuously monitor a fixed location on Earth. Mathematical analysis is done based on the mission geometry. Constellation is designed by appropriate selection of true anomaly and RAAN separation from the closed-form solution. Maximum access time is analyzed with respect to the ground location on Earth for different orbit inclinations. The geometry of footprint overlap

area is analyzed in both two and three dimensions, and a closed-form expression is obtained for maximum swath for continuous coverage.

Results are validated using Systems Tool Kit (STK).¹

Acknowledgements Authors express their sincere thanks to Shri. K. Rambabu, Scientist—‘H,’ Director, DSST, for giving the opportunity and for his invaluable support and encouragement to work extensively on small satellite LEO constellation design.

References

1. Tomas S, David WE (1994) Determination of look angles to geostationary communication satellites. *J Surv Eng* 120(3), paper no 7382
2. Shkeelzen C, Bexhet K, Algenti L, Alban R (2014) The coverage analysis for low earth orbiting satellites at low elevation. *Int J Adv Comput Sci Appl* 5(6):6–10
3. Zwillinger D (2003) *Standard mathematical tables and formulae*, 31st edn. Chapman & Hall/CRC, Boca Raton
4. Beyer WH (ed) (1991) *Standard mathematical tables and formulae*, 29th edn. CRC Press, Boca Raton
5. Curtis HD (2014) *Orbital mechanics for engineering students*, 3rd edn. Elsevier, Amsterdam. ISBN: 978-93-5107-191-4
6. Vallado D (2013) *Fundamentals of astrodynamics and applications*. Microcosm Press, Portland



A. Vairavan received Bachelors degree in Aeronautical Engineering from Bharathiar University, Coimbatore, India, and Masters degree in Aerospace Engineering from Indian Institute of Science, Bangalore, India. Currently, he is working as a scientist in Directorate of Space Systems and Technology, RCI. His research interests include orbit and attitude dynamics of satellites, spacecraft formation flying, satellite constellation design, guidance, navigation and control of aerospace vehicles.

¹Systems Tool Kit (STK) is the premier software for providing four-dimensional modeling, simulation, and analysis of objects from land, sea, air, and space in order to evaluate system performance in real or simulated time. ©Analytical Graphics, Inc., as per Web site information.



Rukmini Banda did her graduation in B.Sc. (Hons) and post-graduation in M.Sc. Tech with electronics from S. V. University Tirupathi from Andhra Pradesh. She joined as a scientist in DRDO and worked for 10 years on infrared imaging payloads for aerospace applications. After that, she worked for on board mission computer and embedded systems software for Air Defence program for a period of 10 years. At present, she is the head for System Engineering Division under the Directorate of Satellite Systems and Technologies. Her research interests include spaceborn payload, satellite constellation design, and space mission software.

Small Satellite System Engineering and Production

Design, Development and Validation of Fault-Tolerant Processor and Integrated Development Environment for Space and Defence Applications: Indigenous Initiative



P. Balasubramanian, B. Kusuma Kumari, S. Kalyan Kumar, Anil N. Terkar, Chnab Sankar, Sudhanshu Kumar, Vikram Singh Parihar, J. V. R. Sagar and C. Ramesh Reddy

Abstract Space and defence electronics system demands higher reliability for its operation in harsh (Maurer et al. in John Hopkins APL Tech Dig 28, 2008 [1]) and tough application environments. Development of processor (Azambuja et al. in IEEE Trans Nucl Sci 59, 2012 [2]) based electronics systems has advantages over sequencer logics, viz. high operating frequency, handle complex algorithm for autonomous operations, supports multiinput and multioutput systems, low form factor, ultra-low-power consumption and increased reliability. The operation of processor under various environmental conditions and its uninterrupted operations pave way to achieve successful missions. Most of the on-board computers for the space and defence systems are subjected to harsh environments due to cosmic radiations(aerial), high temperature, vibrations, sand and dust. Modular redundancy concepts aid to improve reliability however at the cost of increased form factor and enhanced power requirements. Researchers across the globe evolved with various methods and techniques to increase the ruggedness of the electronics systems. Traditional design hardening techniques viz. modular redundancies, parity algorithms, cyclic redundancy checks, single error correction and double error detection are in use to develop the fault-tolerant on-board computers. Since most of the fault-tolerant processors developed using in-house design, process hardening techniques for specific purpose, the availability of the same for the strategic programs and critical applications is limited

P. Balasubramanian

DRDO Research and Innovation Centre (RIC), IIT Madras Research Park, Chennai 600113, India

e-mail: pbalasubramanian@ric.drdo.in

B. Kusuma Kumari · S. Kalyan Kumar · A. N. Terkar (✉) · C. Sankar · S. Kumar · V. S. Parihar · J. V. R. Sagar

ANURAG, Hyderabad, India

e-mail: a_terkar@anurag.drdo.in

B. Kusuma Kumari

e-mail: kusuma@anurag.drdo.in

C. Ramesh Reddy

RCI, Hyderabad, India

© Springer Nature Singapore Pte Ltd. 2020

PSR. S. Sastry et al. (eds.), *Advances in Small Satellite Technologies*,

Lecture Notes in Mechanical Engineering,

https://doi.org/10.1007/978-981-15-1724-2_40

and export controlled. To mitigate the scenarios, an indigenous effort has been made to architect, design, develop and validate the fault-tolerant processor using DRDO processor core (Series-A). The core is indigenously developed by DRDO. Using the fault-tolerant design methods, the indigenous processor core is upgraded to a fault-tolerant core. The core is RISC-based 32-bit architecture. The non-fault tolerant (FT) core is architected to incorporate the FT feature using the in-house and traditional techniques, viz. modular redundancy, single error correction and double error detection for FFs and registers, parity logics for memories. To provide the operational compatibility and to estimate the performance of FT-core using the user's application algorithm, an integrated development environment (IDE) is designed, developed and validated. The FT-core with a frequency of up to 50 MHz in FPGA is validated using the application program for the function-A (aerial) and function-B (ground) strategic systems. The functional performance was on par with the industry architecture. The timing performance is satisfactory and met the user's functional requirement. To meet the high performance and computational intensive requirements of the futuristic programs, the FT-core to be developed using dual or quad-core approach with appropriate fault-tolerant techniques.

Keywords Low Earth Orbit (LEO) · Reliability · Fault Tolerant Processor · Compiler · Validation and On-board Computer

1 Introduction

Worldwide system on chip (SOC) concept is gaining popularity and development of integrated processor with other logics in a single chip has more advantages than the traditional modular processor and glue logics. The Moore's law provides opportunity to integrate more and more logics in the same form factor with the reduced operating voltage. Even though there are significant advantages in Moore's law, several challenges in terms of signal integrity, leakage currents and faults due to cosmic radiation are prominent.

The shrink in feature dimension paved way to miniaturization of the semiconductor system on chip has opened new avenue of challenges related to leakage power dissipation, signal integrity, low-power designs and increased the probability of failures due to cosmic radiations. Cosmic radiation originates from the outer space interacts with the atmosphere and generates particles with high energy. These particles bombard the system on chip and create ionization in-turn generate the charge. The charge created generates single-event transient upsets in combinatorial logics and eventually produces a single-event upset in FFs/storage elements. Since the system on chip functions are designed using combinatorial and sequential logics, the probability of functional failure increases. The effect of shrink in feature size dimension increases the probability by multiple folds. Worldwide various methodologies are adopted to mitigate the effects of failures due to cosmic radiation using radiation hardening by process, radiation hardening by design and shielding methods.

The space and aerial defence vehicles experience the effects of cosmic radiation above 5 km altitude. The high energy particle emitted from the outer space interacts with the atmosphere and produces protons, neutrons and other high energy particles. These particles bombard the SOC and can create ionization in the silicon. The ionization effects produced depends on the particle velocity, angle of inclination with the surface volume (silicon) and its linear energy transfer. The ionization creates a single-event transient in the combinatorial logics and subsequently gets latched as single-event upsets in the sequential logics. The single-event upset can change the logic values in the flip-flops and memories. The logics associated with the FFs and memories elements produces erroneous results. Since the processor comprises several sequential and combinatorial logics, a higher probability of faults generated due to radiation or thermal effects exists. The space and defence vehicles on-board computer need to be hardened and fault tolerant in spite of various environmental conditions. The mission computer needs to be rugged and tolerant for any failures and especially needs to protect and continue the operation.

The radiation hardening by process is complex and export controlled. The hardening by design uses the traditional redundancy techniques, cyclic redundancy checks, parity algorithms and single error correction and double error detection (SECCED) [3] methods to build the fault-tolerant computing platform. Since most of the fault-tolerant computing platforms are used for strategic applications, limited design knowledge and product exist with export control. Considering the situation and the potential development of fault-tolerant computing platform using the indigenous DRDO processor core and scaling up for various high frequency requirements can open-up the path to support the development of various indigenous futuristic strategic programs. This article briefs the fault-tolerant requirements for the processor core function, re-architecture to build the FT-core, development of integrated development environment for the FT-core, validation and results.

2 Fault-Tolerant Requirements

The applications viz. function-A OBC on-board controller of a slow moving aerial vehicle designed to reach up to an altitude of 22 km, and function-C OBC of a high altitude very long endurance platform is designed to reach up to an altitude of 800 km. The primary requirements for both the platforms are below.

S. No.	Threat	Effects	Mitigation
1.	Single point failures due to the effect of cosmic Radiation [4]/power disturbance/thermal imbalance	Single-event transient (SET)—combinatorial logic	Fault-tolerant architecture to arrest/suppress—propagation of SET or Evolve with a voter algorithm to select the correct output

(continued)

(continued)

S. No.	Threat	Effects	Mitigation
2.		SEU single-event upset—FFs/registers	Fault-tolerant architecture [5] using modular redundancy or cyclic redundancy check or parity logics to discard the failed and to select the correct output
3.		No timing or performance degradation of function/execution	Re-architecture the base processor using space redundancy techniques and algorithms

3 FT-Processor Architecture

3.1 Base Architecture

Series-A processor core is indigenously developed by ANURAG DRDO. It is a 32-bit RISC microprocessor. The CPU is implemented using five-stage pipeline. The architecture supports general-purpose registers (GPR), special purpose registers and floating point registers (FPR). These special purpose registers are used for processor housekeeping and accessing peripheral. Special registers include a stack pointer, control/status word, etc.

3.2 FT Architecture

Series-A processor has been modified to fault-tolerant Series-A to mitigate the SEU occurring in registers and pipeline flip-flops. Appropriate techniques of Triple Modular Redundancy (TMR), single error correction double error detection (SEC-DED) and other required logics/algorithms have been applied to these registers and flip-flops.

3.3 Processor Pipelined Flip-Flops

A commonly known method for SEU mitigation [6] is Triple Module Redundancy (TMR) with voting. This mitigation scheme uses three identical logic circuits performing the same task in parallel with corresponding outputs being compared through

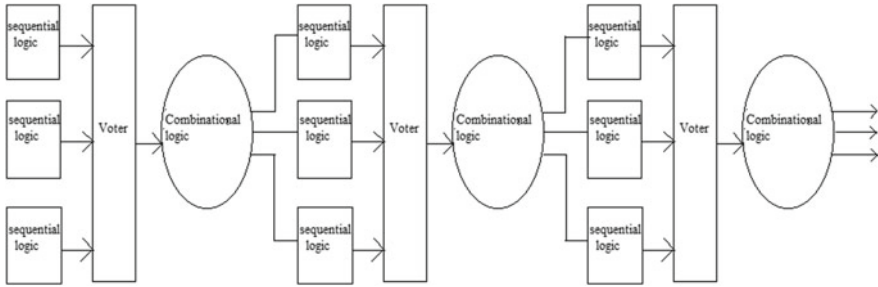


Fig. 1 TMR pipeline registers of Series-A processor

a majority voter circuit. The most common example of TMR is a D-type flip-flop that has been triplicated and to which a voter has been added on its output. By replacing all flip-flops in design with the circuit, the design is protected against SEUs in the flip-flops. Figure 1 shows how TMR pipeline registers connected between each stage.

3.4 SEC-DED for GPR and FPR

The basic Hamming code can detect and correct an error in only a single bit. By adding another parity bit to the coded word, the Hamming code can be used to correct a single error and detect double errors. Figure 2 shows how the GPR and FPR registers were implemented for SEC-DED.

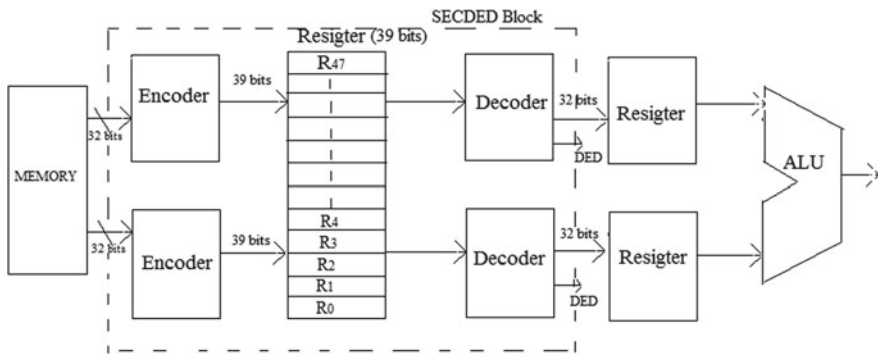


Fig. 2 SECDED block diagram of FT-Series-A

4 Implementation in FPGA and Results

4.1 Area/Timing

Series-A processor and FT-Series-A processor were implemented on custom FPGA board targeting Xilinx Artix-7 FPGA. The utilization and timing report of both Series-A and FT-Series-A are reported as shown below.

Series-A utilization report

Name	Slice LUTs	Slice registers	Slice	LUT as logic	LUT flip-flop pairs
u_alu_top	14,679	7170	5110	14,679	2339
u_alu	14,679	7170	5110	14,679	2339
IDpFpu	3215	0	976	3215	0
IRegFile	5771	6201	2718	5771	1839
ISpFpu	1636	0	485	1636	0
Decoder + execution unit	4057	969			

FT-Series-A utilization report

Name	Slice LUTs	Slice registers	Slice	LUT as logic	LUT flip-flop pairs
u_alu_top	21,838	15,450	7170	21,838	3726
u_alu	21,838	15,450	7170	21,838	3726
IDpFpu	3201	0	932	3201	0
IRegFile	11,529	12,647	4376	11,529	1738
ISpFpu	1652	0	504	1652	0
Decoder + execution unit	5456	2803			

Comparison of Series-A and FT-Series-A processors utilization report

ARTIX-7 XC7A200T (FPGA)	Series-A	FT-Series-A
Slice Registers (269,200)	7170 (2.66%)	15,450 (5.73%)
Slice LUTs (134,600)	14,679 (10.9%)	21,838 (16.22%)
Slice (33,650)	5110 (15.18%)	7170 (21.3%)

Timing in Artix-7 @ 45 MHz

Timing	Series-A	FT-Series-A
Slack	0.18	0.01
Hold	0.04	0.03

5 Validation and Simulation

The verification of TMR logic in FT-Series-A RTL is carried out at module level. In each module, error is propagated randomly to one of TMR flip-flops at various instants of time using select logic as shown in Fig. 3.

The 32-bit register file incorporating the SECDED is verified by introducing single error and double errors. The validation approach depicted in Fig. 4 is self-explanatory.

The register file has been verified with 10,000 different random inputs from hex file. All possible error combinations have been simulated for these inputs.

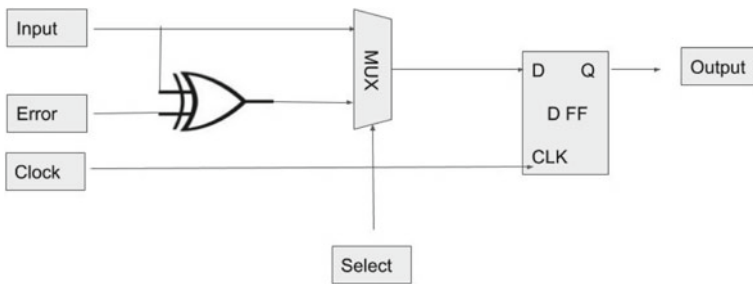


Fig. 3 Error feed mechanism

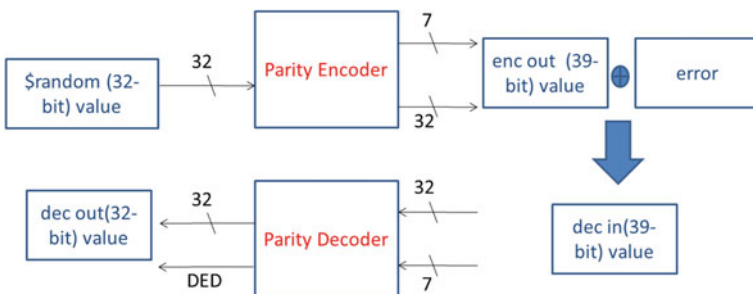


Fig. 4 Block diagram of FT-Series-A validation approach

6 AIDE-FT

The integrated development environment (IDE) provides user-friendly interface to the application developers by integrating various software development tools like text editor, compiler, assembler and linker, etc., as required for developing applications. For the purpose of assisting the application development with ANURAG's indigenous fault-tolerant version of Processor, i.e. FT-Series-A, an IDE named AIDE-FT (ANURAG's integrated development environment for fault-tolerant Series-A) based on Eclipse IDE infrastructure has been developed. It integrates processor Series-A C cross compiler tool chain based on GCC. A tool chain consists of many components, e.g. compiler, assembler, linker, archiver, language-specific standard libraries, etc. The compiler tool chain for Series-A is based on open-source compiler GCC version 4.1.2. GCC is an open-source production level compiler and extensively used by industry.

6.1 Base Architecture

Architecture of AIDE-FT is described in Fig. 5.

- Platform Runtime and Plugin Architecture

The Eclipse Platform runtime provides the core frameworks and services upon which all applications are created. It also provides the platform runtime in which Eclipse plugins are loaded and executed. A plugin is the smallest unit that provides functionality to Eclipse Platform and can be developed and delivered separately.

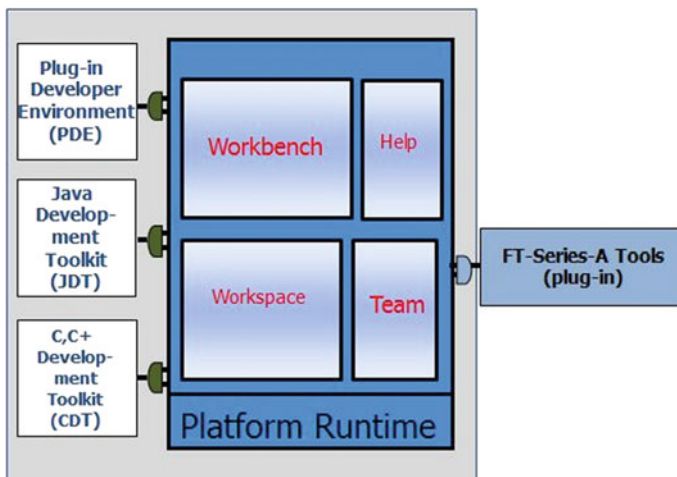


Fig. 5 Eclipse platform architecture

Usually, a small tool is represented as a single plugin, whereas a complex tool functionality is split across many plugins.

- Workspaces
The workspace consists of user-specified one or more projects, where each project maps to a corresponding directory or folder in the file system.
- Workbench and UI Toolkits
The Eclipse Platform UI provides an extensible UI to the user, and it is built around a workbench that provides the overall structure.
- Team support
The Eclipse Platform provides version and configuration management with an associated repository for a project placed in the workspace.

6.2 AIDE-FT: Tools Integration

By default, Eclipse IDE provides interface with native compiler tool chain. To provide interface with FT-Series-A compiler toolset, plugins were developed using plugin development environment (PDE) [9] and (C, C++ development tool kit (CDT) [10], which integrates the FT-Series-A compiler toolset, i.e. FT-Series-A C cross compiler, linker, assembler, libraries, etc., to the Eclipse Platform. This integration was carried out in such a way that AIDE-FT provides seamless interface to the FT-Series-A processor cross compiler tool chain. It generates ‘managed make’ which describes the compilation process of application program by FT-Series-A compiler tools and makes the application ‘build process’ seamless. By default, ELF executable will be generated by compiling application program with this tool chain. As the monitor of FT-Series-A board supports SREC file format for loading and running, plugins were extended such that both ELF and SREC executables are generated by default. Two modes of project creation were supported in AIDE-FT, which are as follows:

1. Series-A Standalone: for standalone application.
2. Series-A Debug: In this mode, debug information will be added in executable, which is necessary for debugging (Fig. 6).

6.3 AIDE-FT: Load, Run and Debug with FT Board

FT-Series-A board has been using serial port for communication with the host system through serial communication program ‘minicom’. Load and run command need to be evoked on minicom terminal to execute the program manually. To remove this manual process, ‘minicom’ was integrated with AIDE-FT. But it only helps in invoking the ‘minicom’, and user has to again type the load and run command on minicom terminal. To solve this problem of manually providing the command, an

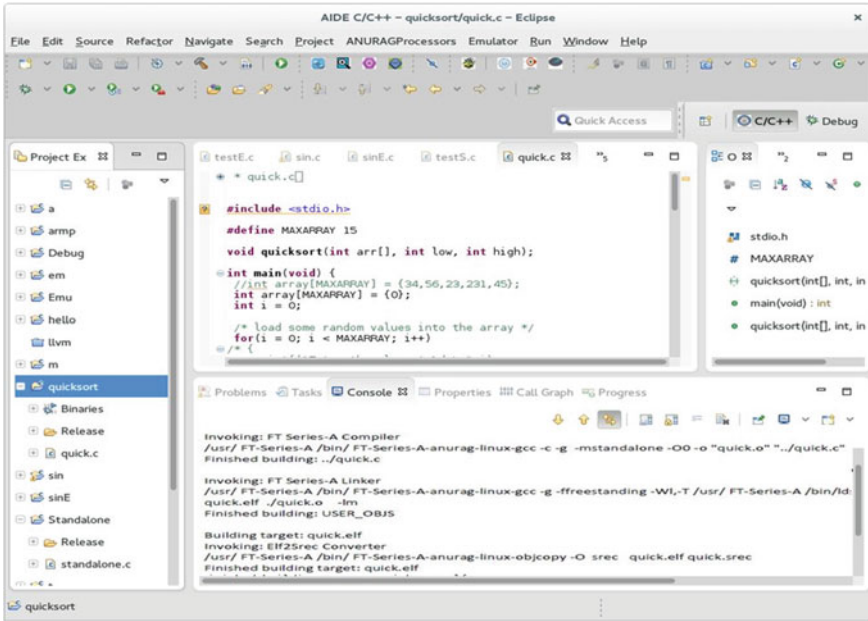


Fig. 6 AIDE-FT snapshot

automate mechanism was developed using expect and ‘tcl’ tools, which automates the loading and running of the executable without any manual intervention. This mechanism also takes care of calculating the load and run addresses of the executable.

Two modes of user application for execution and debug are provided in the AIDE-FT:

- i. Load and Execute in Hardware
- ii. Load and Debug in Hardware.

In both modes, automatic loading and execution of binary were provided. X-term is integrated in the AIDE-FT for displaying the automatic loading, execution, input and output on the host system (Fig. 7).

For application debugging, Series-A remote debugger based on GDB was integrated in AIDE-FT. User can use breakpoints, run step by step, analyse the values of variables and processor registers, etc. (Fig. 8).

6.4 Integration Testing

Various functionalities provided by the FT-Series-A specific developed plugins, e.g. downloading of the file, execution and remote debugging of the application have been tested through automation. Standard Widget Toolkit Bot (SWTBot) [11] provides

```
ANURAG XTerm
Welcome to minicom 2.6.2
OPTIONS: I18n
Compiled on Aug  7 2013, 13:32:43.
Port /dev/ttyS0, 11:34:00
Press CTRL-A Z for help on special keys

RICSoC>
RICSoC> sre

  Load SREC File from HyperTerminal
#####
SREC Loading done !!
10000060

RICSoC>
RICSoC>

RICSoC> run 10000060

Jumping to Location : 0x10000060
Hello..
RICSoC>
RICSoC> █
```

Fig. 7 Load and run view

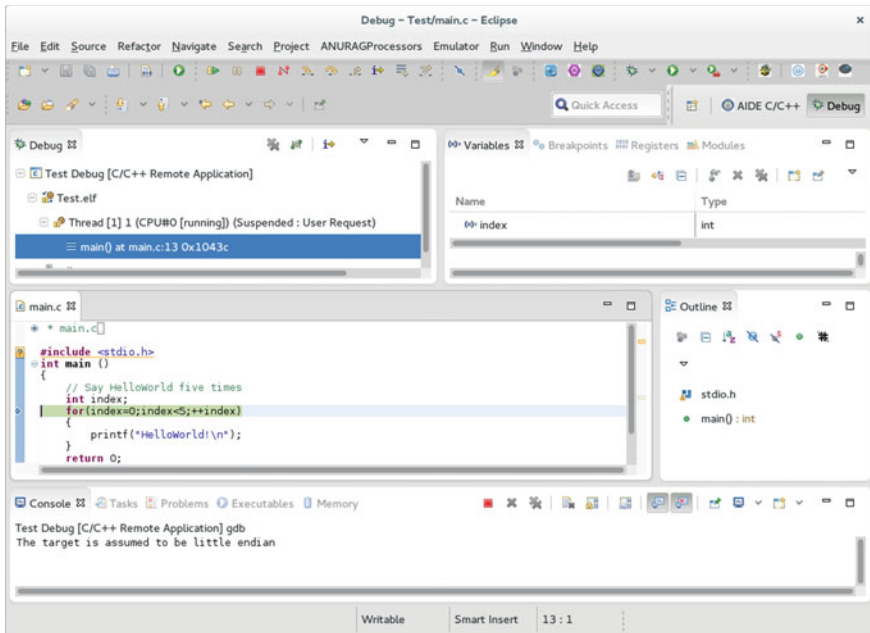


Fig. 8 Debug session

an automated testing framework with the Eclipse IDE. SWTBot is an open-source Java-based UI/functional testing tool for testing SWT, Eclipse and Graphical Editing Framework (GEF)-based applications. SWTBot provides Test Recorder and Generator that user can use to generate test case simply by recording the UI actions, as an end-user would perform them.

SWTBot provides application programming interfaces (APIs) that are very simple to read and write. These APIs also hide the complexities involved with SWT and Eclipse. This makes it useful for UI/functional testing by everyone, not just developers. SWTBot also provides its own set of assertions which are useful for SWT.

7 FPGA Board

The FT-serial-A is implemented in the Xilinx-based FT board to validate the performance for application-specific users algorithms. The FT board consists of features AHRS unit, gauge/differential pressure sensor, absolute pressure sensor GPS, IMU, MIL 1553 and RF link interfaces, and different PWM, digital control signal interfaces used to test and develop algorithms for flight control and navigation control of typical airborne system. The board architecture, block diagram and interfaces are shown in Fig. 9.

The 3D view of the components [7] mounted board is shown in Fig. 10.

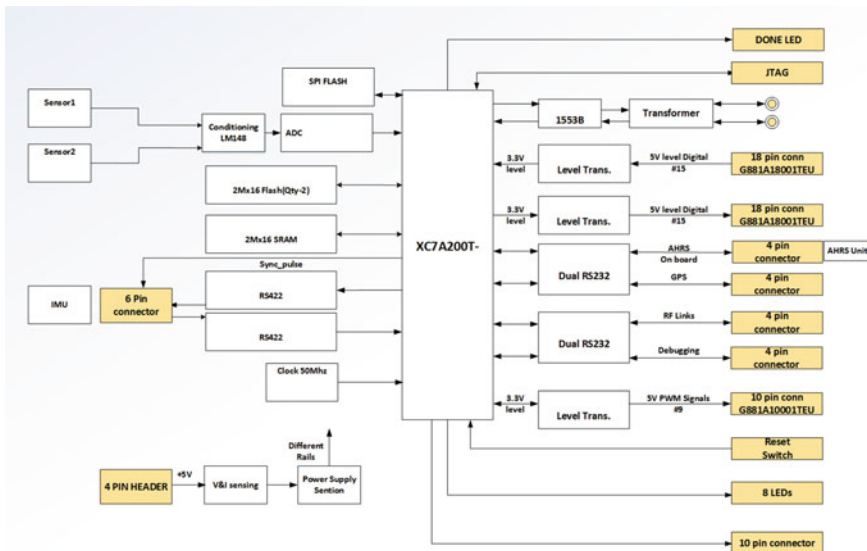


Fig. 9 Architecture and interface block diagram of FT board

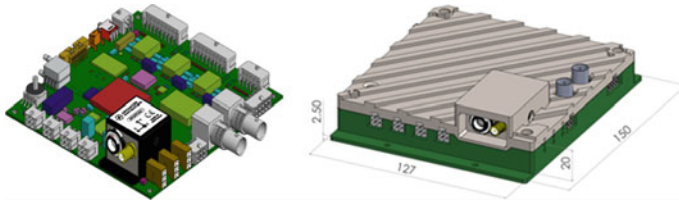


Fig. 10 3D view of the FT board and enclosure

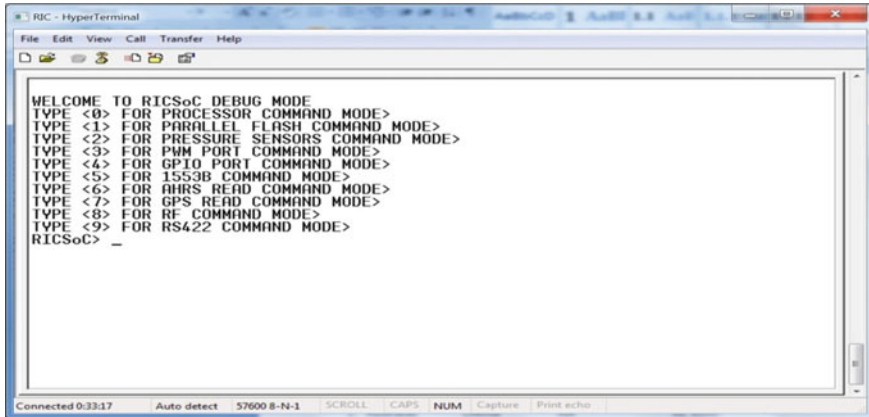


Fig. 11 Boot instruction execution and results display

8 Validation

The board with FT-core and interfaces is validated. The monitor program with instruction is shown in Fig. 11.

AHRS and GPS interface validation:

FT-core is programmed to read the AHRS and GPS data from the sensor and displayed the latitude, longitude, roll and pitch data variance is shown in Fig. 12.

9 Conclusion

The paper summarizes the architecture, design, development, validation and integrated testing of fault-tolerant processor, integrated development environment and application board with sensors, interfaces and on-board logics [8]. The FT architecture developed is validated using on-board software for ground and aerial vehicle

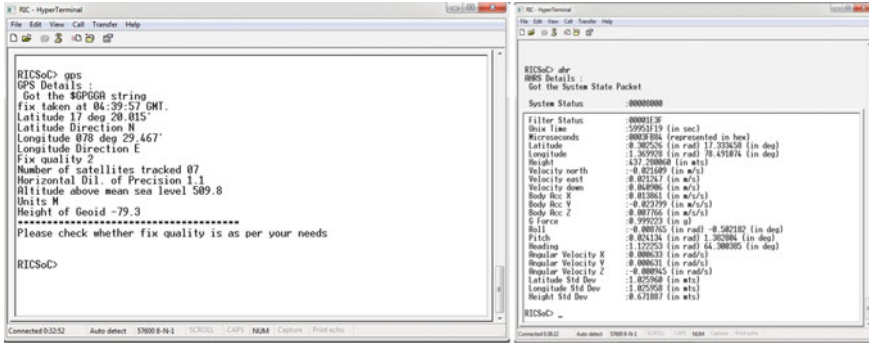


Fig. 12 AHRS and GPS data read and display

applications. The performance in terms of functionality is found satisfactory. The timing cycles need to be re-validated using the higher version of the processor. Effort to perform environmental qualification and certification is in progress.

10 Future Plans

The fault-tolerant computing technology has strong potential for various strategic, space, industrial, medical and commercial applications. Worldwide efforts are initiated to develop fault-tolerant computing platform which can pay way for the development of self-healing electronics systems. With the indigenous effort, it is planned to develop dual core, quad-core and multicore FT-processor architecture to obtain high performance and using design methodologies to develop low-power processors to support the advanced futuristic programs.

Acknowledgements The author acknowledges the encouragement and support provided by Dr. V. Natarajan, Director, RIC to continue and pursue the research activity. The author acknowledges the support provided by RIC team to progress and successfully evolve with the results.

References

1. Maurer RH, Fraeman ME, Martin MN, Roth DR (2008) Harsh environments: space radiation environment, effects, and mitigation. John Hopkins APL Tech Dig 28(1)
2. Azambuja JR, Pagliarini S, Altieri M, Kastensmidt FL, Hübner M, Becker J, Foucard G, Velazco R (2012) A fault tolerant approach to detect transient faults in microprocessors based on a non-intrusive reconfigurable hardware. IEEE Trans Nucl Sci 59(4)
3. Tam S (Xilinx) (2006) Single error correction and double error correction. XAPP645 (v2.2), Aug 2006

4. Todd B, Uznanski S (CERN, Geneva, Switzerland) (2014) Radiation risks and mitigation in electronic systems. In: Proceedings of the CAS-CERN Accelerator School: Power Converters, Baden, Switzerland, 7–14 May 2014
5. Wang L-T, Stroud CE, Toubia NA (2008) System on chip test architectures—nanometer design for testability, 1st edn. Elsevier, Amsterdam
6. Space product assurance: techniques for radiation effects mitigation in ASICs and FPGAs handbook (ECSS-Q-HB-60-02A) dated 1st Sept 2016
7. Space product assurance: radiation hardness assurance—EEE components (ECSS-Q-ST-60-15C) dated 1st Oct 2012
8. Agarwal S, Bhatia R, Padmavathi N, Sudhakar S, Udupa S (2013) System on chip approach for onboard computer. In: IEEE international conference on signal processing, computing and control (ISPC), Sept 2013, Solan, India
9. www.eclipse.org/pde
10. www.eclipse.org/cdt
11. www.eclipse.org/swtbot

On-Orbit Real-Time Avionics Package Identification Using Vision-Based Machine Learning Techniques



B. S. Sajeendran and R. Durairaj

Abstract Capability for on-orbit inspection using autonomous robots is important in manned space station/capsule operations. Due to the unpredictable lighting conditions on orbit, machine learning-based package identification and detection is a good candidate for inspection operations. In this work, the AI-based technique has been used to identify packages of interest from a set of packages in the orbital platforms. Images of different packages on the platform are used for the training using a simple neural network for fast inference of packages in the frame.

Keywords Object detection · Computer vision · Machine learning · Inspection

1 Introduction

With the current trends in robotic space exploration, it is critical to develop technologies for assisting the astronauts in intra- and extra-vehicular activities of which on-orbit inspection and repair are of major significance. Flying robots such as AERCam Sprint and SPHERES [1, 2] have been used for this by NASA in the past. Though teleoperation has been traditionally used for inspection using robotic arms/flying robots, autonomy is preferred to reduce the time that astronauts spend on such tasks. In this work, it is proposed to demonstrate artificial intelligence (AI)-based package identification onboard space platforms as a precursor to autonomous operation. The paper presents the challenges in inspection/identification under varied lighting conditions and a description of the machine learning technique used for this application. Further, the implementation aspects are discussed, followed by results and summary.

B. S. Sajeendran (✉) · R. Durairaj
Artificial Intelligence and Space Robotics Division, ISRO Inertial Systems Unit,
Vattiyookavu, Trivandrum, India
e-mail: sajeendran_bs@vssc.gov.in

© Springer Nature Singapore Pte Ltd. 2020
PSR. S. Sastry et al. (eds.), *Advances in Small Satellite Technologies*,
Lecture Notes in Mechanical Engineering,
https://doi.org/10.1007/978-981-15-1724-2_41

2 Problem Definition

The orbital platforms consist of the avionics packages for the launch vehicle operation. A flying robot is assumed to approach the platform from the side (in a plane perpendicular to the roll axis) during which the inspection operation is planned. The packages will be in the field-of-view of the camera within about 2 m from the platform. The identification of various packages in the image frame poses challenges due to varying lighting conditions and orientation of the robot with respect to the packages. Also, overlapping of packages in the image frame causes occlusion preventing the correct package identification. The fuel tank and the cable harnesses also pose challenges in the vision algorithm.

3 Methods

As mentioned in the problem definition, the unpredictable environment poses challenges for a conventional vision algorithm design. A machine learning-based algorithm will be better suited for the situation as the packages on board the PS4 are predetermined and the images can be used for training purposes.

3.1 Toolchain

In order to leverage identical systems for training as well as the inference stages, Keras library with Tensorflow backend is selected. Keras provides a high-level API for NN definition using python scripts and simplifies the task of training and inference without dwelling much into the computational methods used by Tensorflow. The model developed from training the NN is transferred as an HDF5 file that can be deployed in the edge devices for inference purposes.

3.2 Hardware Selection

3.2.1 Training Hardware

For training purpose, a GPU-based Linux system is used for accelerating the training time. The specifications of the system are listed in Table 1.

Table 1 Hardware for NN training

GPU	Nvidia GeForce 1050 Ti, 768 NVIDIA CUDA [®] cores
Operating system	Ubuntu 16.06
CPU	Intel Core i5
Tensorflow	1.10.0
Keras	2.2.4

3.2.2 Inference Hardware

For on-orbit operation of the inspection hardware, the neural network has to be deployed on embedded edge devices capable of handling the low power and fast development time along with support for NN training and inference toolchain supports. Based on these requirements, two hardware were identified.

The Nvidia Jetson TX2i is a GPU-based embedded board with industrial-grade components supporting Tensorflow. It has quad-core ARM processor and dual-core Denver processor along with 256 CUDA cores. It has a power utilization of 15 W.

The second hardware evaluated was the Raspberry Pi 3 B+ which is an open-source single board computer (SBC) with quad-core ARM CPU and Mali GPU. Official Tensorflow support is provided for Raspberry Pi 3 by Google and the low cost of INR 1000 and a power consumption of 5 W with support from open-source community are the advantages of the board. Even though the performance is low compared to the Nvidia Jetson board, for evaluation of neural network workloads, Raspberry Pi 3 B+ is selected.

3.3 Training Data

The video recorded from the laboratory environment is converted to images for training purpose. To simulate the unpredictable environment on space, different brightness settings and blurring effects were added to prevent over-fitting and under-fitting in the training with the help of data augmentation library available in Keras. Two packages were selected and 300 images were used for each package.

3.4 Neural Network Selection

From literature survey, different neural networks were compared based upon the size of the model and the total number of parameters/total number of multiply accumulation operations (MACs). Since the prime objective is to deploy the network to an embedded device, the focus is given to mobile networks which are small in size

Table 2 Literature survey results for running NN on Raspberry Pi 3

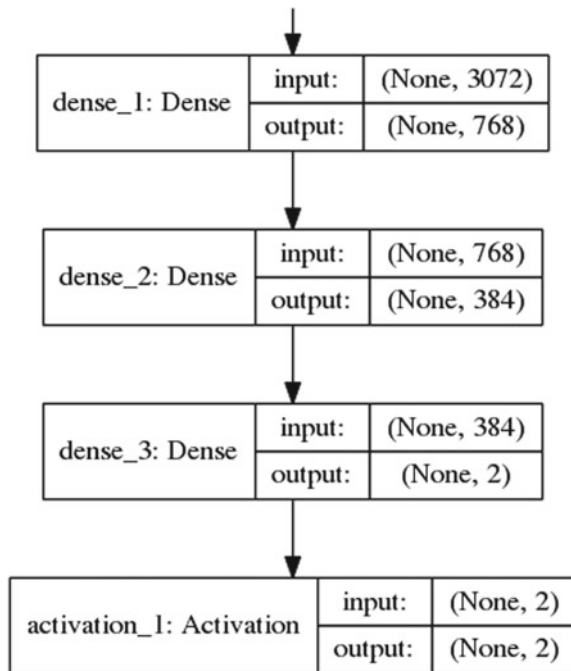
Network architecture/framework	Calculation time for one frame
Darknet/YOLO	450 s
Darknet/Tiny YOLO	40 s
Tensorflow object detection API/SSD	26 s
MXnet/SSD	88 s
Caffe/YOLO	5 s
MobileNet/SSD	250 ms (80–90% CPU usage)
Simple neural network (non-convolutional) [5]	<250 ms

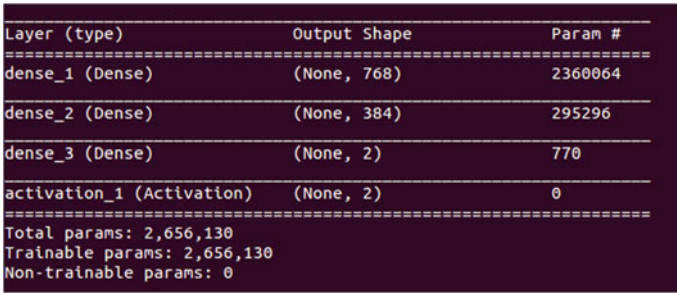
and lighter in terms of computations. Performance of running some standard neural network on Raspberry Pi 3 is evaluated [3] and summarized in Table 2.

Also, a custom CNN deployed for structural health monitoring [4] shows that ~30% of RAM and ~30% of CPU resources are used for a neural network of 37.15 lakh parameters. Raspberry Pi 3 took 8 s for processing a single frame. As expected the convolutional layer consumes most of the CPU workload.

In order to evaluate a faster and lighter method, a non-convolutional neural network is run on the Raspberry Pi 3. The details of the network are mentioned in Fig. 1

Fig. 1 Simple neural network architecture





```
Layer (type)          Output Shape          Param #
-----
dense_1 (Dense)      (None, 768)          2360864
dense_2 (Dense)      (None, 384)          295296
dense_3 (Dense)      (None, 2)            770
activation_1 (Activation) (None, 2)            0
-----
Total params: 2,656,130
Trainable params: 2,656,130
Non-trainable params: 0
```

Fig. 2 Summary of parameters

and the parameters are summarized in Fig. 2.

This simple neural network is designed based on hyperparameter tuning and is useful for binary classification. It takes as input a $32 \times 32 \times 3$ image resized to 3072×1 arrays and is input to two dense layers of size 768 and 384, respectively. The weights are initialized using uniform distribution and a softmax activation layer is used at the output for classification. The network has a size of 22 MB and 26.56 lakhs parameter.

In comparison, the Mobilenet SSD, a standard CNN for multiple object classification with 68 lakh parameters took a processing time of 6 s on Raspberry Pi 3 but takes almost 80–90% of processing time. Larger number of parameters led to more memory usage as well.

3.5 Inference

The inference is done using the Raspberry Pi 3 B+ running identical operating system as the training platform (Raspbian Stretch vs. Ubuntu: both Debian-based). Hence, the code used for laboratory experiments is easily ported to the embedded hardware. The testing data is separated from the training data in order to have a fair evaluation of the model.

4 Test Setup

The final setup for testing the inference speed consists of a Raspberry Pi 3 running Raspbian Stretch using Picam. Even though the resolution of Picam is small (5 MP), it is good enough for laboratory simulations. The test setup is shown in Fig. 3. The

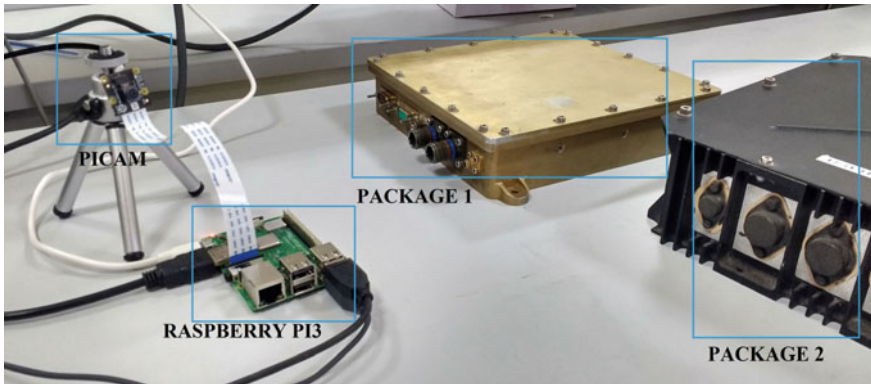


Fig. 3 Laboratory test setup for package detection

image snapshots are captured and stored at 2 fps and the network inference reads the images from the disk.

5 Results

Using the training data from ground-based video capture under single lighting condition, the simple neural network is capable of detecting the packages even under blurred conditions. The two packages used for classification are Inertial Systems Unit (ISU) and Navigation, Guidance and Control Package (NGCP).

The training converges within 2 epochs for the simple neural network with loss less than 0.1.

The loss function used is binary cross-entropy with stochastic gradient descent as the optimizer (Figs. 4 and 5).

As shown in Figs. 6 and 8, the ISU package is identified with a probability of 93% and 97%, respectively, even in the presence of blur and partial image. Similarly, in Figs. 7 and 9, the NGCP package is identified with probability of 93% and 98%, respectively. The simple neural network could do this in real time on Raspberry Pi hardware. In comparison, the LeNet SSD is capable of inferring the object at >4 fps at real time, but is designed for handwriting recognition where the input images are smaller in size. The MobileNet SSD is designed for mobile applications. However, it took ~6 s for a frame on the Raspberry Pi 3 hardware.

Fig. 4 Prediction accuracy variation during training

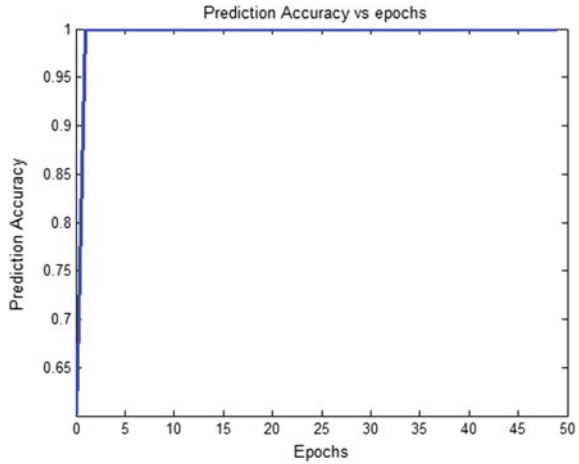
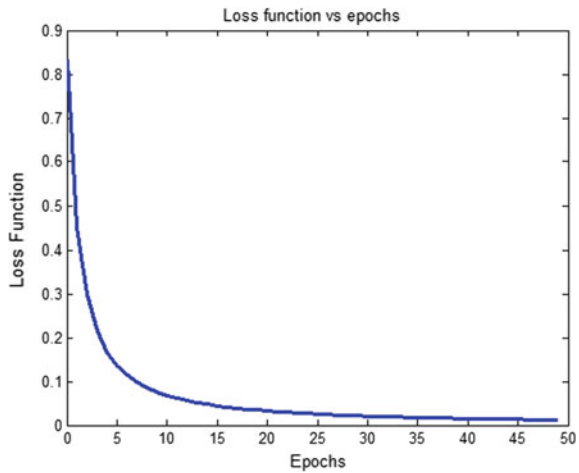


Fig. 5 Loss function variation during training



6 Summary

The package identification using machine learning is developed using standard neural networks and the results are satisfactory. However, for practical deployment in space environment on edge devices, lighter and efficient networks are needed. One such neural network without using the computationally heavy convolutional layer is evaluated on open-source embedded hardware. Other methods like compression techniques can be pursued for further reduction in model size at the cost of computational complexity [6]. Further, speedups have been reported by using accelerators on Raspberry Pi 3 platform like the Intel Neural Compute Stick.



Fig. 6 ISU with blur identified at 92% accuracy



Fig. 7 NGC with blur identified at 98% accuracy



Fig. 8 ISU without blur identified at 97% accuracy



Fig. 9 NGC with blur identified at 98% accuracy

Acknowledgements We would like to thank our colleagues of AISRD team for the support provided during testing and the design works. We would also like to thank Sri. Haridas TR for the detailed reviews and feedbacks. Furthermore, the guidance from our Group Director, Sri. Sasikumar S. is appreciated as well.

References

1. Keller BS, Tadikonda SS, Mapar J (2002) Autonomous acquisition, rendezvous, & docking using a video guidance sensor: experimental testbed results. In: AIAA guidance, navigation, and control conference and exhibit, Monterey, CA, Aug 2002
2. Nolet S, Miller DW (2007) Autonomous docking experiments using the SPHERES testbed inside the ISS. In: Howard RT, Richards RD (eds) Sensors and systems for space applications, Proceedings of SPIE, vol 6555. SPIE—The International Society for Optical Engineering, Bellingham, WA, pp 1–2
3. <https://stackoverflow.com/questions/42354824/ssd-or-yolo-on-raspberry-pi>
4. Monteiro A, de Oliveira M, Oliveira R, Da Silva T (2018) Embedded application of convolutional neural networks on Raspberry Pi for SHM. Electron Lett 54. <https://doi.org/10.1049/el.2018.0877>
5. <https://www.pyimagesearch.com/2016/09/26/a-simple-neural-network-with-python-and-keras/>
6. Iandola FN, Han S, Moskewicz MW, Ashraf K, Dally WJ, Keutzer K (2016) SqueezeNet: Alexnet-level accuracy with 50x fewer parameters and <0.5 MB model size

Quality Assurance Practices for Student Satellite Teams



Yash Sanghvi, Anmol Sikka and Aniruddha Ravindra Ranade

Abstract Pratham, IIT Bombay's first student satellite was launched on September 26, 2016 onboard PSLV C-35. The intended mission life was of 4 months. The satellite was operational but the mission was not successful as only beacon signal was received and not the downlink signal. During the post-launch analysis, the team realized the importance of maintaining the quality. The IIT Bombay Student Satellite Team then started working on instituting quality assurance and management practices within the team. In the process, we listed and made few guidelines that can be useful for initiating and managing quality assurance in Student Satellite Projects across the world. This paper talks about our initial analysis and then lists down various activities to be performed to assure quality.

Keywords Quality assurance · Student satellite · ICSS2019

1 Introduction

Of the ~10 student satellites launched by ISRO so far, not even a single mission was 100% successful. Pratham also achieved only 90% success. Hence, achieving the reliability and the robustness of the satellite becomes a greater challenge before venturing into challenging payloads. The team realized the importance of establishing quality assurance (QA) practices to ensure reliability and robustness.

The team started with surveying quality practices followed at ISRO [1] and listed down the constraints faced by a student satellite team. Based on this preliminary analysis, it was realized that the model with QA as a separate subsystem does not seem appealing. Everything and anything in the satellite were divided into two sections:

Y. Sanghvi · A. Sikka · A. R. Ranade (✉)

Student Satellite Lab, Aerospace Department, IIT Bombay, Powai, Mumbai 400076, Maharashtra, India

e-mail: aniruddha.ranade@iitb.ac.in

A. Sikka

e-mail: anmolsikka@iitb.ac.in

URL: <https://sites.google.com/view/sikka-anmol/>; <https://www.aero.iitb.ac.in/satlab/>

© Springer Nature Singapore Pte Ltd. 2020

PSR. S. Sastry et al. (eds.), *Advances in Small Satellite Technologies*,

Lecture Notes in Mechanical Engineering,

https://doi.org/10.1007/978-981-15-1724-2_42

part (hardware) and code (software). Activities and practices to be performed for both the sections were listed. In the later section of the paper, the breakdown of activities to be performed by different personnel of the team is covered. Finally, a brief overview of subsystem-specific QA is given.

2 Quality Management in ISRO

On initial thought and surveying quality management in ISRO, the following points were noted:

1. Approx. 1/6th of the total strength of ISRO is engaged full time in assuring quality.
2. The personnel involved are from various backgrounds such as design engineering, systems engineering, environmental engineering, and analytical and statistical engineering.
3. Quality is ensured through various practices like reviews, standardizations, non-conformance control, tests, reliability analysis, configuration management, and control.

3 Constraints Faced by Student Satellite Teams

In student satellite teams, a similar model as followed by ISRO is not possible due to the following constraints:

1. An undergraduate typically joins the team in first or second year and on average lasts for **3 years** in the team.
2. A person typically takes **around a year** to familiarise with one subsystem of the satellite.
3. A new team member would typically ask interesting and fundamental questions, but these questions might not be structured and directed, and many will be doubts rather than quality control questions. A QA team would need a combination of **both experienced members and amateurs**.

Keeping these constraints in mind, the idea of quality assurance (QA) as a **separate subsystem was scrapped**.

Following factors were also listed:

- **Shift in Accountability**

A designer would become relaxed, knowing that the QA person would point out all flaws. Having a separate subsystem would result in the accountability shifting from the designer to the QA person.

● **Imbibing the Mindset**

QA should be an integral part of the thought process of the team members. Only when a person questions someone else does she/he realizes what to keep in mind while designing.

● **Lack of Expertise**

By the time, a person can fairly understand a subsystem; she/he has already spent two years and is nearing graduation. These people need to serve as subsystem heads and train new members. Devoting them full time for quality does not seem promising.

Thus, the model with QA as a separate subsystem does not seem appealing for implementation in student satellite teams. Quality management and assurance need to be an integral part of the whole team’s working. Each person should be involved in QA-related activities at various levels. The breakdown of activities to be performed by different personnel of the team will be covered later in the paper.

4 Definitions

Anything in a satellite is divided into two sections: part and code.

Anything that can be held and bought/manufactured/made as a separate unit is a part. For example, a screw is a part, a side panel and even the complete satellite is a part.

The smallest testable block is considered as a code. For example, a function to convert analog quantity to digital quantity can be tested without the help of any other functions. Hence, this function will be considered a code.

The activities to be performed to maintain the quality was divided according to the definitions are given above, i.e., part and code. It can be broadly classified as done in Table 1.

Table 1 Division of activities

Part (hardware)	Code (software)
<ul style="list-style-type: none"> • List down the objectives/requirements • The design on paper/in software • Buy/procure or manufacture/make/process • Handle and store • Document 	<ul style="list-style-type: none"> • List down the objectives/requirements • Design/write pseudo-code or algorithm • Write actual code • Store • Document

5 Activities for Parts

Based on Table 1, we further expanded activities under each task.

5.1 List Down Objectives/Requirements

This task ensures that the purpose served by the part is known. The part under consideration is characterized and given requirement specifications.

A list of QA activities was made to ensure that the task is achieved successfully.

- A **functional decomposition** of the whole subsystem will be prepared which will help to identify the role of the part in the overall scheme of the things.
- An **exhaustive list of requirements** will be made within each subsystem.
- The requirement of **redundancy** will be checked for each part.

5.2 Design

At the start of the design phase, the team should note down the standards and conventions which should be followed. Also, while the requirements captured in the above step were in a top-down fashion, the design should commence in a bottom-up fashion.

5.2.1 Design on Paper

Generally, at the start of brainstorming, a rough design is made on paper. This design basically serves as a way to find out, if the requirements listed earlier are satisfied. Also, in the process, additional constraints that may be posed by the design are identified. No optimization is required at this stage.

A list of QA activities was made to ensure that the task is achieved successfully.

- A **checklist of requirements** satisfied to be ticked for each design.
- **Additional constraints** imposed should be listed and added to the requirements of the corresponding part.
- The relevant parameters for the selected as well as rejected designs should be noted.
- The failure scenarios for the design should be noted down.
- A rough prototype (breadboard circuit) can be made based on this design to establish proof of concept. Results of the tests on the prototype should be noted.

5.2.2 Design in Software

On software like SolidWorks or EagleCAD, a detailed design is made, primarily for parts to be manufactured/made. How sub-parts are interconnected is mentioned in detail in this design.

A list of QA activities was made to ensure that the task is achieved successfully.

- A **checklist of requirements** satisfied to be ticked for each design.
- Again, **additional constraints** imposed should be listed and added to the requirements of corresponding parts.
- Each iteration of the design is to be stored with **version control** using proper nomenclature.
- Proper simulations are to be performed to validate the design. All the results are to be noted and **verified analytically**.
- A list of tests is to be devised to ensure no glitches in the design.
- Failure scenarios are to be identified and taken care of.

5.3 Buy/Procure or Manufacture/Fabricate

First decision to be taken here is whether to buy/procure or manufacture/fabricate the part in-house. Following factors were identified to be analyzed to reach a decision:

1. Criticality of the part for mission success
2. Resource availability
3. Past experience
4. Expertise within the team
5. Complexity
6. Time and finances
7. Availability of documentation of the part

Note: The above factors are not in any order of priority.

5.3.1 Buying/Procuring

- A **list of vendors** is to be maintained for each class of components based on past experience and ISRO's inputs. A **quality certificate** should be obtained from a new vendor being added to the list.
- A **Preferred Part List (PPL)** is to be made from the range of components provided by these vendors.
- A team consisting of relevant members and systems engineers is to be constituted in case no components conform to the requirements (**non-conformance control**).
- After procuring any component, a functional test is to be performed to establish its performance and only then shall it be integrated into the assembly of components.

5.3.2 Manufacturing

- A **list of preferred manufactures** is to be maintained for each class of components based on past experience and ISRO's inputs.
- Also, a **Preferred Materials List (PML)** is to be made for parts to be machined.
- Each manufacturing process is to be characterized with critical parameters noted.
- The final software design is to be **checked OK** before sending it for manufacturing.
- A list of tests is to be devised which will be performed on each manufactured/fabricated component. All failures to be reported to further refine the tests.

5.4 Handling and Storage

- The clean room class is to be maintained along with the list of clean room guidelines to be followed.
- **Proper ESD precautions** have to be taken when handling sensitive components.
- A **proper inventory of components** is to be made and it should be regularly updated.
- Any component-specific handling and storage requirements are to be noted at the design/procurement stage itself and arrangements is to be made for the same.

6 Activities for Code

Many activities listed under part have a direct correspondence with code. All such activities will not be listed again. Only the activities specific to code will be listed down below.

6.1 List Down Objectives/Requirements

This task as in parts ensures that the purpose served by the code is known. Therefore, the list of QA activities performed will be the same as that in parts.

6.2 Design

The design will again follow a bottom-up approach; the smallest function being designed first.

- At this stage, software written for a given purpose is to be broken down into constituent functions and variables. This can be achieved through a state diagram where all events/tasks, the possible input parameters, and the interconnections are shown.
- **Rules of thumb and proper nomenclature** practices for functions and variables need to be established.
- All variables and their expected range of values are to be validated by asking ‘What if?’ questions. For example, What if the value of this variable becomes negative?
- All errors made in the process of writing the code are to be documented to further refine the QA process.

6.3 *Write Actual Code*

- The code is to be written block by block, or function by function with proper commenting standards established and followed throughout.
- The code is to be tested on emulators before testing on the actual hardware. **Emulators** should be standardized, like the Preferred Parts List (PPL) in the case of hardware.
- **Test cases** are to be devised for each block and only after clearing the tests should one proceed to write the next block.
- Needless to say, all the test results are to be documented along with the mistakes that should improve the QA process.

6.4 *Storage of Code*

- **Proper version control** and file nomenclature practices are to be followed.
- The final codes that have cleared the QA should be stored in a master repository.
- Only the relevant subsystem head and the project manager should have the authorization for editing this repository.

7 **Documentation (For Part and Code)**

Documentation is not a task to be done in the end; rather it should follow in parallel with the other tasks. At various points in the paper, many documentation tasks have been mentioned, such tasks are not listed again.

- **Standard templates** are to be made for documenting each of the above steps.

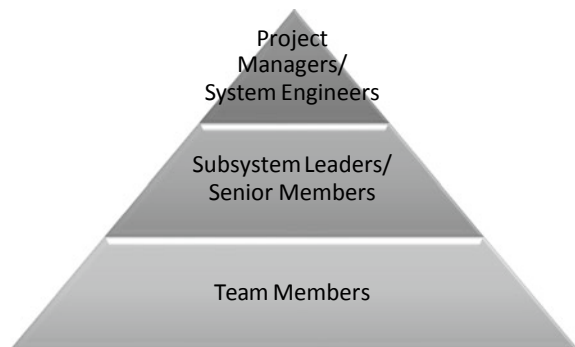
- All the meetings and discussions with engineers and scientists from the launch/space agency (the key takeaways) are to be documented.
- The relevant discussions during the testing are to be documented as well.
- **An inventory of documents** is to be maintained for easily finding the right document from the numerous files.
- All the bills, gate-passes, etc., are to be maintained for future reference.
- The objectives, design, algorithm, subtle aspects of the actual code, and storage methodology should all be documented.

8 Breakdown of Activities Performed by Different Personnel

The thought process of QA should be imbibed in the entire team. The roles of various members in the team are divided in a hierarchy as shown in Fig. 1.

- The project manager will be maintaining the various inventories and overseeing the activities being performed across subsystems. The proper transfer of the QA mindset to each next generation is also ensured by the project manager.
- The subsystem leaders will be overseeing the subsystem-specific activities. Allocation of work to team members regarding quality check, writing test cases, and codes will also be done by subsystem leaders.
- Team members need to cooperate with each other for the whole QA system to run smoothly.

Fig. 1 Team hierarchy



9 Subsystem-Specific Quality Assurance Activities

The team has made quality assurance and management practices to be followed specific to each particular subsystem such as mechanical, controls and electrical and communication subsystem.

- A method to maintain version control on models made on SolidWorks has been devised using Google Sheets. An example of the legend is given in Fig. 2.

Alphabetic Code (AAA)	Numerical Code (NNN)	Component	Comments
ADS	001	Antenna Deployment System	
ADS	002	Antenna	
ADS	003	Guide Rail	
ADS	004	ADS Base	
ADS	005	ADS-Solar Panel Platform 1	
ADS	006	ADS-Solar Panel Platform 2	
BAT	001	Battery Pack	
BAT	002	Battery Box	
CGE	001	Top face	Satellite Structural Cage
CGE	002	Bottom face	
CGE	003	Vertical Supports for Cage	
CGE	004	Full cage	
CGE	005	Vertical Support with 0 MagTorq	
CGE	006	Vertical Support with 1 MagTorq	
CGE	007	Vertical Support with 2 MagTorq	
PCB	001	Stacking PCB Board	
GPS	001	GPS Patch Antenna	
GPS	002	GPS Module	
GPS	003	GPS Box	
MAG	001	Magnetorquers 1U	
MAG	002	Magnetorquers 2U	
MAG	003	Magnetorquers 1U (Top Face)	
MAG	004	Magnetorquers Side Frame	
ROD	001	Vertical PCB rod	
SOS	001	Top Stand-Off Screw	
SOS	002	Middle Stand-Off Screw	
SOS	003	Bottom Stand-Off Screw	
SOL	001	Solar Side Panel	
SOL	002	Solar Top Panel	
SOL	003	Solar Bottom Panel	

Fig. 2 Legend for naming SolidWorks CAD files

- GitHub version control, writing test cases and test codes for every set of simulations in attitude determination and control subsystem are done along with proper documentation. The template for the QA report of code files is given in Fig. 3.
- Electrical and communications subsystem thoroughly check each PCB before and after fabrication and record of the same is maintained through detailed documentation. The template for the documentation is given in Fig. 4.

Quality Assurance Report Code.py

QA requested by: ABC

Date: 20/5/2018

Reviewer: XYZ

- Permanent links:**
- 1.
 - 2.
 - 3.
 - 4.

QA suggestions:

1. Add formula for func1 in comments
2. '+' sign is missing in func2 line2
3. V_ not added for vector variable pos_i
4. Add definition of equinox in README file

Implementation:

1. All changes are implemented

- Post-QA permanent links:**
- 1.
 - 2.
 - 3.
 - 4.

QA requested by: PQR

Date: 6/8/2018

Reviewer: KLM

- Permanent links:**
- 1.
 - 2.
 - 3.
 - 4.

QA suggestions:

1. Test cases for func5 not sufficient
2. Normalize the unit vector in func5
3. Add reference to sun-model report in code

Implementation:

1. No need for normalization according to reference XYZ book.
2. All other changes are implemented

- Post-QA permanent links:**
- 1.
 - 2.
 - 3.
 - 4.

Fig. 3 Template for QA report of any code file

QA Check for PCBs

This document enlist procedures to be completed before ordering fabrication of PCB

Pre-Fab PCB Review	1
Details of PCB	2
List of Electrical Interfaces	2
List of Mechanical Interfaces	2
Checklist for QA Check & Review Questions	3
Comments	4
Approval	4
Soldering Instructions	5
Post-Fab PCB Review	6
Approval	6
Appendix	8

Pre-Fab PCB Review

PCB Name	
Schematic Designer(s)	
Board Designer(s)	
Reviewed by	
Date of Review	

Details of PCB

PCB Name	
Function(s) of PCB	

Fig. 4 Template for PCB fabrication documentation report

Reference

1. Madhavan Nair G, Chairman ISRO (2004) Quality management—ISRO's experience

Challenges in Design of Very High-Speed Data Acquisition System for High-Altitude Application



M. S. P. Srikar, H. R. Naveen Kumar, S. Amruth Kumar, N. Veena, Vasanth, S. S. Rana, Vinod Chippalkatti, R. K. Niranjan and N. Sarada

Abstract This paper chronicles the design of a very high-speed data acquisition system (DAS) which is qualified with a novel architecture for high-altitude applications. The state-of-the-art system is realized with DDR SDRAM modules as the storage media and the controller are designed with AX2000 FPGAs from Microsemi. The design of this high-altitude system matches the reliability requirements using system-level methodologies. The main features of the data acquisition system are the capability to acquire and retrieve up to 12,000 pulses with variable real-time programmable pre-pulse and post-pulse data. The system has modular design approach. Some of the main design challenges are highlighted here.

M. S. P. Srikar · H. R. N. Kumar · S. A. Kumar (✉) · N. Veena · Vasanth · S. S. Rana · V. Chippalkatti

M/s Centum Electronics Ltd., Bengaluru, India
e-mail: amruths@centumelectronics.com

M. S. P. Srikar
e-mail: srikarm@centumelectronics.com

H. R. N. Kumar
e-mail: naveenkumarhr@centumelectronics.com

N. Veena
e-mail: veenan@centumelectronics.com

Vasanth
e-mail: vasanth@centumelectronics.com

S. S. Rana
e-mail: ssrana@centumelectronics.com

V. Chippalkatti
e-mail: vinod@centumelectronics.com

R. K. Niranjan · N. Sarada
Defense Electronics Research Laboratory, Hyderabad, India
e-mail: niranjan.rk@dlrl.drdo.in

N. Sarada
e-mail: sarada.n@dlrl.drdo.in

Keywords AX2000 FPGA · Data acquisition system · Pulse width · Pulse repetition interval · DDR SDRAM

1 Introduction

Data acquisition system acquires and stores digitized samples in memories such as SRAM and DRAM. High-bandwidth requirements of data acquisition systems demand for large-capacity storage device. Due to high density of memory cells per unit area, the DRAMs are preferable for these applications. Further, to manage high-speed data rate, the usage of dual data rate (DDR) SDRAM is preferred. However, DRAM, being capacitor-based devices, has to be periodically refreshed to prevent the loss of stored data. With an increase in the input data rate in field-programmable gate array (FPGA)-based DAS, the speed of operation of FPGA increases. In case of single-event upset (SEU) occurrence in high-altitude-based data acquisition systems, the data integrity is compromised. Therefore, the high-altitude-oriented DAS is also expected to have some sort of recovery and resistance mechanisms to SEU [1]. This paper broadly illustrates the various challenges faced while designing and developing a high-speed SEU tolerant data acquisition system for high altitude for the purpose of surveillance.

The specifications of the data acquisition system are mentioned in Table 1.

2 Background

DDR SDRAM-based data acquisition systems consist of a DDR controller which performs the write and read operations to the memory by generating the appropriate control signals such as RAS, CAS, WE, and chip select (CS) along with address. The DDR controller periodically generates a refresh command in order to recharge the contents of the DRAM. Apart from DDR controller-generated control signals, the data flow to the memory is handled.

Data acquisition system consists of following major parts:

Table 1 Specifications of data acquisition system

Input data rate	8 Gbps
DDR SDRAM clock frequency	84.3 MHz (dual edge sampling)
Maximum output data rate to DDR SDRAM	144 bits @ 84.3 MHz * 2 ~24.3 Gbps
FIFO write clock frequency	83.3 MHz/3
FIFO read clock frequency	84.3 MHz

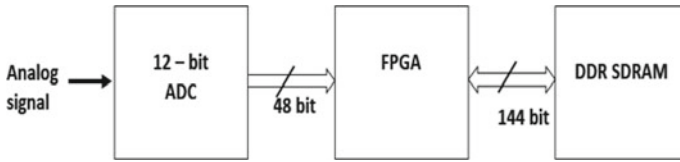


Fig. 1 Block diagram of DAS

1. Analog to digital converter (ADC)
2. DDR controller FPGA
3. DDR SDRAMs.

This is shown in Fig. 1.

The major challenges faced while developing the system are as follows:

1. Handling of high throughput data at FPGA input.
2. Three Nos. of 96 bits width and 64 bits depth FIFOs controller design.
3. Development of DDR controller to meet the input throughput and system functionality requirements at the same time.
4. Maintaining the integrity of the data.

3 Methodology

The DDR controller finite-state machine (FSM) program is coded using very high-speed integrated circuit hardware description language (VHDL) in Libero IDE software targeting AX2000 FPGA of Microsemi. The flow followed while developing and testing the DDR controller is shown in Fig. 2. The design was written in VHDL and simulated at pre-synthesis, post-synthesis, and post-layout stages before programming the FPGA. Efficient clock trees were created for some high fan-out signals to achieve timing closure.

4 Realization

4.1 Handling of High Input Throughput at FPGA Input

The input analog data to DAS is sampled and quantized using a 12-bit ADC using a 333.33 MHz clock at both edges, effectively making the sample rate as 666.5 MHz. In order to reduce the speed of operation in the FPGA, 1:4 Demux option available in ADC is utilized to step down the frequency of operation by 4 times. As a result, 48-bit (4 ADC samples) data lines are connected to the FPGA in a source-synchronous fashion. This data is transferred to FPGA with a clock rate of 83.33 (333.333/4)

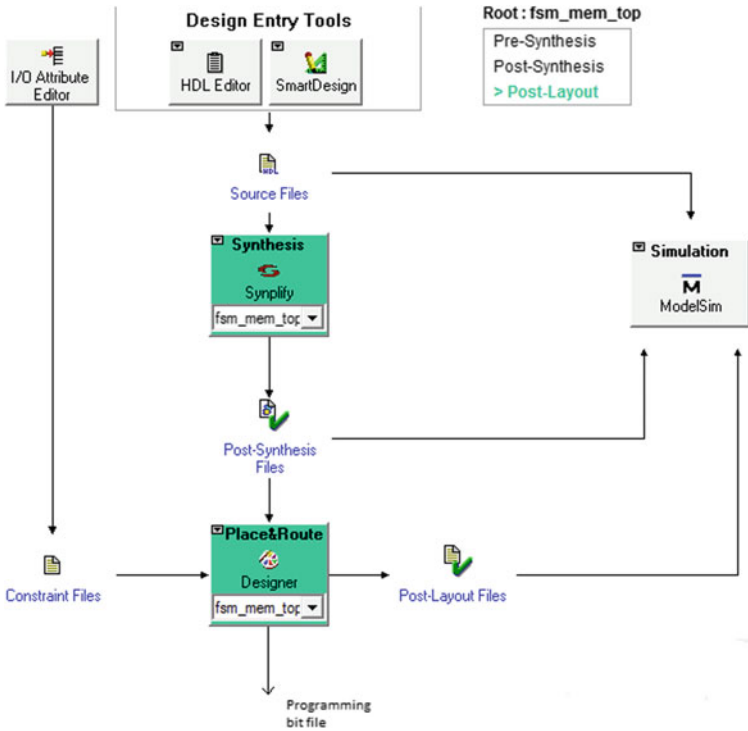


Fig. 2 Design flow

in dual edge sampling (DES) mode. Data is registered using a DDR register macro available inside the FPGA. The 48 bit obtained at each falling and rising edges is concatenated into a single 96-bit bus inside the FPGA.

4.2 FIFO and DDR Configurations

The DDR write data rate and FPGA input data rate have to be matched to ensure that there is no data loss. Additionally, the DDR memory has to be periodically refreshed. Keeping in mind the refresh requirements of memory, the DDR write operation is made periodic in burst manner with a burst count of 8. Since the write to DDR memory is not continuous, the FPGA input data is stored in 3 FIFOs of 96 bit width and 64 addresses depth, each having one-third clock frequency of the data clock rate at FPGA input with a duty cycle of 33.3% and 60° phase difference as shown in Fig. 3. This is done to step down the frequency of operation of FIFOs.

Upon writing the 32 address spaces in 3rd FIFO, a DDR write operation is initiated as data for 64 words (8 accesses of 8 bursts) are accumulated. When 32 addresses are written to 3rd FIFO,

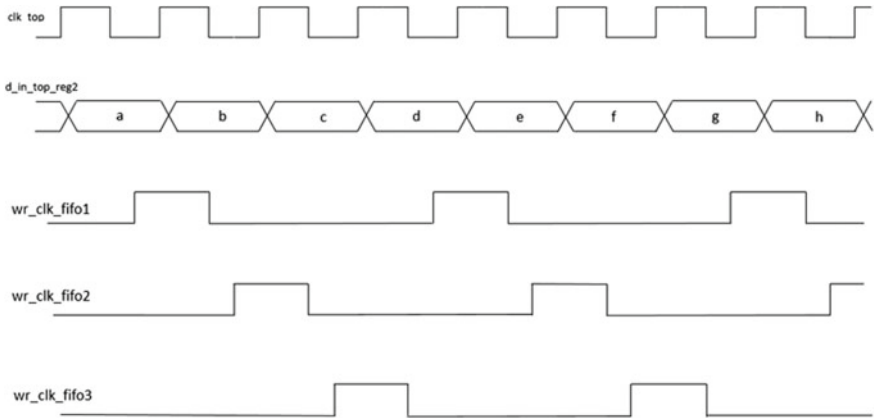


Fig. 3 FIFO clock generation

Total number of addresses to be read from all 3 FIFOs = $32 * 3 = 96$.

As the data is written to FIFOs at a rate of 83.3 MHz clock, the total time for writing 32 address spaces into each FIFO = (number of address spaces) written * (time period of 83.3 MHz)

$$= 96 * 12.004 \text{ nsec}$$

$$= 1152.46 \text{ nsec.}$$

To reduce the overhead time, the DDR memory is operated in 8 continuous bursts manner with a burst length of 8, i.e., 64 addresses are written in one write access to DDR memory. Also, the DDR memory auto-precharge provision is availed for closing the row. The DDR controller operates at 84.375 MHz. The T_{rcd} and T_{rp} values for the DDR SDRAM used are 15 ns each [2]. Therefore, the timing requirements for the write operation are mentioned below.

$$\text{Total time for write operation to DDR} = 1 \text{ clock} + T_{rcd} + (5 \text{ clocks}) * 8 + T_{rp}$$

$$= 11.85 + 15 + (5 * 8 * 11.85) + 15 \text{ nsec}$$

$$= 515.85 \text{ nsec}$$

where T_{rcd} —activate to write/read minimum time requirement of DDR memory and T_{rp} —precharge command period.

As the writing time of data to DDR memory is lesser than the time required for accumulation of $32 * 3$ addresses in 3 FIFOs, FIFO with a depth of double the times of 32, i.e., 64, is sufficient to prevent overflow of data.

4.3 Resistance to SEU

A logic has been incorporated to skip the erroneous pulses if an SEU occurs while transferring the data from FPGA to DDR memory or vice versa.

4.4 Architecture of DDR Controller

4.4.1 DDR Memory Partition

The DAS has the capacity to acquire 12,000 pulses of data. To achieve this goal, the DDR SDRAM is divided into three partitions: Partition #1 (P1), Partition #2 (P2), and Partition #3 (P3) as shown in Fig. 4.

P1 consists of 12,000 circular buffers of 2048 address spaces each. It stores the pre-pulse data while acquiring 12,000 pulses. P2 stores the pulse and post-pulse data during the pulse acquisitions. The pre-pulse and post-pulse addresses are dynamically computed in real time during the acquisition. P3 stores the addresses and the pulse parameters such as TOA and PW. for each and every pulse acquired which is required during the data read out from the DDR SDRAM. The DDR memory partition is shown in Fig. 4.

4.5 DDR Controller FSM

To write and read data from DDR SDRAM, six states have been defined as shown in Fig. 5. The FSM is operated at 84.3 MHz to meet the requirements of the input data rate. One hot encoding technique is used to reduce the switching rate while FSM changes states. The various states of FSM are mentioned below.

Idle: When the power-on reset (POR) is asserted on the system, the FSM is reset to this state. When no more requests are left to be serviced by FSM, it switches to this state.

Write: In this state, the 64 address spaces of DDR memory are written with data continuously.

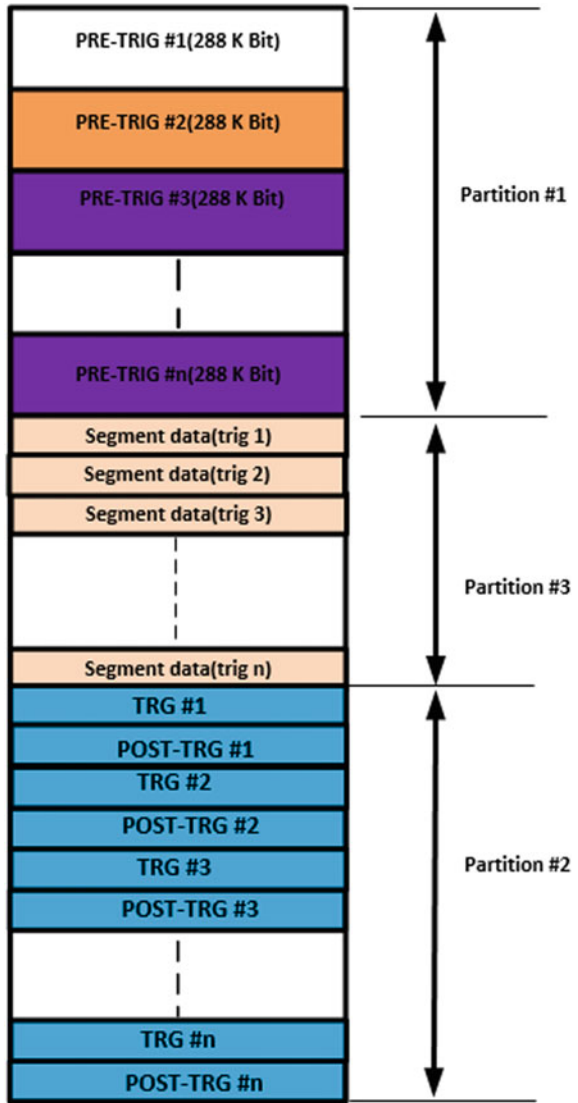
Segment write: In this state, the pulse parameters such as time of arrival (TOA), pulse width (PW), and the addresses corresponding to the pulses are written into the memory with a burst length of 8.

Segment read: In this state, the pulse parameters written during segment write are read out with a burst length of 8.

Read: In this state, the sampled pulse data is written into memory during write state is read out with a burst length of 8.

Config: In this state, the FSM loads the configurable registers of DDR with appropriate values given in Table 2. This state is also used to periodically refresh the contents

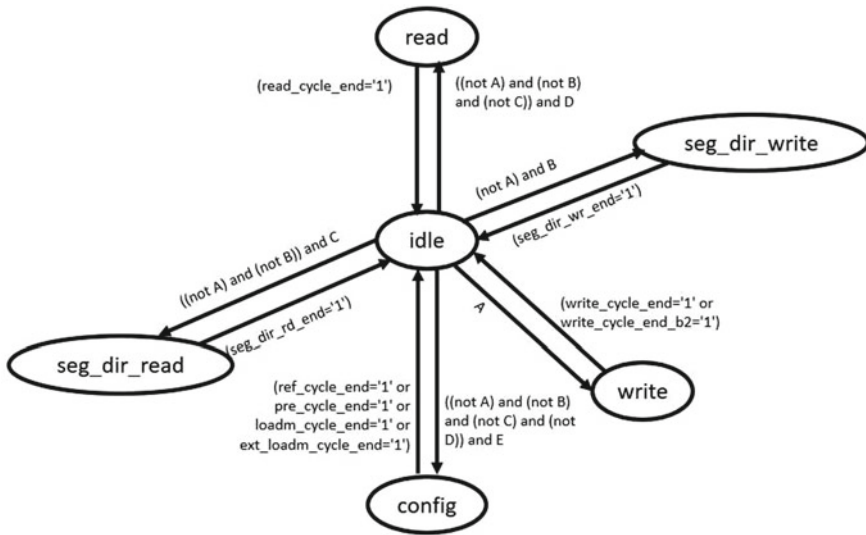
Fig. 4 DDR memory partition



of the memory.

4.6 Data Flow

To meet the high input data rate specification on AX2000 FPGA, the 96-bit input data was pipelined and stored in three FIFOs. Each FIFO has a write clock of one-third



- A - wr_sync='1'
- B - (seg_dir_wr_sync='1' and (read_mask_sync_100='1' or start='0'))
- C - (seg_dir_rd_sync='1' and (read_mask_sync_100='1' or start='0'))
- D - (rd_sync='1' and (read_mask_sync_100='1' or start='0'))
- E - ((rf_sync='1' and ((idle_cycle_mask_final_100='0' and start='0') or read_mask_sync_100='1')) or pre_sync='1' or loadm_sync='1' or ext_loadm_sync='1')

Fig. 5 FSM state diagram

Table 2 DDR memory configurations

Field	Configuration
CAS latency	2.5
Burst length	8
Burst type	Sequential
Operating mode	Normal

clock rate of the input data’s clock frequency. The read clock of the FIFO is a gated clock which is enabled when the DDR controller is in write state. The three 96-bit data output from FIFOs are reorganized into two 144-bit signals that are pipelined and alternatively written into the DDR SDRAM during burst access. The data flow architecture is shown in Fig. 6.

5 Analysis and Testing

In order to check the data integrity at high frequency, simulations were performed at various stages of design. A test bench was written to feed data as input to FPGA. The post-layout simulation was performed, and the flow of data was found to be proper

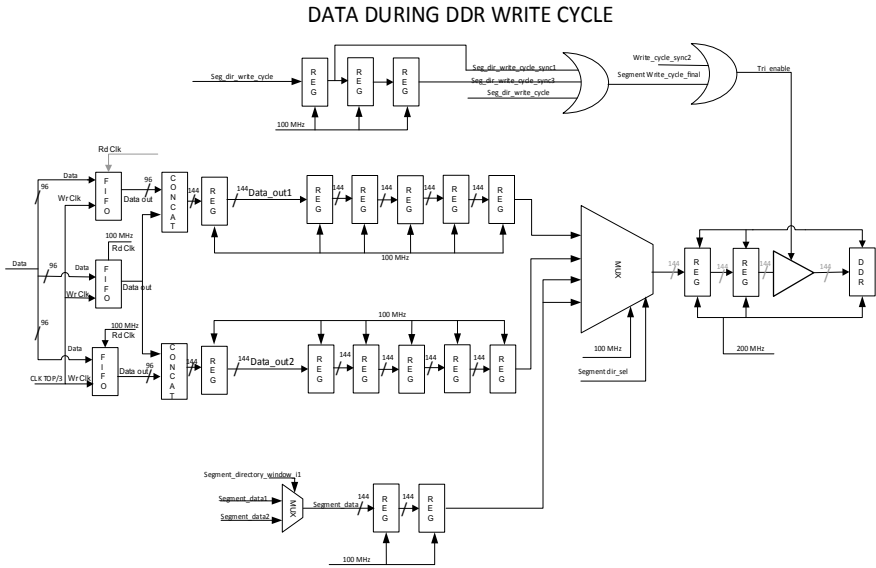


Fig. 6 Data flow in FPGA

and error free. The generation of DDR control signals by DDR controller during write cycle is shown in Fig. 7.

The clock constraints were defined in the timing analyzer, floor planning of certain registers was done, and clock trees were created for high fan-out signals to achieve timing closure [4]. The multi-cycle paths and false paths in the design were segregated accordingly in the timing analyzer.

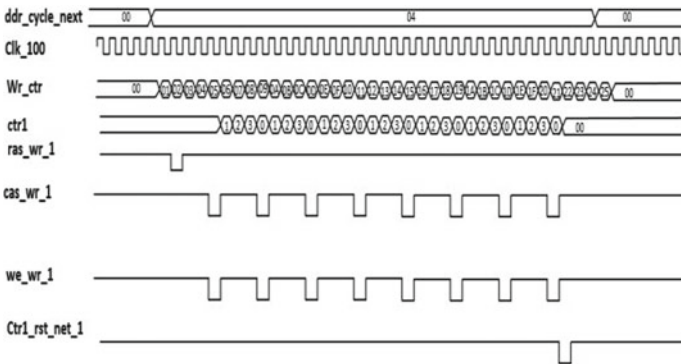


Fig. 7 DDR write interface signal generation

6 Conclusion

During the design and development of high-altitude DAS, SEU effects should be taken into consideration. The interfaces with high-speed ADCs should be handled with care for data reliability. A mechanism has been evolved to match the input data rate from ADC to output data rate to DDR memory.

Acknowledgements The design and implementation of the contents of this paper was carried out by the M/s Centum Electronics, Bengaluru, along with DLRL, Hyderabad.

References

1. Scheick LZ, Swift GM, Guertin SM (2001) SEU evaluation of SRAM memories for space applications. IEEE Trans Nucl Sci 47
2. Micron DDR SDRAM MT46V64M16 datasheet
3. Axcelerator Family FPGAs datasheet
4. Timing Analysis of RTAX-S/SL/DSP Design Using Libero IDE v9.2, Microsemi

Space Applications

Design of Indian Navigation Satellite System-Based Traffic Management for Entire City



Shwetank and Shailendra C. Badwaik

Abstract Indian Space Research Organization (ISRO)'s satellite technology has emerged on the global scale with its own IRNSS (Indian Regional Navigation Satellite System)—NavIC (Navigation with Indian Constellation) in outer space, and this paper aims to exploit one of its applications in traffic management for the complete city with inter-connected squares. This paper projects a novel design towards using NavIC to determine position of the vehicles, and as per their directional motion, number of vehicles moving towards particular road of any designated traffic square is determined. Suitable state machine and flow diagram are designed considering the real-time data. “Hand-over” mechanism is proposed to reduce the design complexity in terms of software implementation. Accordingly, the counter is made adaptive and dynamic. The finite-state machine (FSM) consists of 50 states, and very high-speed integrated circuit hardware description language (VHDL) coding and simulation are done using Libero SoC v11.9, Xilinx ISE 14.7 and ModelSim Microsemi 10.5c.

Keywords NavIC · VHDL · FSM

1 Introduction

Today, with increasing population day-by-day and with growing human needs, a number of vehicles are increasing with alarming pace. Specially, when it comes to a highly populated and developing nation like India, situation becomes more chaotic. Understanding the complexity of traffic situations, there is a need of intelligent, well organized and smart technology-based implementation on a large scale and

Shwetank (✉)

Solar Panel Division, Power Systems Group, U.R. Rao Satellite Center,
Bangalore, Karnataka 560017, India
e-mail: shwetank@urisc.gov.in

S. C. Badwaik (✉)

Department of Electronics and Telecommunication Engineering,
Sinhgad College of Engineering, University of Pune, Maharashtra 411041, India
e-mail: scbadwaik.scoe@sinhgad.edu

Table 1 Data about traffic signals and vehicle number rise [2, 3]

Content	Data
Number of traffic light signals—Bangalore	353
% vehicle rise in Bangalore in the last 40 years	6099
Number of registered vehicles in Bangalore (approx.)	80 lacs

perhaps in an inter-connected way where technologies itself can communicate. Over the years, different ways of traffic handling techniques have been proposed with associated different technological methods. These include sensor based [1], image processing based, etc., which are based on measuring either traffic intensity or traffic density. Some of these methods have already been implemented in developed nations where the condition is not quite alarming or crowded. However, in many developing nations, the need for highly advanced traffic management system is solicited. To project the need of applicable and real-time satellite-based design, we cite case of Indian capital—Delhi or other metropolitan cities of India which finds the spotlight in newspaper every now-and-then due to problems caused by heavy traffic conditions especially during peak office hours or on special festive occasions. A study finds that Delhi itself has 830 traffic signals [2] under operation (as per Delhi traffic police data, 2018), etc. (data is indicated in Table 1), of which many roads are one way and to add to it, a very high percentage of them are programmed for fixed counters irrespective of the traffic condition of the four sides of a square.

1.1 Introduction to NavIC

NavIC is Indian Regional Satellite Positioning and Navigation System (SPS) which provides real-time positioning and timing services covering India and the region extending up to 1500 km surrounding India. It is having a total constellation size of 7 IRNSS satellites with orbital height of 36,000 km capable of providing accuracy of 5–10m. The NavIC operates at the signal frequency in L5 (1176.45 MHz) and S bands (2492.028 MHz). Today, the mobile services in India are using GPS facility for the navigation purpose which operates only in L frequency band. With Indian navigation system being operational and having proven to be more accurate, some of the companies have started to manufacture NavIC receiver (Rx) chips taking into account the operating signal frequency range dedicated for NavIC. This motivates the idea of traffic control/management with real-time positioning information available with the inclusion of such receiver chips in mobile. At the same time, the idea of implementation of traffic control system promotes the inclusion of NavIC Rx in the vehicles too understanding possible additional advantages discussed later in the paper.

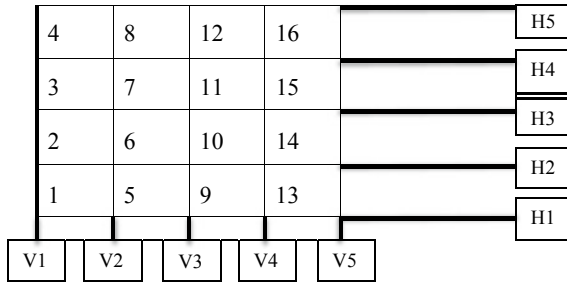


Fig. 1 Division of sectors on the basis of coordinates (where V: longitude and H: latitude)

2 System Design

This novel design aims at exploiting the modular approach by dividing complete city into certain number of sectors/regions on the basis of latitude and longitude, and each sector is then further divided on the basis of number of traffic signals operating in the corresponding sector. It inculcates following five main ideas with each having its own role to play in the complete design.

- Design operates in two domains—vehicle domain and traffic signal domain
- It highlights the importance of a master control station (MCS) for each sector
- Inherent “Hand-over” mechanism
- The duality of satellite communication system and mobile communication
- Necessity of inclusion of NavIC receivers in the vehicles/mobiles
- Need for inter-communication among technologies.

To realize the practical applicability, the design emphasizes on the available data and some calculations which can show the fruitfulness in real-time scenario. It takes the case of Bangalore city of India which is also known as the software, electronics hub and the Silicon Valley of India which forecasts the workforce arena the city holds and stringent need of technologically advanced traffic control system.

Table 1 shows 353 traffic signals operating in Bangalore city. Design divides the city into 16 sectors which on an average computes approx. 20–22 traffic signals that are operating in each sector. These sectors are identified with the latitude and longitude range in which they lie (Figs. 1 and 2).

Using the latitudes and longitudes values of each division, the sectors ($C_i, 1 \leq i \leq 16$) are defined, and it is shown in Table 2. The actual values have been multiplied by 10^6 to get perfect integers. Also, at the traffic signal domain, the comparisons are made using the location coordinates which have been similarly multiplied by 10^6 . This makes comparison easier as so many such values are received at the MCS and traffic signal when transmitted by huge number of vehicles (discussed later in the paper). The intension is to make the coding/programming simulation easier (Fig. 3).

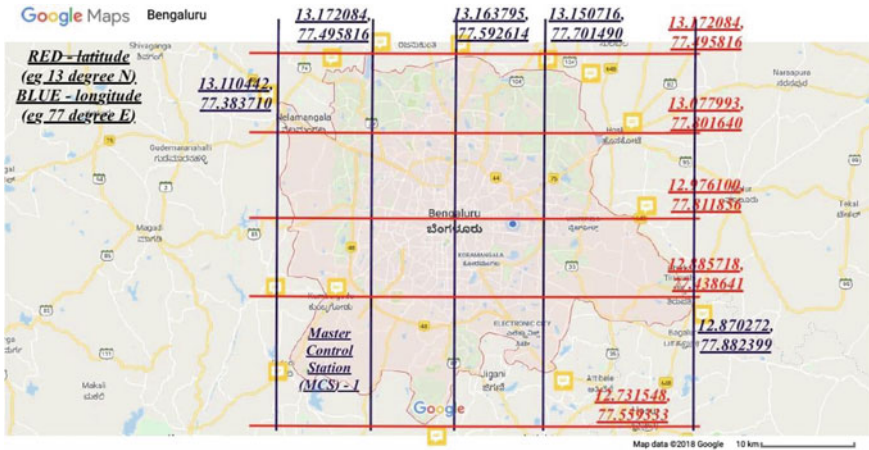


Fig. 2 Map of Bangalore with its latitude and longitude mentioned on the selected points

Table 2 The values used in the FSM corresponding to H and V

Sector (C_i)	Belongs to ($(H_j, H_k), (V_j, V_k)$)
C_1	$((12731548, 12885718), (77383710, 77495816))$
C_2	$((12885718, 12976100), (77383710, 77495816))$
C_3	$((12976100, 13077993), (77383710, 77495816))$

(continued)

where $1 \leq \{j, k\} \leq 5$ and C_i belongs to $((H_j, H_k), (V_j, V_k))$ means $H_j < \text{latitude} < H_k$ and $V_j < \text{longitude} < V_k$.

These are the conditions to be checked to make transition to different sectors. This is shown in Fig. 5 using Finite State Machine (FSM).

2.1 Explanation of Ideas of Design, Their Implementations and Future Prospects

2.1.1 Vehicle Domain

All the vehicles/mobiles in the city need to be equipped with the NavIC R_x chips (even if installed in mobiles, today mobiles have become integral part of human. So, they tend to carry mobiles while using vehicle) which enable them to have their continuous real-time location available in terms of V and H with the help of IRNSS satellites operational in the Indian GEO orbits (discussed in Sect. 1.1). Also, the chips should be able to perform computation to tackle the data comparison and for coordinates transfer to the concerned MCS and traffic signal. For each vehicle, initial screening

Table 2 (continued)

Sector (C_i)	Belongs to $((H_j, H_k), (V_j, V_k))$
C_4	$((13077993, 13172084), (77383710, 77495816))$
C_5	$((12731548, 12885718), (77495816, 77592614))$
C_6	$((12885718, 12976100), (77495816, 77592614))$
C_7	$((12976100, 13077993), (77495816, 77592614))$
C_8	$((13077993, 13172084), (77495816, 77592614))$
C_9	$((12731548, 12885718), (77592614, 77701490))$
C_{10}	$((12885718, 12976100), (77592614, 77701490))$
C_{11}	$((12976100, 13077993), (77592614, 77701490))$
C_{12}	$((13077993, 13172084), (77592614, 77701490))$
C_{13}	$((12731548, 12885718), (77701490, 77882399))$
C_{14}	$((12885718, 12976100), (77701490, 77882399))$
C_{15}	$((12976100, 13077993), (77701490, 77882399))$
C_{16}	$((13077993, 13172084), (77701490, 77882399))$

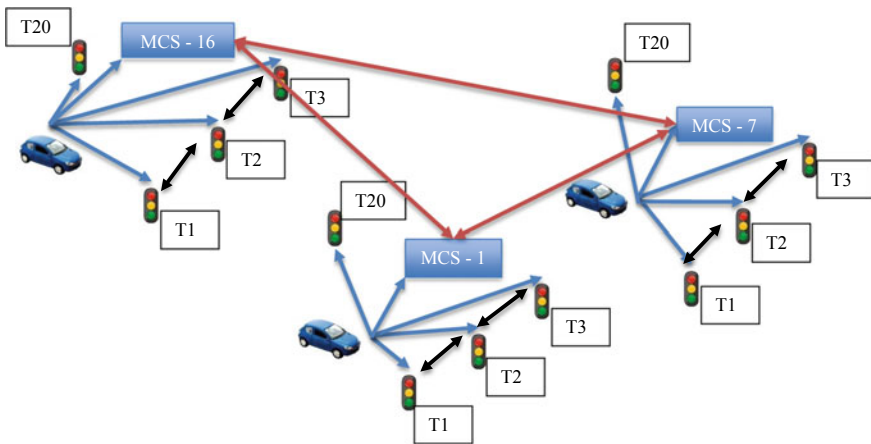


Fig. 3 Complete model of the proposed design with vehicle, traffic signal and master control station

is done by comparing its real-time coordinates with the available set of coordinates $((H_j, H_k), (V_j, V_k))$ given in Table 1. This decides the sector in which vehicle lies which is followed by deciding the traffic signal towards which vehicle is approaching or has already reached that signal. This decision is also made at the vehicle domain; for this, we define a pre-determined range “ r_s ” using coordinate_latitude_range and coordinate_longitude_range: where $1 \leq s \leq 4$ for all four sides of the traffic signal (Fig. 4).

Once the traffic signal is decided, vehicle sends data to traffic signal indicating its presence in ‘ r_s ’. After this, the design switches to traffic signal domain. This is

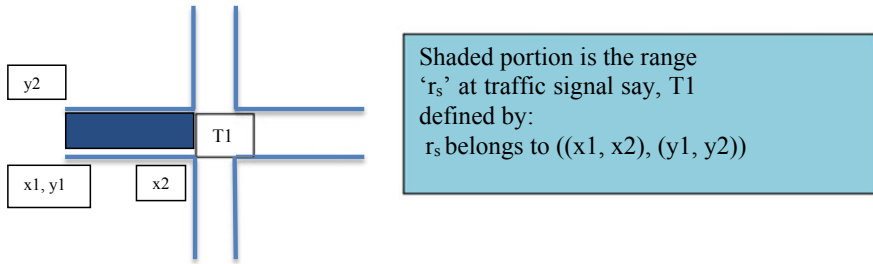


Fig. 4 At the traffic signal—to decide the range in which the vehicle count is to be calculated

shown in Fig. 5 indicating the transition from Sector ‘m’ to traffic signal symbolized by T1–T20. The figure also shows the transition to different sectors in the city once respective conditions (C_i) are met.

The design has inherent feature of “Hand-over” [4] mechanism where the vehicle switches from one sector to the other during the movement. Subsequently, it deals with the coordinates of the respective sector.

2.1.2 Traffic Signal Domain

The statistics in Table 1 shows that Bangalore registers approx. 80 lacs vehicles which indicates on an average (a crude number for analysis purpose) 5 lacs vehicles/sector and out of which even if we assume 1 lac of them running on the road this indicates the quantum of vehicles that need to be tackled by the signals. With proposed design, these vehicles are continuously transmitting their status to some or the other signal. So, in order to have a vehicle count at both the MCS and signal, the vehicle/mobile has to send a unique identification code. Traffic signals are to be equipped with dedicated electronics for the data reception and further computation. This is done by four variables: vehicle_count_east, vehicle_count_west, vehicle_count_north and vehicle_count_south followed by comparison among them. The side with highest number of vehicles is given green signal. The design also manages intermediate Green signals for those sides which do not face heavy traffic conditions which we term as “Intermediate Slots” for say 10–15 s. The design implements “Adaptive and Dynamic” features [1] depending on the number of vehicle count on each sides of the signal to which the decision is made at the end of each counter cycle for the next counter duration (We have taken 60, 40 and 10 s to demonstrate the implementation of the design denoted by counter60, counter40, counter10 in Fig. 6). This is shown in the simulation results by “count_out” in Fig. 8. It aims to abolish the fixed counter approach prevailing on the existing traffic signals today.

At the signal, first set of condition checks corresponds to active sides; i.e., the sides on which the vehicles are present, in the pre-defined range ‘ r_s ’ which is calculated as ${}^4C_1 + {}^4C_2 + {}^4C_3 + {}^4C_4 = 15$ discussed in Table 3, and then further, the conditions are checked on the basis of vehicle count to decide the signal counter.

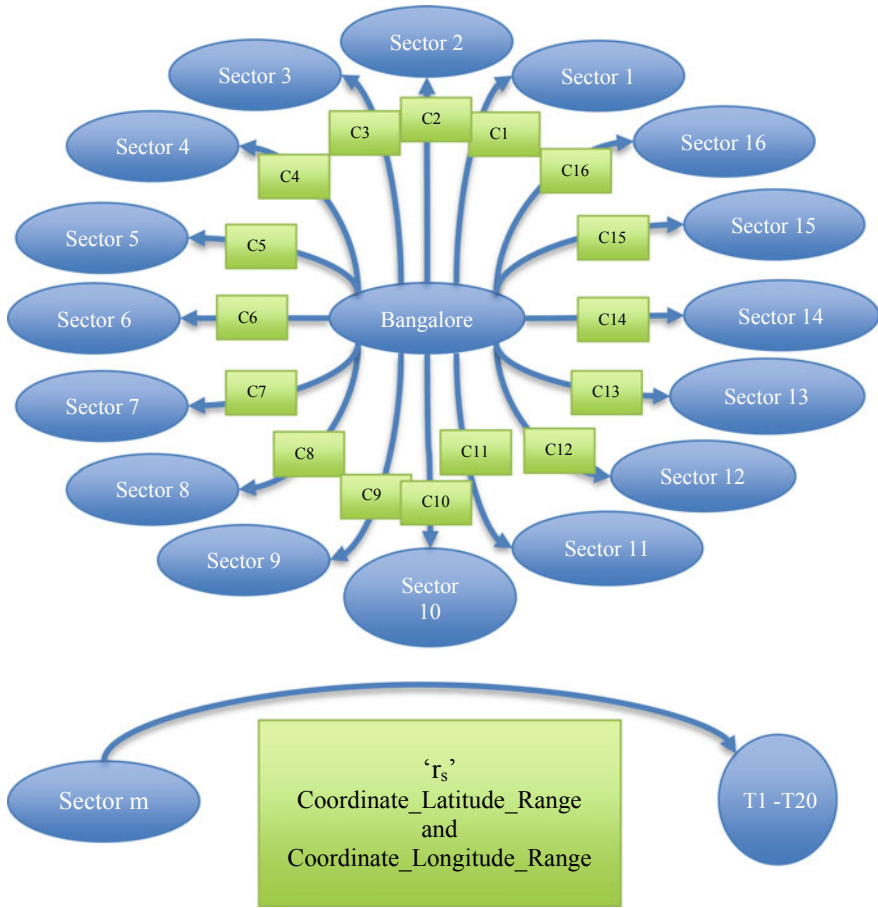


Fig. 5 Finite state machine at the vehicle domain ($S_m, 1 \leq m \leq 20$)

Table 3 Hardware descriptive language (HDL) synthesis report

Possible combinations	Number of active sides
4C_1	One (e.g. s_east = '1' or s_west = '1' or s_north = '1' or s_south = '1')
4C_2	Two (e.g. (s_east = '1' and s_west = '1') or (s_east = '1' and s_north = '1') etc.)
4C_3	Three (e.g. (s_east = '1' and s_west = '1' and s_north = '1') etc.)
4C_4	Four (i.e. (s_east = '1' and s_west = '1' and s_north = '1' and s_south = '1'))

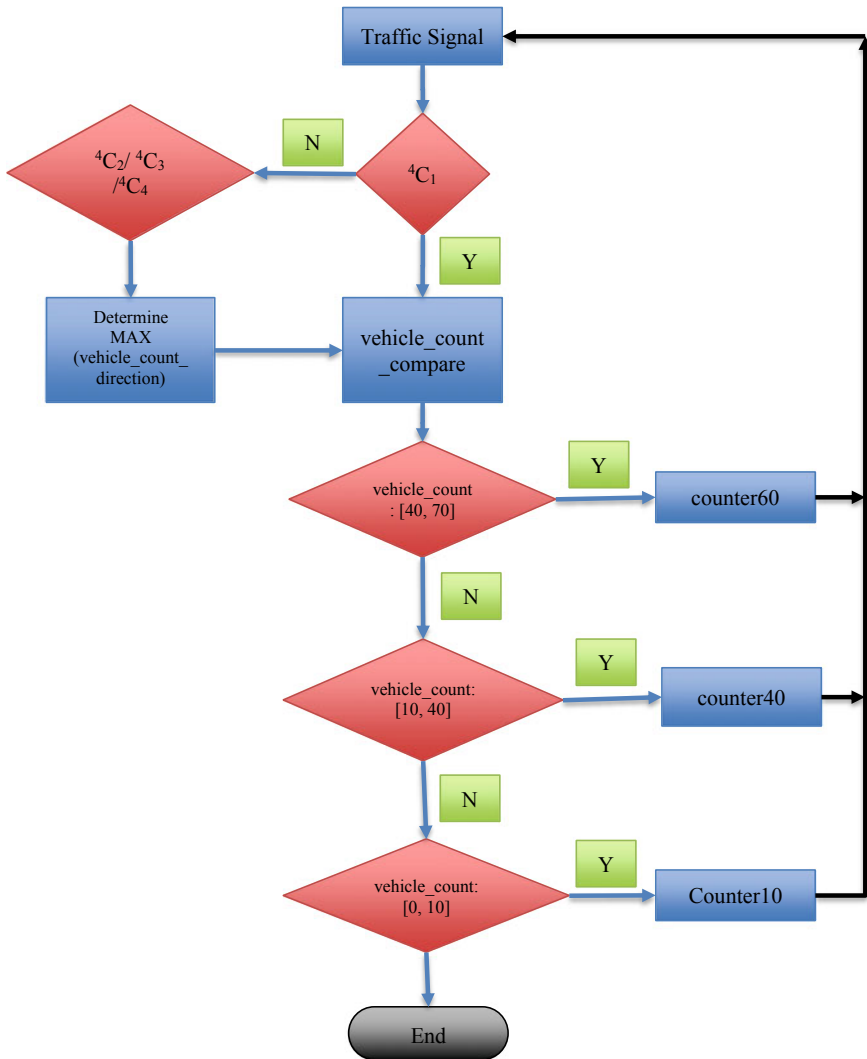


Fig. 6 Highly simplified flow chart to describe state transitions at traffic signal domain

2.1.3 Master Control Station

MCS holds the key to real-time monitoring of any vehicle with the continuous data/location coordinates availability as location coordinates of vehicle are to be continuously sent to the MCS. This MCS is actually the traffic police control which are already available in the city for security/safety provisions. To further enhance monitoring prospects specially during some festival occasions and some chief guest visits when safety protocols get violated, security is at high risk; crime possibilities

see a rise; the idea of technologies communicating among each other may turn out to be quite fruitful. The design proposes:

- Traffic signal communicating with the adjacent next signals: this ensures vehicle count information being communicated to enhance the intelligence of the near-by signals.
- Inter-MCS communication: The data can be shared to allow the possible follow-ups in time of need.

3 Results and Discussion

The VHDL coding is done on Xilinx ISE 14.7 and Libero SoC v11.9. The RTL schematic is generated using Xilinx ISE 14.7, and simulation is carried out on ModelSim Microsemi 10.5c. Below is the synthesis report representing the number of Adders/Subtractors/Multiplexers/Registers and Comparators used in the design implementation using VHDL (Table 4).

The VHDL code is programmed on Actel ProASIC3 FPGA kit which is operated at 40 MHz clock frequency. The FSM design consists of 50 states, and the outputs are seen in form of the traffic signal counters, the green, red and yellow lights for the dynamically updated durations depending upon the traffic conditions at a given square (Fig. 7).

The simulation results are shown using timing diagram which represents providing green signal on the east side towards which vehicle count is found to be maximum. Result shown in Fig. 8 is the condition when vehicle coordinates are $C = ((12731548, 12885718), (77383710, 77495816))$ which moves the FSM to sector1, i.e., C_1 . In this sector, choosing suitable simulation conditions and providing vehicle_count = 50 (in the timing diagram, the values are represented in hexa-decimal, i.e., 32) as an example to conduct. Count_out is the traffic signal counter which is counting from 00 to 04 as a part of 60 s count duration for given vehicle count of 50. As soon as 60 s counter starts, r1 goes “0” and g1 goes “1” (1: east direction). Count_sec is

Table 4 Hardware descriptive language (HDL) synthesis report

HDL synthesis report	HDL synthesis report
<i>#Adders/subtractors 3</i>	<i>#Comparators 22</i>
26-bit adder 1 32-bit adder 1 6-bit adder 1	32-bit comparator greater 2 2
<i>#Registers 15</i>	<i>#Multiplexers 79</i>
1-bit register 5 26-bit register 1 32-bit register 6 6-bit register 3	1-bit 2-to-1 multiplexer 10 26-bit 2-to-1 multiplexer 1 32-bit 2-to-1 multiplexer 14 6-bit 2-to-1 multiplexer 54
	<i>#FSMs 5</i>

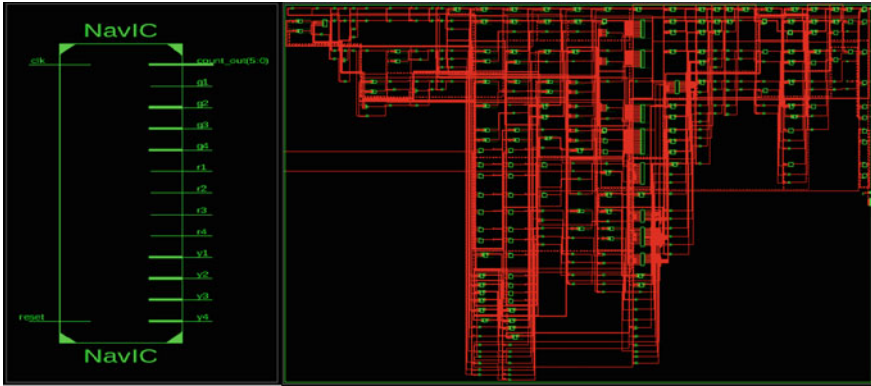
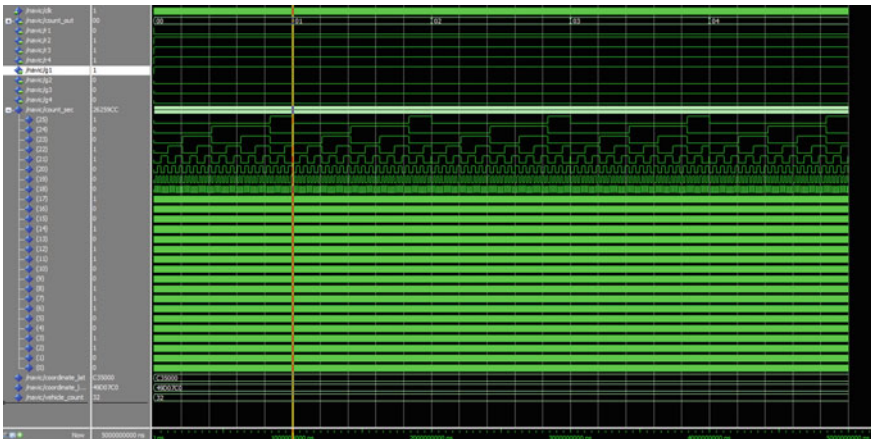


Fig. 7 RTL schematic of the complete design for simulation



can be inculcated in a dedicated fashion. At the same time, it requires very faithful communication/Internet connectivity for this highly technologically advanced proposal which is not only a particular traffic signal centric, rather it aims for the complete city with possibilities of data-sharing feature among the signals as well as among the master control centres.

Acknowledgements We sincerely thank Deputy Director, Communication and Power Area and Group Director, Power Systems Group, for their support and approval of the paper.

References

1. Singh S, Badwaik SC (2011) Design and implementation of FPGA-based adaptive dynamic traffic light controller. In: ETNCC'11, Udaipur
2. Delhi Traffic Police Website. <https://delhitrafficpolice.nic.in/be-road-smart/signals/>
3. Economic Times Report (2017) <https://economictimes.indiatimes.com/news/politics-and-nation/number-of-vehicles-in-bengaluru-rises-by-a-mind-boggling-6099-in-40-years/articleshow/57807459.cms>
4. Handover mechanism. <https://en.wikipedia.org/wiki/Handover>

Techno-Commercial Aspects of Space-Based Startups Ecosystem in India



Hemant M. Jain and Yashesh P. Rana

Abstract Internationally, space industry is going under transformational evolution which in turn is giving rise to new business model and opportunities to entrepreneurs, innovators and startups. Space sector in India is ready to take a next leap as its pioneer Indian Space Research Organization (ISRO) has come a long way by securing the podium place on launching 104 satellites into the intended orbit successfully. This exponential growth has propelled and fuelled the dream of many startups and innovators who are eager to contribute and explore the endless boundaries of space. This paper envisages that the opportunities startups can grab in space segment by learning to explore technological innovation and become commercially revenue garnering entity. Startup India initiative by the Indian Government and establishment of six space technology-based incubators by ISRO will build a strong ecosystem for nurturing the innovation and startups.

Keywords Startups · Small satellite · CubeSat · Space technology · Incubators · ISRO

1 Introduction

Space programme in India, from the days of its inception, has developed technologies for peaceful purpose and civil applications. The orientation of this national mission was towards only one objective envisioned by Dr. Vikram Sarabhai, utilizing space technology to solve the real problems of man and society. Indian Space Research Organization (ISRO), the apex body of Indian space programme, has contributed immensely for national development since decades. It has come a long way to fulfil the requirement of space-based citizen services and has attained the podium place

H. M. Jain (✉) · Y. P. Rana
Space Applications Centre, ISRO, Ahmedabad, India
e-mail: hemant.jain@sac.isro.gov.in

Y. P. Rana
e-mail: yprana@sac.isro.gov.in

© Springer Nature Singapore Pte Ltd. 2020
PSR. S. Sastry et al. (eds.), *Advances in Small Satellite Technologies*,
Lecture Notes in Mechanical Engineering,
https://doi.org/10.1007/978-981-15-1724-2_45

by setting up the world record of launching 104 satellites into the intended orbit successfully. ISRO has always been supported by private industries as well as small and medium enterprises (SMEs) by developing and providing components for spacecraft and launch vehicle subsystems. ISRO has been trying to build and nurture the capabilities of private industries since many years. To strengthen it further, private sector consortium is identified not only for integrating satellites but also for providing value engineering to small satellite launch vehicle (SSLV) to meet the surge in demand for the launch. Indian space industry is undergoing a veritable revolution, and there is a remarkable opportunity for innovators and space technology-based startups to capitalize this reform.

2 Global Space Industry and Startups

2.1 Preamble—Space Age

From the early days of space exploration, it has been found to be an efficient tool for driving the basics of science and technology. The complexity to demonstrate the space technology was so challenging that it has given rise to new approaches. Space sector was always regulated and governed by government and state-owned organization. “Space Race”, i.e. the cold war between two rival nations, the USA and Soviet Union gave birth to new dynamics of science to the world. Their technological rivalry brought out a contest of developing communication and earth observation satellites, exploring celestial bodies as well as other planets for the survival of mankind. The high cost of launch drove designer to make smart material with high performance and durability. Critical knowledge gained by sending experimental satellites in the initial years was utilized to evolve technologies for making more robust and reliable payloads. Over the time, criticality of complex space mission urged premium space agencies to collaborate and utilize expertise of each other to amplify the accomplishment of the mission. National Aeronautics and Space Administration (NASA), Russian Federal Space Agency (Roscosmos) along with European Space Agency (ESA), Japan Aerospace Exploration Agency (JAXA) and Canadian Space Agency collaborated for joint development, operation and utilization of a permanently inhabited space station in low earth orbit. This cooperative programme gave birth to International Space Station (ISA).

2.2 Space Evolution

The economic exploitation of satellite to provide surveillance network for defence, civil communication and earth observation of natural resources was controlled tightly by the government regulations. Building satellite, launching it and maintaining

ground infrastructure were complex and costly affair. So, access to space was preserved to only those nations who were having privilege of being technically advance and economically sound. The balance of space power began to shift with advent of innovation and widespread availability of miniaturized electronic components as well as smart and reliable technical materials. This enabled physically smaller satellites to be built by smaller teams with modest facilities.

Conventional large satellites are designed and built with rigorous well-defined processes which assure quality and system reliability. Revolution in production techniques for consumer market encouraged the utilization of commercial-off-the-shelf (COTS) devices and components for space segment [1]. Adaptation of innovative COTS technologies was not limited to hardware components. It was also exploited for complex software to ensure proper functionality of the system. COTS technologies came as a rescuer for the projects which were imposed with limitation of budget, volume and mass. The era of the 1980s was largely dedicated to the utilization of small satellites for training and education purpose. The pace of development and complexity accelerated in the late 1990s. Small satellite later on attracted its attention from military and surveillance department across the globe because of its offered potential advantages. The new objective was framed for space domain. Developing new small launch vehicle as well satellites having standardized plug-and-play bus architecture which can shorten development time of missions.

Constellations of satellites in low earth orbit (LEO) offered persistent widespread or global coverage. Early 1990s saw many commercial proposals to set up constellation of small satellites to take advantage of digital communication and provide low-rate data and mobile voice communication. Satellite constellations targeting real-time voice and data communication was established by Globalstar and Iridium [2]. Both of them initially failed due to mismatch between the market demand and cost of technology development, large number of satellites and infrastructure requirement. This event caused the loss of confidence of angel investors for financial funding in any such proposals for almost more than a decade. RapidEye was the first fully commercial operational class earth observation system using constellation of five microsatellites. Its commercial operation also faced difficulties like Globalstar and Iridium. After its multiple acquisitions, it became a profitable operation once the capital cost was written off.

2.2.1 CubeSats

A significant impetus for producing affordable, smaller satellites came in 1999 when two professors, Jordi Puig-Suari of California Polytechnic State University and Bob Twiggs of Stanford University, challenged their graduate students to design and build miniature spacecraft [3]. That resulted in the creation of a whole new CubeSat, or nanosatellite industry. CubeSat is a particular form of nanosatellite that is made up of multiples of $10 \times 10 \times 10 \text{ cm}^3$ units with a mass of about 1.33 kg. They can be 1U, 2U 3U or 6U in size. CubeSats are small, modular and inexpensive to build and launch. They are opening up space exploration and opportunities for research and

technology development for everyone. Until 2013, majority of CubeSat launched were from academia. Post 2014, most deployment of CubeSats was for commercial missions. The revolution of CubeSats has inspired¹ Interorbital Systems to develop TubeSat which is a personal satellite kit served at educational platform. For academia, the smallest unit of kit is available at as low as \$8000 which includes launching cost to LEO. Recently, CubeSats achieved its major milestone by performing major role in NASA's ambitious interplanetary Mars InSight mission. Mars Cube One (MarCO) twin CubeSats were used demonstrated the technology to perform communication and navigation experiment [4].

2.3 *NewSpace and Global Startups*

NewSpace: it is a phrase today that is commonly used to describe the emergence of space segment having steady and pragmatic approach with a sense to explore and exploit the innovative COTS technologies. The modest resources need to design and build the small satellites which had attracted entrepreneurs and innovative small startups companies. They have shown their capabilities to provide end-to-end solution services across all platforms and confident enough to raise substantial investments for their ventures. There are myriad of new business proposals and startups in space segment. This democratization of space sector has encouraged around 400 emerging space companies across the world, and they are supported by strong investor appetite. Startups are empowering themselves to scale their offerings of products and services and integrate itself into \$300 billion supply chain of space industry.² Globally, small satellite market is expected to grow at a compound annual growth rate (CAGR) of 18.8% and estimated to be valued around \$7.66 billion [5]. Figure 1 from SpaceWorks report shows the launch history and market forecast for nano/microsatellite. SpaceWorks estimates the launch of around 2600 nano/microsatellite in the next five years.

Global Space Technology Startups: communication satellite business for decades now is dominated by geostationary satellites, and attempt to provide ubiquitous broadband data and voice services across globe using LEO in the past has faced big financial debacle. But, now technology advancement and the need of low latency communications have encouraged new preposition of satellite constellations in multiple plane. Startup companies like SpaceX backed Space Exploration Technologies Corporation, OneWeb and aviation giant Boeing are planning to develop, deploy and operate the constellation of large number of satellites in LEO to provide high bandwidth broadband services across the globe.

Advent of small satellite coupled with cloud computing, advanced data processing, etc., have brought transformation in earth observation. Planet Lab (now Planet) was

¹<http://www.interorbital.com/Tubesat.%20Kits>—IOS TubeSats Kits.

²SpaceWorks Report “Nano/Microsatellite Market Forecast, 8th Edition.

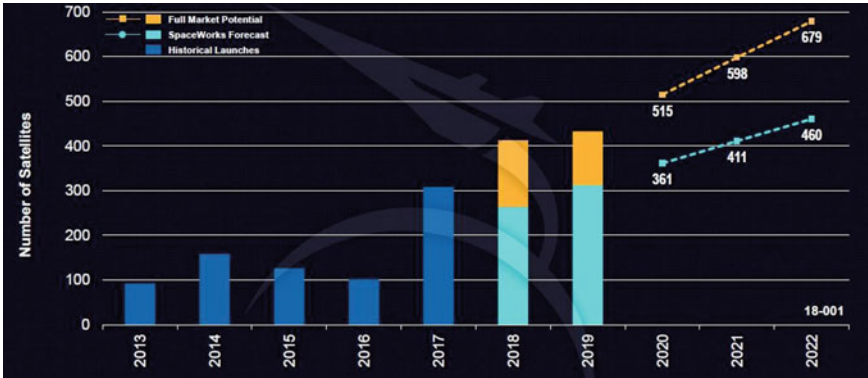


Fig. 1 Nano/microsatellite launch history and market forecast

founded as a startup by former NASA employees.³ It operates the world’s largest fleet of satellites in the orbit, 190 satellites, which includes “Doves”, flock of CubeSats and few RapidEye and SkySats—microsatellites constellation [6]. It has capitalized traditional EO business by using satellite imagery for commercial purposes. Spire Global, startup initially funded for developing satellite via crowdfunding, is a geospatial analytics firm focusing on providing information related to weather, to monitor global trade, shipping, illegal fishing and maritime awareness. SpacePharma, startup one of its kind, provides researcher access to unique environment of microgravity using cutting-edge remote-controlled laboratories. They provide platform to global players from pharmaceutical, biotechnology, material/chemical science and nutrition industries with the opportunity to accelerate breakthrough discovery processes—for new drugs and vaccines, crystals and materials, as well as accelerate the study of human genomes and the origin of diseases.

Rocket Lab, California, USA-based startup, provides launch service for small satellite from its space port established in New Zealand. It has pushed the frontier of space technology by using carbon composite material for rocket casings and 3-D printing for manufacturing electric-fed Rutherford rocket engines. It has brought the launching cost to competitive price after its recent first successfully launch.⁴ Their list price of launching 100–225 kg payload in LEO is \$5 million. Rocket Lab will be having an enormous impact on the economy of New Zealand. Virgin Orbit, a subsidiary of Virgin Group, is developing a new rocket called LauncherOne. This vehicle is an example of exemplary innovation as it is designed to take off from the sky rather than from the ground and put small satellites in LEO. Blue Origin has

³Planet EO Satellite Constellation—<https://www.planet.com/products/planet-imagery/>.

⁴Boyle, Alan. “Rocket Lab’s low-cost Electron launcher puts satellites in Orbit from New Zealand”, GeekWire, November 10, 2018, <https://www.geekwire.com/2018/rocket-lab-electron-rocket-sends-satellites-into-orbit-from-new-zealand/>.

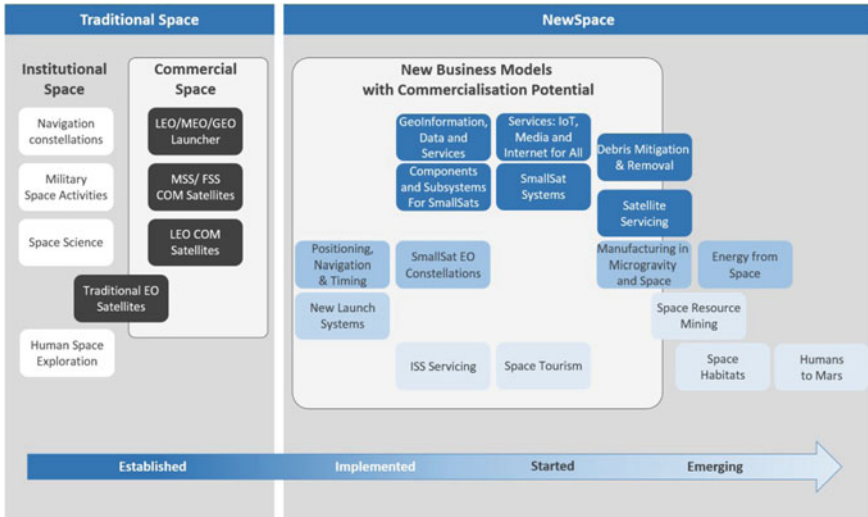


Fig. 2 Trends in space industry: global view

developed an innovative reusable rocket system, New Shepard. It is designed to take astronauts as well as research payloads past Karman line which is internationally recognized boundary of space.

Trends in Space Sector: globally, plethora of opportunities can be gauged for the space segment startups. Figure 2 depicts the trends prevailing in space industry. In traditional era, space industry was more focusing upon exploration of routine segment, i.e. communication, navigation and remote sensing, for civil application and developing space-based surveillance network for strategic application. Convergence of technologies, advancement in process and diversity in product have established a new business model to exploit the commercial potential of space segment.

Modern day information technologies such as Big Data Analytics, Cloud Computing etc. are used to simply ground station solution and beaming imagery data at affordable price. New concepts such as satellite servicing technology, i.e. unprecedented flexibility to service the satellite in space, space-based energy project and space mining are being explored by new-age stakeholders of space industry. Highly ambitious business ideas such as space tourism and colonization to Mars are under assessment and yet to prove their solidity. NewSpace unlocks many opportunities for emerging enterprise and startups to contribute and offer greater value proposition [7].

3 Indian Space Industry and Startups

3.1 Overview

India started investing in space programme in the 1960s, and it has been five decades now. ISRO started its journey by making small satellites (Rohini Series) and scientific payloads. Parallel to this activity, it also started to dedicate its efforts to become self-sufficient in launch vehicle area. Today, ISRO has achieved many major milestones in the space segment and is considered as one of the most credible players of global space industry. It has achieved the success rate on record high note because of exceptional repetitive performance of its “work horse”—Polar Satellite Launch Vehicle (PSLV). To fulfil the national requirement of space-based citizen services, ISRO has successfully developed one of the best remote sensing and communication satellites. India’s own navigation satellite constellation will be marking its operational inception soon. ISRO achieved its greatest feat and joined the elite club by successfully completing Mars Mission in the first attempt. The journey of Indian space programme so far would not have achieved so many milestones without unprecedented support of government, private industry partners and SMEs [8].

For commercial exploitation, ISRO has disseminated its know-how through licensing the technology transfer [9]. These offerings till today are economically made available at very low price if the social benefit factor is predominant. These efforts have resulted into vendor development. The emergence of turnkey solution provider in satellite and launch segment from the private industry front does not exist. The main reason behind it is space segment being capital intensive, meticulous technical understanding, and it demands some radical changes in policy framework. Looking at the enhanced national demand of the satellites for varied concern areas from defence to civil applications, ISRO has decided to transfer their workload to the consortium of private firms. This consortium will not only build and integrate the satellites but also provide the service of their engineering skills for making launch vehicle too.

3.2 Space Technology Startups: India

Space sector is a niche market, and tapping the new prospects is important for startups to be on progressive path for long-term sustainability. This decade has seen many enthusiastic startups plunging into space segment. There are handfuls of space startups from India, and one name that strikes first in mind is Bengaluru-based TeamIndus—Axiom Research Labs. Their team came in limelight as it was the only team from India to participate in Google’s Lunar X Prize competition and was one of the finalists. The startups not just received \$1 million as a terrestrial prize but also got praised across the world for their exceptional efforts. Earth2Orbit is considered as the first space startup in India which started as launch advisory service

firm in 2008 and now have oriented towards geospatial analytics targeting sectors ranging from environment and agriculture to development of smart cities. Dhruva Space is also one of the early movers came into existence in 2012. They are into designing, development and integration of small satellite. Astrome Technologies, startup incubated at Indian Institute of Science (IISc) Bengaluru, is looking to explore the satellite technology-based application market in India. Their ambitious business model is seeking to provide broadband Internet service using constellation of satellites. SatSure, a data analytics company, integrated modern-day concept Internet of things (IoT) technology with remote sensing and assisting EO in commoditization satellite-based solutions [10].

New Delhi-based Xovian, since 2011, is engaged in conducting educational and research-based activities related to space to bridge the innovation gap between academia and industry. They have a vision to provide low-cost sustainable solutions for satellite fabrication. Mysore-based Bellatrix Aerospace is one of the most audacious aerospace startup in India who have dreamt of building an orbital launch vehicle and satellite propulsion systems at low-cost. They are developing their rocket by using the next generation material such as carbon composites. One cannot end this list without including the team who built the world's lightest Femto satellite weighing just 0.64 grams and named it Kalam SAT paying tribute to Dr. A.P.J. Abdul Kalam. They developed their satellite with reinforced carbon fibre polymer which was fully 3-D printed, and it was ultimately launched by NASA. These startups are optimistic to fly their ambitious business plan with their own space mission by some way or the other. Most of them are at a nascent stage and will be requiring not just substantial investment but also precise mentoring for sustaining in cyclic economy of space [11].

4 Role of Incubators

ISRO has successfully launched nine satellites developed by educational and research institutions of India. Majorly, these satellites were experimental and educational with a purpose to demonstrate the capabilities of these institutes in space segment. ISRO has provisioned the participation of academia for building a payload successfully and launching them in orbit. The main reason behind less participation of universities in space programme is the lack of programmatic approach towards developing itself as efficient stakeholder. The absence of infrastructure, facilities and policies adds up to this issue. NASA, ESA and JAXA have encouraged the participation from universities with the initiatives like CubeSat's development. Such programmes have increased the scientific awareness and garnered the innovative solutions to many societal problems. ESA Space Solutions, which is an incubator supported by⁵ ESA, has incubated 600 startups in the last 20 years. These startups could sustain because of the availability of funding and investment for their business and enough support from the policy of their respective government.

⁵34th Space Symposium USA, April 2018.

In India, most of the startups germinate from the academia. Further, they are guided and nurtured by incubators and accelerators. Academia can play a big role for building the strong pillars in these startups by inculcating in them stout technical intellect. The next level of scaling up of these startups can be worked out with the help various premium incubators established across the academic institutions, universities and commercial forums such as Federation of Indian Chamber of Commerce and Industry (FICCI), Confederation of Indian Industry (CII), etc.⁶ ISRO has planned to set up six incubators across country to groom space startups. This initiative could help imminent startups to work upon cutting-edge technologies and provide practical solutions which complements to traditional space industry approach and process cycle. The inauguration of the first incubator under ISRO's mentorship was opened in the capital of Tripura, at Agartala [12]. The next five incubators will be set up in the next six months. The identified locations are Jalandhar in Punjab, Bhubaneswar in Odisha, Nagpur in Maharashtra, Indore in Madhya Pradesh (MP) and Tiruchirappalli in Tamil Nadu (TN). The reason for selecting these cities and states was negligible presence of space activity but strong academic institutions and industry presence. Each centre will be set up at a cost of ₹2 crores and will help the startups to develop prototypes of components required for space technology, in partnership with industry. These initiatives will help to boost the innovation focused space research and would complement the economic growth of the nation.

5 Swot Analysis

Strength: space industry in India is undergoing paradigm shift, and this phase brings in lot many opportunities for startups to capitalize. SWOT analysis is used here as a foundational assessment model to measure the competitive position of space segment in Indian economy and to identify the ways startups can carve in this market for their sustainable survival and growth. The startup ecosystem in India is under transition for a decade now, and its 37th ranking position in global startup ecosystem index shows its trajectory moving towards growth inclination. The major strength of startups in space segment is availability of intellectual human resources and vast talent pool who understands the technology domain very well. COTS technologies have not only brought the economies of scale in the manufacturing of space grade components, but also, it has reduced the time cycle of delivery in upstream as well as downstream segment. There is huge under-served market which is yet to be catered by traditional space satellite, and this acts as catalyst for the existing space tech startups. Government's StartupIndia initiative is a holistic approach by governing agencies. Support provided by them includes legal advisory, investment and funding, IPR protection, tax exemption, exigency exit plan, etc. It is a great initiative towards cluster mapping of resources and helping startups to build end-to-end space activity-based products and services (Fig. 3).

⁶5th Edition of SPACETRONICS & DEFTRONICS, Bengaluru, Sept 2018.

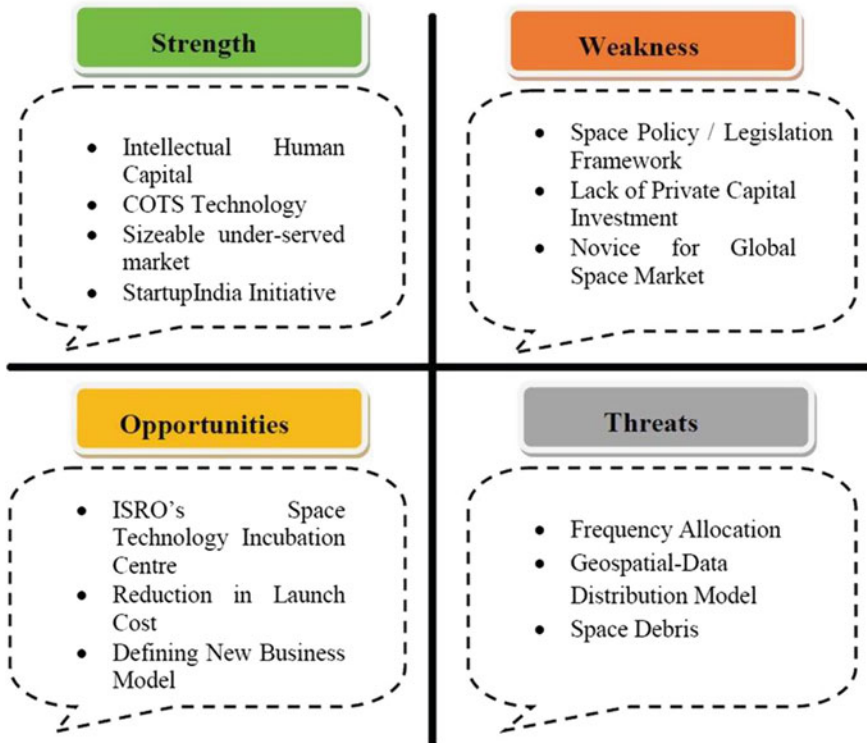


Fig. 3 SWOT analysis

Weakness: space activities in India from its inception are regulated by government policies and state agency. The present situation demands legal and legislative framework for space activities in India. In this direction, Space Activity Bill 2017 was drafted to regulate proper legal environment for service providers, public as well as private entity in space segment and encourage their participation in harnessing space technology for national development. Private venture capital and angel investors are not betting actively on space tech startups. Innovators and startups are finding it difficult to attract funds for their innovative business model to explore the outer space dynamics. There are very few space activities-based startups in India, and they are very novice to mark their presence in the global market. These weaknesses can be mitigated by contributing towards critical project such as Mars Mission and branding it to win confidence of various stakeholders of space ecosystem.

Opportunities: the opportunities for initiators in space domain are plenty. Startups can differentiate themselves from those 500-odd SMEs that serve ISRO by providing diversified business model. ISRO's initiative towards setting up Space Technology Incubation Centre in six different cities across India will help promising innovators and startups to create cutting-edge space technologies. This programme will help to expand the horizon of space segment in India. Globally, in satellite launch service,

Rank ¹	Name	Stated IOC	Payload to SSO (kg)	Target Launch Price	Major Recent Milestone
1	 Electron	2018	150	\$33K/kg	Successful orbital launch and satellite deployment
2	 Kuaizhou 1A ↑	2017	250	\$57K/kg	Successful orbital launch and satellite deployment
3	 LauncherOne	2018	300	\$40K/kg	Secured \$1B investment from Saudi Arabia Public Investment Fund
4	 Small Satellite Launch Vehicle (SSLV) ↑	2019	700	\$12K/kg	Development announced by Indian Space Research Organization
5	 Vector-R	2018	28	\$54K/kg	Successful suborbital flight demonstration
6	 Arion 2 ↑	2021	83	\$38K/kg	Secured \$2.5M grant from the European Commission

Fig. 4 Small satellite launch vehicle forecast—SpaceWorks report 2018

ride-share model is prevailing because of the congestion observed in launch window. But, there is growing demand and need of affordable and dedicated launch vehicle because of the proliferation of small satellite market. This surge is anticipating the reduced launch cost across the world. Figure 4 presents the forecast made in SpaceWorks report 2018 related to small satellite launch vehicle coming up in near future [13]. Once the SSLV is operational, it will be the most economical launch service offered for deploying a satellite in the space.

Threats: threats inflicting on space tech startups in India are same as those inherent in international space ecosystem. The International Telecommunication Union (ITU) is the global body that assigns radio frequency and allocates them in division across the globe. The spectrum allocation and frequency interference are big issues prevailing in space fraternity, and this can only be solved by international cooperation and agreements among countries. The repository of geospatial data is maintained under government-authorized agency in India. The large quantum of geospatial data and information is acquired through public funds. The licensing mechanism for distributing these data under defined policy weighs in favour of government users. For private entity, the usage is restricted, and to access it, they have to go through cumbersome process. Space debris issue is vociferously discussed because of overcrowding of satellites and increased space activities [14]. There is an international forum which takes care of it with the help of various radar based-tracking systems developed by premium space agencies of the world.

The current outlook for startups in space industry of India is affirmative. For private entity, the exploration of space corridor is at very nascent stage. Incorporation of new business model from burgeoning startups and introducing business-friendly legal and policy framework will encourage the space activity environment in the nation.

6 BCG Matrix Analysis

The Boston Consulting group’s product portfolio matrix (BCG matrix) is designed to help with long-term strategic planning. It helps business seeking growth opportunities by reviewing its portfolio of products and enables them to decide whether to invest, to discontinue or to develop new products. It is also known as the growth/share matrix. Here, the attempt is to analyse various domains where the space tech startups in India can explore to build viable and sustainable businesses solving real problems. The matrix is divided into four quadrants based on market growth and market share of the business portfolio (Fig. 5).

Quadrant 1—Star: the first quadrant relates to “Star” for those business provinces having big share of intensely growing market. It requires enduring investment to retain its market leader position. New Ventures can get into earth observation and geospatial small satellite constellation as it has huge potential to provide vital information which can be utilized for optimum management of scarce resources. Excellent location-based service can be offered if an open access to satellites images is given under carefully drafted statutory framework. Startups can fore into sub-system level

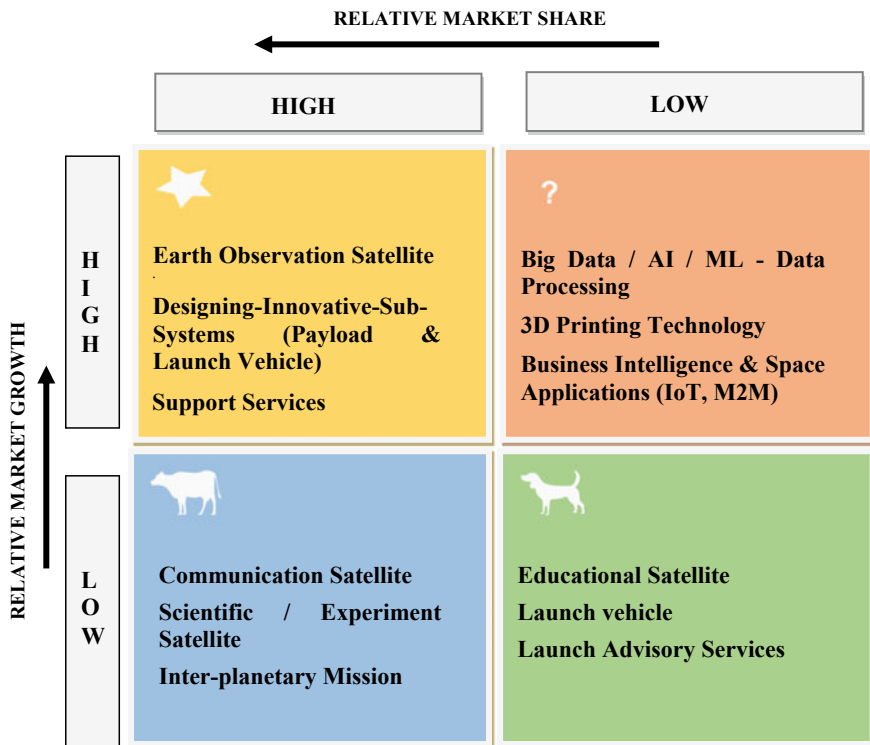


Fig. 5 BCG matrix

activities which can complement the progress of the design and development of the spacecraft and launch missions. Startups can leverage the modern-day expertise such as micro-electro-mechanical systems (MEMS) technologies, electric propulsion, laser-based communication and additive manufacturing to contribute towards diminutive cost and volume of satellite architecture. Space tech startups can contribute at various platforms to build the satellite such as structure and mechanics, thermal systems, on-board data handling (OBDH), altitude and orbital control system (AOCS), power systems and ground systems.

Quadrant 2—Question Mark: the second quadrant represents “Question Mark”. The domains in this section would require more investment and deliberation to adapt with the changing dynamics of the market. Ardent efforts towards it would make them a game-changer, but apprehensive attempt would bring a debacle. Usage of technologies like artificial intelligence (AI), machine or deep learning (MI) in geospatial imagery would bring transformation in large number of sectors. They are helpful in predictive analysis and would complement many business models. Adaption of 3-D printing in manufacturing process is in demand these days. Additive manufacturing or 3-D printing technology has made its debut in space segment already in India. It has gained momentum in manufacturing process because of its ability to deliver consistent results. Startups should guide their focus in developing innovative space application-based business model. These dynamic ideas should not only have profit-oriented deliverables but their business intelligence should also address routine unresolved issues. Their user-centric approach can be achieved by complementing space applications with modern-day novel evolutions such as Internet of Things (IoT) and machine-to-machine (M2M) data exchange. One such exemplary project has executed by Bengaluru-based firm Telematics4U (T4U) services. The model named as Auto Community Empowerment Platform (ACEP) promises revenue for advertising agencies and improved livelihood for auto drivers. NavIC messaging receiver developed by ISRO is playing a key role in this pilot project. NavIC receiver is aiding this concept by providing location-based service [15].

Quadrant 3—Cow: the third quadrant signifies “Cow” for those established business models which guarantees continuous flow of funds from the market having a stagnant growth. Their products get mature and become well-established over the time. Innovators and tech startups should focus on deployment of small satellite constellation which can provide digital connectivity and broadband services with low latency. These initiatives would boost the government’s mission of Digital India and would act as a catalyst for various critical services such as health care, education and financial services. Scientific or experimental payload design and development area is very niche, and startups, by plunging into this domain, can really bring some radical changes in the way meteorological or climatic changes are analysed and mitigated. Interplanetary missions are very challenging but assure long-term growth if successfully worked out. Startups which can attract the best of minds from the talent pool can initiate such projects.

Quadrant 4—Dog: the fourth quadrant is termed as “Dog” where the business/product/service have barren possibilities of progress. They drain the resources and have no market share to garner the revenue. Looking at the current dynamics and

trends in space segment, startups from India should avoid investing in and inclining their efforts in making educational or technology demonstrating satellite. The reason behind this proposition is Indian market's adaptability towards "Leapfrogging". The time has come to match up with the pace of global space economy, so developing satellite to assess capabilities should circumvent. In launch segment, ISRO is having its stronghold, and the amount of resources availability with them it would be difficult for any startup to bring down the economies of scale in this area. Providing launch advisory services in India could not pick up its pace as on the global level, many firms have already matured themselves into this business, and they are considered as a barrier for any new entrant.

7 Conclusion

Space sector in India is experiencing a transformational evolution. There is paradigm shift in traditional approach, and the focus is to encourage the role of private enterprise and startups in space segment to achieve new horizon. Path-breaking innovations, marginalization of cost and availability of key space-grade components have fuelled the motive of few innovators and space technology startups. The success of Moon and Mars mission of ISRO and proliferation of small satellite programme across the globe has provided opportunities to startups to emerge as game-changer in outer space-related activities of India. Space tech startups ecosystem in India is at nascent stage, but it is having apt time for tapping the opportunities prevailing in this area. Innovator and startups can provide end-to-end product and service business model which make them distinct from SMEs. Change in policy and legal framework and mentorship model proposed by ISRO in the form of incubators will gain the confidence of the investors to provide funding for space activity-based business ventures.

Acknowledgements We express our gratitude towards Shri D K Das, Director, Space Applications Centre (SAC), ISRO, Ahmedabad, and Shri N M Desai, Associate Director, SAC, for their valuable guidance and support. We would like to appreciate the efforts put in by Shri A. P. Shukla, Shri Anup Vora and Dr. Dhruvi Bharwad for reviewing the paper.

References

1. Sweeting MN (2018) Modern small satellites—changing the economics of space. Proc IEEE 106:343–361. <https://doi.org/10.1109/JPROC.2018.2806218>
2. Gao S, Sweeting MN, Nakasuka S, Worden SP (2018) Issue small satellites. Proc IEEE 106(3):339–342. <http://ieeexplore.ieee.org/stamp/stamp.jsp?tp=&arnumber=8303878&isnumber=8303007>
3. Loff S (2015) CubeSats overview. Retrieved from https://www.nasa.gov/mission_pages/cubesats/overview (July 22)
4. Harris M (2018) A revolution in a box—physics world. Retrieved from <https://physicsworld.com/a/a-revolution-in-a-box/> (July 3)

5. Prasad VS (2018) SmallSat launch market to Soar Past \$62 Billion by 2030. Retrieved from <http://interactive.satellitetoday.com/via/july-2018/smallsat-launch-market-to-soar-past-62-billion-by-2030/> (June 8)
6. Thornhill J (2018) How CubeSat satellites are changing the world (and your privacy). *Financ Rev* (22 Feb 2018). <https://www.afr.com/technology/how-cubesat-satellites-are-changing-the-world-and-your-privacy-20180220-h0wcol>
7. How new business models will disrupt old space industry. Noosphere The Top Six Current Launch Systems for Accessing Space Comments, noosphereventures.com/how-new-business-models-will-disrupt-old-space-industry/
8. Prasad N (2015) India's small satellite mission—time for the next leap forward
9. Prasad N, Rajagopalan RP (2017) Space India 2.0: commerce, policy, security and governance perspectives. Observer Research Foundation
10. Nair D (2018) Indian startup ecosystem ranked at number 37, much below China, Singapore, and South Korea. *YourStory.com*, Yourstory, 31 Mar 2018. <https://yourstory.com/2018/03/indian-startup-ecosystem-ranked-at-number-37/>
11. Prasad N (2018). Don't Panic! The Hitchhiker's guide to creating a space startup in India. Retrieved from <https://thewire.in/space/dont-panic-the-hitchhikers-guide-to-creating-a-space-startup-in-india> (Feb 28)
12. (n.d.). Retrieved from <https://www.isro.gov.in/update/18-sep-2018/inauguration-of-space-technology-incubation-centre-national-institute-of>
13. SpaceWorks Report. Nano/microsatellite market forecast, 8th edn
14. Scoles S (2017) The space junk problem is about to get a whole lot gnarlier. *Wired*, Conde Nast (9 Aug 2017). www.wired.com/story/the-space-junk-problem-is-about-to-get-a-whole-lot-gnarlier/
15. Mudur N (2016) Space tech will now aid auto passengers in city. Retrieved from <https://bangaloremirror.indiatimes.com/bangalore/others/space-tech-will-now-aid-auto-pasengers-in-city/articleshow/53986337.cms> (Sept 2)

Space Robotics and Mechanical

Thermal Investigation of Power Supply Module (QDR-PSM) for Space Application Using Numerical and Experimental Approach



B. K. Sharath, Santosh Jotteppa, Shashank Dibbi, Vinod Chippalkatti, P. Rajendran and M. Uma Ravindra

Abstract Power supply module is designed to provide input power to digital system and radio frequency system for space application. High power and package density in electronics are continuously increasing, which create more heat in the system. Thermal management in space application is even more challenging since the cooling of these systems primarily relies on conduction and radiation by ignoring convection for space application. The effective heat removal from a component and PCB to mechanical housing is through conduction and partly with radiation. In fact, thermal design in electronics through thermal modelling and simulation is becoming an integral part of the electronics system design process because it is normally less time consuming and also low expensive compared to the experimental cut-and-try approach. In paper, thermal design, analysis and testing of DC–DC power supplies module have been explained in detailed. Thermal analysis has been carried out using computational fluid dynamics technique, by considering total heat dissipation of 40 W. Thermal model was created using Ansys Icepak, and all active and highly dissipating component are modelled. Conduction and radiation mode of heat transfer are considered during the analysis by maintaining the base plate temperature at 55 °C. Based on the analysis results, the convertor has been manufactured, assembled and electrically tested. Thermal testing has been carried out at ambient air temperature of 25 °C for identifying the hot spot in the convertor using thermal camera before it is tested at high temperature. Thermal cycle testing of space grade DC–DC convertor

B. K. Sharath (✉) · S. Jotteppa · S. Dibbi · V. Chippalkatti
Centum Electronics Limited, Bangalore, Karnataka 560106, India
e-mail: sharathbk@centumelectronics.com

S. Jotteppa
e-mail: santoshj@centumelectronics.com

S. Dibbi
e-mail: shashankd@centumelectronics.com

V. Chippalkatti
e-mail: vinod@centumelectronics.com

P. Rajendran · M. Uma Ravindra
DLRL, Hyderabad, Telangana 500053, India

is performed in thermo vacuum chamber at extreme cold temperature of negative 15 °C and extreme hot temperature of 55 °C under 1×10^{-5} torr pressure condition, during which electrical functionality of the module is monitored and temperature of active component is measured and the results of the thermal analysis and testing are elaborated and compared.

Keywords Thermal analysis · Computational fluid dynamics · Electronics cooling for space · DC–DC convertor

1 Introduction

DC–DC convertors are normally designed for space application are in the power range of 5–100 W delivered come in a variety of package sizes and shapes. The demand for more sophisticated and reliable products for satellite application had pushed electronics packaging into grater challenges. Industry trends are continuously driving package sizes downward and increasing without a conforming allowance for size to facilitate for heat management. Specification demands from customer are such that to need to maintained the temperature of component below 110 °C without disturbing the external dimensions, when it is operated at extreme temperatures.

In thermal design process of a complex electronics system, it is very essential to get accurate data at various location temperature in front-end design phase. Hence, it is almost essential to use computational fluid dynamics (CFD) tool for analysing the module during design. Computational fluid dynamics (CFD) has been progressively becoming a powerful tool in the heat transfer problems since a CFD tool has a capability of predict temperature at any locations inside a system.

In this paper, thermal design verification and validation of DC–DC convertor which convert 42 V/5A DC input to six different DC output. The paper also elaborates on thermal design, thermal modelling and testing of DC–DC convertor are discussed in detail. The thermal analysis is carried using computational fluid dynamics (CFD) technique. Conduction and radiation mode of heat transfer are considered by maintaining the base plate temperature at 55 °C, and thermal cycling is carried out in thermal vacuum chamber for the extreme temperatures in cycle, and results of analysis and testing are compared.

2 Thermal Design

Thermal design of power supply modules is challenging for space application to meet the stringent environmental condition due to the nonexistence of convection cooling. The module has been designed with dimension of 220 mm × 218 mm × 90 mm and with the mass of 3400 g. Mechanical housing of power supply module

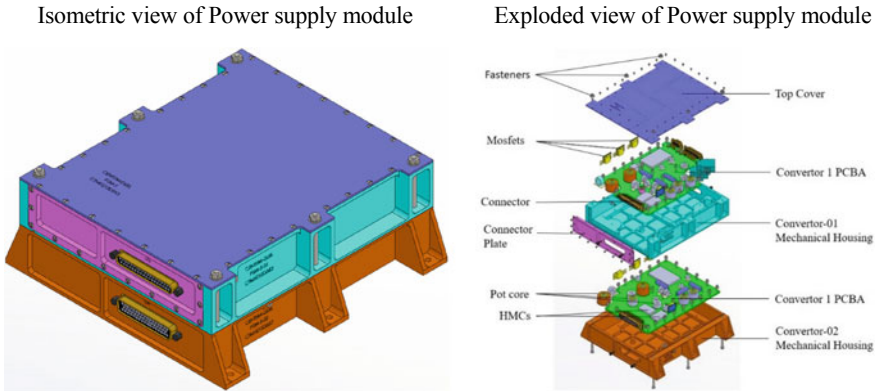


Fig. 1 Mechanical housing with PCBA of power supply module

is designed with two number of converters. Converter-2 has the highest power dissipation among two, and to provide the lower thermal path, it is placed on the bottom side, and Converter-1 is placed on the top side [1]. The mechanical parts have been designed with aluminium alloy material and part are coated with black anodized to increase heat transfer though radiation and Module will be stacked together and will be mounted on the satellite deck (Fig. 1).

Mechanical housing is designed with necessary thermal ribs, which will facilitate the heat flow from printed circuit board (PCB) to housing. For better thermal contact with the mechanical housing and PCB, it has been provided with sufficient number of holes to fix to the housing using fasteners. The component like pot core and toroidal cores is placed on the PCB, for better heat transfer fixed using screw, thermal interface material is used beneath the core, and potting is also done to ensure good contact for better heat transfer. Highly dissipating components like hybrid microcircuits (HMC) and transformers are mounted on the PCB using thermal interface material, and also, highly heat-dissipating components like MOSFETs and diode are directly mounted on the mechanical housing using thermal interface material, which is having good thermal conductivity and electrically insulating property. Thermal vias have been provided in the PCB with continuous array, and also, PCB area below the thermal vias is made in contact with the thermal guides provided in the mechanical housing which will assist in the heat transfer, thereby drastically reduce the temperature in low thermal conductive glass epoxy [2].

3 Methodology

3.1 Thermal Simulation Methodology

Thermal design of electronics for the space application should be very precise, so accurate modelling needs to be created by using computational fluid dynamics technique. CAD step models have been used for creating the thermal model of the convertor and its components. All components which are critical from thermal point of view are modelled, some of the components like resistors, capacitors, etc., are not modelled, heat has been considered as uniformly distributed load (UDL) on the PCB for modelling simplification, and the PCB is modelled in details by constructing each layers including insulator material and copper [3].

3.1.1 Computational Fluid Mechanics

Computational fluid dynamics (CFD) is that deals with fluid mechanics that numerical equations and analyse problems that involve fluid flows. CFD modelling technique has been extensively used in different engineering industries like aerospace, energy, oil and gas, etc. CFD model assists to validate the results and resolve the cooling issues in electronics system. CFD analysis helps to determine thermal design defects and assists in framing correcting the thermal design, significantly reduce the cost to manufacture the product and time for running the several laboratory experiments to understand issue to implicate the better or new design. CFD modelling has become a standard technique for designing new electronics system. The commercial software used in the study is ANSYS ICEPAK. The computational representation of the thermal model is taken by the CFD fluent solver, and it is iteratively solved for different equations, i.e. continuity, momentum and energy based on the generated mesh.

Continuity Equation:

$$\frac{\partial u}{\partial x} + \frac{\partial v}{\partial y} + \frac{\partial w}{\partial z} = 0 \quad (1)$$

Momentum Equation in X-direction:

$$u \frac{\partial u}{\partial x} + v \frac{\partial u}{\partial y} + w \frac{\partial u}{\partial z} = f_x - \frac{1}{\rho} \frac{\partial p}{\partial x} + \nu \left(\frac{\partial^2 u}{\partial x^2} + \frac{\partial^2 u}{\partial y^2} + \frac{\partial^2 u}{\partial z^2} \right) \quad (2)$$

Momentum Equation in Y-direction:

$$u \frac{\partial v}{\partial x} + v \frac{\partial v}{\partial y} + w \frac{\partial v}{\partial z} = f_y - \frac{1}{\rho} \frac{\partial p}{\partial y} + \nu \left(\frac{\partial^2 v}{\partial x^2} + \frac{\partial^2 v}{\partial y^2} + \frac{\partial^2 v}{\partial z^2} \right) \quad (3)$$

Table 1 Mechanical properties used during the analysis

S. No.	Material	Density (gm/cc)	Thermal conductivity (w/mk)	CTE (10E-6/°k)	Remarks
1	Aluminium Alloy 6061	2.7	170	23.6	Mechanical housing
2	Copper	8.9	390	16.5	PCB
3	Glass Epoxy (FR4)	1.8	0.2	11.7	PCB
4	Kovar	8.83	17.3	5.02	HMC
5	Ferrite	4.85	3.5		Component
6	Alumina	3.8	21	6.5	Component

Momentum Equation in Z-direction:

$$u \frac{\partial w}{\partial x} + v \frac{\partial w}{\partial y} + w \frac{\partial w}{\partial z} = f_z - \frac{1}{\rho} \frac{\partial p}{\partial z} + \nu \left(\frac{\partial^2 w}{\partial x^2} + \frac{\partial^2 w}{\partial y^2} + \frac{\partial^2 w}{\partial z^2} \right) \tag{4}$$

Energy Equation:

$$u \frac{\partial T}{\partial x} + v \frac{\partial T}{\partial y} + w \frac{\partial T}{\partial z} = \alpha \left(\frac{\partial^2 T}{\partial x^2} + \frac{\partial^2 T}{\partial y^2} + \frac{\partial^2 T}{\partial z^2} \right) + \phi \tag{5}$$

where in above equation, (u, v, w) are the component of the fluid velocity, and (f_x, f_y, f_z) are body force in direction of (x, y, z) direction; p is pressure; T is temperature, ϕ is viscous dissipation.

3.1.2 Component Modelling

All electronics component which are having inherent capacity to generate heat when they electrically operated, so thermal model is created with all active component. Components modelling is one of the important criteria during the modelling for the accurate temperature. Component which having thermal resistance from junction to case are modelled with 2R type and component with are not having junction are modelled using material properties that are used in the components [4]. Materials properties used during the analysis are tabulated in Table 1.

3.1.3 Printed Circuit Board

Multilayer printed circuit board is made by FR4 (glass epoxy) layer with copper layer is alternatively packed. Design of PCB has major impact in thermal management of

electronics for space application since heat generated in the component and trace in the PCB has to be transferred to mechanical housing in through conduction only. So providing thermal layer in the PCB plays vital role in thermal management (Table 2).

PSM consists of one number of PCB in each convertor, having thickness of 3 mm and 12 layers in each PCBs. Four thermal layers are provided with more than 80 percentage copper spreading in order to increase the thermal conductivity of in plane and out of plane. Thermal conductivity of PCB is calculated using below equation,

$$K_{\text{inplane}} = \frac{\sum_{i=1}^{i=n} k_i t_i}{\sum_{i=1}^{i=n} t_i} \quad \& \quad K_{\text{Outplane}} = \frac{\sum_{i=1}^{i=n} t_i}{\sum_{i=1}^{i=n} \frac{t_i}{k_i}}$$

Using above formula, the PCB thermal conductivity is calculated as, for Convertor 01, $K_{\text{Inplane}} = 62.42 \text{ W/mk}$ and $K_{\text{Outplane}} = 0.327 \text{ w/mk}$. For Convertor 02, $K_{\text{Inplane}} = 76.4 \text{ W/mk}$, $K_{\text{Outplane}} = 0.327 \text{ W/mk}$.

3.1.4 Power Dissipation

Power supply module is designed to provide required electrical output for given electrical input, and during this conversation process, there will electrical loss in module, which results to producing heat in the component. Power supply module for space application designed in such way that it should have minimum loss/ higher efficiency in the module [5].

$$\text{Heat generated } (Q) = \text{Electrical Input } (VI)_{\text{In}} - \text{Electrical output } (VI)_{\text{Out}}$$

where Q is heat generated in the system and V is voltage and I Current. In PSM module having total heat dissipation of 40 W, in which Convertor-1 is having heat dissipation of 17.82 W and Convertor-2 which is having dissipation 21.98 W. During this study, heat dissipation in each component is given below (Table 3).

3.1.5 Grid Generation and Boundary Condition

The grid generation plays a vital role in the CFD results, so it is very important to take care of grid size during generation, improper grid size has major impacts, and selection of fine mesh leads to increase in the computational cost as well as the time and usage of course mesh which leads in the improper solution. So selecting different mesh size for different region is depending upon on heat flux [6] (Table 4).

Initial and boundary conditions are important parameter for analysis. The boundary conditions are applied in analysis are such a way that it is almost similar to the test/end-use operating requirements to get the accurate results. The analysis is carried

Table 2 PCB stackup details of Converter 01 and Converter 02

Converter 01 stack up details

Board dimensions: 1150x150, 220x153x2.7 mm PMM 4.5.1					
Description of Layer	Copper %	Layer	Code: mils / μ m	Name	Isolation in mm
Electrical Copper	48.7326383	Layer 01	0.007 FRA 1150 (11.50k) (PC-4-H1000N) (11.50k)	core	0.01
Thermal Copper	81.5345365	Layer 02	1 X 2.118 ± 0.024F Prepreg 1150 (11.50k)	prepreg	0.1
Electrical Copper	48.5348179	Layer 03	0.007 FRA 1150 (11.50k) (PC-4-H1000N) (11.50k)	core	0.2
Electrical Copper	46.2492596	Layer 04	1 X 2.118 ± 0.024F Prepreg 1150 (11.50k)	prepreg	0.1
Thermal Copper	81.6054321	Layer 05	0.007 FRA 1150 (11.50k) (PC-4-H1000N) (11.50k)	core	0.2
Electrical Copper	46.2492596	Layer 06	1 X 2.118 ± 0.024F Prepreg 1150 (11.50k)	prepreg	0.1
Electrical Copper	48.7326383	Layer 07	0.007 FRA 1150 (11.50k) (PC-4-H1000N) (11.50k)	core	0.2
Thermal Copper	81.5345365	Layer 08	1 X 2.118 ± 0.024F Prepreg 1150 (11.50k)	prepreg	0.1
Electrical Copper	48.8523282	Layer 09	0.007 FRA 1150 (11.50k) (PC-4-H1000N) (11.50k)	core	0.2
Electrical Copper	48.6972528	Layer 10	1 X 2.118 ± 0.024F Prepreg 1150 (11.50k)	prepreg	0.1
Thermal Copper	81.5345365	Layer 11	0.007 FRA 1150 (11.50k) (PC-4-H1000N) (11.50k)	core	0.2
Electrical Copper	48.6821442	Layer 12	1 X 2.118 ± 0.024F Prepreg 1150 (11.50k)	prepreg	0.1
Electrical Copper	50.4892389	Layer 13	0.007 FRA 1150 (11.50k) (PC-4-H1000N) (11.50k)	core	0.2
Total copper details					2.68
Total: 2.7 ± 10%					

Converter 02 stack up details

Board dimensions: 1150x150, 220x153x2.7 mm PMM 4.5.2					
Description of Layer	Copper %	Layer	Code: mils / μ m	Name	Isolation in mm
Electrical Copper	48.7326383	Layer 01	0.007 FRA 1150 (11.50k) (PC-4-H1000N) (11.50k)	core	0.01
Thermal Copper	81.5302934	Layer 02	1 X 2.118 ± 0.024F Prepreg 1150 (11.50k)	prepreg	0.1
Electrical Copper	44.8277231	Layer 03	0.007 FRA 1150 (11.50k) (PC-4-H1000N) (11.50k)	core	0.2
Electrical Copper	46.5338808	Layer 04	1 X 2.118 ± 0.024F Prepreg 1150 (11.50k)	prepreg	0.1
Thermal Copper	88.3127746	Layer 05	0.007 FRA 1150 (11.50k) (PC-4-H1000N) (11.50k)	core	0.2
Electrical Copper	43.7401263	Layer 06	1 X 2.118 ± 0.024F Prepreg 1150 (11.50k)	prepreg	0.1
Electrical Copper	48.7326383	Layer 07	0.007 FRA 1150 (11.50k) (PC-4-H1000N) (11.50k)	core	0.2
Thermal Copper	88.1716195	Layer 08	1 X 2.118 ± 0.024F Prepreg 1150 (11.50k)	prepreg	0.1
Electrical Copper	49.8877348	Layer 09	0.007 FRA 1150 (11.50k) (PC-4-H1000N) (11.50k)	core	0.2
Electrical Copper	49.5507263	Layer 10	1 X 2.118 ± 0.024F Prepreg 1150 (11.50k)	prepreg	0.1
Thermal Copper	88.1782363	Layer 11	0.007 FRA 1150 (11.50k) (PC-4-H1000N) (11.50k)	core	0.2
Electrical Copper	50.4892389	Layer 12	0.007 FRA 1150 (11.50k) (PC-4-H1000N) (11.50k)	core	0.1
Total copper details					2.68
Total: 2.7 ± 10%					

Table 3 Heat dissipation details of PSM

Convertor 01				Convertor 02			
S. No.	Components	Placement	Dissipation (W)	S. No.	Components	Placement	Dissipation (W)
1	RL1	Wall Mount	0.4	1	D8	Wall Mount	5.85
2	RL2	Wall mount	0.4	2	D11	Wall Mount	1.385
3	D16	Wall Mount	5.85	3	D14	Wall Mount	0.133
4	D19	Wall Mount	0.25	4	Q1	Wall Mount	2.712
5	D22	Wall Mount	0.12	5	D2	Top PCB	0.1
6	Q1	Wall Mount	2	6	D3	Top PCB	0.1
7	L1	Top PCB	0.125	7	L1	Top PCB	0.44
8	L2	Top PCB	0.125	8	L2	Top PCB	0.454
9	L3	Top PCB	0.298	9	L6	Top PCB	0.867
10	L4	Top PCB	0.368	10	L4	Top PCB	0.1
11	L5	Top PCB	0.388	11	L5	Top PCB	0.625
12	L9	Top PCB	0.785	12	L7	Top PCB	0.136
13	L7	Top PCB	0.1	13	L8	Wall Mount	1.231
14	L8	Top PCB	0.638	14	L9	Top PCB	0.245
15	L10	Top PCB	0.233	15	L10	Bottom PCB	0.169
16	L12	Top PCB	0.12	16	TR1	Bottom PCB	0.56
17	L11	Top PCB	0.138	17	R6	Bottom PCB	0.106
18	TR1	Top PCB	0.351	18	R58	Top PCB	0.16
19	R66	Bottom PCB	0.16	19	R53	Bottom PCB	0.2
20	R61	Bottom PCB	0.2	20	R91	Bottom PCB	0.2
21	R83	Bottom PCB	0.2	21	R49	Bottom PCB	0.15
22	R57	Bottom PCB	0.15	22	R57	Bottom PCB	0.17
23	R65	Bottom PCB	0.17	23	R46	Bottom PCB	0.2
24	R54	Top PCB	0.2	24	R47	Top PCB	0.2

(continued)

Table 3 (continued)

Convertor 01				Convertor 02			
S. No.	Components	Placement	Dissipation (W)	S. No.	Components	Placement	Dissipation (W)
25	R55	Top PCB	0.2	25	R48	Bottom PCB	0.2
26	R56	Bottom PCB	0.2	26	HMC-A	Top PCB	1.0497
27	HMC-A	Top PCB	1.0497	27	HMC-D	Top PCB	0.3908
28	HMC-C	Top PCB	0.1745	28	HMC-C	Top PCB	0.1654
29	HMC-D	Top PCB	0.342	29	PCB		3.6811
30	PCB		2.087	Total heat dissipation			21.98
Total heat dissipation			17.8222				

Table 4 Mesh details used in the assembly

Details of mesh used in analysis			Quality of mesh used in analysis		
Mesh details			Quality details		
S. No.	Description	Number	S. No.	Description	Range
1	No. of nodes	8,271,263	1	Face alignment	0.2546–1
2	No. of elements	6,866,231	2	Volume	2.21e–13 to 1.45e–6
			3	Skewness	0.0575–1

out for conduction and radiation mode of heat transfer. The base plate of package is maintained at 55 °C, and cabinet wall is maintained at 55 °C, complete module is under the radiation interaction, and inside cabinet vacuum properties are considered [7].

3.1.6 Results

The steady-state thermal analysis of power supply module has been carried out by considering total heat dissipation of 40 W for conduction and radiation mode of heat transfer. Using commercial available Ansys Icepak software with inbuilt fluent solver. The temperature distribution plots for the assembly are shown in Fig. 2.

Figure 2 shows temperature plot of PSM, the maximum temperature in the Convertor 1 is 90.13 in the L8 component, and maximum temperature in the Convertor 2 is 85.99 in the L5 component.

Temperature distribution in the mechanical housing of complete of power supply module, Convertor 01 with PCB assembly and convertor 2 with PCB assembly are shown in Fig. 3 and have maximum temperature of 90.13 °C [8].

It can be noticed in Fig. 4 that inside the cabinet, minimum temperature maintained

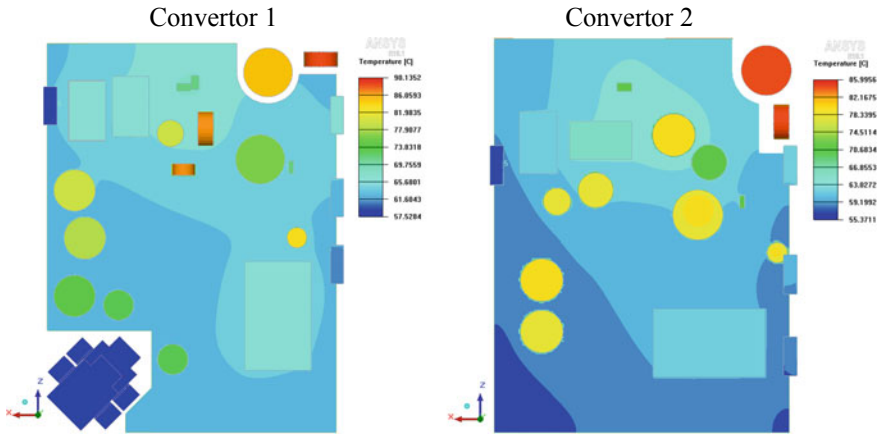


Fig. 2 Temperature distribution in the mechanical housing with PCBA

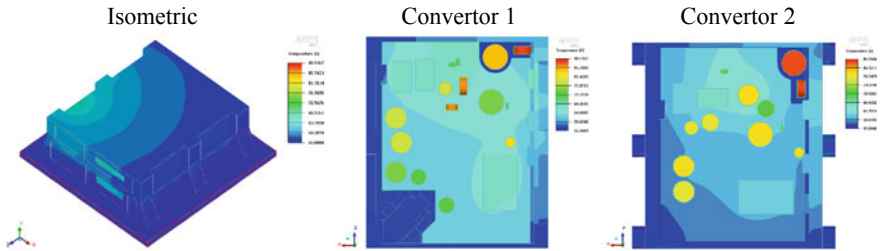


Fig. 3 Temperature distribution in the mechanical housing with PCBA

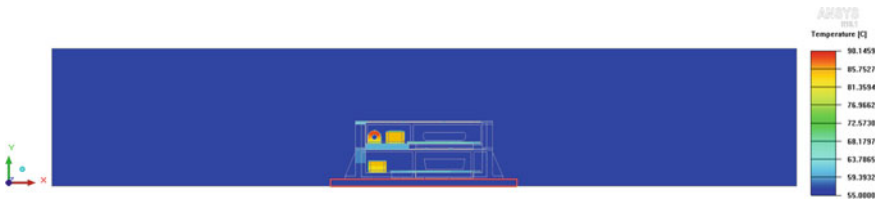


Fig. 4 Temperature distribution in cabinet and mechanical housing with PCBA

is 55 °C, and maximum temperature obtained is 90.15 °C that is observed in the component L8. Table 5 shows the critical temperatures of the components in the power supply module.

Table 5 Temperature details of the component

Convertor 01				Convertor 02			
S. No.	Component	Placement	Temperature (°C)	S. No.	Component	Placement	Temperature (°C)
1	RL1	Wall Mount	57.91	1	D8	Wall Mount	72.42
2	RL2	Wall mount	57.76	2	D11	Wall Mount	62.04
3	D16	Wall Mount	76.75	3	D14	Wall Mount	57.78
4	D19	Wall Mount	63.46	4	Q1	Wall Mount	64.80
5	D22	Wall Mount	58.24	5	D2	Top PCB	64.89
6	Q1	Wall Mount	65.24	6	D3	Top PCB	64.00
7	L1	Top PCB	74.39	7	L1	Top PCB	78.67
8	L2	Top PCB	74.19	8	L2	Top PCB	79.95
9	L3	Top PCB	76.09	9	L6	Top PCB	85.03
10	L4	Top PCB	79.82	10	L4	Top PCB	79.56
11	L5	Top PCB	80.91	11	L5	Top PCB	85.99
12	L9	Top PCB	86.16	12	L7	Top PCB	72.69
13	L7	Top PCB	83.71	13	L8	Wall Mount	79.92
14	L8	Top PCB	90.13	14	L9	Top PCB	78.70
15	L10	Top PCB	87.76	15	L10	Bottom PCB	79.33
16	L12	Top PCB	87.81	16	TR1	Bottom PCB	79.60
17	L11	Top PCB	80.76	17	R6	Bottom PCB	64.16
18	TR1	Top PCB	73.45	18	R58	Top PCB	71.63
19	R66	Bottom PCB	72.67	19	R53	Bottom PCB	69.67
20	R61	Bottom PCB	74.66	20	R91	Bottom PCB	69.21
21	R83	Bottom PCB	73.45	21	R49	Bottom PCB	69.12
22	R57	Bottom PCB	72.10	22	R57	Bottom PCB	67.78
23	R65	Bottom PCB	73.35	23	R46	Bottom PCB	70.26
24	R54	Top PCB	72.42	24	R47	Top PCB	72.99

(continued)

Table 5 (continued)

Convertor 01				Convertor 02			
S. No.	Component	Placement	Temperature (°C)	S. No.	Component	Placement	Temperature (°C)
25	R55	Top PCB	72.41	25	R48	Bottom PCB	70.19
26	R56	Bottom PCB	74.33	26	HMC-A	Top PCB	62.48
27	HMC-A	Top PCB	66.47	27	HMC-C	Top PCB	62.42
28	HMC-C	Top PCB	66.85	28	HMC-D	Top PCB	65.68
29	HMC-D	Top PCB	66.99				

3.2 Thermal Testing Methodology

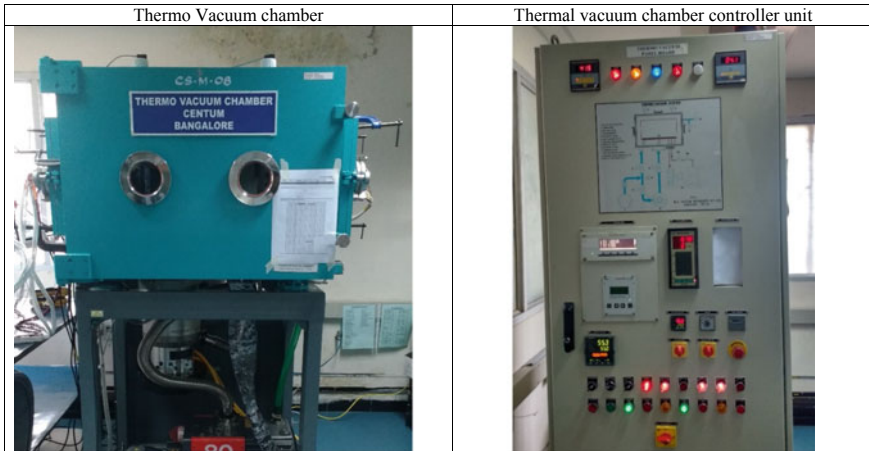
Thermal performance of power supply module is realized by subjecting to environmental test under thermo vacuum condition with very low pressure condition, which is advanced test for space environmental. Power supply module for space application will be exposed to harsh thermal cycling under vacuum condition and also need to undergo repeated and wide changes in operating temperature, as well as functionality at extreme temperature [9].

3.2.1 Thermal Vacuum Chamber

Thermal vacuum chamber is one of risk mitigation test methods for space application. Chamber artificially replicates the vacuum environmental with different range of temperature. This helps in the predicting the temperature, performance of power supply module and also flaws (if any) in the module well in advance before exposing to real time [10] (Table 6).

Table 6 Temperature details of component obtained during a below table the

S. No.	Particular	Description
1	Make	Vacuum Techniques Pvt Ltd, Bangalore
2	Model	2006
3	Temperature range	-55 to +100 °C
4	Power Dissipation	70 W
5	Vacuum range	$>1.0 \times 10^{-5}$ torr
6	Base plate size	650 mm × 650 mm
7	Coolant	Ammonia
8	Heaters	IR Heaters
9	Number RTD	012



3.2.2 Testing Approach

Thermal vacuum cycle testing of electronics product helps in predicting performance and reliability of an electronics package and also facilitates to validate the thermal analysis results under the thermo vacuum condition. Following step are involved have been used for during testing.

Hot spots in the analysis and component which are critical from thermal point of view are identified, and they are attached component temperature sensors to measure the temperature. Thermal sensor is applied with adhesive in order to have proper contact between the sensor head and component (Fig. 5).

Power supply module is placed thermal vacuum chamber and fixed to base plate of chamber with the help of fasteners by applying proper torque. Chamber controller

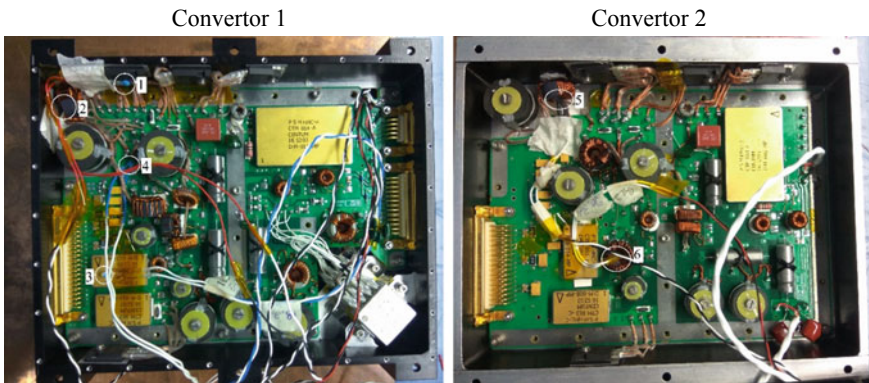


Fig. 5 Thermal sensor is attachment for critical component

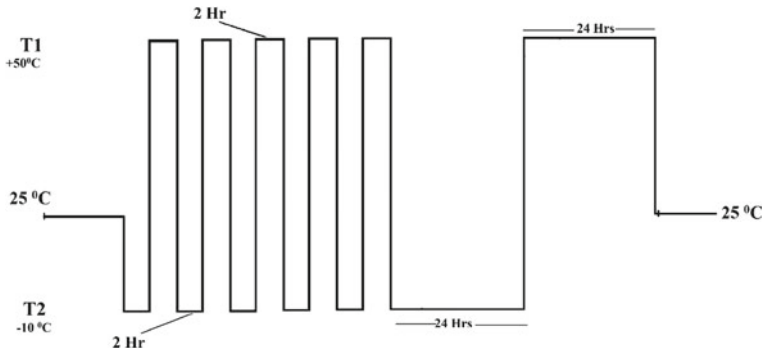


Fig. 6 Operational thermal vacuum cycling testing profile

RTD is mounted in diagonal fashion to the package to maintain the temperature of the base at constant. RTD temperatures are taken to control the base plate temperature of thermal vacuum chamber at 55 °C. Power supply module is subjected to thermal cycle as shown in Fig. 6, module is subjected to extreme temperature ranging from -10 to 55 °C with pressure condition of 1×10^{-5} torr during which module is continuously ON with fully loaded condition. The initial five cycle of profile is subjected to dwell period of 2 h, last cycle of profile is with 24 h dwell period, and during dwell period, electrical functionality and temperatures are continuously monitored at each extremes temperature.

3.2.3 Thermal Test Results

Power supply module operating in full load condition under thermal vacuum cycle, during which continuous electrical functionality data are acquired and Temperature of component are monitored at regular interval of 10 min for complete profile. Positive dwell period of last cycle in which temperatures reached at equilibrium state. Temperature of the component is tabulated in Table 7.

The temperature obtained during the thermal vacuum testing is compared with temperatures of analysis. Compassion of simulation and testing results are tabulated

Table 7 Temperature of the component during thermal vacuum cycle

S. No.	Component	Convertor	Testing results
1	D16 Diode	Convertor 1	76.45
2	L8 Inductor		86.33
3	HMC-D		63.76
4	D8 Diode	Convertor 2	81.12
5	L6 Inductor		82.76
6	L9 Inductor		80.31

Table 8 Temperature of the critical component during thermal vacuum cycle

S. No.	Component	Analysis	Testing results	Percentage of error
1	D16 Diode	76.7561	76.45	0.39
2	L8 Inductor	90.1352	86.33	4.22
3	HMC-D	66.9928	63.76	4.82
4	D8 Diode	72.4273	71.12	1.80
5	L6 Inductor	85.0377	82.76	2.67
6	L9 Inductor	78.7096	80.31	2.03

in Table 8, and the maximum percent of variation between simulation and thermal vacuum cycle test is found to 5% which is found in the HMC component.

4 Conclusion

In this paper, we have emphasized the thermal design, methodology involved in the analysis and thermal testing of power supply module for the space application. Thermal simulation facilitates to select optimal design and identify the flaws during the design phase, so it can be rectified in design stage, so that product cycle, time and cost can be reduced. The summarized as, thermal analysis of Power supply module is performed for the dissipation of 40 W with conduction with radiation mode of heat transfer. To study thermal design adequacy to meet the intended specification and component are well are well below the operating temperature specified by the manufacturer. After finalizing the design, part is manufactured and assembled. For thermal vacuum testing, hot spot is identified from the analysis data, and they are attached with thermal sensor to monitor the temperature of hot spot component. This has enhanced confidence on the boundary conditions used to define the vacuum conditions during thermal analysis since the results are matching with physical vacuum test, and hence, the same concept will be used for all spacecraft packages design and analysis.

References

1. Lee RKW, Montero MG, Wright PK (2003) Design methodology for the thermal packaging of hybrid electronic mechanical products. In: ASME, design engineering technical conferences, DAC-48790, pp 1–10
2. Bar-Cohen A (1992) State-of-the-art and trends in the thermal packaging of electronic equipment. ASME J Electron Packag 114:257–270
3. Moghaddam S, Rada M, Shooshtari A et al (2003) Evaluation of analytical models for thermal analysis and design of electronic packages. Microelectron J 34(3):223–230

4. Maleki H, Shamsuri AK (2003) Thermal analysis and modeling of a notebook computer battery. *J Power Sources* 115:131–136 (Elsevier Science)
5. Lau JH, Yue TG (2009) Thermal management of 3D IC integration with TSV. In: *IEEE electronic components and technology conference*, pp 635–640
6. Hanreich G, Nicolics J, Musiejovsky L (2000) High resolution thermal simulation of electronic components. *Microelectron J* 40(12):2069–2076
7. Planas Almazan P (1997) Accuracy of Monte Carlo ray-tracing thermal radiation calculations: a practical discussion for an Active vs Passive Cooling design. In: *Sixth European symposium on space environmental control systems*, Netherlands. European Space Agency, SP-400, pp 579–591
8. ANSYS Icepak 12.1, user's guide Nov 2009
9. Jotteppa S, Singh B, Prasad S, Chippalkatti VS, Garvalia RN, Domadia KG, Parmar RM, Dave RK, Samudraiah DRM (2012) Analysis and experimental verification of space grade power supply performance under thermo-vacuum environment. *Int J Aerosp Sci* 1(3):43–48 (Scientific & Academic Publishing)
10. Avagyan VS, Danielyan VA, Gevorgyan AA, Simonyan AS, Mkrtychyan TH, Vardanyan VV (2014) Vacuum apparatus for thermal testing of electronic equipments. In: *2014 Tenth international IEEE vacuum electron sources conference (IVESC)*, Sept 2014

Analytical Thermal Modeling of Deployed and Body Mount Solar Panel and Its Comparison with Numerical Approaches for Small Satellite



G. Ramu and Prateek Nagvanshi

Abstract This paper involves a detailed thermal mathematical modeling of 300 mm × 300 mm deployed and body mounted solar panel of 10 kg sun-pointing Low Earth Orbit small satellite. An analytical calculation of solar panel both deployed and body mounted is performed using energy conservation principle. The system-level satellite thermal model along with solar panels is generated and solved numerically. In this paper, two configuration of body mounted solar panel in detailed system-level thermal model is studied. Firstly, the solar panel is fully conduction coupled with body structure panel. Secondly, conduction coupling is restricted by using 3 mm thick GFRP insulator at fastening points and resulting heat transfer by radiation is also studied. Also, the worst hot case temperatures of solar panel both deployed and body mount predicted by analytical approach is compared with numerical approach of the detail system-level thermal model. Hence, the presented method is beneficial for predicting the temperature profile of solar panel under worst hot condition.

Keywords Solar panel thermal analysis · Analytical calculation · Numerical approach

Nomenclature

η	Solar cell efficiency
α	Surface absorptivity
α_{eff}	Effective solar cell absorptivity
ε	Surface emissivity
T	Temperature
σ	Stefan Boltzmann constant ($5.67 \times 10^{-8} \text{ W/m}^2\text{K}^4$)
Q	Heat rate (W)

G. Ramu (✉) · P. Nagvanshi
Directorate of Space System and Technologies, Research Centre Imarat (RCI), Defense Research and Development Organization (DRDO) Lab, Hyderabad 500069, India
e-mail: ramu.g@rcilab.in

q	Heat flux (W/m^2)
Q_{Lugs}	Heat rate through fasteners (W)
$Q_{\text{b/w rad}}$	Heat rate between backside of solar panel to structure panel (W)
f	Solar albedo factor
K	Thermal conductivity (W/mK)
K_t	Solar panel conductance ($\text{W}/^\circ\text{C}$)

1 Introduction

Solar panel generates power required for spacecraft operations. During orbiting Earth, the solar panels experiences large variation in thermal environment in sunlit and eclipse period of Earth. Thus, it is of great importance to do the thermal analysis of solar panel to ensure safe working of satellite throughout its mission life. The temperature variation range of typical solar array of LEO satellite is -100 to 100 $^\circ\text{C}$. Therefore, it is necessary to forecast the worst hot and cold case temperature of solar arrays. The main objective of satellite thermal design is to ensure the spacecraft components temperatures are within allowable limits throughout the mission phase.

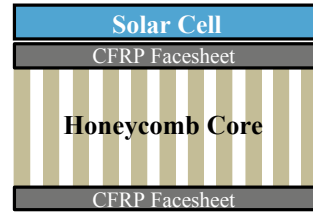
Much research has been carried out on the thermal analysis of solar array. Li et al. [1] have investigated on predicting the temperature profile of composite solar array for Low Earth Orbit (LEO) and Geosynchronous Orbit (GEO). Kim and Han [2] researches on the thermal investigation of fixed type solar array for LEO satellite.

Many researches have been carried out to predict the temperatures of deployed solar panels. But still, it is required to do the thermal analysis of satellite component for the safe operation of satellite throughout the mission life. The present LEO satellite has two deployable and one body mount solar arrays. This paper researches on the development of a detailed thermal mathematical modeling of deployed and body mount solar panel of a LEO satellite. An analytical calculation of solar array is performed using energy conservation principle. Here, the finite element method is used to predict the in-orbit temperature variation of solar array. Then, the worst hot case temperature from analytical method is compared with detailed system-level thermal model. Also, two configuration of body mount solar panel is studied and compared.

2 Solar Array Configuration

Here, solar array is in sun oriented panel of the satellite. There are two deployable and one body mount solar panel. Each solar panel is of $300\text{ mm} \times 300\text{ mm}$ size which consists of solar cells and 0.5 mm CFRP substrate with 12 mm thick low-density aluminum honeycomb core. M/s Azur space make solar cells are of size $80\text{ mm} \times 40\text{ mm}$ (Fig. 1). The solar cell efficiency is 28% at the beginning of life and at the end

Fig. 1 Solar panel construction



of life it is considered as 22%. Solar absorptivity of solar cells is 0.92 and emissivity is 0.82. These solar cells are bonded on the substrate using adhesives as shown in Fig. 2.

Solar cells convert incident solar energy into electric energy. But some energy is converted into heat energy. Hence, it is necessary to calculate effective absorptivity of solar array by considering solar cell power generation efficiency Ref. [2]. The effective absorptance (α_{eff}) of a solar cell is calculated by the following equation

$$\alpha_{\text{eff}}q_{\text{Solar}} = \alpha_{\text{solar cell}}q_{\text{Solar}} - \eta_{\text{solar cell}}q_{\text{Solar}} \quad (1)$$

Consequently, α_{eff} is calculated as 0.70.

3 Solar Panel Thermal Analysis Methodology

Satellite thermal analysis is concerned with predicting the temperature of satellite and its components in assumed heating environment. The predictions are made by using energy conservation principle. In this chapter, orbit environment heating fluxes are calculated and incorporated in energy balance equation to predict worst hot case temperature of solar panel.

3.1 Analytical Method for Solar Panel Thermal Analysis

The worst hot case temperature is predicted by applying energy conservation principle. For the ease of calculation, the following assumption is considered:

- Honeycomb panel is considered as two nodes lumped mass [3].
- Steady-state heat transfer is assumed.
- Sun-pointing attitude of solar array.
- Constant heat loads are considered on the solar arrays.
- Satellite body is considered as constant temperature.

3.2 Calculation of Space Heat Loads

Spacecraft heating can be classified into two categories. The first is orbit environment heating fluxes. The second category is internal dissipation, i.e., heat generated due to operating electronics, heaters, and shunts. The external heating loads experienced by satellite solar array while orbiting Earth includes solar flux and Earth radiation as shown in Fig. 2. The solar flux S above Earth atmosphere is 1410 Wm^{-2} [3]. The heat flux falling on the surface is given by,

$$q_{\text{Solar flux}} = \alpha_{\text{eff}} S \cos \delta \tag{2}$$

where $q_{\text{Solar flux}}$ (Wm^{-2}) is absorbed energy when the solar vector impinges at angle δ off the surface normal and α_{eff} is the effective solar absorptivity of the solar panel. For sun-pointing solar array δ is 0.

The Earth irradiation flux absorbed by solar array (q_{IR} in Wm^{-2}) is given by,

$$q_{\text{IR}} = \varepsilon E \tag{3}$$

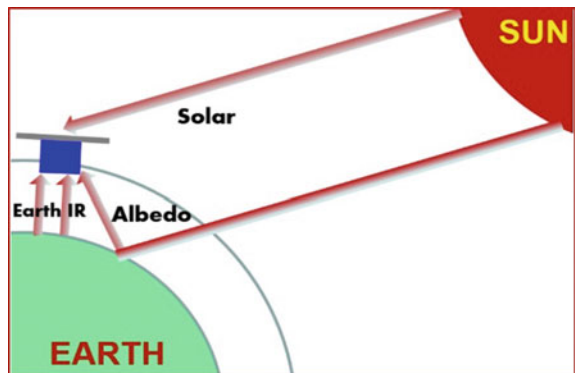
where E is the emitted radiation from the planet Earth which has a nominal value of 236 Wm^{-2} [4] and ε is the emissivity of solar array seeing the deep space.

Similarly, the radiation reflected from Earth is represented in terms of solar albedo factor f , which is usually stated as a fraction f of solar constant. It varies both seasonally and geographically, but good approximation can be obtained by using $f = 0.36$. The Earth albedo flux (q_{Albedo} in Wm^{-2}) is given by [4],

$$q_{\text{Albedo}} = f \alpha S \cos \varphi \tag{4}$$

where α is the surface absorptivity and φ is the reflection angle.

Fig. 2 Satellite thermal environment



3.3 Analytical Calculation of Deployed Solar Panel Temperature

Based on energy conservation principle, the steady-state heat balance on a deployed solar array is shown in Fig. 3 can be written as,

$$Q_{in} = Q_{out} \quad (5)$$

$$Q_{Solar} + Q_{IR} + Q_{Albedo} = Q_{Radiation\ to\ space} \quad (6)$$

3.3.1 Solar Panel Conductance (K_t)

Consider the solar panel schematically shown in Fig. 4. The overall heat balance can be represented on the two nodes located opposite to each other on the solar panel and is coupled by a conductance that can be estimated from $K_t = 1/R$, where K_t is conductance in $W/^\circ C$ and R is heat resistance of solar panel in $^\circ C/W$. The heat resistance (R) of solar panel is given by,

$$R = L/K A \quad (7)$$

where L is thickness of panel in meters, K is effective thermal conductivity of solar panel in W/mK , and A is the area of solar panel in m^2 , i.e., $0.09\ m^2$. Hence, the value of R is $0.25\ ^\circ C/W$ and $K_t = 4\ W/^\circ C$.

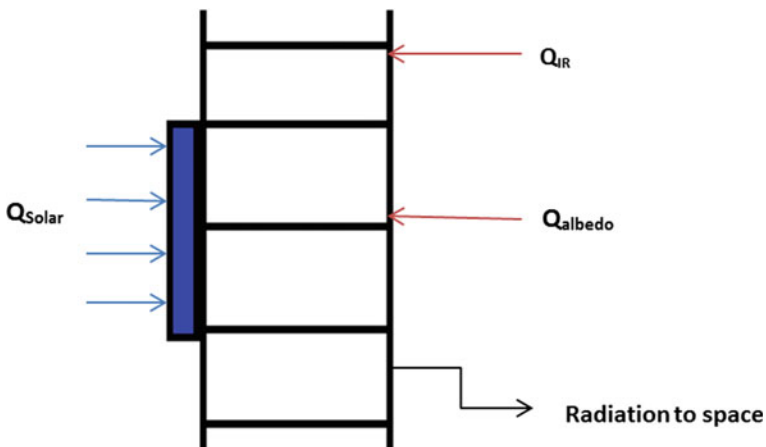


Fig. 3 Heat transfer in deployed solar panel

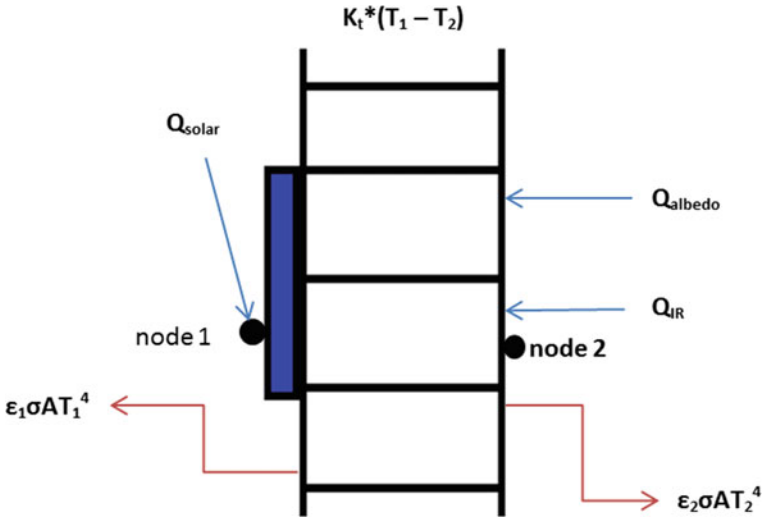


Fig. 4 Heat balance on deployed solar panel

3.3.2 Steady-State Heat Balance Calculations Q_{in} and Q_{out}

Using Eqs. (2), (3), (4) and the parameter from Table 1 the external heat loads at node 1 and node 2 in Fig. 4 can be calculated as, $Q_{Solar} = 88.83$ W, $Q_{IR} = 14.3$ W, and $Q_{Albedo} = 11.23$ W. Here, the deployed solar panel cell side and bottom side are facing deep space. Hence, the heat will be radiated from both the surface of the panel to the space as shown in Fig. 4. Steady-state heat balance on node 1 and node 2 gives,

$$(\alpha_{Solar\ cell} - \eta_{Solar\ cell})Aq_{Solar\ flux} = \epsilon_1\sigma AT_1^4 + K_t(T_1 - T_2) \tag{8}$$

$$K_t(T_1 - T_2) + Q_{IR} + Q_{albedo} = \epsilon_2\sigma AT_2^4 \tag{9}$$

Equations (8) and (9) are nonlinear and are solved numerically using MATLAB software which gives $T_1 = 71.3922$ °C and $T_2 = 64.3251$ °C. The temperature

Table 1 Thermo-optical properties of deployed solar array

S. No.	Parameter	Values	Remarks
1	ϵ_1	0.82	Emissivity of cell side solar array
2	ϵ_2	0.84	Emissivity of backside of solar array
3	$\eta_{solar\ cells}$	22.0%	At end of life
4	$\alpha_{solar\ cells}$	0.94	Absorptivity of solar cells

difference between the solar panel cell side and back side is approximately 7 °C because cell side facesheet is receiving more heat flux as compared to back side facesheet.

3.4 Analytical Calculation of Body Mount Solar Panel Temperature

The body mount solar panel is fixed at negative pitch panel which is sun oriented during power generation and it is fastened to structure panel at six locations. It is conductively isolated by maintaining a gap of 3 mm and by using GFRP washers at fastening locations. Radiation coupling with good view factor between back sides of body mount solar panel to the negative pitch structure panel is considered. It is also assumed that there will be no conduction from the back face of the structure panel.

Figure 5 shows the schematic of heat transfer in body mount solar panel. As discussed earlier, the overall heat balance can be represented on the two nodes located opposite to each other on the solar panel and is coupled by a conductance. The thermo-optical properties used for calculation are provided in Table 2.

Based on energy conservation principle, the steady-state heat balance on node 1 of a body mount solar array is shown in Fig. 5 can be written as,

$$(\alpha_{\text{solar cell}} - \eta_{\text{solar cell}})Aq_{\text{solar flux}} = \epsilon_1 \sigma AT_1^4 + K_t(T_1 - T_2) \tag{10}$$

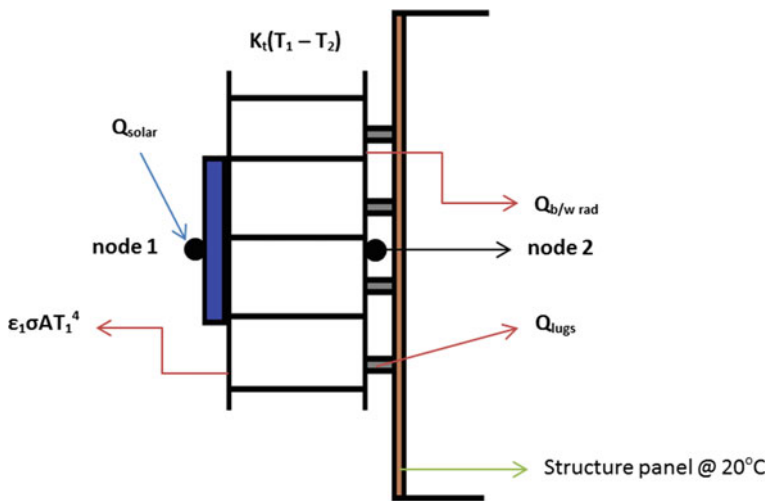


Fig. 5 Heat balance on body mount solar panel

Table 2 Thermo-optical properties and parameters for body mount solar panel

S. No.	Parameter	Values	Remarks
1	ϵ_1	0.82	Emissivity of cell side solar array
2	ϵ_2	0.718	Effective emissivity between backside of solar panel and structure panel
3	T_{str}	293 K	Structure panel temperature

Similarly, the steady-state heat balance on node 2 of a body mount solar array can be written as,

$$K_f(T_1 - T_2) = Q_{Lugs} + Q_{b/w \text{ rad}} \quad (11)$$

where Q_{Lugs} is the heat transfer through fasteners and considering $0.2 \text{ W/}^\circ\text{C}$ conductance value and $Q_{b/w \text{ rad}}$ is the radiation heat transfer between back sides of solar panel to the structure panel. On rearranging the equation, we get,

$$K_f(T_1 - T_2) = 0.2 \times (T_2 - T_{str}) + \epsilon_2 \sigma A (T_2^4 - T_{str}^4) \quad (12)$$

Equations (10) and (12) are nonlinear and are solved numerically using MATLAB software which gives $T_1 = 67.8534 \text{ }^\circ\text{C}$ and $T_2 = 61.1349 \text{ }^\circ\text{C}$. Hence, the top and bottom solar panel temperature are $68 \text{ }^\circ\text{C}$ and $61 \text{ }^\circ\text{C}$, respectively. Using temperatures T_1 and T_2 we can say that total heat energy coming to structure panel is $Q_{Lugs} + Q_{b/w \text{ rad}} = 26.86 \text{ W}$, out of which 18.64 W is due to radiative heat transfer between the back side of body mount solar panel and structure panel.

4 Numerical Approach for Thermal Analysis of Solar Panel

The solar panels are mounted on the negative pitch of satellite. There are two deployable and one body mount solar panel. Using, lumped mass approximation [5], the steady-state temperature in worst hot conditions can be calculated by a simplified analytical approach, but it cannot simulate the in-orbit temperature variation within the solar panels.

This section deals with the development of the solar panel thermal model using finite element method to predict in-orbit temperatures. In this chapter, two configurations of body mount solar panel is discussed and compared. Firstly, conduction coupling is restricted by using 3 mm thick GFRP insulator at fastening points and resulting heat transfer by radiation is also studied. Secondly, the solar panel is fully conduction coupled with body structure panel.

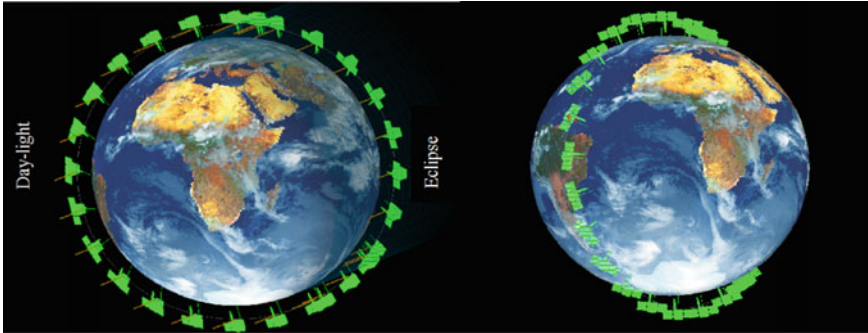


Fig. 6 Satellite positions from top of the orbit plane (left) and from sun point of view (right)

4.1 *Orbital Conditions for a Detail System-Level Thermal Model*

As mentioned in Sect. 3.1, the solar array is sun oriented panel of the satellite, so that the solar cell can generate maximum amount of solar energy. In analytical approach, the orbit and satellite attitude is not considered, whereas the orbit and attitudes of satellite must be considered in detailed system-level thermal analysis. The altitude of satellite is 640 km with orbit inclination of 97.91° . The equatorial crossing time of satellite is 09:30 AM and the orbit period is 5842.33 s. The in-orbit satellite attitude of a detailed system-level thermal model viewed above an orbit plane and the location of satellite in-orbit from sun point of view are shown in Fig. 6.

4.2 *Solar Panel Thermal Model*

As discussed in Sect. 2, there are three solar arrays, two deployable, and one body mount solar array. The two deployable solar arrays are attached to structure panel by mechanical hinges. Solar panels are of $300\text{ mm} \times 300\text{ mm}$ and a thickness of 12 mm with 0.5 mm CFRP substrate and 12 mm thick aluminum honeycomb core. The detailed solar array is modeled using shell elements which consist of 20×20 nodes on solar panel top and back surface. Optical properties are assigned on solar cell side which is sun facing surface and back side which is anti-sun looking side. Solar panel thickness is modeled and thermal conductance coupling is assigned between two shell elements. The schematic of solar array with node division is shown in Fig. 7.

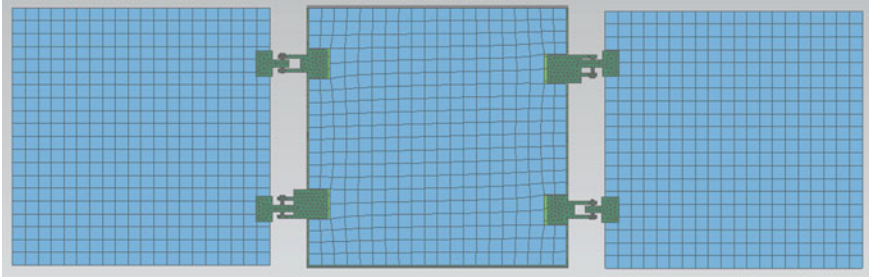


Fig. 7 Node division on solar panels

4.3 Method for Detailed Solar Panel Thermal Analysis

Thermal model is created by assigning thermo-optical properties of surfaces, thermo-physical and material properties. The contact conductance, thermal resistance or heat transfer coefficient between the nodes is assigned based on our judgment. The method adapted here is the solar panel is divided with the help of nodes throughout the surface and is thermally coupled to predict the in-orbit temperature.

The solar panel consists of solar cells, CFRP facesheets, and a honeycomb core. In geometric configuration, two facesheets are created and are discretized with uniform 20×20 nodes. The thermal capacitance (mC_p) of 1789 J/K is distributed uniformly on each and every node of solar panel. The optical properties of both facesheets given in Tables 1 and 2 are assigned; i.e., the effective thermo-optical properties are assigned on solar cell side facesheets and thermo-optical properties of black paint are used on the anti-sun looking side of solar panels. The effective thermal conductivity of solar array is calculated as 0.54 W/mK [5].

The current geometric mathematical model (GMM) is developed by using NX-CAD software. The thermal mathematical model (TMM) is further solved implicitly by conjugate gradient method using Siemens NX-Nastran software packages [6].

5 Thermal Analysis of Detailed System-Level Solar Panel

An analysis is carried out on the developed numerical model to understand the temperature variation within the solar array. From the numerical model, the temperature field is generated and the thermal aspects of the solar panel are discussed in this chapter.

5.1 Result Discussion

The temperature profile obtained from detailed model of the solar array is shown in Fig. 8. The three nodes temperature shown in graph corresponds to the solar cell side, solar panel backside, and body mount solar panel cell side. This figure gives the temperature difference between the cell side and bottom side of the solar panel surface. From the analysis, it is found that the temperature difference on the surface of cell side solar panel is as high as 14.6 °C. This is because of mechanical hinges which act as a heat conductive path between solar panel and satellite structure panel. Further, the temperature difference between cell side and back side is maintained at 5.42 °C during sunlit period and no temperature difference is maintained during eclipse period. The temperature difference is maintained because of the less thermal conductivity of honeycomb material. The analysis predicts the maximum temperature of 70.48 °C and the minimum analysis temperature of -70 °C. Similarly, the maximum temperature of body mount solar panel is 69.50 °C. Therefore, we can say that the maximum and minimum temperature of solar panel is within acceptable range and its thermal safety is verified under worst hot case condition.

An additional case study as shown in Fig. 9 is done to see the solar panel and inside electronic package temperature, if the body mount solar panel is mated (conduction coupled) with structure panel (no gap) and mounting lugs also not insulated with GFRP. From the analysis, the body mount solar panel temperature is dropped to 42.69 °C at the sunlit period this attributed extra heat loss to the satellite body. At the same time, all inside electronic packages temperatures are increased by approximately 10 °C due to extra heat load from solar panel and the radiator sizes were kept

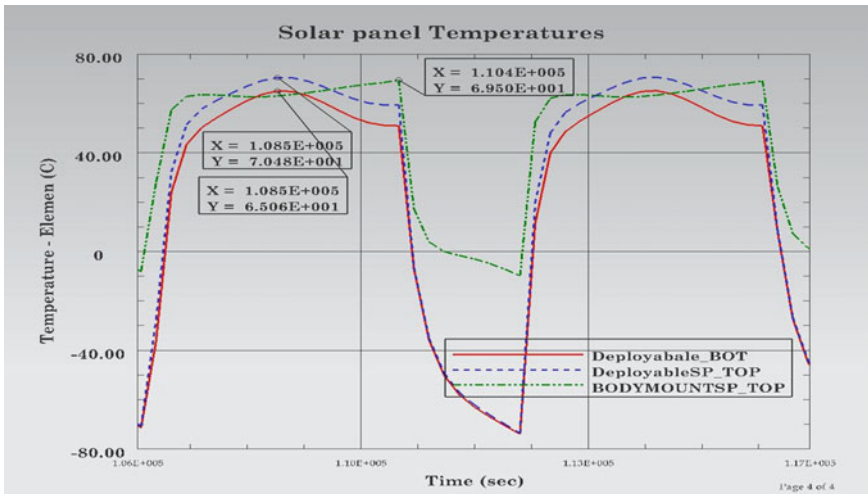


Fig. 8 In-orbit temperature variation of solar arrays

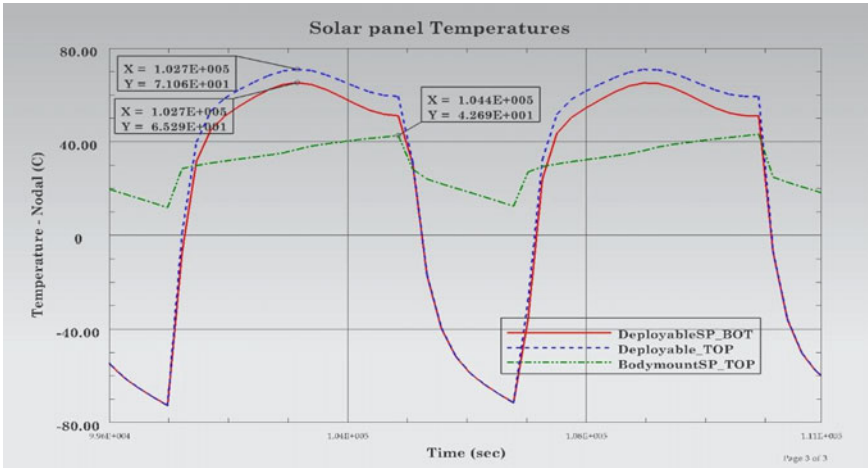


Fig. 9 Solar panel temperature with good contact between solar panel back and structure panel

same for both cases. Hence, for the safe operation of satellite electronic package, the body mount solar array conductively isolated by maintaining a gap of 3 mm and by using GFRP washers at fastening locations is considered.

5.2 Comparative Study of Analytical and Numerical Method

The computational time and effort for a detailed thermal model are much more as compared to analytical method. So it is useful to do the analytical solution before the development of system-level finite element model. The temperature obtained from analytical solution is 71 °C for deployed solar panel and 68 °C for body mount solar panel.

In this study, the analytical solution gives the worst hot case temperature of solar panel. As discussed previously, the maximum temperature of sun looking side and bottom side solar panel in the detailed satellite thermal analysis is 70.48 °C and 65.06 °C, respectively. Also, the body mount solar panel cell side temperature is 69.50 °C. The analytical temperature and the temperature obtained from detailed system-level thermal analysis of solar array are closer; hence, we can say that the current analytical approach is applicable to predict the solar array temperature in worst hot case condition.

6 Conclusion

An analytical calculation for solar array is performed using energy conservation principle on two-node thermal model with external thermal heat loads. Some assumptions were also considered to simplify a thermal model.

A detailed system-level finite element model of satellite is generated and solved numerically. The in-orbit temperature profile on the solar panel cell side and bottom side can be understood from the numerical solution. Moreover, the two configuration of body mount solar panel is discussed. Later, in the study, it is found that the body mount solar panel temperature is on lower side which attributed extra heat loss to the satellite body.

The analytical temperature and the temperature obtained from detailed system-level thermal analysis of solar array give reasonable comparison. This shows that the solar panel temperature can be predicted by using this analytical approach. Hence, it can be concluded that the assumption which we made in analytical approach is correct and the usefulness of analytical as well as numerical approach is also studied successfully. The maximum and minimum temperature of solar array is also confirmed within acceptable temperature range.

References

1. Li J, Yan S (2013) Thermal analysis of composite solar array subjected to space heat flux. *Aerosp Sci Technol* 27:84–94
2. Kim HK, Han CY (2010) Analytical and numerical approaches of a solar array thermal analysis in a low earth orbit satellite. *Adv Space Res* 46:1427–1439
3. Karam RD (1998) *Satellite thermal control for system engineers*. American Institute of Aeronautics and Astronautics, Reston
4. Thornton E (1996) *Thermal structures for aerospace application*. American Institute of Aeronautics and Astronautics. ISBN 1-56347-190-6
5. Gilmore DG (2002) *Spacecraft thermal control handbook*. American Institute of Aeronautics and Astronautics. ISBN 1-884989-11-X
6. NX 9 Thermal Solver TMG Reference Manual

Design Approach to Antenna Deployment System for Nano-Satellite Applications



Aditya Patki, Karan Jagdale and Mrigi Munjal

Abstract This paper presents an approach to design an antenna deployment system (ADS) for nano-satellite applications. The known material properties, simulations on ANSYS for structural loads, mission requirements and simulations on HFSS for antenna characteristics were used to reach a design for the current version of the ADS. Mechanical testing was carried out to test the recovery of the antenna from the coiled state. The test ascertained the thickness and fabrication process to be used. The antenna was decided to be a dipole antenna operating at 145 MHz based on simulations as well as mission requirements.

Keywords Antenna deployment system · Nano-satellite · Beryllium copper alloy · Burn wire circuit

1 Introduction

The antenna deployment system (ADS) has the purpose to deploy antenna once the satellite enters the orbit. ADS has become an essential component of any pico- or nano-satellite design due to space constraints during launch. These constraints do not allow the use of fixed antennas like those in larger satellites. The paper presents the specifications of the designed ADS, the test results of mechanical and communication testing and the structural and antenna simulation results. Conclusions regarding the design decisions made on the basis of mission requirements, simulations and test results are presented in the final section. The mechanism employed is a burn wire circuit which triggers the release of the strain energy present in the deformed antenna held in its undeployed curved state [1]. This trigger is caused by the burning of a nylon wire using a nichrome resistor-based circuit. The antenna is hence deployed and achieves its straight configuration. The deployment is detected by deployment switches positioned on the edge of sub-chassis.

A. Patki (✉) · K. Jagdale · M. Munjal
Student Satellite Lab, Aerospace Department, IIT Bombay, Mumbai, Maharashtra 400076, India
e-mail: 160100001@iitb.ac.in
URL: <https://www.aero.iitb.ac.in/satlab/>

© Springer Nature Singapore Pte Ltd. 2020
PSR. S. Sastry et al. (eds.), *Advances in Small Satellite Technologies*,
Lecture Notes in Mechanical Engineering,
https://doi.org/10.1007/978-981-15-1724-2_48

2 General Specifications and Design

2.1 *Sub-chassis Assembly*

The sub-chassis that the antenna is wrapped around in undeployed state is made of a polyimide material from DuPont India called Vespel[®] SP-3. The shape is designed to be roughly the biggest circle possible to fit in the area of the PCB.

2.2 *Antenna*

The current design of the antenna is a half-wave dipole antenna operating at 145 MHz. The current dimensions of the antenna are $0.4 \times 4 \times 487$ mm. The choice of material for the antenna is beryllium copper alloy.

2.3 *Circuit Design on the Printed Circuit Board*

The sub-chassis assembly is mounted on an FR-04 printed circuit board. The printed circuit board has an SMA connector for coaxial connection for the antenna feed. Tapered traces on the board are used for matching impedance of antenna to impedance of feed. The burner circuitry receives power and input from the communications board. The current is passed through a nichrome wire when the deployment has to occur. The board also includes a current limiter IC which ensures that the current does not go beyond 1 A to avoid damage due to overcurrent.

2.3.1 *Tapered Feed and Interfacing with Antenna*

Impedance matching is done by tapered traces on PCB. One end of trace has an impedance of 50Ω which is connected to SMA, and other end has an impedance of 114Ω which is connected to antenna. Interfacing of the antenna to the trace is done with the help of a small metal block screwed to the antenna and in contact with the trace.

2.3.2 *Burner Circuit*

Burner circuit will be used for heating nichrome wire to burn the nylon wire to deploy the antenna. The current limiting IC NCP380 along with its peripheral circuit is used to limit the current in nichrome.

2.4 Burn Wire Mechanism and Deployment Switches

The antenna is held down in the stowed state wrapped around the polymeric sub-chassis with the help of 0.16 mm nylon wire. The nylon wire will be thermally cut with a nichrome wire at the time of deployment. Cutting of the nylon wire will result in the release of the strain energy, and the antenna is deployed.

SPDT switches on the board which are pressed down by the antenna in the undeployed state are released once the antenna is successfully deployed. Deployment is signaled to the communication subsystem.

3 Simulation and Testing

This section covers the development of the proof of concept setup, structural simulations of the system, antenna simulations, prototype development and testing of the prototype.

3.1 Proof of Concept Setup

The proof of concept setup was built with a tape spring used as the antenna, and nichrome wire (heating element) of 24 AWG was used for melting nylon wire. The tape spring was used to simulate the recoverable nature of the antenna to be used. Nichrome wire was chosen as the heating element in the burn wire mechanism due to its heritage in space as an effective heating element and easy availability. Tests were carried out on the setup to establish its feasibility and practical potential. The tests were carried out at 28 °C in a temperature-controlled environment. The tests were successful, and hence, the idea was taken to the design phase.

3.2 Simulations

3.2.1 Structural Simulations

The structural simulations were carried out on ANSYS 16.2. Boundary conditions for structural simulations were as experienced in a Poly-Picosatellite Orbital Deployer. A 1U satellite structure was simulated which had the ADS mounted on it. The configuration of the ADS with respect to the satellite is that it is mounted on the side that always faces away from the sun. Such a design helps to protect the ADS mounted on the outside from directly incident sun's radiation.

The loadings applied on the satellite are similar to those experienced by a satellite during a PSLV launch. Static structural, modal, harmonic vibrations and random vibrations simulations were carried out for ascertaining the design qualification. The results obtained from the simulations verified the design integrity during launch.

3.2.2 Antenna Simulations

Antenna simulations were carried out assuming satellite as a hollow metallic box. Simulations were performed for monopole as well as dipole antennas. Length and cross-section of the antenna were optimized on HFSS software to minimize S11 parameter. Gain, S11, radiation pattern, and Smith chart were obtained and analyzed.

Satellite is assumed as a hollow box made up of aluminum for simulations. For dipole antenna simulation, feed to the antenna was modeled as coaxial feed. Optimized length of one element of dipole came out to be 487 mm. The material used for antenna elements was beryllium copper having conductivity 10^7 S/m.

Similar simulations were done by using steel as material for antenna elements with a conductivity of 1.45×10^6 S/m. The optimized length was same as beryllium copper.

3.2.3 Bend Tests

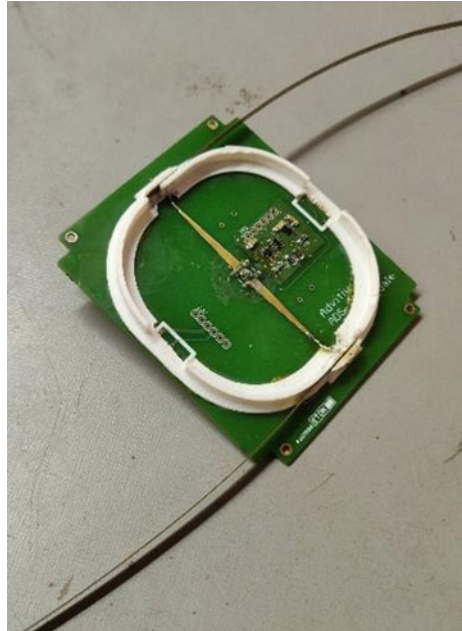
A bend test is a method for estimating yield properties of certain materials. Bend tests for ductility provide a simple way to evaluate the quality of materials by their ability to resist yielding or permanent deformation under one continuous bend. Bend tests were carried out to determine the best possible thickness and manufacturing process to fabricate the antenna.

The test was carried out for a duration of two weeks by storing antennas in the undeployed state. This was achieved by wrapping the antennas around a circular setup of 8 cm radius. The bend was defined as the angle between tangents at the two ends of the antenna after deployment.

3.3 Prototype

The sub-chassis was made of 3D printed PLA. PLA was chosen for sub-chassis for prototyping because of ease of 3D printing it and hence ensuring rapid prototyping of ADS with equivalent electrical characteristics. These characteristics were essential to carry out the preliminary tests for antenna characterization. The rest of the specifications for antenna, burner circuit and the impedance matching circuit were as mentioned in Sect. 2 (Fig. 1).

Fig. 1 Antenna deployment system prototype



4 Results

4.1 Structural Simulations

The random vibration simulations gave a maximum stress value of 6.32 MPa on the PCB which supports the antenna setup. The obtained stress levels are well below the yield stress of the material (FR-4) of PCB. The rest of the analysis gave stress levels much lower than this (Figs. 2, 3, 4 and 5).

4.2 Antenna Simulations

4.2.1 Structure Used in Simulation

See Fig. 6.

4.2.2 Results Obtained from Analysis

- (1) Material of antenna—Beryllium copper; radiation pattern, gain table and S11 (Figs. 7, 8 and 9; Table 1)

Fig. 2 Harmonic vibration stress levels

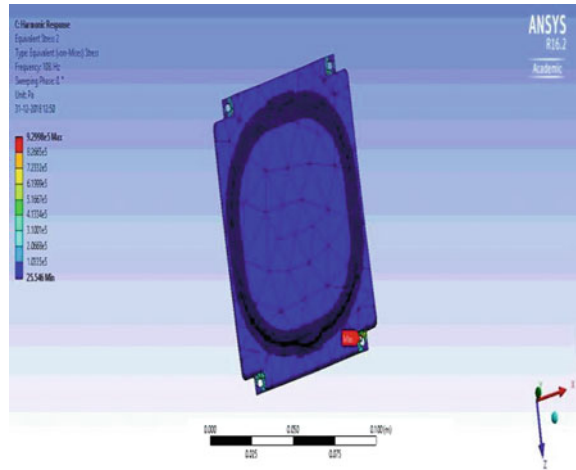
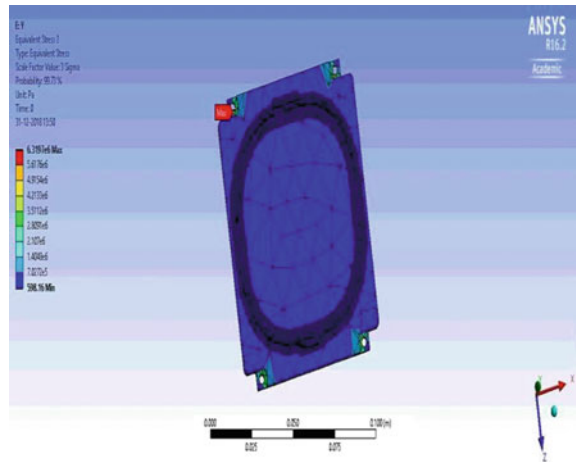


Fig. 3 Random vibration stress levels



- (2) Material of antenna—Steel; radiation pattern, gain table and S11 (Figs. 10, 11 and 12; Table 1).

4.3 Bend Tests

The bend tests were initiated at a bend angle of 0° . The results were obtained for samples of thicknesses 0.3 and 0.4 mm that were produced using shear cutting and wire EDM. The best results were obtained for a 0.4 mm thickness antenna and machined using wire EDM which gave a final bend of 35° .

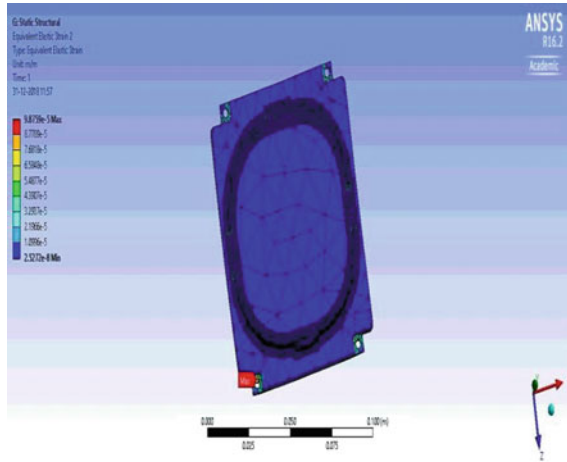


Fig. 4 Static analysis strain levels

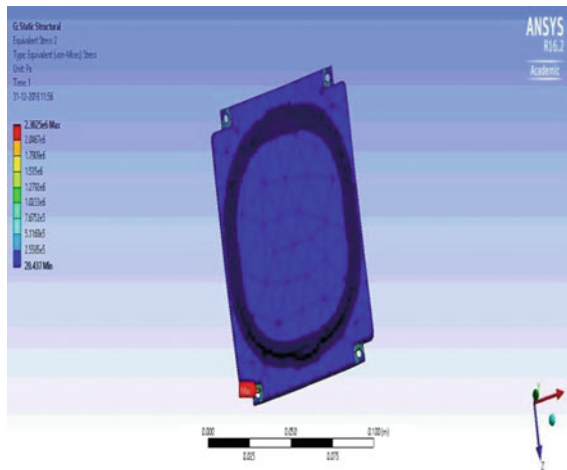


Fig. 5 Static analysis stress levels

5 Conclusions

- High modulus of resilience plays an important role in the mechanical design of antenna to ensure minimum residual bend after deployment.
- The minimum radius of curvature of the antenna around the sub-chassis also affects the permanent deformation in antenna after deployment. This was considered while designing the sub-chassis.

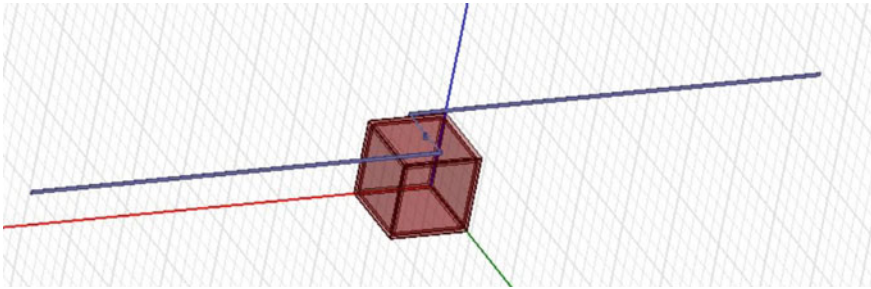


Fig. 6 Model used for antenna simulations on HFSS

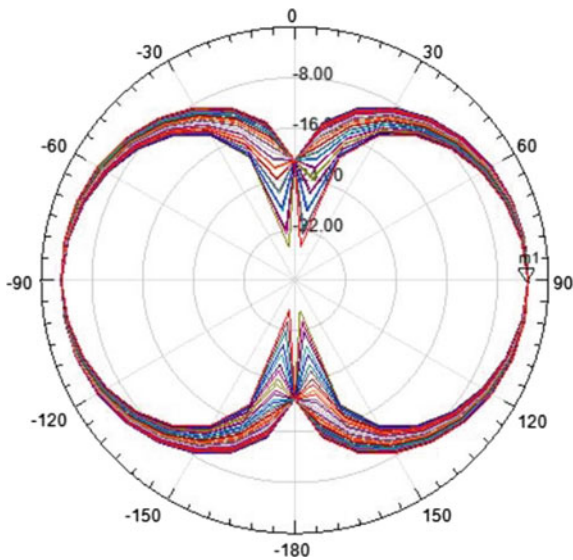


Fig. 7 Radiation pattern—Different lines are for different values of azimuthal angle

Name	Theta	Ang	Mag
m1	90.0000	90.0000	-3.0886

Fig. 8 Gain Table—Theta is polar angle. Ang is azimuthal angle

- The simulations on HFSS indicated that this choice of antenna did not worsen the performance by a large margin as compared to aluminum or copper because the gain saturates as the conductivity crosses a certain threshold as investigated in [2].
- Optimizations of length and thickness of antenna were carried out on HFSS software to minimize S11.

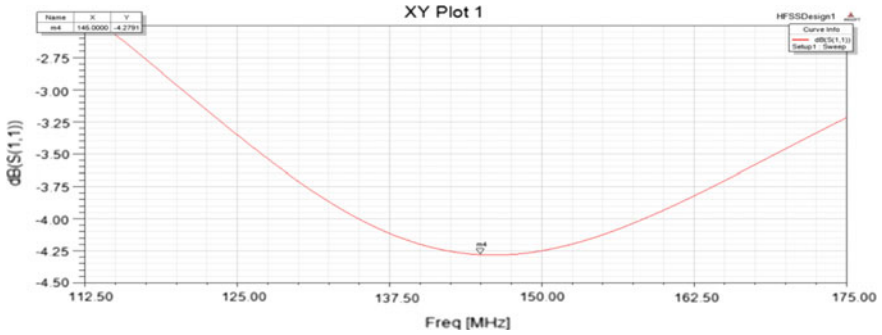


Fig. 9 S11 graph

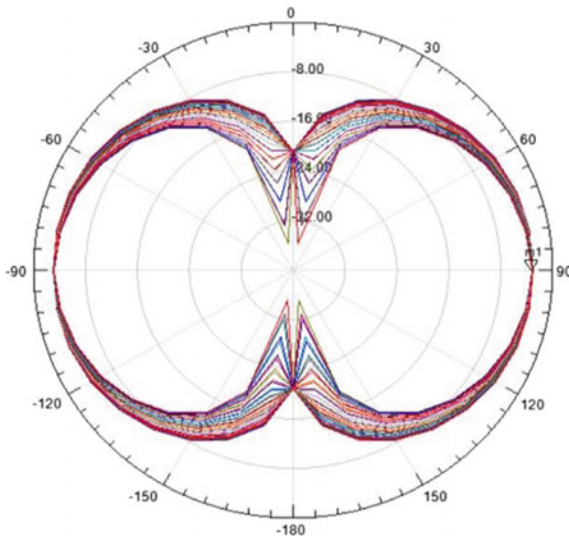


Fig. 10 Radiation pattern—Different lines are for different values of azimuthal angle

Name	Theta	Ang	Mag
m1	90.0000	90.0000	-2.9908

Fig. 11 Gain Table—Theta is polar angle. Ang is azimuthal angle

- The bend test results confirmed the best fabrication process. This is as predicted by theoretical concepts of heat input, mechanical distortions and residual stresses in manufacturing processes which alter material properties.
- The structural simulations indicated that the design of the PCB and antenna sub-chassis would be able to handle the launch loads.

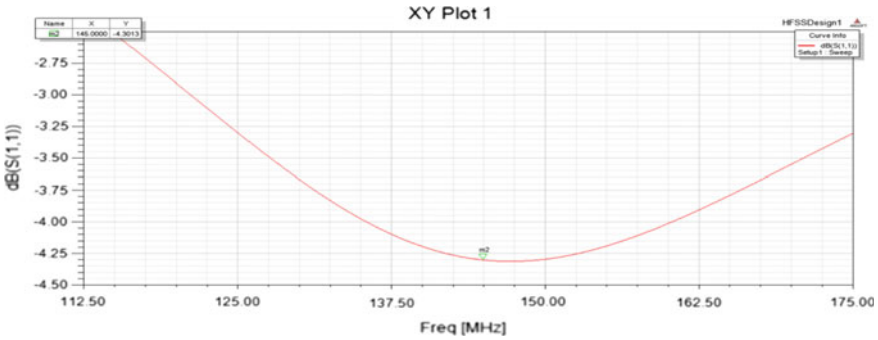


Fig. 12 S11 graph

Table 1 Results from antenna simulations

Antenna specifications	Length (cm)	Gain (dB)	S11 (dB)
Monopole, steel $\sigma = 1.45 \times 10^7$ S/m	64	-3.6	-4.75
Dipole, steel $\sigma = 1.45 \times 10^7$ S/m	48.7	-2.99	-4.3
Dipole, beryllium copper $\sigma = 1 \times 10^7$ S/m	48.7	-3.09	-4.27

- Dipole antenna has a higher gain as compared to monopole and satisfies mission requirements; hence, it was selected for the ADS design. The S11 would be taken care of by the impedance matching circuit on the board.
- The performance parameters for antenna comparison were determined as gain, residual bend and S11.

6 Future Tasks

Testing of the ADS setup needs to be carried out in vacuum to measure performance parameters of the antenna and correlate it with simulation results. Iterative improvements in impedance matching circuitry are required to ensure maximum power transfer. Additionally, testing of the ADS setup needs to be carried out in vacuum to simulate deployment in orbital conditions.

Acknowledgements We would thank the entire faculty involved in this project, especially Prof Varun Bhalerao and Prof Prabhu Ramachandran, our Faculty Advisers for giving us timely inputs and suggestions and also freedom and space for our design. We would like to thank Prof Salil Kulkarni for his guidance and suggestions for the satellite. We extend thanks to IRCC, IIT Bombay, for providing us funds needed for a project of this magnitude. We wish to thank the Aerospace Department, IIT Bombay, for providing us laboratory space. We would like to thank IIT Bombay as a whole for creating an environment conducive for growth and excellence. We would also like

to have this opportunity to thank Pratham and its team for the team culture they had setup and the learning they passed on to us along with the dream.

References

1. Madinabeitia G (2008) Antenna deployment system. Retrieved from <http://www.goldstem.org/Swiss%20Cube/10%20-%20Mechanisms/S3-C-STRU-1-1-Antenna%20Deployment%20System.pdf>. Accessed 20 June 2018
2. Shahpari M, Thiel David V (2015) The impact of reduced conductivity on the performance of wire antennas, *IEEE Trans Antennas Propag* 63(11)

Satellite Structure of Advitiiy (Second Student Satellite of IIT Bombay)



Hemil Kothari, Pushkar Lohiya, Abu Zubair and Shreeya Singh

Abstract The Student Satellite Team, IIT Bombay aims to develop India's lightest actively controlled satellite. Major concern for the team is to keep the mass as low as possible while making the satellite structurally capable to bear random vibration, static and harmonic loads. The work below presents an approach towards designing satellite structure by considering mass minimization while maintaining the structural integrity of the satellite in launch and in-orbit environment.

Keywords Cubesat · PCB rods · Configuration layout · Mass budget

1 Introduction

After the successful launch of Pratham (First Student Satellite of IIT Bombay) [1], the Student Satellite Team, IIT Bombay is now aiming for developing India's lightest actively controlled satellite with mass less than 1 kg. This paper highlights the approach towards designing Advitiiy while accommodating major constraints of mass and size. The mass has to be kept as low as possible due to the mission statement. The satellite structure should bear Polar Satellite Launch Vehicle (PSLV) launch loads and protects its components from orbit environment. The team first developed a conceptual design on the basis of initial requirements of component placement and did further iterations to improve the design. Each iteration was analysed on the basis of manufacturing feasibility, mass and structural capability.

H. Kothari (✉) · P. Lohiya · A. Zubair · S. Singh
Student Satellite Lab, Aerospace Department, IIT Bombay, Mumbai, Maharashtra 400076, India
e-mail: hemilkothari@iitb.ac.in
URL: <https://www.aero.iitb.ac.in/satlab/>

© Springer Nature Singapore Pte Ltd. 2020
PSR. S. Sastry et al. (eds.), *Advances in Small Satellite Technologies*,
Lecture Notes in Mechanical Engineering,
https://doi.org/10.1007/978-981-15-1724-2_49

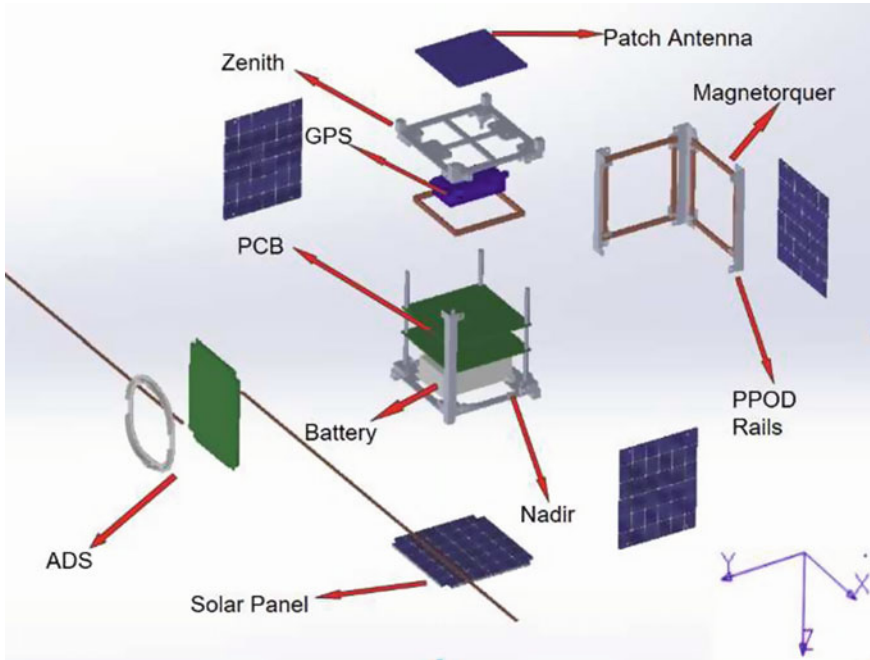


Fig. 1 Configuration layout of advitiy

2 General Specifications

Satellite structure, with dimensions $11.35 \times 10 \times 10 \text{ cm}^3$, was designed for 1U configuration and ISIS PPOD [2] compatibility is ensured. The configuration and list of components which can be accommodated in the satellite are shown in Fig. 1. It can withstand PSLV launch loads and has a mass of less than 900 g. Structure materials are chosen as Al6061-T6.

We are not using magnetorquers' frame as it will increase mass instead magnetorquers coils are mounted on the frame (PPOD rails Fig. 1) with the help of stubs and adhesives. PCBs are stacked over each other using standoff screws (Fig. 1).

3 Configuration Layout

The satellite structure is modelled in the SolidWorks software and the axes are defined in accordance with the convention followed by the controls subsystem (Tables 1, 2).

Table 1 Axes in the body frame

X-axis	Lagging to leading
Y-axis	Sunside to anti-sunside
Z-axis	Zenith to nadir

Table 2 Components to be incorporated into the satellite

Component name	Quantity
Antenna deployment system	1
GPS Antenna (patch antenna)	1
GPS receiver	1
PCB	2
Battery	1
Magnetorquer	3
Solar panel	4

The satellite is broken down into two parts for the placement of components:

1. Stacked components
2. Side-mounted components

The stack consists of the PCBs, while the side mounts of the various sides house the other components.

Stacked PCBs

The PCBs belonging to the communications and electrical subsystems are placed in a stacked form within the satellite with the help of four vertical PCB rods each of which is an assembly of three standoff screws.

Zenith-mounted components

GPS antenna, GPS receiver module and a magnetorquer are the components placed near zenith face.

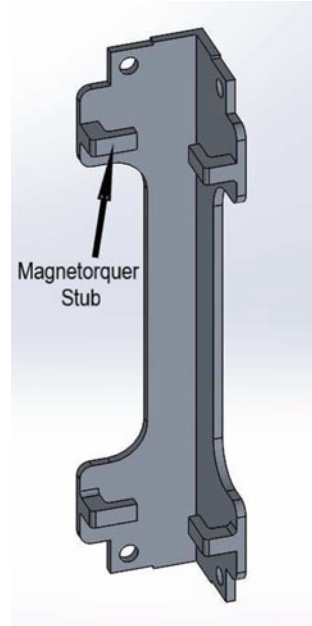
Nadir-mounted components

Battery pack and a solar panel are the components near the Nadir face.

Remaining four sides are frameless with 4 PPOD rails acting as vertical edges for them. PPOD rails (as shown in Fig. 2) are vertical support of structure and they are in contact with PPOD before deployment. The dimensions of PPOD rails have been decided appropriately so as to make the satellite PPOD compatible.

Sunside- and Leading-mounted components

A magnetorquer and a solar panel are the components mounted close to each of these two faces. Magnetorquers are mounted with the help of “Stubs” present on PPOD rails.

Fig. 2 PPOD rails**Anti-sunside-mounted components**

Antenna deployment system is mounted on the outside.

Lagging-mounted components

Lagging side only has a solar panel mounted on the outside.

4 Mass Budget

The complete satellite has a mass of 893 g. Mass of major components is shown in Table 3. Advitiy aims to be India's lightest actively controlled satellite, hence developing a satellite with mass less than 980 g. Developing a structure with minimum possible mass and yet high strengths are essential. This can be realized if all the critical components such as structure, battery, PCBs required for basic control and regulation of the satellite can be fit into a mass of 500–600 g. With some modifications to the basic structure, the mass would be in the ballpark range of 980 g.

Table 3 Mass budget

Components	Quantity	Mass (g)
Antenna deployment system	1	60
PCB	2	130
Battery box + battery pack	1	120
Magnetorquers	3	96 (3 × 32)
GPS receiver + antenna	1	80
Solar panel	4	200 (4 × 50)
Satellite frame	NA	127
Integration	NA	80

5 Salient Features of Satellite Structure

Entire satellite is PPOD compatible. Antenna deployment system modelled on anti-sunside includes PCB, dipole antenna that will deploy along the X-axis and a sub-chassis with space constraints taken care of. PCBs are stacked on a PCB rod consisting of three stand off screws for easier integration. Magnetorquers are mounted on stubs located on PPOD rails for better manufacturability. This arrangement of magnetorquer has lower mass than the case when separate frames were being used.

6 Material Assignment

Table 4 shows the material assigned to a particular component. The material of the satellite plays a critical role along with the geometry to help to maintain the structural integrity during launch. The material must also be light enough to keep the mass under specification levels. The antenna guide rail has to be nonconducting and light weight so a light, structurally capable material was required. Vespel SP-3 was decided for antenna guide rails. Currently, the battery box material is chosen as Al6061-T6. We

Table 4 Materials

Components	Material
Antenna	Beryllium copper
PCB	FR04
Antenna sub-chassis	Vespel SP-3
Solar panels	Al6061-T6
Frame	Al6061-T6
Battery box	Al6061-T6
Magnetorquers	Copper

can shift to a light material if temperature distribution over the satellite permits. The solar panels are assumed to be of Al6061-T6 and their density is calculated using their mass and volume.

7 Simulation and Set-up

Simulation of satellite was done by placing it in a PPOD and applying PSLV boundary conditions on the PPOD. Simulations and modelling were done in ANSYS and SolidWorks, respectively. Satellite model was simulated for random vibration, static and harmonic loading.

Boundary Conditions—Satellite is simulated inside PPOD under launch loads. The base of PPOD is attached to the launch vehicle so it is defined as fixed support for launch loads simulation (Fig. 3).

Modelling

- Electrical, communication and ADS PCBs are modelled as uniformly distributed mass by averaging the density over the volume (taking mass and dividing it by total volume).
- The antenna is not modelled explicitly in simulation but its mass is accounted in the PCB of ADS.
- Exact dimensions and model of the patch antenna is not known, so to take account of its mass, it is modelled as a plate and its mass is taken from standard patch antennas.
- PCBs and battery mass are scaled down from Pratham (1st Student Satellite of IIT Bombay).
- Magnetorquers are not modelled as the bundle of separate wires, it is assumed as the bulk of copper (modelled as isotropic in nature).
- Epoxy which is used for fabricating magnetorquers is not modelled in simulations.

Fig. 3 Fixed support

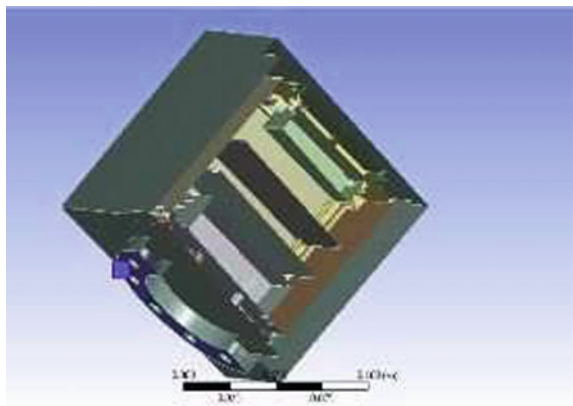
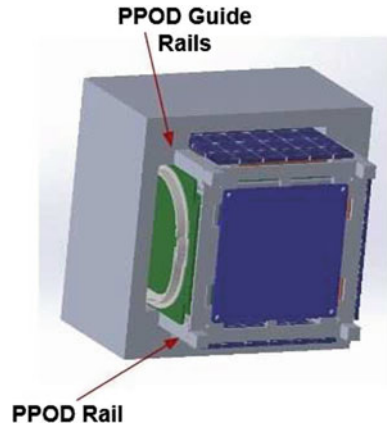


Fig. 4 Rough contact



- **Contacts**
 - Bonded contacts are modelled to simulate adhesives used between two surfaces and are defined between the battery pack and battery box, and between guide rails and PCB.
 - Rough contacts are modelled at the contact between the PPOD rails and PPOD guide rails as shown in Fig. 4. Rough contact has infinite friction coefficient and separation between PPOD and satellite takes place when the normal force is zero.
- **Joints**
 - Fixed rigid joints have been used to model screws. Concentric surfaces were interfaced with the joint to simulate the bond.
 - Fixed joints—All degrees of freedom are constrained.

8 Results

- First modal frequency of 281.42 Hz was on PCB which is well within range, i.e. frequency should be greater than 90 Hz (according to ISRO guidelines). Mass participation was extracted for first 300 modal frequencies (Table 5).

Table 5 Mass participation

Axis	Mass participation (%)
X-axis	77.78
Y-axis	79.67
Z-axis	86.4

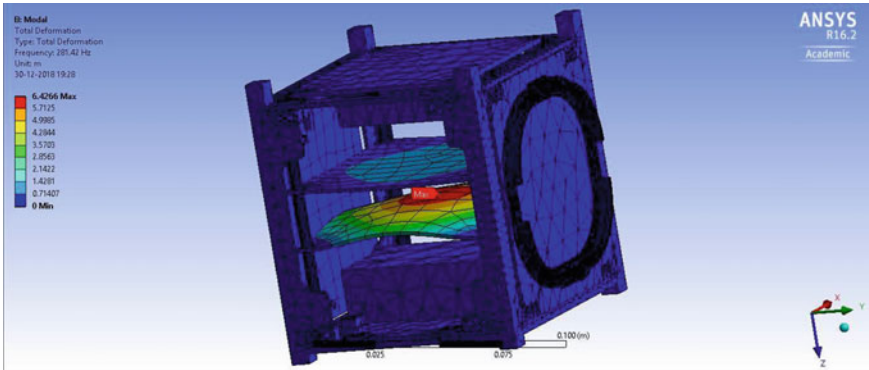


Fig. 5 Modal simulation

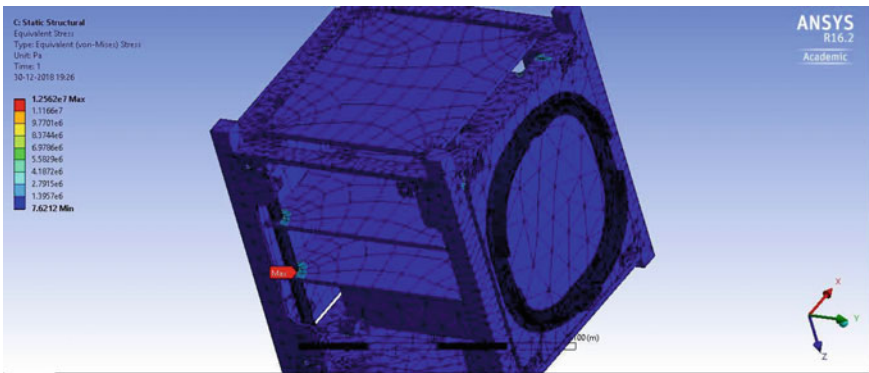


Fig. 6 Static structural simulation

- All the maximum stresses are well within limits with sufficient factor of safety (Figs. 5, 6, 7 and Table 6).
- From the above results, we can infer that the obtained values are well within the operational limits. The most critical component in our satellite structure is the PCB rod and the PCB. Therefore, for these parts, mesh refinement was done and more accurate results were obtained.

9 Future Work

- Screws have to be sub-modelled to find stress distribution on screws and it will help in deciding the dimensions of the screws to be used.

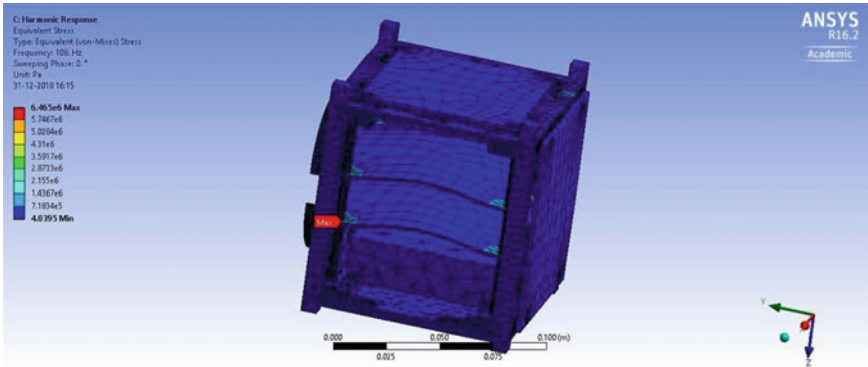


Fig. 7 Harmonic simulation

Table 6 Simulation results

	First modal frequency (Hz)	Stress (MPa)	Random vibration (max stress-MPa) with 99.73% confidence	Harmonic (max stress-MPa)
Results	281.42	12.562	30.335	6.465
Operational limits	90 (min)	275	275	275
Factor of safety	3.13	21.9	9.066	43.51
Component	PCB	PCB rod	PCB rod	PCB rod

- We need to gain more clarity on the meshing method for finite element simulations’ of the satellite model as it would help to improve the accuracy of the results and also lower the computational time involved in the simulations.

Acknowledgements We would first like to extend a special thanks to ISRO small satellite group director Dr. S.A. Kannan for guiding us and a big thanks to the whole ISRO team for inspiring young minds to venture into the domain of space science and engineering. We would thank the entire faculty involved in this project, especially Prof Varun Bhalerao and Prof Prabhu Ramachandran, our Faculty Advisers for giving us timely inputs and suggestions as also freedom and space for our design. We would like to thank Prof Salil Kulkarni for his guidance and suggestions for the satellite. We extend thanks to IRCC, IIT Bombay for providing us funds needed for a project of this magnitude. We thank Prof Hemendra Arya for his course on System Engineering which has helped us in organizing the project well. We wish to thank the Aerospace Department, IIT Bombay for providing us laboratory space. We would like to thank IIT Bombay as a whole for creating an environment conducive for growth and excellence. We would also like to have this opportunity to thank Pratham and its team for the team culture they had set-up and the learning they passed on to us along with the dream. Finally, we would like to thank the families of our team members who support us.

References

1. Pratham. <https://www.aero.iitb.ac.in/satlab/pratham>
2. ISIS PPOD. https://www.isispace.nl/brochures/ISIS_ISIPOD_Brochure_v.7.11.pdf

Retraction Note to: Usage of COTS/EEE Parts in Space Applications—An Overview



H. V. Harish

Retraction Note to:
Chapter “Usage of COTS/EEE Parts in Space Applications—An Overview” in: PSR. S. Sastry et al. (eds.), *Advances in Small Satellite Technologies, Lecture Notes in Mechanical Engineering*, https://doi.org/10.1007/978-981-15-1724-2_33

The Editors have retracted this book chapter “Usage of COTS/EEE Parts in Space Applications—An Overview” because it contains material that substantially overlaps with content from a blog post by a different author [1].

All authors agree to this retraction.

[1] Dan Friedlander (2016, November 4th) COTS/EEE parts in space applications: evolution overview, revolution forward view. Intelligent Aerospace. <https://www.intelligent aerospace.com/satcom/article/16538751/cotsee-parts-in-space-applications-evolutionoverview-revolution-forward-view>.

The retracted version of this chapter can be found at https://doi.org/10.1007/978-981-15-1724-2_33

© Springer Nature Singapore Pte Ltd. 2021
PSR. S. Sastry et al. (eds.), *Advances in Small Satellite Technologies*,
Lecture Notes in Mechanical Engineering,
https://doi.org/10.1007/978-981-15-1724-2_50

C1